

**1-D, 2-D, 3-D Hybrid Based on Carbon Nitride and Metal
or Metal Oxide Nanostructures: Materials for
Environmental and Electrochemical Energy Applications**

By

**Manas Kumar Kundu
CHEM11201204004**

**National Institute of Science Education and Research Bhubaneswar, Odisha –
752050**

*A thesis submitted to the
Board of Studies in Chemical Sciences
In partial fulfillment of requirements
for the Degree of*

DOCTOR OF PHILOSOPHY

of

HOMI BHABHA NATIONAL INSTITUTE

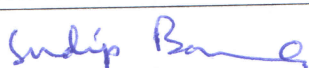
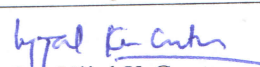
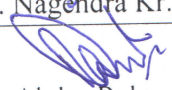


July, 2019

Homi Bhabha National Institute

Recommendations of the Viva Voce Committee

As members of the Viva Voce Committee, we certify that we have read the dissertation prepared by **Manas Kumar Kundu** entitled "**1-D, 2-D, 3-D Hybrid based on Carbon Nitride and Metal or Metal Oxide Nanostructures: Materials for Environmental and Electrochemical Energy Applications**" and recommend that it may be accepted as fulfilling the thesis requirement for the award of Degree of Doctor of Philosophy.

Chairman -		Date: 12.07.19
	Prof. A. Srinivasan	
Guide / Convener -		Date: 12/07/19
	Dr. Sudip Barman	
Examiner -		Date: 12/7/19
	Dr. Ujjal K Gautam	
Member 1 -		Date: 12-7-19
	Dr. Prasenjit Mal	
Member 2-		Date: 12-07-19
	Dr. Nagendra Kr. Sharma	
Member 3 -		Date: 12-07-19
	Dr. Abdur Rahaman	

Final approval and acceptance of this thesis is contingent upon the candidate's submission of the final copies of the thesis to HBNI.

I/We hereby certify that I/we have read this thesis prepared under my/our direction and recommend that it may be accepted as fulfilling the thesis requirement.

Date: 12.07.2019

Place: Bhubaneswar


(Dr. Sudip Barman)
Guide

STATEMENT BY AUTHOR

This dissertation has been submitted in partial fulfillment of requirements for an advanced degree at Homi Bhabha National Institute (HBNI) and is deposited in the Library to be made available to borrowers under rules of the HBNI.

Brief quotations from this dissertation are allowable without special permission, provided that accurate acknowledgement of source is made. Requests for permission for extended quotation from or reproduction of this manuscript in whole or in part may be granted by the Competent Authority of HBNI when in his or her judgment the proposed use of the material is in the interests of scholarship. In all other instances, however, permission must be obtained from the author.

Manas Kr. Kundu
12/07/2019

Manas Kumar Kundu

DECLARATION

I, hereby declare that the investigation presented in the thesis has been carried out by me. The work is original and has not been submitted earlier as a whole or in part for a degree / diploma at this or any other Institution / University.

Manas Kr. Kundu
12/07/2019

Manas Kumar Kundu

List of Publications arising from the thesis

Journal Published

1. **Kundu, M. K.**; Bhowmik, T.; Mishra, R.; Barman, S. *ChemSusChem*, **2018**, 11, 2388-2401.
2. **Kundu, M. K.[†]**; Sadhukhan, M.[†]; Barman, S. *J. Mater. Chem. B* **2015**, 3, 1289-1300. († equal contribution)
3. **Kundu, M. K.**; Bhowmik, T.; Barman, S. *J. Mater. Chem. A* **2015**, 3, 23120-23135.
4. Bhowmik, T.[†]; **Kundu, M. K.[†]**; Barman, S. *RSC Adv.* **2015**, 5, 38760-38773.(† equal contribution)

Communicated

1. **Kundu, M. K.**; Mishra, R.; Bhowmik, T.; Barman, S., Three-dimensional Hierarchically Porous Iridium oxide-Nitrogen doped Carbon Hybrid: An Efficient Bifunctional Catalyst for Oxygen Evolution and Hydrogen Evolution Reaction in Acid (Manuscript under revision).

Under Preparation

1. **Kundu, M. K.**; Barman, S. Silver Nanostructures: an Extraordinary Active Catalyst for Hydrogen Evolution reaction and Oxygen Reduction Reaction.

Journals not included in thesis

1. **Kundu, M. K.[†]**; Mishra, R.[†]; Bhowmik, T.; Barman, S. *J. Mater. Chem. A*, **2018**, 6, 23531-23541

2. Sadhukhan, M.; Bhowmik, T.; **Kundu, M. K.**; Barman, S., *RSC Adv.* **2014**, *4*, 4998-5005.
3. Bhowmik, T.; **Kundu, M. K.**; Barman, S. *ACS Catal.* **2016**, *6*, 1929-1941.
4. Bhowmik, T.; **Kundu, M. K.**; Barman, S. *Int. J. Hydrogen Energy* **2016**, *41*, 14768-14777.
5. Bhowmik, T.; **Kundu, M. K.**; Barman, S. *ACS Appl. Mater. Interfaces* **2016**, *8*, 28678-28688.
6. Bhowmik, T.; **Kundu, M. K.**; Barman, S. *Int. J. Hydrogen Energy* **2017**, *42*, 212-217.
7. Bhowmik, T.; **Kundu, M. K.**; Barman, S. *ACS Appl. Energy Mater.* **2018**, *1*, 1200-1209.
8. Sadhukhan, M.; **Kundu, M. K.**; Bhowmik, T.; Barman, S. *Int. J. Hydrogen Energy* **2017**, *42*, 9371- 9383.

Conferences and Presentation

1. **Poster Presentation:** Bengaluru India Nano, held on 7-8 December, 2017 in Bengaluru.
2. **Poster Presentation:** Inter IISER & NISER Chemistry Meet (IINCM), held on 22-24 December, 2017 at NISER, Bhubaneswar.
3. Indo-French symposium, held at NISER, Bhubaneswar, February 2014.
4. Workshop, jointly organized by Electron Microscope Society of India (EMSI) and NISER, held on 16-17th July, 2018 at NISER, Bhubaneswar.
5. ACS on Campus Meet held on 23 July at NISER, Bhubaneswar.

Manas K. Kundu
12/07/2019

Manas Kumar Kundu

*Dedicated
To*

My Parents & Brother

ACKNOWLEDGEMENTS

None of this work would have been possible without generous help and support of kind people around me. Firstly, I would like to express my sincere gratitude to my thesis supervisor Dr. Sudip Barman for his valuable guidance, outstanding motivation, especially for allowing me independently free exploration and giving me generous support throughout my Ph.D. study and research.

For the financial support during my Ph.D. I thank to Department of Atomic Energy (DAE), India. I gratefully acknowledge the Homi Bhaba National Institute (HBNI), India for academic registration and National Institute of Science Education and Research (NISER), Bhubaneswar, India for research Infrastructure. I would like to recognize my doctoral committee members Prof. Alagar Srinivasan, Dr. Prasenjit Mal, Dr. Nagendra Kr. Sharma and Dr. Abdur Rahaman and all other faculty members in SCS for their support and useful suggestions.

I warmly thank to my lab mates, Dr. Mriganka Sadhukhan, Dr. Tanmay Bhowmik, Sarat Kanrar, Ranjit Mishra, Dr. Susanta Kr. Bera, Amit, Amal and Subham. It has been a pleasure to work and sharing lab with you. Their cheerful accompany have provided friendly environment inside and outside laboratory, make this journey smooth.

I thank all of my NISER friends, especially Dr. Basujit chatterjee, Dr. Saikat Maity, Dr. Tapas Achar, Dr. Milan Barman, Dr. Sourav Palchowdhury, Dr. Arindam Ghosh and Dr. Somnath Koley, Subhayan Chakraborty, Khokan Chowdhuri for the memorable moments. I would also like to thank my friends from outside NISER, Dr. Amit Kumar Mondal, Dr. Sisir Maity, Dr. Ajay Jana, Debnath Chatterjee for their support and encouragement.

Finally, I would like to thank my family members who witnessed every step of the way and provided me support and confidence in all aspects to let me accomplish my dream of Ph.D. I

wish to express my sincere gratitude to Mr. Naba Kumar Kundu & Mrs. Depali Kundu (parents), Mr. Tapas Kr. Kundu (brother), Mrs. Adrija Mandal (sister-in-law), Mr. Rituraj Kundu, Mr. Bimal Pal, Mr. Amal Pal, Dr. Shyamal Kanti Pal and Mrs. Tumpa Pal for their patience, encouragement and providing me the happiest moments. Thanks to all for your unconditional love.

Manas Kr. Kundu
12/07/2019

...Manas Kumar Kundu

CONTENTS

Title	Page No
Summary	xiv
List of figures	xvi
List of tables	xxxiii
List of schemes	xxxv
Chapter 1	Nanocomposite for Environmental and Electrochemical Energy Conversion Applications
1.1	Abstract 36
1.2	Introduction 37
1.3	Fuel cells 42
1.4	Various Reactions Involved in RFCs 45
1.5	Electrolyser 54
1.6	Theoretical Aspect of Electrochemical Reaction 58
1.7	Kinetics of Electrochemical Reaction 60
1.8	Glucose and H ₂ O ₂ sensing 65
1.9	Removal of Dye 69
1.10	Nanoparticle: An Overview and Preparation 71
1.11	Synthesis Procedures of Metal Nanoparticles in Liquid Phases 77
1.12	Aims of the Present Thesis 80
1.13	Scopes and Challenges of the Present Thesis 81
1.14	References 81

Chapter 2	General Experimental Methods and Techniques	
2.1	Introduction	89
2.2	Materials	89
2.3	Instruments and instrumental techniques	90
2.4	References	106
Chapter 3	Gold Aerogel Supported on Graphitic Carbon Nitride: Synthesis, Characterisation and Applications in Oxygen Reduction Reaction and Hydrogen Evolution Reaction	
3.1	Abstract	108
3.2	Introduction	109
3.3	Experimental section	113
3.4	Results and discussions	115
3.4.1	Characterization of Au aerogel composites	115
3.4.2	Electrochemical Characterization	125
3.4.3	ORR studies on Au –aerogel-CN _x catalysts in alkaline medium	128
3.4.4	ORR studies on Au-aerogel-CN _x catalysts in acidic medium	136
3.4.5	HER studies on Au-aerogel-CN _x catalyst in acidic medium	142
3.5	Conclusion	147
3.6	References	148
Chapter 4	One dimensional Pt Nanostructures/Carbon Nitride hybrid: Synthesis and its Applications as Highly Efficient Catalyst in Hydrogen Evolution/Oxidation Reactions at Different pH Values	
4.1	Abstract	158
4.2	Introduction	159

4.3	Experimental section	163
4.4	Results and discussions	165
4.4.1	Characterization of Pt-(PtO _x)-NSs/C composite	165
4.4.2	HER Activity of Pt-(PtO _x)-NSs/C in Acid and Alkaline medium	171
4.4.3	HOR Study on Pt-(PtO _x)-NSs/C Surfaces over a Broad pH Range	179
4.4.4	Factors responsible for the high catalytic activity	190
4.5	Conclusions	191
4.6	References	192

Chapter 5 Three-dimensional Hierarchically Porous Iridium Oxide- Carbon Nitride Hybrid: Synthesis and their Applications in Overall Water Splitting

5.1	Abstract	207
5.2	Introduction	208
5.3	Experimental section	210
5.4	Results and discussions	211
5.4.1	Characterization of 3D-IrO ₂ /N@C composite	211
5.4.2	Oxygen Evolution Reaction (OER) Activity of 3D-IrO ₂ /N@C hybrid in acidic medium	217
5.4.3	Hydrogen Evolution Reaction (HER) by 3D-IrO ₂ /N@C hybrid in acidic medium	224
5.4.4	Factors responsible for the high catalytic activity of 3D-IrO ₂ /N@C	229
5.5	Conclusion	231
5.6	References	232

**Chapter 6 Interconnected 1-D Silver Nanowires Supported on Carbon Nitride:
A Stable and Highly Efficient Electrocatalyst for Hydrogen Evolution
Reaction and Oxygen Reduction Reaction**

6.1	Abstract	239
6.2	Introduction	240
6.3	Experimental section	243
6.4	Results and discussions	244
6.4.1	Characterization of AgNWs-CN _x composite	244
6.4.2	Electrochemical HER process in acidic medium	249
6.4.3	HER activity of ac-AgNWs-CN _x catalyst in Basic Medium	254
6.4.4	ORR studies on ac AgNWs catalysts in alkaline medium	255
6.4.5	ORR studies on ac AgNWs catalysts in acidic medium	260
6.4.6	Factors responsible for high catalytic activity	261
6.5	Conclusion	264
6.6	References	264

**Chapter 7 Two Dimensional Assembly of Silver Nanoparticles on Carbon
Nitride Sheets and their Applications in Non-enzymatic Sensing of
Hydrogen Peroxide and Glucose**

7.1	Abstract	271
7.2	Introduction	272
7.3	Experimental section	275
7.4	Results and discussions	276
7.4.1	Growth and Assembly AgNPs on Carbon Nitride sheets	280
7.4.2	Electrochemical Applications	285
7.5	Conclusion	294
7.6	References	295

Chapter 8	Ultra Small Gold Nanoparticles on 2 Dimensional Graphitic Carbon Nitride: An Efficient Catalyst for Ultrafast Reduction of 4-nitrophenol and Removal of Organic Dyes from Water	
8.1	Abstract	302
8.2	Introduction	303
8.3	Experimental section	308
8.4	Results and discussions	310
8.4.1	Catalytic reduction of 4-Nitrophenol	315
8.4.2	Adsorption of organic dyes	317
8.4.3	Desorption of adsorbed dyes	322
8.4.4	Photocatalytic degradation of organic dyes	324
8.5	Conclusion	335
8.6	References	336
Chapter 9	Summary of the Thesis	344

Summary

The rapid rise of energy demand and the depletion of fossil fuels are the driving force for exploring the renewable energy sources. Among several renewable energy techniques, water electrolyzers (WEs) and fuel cells (FCs) are the two important method for energy storage and conversion. The regenerative fuel cell consist of four different reactions, such as hydrogen oxidation reaction (HOR), oxygen reduction reaction (ORR) in FCs stack and hydrogen evolution reaction (HER), oxygen evolution reaction (OER) in WEs stack. The most active catalyst for HER, ORR and HOR is commercial Pt/C whereas IrO₂ is the best catalyst for OER. However, their electrocatalytic stability, abundance and energy efficiency is significantly low and that restricted the practical application of FCs and WEs devices. We have synthesized various dimensions metal/metal oxide nanostructures and their activity towards HER, HOR, ORR, OER was explored.

Au-aerogel supported on CN_x catalyst exhibited superior catalytic activity towards HER and ORR. The Au-aerogel-CN_x composite shows ORR onset potentials at 0.92 V and 0.43 V (vs RHE) in 0.5 M KOH and H₂SO₄ solution. The activity of Au-composites is morphology dependent and ORR and HER performances on porous Au-aerogel-CN_x composites is better than that of AuNPs-CN_x catalyst and commercial flat gold electrode.

The HER activity of Pt-(PtO_x)-NSs/C catalyst is 4 and 6.5 times better than commercial Pt/C in acid and base. The HER/HOR activity of Pt-(PtO₂)-NSs/C and PtO_x-free PtNSs/C catalysts are comparable in acid. The presence of PtO_x in Pt-(PtO_x)-NSs/C makes this Pt-catalyst 5 fold higher HER/HOR active in base media than that of PtO_x free PtNSs/C catalyst al. We have demonstrated hydrogen binding energy and oxophilicity are the two equivalent descriptors for HER/HOR in basic media. Here we propose a bi-functional mechanism for the enhanced alkaline HER/HOR activity of Pt-(PtO_x)-NSs/C catalyst.

In 0.5 M HClO₄, 3D-IrO₂ supported on N@C exhibited superior activity towards OER with a low overpotential of 280 mV at 10 mA/cm², a low Tafel slope of 45 mV/dec and ~98% faradic efficiency. The mass activity and turnover frequency (TOF) at an overpotential are also 32 times higher than that of commercial IrO₂. The HER performance of this 3D-IrO₂/N@C is comparable to that of commercial Pt/C catalyst in acid. This 3D-IrO₂/N@C catalyst was also applied as cathode and anode for over-all water splitting.

AgNWs supported on CN_x showed superior activity towards HER in acid and base with onset potential of 0 mV in both the medium. It requires over-potentials of 25 mV and 85 mV to achieve the current densities of 10 and 50 mA/cm² respectively in acid whereas 110 mV and 290 mV needed to attain the same current densities in base. Furthermore, this AgNWs-CN_x catalyst showed superior activity towards ORR and comparable to that of Pt/C in base. This catalyst also showed excellent methanol tolerance and superior durability in ORR.

The development of rapid and reliable methods for highly sensitive, selective glucose and H₂O₂ detection is necessary in many fields such as clinical diagnostics, food industry, sustainable fuel cell, environmental analysis. The 2-D hybrids of Ag nanoparticles and carbon nitride were applied for sensitive sensing of glucose and H₂O₂ in aqueous media. The lowest detection limits achieved by this Ag-CN_x electrode for H₂O₂ and glucose were 0.6 nM and 0.6 μM respectively.

Released contaminants from industries create havoc pollution. Among these toxic threats, dyes are more concerned to us because of their high chemical and biological stability which makes difficult to remove from water. Ultra-small AuNPs supported on CN_x was found to be very effective for removal of various organic dyes through absorption and photocatalysis. Excellent photo degradation rate constants for RhB (0.024 min⁻¹), MB (0.024 min⁻¹) and MR (0.02 min⁻¹) were observed although high concentration of dyes were used for degradation.

LIST OF FIGURES

Sl. No.	Figure Caption	Page No.
1	Figure 1.1 (a) Percentage Energy consumption from different Sources. (b) Predicted energy consumption through years.	38
2	Figure 1.2 Schematic diagram of non-combustive fuel cell.	42
3	Figure 1.3 A schematic representation of the Fuel cell Stack.	43
4	Figure 1.4 Schematic diagram of a RFCs showing the two main components: Fuel cell and electrolyzers.	44
5	Figure 1.5 Various electrochemical processes with polarisation curves.	46
6	Figure 1.6 Schematic representation of Proton Exchange Membrane Fuel cell (PEMFCs).	48
7	Figure 1.7 (a-b) Possible reaction mechanism of HOR in alkaline condition with effect of OH ⁻ ion in electrolyte and (c-d) effect of adsorbed OH _{ad} on the surface of catalyst.	50
8	Figure 1.8 Schematic diagram of water electrolyser.	55
9	Figure 1.9 Volcano plot for (a) over-all electrochemical processes, (b) HOR, (c) HER and (d) ORR (e) OER	60
10	Figure 1.10 (a) Butler-Volmer plot, (b) Tafel Plot for electrochemical reaction.	64
11	Figure 1.11 Schematic representation of enzymatic glucose oxidation mechanism for first, second and third generation biosensors.	67
12	Figure 1.12 A schematic representation of (a) adsorption theory with adjacent adsorption site of nanostructured electrode and (b) IHOAM model.	68
13	Figure 1.13 Schematic representation of mechanism of Dye degradation.	70
14	Figure 1.14 Examples of different supporting materials used to stabilise nanoparticles.	75

15	Figure 1.15	Proposed structures of g-C ₃ N ₄ with (a) heptazine building block, (b) s-triazine building block.	76
16	Figure 2.1	Schematic illustration of (a) an X-ray scattering and (b) alignment of X-ray source and detector.	91
17	Figure 2.2	Schematic diagram of FE-SEM.	93
18	Figure 2.3	Schematic representation of working principle of XPS.	95
19	Figure 2.4	Photograph of conventional three electrode setup of Autolab instrument.	99
20	Figure 2.5	Voltage vs time profile of (a) cyclic voltammetry and (b) linear sweep voltammetry.	100
21	Figure 3.1	p-XRD of g-CN _x , AuNPs-CN _x and Au-aerogel-CN _x composite.	115
22	Figure 3.2	TEM images of (a) g-CN _x sheet (b) AuNPs on CN _x (AuNPs-CN _x composite) showing highly dispersed ultra-small AuNPs on the CN _x sheets (c, f) Low resolution TEM images of Au-aerogel supported on CN _x showing porous morphology. (d, e) Mid resolution TEM images of Au-aerogel showing interconnected Au nanochains and CN _x support.	117
23	Figure 3.3	(a) SAED images of Au-aerogel-CN _x (b) HRTEM images of Au-aerogel-CN _x showing preferential growth along Au (111) plane.	118
24	Figure 3.4	FESEM images of Au-aerogel-CN _x shows highly porous morphologies of interconnected nanoparticles.	118
25	Figure 3.5	(a) TEM images of AuNPs-CN _x formed from ultrasound treatment of HAuCl ₄ with CN _x (inset: particle size distribution graph, particle size are in the range of 1 nm - 2.5 nm). (b, c) TEM images of Au-CN _x composite (formed from ultrasonic treatment on 0.162 mmol of HAuCl ₄ and 0.10 mmol of NaBH ₄) showing highly dispersed AuNPs of less than 1 nm on CN _x sheet in Figure 3.5b and few nano chains on S1c. (d, e) TEM images of Au-aerogel-CN _x formed when 0.162 mmol HAuCl ₄ and 0.53 mmol NaBH ₄ was used and (f) TEM images showing 6-8 nm AuNPs distributed on CN _x sheet. (g, h) TEM images of Au-aerogel-CN _x formed when 0.235 mmol of HAuCl ₄ and	119

		0.79 mmol of NaBH ₄ was used. (i) HRTEM image of Au-aerogel-CN _x .	
26	Figure 3.6	TGA curves of Au-aerogel(1)-CN _x , Au-aerogel(2)-CN _x , AuNPs-CN _x and CN _x .	120
27	Figure 3.7	(a) UV-Visible spectrum of g-CN _x and Au-aerogel-CN _x . (b) FT-IR spectra of CN _x (red line), AuNPs-CN _x (green line) and Au-aerogel-CN _x (blue line).	121
28	Figure 3.8	(a) XPS survey scan of Au-aerogel-CN _x . XPS spectrum of (b) Au 4f orbital and (c) C1s for Au-aerogel-CN _x (black line), AuNPs-CN _x (blue line), g-CN _x (red line). (d) Comparison of N2p XPS spectra of g-CN _x , AuNPs-CN _x , Au-aerogel-CN _x .	122
29	Figure 3.9	(a) CVs of 0.5 mM Fe(CN) ₆ ^{3-/4-} solution at GCE, AuNPs-CN _x and Au-aerogel-CN _x modified GC electrode. Electrolyte: 0.05 M H ₂ SO ₄ solution. (b) CVs of AuNPs-CN _x , commercial flat Au electrode, Au-aerogel(1)-CN _x , Au-aerogel(2)-CN _x in N ₂ saturated 0.5 M H ₂ SO ₄ solution and (c) CVs of AuNPs-CN _x , commercial flat Au electrode, Au-aerogel(1)-CN _x , Au-aerogel(2)-CN _x in N ₂ saturated 0.5 M KOH solution. scan rate 100 mV sec ⁻¹ .	126
30	Figure 3.10	electrodes (a) LSV curves at Au-aerogel(1)-CN _x /GCE, Au-aerogel(2)-CN _x , AuNPs-CN _x , CN _x modified GC electrode in presence of oxygen saturated KOH medium and Au-aerogel(2)-CN _x in presence of nitrogen saturated solution. (b) Comparison of LSV polarization curve of Au-aerogel-CN _x , Pt/C-GCE with 1000 rpm rotation speed.	129
31	Figure 3.11	(a) ORR polarisation curves of AuNPs-CN _x /GCE. (b) K-L plot of the ORR of AuNPs-CN _x /GCE. (c) ORR polarisation curves of Au-aerogel(1)-CN _x /GCE. (d) K-L plot of the ORR of Au-aerogel(1)-CN _x /GCE. (e) Au-aerogel(2)-CN _x /GCE at different rotation speed at 0.5 M oxygen saturated KOH solution at a scan speed 100 mV sec ⁻¹ with Au loading of 0.130 mg cm ⁻² . (f) K-L plot of the ORR of Au-aerogel(2)-CN _x /GCE. (g) Voltametric profile of Au-aerogel-CN _x , AuNPs-CN _x and GCE in 0.1 M KOH solution containing 2mM Pb(NO ₃) ₂ solution at a scan rate 10 mV sec ⁻¹ . The main Pb desorption peaks from Au surfaces are marked. (h)	130

- Mass transfer corrected Tafel slope of different catalyst was shown. All ORR experiments were done at oxygen saturated 0.5 M KOH solution by a scan speed 100 mV sec⁻¹. Au loading: 0.130 mg cm⁻².
- 32 **Figure 3.12** (a) CVs of Pt-C in N₂ saturated (green line), O₂ saturated (blue line) and O₂ saturated 2 M methanol (red line) in 0.5 M KOH solution (b) Au-aerogel-CN_x in N₂ saturated (green line), O₂ saturated (blue line), O₂ saturated 2 M methanol (red line) 0.5 M KOH solution. Scan rate 100 mV/sec (c) Chronoamperometric stability in 0.5 M alkaline medium at Au-aerogel-CN_x, AuNPs-CN_x and 10% Pt-C at 0.7 V(RHE). 132
- 33 **Figure 3.13** (a) LSV curve by AuNPs-CN_x, Au-aerogel(1)-CN_x, Au-aerogel(2)-CN_x, and flat AuE in presence of oxygen saturated 0.5 M H₂SO₄ solution. (b) CVs of different catalyst at O₂ saturated 0.5 M H₂SO₄ : Au-aerogel(2)-CN_x (red line), Au-aerogel(1) -CN_x (blue line) AuNPs-CN_x (green line), flat Au electrode (purple line) and Au-aerogel(2)-CN_x in N₂ atmosphere. Scan rate 100 mV sec⁻¹. 136
- 34 **Figure 3.14** (a) ORR polarisation curves of AuNPs-CN_x/GCE. (b) K-L plot of the ORR of AuNPs-CN_x/GCE (c) ORR polarisation curves of Au-aerogel(1)-CN_x/GCE. (d) K-L plot of the ORR of Au-aerogel(1)-CN_x/GCE (e) ORR polarisation curves of Au-aerogel(2)-CN_x/GCE at different rotation speed at 0.5 M O₂saturated H₂SO₄ solution at a scan speed 100 mV sec⁻¹ with Au loading of 0.130 mg cm⁻². (f) K-L plot of the ORR of Au-aerogel(2)-CN_x/GCE constructed from the polarisation curves. (g) Mass corrected tafel slope of different catalyst was shown 137
- 35 **Figure 3.15** (a) Chronoamperometric responses of Au-aerogel-CN_x and AuNPs-CN_x at 0.15 V. (b) Stability of catalyst at up to 10000th cycles. All ORR experiments were done at oxygen saturated 0.5 M H₂SO₄ solution at a scan speed 100 mV sec⁻¹. Au loading: 0.130 mg cm⁻² 138
- 36 **Figure 3.16** HER performance by various electrode (a) LSV polarisation curves of Pt/C, Au-aerogel-CN_x, AuNPs- 143

CN_x, Au electrode, CN_x, GCE at N₂ saturated 0.5 M H₂SO₄ solution (Scan rate 10 mV Sec⁻¹, rotation speed 1000 rpm) (b) Base line corrected LSV polarisation curves of Au-aerogel-CN_x, AuNPs-CN_x, Au electrode. (c) HER Tafel plot (log j vs potential) of Pt/C, Au-aerogel-CN_x-GCE, AuNPs-CN_x, Au electrode. (d) HER activity of Au-aerogel-CN_x electrode at first cycle and after 10000 times scan (at scan speed 50 mv sec⁻¹). Inset: chronoamperometric responses of Au-aerogel-CN_x for a long time (10 hrs) at -0.15 V (RHE). Au loading: 0.130 mg cm⁻²

37	Figure S3.1	FT-IR spectra of (a) freshly prepared Au-aerogel-CN _x (blue line) and solid obtained from evaporation of water dispersion of Au-aerogel-CN _x (red line). (b) Freshly prepared AuNPs -CN _x (purple line) and solid, obtained from evaporation of water dispersion of AuNPs -CN _x (green line).	155
38	Figure S3.2	(a, b) The deconvoluted spectra of C1s and N2p XPS spectra of CN _x . (c) Comparison of N2p XPS spectra of g-CN _x , AuNPs-CN _x , Au-aerogel-CN _x	155
39	Figure S3.3	CVs curve for 0.5 mM K ₄ [Fe(CN) ₆] ^{3-/4-} redox couple in 0.05 M H ₂ SO ₄ at different scan rate and corresponding current vs square root of scan rate plot of (a, b) Au-aerogel-CN _x (c, d) AuNPs-CN _x and (e, f) bare GCE	156
40	Figure 4.1	(a) p-XRD of Pt-(PtO _x)-NSs/C composite	166
41	Figure 4.2	(a, b) FESEM images of Pt-(PtO _x)-NSs/C composite	166
42	Figure 4.3	(a,b) TEM images of Pt-(PtO _x)-NSs/C composite showing the nanowires morphology. (c) SAED image (d) HRTEM image	168
43	Figure 4.4	XPS survey scan of (a) Pt-(PtO _x)-NSs/C (b) PtNSs/C composite. (c) Comparison of Pt4f XPS spectra of Pt-(PtO _x)-NSs/C and PtNSs/C composite.(d) Deconvoluted Pt4f XPS spectra of Pt-(PtO _x)-NSs/C composite	169
44	Figure 4.5	Cyclic voltammograms of porous Pt-(PtO _x)-NSs/C (a) 0.1 M HClO ₄ and (b) 0.1 M KOH electrolyte was	170

showing H adsorption and desorption peaks clearly.
(Scan rate 30 mV/sec, N₂ atmosphere, Pt loading 8 μg)

- 45 **Figure 4.6** HER performance of various electrodes (a) LSV polarization curves of Pt-(PtO_x)-NSs/C, commercial Pt/C, PtNSs/C, N@C and GCE in 0.5 M H₂SO₄ with scan rate 10 mV/s at 1600 rpm rotation. Comparison of (b) Geometric current density (c) SA (d) MA of Pt-(PtO_x)-NSs/C, PtNSs/C and commercial Pt/C. (e) The HER Tafel plot of Pt-(PtO_x)-NSs/C, commercial Pt/C and PtNSs/C 172
- 46 **Figure 4.7** (a) Chronoamperometric responses of Pt-(PtO_x)-NSs/C, commercial Pt/C and PtNSs/C catalyst at η = -25 mV in (RHE). (b) Chronoamperometric stability of Pt-(PtO_x)-NSs/C for 40 h 173
- 47 **Figure 4.8** (a) LSV polarization curves of Pt-(PtO_x)-NSs/C, commercial Pt/C, PtNSs/C and N@C in 0.5 M KOH. Comparison of (b) Geometric current density (c) SA (d) MA of Pt-(PtO_x)-NSs/C, PtNSs/C and commercial Pt/C. (e) The HER Tafel plot of Pt-(PtO_x)-NSs/C, commercial Pt/C 173
- 48 **Figure 4.9** (a) LSV curves on the Pt-(PtO_x)-NSs/C catalyst at the first cycle and after 1000 cycles (scan rate 50 mV/s). (b) Chronopotentiometric stability of Pt-(PtO_x)-NSs/C, commercial Pt/C at 10 mA cm⁻² 174
- 49 **Figure 4.10** (a) LSV polarization curves of Pt-(PtO_x)-NSs/C, commercial Pt/C, N@C and GCE in 1 M KOH with scan rate 10 mV/s at 1600 rpm rotation. Comparison of (b) Geometric current density (c) SA (d) MA of Pt-(PtO_x)-NSs/C, and commercial Pt/C in 1 M KOH. (e) Chronoamperometric study of Pt-(PtO_x)-NSs/C in 1 M KOH at constant current density of 10 mA/cm² 175
- 50 **Figure 4.11** (a) Nyquist plot of Pt-(PtO_x)-NSs/C at different overpotentials and its corresponding semicircle fit. Inset: an equivalent circuit for the fitting of the EIS spectra. (b) logR_{ct}⁻¹ vs overpotential plot of Pt-(PtO_x)-NSs/C composite. iR-corrected and non iR-corrected comparison of (c) geometric current density and (d) SA for Pt-(PtO_x)-NSs/C and commercial Pt/C at different base concentrations 177

51	Figure 4.12	(a, b) HER/HOR polarization curves (going positive direction) of Pt-(PtO _x)-NSs/C in 0.1 M HClO ₄ and 0.1 M KOH solution saturated with H ₂ (~1 atm) with different rotation speeds at a scan rate of 10 mV/s (inset: Koutecky–Levich plot at 0.15 V and 0.3 V in RHE). (c-d) Kinetic current vs potential plot (Butler-Volmer plot) of Pt-(PtO _x)-NSs/C and PtNSs/C-(RT) at 0.1 M HClO ₄ and 0.1 M KOH	178
52	Figure 4.13	(a) HOR polarization curves of Pt-(PtO _x)-NSs/C. (b) Normalized HOR polarization curve in different buffer solutions for Pt-(PtO _x)-NSs/C. (c) HOR polarization curves of PtNSs/C. (d) Normalized HOR polarization curve in different buffer solutions for PtNSs/C. All experiments were done in H ₂ saturated different buffer solutions at 10 mV/sec scan rate with 1600 rpm	182
53	Figure 4.14	(a) Required HOR overpotential for both the catalysts at half of the normalized current density (0.5 <i>i</i> _{lim}) at different pH. (b) The limiting HOR current density for both the catalysts at different pH solutions. All polarization curves are <i>i</i> R corrected accordingly	183
54	Figure 4.15	CVs of (a) Pt-(PtO _x)-NSs/C and (b) PtNSs/C in different pH for Pt (110) and Pt (100) in N ₂ saturated medium at 30 mV/sec. (c) The plot of HBE vs pH of Pt-(PtO _x)-NSs/C and PtNSs/C	183
55	Figure 4.16	(a) CO stripping voltammetry of Pt-(PtO _x)-NSs/C and PtNSs/C catalyst in acid medium (b) Comparison of onset potential of CO stripping with different pH of Pt-(PtO _x)-NSs/C and PtNSs/C	184
56	Figure 4.17	HER/HOR overpotential required for 1mA/cm ² current density for Pt (110) and Pt (100) plane of Pt-(PtO _x)-NSs/C and PtNSs/C composite	185
57	Figure 4.18	Schematic diagram of bi-functional mechanism of HOR on Pt-(PtO _x)-NSs/C catalyst in basic medium	186
58	Figure 4.19	(a) HER activity of (current normalized by surface area of the catalyst) of Pt-(PtO _x)-NSs/C and Pt/C in acid and alkaline medium and (b) corresponding SA plot of both the catalysts at η= 0.1	188

59	Figure 4.20	Schematic representation of bi-functional mechanism of HER on Pt-(PtO _x)-NSs/C catalyst in basic medium	189
60	Figure S4.1	(a, b) TEM images(c) FESEM images of Pt-(PtO _x)-NSs/C composite	197
61	Figure S4.2	p-XRD of PtNSs/C composite	197
62	Figure S4.3	(a,b) FESEM images of PtNSs/C composite showing the interconnected PtNPs.	198
63	Figure S4.4	Comparison of high resolution XPS spectra of (a) C1s (b) O1s (c) N1s of Pt-(PtO _x)-NSs/C and PtNSs/C composite	199
64	Figure S4.5	(a,b) EDS spectrum of Pt-(PtO _x)-NSs/C where it clearly confirms the presence of carbon, nitrogen, oxygen and platinum	199
65	Figure S4.6	(a, b) EDS spectrum was taken on PtNSs/C where it clearly confirms the presence of carbon, nitrogen, oxygen and platinum	199
66	Figure S4.7	CV curves of Pt-(PtO _x)-NSs/C, Pt/C in KOH electrolyte of different concentrations. All CV experiments were performed with 30 mV/s scan rate with a constant Pt loading of 28.57 μg/cm ²	200
67	Figure S4.8	CV curves of (a) Pt/C and (b) Pt-(PtO _x)-NSs/C in 0.5 M H ₂ SO ₄ .ECSA was calculated from the shaded UPD-H _{des} region. All CV experiments were performed with 30 mV/s scan rate with a constant Pt loading of 28.57 μg/cm ²	201
68	Figure S4.9	Pt 4f XPS spectra of Pt-(PtO _x)-NSs/C (a) before and (b) after HER study. (c) TEM image of Pt-(PtO _x)-NSs/C after HER stability	201
69	Figure S4.10	(a) HER LSV curves of Pt-(PtO _x)-NSs/C, Pt/C, CN _x and GCE in 0.1 M KOH with scan rate 10 mV/s. Comparison of (b) geometric current density (c) SA (d) MA at -0.1 and -0.2 V of Pt/C and Pt-(PtO _x)-NSs/C	202
70	Figure S4.11	iR and diffusion corrected polarization curve at 1600 rpm in (a) 0.1 M HClO ₄ (b) 0.1 M KOH	202

71	Figure S4.12	CO stripping voltammograms of Pt-(PtO _x)-NSs/C at different pH solutions	203
72	Figure S4.13	CO stripping voltammograms of PtNSs/C at different pH	203
73	Figure S4.14	Niquist plot of different catalysts (a) Pt-PtO ₂ (without support), Pt-PtO ₂ + CN _x physical mixture, Pt/C, Pt-(PtO _x)-NSs/C and (b) N@C in 0.5 M KOH at a constant voltage -20 mV (RHE). (c) HER activity of different catalysts Pt-PtO ₂ (without support), Pt-PtO ₂ + CN _x physical mixture, Pt/C, Pt-(PtO _x)-NSs/C in 0.5 M KOH and (d) Chronopotentiometric HER stability of Pt-PtO _x (without support), Pt-(PtO _x)-NSs/C in 0.5 M KOH	204
74	Figure 5.1	UV-Visible spectra of H ₂ IrCl ₆ and N@C mixture in different time	211
75	Figure 5.2	(a) p-XRD of 3D-IrO ₂ /N@C hybrid. (b) p-XRD of 3D-IrO ₂ /N@C on Ti foil (blue line) and only Ti foil heated at 400 °C	212
76	Figure 5.3	FESEM images of 3D-IrO ₂ /N@C prepared at (a) 400 °C (b, c) 500 °C	213
77	Figure 5.4	(a) HRTEM image of 3D-IrO ₂ /N@C (b) SAED image of 3D-IrO ₂ /N@C hybrid	214
78	Figure 5.5	FESEM image of (a) N@C (b) N@C-Ir ⁴⁺ complex before heating. The FESEM image 3D-IrO ₂ /N@C prepared at (c) 300 °C (d) 400 °C (inset: high magnification image) (e, f) 500 °C	214
79	Figure 5.6	(a, b) EDS line profile and elemental weight percentage of the 3D-IrO ₂ /N@C hybrid (heated at 400 °C). (c-g) STEM image and TEM-EDS elemental mapping of 3D-IrO ₂ /N@C	215
80	Figure 5.7	(a) XPS survey scan of 3D-IrO ₂ /N@C hybrid. High-resolution XPS spectra of (b) Ir4f (c) O1s (d) C1s of 3D-IrO ₂ /N@C hybrid	216
81	Figure 5.8	(a) LSV polarisation curves of 3D-IrO ₂ /N@C, comm. IrO ₂ , comm. Pt/C in 0.5 M HClO ₄ with scan rate 10 mV/s (b) Required overpotential required for	218

		achieving 10 mA cm ⁻² current density for of 3D-IrO ₂ /N@C catalyst	
82	Figure 5.9	(a) MA of 3D-IrO ₂ /N@C, comm. IrO ₂ , comm. Pt/C at 1.58 V. (b) MA of 3D-IrO ₂ /N@C and comm. IrO ₂ at different overpotentials (c) TOF of 3D-IrO ₂ /N@C and comm. IrO ₂ at different overpotentials. (d) Tafel slope of 3D-IrO ₂ /N@C and comm. IrO ₂	219
83	Figure 5.10	(a) Steady-state chronoamperometric stability of 3D-IrO ₂ /N@C and comm. IrO ₂ in 0.5 M HClO ₄ at a constant potential of 1.51 V. (b) Theoretical and experimental measured O ₂ by the 3D-IrO ₂ /N@C electrode at 25 mA cm ⁻² current density. (c) LSV polarization curve normalized by mass of the catalyst of 3D-IrO ₂ /N@C on Ti foil and GC surface	220
84	Figure 5.11	(a) OER activity of 3D-IrO ₂ /N@C at different metal loading in the electrode. (b) Mass activity (with respect to Ir) of 3D-IrO ₂ /N@C with different Ir loading in the 3D-IrO ₂ /N@C catalyst. (c) (a) LSV curves (b) Mass activity of 3D-IrO ₂ /N@C catalysts prepared at different calcination temperature ranging from 100 to 600 °C. Amount of Ir loading kept same (120 μg _{Ir} cm ⁻²)	221
85	Figure 5.12	(a) p-XRD of 3D-IrO ₂ /N@C before and after 10 hrs of OER stability. High resolution 4f XPS spectra of (b) Ir (c) O1s (d-e) FESEM images of 3D-IrO ₂ /N@C after 10 hrs OER stability	223
86	Figure 5.13	HER performance of various electrodes: (a) LSV polarization curves of 3D-IrO ₂ /N@C, comm. IrO ₂ , comm. Pt/C in 0.5 M HClO ₄ with scan rate of 10 mV/s in N ₂ saturated medium. (b) Overpotential required to achieve 10 mA/cm ² current density for 3D-IrO ₂ /N@C, comm. Pt/C and comm. IrO ₂ catalyst. (c) MA of 3D-IrO ₂ /N@C, comm. Pt/C and comm. IrO ₂ at -50 mV. (d) Tafel slope of 3D-IrO ₂ /N@C, comm. Pt/C and comm. IrO ₂ (e) Steady-state chronoamperometric stability (at 35 mV) of 3D-IrO ₂ /N@C and comm. Pt/C in 0.5 M HClO ₄	225
87	Figure 5.14	(a) LSV polarization curve of overall water splitting using 3D-IrO ₂ /N@C as a cathode as well as an anode in 0.5 M HClO ₄ at 10 mV/s scan rate. (b) The	227

		chronoamperometric response of 3D-IrO ₂ /N@C at 1.55 V. Inset: Photograph of cathode and anode	
88	Figure 5.15	(a) CV curves of 3D-IrO ₂ /N@C hybrid with a different scan rate starting from 30 to 300 mV/s. CV curves of (b) comm. IrO ₂ (c) Ti foil in a potential range 0.75- 1.25 V (vs RHE) with different scan rate in 0.5 M HClO ₄ . (d) Linear plot of double layer current vs scan rate 3D-IrO ₂ /N@C comm. IrO ₂ and Ti foil in 0.5 M HClO ₄ at a potential of 1.1 V in RHE	228
89	Figure 5.16	(a) EIS spectra of 3D-IrO ₂ /N@C in 0.5 M HClO ₄ at different voltages. Inset: Equivalent circuit for the fitting of the EIS curves. (b) Comparison of EIS spectra of the different catalysts at 1.52 V. (c) Comparison of EIS spectra of 3D-IrO ₂ /N@C, a physical mixture of IrO ₂ and CN _x , IrO ₂ (IrO ₂ was synthesized by heating Ir salt at 400 ⁰ C) and (d) CN _x at 1.52 V (RHE)	229
90	Figure 6.1	p-XRD of AgNWs-CN _x composite	245
91	Figure 6.2	(a-d) TEM images of AgNWs-CN _x composite in low and high magnification showing interconnected nanochains of Ag. (e) SAED profile of corresponding AgNWs-CN _x composite. (f) HRTEM images of Ag in AgNWs shows preferential growth on Ag(111) surface	246
92	Figure 6.3	(a-c) FESEM images of interconnected AgNWs-CN _x	247
93	Figure 6.4	(a) FESEM image of interconnected AgNWs. (b) EDS profile of AgNWs-CN _x composite taken from Figure 6.5a. (c, d, e) Corresponding EDS mapping for element Carbon, Nitrogen, Silver respectively	248
94	Figure 6.5	(a) XPS survey scan of AgNWs-CN _x and XPS spectra of (b, c, d) Ag3d, C1s, N1s spectra of AgNWs-CN _x .	249
95	Figure 6.6	(a) HER performance of ac-AgNWs-CN _x with repeated LSV polarization scan at 50 mv/sec scan rate. (b) LSV polarization of Pt/C, ac-AgNWs-CN _x , CN _x and GC at 10 mv/sec scan rate. (c) HER Tafel plot (log j vs potential) of ac-AgNWs-CN _x and Pt/C. (d) EIS study of ac-AgNWs-CN _x at different overpotential at onset of HER (-0.01 to 0.03). (e) log R _{ct} ⁻¹ vs Potential plot shows the Tafel slope value is 30	250

mv/dec. (f) HER activity of ac- AgNWs-CN_x at 1st cycle and 15,000th cycle. Inset: Chronoamperometric study of ac-AgNWs-CN_x and Pt/C electrode for long time (>35 hr). Experimental condition: 0.5 M H₂SO₄, N₂ atmosphere, 1600 rpm rotation.

- | | | | |
|-----|--------------------|---|-----|
| 96 | Figure 6.7 | (a) LSV polarization curve of Pt/C, ac-AgNWs-CN _x , CN _x and GC at 10 mV/sec scan rate. (b) HER Tafel plot (log j vs potential) of ac-AgNWs-CN _x and Pt/C. (c) HER activity of ac-AgNWs-CN _x at 1st cycle and 1500th cycle. (d) Chronoamperometric study of ac-AgNWs-CN _x electrode and Pt/C for long time (30 hr). Experimental condition: 0.5 M KOH, N ₂ atmosphere, 1000 rpm rotation. ac-AgNWs-CN _x was used after 4000 LSV scan in H ₂ SO ₄ . | 252 |
| 97 | Figure 6.8 | (a) LSV polarisation curve of Pt/C, ac-AgNWs-CN _x , CN _x and GC in O ₂ saturated 0.5 M KOH at 100 mV/sec scan rate. ac-AgNWs-CN _x was used for ORR studies. (b) LSV polarisation curve of ac AgNWs at different rotation varied from 200 to 2150 rpm. (c) K-L plot of ac-AgNWs-CN _x electrode constructed from Figure b (d) ORR Tafel plot (log j vs potential) of ac-AgNWs-CN _x and Pt/C. | 256 |
| 98 | Figure 6.9 | (a) ORR activity of ac-AgNWs-CN _x at 1 st cycle and 1000 th cycle in a O ₂ saturated 0.5 M KOH. (b) Comparison of ORR LSV cycling stability between Pt/C and ac-AgNWs-CN _x . (c) CV of ac-AgNWs-CN _x and Pt/C in a N ₂ saturated 0.5 M KOH contain 1 M methanol. (d) LSV curve of ac-AgNWs-CN _x in an O ₂ saturated 0.5 M KOH contain 1 M methanol shows methanol tolerance of the electrode | 258 |
| 99 | Figure 6.10 | (a) LSV polarisation curve of Pt/C, ac-AgNWs-CN _x , CN _x and GC in O ₂ saturated 0.5 M H ₂ SO ₄ at 100 mV/sec scan rate (b) LSV polarisation curve of ac-AgNWs-CN _x at different rotation varied from 250 to 2500 rpm. (c) K-L plot of ac-AgNWs-CN _x electrode. (d) ORR activity of ac-AgNWs-CN _x at 1 st cycle and 10,000 th cycle in an O ₂ saturated 0.5 M H ₂ SO ₄ | 261 |
| 100 | Figure 6.11 | (a) CVs of 0.5 M [FeCN ₆] ^{3-/4-} solution at GCE and ac-AgNWs-CN _x electrode in N ₂ saturated 0.1 M H ₂ SO ₄ solution. (b, d) CVs of GC electrode and ac-AgNWs- | 263 |

		CN _x electrode in different scan rate ranging from 100 to 700 mV/sec. (c, e) Cathodic and anodic current vs (scan rate) ^{1/2} plot shows a linear fit in both the electrode	
101	Figure S6.1	(a-c) TEM images of AgNWs composite in low and high magnification showing interconnected nanochains of Ag. (d) HRTEM images of Ag in AgNWs. (e) TEM EDS profile has taken on AgNWs-CN _x composite	268
102	Figure S6.2	CVs of AgNWs-CN _x in O ₂ saturated and N ₂ saturated 0.5 M H ₂ SO ₄	268
103	Figure 7.1	(a) FT-IR spectra and (b) UV-Visible spectra of free g-CN _x and in the presence of Ag ⁺ ions	276
104	Figure 7.2	p-XRD of g-CN _x and Ag-CN _x composite	278
105	Figure 7.3	Two dimensional self assembly of silver nanoparticles on CN _x sheets: (a) and (b) TEM images showing AgNPs highly dispersed on CN _x sheet (c) EDX spectrum on this sheet. (d) Size distribution of AgNPs	279
106	Figure 7.4	Comparison of XPS spectra of (a) C1s, (b) N1s of Ag-CN _x , Ag ⁺ -CN _x and CN _x , (c) Ag 3d XPS spectra of Ag-CN _x , Ag ⁺ -CN _x	280
107	Figure 7.5	FESEM images showing assembly of AgNPs on CN _x sheets prepared from evaporation of (a) zero hrs (b) 7 hrs (d) 14 hrs old stock solution on Si wafer. (c) SEM image of ordered 2D assembly of AgNPs on a very thin CN _x sheet from 7 hrs old stock solution on Si wafer (inset of (c) showing heptamer arrangement of AgNPs)	281
108	Figure 7.6	SEM images of AgNPs dispersed on CN _x sheets prepared from evaporation of 7 hrs old solution. The average sizes in (a), (b) and (c,d) are 3-4 nm, 5-6 nm and 8-10 nm respectively	283
109	Figure 7.7	Comparison FT-IR spectra of Ag ⁺ -CN _x and Ag(0)-CN _x	284
110	Figure 7.8	(a) CVs of 2 mM H ₂ O ₂ in 0.01M PBS at bare and Ag-CN _x /GC electrode. (b) CVs of Ag-CN _x /GC electrode	285

		in absence and presence of 2 mM H ₂ O ₂ in 0.01M PBS (pH=7) solution	
111	Figure 7.9	(a) Amperometric response of Ag-CN _x /GC electrode on successive addition of H ₂ O ₂ into 0.01M PBS with stirring. Inset: lower concentration regime. (b) Lower concentration regime (c) Calibration curve of current vs. H ₂ O ₂ concentration	286
112	Figure 7.10	Amperometric responses of Ag-CN _x /GC electrode at a potential of -0.7V on subsequent addition of 5 mM dopamine (DA) 5 mM ascorbic acid (AA), 5 mM D-Glucose, 5 mM L-Glycine, 5 mM L-Cysteine, 5 mM L-Tyrosine, 5 mM L-Tryptophan and 5 mM H ₂ O ₂	287
113	Figure 7.11	(a) CVs of Ag-CN _x /GC and only GC electrode in presence of 2 mM H ₂ O ₂ and Ag-CN _x /GC electrode in absence of H ₂ O ₂ in 0.05 M NaOH solution (b) Amperometric response of Ag-CN _x /GC electrode on successive addition of H ₂ O ₂ into 0.05M NaOH with stirring. (c) Lower concentration regime of amperometric curve. (d) Calibration curve of current vs. H ₂ O ₂ concentration	288
114	Figure 7.12	(a) CVs of 20mM glucose in 0.05M NaOH at bare GC and Ag-CN _x /GC electrode. (b) CVs of Ag-CN _x /GC electrode in absence and presence of 20 mM glucose in 0.05 (M) NaOH solution	289
115	Figure 7.13	(a) Amperometric response of Ag-CN _x /GC electrode on successive addition of glucose into 0.05 M NaOH with stirring at 1.0 V. (b) Calibration curve of current vs. glucose concentration at 1.0 V. (c) Calibration curve of current vs. glucose concentration (100 μM - 2 mM) (d) Calibration curve of current vs. glucose concentration (2 mM - 30 mM)	291
116	Figure 7.14	(a) Amperometric response of Ag-CN _x /GC electrode on successive addition of glucose into 0.05M NaOH with stirring at 1.5 V (b) Lower concentration regime of amperometric curve. (c) Calibration curve of current vs. glucose concentration (lower concentration regime)	292
117	Figure S7.1	SAED image of AgNPs taken from Figure 7.6(b)	298

118	Figure S7.2	(a) C1s and (b) N1s XPS spectra of CN _x	298
119	Figure S7.3	(a, b) TEM images of CN _x sheets prepared from g-CN _x	299
120	Figure S7.4	AFM images of thin CN _x sheets and its height profile shows thickness 2.0 to 2.5 nm	299
121	Figure S7.5	SEM image of AgNPs assembly on CN _x sheet	300
122	Figure S7.6	(a) and (b) SEM images showing ordered assembly of AgNPs on thin CN _x sheets	300
123	Figure S7.7	SEM image of highly ordered 2D assembly	301
124	Figure 8.1	p-XRD of g-C ₃ N ₄ and Au-CN _x composite	310
125	Figure 8.2	(a, b) TEM images of g-carbon nitride	311
126	Figure 8.3	(a, b, c) TEM images of Au-CN _x composite shows ultra-small AuNPs are highly dispersed on the CN _x sheets. (d) Size distribution plot of Au NPs taken from Figure 2d. (e, f) SEAD and EDS spectra of Au-CN _x composite respectively, has taken from Figure 8.3a	311
127	Figure 8.4	EDS spectra Au-CN _x composite prepared on silicon wafer	312
128	Figure 8.5	TGA spectra of Au-CN _x (blue line) and CN _x (red line) at N ₂ atmosphere	313
129	Figure 8.6	(a) XPS spectra of 4f orbital of Au (b, c) The deconvoluted spectra of 1s carbon(C) and nitrogen(N) of Au-CN _x respectively	315
130	Figure 8.7	(a) UV-Visible spectra for the reduction 4-NP catalysed by Au-CN _x composite. 4-NP is represented by green colour curve, red color curve is in presence of only NaBH ₄ without catalyst and blue color curve represent reductive product 4-AP. (b) The stability of the Au-CN _x catalyst with 5 successive cycles keeping the conditions same at every cycles	316
131	Figure 8.8	(a, d) UV-Visible absorption spectra of aqueous solution of RhB and MB respectively at different time interval in presence of Au-CN _x catalyst. (b, e) Plot of C/C ₀ vs time for RhB and MB dyes respectively where C ₀ is initial concentration of dyes (70 ppm) and C is the concentration at different time interval.(c, f)	320

Fitting of different isotherm model with adsorption of RhB and MB on Au-CN_x surfaces respectively. All the experiment was done with 1 ml of 70 ppm dyes with 1 mg Au-CN_x catalyst

132	Figure 8.9	(a) UV-Visible absorption spectra of aqueous solution of MR at different time interval in presence of Au-CN _x catalyst. (b) Plot of C/C ₀ vs time for MR dyes respectively where C ₀ is initial concentration of dyes (20 ppm) and C is the concentration at different time interval. (c) Fitting of different isotherm model with adsorption of MR on Au-CN _x surfaces. All the experiment was done with 1 ml of 20 ppm dyes with 1 mg Au-CN _x catalyst	321
133	Figure 8.10	(a, b) Change of Zeta potential of g-CN _x and Au- CN _x composite with different pH respectively. (c, d) The adsorption–desorption cycle of RhB and MB respectively	321
134	Figure 8.11	Degradation of 30 ppm RhB, 35 ppm MB, and 35 ppm MR dye by Au-CN _x under irradiation of visible light, natural sunlight, and UV light. (a, d, g) The change of UV-Visible absorption spectra of RhB, MB, MR over Au-CN _x catalyst on irradiation of visible light respectively. (b,e,h) Change of the concentration. (c) of RhB, MB, and MR relative to their initial values (C ₀) with time on irradiation of different lights. (c, f, i) The pseudo first order kinetics plots of RhB, MB, MR degradation under different UV, Visible and natural sunlight respectively	323
135	Figure 8.12	(a) Reusability of Au-CN _x catalyst for degradation of 30 ppm RhB dye where conditions of each cycle are kept same	325
136	Figure 8.13	(a) Fluorescence emission spectra of g-CN _x and Au-CN _x composite (b) Scavenger effect on rate of 30 ppm RhB dye degradation	326
137	Figure 8.14	(a) UV-vis absorption spectra for degradation of RhB under irradiation of visible light. (b) Normalized absorption spectra of different N-de-ethylated intermediate products taken from Figure 8.14a	327

138	Figure 8.15	ln (C_0/C) vs time plot of different concentration of RhB under visible light illumination	328
139	Figure 8.16	pH dependent degradation efficiency of 70 ppm RhB with Au-CN _x catalyst	329
140	Figure 8.17	(a-e) represent LC-MS mass spectra of different N-alkylated intermediate, formed during degradation of RhB	330
141	Figure 8.18	A proposed mechanism of photocatalytic degradation of dyes (a) under sunlight or visible light and (b) under irradiation of UV light in presence of Au-CN _x catalyst	333
142	Figure S8.1	AFM images of thin CN _x sheets and its height profile shows thickness 2.0 to 2.5 nm	342
143	Figure S8.2	Degradation of 250 ppm RhB dye by Au-CN _x under visible light after 10 hour adsorption. (a) The change of UV-Visible Spectra at different time intervals, (b) C/C ₀ vs time plot	343
144	Figure S8.3	pXRD of recycled (after 3 rd catalytic cycles) catalyst	343

LIST OF TABLES

Sl. No.	Table Caption	Page No.
1	Table 2.1 List of the chemicals along with formula and company name	89
2	Table 2.2 The details description of Bode and Nyquist plot	101
3	Table 2.3 The components and their indication for equivalent circuit	102
4	Table 3.1 Electrochemical parameters deduced from Figure S3.3 such as ΔE_p and slope of cathodic and anodic current of Au-aerogel-CN _x , AuNPs-CN _x and bare GCE	127
5	Table 3.2 ECSA of different catalysts in acidic and basic medium	128
6	Table 3.3 Different parameter of synthesized catalyst at 0.5 M KOH	131
7	Table 3.4 Comparison of ORR the activity of different catalysts in acidic and alkaline media	139
8	Table 3.5 Different parameter of synthesized catalysts in acidic media	142
9	Table 3.6 Comparison of HER activity of different reported catalyst in acidic media	146
10	Table 4.1 Different HER parameter in acidic and alkaline medium	176
11	Table 4.2 Kinetic parameter of Pt-(PtO _x)-NSs/C extracted from Butler-Volmer fitting at 0.1 M H ₂ SO ₄ and KOH	180
12	Table S4.1 Comparison of HER activity of Pt-(PtO _x)-NSs/C in 0.5 M H ₂ SO ₄ with other reported catalysts	205
13	Table S4.2 Comparison of HER activity of Pt-(PtO _x)-NSs/C in 0.5 M KOH with other reported catalysts	206

14	Table 5.1	Comparison of OER activity of different catalysts in 0.5 M HClO ₄	222
15	Table 5.2	Comparison of HER activity of different catalysts in 0.5 M HClO ₄	226
16	Table S5.1	Comparison of OER activity of 3D-IrO ₂ /N@C in acidic medium with other reported catalysts	237
17	Table S5.2	Comparison of HER activity of 3D-IrO ₂ /N@C in 0.5 M HClO ₄ with other reported catalysts	238
18	Table 6.1	Summarized HER activity of ac-AgNWs-CN _x and Pt/C in 0.5 M H ₂ SO ₄	251
19	Table 6.2	Summarized HER activity of ac-AgNWs-CN _x and Pt/C in 0.5 M KOH	254
20	Table 6.3	Different parameter of ac-AgNWs-CN _x in ORR	259
21	Table 6.4	Different parameters obtained from the CV of [FeCN ₆] ^{3-/4-} by the ac-AgNWs-CN _x and GCE electrode	264
22	Table S6.1	Comparison of HER activity of different catalysts with ac-AgNWs-CN _x on GC electrode in acidic medium	269
23	Table S6.2	Comparison of HER activity of different catalysts with ac-AgNWs-CN _x on GC electrode in basic medium	270
24	Table 7.1	Comparison of detection limit and sensitivity of Ag-CN _x /GC sensor with reported non enzymatic H ₂ O ₂ sensors	290
25	Table 7.2	Comparison of detection limit and sensitivity of Ag-CN _x /GC sensor with reported non enzymatic glucose sensors	292
26	Table 8.1	Comparison of activity of different catalyst on 4-NP reduction	317
27	Table 8.2	Parameters of different isotherm model of RhB dye	319
28	Table 8.3	Parameters of different isotherm model of MB dye	319

29	Table 8.4	Comparison of rate constant for photocatalytic degradation of different dyes.	335
30	Table S8.1	Parameters of different isotherm model of MR dye	342

LIST OF SCHEMES

Sl. No.	Scheme Caption		Page No.
1	Scheme 3.1	Schematic representations of formation of Au-aerogel and AuNPs on CN _x sheet	123
2	Scheme 7.1	Schematic diagram of evaporation induced ordered self-assembly of AgNPs on CN _x sheet on a solid surface	282
3	Scheme 8.1	Schematic diagram of de-ethylation process of RhB on the surface of Au-CN _x composite under irradiation of light	331

CHAPTER 1

Introduction: Nanocomposite for Environmental and Electrochemical Energy Conversion Applications

1.1 ABSTRACT

In this present thesis, our prerequisite of current and future energy have been reviewed and the need of renewable/alternate energy conversions and storage procedures are being explored. The insight of the fuel cells and water electrolyzers are discussed also. This section gives a general portrayals, reaction mechanisms and kinetics of different fuel cell reactions, for example, hydrogen oxidation reaction (HOR), oxygen reduction reaction (ORR) and water electrolyser reactions, to be specific, hydrogen evolution reaction (HER), oxygen evolution reaction (OER). Brief accounts of theoretical backgrounds for the development of various efficient electrocatalysts for different renewable processes have been exploited. A general description in the electrochemical sensing of glucose, hydrogen peroxide (H_2O_2) and photocatalytic dye degradation have been discussed. This chapter also describes a brief idea about the different dimensions of nanoparticles, stabilisation of the nanoparticles by using support and their synthesis procedures. At the end, aims of the present thesis has been revealed.

1.2. INTRODUCTION

Last few years, we have become more reliant on non-renewable based energy technologies. Upto 17th century our energy requirement was satisfied by several renewable energies like water, wind, firewood. These energy sources are directly or indirectly related to the sun, since solar energy is mainly responsible to produce these energies. Mankind faced a drastic increase in energy demands from 18th century onwards due to the increased dependence on machines and technologies. Maximum contribution towards the energy requirements came from coal, oil and natural gas¹. The fossil fuel had replaced the several ancient energy sources except the energy harvested from water. The fossil fuel are blend of hydrocarbons started from the decayed remains primordial creatures and plants, in a roundabout way, their energy likewise begin, from the sun. Be that as it may, the fossil fuel are utilized at a far more prominent rate than their formation for example energy put away for more than billions of years was overwhelmed by in about hundred years. Almost 80% of usable energy produced from fossil fuels such as oil, coal and gas (Figure 1.1. a). United States Energy Information Administration (US-EIA) revealed that, world-wide energy intake is 14 Terawatt hour (TWh) per year nearly and at the end of the year 2050 it will nearly become double (Figure 1.1. b)². Fossil fuels are not are not feasible energy sources and they will at some point or another exhaust. Apart from that, they are the reason for the large amounts of unsafe gases, responsible for ozone layer depletion as well as global warming, which is certainly a threat towards human civilization. It results in the temperature

increase of our planet and compromising the lives on it. Furthermore, due to the temperature upswing, the polar ice of Arctic and Antarctic has been constantly melting which is creating the sea levels higher ^{3,4}.

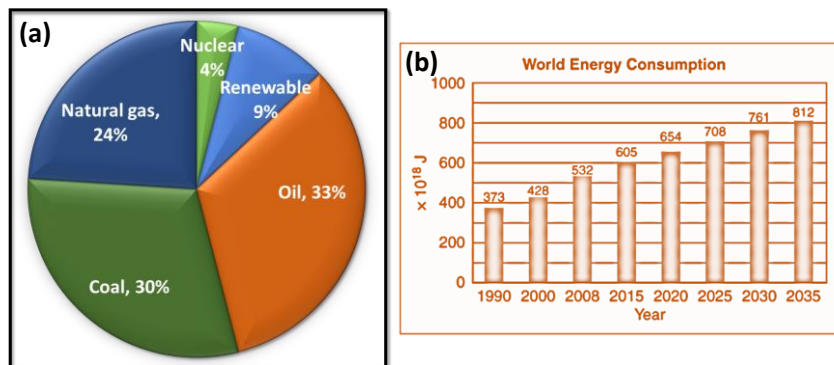


Figure 1.1. (a) Percentage of energy consumption from different Sources. (b) Predicted world energy consumption for upcoming years (Adopted from Wikipedia).

Middle East nations have vast storage of fossil fuels and other nations are reliant on them for the continuous supply. Incomplete combustion of these fossil fuels also produces several toxic gases such as nitrogen dioxide, nitrogen monoxide, sulphur dioxide and carbon monoxide *etc.* These are the major air pollutants that can cause severe damage to the human health and plant growth leading to complete breakdown of human civilization. Coal mining has created many unlucky deaths throughout the year and oil spilling in seas during transport sometimes has shattered our ecosystems. Least can be done until & unless we focus on the renewable energy sources. After 1950, we initiated to use uranium, a source of nuclear energy. But uranium, like other fossil fuels, is also non-renewable and setting up a plant is too costly. Renewable energy can be derived from unlimited sources. Over the past few

years, we have started to proceed with new renewable energy sources and has upraised older one. Renewable energy offers openings for an infinite, viable energy resource with less environmental pollution. It is unpleasant reality that lots of industries around the globe are still reliant on fossil fuels for producing electricity. Undoubtedly, power production efficiency of these fuels are very effective, but these are not meant for the long run. Fossil fuels will drain eventually and the industries have to must return to renewable sources.

1.2.1. Difference between Renewable and Alternative Energy Sources

Appropriate renewable energy can be assumed as energy sources refilled by natural procedures when we make them use. Sun is the ultimate sources of all energy and it is true for the renewable energy sources as well. Direct use of solar energy i.e. solar heating process or indirect use e.g. hydroelectric energy, wind energy, and energy from biomass. Storage of renewable energy can be exhausted if we use them very fast which they become replenished. On the other side, judicious uses of this type energy can last endlessly. Also, some other alternatives sources are present and they are not renewable. In spite of the fact, these are “alternative energy” instead of calling “renewable energy”, these energy sources are more productive than more established advances. Utilizing this, they help us make our current energy supplies last more and give us additional time before we come up short of fossil and nuclear fuels. There are a few sustainable power sources that are being used today. Recorded underneath are brief depictions of these assets.

1.2.2. Renewable energy and other alternative energy sources

Hydropower:

Hydropower is one of the first-born and leading renewable energy source producing electricity from the energy of flowing water. This is made by development of huge water reservoir and after that discharging water through turbines to reap power. Emission less energy are produced from hydropower but making reservoir can create significant ecological problems for quality of water, water bodies and wildlife habitat.

Biomass:

Biomass is another important renewable energy source. Biomass fuel mainly constitutes of organic components such as industrial, rural waste, wood and so on. It can substitute 15% of coal utilization as a fuel in common power supply. Biomass contains less sulphur, which implies less measure of sulphur dioxide will be discharged in our climate. Gasification of biomass produce methane gas and combustion of methane in boiler are used to run steam turbines or used in gas turbines directly and replying engines. Several industries i.e. sawmills and paper mills frequently ignite their wood waste to harvest heat and electricity.

Geothermal:

The warmth stockpiling inside the earth is utilized by geothermal power plants to yield steam, which produce forces to the turbines that produce electrical energy. Geothermal

power plants can even draw high temperature water stored underground or can warm water by driving it into warm, dry stones. Heat energy, put under earth surface are recovered by exhausting wells. Boring and inspection for profound assets is in all respects expensive. It may incite the possibility that this geothermal energy can't be viewed as inexhaustible, as at some point in future the centre of the earth will be cold. In any case, that require tremendous time which can thus consider it as practically inexhaustible. It has verifiably been restricted to territories close to the tectonic plate boundaries.

Wind Power:

The energy of the flowing air revolving the specially designed aerodynamic blades connected to a hub produces wind power. The hub then is coupled to a shaft that revolves a generator. Large scale wind turbines size varies from 50 kW to over four MW. Under 50 kW are appropriate for domestic and farming use. Wind has been the fastest growing energy source in the western countries over the past few years and very significant developments in wind energy technology has been noticed.

Solar Energy:

Recent day's solar cell is well known to all of us because of its wide spread applications. Solar energy is converted to several form of energy such as solar electricity, solar hot water and photovoltaic (PV). Sunlight is directly converted to electrical energy using solar cells in PV technology. PV technology is more real for domestic use as operation

is simple and hassle free. In PV technology a semiconductor material is used that shows photovoltaic effect in presence of sunlight.

1.3. Fuel Cells

A fuel cell is an electrochemical device/cell that transforms the chemical energy to electrical energy through an electrochemical reaction occurring in an electrode⁵. A fuel cell is an alternative energy device. But it is worth mentioning that, not necessarily it should be renewable energy device until and unless the source of the fuel used in the cell is renewable. On the other hand it is comparable with battery but unlike a battery, whose energy production capacity is restricted to the amount of chemicals stored inside, a fuel cell has the continuous capability of creating energy on condition that fuel is provided⁵ (Figure 1.2). Conventional fuel cells electrochemically combine hydrogen and oxygen to yield electricity without combustion. The source of oxygen is air, while the other component hydrogen could easily be produced from water (using electricity).

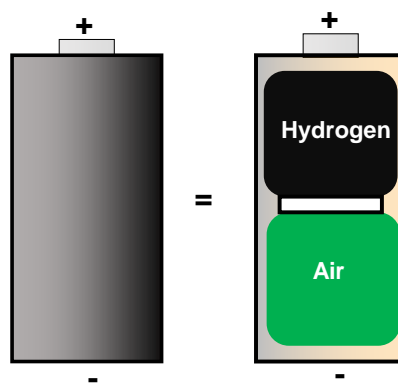


Figure 1.2. Schematic diagram of battery and non-combustive fuel cell.

This technology is more than 150 years old and it shows boundless promises in fuelling vehicles and providing energy for domestic applications. One fuel cell is equivalent to a 1 volt battery. We can easily produce large amps of electricity by staking of a large number of individual fuel cells as shown in Figure 1.3.

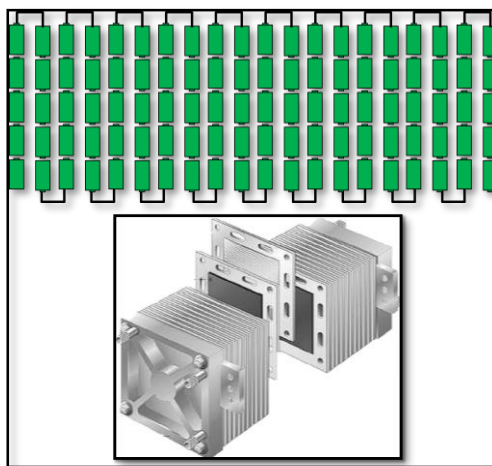


Figure 1.3. A schematic representation of the Fuel cell Stack (Adopted from Jolt Plastics innovation).

Renewable Fuel cells (RFCs) constitute of mainly two sections- one is fuel cell stack and another is electrolyser stack⁶ (Figure 1.4). Generally, H_2 behaves as the energy carrier which reserves renewable electricity by electrochemical splitting of water into the corresponding H_2 and O_2 in an ‘electrolysis mode’. This H_2 is further stored on-site and for the time being it is consumed; providing electricity whenever it is needed. Furthermore, RFCs are exclusively used in different vehicles, aircrafts and supply power for residential as well as commercial purposes. Being economically inexpensive, RFCs constitutes are used for centralized grid energy storages. Among the different fuel cells, H_2 - O_2 - H_2O fuel cell⁷ is a fascinating candidate for future renewable energy conversion technology; where electricity is generated from the chemical energy of H_2 , used as flexible energy carrier⁸.

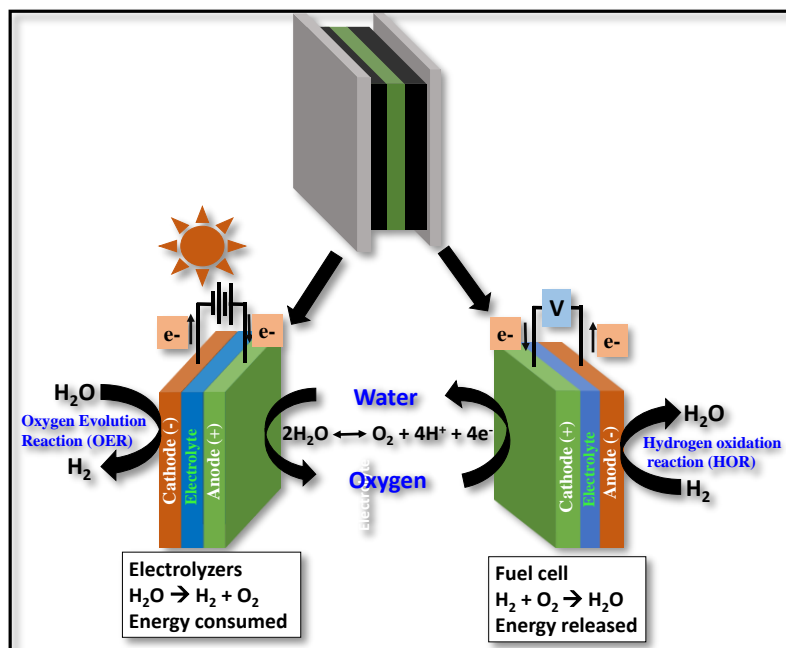


Figure 1.4 Schematic diagram of a RFCs showing the two main components: Fuel cell and electrolyzers.

The electrolyser can generate fuels from renewable resources (i.e. water) and store the electrical energy as of chemical bond. Depending upon the nature of the electrolytes, RFCs are generally classified into two types; (1) proton exchange membrane (PEMFC) and (2) anion exchange membrane (AEMFC). The PEMFC system is generally worked under acidic electrolytic (i.e. lower pH) environment wherein the protons (H) are generated from electrolytes or products of anodic reactions, exchanged between anodic and cathodic compartments⁹. AEMFC system is mainly worked under alkaline electrolyte environments (i.e. higher pH) and exchanges hydroxyl anion between anodic and cathodic compartment.¹⁰

1.3.1. Parts of Fuel cell:

These are the following four parts constitutes the FCs.

a) Anode: Anode is the negative pole of FCs and it uptakes the electrons that are generated from the oxidation of H_2 molecule and can be transported through an outer circuit.

b) Cathode: Cathode is the positive side of FCs which is in charge for conducting the electrons back from the outer circuit again, produced reduced oxygen and then recombines oxidized hydrogen to form water.

c) Electrolyte: It is a solid or liquid part of the Fuel cell that helps to transfer charger between the two electrodes.

d) Catalyst: Catalysts are special class of materials that facilitates the reaction of oxygen and hydrogen. In general, the thin film coated platinum on carbon paper or cloth acts as catalyst surface

1.3.2. Types of Fuel cell

There are several types of fuel cell till now invented. Few of them are as following

(a) Proton Exchange membrane fuel cell (PEMFC)

(b) Alkaline fuel cell (AFC)

(c) Phosphoric-acid fuel cell (PAFC)

(d) Solid oxide fuel cell (SOFC)

(e) Molten carbonate fuel cell (MCFC)

But PEMFC has some advantages over the other fuel cells such as its low operating temperature, higher power efficiency than the other fuel cell, small in size, thus easily portable, cheap.

1.4. Various Reactions Involved in RFCs

The RFCs mainly consist of four different reactions namely hydrogen oxidation reaction (HOR), oxygen reduction reaction (ORR) in fuel cell stack and hydrogen evolution reaction (HER), oxygen evolution reaction (OER) in water electrolyzer stack. All the

electrochemical processes occurred in the RFCs and corresponding over potentials are shown in Figure 1.5.

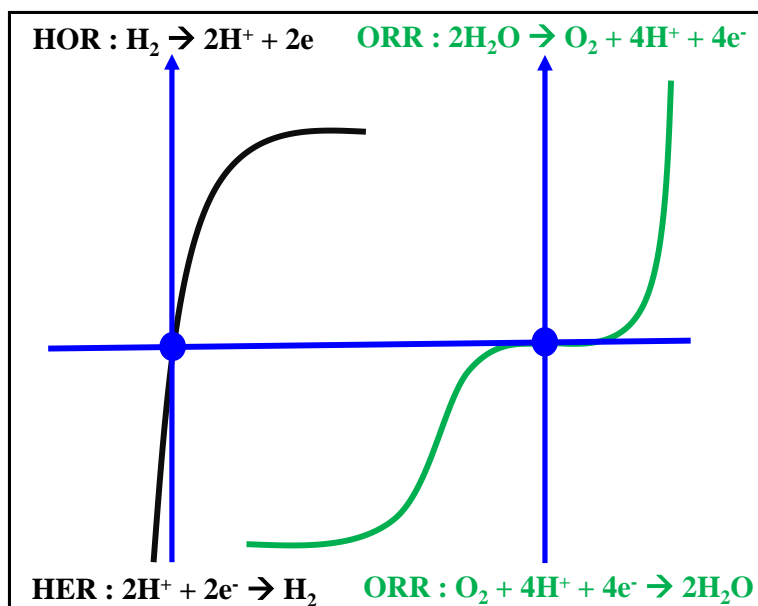


Figure 1.5. Various electrochemical processes with polarisation curves (Adopted from Chem. Soc. Rev., 2015, 44, 2060 with permission of The Royal Society of Chemistry).

The sequential steps occurs in FCS are shown in Figure 1.5, Figure 1.6 and demonstrated as follows:

First step: Hydrogen fuel and oxygen is directed to anode and cathode compartment.

Second step: In anode, hydrogen get oxidised into hydronium ion (H_3O^+) which is known as hydrogen oxidation reaction (HOR).

Third step: In the cathode compartment oxygen is reduced into hydroxide ion (OH^-) which is known as oxygen reduction reaction (ORR).

Step IV: The positive H_3O^+ ions from anodic side cross the PEM membrane and combined with OH^- ion (anodic compartment) to generate water.

Step V: Electron is moved through external circuit from anode to cathode and generated electricity.

The half- cell reactions have been discussed as follows:

1.4.1. Hydrogen Oxidation Reaction:

In the PEMFCs, H_2 and O_2 are used as reactant for HOR at anode and ORR at cathode in strong acid environment (Figure 1.6). PEMFCs cell has higher power effectiveness and eco-friendly due to their more ability to convert H_2 into H_2O . But it requires suitable catalyst for this process, else the process will be slow and required higher potential. The trend of activity is followed the order $Pt > Ir >> Rh > Pd$ ^{11,12}. Platinum being a precious metal, can promise a sensibly decent HOR performance in significantly less loading of ($\leq 0.05 \text{ mg}_{Pt} \text{ cm}^{-2}$) at the anode side of PEMFCs. But due to the sluggish kinetics, ORR occurred at the cathode side requires a high loading of Pt ($0.2\text{--}0.4 \text{ mg}_{Pt} \text{ cm}^{-2}$). Therefore, it creates a bottlenecks of commercialization of PEMFCs and currently suffers from the lack of cathodic electrocatalysts with high activity, stability, and low cost. Compared to the PEMFCs based technologies, AMFCs or alkaline electrolyzer are exceedingly attention-grabbing as highly active, earth plentiful and inexpensive transition metal catalysts for ORR and OER are available in alkaline media^{13,14}. Another benefit of AFCs over PEMFCs is much higher stability of transition metal catalysts towards ORR and OER in basic condition^{15,16}. However, even for the commercial Pt/C electrocatalyst the HOR kinetics in alkaline media is two orders of magnitude lower than that of in acidic media and this remains a great challenge to the scientific community. Therefore, it requires a high stocking of Pt at the anode of AMFCs to achieve a considerable activity.

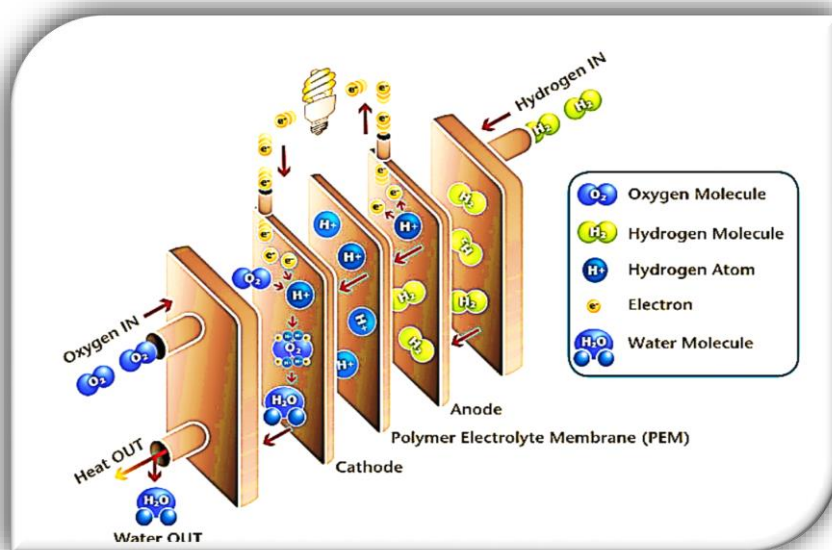
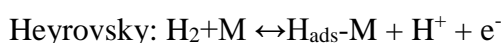


Figure 1.6. Schematic representation of PEMFCs (Adopted from Fuel Cell Store, USA)

Thus, extremely effectual HOR catalysts are of prime important for the development of AFCs and alkali electrolyzers till now. The insights of HER/HOR in basic media should comprehend for the advancement of new effective HER/HOR catalysts for AMFCs and alkaline electrolyzer. Two conflicting mechanisms are reported so far¹⁷⁻²² for the lower performance of HOR in basic media – (1) influence of hydrogen binding energy (HBE) and (2) influence of OH⁻ adsorption (oxophilicity) of the metal. Acidic media, HOR/HER follows via either Tafel-Volmer or Heyrovsky-Volmer mechanism^{17,18, 23}.



Therefore, in acid media, undoubtedly HBE is the foremost descriptor for HOR/HER^{18, 24,25}.

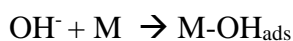
In alkaline medium the reaction proceed via following steps:



It is not clear of the role OH^- ion in alkaline media²⁶. Several scientific community recommended that proton (H^+) is formed from desorption of H_{ads} and then quick recombination of H^+ and OH^- ions to form water (Figure 1.7 a, b).



Thus, in this mechanism like acid medium HBE is the prime descriptor for HOR/HER in basic media^{11, 27-29}. A different possibility is also exist here. Catalyst surface can adsorb OH^- ions to form OH_{ads} species which can react with neighboring H_{ads} to generate water molecule.



If the catalyst surface adsorbed OH^- ions then reaction between H_{ads} and OH_{ads} occurs through the bi-functional mechanism. Thus, the catalyst surface with higher OH^- adsorption will heighten the HOR activity in basic media^{20,30} (Figure 1.7 c and d). Therefore, either HBE or oxophilicity of the catalyst is the main descriptor for the HOR in basic media. Y. Yan^{18,27} *et al.* have revealed that HBE is sole descriptor for HER/HOR and volcano-shaped curves were acquired when HBE and HER/HOR exercises of various monometallic metals surface are plotted. Durst and coworkers³¹ additionally demonstrated higher HBE can be connected by the poor HER/HOR action in basic media.

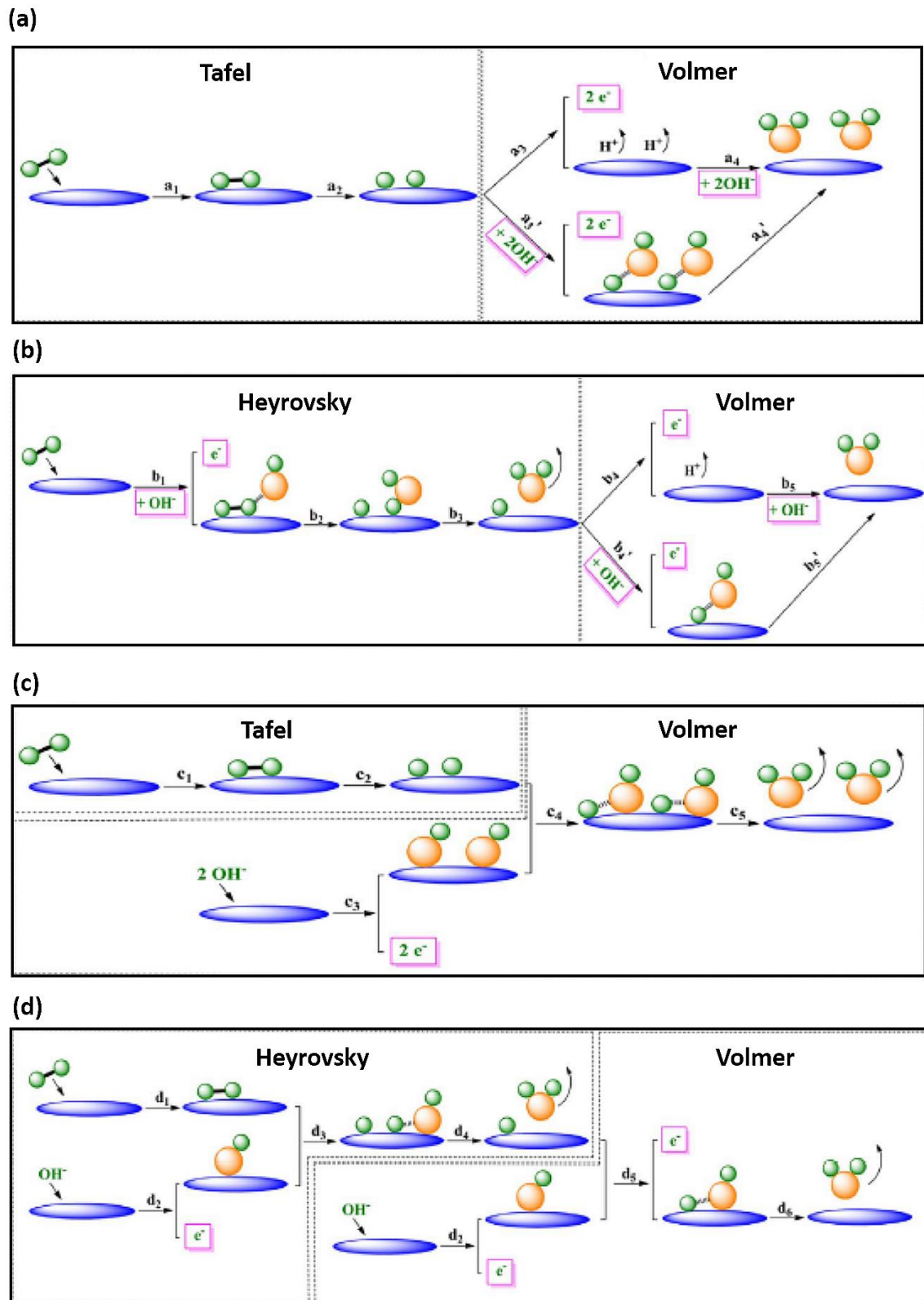


Figure 1.7. (a-b) Possible reaction mechanism of HOR in alkaline condition with effect of OH^- ion in electrolyte and (c-d) effect of adsorbed OH_{ad} on the surface of catalyst (Adopted from Nano Energy 2018, 44, 288 with permission of The Elsevier).

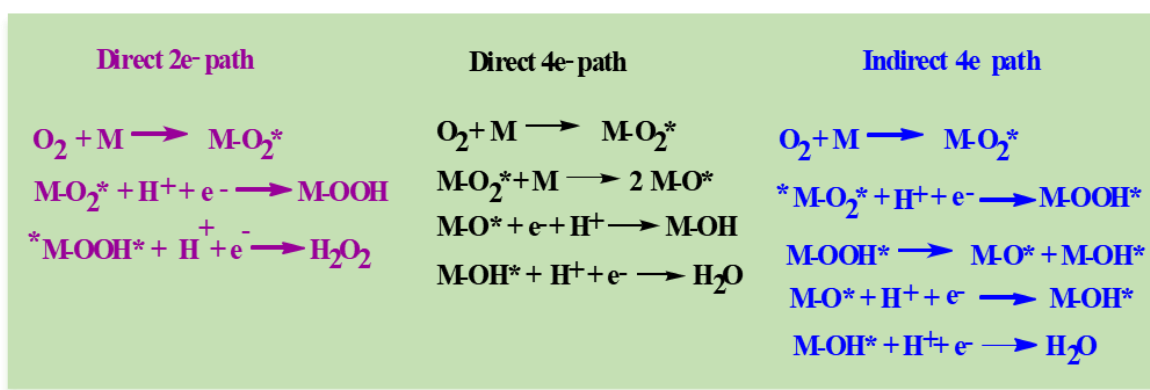
J. X. Wang³² *et al.* have shown due to the alteration of total HBE to a lesser value, Ru-Pt core-shell nanoparticle can enhance multiple times of HOR/HER mass activity with contrast to bulk Pt. Wang and coworkers²⁸ have expressed HOR action of PtRu composite impetus in basic media is two-fold than that of Pt in spite of the fact that on-set potential for OH⁻ adsorption of Pt is lower recommending that oxophilicity of metals doesn't assume a noteworthy job in HOR activity. S. S Wong³³ *et al.* has reasoned that the electronic impact forced on Pt by Ru considerably control HBE values which governor the HOR action. As of late, our group²⁹ additionally demonstrated that HBE is the singular descriptor for HOR in basic media for Pd-CN_x composite. Then again, D. Strmcnik *et al.*²⁰ revealed that oxophilicity of metals assumes noteworthy job to decide the HER/HOR activity in basic medium. They have recommended that the poor HOR movement in basic media is expected to non-accessibility of OH_{ads} species in the impetus surface and furthermore demonstrated that HOR action can be improved by alloying Pt with more oxophilic metals, for example, Ni. Although HOR/HER in alkaline medium were studied in several reports (Figure 1.7 c-d), it is still not flawless why the HOR activity in basic medium is poor. Thus there is a need of methodical revision to apprehend the HOR/HER in alkaline medium.

1.4.2. Oxygen Reduction Reaction:

Electrochemical oxygen reduction reaction (ORR) is an important cathodic half-cell reaction in fuel cells. ORR is the main reaction for PEMFCs including direct methanol or formic acid fuel cell (DMFCs/DFFCs), Zn-Air batteries and Li-Air batteries. Platinum is the best known catalyst for the ORR. But, the high cost and scarcity of platinum prevent its wide spread commercialization. It is important to develop ORR active cathode for commercialization of fuel cell. Enormous efforts have been spent during the past decades on

finding an economically viable novel and better catalyst for this purpose. Recently noble metal nanoparticles were found to be most promising electrocatalyst due to their high surface area and their cost effective of production since small amount of metal are used in their synthesis^{34,35}. Pt_3Ni ³⁶ and Pt_3Co ³⁷ alloys have shown better performance than pure Pt. Research so far attributes the improved activity to a change in band structure. Maintaining low costs is often the key in the universal adoption of a technology, and the use of platinum based catalysts is in direct conflict with this principle. Two approaches have been proposed to rectify the issue regarding the high cost of platinum: (1) increase the utilization or effectiveness of platinum catalysts, so less platinum need to be used, or (2) completely replace platinum catalysts with non-precious alternatives. In the long term, it is far more desirable to take the second approach and completely replace platinum with non-precious metal catalysts as the first approach does not address the issue of limited world supply of platinum. The development of low cost of highly active ORR catalysts consisting of abundantly found materials will greatly benefit the commercialization of PEM fuel cell and metal-air battery technologies. A common approach to developing low cost active ORR catalysts is the use of high surface area carbon along with a transition metal and nitrogen pore filler. Pyrolysis of the carbon/transition metal/nitrogen precursor results in active ORR catalysts exhibiting high stability in both alkaline and acidic conditions. A second approach is to synthesize transition metal macrocyclic molecules but these macrocycles are not stable in acidic conditions without adjusting the molecular structure of the macrocycle. The main

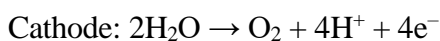
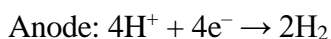
goal of this research is the development of highly active nanostructured non-precious ORR catalysts for both acidic and alkaline conditions. The electrochemical oxygen reduction reaction (ORR) is a fundamental cathodic process occurred in fuel cells. The ORR is a complex multi electron transfer reaction with involving different elementary steps with different intermediates. The reaction steps in acidic medium are as follows:



Oxygen can electrochemically reduce either directly to water via (direct 4e reduction, $O_2 + 2H_2O + 4e^- \rightarrow 4OH^-$) or through the formation of H_2O_2 (2e reduction, $O_2 + 2H_2O + 2e^- \rightarrow OH_2^- + OH^-$) and then this peroxide can be reduced to water (series 4e pathway, $OH_2^- + H_2O + 2e^- \rightarrow 3OH^-$) or chemically decomposed on electrode³⁸. In this regard production of H_2O_2 is not desirable for fuel cell as it corrode the membranes in cell assembly. Sometimes, it can also undergo one electron pathway to form superoxide species (O_2^-) in non-aqueous aprotic solvents or in alkaline medium. Several efforts have been made for preparation of noble metal based catalysts to reduce the ORR over-potential as well as the H_2O_2 formation.

1.5. Electrolyser:

Electrolysers, split water into hydrogen and oxygen by the means of using electricity. It happens through an electrochemical reactions ($2 \text{H}_2\text{O} \rightarrow 2 \text{H}_2 + \text{O}_2$) that does not require any heavy machinery or revolving parts, which makes it extremely hassle free. It is entirely trustworthy and can deliver extremely pure hydrogen in a non-dirtying way as far the source of the electric is sustainable. The ultrapure hydrogen created from an electrolyser is ideal for use in the energy productions. There is not a much deference in an electrolyser and hydrogen fuel cell, aside from the reaction that happen in the anode and cathode are switched. In a fuel cell, the anode is the place hydrogen gas is devoured, and in an electrolyser, the hydrogen gas is delivered at the cathode. Electrical energy is extremely necessary for the electrolysers to finish the reactions. In ideal case, the electrical energy required for the electrolysis reaction should originate from sustainable power sources, for example, wind, sun based or hydroelectric sources. A few instances of uses in which electrolyzers would be especially in fuel cell-controlled vehicles, and convenient gadgets. As illustrated in Figure 1.8 electrolysers do have a positive (anode) and a negative (cathode) terminal, like a battery. H_2 gas is produced on the negative terminal whereas O_2 gas is produced on the positive (Figure 1.8). We can collect these gases in empty cylinders and use them in our needs. These are the following reactions occur in electrolyzers:



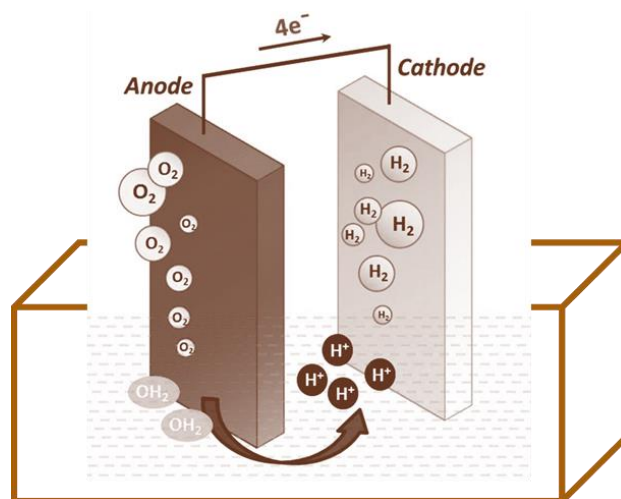


Figure 1.8. Schematic diagram of water electrolyser (Adopted from *Nanoscale*, 2016, 8, 15033-15040 with permission of The Royal Society of Chemistry).

The electrolyser technology can be classified into two categories: 1) Proton electrolyte membrane water electrolyser (PEMWEs) and 2) Alkaline electrolyte membrane water electrolyser (AEMWEs). The first commercially available AEMWEs has 40-80% efficiency of current density in-between $250\text{-}500\text{ mA cm}^{-2}$ whereas PEMWEs has the same efficiency with the current density ranges from $1500\text{ to }2000\text{ mA cm}^{-2}$. Although both the processes have same efficiency, PEMWEs has several advantages over AEMWEs because of its higher current density, low operational temperature and it has produced high purity of H_2 . In addition, cheap material is being used in AEMWEs unlike the case of PEMWEs. Therefore, both the processes are equally vital for the enlargement of WEs technology.

1.5.1. Hydrogen Evolution Reaction (HER):

Hydrogen is well known as one of the greenest fuel and energy bearer. Yet, creation of unadulterated hydrogen is a difficult undertaking. Electrocatalytic water splitting is one of the sustainable method to deliver unadulterated H_2 . HER occurs in the cathode and Pt, undoubtedly is the most vigorous catalyst in acid. The main drawback of Pt-based catalysts

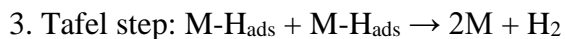
are high price, scarcity and poor stability of in acid media that hinder its wide spread applications. This drawback can be removed by using low cost transition metal catalyst or alloying transition and noble metal or minimum use of noble metal for desired activity. So it is the important to develop Pt nanostructured material with varying size and morphology for their high catalytic activity and high stability so that a very low amount of catalyst serve a desired amount of hydrogen generation. Several transition metal catalyst is also possess good HER activity in acidic medium^{39,40} such as cobalt phosphide (CoP), iron phosphide (FeP), Molybdenum phosphide (MoP), molybdenum sulphide (MoS₂), molybdenum selenide (MoSe₂). Though Pt supported on carbon is the best catalyst in acidic medium but its activity is 2 orders lower in base¹². Suggested by the reaction chemistry, there is an additional energy barrier present in alkaline medium for HER and the electrocatalyst has to overcome this barrier⁴¹. It has been experimentally found that the catalyst with an additional active component which enhance the water dissociation step has higher HER activity in alkaline medium. For instance Markovic group²⁰ has established the Ni(OH)₂ ornamented on Pt catalyst to increase the HER activity of Pt by depressing the energy barriers for water dissociation. Several single non noble metal or mixed non noble/transition metal based catalysts was well known for their HER activity in alkaline medium. The HER reaction mechanism are as follows:

HER mechanism in acidic condition:

1. Volmer step: $M + H_3O^+ + e^- \rightarrow M-H_{ads} + H_2O$
2. Heyrovsky step: $M-H_{ads} + H_3O^+ + e^- \rightarrow M + H_2 + H_2O$
3. Tafel step: $M-H_{ads} + M-H_{ads} \rightarrow 2M + H_2$

HER mechanism in alkaline condition:

1. Volmer step: $M + H_2O + e^- \rightarrow M-H_{ads} + OH^-$
2. Heyrovsky step: $M-H_{ads} + H_2O + e^- \rightarrow M + H_2 + OH^-$



M is the catalyst surface.

1.5.2. Oxygen Evolution Reaction (OER):

Water electrolysis is extremely inhibited by the kinetically sluggish OER as it is not favourable both kinetically and thermodynamically. A huge amount of struggles have been dedicated to improve catalysts for the OER process. Systematically OER in acid solutions was studied by Miles and Thomason and they showed the activity trend of OER is Ir > Ru > Pd > Rh > Pt > Au > Zr > Ti > Ta⁴². In acidic medium noble metal Ru, Ir-oxide and their compounds show best OER activity and the activity order is Ru > Ir > Pt. But IrO₂ shows better stability than RuO₂. Hence IrO₂ is considered as state of art catalyst in acidic medium for OER. On the other hand, 3d transition metals like iron, cobalt, nickel etc. catalyze the better OER activity in alkaline medium than under acidic medium⁴³. OER activity in alkali medium for transition metal catalyst depends on the OH–M^{2+δ} bond strength. The OER activity trend is as NiO_x > CoO_x > FeO_x > MnO_x as observed by Trotochaud *et.al.* and their catalytic activities for OER is directly proportional to the OH–M^{2+δ} bond strength (0 < δ < 1.5) with the order of Ni < Co < Fe < Mn⁴⁴. This bond strength can be tweaked by alloy formation. Such as alloying Ni with Cu and Mn decreases the OER activity while doping of Co and Cr increases the OER activity. Similarly it is established that tailoring of Fe ominously upsurges the OER activity. As for example Ni-Fe film prepared by Louie and Bell shows when 40% Fe is present in the film then OER activity is 2 times higher with compared to Ni film and 3 times higher with compared to a Fe film⁴⁵. Oxides with layer structure including metal hydroxides (M(OH)₂; M = transition metals) and metal oxyhydroxides (MOOH) generally own very high electrocatalytic OER activity. The crystal structure is stack layered conformation, sandwiching with proton between layers. Then the transition metals are situated in the octahedron centre with oxygen anions on the corners as [MO₆] subunits and these subunits

again linked to individually through sharing the edges to form 2-D layers. Consequently, layer structure oxides are known as layered double hydroxides (LDH), and this family is typically cobalt- and nickel based composites because of their outstanding OER activity. One reason behind this is the poor stability of the transition metal based systems under acidic conditions as it is known to leach out in the acidic electrolyte solution.

Unlike HER, OER mechanism is more complicated and involved more number of reaction pathways in both acidic as well as alkaline medium. In alkaline condition, all the proposed mechanism begin with the elementary step of hydroxide co-ordination on the active catalytic site followed by other elementary reaction pathways. The energy barrier associated with each and every elementary step leads to increase in over potential of the catalysts and makes OER more kinetically sluggish. The peroxide intermediate formed on the catalytic interface plays an important role in delivering the di-oxygen molecules during the reaction. The most accepted OER mechanism in alkaline condition is given below⁴⁶.

Overall Reaction	Reaction Pathway	Tafel slope
$4 \text{OH}^- \rightarrow \text{O}_2 + 2\text{H}_2\text{O} + 4\text{e}^-$ Alkaline medium	(i) $\text{S} + \text{OH}^- \rightarrow \text{S-OH} + \text{e}^-$	118
	(ii) $\text{S-OH} + \text{OH}^- \rightarrow \text{S-O} + \text{H}_2\text{O} (\text{l}) + \text{e}^-$	39
	(iii) $\text{S-O} + \text{OH}^- \rightarrow \text{S-OOH} + \text{e}^-$	24
	(iv) $\text{S-OOH} + \text{OH}^- \rightarrow \text{S} + \text{O}_2 (\text{g}) + \text{H}_2\text{O} + \text{e}^-$	17
$2\text{H}_2\text{O} \rightarrow \text{O}_2 (\text{g}) + 4\text{H}^+ + 4\text{e}^-$ Acidic medium	(i) $\text{S} + \text{H}_2\text{O} \rightarrow \text{S-OH} + \text{H}^+ + \text{e}^-$	118
	(ii) $\text{S-OH} + \text{OH}^- \rightarrow \text{S-O} + \text{H}^+ + \text{e}^-$	39
	(iii) $\text{S-O} + \text{H}_2\text{O} \rightarrow \text{S-OOH} + \text{H}^+ + \text{e}^-$	24
	(iv) $\text{S-OOH} \rightarrow \text{S} + \text{O}_2 (\text{g}) + \text{H}^+ + \text{e}^-$	17

1.6. Theoretical Aspect of Electrochemical Reaction:

Electrochemistry expands vastly as the need for sustainable energy increases, thus a huge consideration was rewarded for find out mechanistic pathway of several electrochemical reactions. Sabatier principle in combination with density functional theory (DFT) is a novel way of to understand trends in catalytic activity is. Several studies have been conceded to rationalization of the relative electrocatalytic activities of different

electrode materials in terms of a descriptor. A single parameter called as descriptors which controls the catalytic process. For HER/ HOR and OER/ORR, this descriptor can be represented as the interaction between reaction intermediate and the catalytic surface. When j_0 is plotted vs. $\Delta G_{\max}(U^0)$, a volcano-shaped plot is obtained as shown in Figure 1.9a. Volcano plots play a vital role in electrocatalysis, which was discovered to seventy years ago. Considering Langmuir type adsorption, HER rate expression appeared as a volcano-type plot, where the maximum activity is observed at $\Delta G_{H^*} = 0$ and this is the most common shape. If we consider other adsorption models, other shape of these plots are also probable. Volcano plot also resembles the Sabatier principle and it holds that the suitable binding energies for reactive intermediate species will show highest catalytic activity. As shown in Figure 1.9a, intermediates activation on the surface is problematic when the intermediates bind too weakly (fall into the right side of the plot). However if they bind too strongly (fall into the left side of the plot), all available surface sites are occupied (poisoning effect). So, considering the above fact more favourable is metal surface with moderate binding energies. For HOR/HER, two competitive processes are happened. One is chemical adsorption, other is desorption of H^* atoms on the surface of the electrode and these two simultaneously control the rates of H_2 production (Figure 1.9 b, c). Therefore, G_{H^*} value is considered as the main descriptor for HER. Proposed volcano-type plot associated of J_0 for HER with the thermodynamically derived ΔG_{H^*} is shown in Figure 1.9c. This volcano plot shows a maximum peak at $\Delta G_{H^*}=0$ with two symmetrical linear branches towards $\Delta G_{H^*}>0$ and $\Delta G_{H^*}<0$. However, obtaining the exact thermodynamic value of ΔG_{H^*} is the main challenge regarding the construction of volcano plot. Nørskov *et al.*⁴⁷ first time demonstrated DFT study for the calculation of exact ΔG_{H^*} for different systems for an constructed volcano plot for different metal catalysts as shown in Figure 1.9c which clearly shows that the metals (Ag, Cu, Au), positioned at right side of the volcano plot, adsorb hydrogen weakly and those

which positioned at left side (Mo, Nb, W) adsorb H strongly although both the cases exhibit low J_0 value. However, the elements, much closed to maximum peak point show moderate hydrogen adsorption (Pt, Pd, and Rh, have very high values of J_0). Moreover, the activity trends of different systems for different electrochemical processes such as ORR and OER can be described by volcano plot (Figure 1.9d and 1.9e).

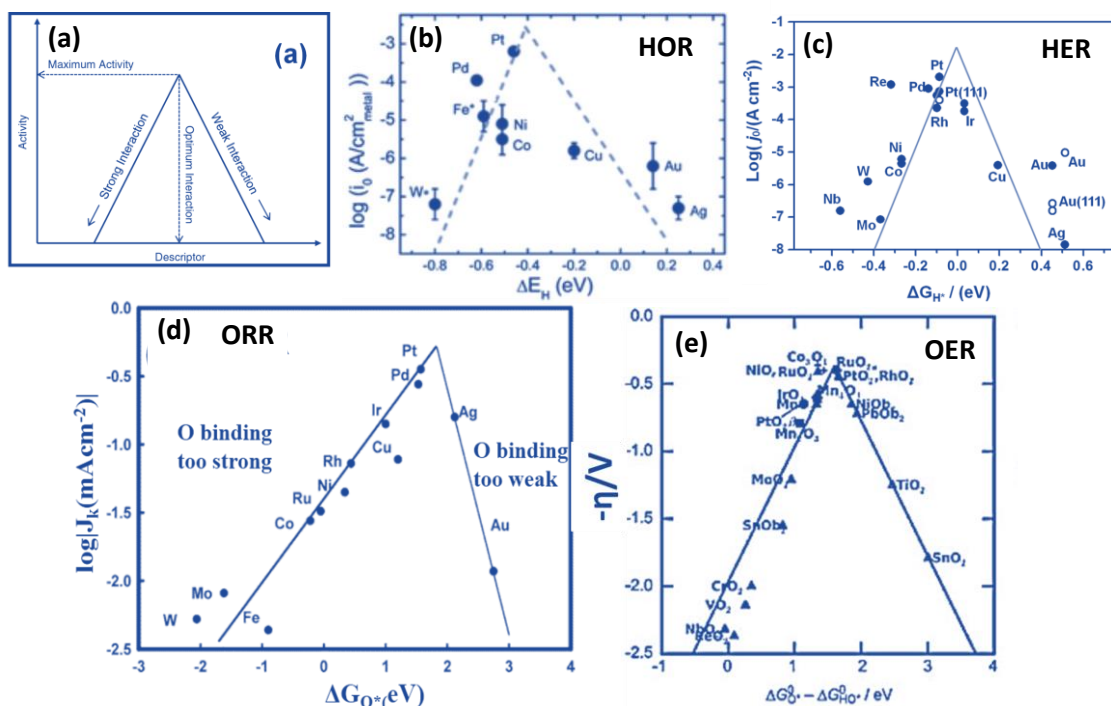


Figure 1.9. Volcano plot for (a) over-all electrochemical processes, (b) HOR, (c) HER and (d) ORR (e) OER. (Adopted from Chem. Soc. Rev., 2015, 44, 2060 with permission of The Royal Society of Chemistry)

In volcano plot, the free energy for OH^* oxidation on catalyst site ($\Delta G_{\text{O}^*} - \Delta G_{\text{HO}^*}$) is used as descriptor for the OER⁴⁸ whereas for ORR^{49,50} the free energy changes for intermediate (O^*) binding (ΔG_{O^*}) is used as descriptor.

1.7. Kinetics of Electrochemical Reaction:

The electrochemical process is all about the transfer of the charge through the interface between electrode and electrolyte solution in an electro chemical reaction. This charge transfer process occur via two main procedures:

1. Faradaic process: in this process charge transfer happened across the interface of electrode and electrolyte.
2. Non-Faradaic process: no transfer of charge across the interface of electrolyte-electrode but the double-layer charging may happen due to some chemical reactions or change in the oxidation states.

Both the faradic and non-faradic process involves at electrode/electrolyte interfaces during any electrochemical process. But, faradic process is the prime importance of study. The overall reaction for faradic process on the electrode surface can be described as:



In an electrochemical reaction, a faradic process can be symbolised as:

$$i_a = FA r_o c_{Ox}$$

Where i_a is current flow from electrode, F is the Faraday's constant (84548 C mol^{-1}), A is the electrode surface area, r_o is the electron transfer rate and c_{Ox} is the concentration of the reactant. Except the rate of the electron transfer from the electrode, all terms, represented here are constant. Furthermore, the rate of the electron transfer is depend on the potentials applied on the electrode. So, in equilibrium state, the potential applied on electrode can be given by

$$\Delta G = - nF\Delta E$$

Where ΔE is the electrode potential, n is the number of electrons transferred and ΔG is the free energy of the activation barrier.

In electrochemistry two important terms are described as follows:

- (a) **Overpotential** (η): It is defined as the difference in electrode potential at equilibrium (E_e) and the potential at a given current density (E_i).

$$\eta = E_e - E_i$$

(b) Charge Transfer Coefficient (α) and Butler-Volmer Equation:

It is defined as the amount of charge transfer at a particular overpotential. The free energy of activation barrier will be defined as:

$$\Delta G_c = \Delta G_{c,eq} + \alpha_c n_e F \eta$$

$$\Delta G_a = \Delta G_{a,eq} - \alpha_a n_e F \eta$$

Where $\Delta G_{c,eq}$ and $\Delta G_{a,eq}$ are the potentials independent activation energy, η is the overpotential applied on electrode F is the faraday's constant, α_a and α_c are the anodic and cathodic charge transfer coefficient. The rate of a reversible electrochemical reaction can be written as:

$$r = k_a c_{ox} - k_c c_{red}$$

Where k_a and k_c are the rate constant of anodic and cathodic process.

According to Arrhenius equation, the rate constant of a reaction is given by

$$k = k_0 e^{-E_a/RT}$$

For anode

$$k_a = k_0 e^{-\Delta G_a/RT}$$

For cathode

$$k_c = k_0 e^{-\Delta G_c/RT}$$

Where k_0 defined as potentials independent rate constant and other terms are defined their usual meaning.

Now putting the value of ΔG_a and ΔG_c we get

$$k_a = k_0 e^{(-\Delta G_{a,eq} + \alpha_a n_e F \eta)/RT}$$

$$k_c = k_0 e^{(-\Delta G_{c,eq} - \alpha_c n_e F \eta)/RT}$$

As the equilibrium activation free energy term is also a potential term, therefore we can write

$$k_a = k_0^a e^{\alpha_a n_e F \eta / RT}$$

$$k_c = k_0^c e^{-\alpha_c n_e F \eta / RT}$$

So now if we put the equation in

$$r = k_0^a c_{ox} e^{\alpha_a n_e F \eta / RT} - k_0^c c_{red} e^{-\alpha_c n_e F \eta / RT}$$

If we transform the rate of the reaction in terms of the current, we get

$$\text{Or } r = \frac{i}{nF} = k_0^a c_{ox} e^{\alpha_a n_e F \eta / RT} - k_0^c c_{red} e^{-\alpha_c n_e F \eta / RT}$$

$$\text{Or } i = nF k_0 (c_{ox} e^{\alpha_a n_e F \eta / RT} - c_{red} e^{-\alpha_c n_e F \eta / RT}) \text{ as } k_0^c = k_0^a = k_0$$

$$\text{Or } i = i_0 (c_{ox} e^{\alpha_a n_e F \eta / RT} - c_{red} e^{-\alpha_c n_e F \eta / RT}) \text{ where } nF k_0 = i_0$$

Here i_0 represented the exchange current density.

So finally we get the classical Butler-Volmer equation:

$$i = i_0 (c_{ox} e^{\alpha_a n_e F \eta / RT} - c_{red} e^{-\alpha_c n_e F \eta / RT})$$

The Butler-Volmer equation⁵¹ is the most fundamental equation for electrochemical kinetics.

The connection between the total current density, exchange current density, transfer coefficient and overpotential (Figure 1.10a) can be correlated by this equation. At higher overpotentials the reaction will be out of equilibrium. Either the anodic or the cathodic current will dominate in the total current density measurement. Then the Butler-Volmer equation will turn into these following forms:

$$\log(i) = \log(i_0) + \frac{\alpha_c \eta F}{2.303 RT} \quad \text{at higher cathodic potentials}$$

$$\log(i) = \log(i_0) - \frac{\alpha_a \eta F}{2.303 RT} \quad \text{at higher anodic potential}$$

These two equations are called as Tafel Equations. The logarithm of the current density ($\log|i|$) vs overpotential plot will give a linear slope, is called Tafel slope (Figure 1.10b)⁵².

Exchange current density (i_0) and Tafel slope $\frac{2.303 RT}{\alpha_{a/c} n_e F}$ can be obtained from Tafel analysis.

The Tafel slope is expressed in units of mV decade⁻¹. The equation may be written in different way as:

$$\eta = a + b \log i_0$$

where a and b are the constant.

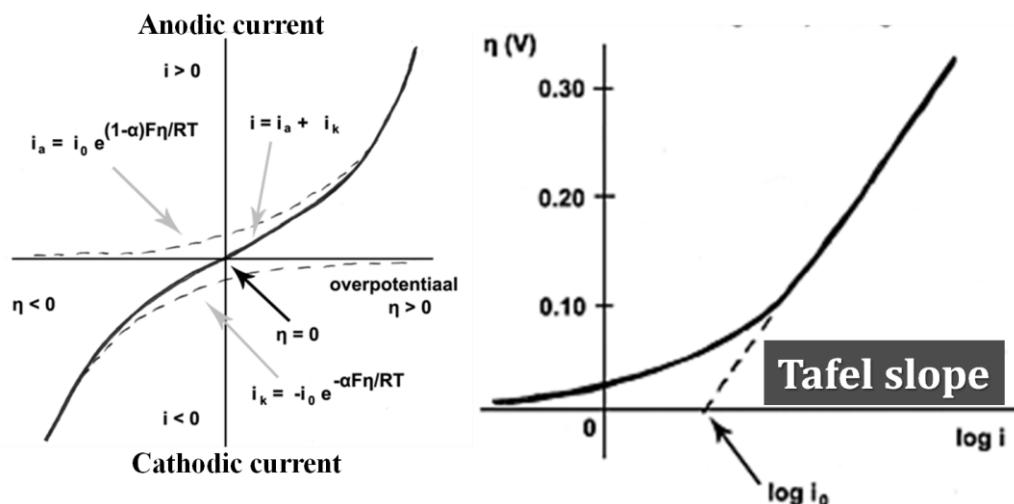


Figure 1.10. (a) Butler-Volmer plot, (b) Tafel Plot for electrochemical reaction. (Adopted from the Global Climate and Energy Project by Thomas Jaramillo, Stanford University)

The Tafel slope determines the electrocatalytic performance of the catalyst in a particular electrochemical reaction over a potential ranges. Smaller the Tafel slope signifies the faster rate of catalysis i.e. required lower potential for a particular current density. The theoretical Tafel slope value for a multistep reaction, comprising a series of elementary steps can be represented by:

$$b = \frac{2.303 \times RT}{\alpha \times F}$$

Where Temperature (T), charge transfer coefficient (α) and R is gas constant, F is the Faraday. The exchange current density (i_0) is equivalent to the rate constant of a heterogeneous catalyst. It provides both the thermodynamics as well as the kinetic information. Higher i_0 value defines no activation barrier (faster rate) in electrolysis reaction whereas; low i_0 reflects the high activation barrier (sluggish reaction).

1.8. Glucose and H₂O₂ sensing

Diabetes mellitus is more commonly known as diabetes, considered by high blood sugar and has become a widespread epidemic now a days. It is one of the reasons of disability in the 3rd – world country and greatly accountable for numerous hitches such as frequent urination, heart disease, increase thirst and blindness. Conferring by the World Health Organization (WHO), roughly 350 million people globally are being suffered from diabetes and, based on present forecasts, diabetes will be the 7th foremost cause for death by 2030. Controlling diabetes is undoubtedly to be one of the most thought-provoking health problems in current scenario. Diabetes mainly occurs because of either insufficient production of the insulin in the body (Type 1 diabetes) or by the failure to usage produced insulin by the body (Type 2 diabetes). So far, regular monitoring of blood glucose in diabetic patient is most vital in order to control glucose concentration⁵³. Therefore, it's of prime importance to develop a fast, reliable and sensitive glucose detector to perceive the blood sugar level and reducing the chance of sickness or further complications. The many years evolution of enzymatic glucose sensors can be concise mostly into three generations⁵⁴. The initial enzymatic detection of glucose was established using glucose oxidase (GO_x) enzyme in the 1960s validated by Lyons and Clark⁵³. In this method amount of oxygen intake by the enzyme-catalysed reaction was examined in this method. This was again improved by Hicks and Updike followed by Guilbault and Lubrano⁵³. They developed a different way to detect glucose based on the detection of hydrogen peroxide. The detection of glucose was all about the catalytic oxidation of glucose by the help of oxygen and an active component of GO_x (i.e. flavin adenine dinucleotide). This produce the redox product of glucolactone and hydrogen peroxide (Figure 1.11). However, main constraints of this generation enzymatic glucose sensors are: strong oxygen dependency, the co-existence of redox-active species

that could interfere in the detection such as amino acids, uric acid, ascorbic acid and other drugs.

The second generation glucose sensor was introduced in 1980s, constructed by using mediators and it is able to simplify electron transfer in the reaction medium (Figure 1.11). However, owing to the possible bio-toxicity of mediators, in-vivo operation of the second generation glucose sensor is questionable. Furthermore, the existence of other redox-active species in blood also affects the accuracy of the glucose sensor as these redox species possibly participates with the mediators.

The third generation of glucose sensor eliminated the employment of the mediator and it work on the direct electron transfer between the electrode and the enzyme. Immobilization of the GO_x is essential here and some porous materials have serve the purpose for immobilisation. Though third generation sensors showed some enhancement over their first and second generation sensors (Figure 1.11), their use still limited from the enzyme's activity which is very sensitive with air, moisture, temperature. The thick enzyme layer also create problems for effective electron transfer.

However, due to several drawbacks of the first, second and third generation glucose sensors, additional progress of glucose sensor is highly expected. This has introduced the glucose oxidation directly on the electrode surface. This is called as non-enzymatic glucose (NEG) sensors and categorises as fourth generation of glucose sensor technology. A tremendous effort is invested on NEG sensing in world-wide, as proved by the whopping number of publications over recent years.

1.8.1. Mechanism of glucose oxidation

Enzymatic sensing of glucose is mainly based on the enzyme, GO_x which is acted as a catalyst, but in NEG sensors, surface atoms themselves performed as the electrocatalysts. In

NEG sensing, electrocatalysts existing at the electrode surface are the prime reasons for the detection limit of glucose sensing.

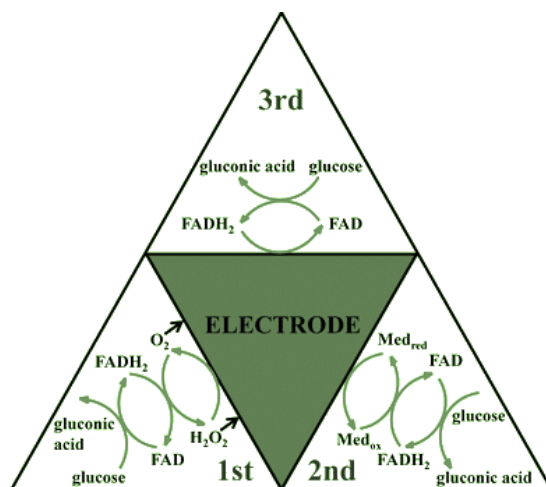


Figure 1.11. Schematic representation for first, second and third generation enzymatic glucose oxidation. (Adopted from Mater. Sci. Eng. C 2017, 70, 1018 with permission of The Elsevier)

To explain the glucose oxidation mechanism, two models have been proposed mainly till now. The first model is familiar as activated chemisorption model, was proposed by Pletcher⁵⁵. According to this model, the glucose molecules adsorption take place on the surface of the electrode initiated the oxidation step by formation of a bond with the glucose molecules and electrode surface. Now, the H-atom besides to the hemiacetal carbon of glucose (see Figure 1.12a) is extracted. This H-atom bonds with the same electrode surface at a position adjacent to the bound glucose. Thereby desorption of the glucose molecule occurs due to the dropping of the glucose–metal bond strength occurred due to the change in the oxidation state of the glucose molecule and metal electrode. The second model, is known as ‘Incipient Hydrous Oxide Adatom Mediator’ (IHOAM) model, proposed by Burke. This model⁵⁶ was originally based on the opinion that the active metal atoms with low lattice stabilization energy on the electrode surface, can improved the reactivity. An incipient hydrous oxide (OH_{ads}) layer is made due to the pre-monolayer oxidation step of

catalyst surface atoms, which is supposed to facilitate the glucose oxidation at the catalyst surface. Figure 1.12b shows a schematic illustration of the IHOAM model. Although both of these models are not widely recognised till now but they can still be used to enlighten glucose oxidation mechanism for noble metal electrodes such as Au and Pt. But these explanations are not fully valid to several transition metals electrodes. Redox centres of the transition metals can describe the glucose oxidation on such metals.

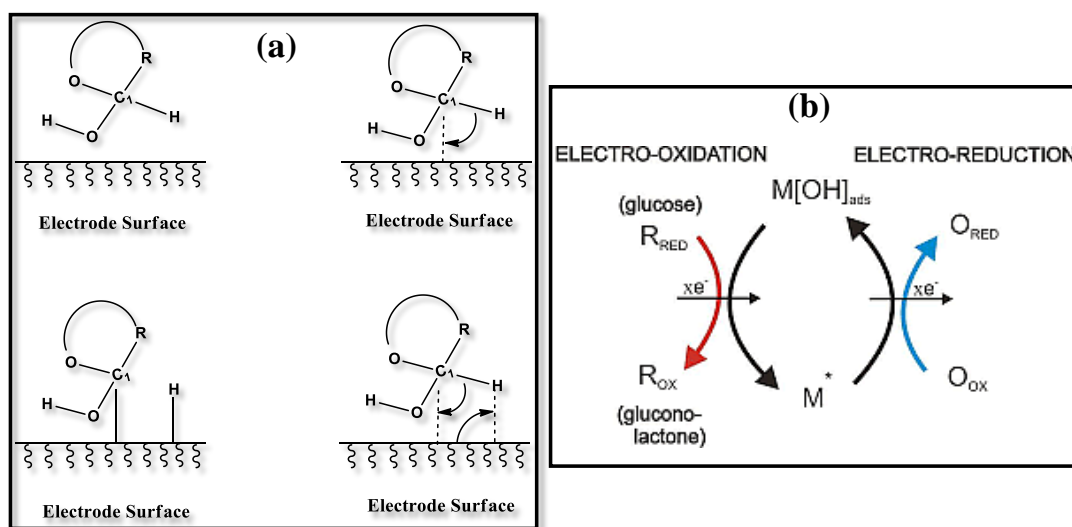


Figure 1.12. A schematic representation of (a) adsorption theory with adjacent adsorption site of nanostructured electrode and (b) IHOAM model. (Adopted from *Anal. Chim. Acta* 2018, 1033, 1 with permission of The Elsevier)

1.8.2. Sensing of H₂O₂

Sensitive, selective H₂O₂ detection by fast and trustworthy methods is essential in many grounds such as medical diagnostics, liquid-fuel cell, chemical, fabric and food industry etc. H₂O₂ is takes part in quite a few biological processes and is one of the vital side products of several enzyme-catalysed reactions in organism. It also plays a vital role as a waving molecules in several biological processes such as immune cell activation, apoptosis etc. Conventional techniques such as titration, fluorometric, chemiluminescent,

electrochemical methods are available for determination of H_2O_2 but electrochemical H_2O_2 sensing can offer a rapid, sensitive and cost effective means⁵⁷. CNT, graphene and metal-metal oxides, metal hexacyanoferrates shows promising activity towards H_2O_2 sensing.

1.9. Removal of Dye

Textile industries expel a lot of dye stuff in the environment creating major pollutant, as organic dye molecules are carcinogenic in water bodies, therefore there is a need to treat the containment of waste water. Not just the textile industries but paper industries, leather tanning, food industries and hair coloring industries in addition increase the concentration of these organic molecules in our environment, therefore it is major challenge to degrade it. Dye has a several adverse effect on human being, plant species and aquatic animals and environment. It is hazardous, carcinogenic, interrupt photosynthesis and increase the COD & BOD⁵⁸. This became an inspiration or motivation for photocatalytic dye degradation. Dyes can be removed from water by either adsorption or by degradations. It is also important of regeneration of the catalyst after treated with dyes. But it is difficult to regenerate dyes after adsorption. Hence degradation method is more fruitful. Dye stuffs also became one of the best candidate to study photocatalytic properties. Dyes are classified in the chemical entity of chromophore. For dye degradation purpose, thiazine has been mostly studied (mostly methylene blue 37%) then are xanthane (consisting of Rhodamine B) and then there are azo dyes, though it is mostly azo dyes which has significant contribution in acting as pollutant in the environment. TiO_2 was one the initial material for photocatalytic dye degradation though it showed activity only in the UV region⁵⁸. UV consist of very low percentage of solar spectra that appears on earth's troposphere, therefore it is preferable for the catalyst to show good visible light activity, also UV light is harmful for most species on earth. Doping the material with different impurities is method to reduce the band gap of the material to make it visible light active for the purpose of photocatalytic degradation. Initially TiO_2 was

doped with different nonmetallic element like nitrogen, carbon, sulphur and their composites⁵⁹⁻⁶⁰, also by different transition metal⁶¹⁻⁶² and coupling with photocatalysts of other semiconductor to achieve desired band gap⁵⁸. Doping can cause for some problem in catalyst regeneration due to the leaching process. Another semiconductor material carbon nitride shows a visible band gap and well known for its photocatalytic activity such as photocatalytic water splitting.

1.9.1. Mechanism of Dye degradation

Dye degradation takes place with two mechanism, indirect mechanism and direct mechanism. In direct mechanism imitate from photo excitation process where photo electron are excited from valence band to conduction band leading to creation of holes (h^+) and net result is electron hole pair (Figure 1.13). The hole react with water to form OH radicals which extremely reactive species and degrade the adsorbed dye.

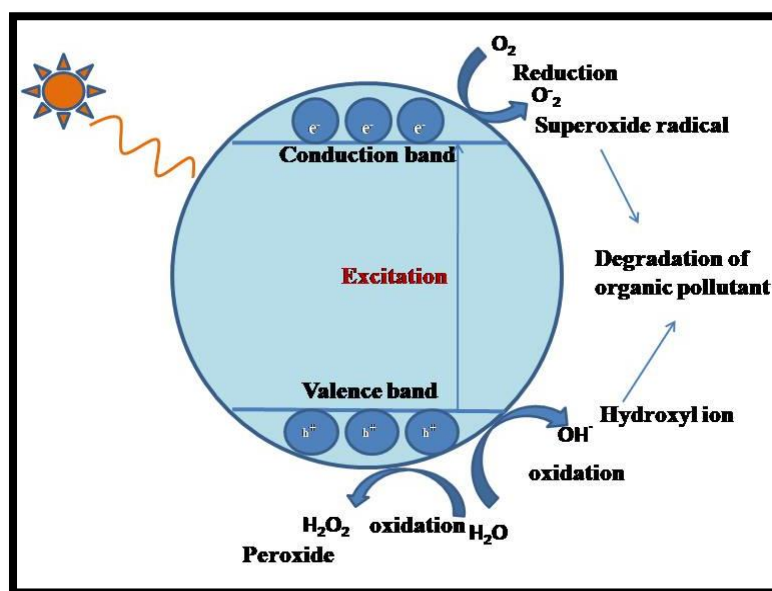


Figure 1.13. Schematic mechanism of dye degradation.

The photo generated electron react with O_2 to form superoxide radical which are another reactive species and formation of superoxide radical will also make sure that no

recombination takes place. In Direct method the ground state dye get excited to triplet excite dye which further gets converted semi oxidized radical later on reacting with superoxide and OH radical getting degraded (Figure 1.13).

1.10. Nanoparticle: An Overview and Preparation

In the previous two decade nanoparticles demonstrates a consistently expanding application to various fields of science. They are the scaffold between bulk materials and atomic or molecular structure. Nano-containing terms that emerge as often as possible in scientific reports, books just as in papers and that have gotten comfortable to the greater part of the general population. The nanosize-world is normally estimated in nanometres (1 nm relating to 10^{-9} m) and it includes frameworks whose measure is above atomic measurements and underneath plainly macroscopic ones (by and large > 1 nm and < 100 nm).

1.10.1. Classifications of nanoparticles

There are different methodologies for classifications of nanomaterials. These are described in below.

Zero dimension nanostructures:

Zero dimension (0-D) nanostructures are known where all the dimensions are restrained within the nanoscale. The wide demonstration of 0-D nanostructures are nanoparticles and quantum dots. The widely used method for synthesis of zero dimension nanostructures is template based method. Several templates have been used so far for synthesizing 0-D nanoparticles. As for example polymer micelles⁶³, carbonaceous saccharide microspheres⁶⁴, porous silica⁶⁵, lyotropic liquid crystal⁶⁶ assemblies used widely for 0-D nanoparticle synthesis. Electro deposition method⁶⁷, hydrothermal method⁶⁸,

microwave assisted solvothermal synthesis method⁶⁹, sol-gel process⁷⁰, CVD technique⁷¹, sonochemical⁷² synthesis method are also used widely.

One dimension (1-D) nanostructures:

1-D materials include nanotubes, nanobelts, nanorods, nanoribbons, nanowires and hierarchical structures. 1-D framework, for example, thin film or fabricated surfaces, has been utilized for quite a long time in gadgets, science and engineering. Fabrication of thin films (1-100 nm) or monolayer is now very common in PV cells or catalysis. LLC template-assisted synthesis method⁷³, electrodeposition method⁷⁴, electroless deposition⁷⁵, hydrothermal synthesis⁷⁶, sol-gel technique⁷⁷, CVD technique⁷⁸ are the most applied methods for the formation of 1D materials.

Two dimension (2-D) nanostructures:

2-D nanostructures have the two dimensions and are not restricted to the nano range. 2-D nanostructures display plate-like shapes. 2-D nano-structures include nanosheets, nanoplates, nanodisks, nanofilms, nanolayers *etc.* 2-D nanostructures possess several low dimension characteristics different from the bulk materials, thus withdrawn a huge interest in nano materials research. As for example graphene a 2-D nanostructure materials has shown enormous applications in nanomaterials field and also are used as promising support material for several nanoparticles⁷⁹⁻⁸¹. First single layer graphene was discovered by Geim and Novoselov⁸² from pyrolytic graphite (HOPG) in 2004 by via adhesive tape. Single layer graphene is important for its high charge transfer, optically more transparent, high thermal conductivity and specific area. After that numerous approaches have been established for the synthesis of few layers graphene. For instance liquid exfoliation method⁸³, mechanical exfoliation method⁸², chemical oxidation and reduction method⁸⁴, CVD method⁸⁵ and chemical synthesis method⁸⁶ can produce high quality graphene. Graphene supported

semiconductors and noble metal NPs shows enormous applications in fuel cell, sensors, photovoltaic and environmental applications^{79-81, 87}. 2-D nanostructures can be synthesized by several chemical process. Several group has prepared nanodisks and nanosheets like structures by using a soft template cetyltrimethylammonium bromide (CTAB) micelle. Noble metal such as Ag, Pd, Pt nanoplates and nanosheets can be synthesized in this method^{88,89}. MnO₂ nanowalls, Co nanowalls, In(OH)₃ nanosheets can be synthesised by electro deposition technique⁹⁰⁻⁹². Several 2-D transition metal oxide nanostructures and carbon based nanostructures can be synthesized by solvothermal method⁷⁰. Formation of 2-D film can be achieved by simple and flexible sol-gel process⁷⁷ and pure 2-D nanostructure can be formed by CVD method⁹³.

Three dimension (3-D) nanostructures:

These materials are in this manner described by having three discretionarily dimensions over 100 nm, bulk nanomaterials can be made out of a numerous arrangement of nanosize materials, most regularly in various directions. As for the nearness of highlights at the nanoscale, 3-D nanomaterials can contain scatterings of nanoparticles, groups of nanowires, and nanotubes or just as multinanolayers (for instance nanodendritic structures, spring-like nanocoils, and nanoflowers). 3-D nanostructures possess high surface area arising from their quantum size effect compared to their bulk counterpart. Therefore it has withdrawn a huge attention to synthesized 3-D nanomaterials with a restrained structure and morphology. Due to the 3-D structure and porosity it allows a better contact with the involved molecules that make 3-D structure a promising candidate for several catalysis battery electrode material. As for example 3-D porous graphene network consists of graphene foam and graphene aerogel shows enormous possibilities in lithium ion batteries and supercapacitors and can be produced by a simple hydrothermal method starting from graphene monolith⁹⁴. ZnO nanosheets and nanorods⁹⁵, TiO₂ hierarchical structure⁹⁶ can also

be made using this method. CVD method is also well known for the growth of 3D nanostructures such as aligned nanowalls and nanowires synthesis⁹⁷.

Nano particles has several advantages over bulk materials. NPs are extremely reactive in catalysis reaction owing to their elevated surface to volume ratio. The reduction of size in the nanoparticles causes a significant change in reduction potential as compared to the bulk materials as their Fermi potential become more negative. This exciting property helps in electron transfer in several catalysis reactions. A change in optical properties was also observed in nanomaterials compared to the bulk materials. For 0-D nanomaterials, where all the dimensions are at the nanoscale, an electron is confined in 3-D space, no delocalisation of electron takes place. For 0-D nanomaterials, where every one of the quantities are at the nanoscale, an electron is kept in 3-D space, no delocalisation of electron happens. For 1-D nanomaterials, electron imprisonment happens in 2-D while delocalization happens along the long axis of the nanowire/rod/tube. On account of 2-D nanomaterials, the conduction electrons will be kept over the thickness however delocalized in the plane of the sheets. The littler in the dimensions of the nanostructure, the more extensive is the partition between the energy levels, prompting a range of discreet energies. But stabilisation of small NPs are really challenging task. Because of their high surface energy they continually will attempt to agglomerate to reduce surface energy. Uninhibited agglomeration of nanoparticles may happen because of alluring van der Waals forces between particles. In order to avoid aggregations organic molecules or polymer was used as capping agent⁹⁸. Similarly mesoporous silica⁹⁹, metal organic framework¹⁰⁰, CNT¹⁰¹ has been used for long time (Figure 1.14). These are called support materials. A support material ideally should have these properties (a) as (i) higher number of stabilisation site for NPs allowing uniform dispersions of NPs on surface for maximum ECSA, (ii) higher porosity that enhances reactants goes in and product goes out (ii) higher electrical conductivity which minimize the

interfacial resistance, (iv) it should be compatible for different fabrications processes (v) higher stability under both transient and operational conditions and (vi) it should be cheap and environment friendly. But the presence of the support materials sometimes hindered the activity of NPs. Porous carbon supported NPs offered a better catalytic activity. As for example carbon black with high surface area was used for commercial noble metal NPs support. But the problem associated with the carbon as it is less stable in strong oxidizing conditions. As for example commercial Pt/C is relatively less stable in PEMFC due to the oxidation of carbon support. Graphene an allotrope of carbon can be used for stabilisation of NPs. Graphene is highly needed as it can be used as a two dimension (2D) catalyst support as high electrical and thermal conductivity, mechanical elasticity and theoretical high surface area is well known for graphene. In any case, two vital hindrances remain in developing enormous scale graphene-supported catalyst systems. Firstly low wettability of graphene in several solution and the second one is the low attachment between nanoparticles and graphene sheets. These result increases the dissolutions of metal NPs and lowers the stability under different electrochemical or heterogeneous catalytic applications.

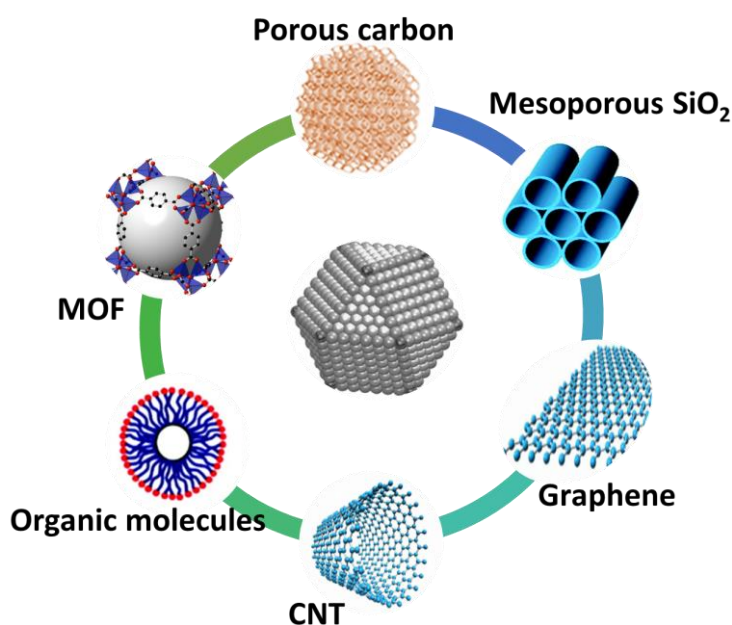


Figure 1.14. Examples of different supporting materials used to stabilise nanoparticles

Several literature reports¹⁰²⁻¹⁰⁴ suggested that heteroatoms (N, S) doped on the graphene improves the metal NPs anchoring ability and the catalytic activity of the graphene. Another two dimensional materials graphitic carbon nitride ($g\text{-C}_3\text{N}_4$) consists of moderate band gap has attracted a significant consideration which turns to be a potential candidate in the photocatalysis, several organic reaction and fuel cell applications. It is a class of polymeric materials consisting mainly carbon and nitrogen¹⁰⁵. Replacing of the carbon atom by a special manner in a carbon materials they can be obtained. First synthesized by Berzelius in 1834 and later named melon by Liebig. In recent decade also its potential value is not discovered for its chemical inertness in strong acidic and alkaline conditions. C: N ratio should be 0.75 for the fully polymerized $g\text{-C}_3\text{N}_4$ and cannot be virtually gained. $g\text{-C}_3\text{N}_4$ can be simply synthesized from cheap materials such as melamine. Thermal condensation is the easiest technique for the synthesis of the nitrogen-rich species, especially melamine which will undergo self-condensation with de-ammonation process. Hypothetically, there are seven phases of CN_x that naturally exist but $g\text{-C}_3\text{N}_4$ is considered the most stable one under ambient conditions¹⁰⁶. The C_3N_4 has two structural isomers- first one ((Fig. 1.15.a) comprises by the condensed tri-s-triazine (heptazine) units and the second one (Fig. 1.15.b) is composed of the condensed s-triazine subunits. Several reports have shown that $g\text{-C}_3\text{N}_4$ is a promising support for several metal NPs^{107,108}.

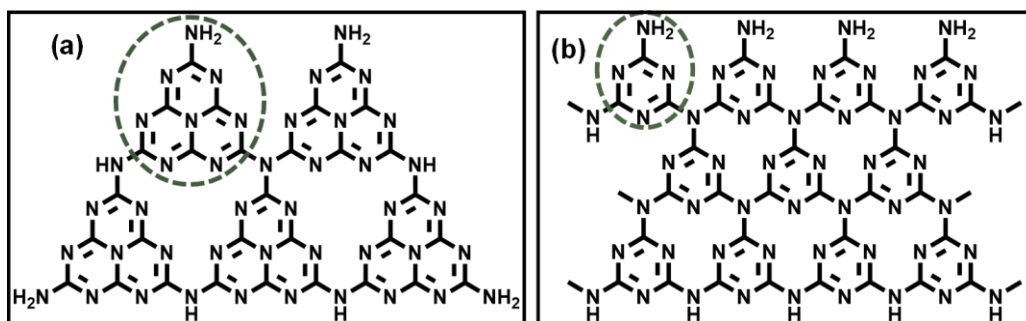


Figure 1.15. Proposed structures of $g\text{-C}_3\text{N}_4$ with (a) heptazine building block, (b) s-triazine building block.

1.11. Synthesis Procedures of Metal Nanoparticles in Liquid Phases:

Several techniques have been reported so far for synthesizing nano materials. These process are listed below.

Colloidal method:

This is the easiest and well established method to synthesis nanoparticles. This method follows the precipitation process in wet chemistry where solutions of different ions are mixed together to form precipitations under controlled temperature and pressure. Eminent scientist Michael Faraday synthesised beautiful red colloidal gold dispersion in 1850s which are still stable and kept at Royal Institute, London. For synthesis of colloidal NPs using of some stabilising agents is necessary otherwise van der walls forces works between the NPS and make them agglomerated. Particles can be stabilised by steric effect and electrostatically. Steric stabilisation can be done by using polymers and surfactants onto the surface of the colloidal NPs. Coating or capping of NPs by the means of molecules that form bonds or chemisorbed NPs are found extremely fruitful process for the stabilisation. As for examples thiols and dithiols are found good stabilizers for MNPs (particularly Au and Ag).

Sol-Gel method:

Sol-gel is another well-established wet chemistry method which offers numerous NPs synthesis with novel, predefined properties at a low production cost. It can be described as formation of a network structure through the condensation reaction reactions of a molecular precursors. A sol is recognised as a steady dispersion of colloidal particles and gel is famous as three dimensional continuous network with enclosed by a liquid phase. The idea behind sol-gel synthesis is as following:

- (a) Dissolve the precursors in a liquid to form a solution i.e. hydrolysis.

- (b) Then dehydration of the solution to form the wet-gel through the van der Waals forces or hydrogen bonding.
- (c) If the gel is dried by evaporation, then the capillary forces will shrink the gel structure network. This collapsed network is called Xerogel. If drying is performed under supercritical conditions i.e. CO₂ super critical drying the gel structure may be reserved and a gel with large number of open pores may be formed. This is called an aerogel which possess very low density.
- (d) Thin film also can be produced by spin coating or dip coating.

The benefits of sol–gel processing are the high purity of the nanostructures and uniform size and shape achievable at low temperatures.

Chemical reduction method:

Chemical reduction method deals with the reduction of precursor salt in aqueous or non-aqueous solution in present of reducing agent. For make it environmental friendly aqueous medium is favourable. Several reducing agent are well known such as gaseous H₂, solvated alkali metal borohydride (NaBH₄, LiAlBH₄), ethylene glycol, hydrazine hydrate (N₂H₄,H₂O) etc.

High-energy milling:

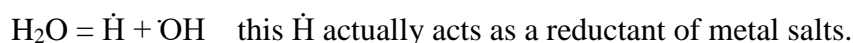
High energy milling is a non-equilibrium process resulting bulk materials to a nanostructures. Following process takes place in high energy milling:

- (a) Deformation in shear bands in materials containing a high dislocation density.
- (b) Random orientation of grains takes place, i.e., low angle grain boundary to high angle grain boundary to grain boundary sliding rotation.
- (c) Annihilation or recombination or rearrangement of dislocation to form sub-grain structure with smaller dimensions.

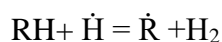
Sonochemical Methods:

Sonochemistry is the effect of ultrasound to chemical process. The mechanism can be described as sonochemical effects in liquids is the result of acoustic cavitation. It is high energy process which operate at 20-40 kHz. It helps to reduce the layers, exfoliate of the nanomaterials as well as reduction of the nanomaterials. The suggested mechanistic pathway¹⁰⁹ for sonochemical formation of metal nanoparticles is described below:

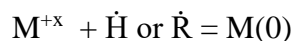
- (a) First sonolysis of water and water converted to \dot{H} and $\dot{O}H$



- (b) Second step is the generation of an secondary radical which promotes the reduction rate



- (c) Third step is the reduction of metal salt by \dot{H} formed from sonolysis of H_2O

**Microwave Irradiation:**

Microwave irradiation methods are very frequently used for synthesis of NPs. It is occurred through an interaction between light waves and polar solvents. It is a greener synthesis method by restricted it low solvent consumption and it is energy efficient. The microwave irradiation on a high dielectric solvent generates very fast and uniform heating which further allows a quick reduction of the metal precursor and deposits on the support materials. Several groups have reported the synthesis of supported metal NPs from the solution of the metal salts by irradiating microwave light. Advantages of microwave irradiation methods over the conventional heating's are (a) reaction parameters can be monitored precisely (b) very fast heating during microwave irradiation decreases the reaction

time. (c) Formation of very small as well as very narrow size distribution (d) formation of highly pure of nanoparticles.

Photodeposition:

Nanoparticles can be synthesized by light assisted method. Different wavelength ranges of light such as visible, UV, X-ray have been used for the reduction and deposition of metal nanoparticles. For example AuNPs can be deposited on TiO₂ surface by the photochemical deposition of a gold precursor (HAuCl₄), using a mercury lamp.

1.12. Aims of the Present Thesis:

- 1) Design and synthesis of 0-D, 1-D, 2-D and 3-D metal or metal-oxide nanostructures by mechanical and/or chemical processes.
- 2) Graphitic carbon nitride (g-CN_x) has been developed as a supported material for different metal and metal oxide nanostructure.
- 3) The g-carbon nitride or nitrogen doped carbon based composite materials have been characterised by p-XRD, FT-IR, XPS and UV-Vis spectroscopy.
- 4) Morphological studies of 0-D, 1-D, 2-D and 3-D hybrid nanomaterials were executed by using FESEM and TEM instrument.
- 5) Different electrocatalytic applications for energy storage and conversion such as HOR, HER, OER and ORR were explored with different g-CN_x based hybrid materials.
- 6) Mechanism of electrocatalytic HOR, HER, OER and ORR on the different catalysts surface were also deliberate.
- 7) Electrochemical impedance spectroscopy (EIS), double layer capacitance, and electrochemical surface area (ECSA) were calculated to understand the factors responsible for superior activity.

- 8) Very small nanoparticles supported on g-CN_x (2D hybrid) was studied for several biomolecules sensing.
- 9) Photocatalytic application of 2D hybrid nanocomposite is also shown in this thesis.

1.13. Scopes and Challenges of the Present Thesis:

The forgoing discussions clearly demonstrate that there is an upsurge in the research activities of nanocomposites owing to their potential applications such as electrochemical energy conversion, sensing as well environmental application. The present thesis is mainly concerned with the rational design, syntheses and characterizations of various supported metal or metal-oxide nanostructures and their various potential applications as electrocatalysts for energy conversions as well as sensing and photocatalytic applications. The main benefit of the present thesis is the easy synthetic procedure for the development of nanocomposites showing efficient catalytic behaviour.

1.14. References:

- (1) Johnston, B.; Mayo, M. C.; Khare, A. *Technovation* **2005**, *25*, 569-585.
- (2) Whitesides, G. M.; Crabtree, G. W. *Science* **2007**, *315*, 796-798.
- (3) Dresselhaus, M. S.; Thomas, I. L. *Nature* **2001**, *414*, 332-337.
- (4) Jacobson, M. Z. *Energy Environ. Sci.* **2009**, *2*, 148-173.
- (5) Winter, M.; Brodd, R. J. *Chem. Rev.* **2004**, *104*, 4245-4270.
- (6) Goodenough, J. B.; Manthiram, A. *MRS Communications* **2014**, *4*, 135-142.
- (7) Pettersson, J.; Ramsey, B.; Harrison, D. *J. Power Sources* **2006**, *157*, 28-34.
- (8) Shao, Y.; Markovic, N. M. *Nano Energy* **2016**, *29*, 1-3.
- (9) Kraytsberg, A.; Ein-Eli, Y. *Energy Fuels* **2014**, *28*, 7303-7330.

- (10) Gottesfeld, S.; Dekel, D. R.; Page, M.; Bae, C.; Yan, Y.; Zelenay, P.; Kim, Y. S. *J. Power Sources* **2018**, *375*, 170-184.
- (11) Durst, J.; Siebel, A.; Simon, C.; Hasche, F.; Herranz, J.; Gasteiger, H. A. *Energy Environ. Sci.* **2014**, *7*, 2255-2260.
- (12) Zheng, J.; Sheng, W.; Zhuang, Z.; Xu, B.; Yan, Y. *Sci. Adv.* **2016**, *2*.
- (13) Safizadeh, F.; Ghali, E.; Houlachi, G. *Int. J. Hydrogen Energy* **2015**, *40*, 256-274.
- (14) Pu, Z.; Liu, Q.; Asiri, A. M.; Sun, X. *ACS Appl. Mater. Interfaces* **2014**, *6*, 21874-9.
- (15) Guo, S.; Zhang, S.; Wu, L.; Sun, S. *Angew. Chem. Int. Ed.* **2012**, *51*, 11770-11773.
- (16) Liang, Y.; Li, Y.; Wang, H.; Zhou, J.; Wang, J.; Regier, T.; Dai, H. *Nat. Mater.* **2011**, *10*, 780-786.
- (17) Sheng, W.; Gasteiger, H. A.; Shao-Horn, Y. *J. Electrochem. Soc.* **2010**, *157*, B1529-B1536.
- (18) Zheng, J.; Sheng, W.; Zhuang, Z.; Xu, B.; Yan, Y. *Sci. Adv.* **2016**, *2*, e1501602.
- (19) Sheng, W.; Zhuang, Z.; Gao, M.; Zheng, J.; Chen, J. G.; Yan, Y. **2015**, *6*, 5848.
- (20) Strmcnik, D.; Uchimura, M.; Wang, C.; Subbaraman, R.; Danilovic, N.; van der, V.; Paulikas, A. P.; Stamenkovic, V. R.; Markovic, N. M. *Nat. Chem.* **2013**, *5*, 300-306.
- (21) Guo, S.; Wang, E. *Nano Today* **2011**, *6*, 240-264.
- (22) Zhu, H.; Zhang, S.; Huang, Y.-X.; Wu, L.; Sun, S. *Nano Lett.* **2013**, *13*, 2947-2951.
- (23) Chen, D.; Ye, F.; Liu, H.; Yang, J. *Sci. Rep.* **2016**, *6*, 24600.
- (24) Sheng, W.; Zhuang, Z.; Gao, M.; Zheng, J.; Chen, J. G.; Yan, Y. *Nat. Commun.* **2015**, *6*, 5848-5854.
- (25) Lu, S.; Zhuang, Z. *J. Am. Chem. Soc.* **2017**, *139*, 5156-5163.
- (26) Cong, Y.; Yi, B.; Song, Y. *Nano Energy* **2018**, *44*, 288-303.
- (27) Sheng, W.; Myint, M.; Chen, J. G.; Yan, Y. *Energy Environ. Sci.* **2013**, *6*, 1509-1512.

- (28) Wang, Y.; Wang, G.; Li, G.; Huang, B.; Pan, J.; Liu, Q.; Han, J.; Xiao, L.; Lu, J.; Zhuang, L. *Energy Environ. Sci.* **2015**, *8*, 177-181.
- (29) Bhowmik, T.; Kundu, M. K.; Barman, S. *ACS Catal.* **2016**, *6*, 1929-1941.
- (30) Wang, G.; Parrondo, J.; He, C.; Li, Y.; Ramani, V. *J. Electrochem. Soc.* **2017**, *164*, F1307-F1315.
- (31) Durst, J.; Simon, C.; Hasché, F.; Gasteiger, H. A. *J. Electrochem. Soc.* **2015**, *162*, F190-F203.
- (32) Elbert, K.; Hu, J.; Ma, Z.; Zhang, Y.; Chen, G.; An, W.; Liu, P.; Isaacs, H. S.; Adzic, R. R.; Wang, J. X. *ACS Catal.* **2015**, *5*, 6764-6772.
- (33) Scofield, M. E.; Zhou, Y.; Yue, S.; Wang, L.; Su, D.; Tong, X.; Vukmirovic, M. B.; Adzic, R. R.; Wong, S. S. *ACS Catal.* **2016**, *6*, 3895-3908.
- (34) Koenigsmann, C.; Scofield, M. E.; Liu, H.; Wong, S. S. *J. Phys. Chem. Lett.* **2012**, *3*, 3385-3398.
- (35) Zhongwei, C.; Mahesh, W.; Wenzhen, L.; Yushan, Y. *Angew. Chem. Inter. Ed.* **2007**, *46*, 4060-4063.
- (36) Lim, B.; Jiang, M.; Camargo, P. H. C.; Cho, E. C.; Tao, J.; Lu, X.; Zhu, Y.; Xia, Y. *Science* **2009**, *324*, 1302-1305.
- (37) Dubau, L.; Lopez-Haro, M.; Castanheira, L.; Durst, J.; Chatenet, M.; Bayle-Guillemaud, P.; Guétaz, L.; Caqué, N.; Rossinot, E.; Maillard, F. *Appl. Catal. B: Environ.* **2013**, *142-143*, 801-808.
- (38) Markovic, N. M.; Schmidt, T. J.; Stamenkovic, V.; Ross, P. N. *Fuel Cells* **2001**, *1*, 105-116.
- (39) Murthy, A. P.; Madhavan, J.; Murugan, K. *J. Power Sources* **2018**, *398*, 9-26.
- (40) Roger, I.; Shipman, M. A.; Symes, M. D. *Nat. Rev. Chem.* **2017**, *1*, 0003.

- (41) Mahmood, N.; Yao, Y.; Zhang, J.-W.; Pan, L.; Zhang, X.; Zou, J.-J. *Adv. Sci.* **2018**, *5*, 1700464.
- (42) McCrory, C. C. L.; Jung, S.; Ferrer, I. M.; Chatman, S. M.; Peters, J. C.; Jaramillo, T. F. *J. Am. Chem. Soc.* **2015**, *137*, 4347-4357.
- (43) McCrory, C. C. L.; Jung, S.; Peters, J. C.; Jaramillo, T. F. *J. Am. Chem. Soc.* **2013**, *135*, 16977-16987.
- (44) Fabbri, E.; Haberer, A.; Waltar, K.; Kötz, R.; Schmidt, T. J. *Catal. Sci. Technol.* **2014**, *4*, 3800-3821.
- (45) Klaus, S.; Cai, Y.; Louie, M. W.; Trotochaud, L.; Bell, A. T. *J. Phys. Chem. C* **2015**, *119*, 7243-7254.
- (46) Morales-Guio, C. G.; Stern, L.-A.; Hu, X. *Chem. Soc. Rev.* **2014**, *43*, 6555-6569.
- (47) Seh, Z. W.; Kibsgaard, J.; Dickens, C. F.; Chorkendorff, I.; Nørskov, J. K.; Jaramillo, T. F. *Science* **2017**, *355*.
- (48) C., M. I.; Hai-Yan, S.; Federico, C. V.; A., H. H.; I., M. J.; G., I. N.; John, K.; F., J. T.; K., N. J.; Jan, R. *ChemCatChem* **2011**, *3*, 1159-1165.
- (49) Rossmeisl, J.; Nørskov, J. K. *Surf. Sci.* **2008**, *602*, 2337-2338.
- (50) Nørskov, J. K.; Rossmeisl, J.; Logadottir, A.; Lindqvist, L.; Kitchin, J. R.; Bligaard, T.; Jónsson, H. *J. Phys. Chem. B* **2004**, *108*, 17886-17892.
- (51) Zheng, J.; Yan, Y.; Xu, B. *J. Electrochem. Soc.* **2015**, *162*, F1470-F1481.
- (52) Shinagawa, T.; Garcia-Esparza, A. T.; Takanabe, K. *Sci. Rep.* **2015**, *5*, 13801.
- (53) Hwang, D.-W.; Lee, S.; Seo, M.; Chung, T. D. *Anal. Chim. Acta* **2018**.
- (54) Zhu, Z.; Garcia-Gancedo, L.; Flewitt, A. J.; Xie, H.; Moussy, F.; Milne, W. I. *Sensors* **2012**, *12*, 5996.
- (55) Pletcher, D. *J. Appl. Electrochem.* **1984**, *14*, 403-415.
- (56) Burke, L. D. *Electrochim. Acta* **1994**, *39*, 1841-1848.

- (57) Chen, W.; Cai, S.; Ren, Q.-Q.; Wen, W.; Zhao, Y.-D. *Analyst* **2012**, *137*, 49-58.
- (58) Ajmal, A.; Majeed, I.; Malik, R. N.; Idriss, H.; Nadeem, M. A. *RSC Adv.* **2014**, *4*, 37003-37026.
- (59) Liu, Y.; Chen, X.; Li, J.; Burda, C. *Chemosphere* **2005**, *61*, 11-18.
- (60) Siddiqa, A.; Masih, D.; Anjum, D.; Siddiq, M. *J. Environ. Sci.* **2015**, *37*, 100-109.
- (61) Andronic, L.; Enesca, A.; Vladuta, C.; Duta, A. *Chem. Engineering J.* **2009**, *152*, 64-71.
- (62) Anas, M.; Han, Dong S.; Mahmoud, K.; Park, H.; Abdel-Wahab, A. *Mater. Sci. Semiconductor Processing* **2016**, *41*, 209-218.
- (63) Nash, M. A.; Lai, J. J.; Hoffman, A. S.; Yager, P.; Stayton, P. S. *Nano Lett.* **2010**, *10*, 85-91.
- (64) Li, Z.; Lai, X.; Wang, H.; Mao, D.; Xing, C.; Wang, D. *J. Phys. Chem. C* **2009**, *113*, 2792-2797.
- (65) Kim, Y.-T.; Han, J. H.; Hong, B. H.; Kwon, Y.-U. *Adv. Mater.* **2010**, *22*, 515-518.
- (66) Ding, J. H.; Gin, D. L. *Chem. Mater.* **2000**, *12*, 22-24.
- (67) Day, T. M.; Unwin, P. R.; Macpherson, J. V. *Nano Lett.* **2007**, *7*, 51-57.
- (68) Xuan Hien, V.; Tu Huy Anh, L.; Quang Trung, K.; Duc Vuong, D.; Duc Chien, N. *Adv. Nat. Sci.: Nanosci. Nanotechnol.* **2010**, *1*, 025014.
- (69) Zawadzki, M. *J. Alloys Compd.* **2008**, *454*, 347-351.
- (70) Yamauchi, T.; Tsukahara, Y.; Yamada, K.; Sakata, T.; Wada, Y. *Chem. Mater.* **2011**, *23*, 75-84.
- (71) Palgrave, R. G.; Parkin, I. P. *J. Am. Chem. Soc.* **2006**, *128*, 1587-1597.
- (72) Kis-Csitári, J.; Kónya, Z.; Kiricsi, I. In *Sonochemical Synthesis of Inorganic Nanoparticles*, Dordrecht, Springer Netherlands: Dordrecht, 2008; pp 369-372.

- (73) Kijima, T.; Yoshimura, T.; Uota, M.; Ikeda, T.; Fujikawa, D.; Mouri, S.; Uoyama, S. *Angew. Chem. Int. Ed.* **2004**, *43*, 228-232.
- (74) Cheng, F.; Wang, H.; Sun, Z.; Ning, M.; Cai, Z.; Zhang, M. *Electrochem. Commun.* **2008**, *10*, 798-801.
- (75) Li, Q.; Walter, E. C.; van der Veer, W. E.; Murray, B. J.; Newberg, J. T.; Bohannan, E. W.; Switzer, J. A.; Hemminger, J. C.; Penner, R. M. *J. Phys. Chem. B* **2005**, *109*, 3169-3182.
- (76) Deng, B.; Xu, A.-W.; Chen, G.-Y.; Song, R.-Q.; Chen, L. *J. Phys. Chem. B* **2006**, *110*, 11711-11716.
- (77) Nath, M.; Parkinson, B. A. *Adv. Mater.* **2006**, *18*, 1865-1868.
- (78) Schmitt, A. L.; Zhu, L.; Schmeißer, D.; Himpfel, F. J.; Jin, S. *J. Phys. Chem. B* **2006**, *110*, 18142-18146.
- (79) Nasrollahzadeh, M.; Issaabadi, Z.; Tohidi, M. M.; Mohammad Sajadi, S. *Chem. Rec.* **2018**, *18*, 165-229.
- (80) Paczosa-Bator, B.; Piech, R.; Wardak, C.; Cabaj, L. *Ionics* **2018**, *24*, 2455-2464.
- (81) Chen, X.; Yasin, F. M.; Eggers, P. K.; Boulos, R. A.; Duan, X.; Lamb, R. N.; Iyer, K. S.; Raston, C. L. *RSC Adv.* **2013**, *3*, 3213-3217.
- (82) Novoselov, K. S.; Geim, A. K.; Morozov, S. V.; Jiang, D.; Zhang, Y.; Dubonos, S. V.; Grigorieva, I. V.; Firsov, A. A. *Science* **2004**, *306*, 666-669.
- (83) Behabtu, N.; Lomeda, J. R.; Green, M. J.; Higginbotham, A. L.; Sinitskii, A.; Kosynkin, D. V.; Tsentelovich, D.; Parra-Vasquez, A. N. G.; Schmidt, J.; Kesselman, E.; Cohen, Y.; Talmon, Y.; Tour, J. M.; Pasquali, M. *Nat. Nanotechnol.* **2010**, *5*, 406.
- (84) Hummers, W. S.; Offeman, R. E. *J. Am. Chem. Soc.* **1958**, *80*, 1339-1339.
- (85) Zhu, Y.; Murali, S.; Cai, W.; Li, X.; Suk, J. W.; Potts, J. R.; Ruoff, R. S. *Adv. Mater.* **2010**, *22*, 3906-3924.

- (86) Yang, X.; Dou, X.; Rouhanipour, A.; Zhi, L.; Räder, H. J.; Müllen, K. *J. Am. Chem. Soc.* **2008**, *130*, 4216-4217.
- (87) Li, Z.; Zhao, H.; Han, H.; Liu, Y.; Song, J.; Guo, W.; Chu, W.; Sun, Z. *Tetrahedron Lett.* **2017**, *58*, 3984-3988.
- (88) Chen, S.; Carroll, D. L. *Nano Lett.* **2002**, *2*, 1003-1007.
- (89) Siril, P. F.; Ramos, L.; Beaunier, P.; Archirel, P.; Etcheberry, A.; Remita, H. *Chem. Mater.* **2009**, *21*, 5170-5175.
- (90) Liu, D.; Garcia, B. B.; Zhang, Q.; Guo, Q.; Zhang, Y.; Sepehri, S.; Cao, G. *Adv. Funct. Mater.* **2009**, *19*, 1015-1023.
- (91) Wei, H.; Peng, G.; Lei, C.; Ligen, Y.; Zhen, L.; Yi, X. *Nanotechnol.* **2006**, *17*, 3512.
- (92) Dutta, D.; Pulsipher, A.; Yousaf, M. N. *Langmuir* **2010**, *26*, 9835-9841.
- (93) Barreca, D.; Ferrucci, A. P.; Gasparotto, A.; Maccato, C.; Maragno, C.; Tondello, E. *Chem. Vapor Depos.* **2007**, *13*, 618-625.
- (94) Yao, X.; Zhao, Y. *Chem* **2017**, *2*, 171-200.
- (95) Cheng, C.; Liu, B.; Yang, H.; Zhou, W.; Sun, L.; Chen, R.; Yu, S. F.; Zhang, J.; Gong, H.; Sun, H.; Fan, H. *J. ACS Nano* **2009**, *3*, 3069-3076.
- (96) Wang, C.; Yin, L.; Zhang, L.; Qi, Y.; Lun, N.; Liu, N. *Langmuir* **2010**, *26*, 12841-12848.
- (97) Kumar, B.; Lee, K. Y.; Park, H.-K.; Chae, S. J.; Lee, Y. H.; Kim, S.-W. *ACS Nano* **2011**, *5*, 4197-4204.
- (98) Van Haute, D.; Liu, A. T.; Berlin, J. M. *ACS Nano* **2018**, *12*, 117-127.
- (99) Huang, Y.; Deng, W.; Guo, E.; Chung, P.-W.; Chen, S.; Trewyn, B. G.; Brown, R. C.; Lin, V. S.-Y. *ChemCatChem* **2012**, *4*, 674-680.
- (100) Liu, H.; Liu, Y.; Li, Y.; Tang, Z.; Jiang, H. *J. Phys. Chem. C* **2010**, *114*, 13362-13369.
- (101) Trépanier, M.; Dalai, A. K.; Abatzoglou, N. *Appl. Catal. A* **2010**, *374*, 79-86.

- (102) Duan, J.; Chen, S.; Jaroniec, M.; Qiao, S. Z. *ACS Catal.* **2015**, *5*, 5207-5234.
- (103) Wang, H.; Maiyalagan, T.; Wang, X. *ACS Catal.* **2012**, *2*, 781-794.
- (104) Ci, L.; Song, L.; Jin, C.; Jariwala, D.; Wu, D.; Li, Y.; Srivastava, A.; Wang, Z. F.; Storr, K.; Balicas, L.; Liu, F.; Ajayan, P. M. *Nat. Mater.* **2010**, *9*, 430.
- (105) Wang, X.; Blechert, S.; Antonietti, M. *ACS Catal.* **2012**, *2*, 1596-1606.
- (106) Teter, D. M.; Hemley, R. J. *Science* **1996**, *271*, 53-55.
- (107) Wang, Y.; Yao, J.; Li, H.; Su, D.; Antonietti, M. *J. Am. Chem. Soc.* **2011**, *133*, 2362-2365.
- (108) Datta, K. K.; Reddy, B. V.; Ariga, K.; Vinu, A. *Angew. Chem. Int. Ed.* **2010**, *49*, 5961-5965.
- (109) Bang, J. H.; Suslick, K. S. *Adv. Mater.* **2010**, *22*, 1039-1059.

CHAPTER 2

General Experimental Methods and Techniques

2.1. INTRODUCTION

This chapter manages the fundamental principles of different instruments which have been utilized in this present thesis. The exploratory subtleties, associated with this theory work for different experiments have been quickly talked about.

2.2. Materials:

The materials and synthetic concoctions engaged with this thesis are legitimately taken from commercially available sample without further purification. A list of the names of materials and synthetic substances engaged with the thesis, alongside their formula, provider is appeared in Table 2.1.

Table 2.1. List of the chemicals along with formula and company name.

Name of Chemicals	Chemical formula	Company name
Formamide	HCONH ₂	Sigma Aldrich
Gold (III) chloride trihydrate	HAuCl ₄ . 3H ₂ O	Sigma Aldrich
Silver nitrate	AgNO ₃	Alfa Aesar
Chloroplatinic acid hexahydrate	H ₂ PtCl ₆ . 6H ₂ O	Merck
Chloroiridic acid	H ₂ IrCl ₆ .xH ₂ O	Sigma Aldrich
Sodium borohydride	NaBH ₄	Merck
Potassium hydroxide	KOH	Merck
Sulphuric acid	H ₂ SO ₄	Merck
Nitric acid	HNO ₃	Merck
Hydrochloric Acid	HCl	Merck
Perchloric acid	HClO ₄	Alfa Aesar

Acetic acid	CH ₃ COOH	Sigma Aldrich
Boric acid	H ₃ BO ₄	Sigma Aldrich
Sodium bicarbonate	NaHCO ₃	Merck
Phosphate buffer solution	PBS	Merck
Platinum on graphitic carbon	Pt/C (40 wt% or 10%)	Sigma Aldrich
Iridium oxide	IrO ₂	Alfa Aesar
Ethanol	CH ₃ CH ₂ OH	Merck
Acetone	CH ₃ COCH ₃	Merck
Isopropanol	CH ₃ CHOHCH ₃	Merck
Water	H ₂ O	Milli-Q Merck

2.3. INSTRUMENTS and INSTRUMENTAL TECHNIQUES

X-ray diffraction (XRD):^{1,2}

X-Ray diffraction (XRD) a non-destructive method used to study the identifications of phase of crystalline materials, which is good enough to get idea of a unit cell. XRD uses X-ray as the light source and as they have wavelength in nanometre region, X-ray scattering from the sample give rise to interference pattern. X-rays are created from X-ray tube which are shaped from warmed tungsten tube encased in a cleared ceramic vessel as cathode and cooled Cu foil as anode. The electrons which are radiated from tungsten are quickened towards a metal (water cooled) and give out the electrons from the internal shells of Cu atoms— coming about an unwinding of valence electron to inward position prompting the creation of X-beam. Cu-source can create X-beam of two trademark wave lengths, for example, Cu K α ($\lambda = 0.154$ nm) and Cu K β ($\lambda = 0.139$ nm). For appropriate obstruction X-beam ought to be monochromatic and utilization of nickel channel ensure that K β gets assimilated and just K α is given out. A light emission beam is centred on the sample and dispersed beam is determined by the detector. 2 theta is angle formed in between incoming

and outgoing direction of beam. The estimation of 2 theta is utilized to quantify the d spacing i.e. interplanar distance of two planes in a crystal utilizing the Bragg's diffraction condition (Figure 2.1):

$$n\lambda = 2d\sin\theta \quad (n \text{ is an integer: } 1,2,3\dots)$$

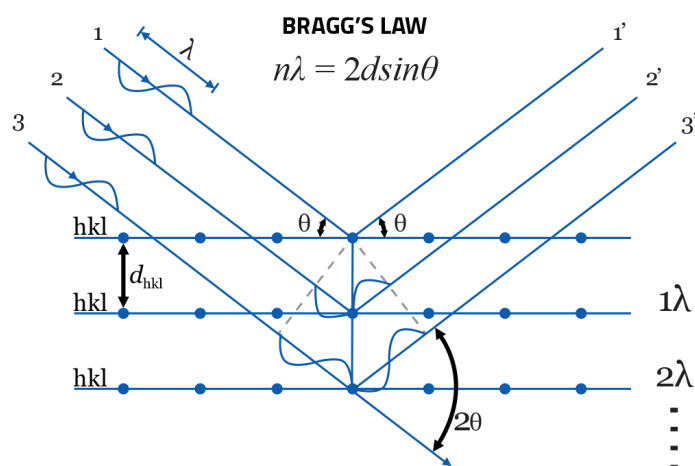


Figure 2.1. Schematic diagram of an X-ray scattering (Adopted from Wikipedia).

In this thesis, X-ray spectra were collected on Bruker DAVINCI D8 ADVANCE diffractometer equipped with Cu $K\alpha$ radiation (λ 0.15406 nm).

Transmission Electron Microscope (TEM):³

TEM is regularly used in the field of material science. Nanowires, quantum dot and various nanoparticles and their quality, shape, size density can be studied using TEM. One can also study the defects, composition and composition of in the semiconductor. The principle of TEM is similar to that of microscope just in place of light, electrons are used. Monochromatic beam of electron is generated by electron gun. This stream is concentrated to a thin, coherent beam by condenser lenses. The beam is concentrated to thin, coherent beam by condenser. The beam is restricted by the condenser aperture, eliminating high angle

electrons. After hitting the specimen some part of it gets transmitted depending on the thickness and transparency of the specimen. This transmitted portion is directed by the objective lens into an image. The image is moved down the column through the intermediate and projector lenses, being magnified all the way. The image strikes the fluorescent screen and light is generated. The darker area represent that less amount of electron could transfer whereas lighter areas of the image represent more electrons respectively .It can be useful for production of image, diffraction pattern depending on the operation mode.

In case of HRTEM both use of scattered and transmitted beam of electron to create an interference image giving out the image of the sample. One can study lattice imperfections and crystal structures of various material in the range of atomic unit with high resolution for the characterization of point defect, dislocation and surface structures.

SAED is selected area electron diffraction pattern, provides the indices based on which we can calculate the d-spacing of crystals. Additionally, the pattern obtained also informs us about the crystallinity of the samples. The crystal planes of the sample, parallel to the direction of propagation of the electron beam will be diffracted according to the Bragg's law. This diffraction pattern is a Fourier transformation of the periodic potential of the electron. These diffracted electrons along with the electrons in the primary interfere causing a back transformation (or inverse Fourier transform) resulting in an image.

In this thesis, the morphology and chemical composition of the as-prepared samples were observed by transmission electron microscopy in JEM –2100, JEOL and JEM –2100F, JEOL operated at 200 kV.

Field Emission Scanning Electron Microscope (FESEM):⁴

FESEM is used to produce high-resolution three-dimensional images, about the morphology. Electrons from the electron gun are emitted in a high vacuum from the cathode and accelerated by the anode. The vacuum assistance is to make sure any atoms and molecules present in the column from interacting with the electron beam and producing good quality imaging. The electron beam is focussed by the condenser lenses. Produced magnetic field is deflected back and forth. The beam, focused by the objective lens to very fine spot (1-5 nm), scans the sample surface in a raster pattern. Surface sample is scanned is done in raster pattern focussing on a very fine spot. Primary electron interacts with surface sample atom producing secondary emission which are detected and image is formed out of it. Angle and velocity of the secondary beam is directly connected to object surface structure.

In this thesis, Field-emission scanning electron microscope (FESEM) data collected on Carl Zeiss, Germany (Model: Σ igma).

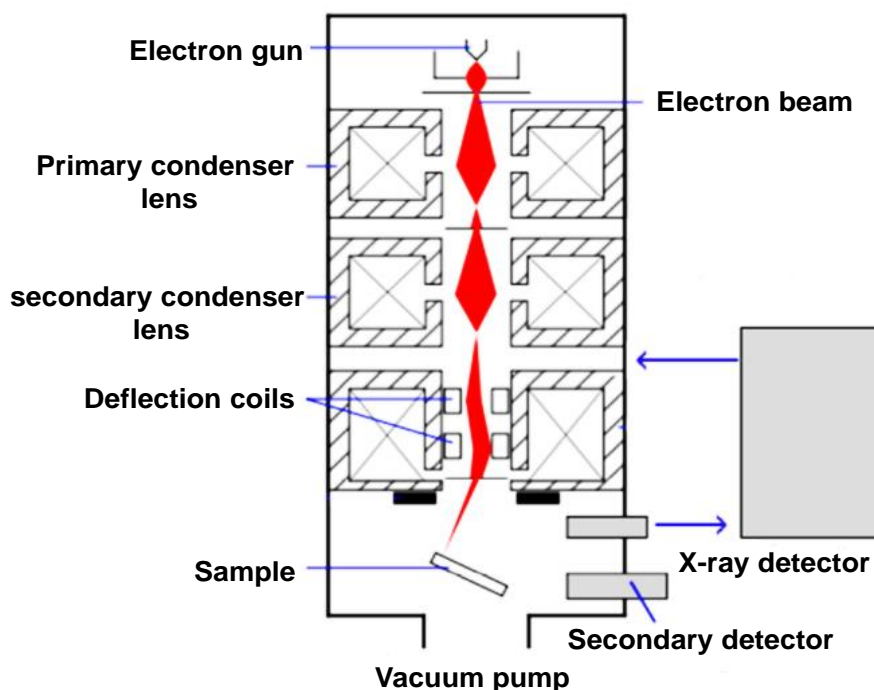


Figure 2.2. Schematic diagram of FE-SEM (Adopted from Wikipedia).

Energy-Dispersive X-ray spectroscopy (EDS):

Elemental composition can be identified and studied through EDS spectroscopy. No need to have separate instrument as EDS is preinstalled with electron microscope SEM and TEM. The working principle is based on the characteristics. X-ray generated during the interaction between sample and incident electron beam. Electron hole pair is formed when incident X-rays interact with the sample. Upon applying a high bias voltage across the crystal, the electrons and holes move to electrodes on opposite sides of the crystal, producing a charge signal which is passed to the pulse processor. The energy of incoming X-rays is proportional to the size of the signal. Therefore from the current from that is produced from each X-ray, the energy of the X-ray can be calculated.

Energy dispersive spectrometer (EDS) were taken from the spectrometer attached to Carl Zeiss (Germany made, Model: Σ igma)

X-ray photoelectron spectroscopy (XPS):⁵

To gather qualitative and chemical information from the substance i.e. to do surface analysis, XPS is used. The elemental composition, electronic state and empirical formula for the substance can be measured using this technique. Al $K\alpha$ X-rays is a source for the X-ray emission causing the photoelectron to be emitted from sample surface. By measuring the photoelectron energy (binding energy) and the intensity of photoelectron peak, chemical state and quantity of an element can be determined. These photoelectrons originate from a depth of <10 nm, therefore the information obtained is from within this depth for XPS measurement.

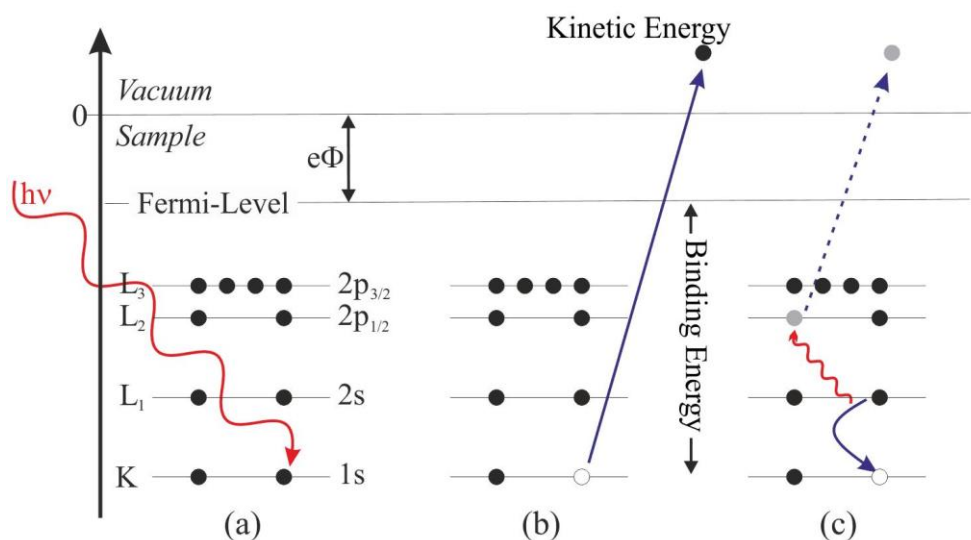


Figure 2.3. Schematic representation of working principle of XPS (Adopted from Wikipedia).

XPS measurements were performed using Kratos Axis Ultra and VG Microtech under ultra-high vacuum condition, using a monochromatic Al K $_{\alpha}$ X-ray was used as the source.

Fourier Transform Infra-red Spectroscopy (FT-IR):⁶

For the study of the functional group present in the molecule a very sensitive instrument called FT-IR is used. FT-IR works in the region of infra-red from electromagnetic spectra. The absorption is the function of the vibrations of bonds present in the molecule. The frequency ranges that can be measured are typically over the range of 4000 – 400 cm⁻¹. Before measuring or studying the sample it is required to first do background emission then one can proceed to measuring emission spectra of the sample. The absorption spectra is directly proportional to the ratio sample spectra to the background spectra. Less amount of the sample requirement and very high sensitivity is major reason why FT-IR is excessively used in chemical characterization.

All FT-IR spectra in this thesis were collected from Perkin Elmer RXI FT-IR spectrophotometer.

UV-Vis spectroscopy:

UV-Visible spectroscopy is an absorption spectroscopy in work in the region of visible (400-1200 nm) and Ultra-Violet (200-400 nm). It work on the principle when sample absorb light the electron excitation takes place from ground state to higher excited state.

It follows Lambert Beer's law which is

$$A = \log\left(\frac{I_0}{I}\right) = \epsilon c l$$

Where A is the optical density or absorbance, I_0 is the incident light intensity and I is the transmitted light, ϵ is the molar absorption coefficient, c is the concentration of the solution of the sample and l is the path length of light beam passing through the solution.

The optical absorbance of the synthesized compounds was studied using Varian Cary 100 Bio UV-visible Spectrophotometer.

Thermo-gravimetric analysis (TGA):

TGA is widely used to examine the thermal stability and chemical composition of the sample. TGA measurement offers evidences about physical phenomena of a sample, such as phase transitions, adsorption, desorption and chemical phenomena such as thermal decomposition. In nitrogen atmosphere the change of weight percentage of the material is studied by heating the substance at variable temperature.

TGA of as synthesized sample was carried out by TA Instrument (Model: Discovery TGA).

Inductive Coupled Plasma-Optical Emission Spectroscopy (ICP-OES):⁸

It is a purely analytical technique and used for the revealing for the individual elements. It is very useful to determine trace amount of metal in any substance such as food, water. It is basically a flame technique with a flame temperature varies from 6000 to 10,000 K. The ICP-OES instrument consists with an atomizer and an analyser. The inductive couple plasma act as atomizer and optical emission spectroscopy as an analyser. It works on the principle of emission, argon act as a carrier gas which pushes through differential vacuum interphase and when it cools down emission rays are released. Emission rays are being directed into the optical emission chamber, corresponding to the photon wavelength followed by the measurement. From the position of the photon rays, the element is determined and the intensity of the photon determines the content ICP-OES measurements have several advantages over other experiments such as:

- (a) Multiple elements can be measured simultaneously using ICP-OES process.
- (b) Low chemical and ionization interference.
- (c) It is very sensitive technique can go in the range of part per billion.
- (d) It can produce very stable result.

In this thesis, ICP-OES was performed on iCAP 7000 Series (Thermo Scientific).

Elemental Analysis:⁸

Elemental analysis is an analytical analysis that can decide the sum (in type of weight percent) of components present in the sample. The CHNS analysis specifically measures the amount of carbon, hydrogen, nitrogen and sulphur in the sample. The sample is followed by combustion process at high temperature in presence of ultra-pure oxygen and then passed through gas chromatography set up, later on thermal conductivity is studied using thermal conductivity detector. In combustion process, (at 1000° C), hydrogen to water; nitrogen to nitrogen gas/ oxides of nitrogen and sulphur to sulphur dioxide and carbon is converted to

carbon dioxide. After that, the gases enter a mixing volume chamber to make a homogeneous mixture at constant temperature and pressure. The homogeneous mixture then passes through a series of thermal conductivity detectors and provides the amounts.

In this thesis, EuroEA Elemental Analyser was used for CHN measurement of as synthesized sample.

Electrochemical measurement:⁹

All electrochemical performance test was done in a conventional three electrode set up as shown in Figure 2.4 and data were recorded from an electrochemical workstation (Autolab, Metrohm, PGSTAT 302N). Glassy carbon electrode (GC, diameter 3 mm and 5 mm) or metal foil electrode (i.e. Ti foil) was used a working electrode whereas platinum wire/mesh and Ag/AgCl in 3 M KCl was used as counter and reference electrode. Before performed any electrochemical study, GC was were polished with alpha alumina powder (0.3 micron) suspended in deionized water on a Nylon polishing pad (Metrohm). After each polishing the GC electrode was rinsed with deionized water and sonicated for 2 min in ethanol. The current density reported herein was normalized by the geometrical area of the working electrode for HER, HOR, ORR, OER and all potentials were shown in reversible hydrogen electrode (RHE) or Ag/AgCl scale. The potential measured in Ag/AgCl were converted into RHE by Nernst equation, $E_{RHE} = E_{Ag/AgCl} + E^0_{Ag/AgCl} + 0.059 \text{ pH}$ where $E_{Ag/AgCl}$ is the working potential, $E^0_{Ag/AgCl} = 0.1976$ at 25°C . Several technique which are used extensively as describes bellow:

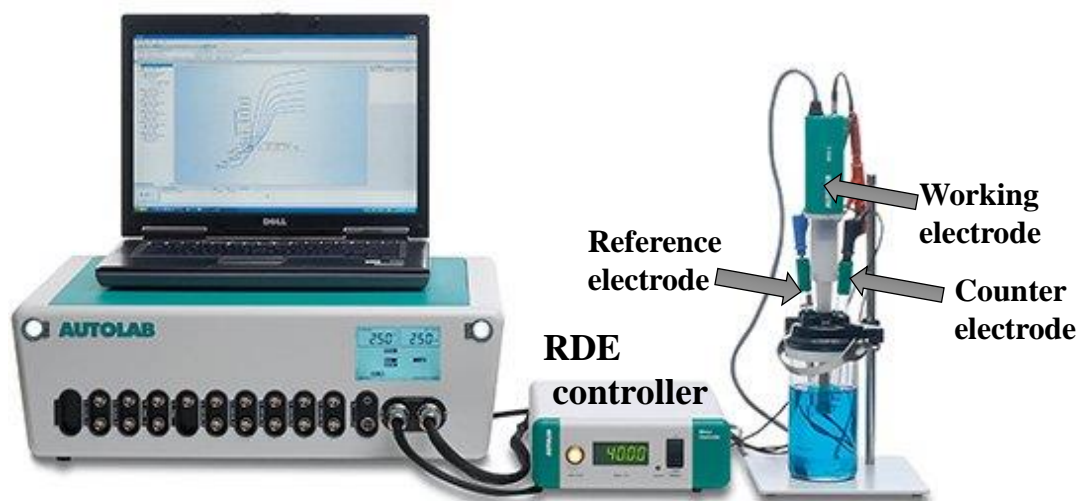


Figure 2.4. Photograph of conventional three electrode setup of Autolab instrument (Adopted from Metrohm).¹⁰

Voltammetry:

Voltammetry is where potential is changed with certain rate and the comparing current is recorded. It is surface fragile technique. It gives the estimation of the current (charge) exchange between electrode and electrolyte interfaces. Two sorts of Voltammetry are for the most part used to understand the electrochemical process¹¹-(a) cyclic voltammetry (CV) wherein the progressions of potential happen straight from one potential (V1) to another potential (V2) and afterward it is changed from V2 to V1. (Figure 2.5.a) (b) Linear sweep voltammetry (LSV) where the potential changes from one potential (V1) to another potential (V2) (Figure 2.5.b) and then don't come to the reverse. Voltammetry procedure can give the current versus potential plot of various interface process however the identification of procedure is troublesome. For a constant potential the steady state current at the interfaces consist with four components: $i = i_{\text{reaction1}} + i_{\text{corrosion}} + i_{\text{reaction 2}} + i_{\text{charge}}$. LSV is a voltammetric method to measure the current density at a working electrode based on the overpotential. Both CV and LSV process are mainly used to study HOR, HER, OER and ORR.

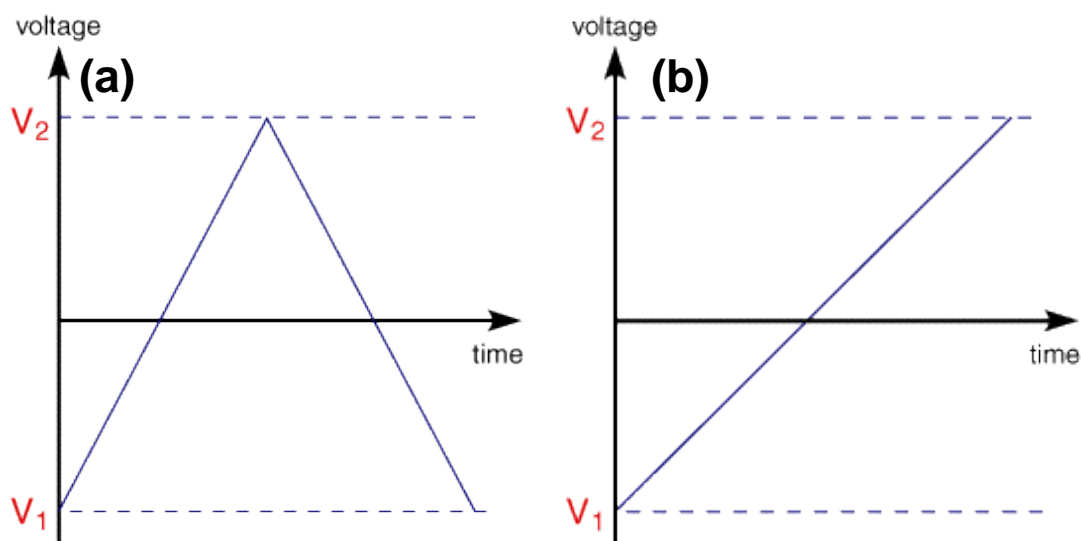


Figure 2.5. Voltage vs. time profile of (a) cyclic voltammetry and (b) linear sweep voltammetry.

Chronoamperometry (CA):

In the CA technique, current is measured at a constant potential with time. Stability of the electrocatalysts can be measured from this method. This technique can also help to measure Tafel slope. Quantitative information such as the amount of total charged passed through the electrode is obtained by the integrating the current over a certain time.

Chronopotentiometry (CP):

CP is a galvanostatic technique where a required current is being fixed and measure the required potential to keep that current varies over time. We can also use the CP to know the stability of the electrocatalysts.

Impedance spectroscopy:¹²

Electrical resistance, R , is correlated to the resistance of circuit elements toward the flow of electrical current. Based on Ohm's law, the resistance is the ratio of input voltage, E , to the output current, I

$$R = \frac{E}{I}$$

Like resistance, impedance also demonstrates the resistance of the circuit toward the electrical current flow. It is represented by real part, but it also has an imaginary impedance component which correlates to the electrical energy storage ability of the circuit. This definition of impedance can be applied in both direct and alternating current. For real circuit, relation between impedance and frequency dependent resistance can be written as

$$Z_{\omega} = \frac{E_{\omega}}{I_{\omega}}$$

Where Z_{ω} is the impedance, E_{ω} is the frequency dependent potential and I_{ω} is frequency dependent AC current.

The sinusoidal potentials response signal for AC current is

$$E(t) = E_0 \sin(\omega t)$$

where potential and measured AC current are also in the same frequency but in different phase.

Table 2.2. The details description of Bode and Nyquist plot.

Parameter	Nyquist plot	Bode plot
Process	The individual electron transfer process was describes.	The individual electron transfer process was describes.
Frequency	Frequency was not well defined.	Frequency was well defined.
Nature	In presence of large impedance, small impedance was not well defined.	Both small and large impedance was defined simultaneously.

Where the radial frequency $\omega = 2\pi f$.

The corresponding AC current signal follows as:

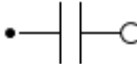
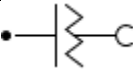
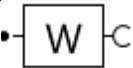
$$I(t) = I_0 \sin(\omega t + \varphi)$$

Where φ is the phase difference and I_0 is the response signal amplitude.

Now in according to the impedance (Z_ω)-

$$Z_\omega = \frac{E_0 \sin(\omega t)}{I_0 \sin(\omega t + \varphi)} = Z_0 \frac{\sin(\omega t)}{\sin(\omega t + \varphi)} = Z_0 \{\cos(\varphi) + i \sin(\varphi)\} = Z_{real} + Z_{imag}$$

Table 2.3. The components and their indication for equivalent circuit.

Equivalent	Impedance	Indication
Resistance	R	
Capacitance	C	
Constant phase element	Q	
Inductance	L	
Warburg Impedence	W	

So total impedance is a complex quantity and has two counterparts one is real part another is imaginary part. The EIS of a compound can be represented by two ways (a) by plotting the real part on x-axis and the negative of the imaginary part on the y-axis, producing a Nyquist plot. (b) Logarithm of both x-axis and y-axis produced Bode Plot. A detail descriptions of the Bode and Nyquist plot are describes in Table 2.2. For a particular circuit if capacitive and resistance elements are parallel to each other than the Nyquist plot would look like the one where low frequency is plotted on the right side and high frequency data

is placed on the left side. The electrochemical cell can be represented by a network frame of passive electrical elements and it's called equivalent circuit. The elements of equivalent circuit are presented in Table 2.3.

Gas chromatography (GC):

GC is a quantification and separation technique for the mixture of components. In GC, retention coefficients of an individual elements take a vital role for the separation of the elements in a liquid or solid stationary phase in a column. It consists with mainly three parts: injector, column and detector. The column, is attached between injector and detector, and placed in an empty space, called oven. Oven, column, injector can be heated at different temperature as per the requirement of the samples. A carrier gas *i.e.* argon is continuously flowed continuously through the column in a certain flow rate (sccm). A gas tight syringe is used to take sample (H_2 , O_2) from the headspace of the electrochemical cell and injects in the injection port. Thereafter, the carrier gas pulled the sample gas through the column and depending on their retention coefficients, different analyte arrived to the detector separately at different time intervals. Thermal conductivity detector (TCD) with argon (Ar) as a carrier is used for the gas phase analysis.

In this study, GC instrument (Thermo Scientific, Model: Trace 1110) equipped with TCD and argon as carrier gas was used.

Faradaic efficiency:

It is comparison between the theoretical and experimental amount of evolved gas in an electrochemical reaction. The amount of the evolved gas from cathode and anode was quantified by GC. A 250 ml five neck sealed glass cell was used for measure the amount of O_2 and H_2 . Before starting the experiment, the glass cell have purged with Ar (99.9%) for 30 min to remove contained O_2 and H_2 . The chronoamperometry experiment was performed

with modified working electrode at a particular current density and at different time interval gas was analyzed with GC instrument. The theoretical amount of gas (O₂ and H₂) was calculated from accumulated charge during galvanostatic electrolysis by assuming 100% faradic efficiency.

$$\text{Theoretical amount (n in mole) of gas (H}_2, \text{O}_2) = \frac{Q}{e \times F} = \frac{I \times t}{e \times F}$$

Where I is the current in Amp, t is time in sec, e is the number of electrons which is 2 for HER and 4 for OER and F is the Faraday constant (96485.3 C mol⁻¹). From these two faradic efficiency of the catalyst towards OER and HER can be easily calculated.

Turn Over Frequency (TOF) Calculation¹³:

Assuming Every metal atom presence on the glassy carbon electrode are involved in OER/HER reaction, the TOF per active site for OER/HER reaction was calculated by following equation:

$$\text{TOF(H}_2\text{/O}_2\text{/s)} = \frac{\text{Total oxygen/Hydrogen turnover per geometrical area of working electrode}}{\text{Total no active site per geometrical area of working electrode}}$$

$$\text{TOF(s}^{-1}\text{)} = \frac{J \times A}{4 \times F \times n}$$

Where J is the current density (mA cm⁻²) at particular overpotential ($\eta = 0.35$ V), A is the geometrical area (cm²), F is the Faraday constant (96485.3 C mol⁻¹) and n is the mole of the active site on the electrode.

Double layer capacitance:

The double layer capacitance (C_{dl}) of the catalyst was measured from the CV plot of the catalyst taken in a non-faradic region with a small potential windows. Before taken the charging-discharging CV plots in different scan rate, working electrode was scanned 20 CV

cycling in a particular potentials region to stabilize the electrode. The slope of the linear plot of current density (mA cm^{-2}) at a particular potential (RHE) vs scan rate, gives the C_{dl} (mF cm^{-2}). In addition also we have calculated the roughness factor (R_f) of the materials was calculated from C_{dl} by

$$R_f = C_{dl}/C_s$$

Where C_s is the double layer capacitance of an atomically smooth planar surface of per unit area under identical conditions. Here, we considered bare GC electrodes as the planar surface. For bare GC electrode C_s is considered as 0.082 mF cm^{-2} .

ECSA calculation from under potential H-desorption method¹⁴:

ECSA was calculated from the hydrogen desorption (UPD- H_{des}) peak of CV curves. After double layer correction UPD- H_{des} peak of CV has been used to calculate the electrochemically active surface area (ECSA) by the following equation:

$$ECSA = S/m \times v \times c$$

Where S is double layer corrected area under hydrogen desorption curve, v is the scan rate (mV/s), c is the required charge to oxidize a monolayer of hydrogen on the platinum surface (mCcm^{-2}), the value of c is 0.21 mC cm^{-2} (required charge per cm^2 for hydrogen monolayer oxidation), m is the Pt loading on the electrode surface (mg).

CO stripping measurement¹⁵:

CO stripping measurement was performed by first holding the electrode potential at 0.1 V (RHE) for full monolayer adsorption of CO on metal surface. Then N_2 was flowed to remove the dissolved CO from the solution. Then CV scan was performed at 30 mV/s where the forward scan represents the CO stripping at different pH. The different pH solution was prepared by mixing of $0.2 \text{ M H}_3\text{PO}_4$ and 5 M KOH .

2.4. References:

1. W. H. Bragg, W.L. Bragg, “The reflexion of X-rays by crystals”. Proc R. Soc. Lond. A; **1913**, 88, 428–38.
2. A. R. West, “Solid state chemistry and its applications”, John Wiley & Sons, New York, 1984.
3. S. Amelinckx, D. V. Dyck, J. V. Landuyt, G.V. Tendeloo, “Electron microscopy: Principles and fundamentals” VCH, University of Michigan, 1997.
4. J. W. S. Hearle, J. T. Sparrow and P. M. Cross, “The use of the scanning electron microscope” J. Appl. Cryst. **1974**, **7**, 513-514.
5. C. D. Wagner. Handbook of x-ray photoelectron spectroscopy: a reference book of standard data for use in x-ray photoelectron spectroscopy, 2010.
6. P. Griffiths; J. A. de. Hasseth; “Fourier Transform Spectroscopy” (2nd ed.), Wiley-Blackwell, 2000.
7. Y. R. Sharma, “Elementary organic spectroscopy; Principles and chemical applications” S. Chand, New Delhi, 1980.
8. J.M. Hollas, Modern Spectroscopy, **2003**, Wiley, Fourth Edition.
9. Allen J. Bard, Larry R. Faulkner “Electrochemical Methods: Fundamentals and Applications” Wiley, 2000.
10. http://www.metrohm-autolab.com/download/Autolab_Brochure_2013_EN_LR.pdf.
11. www.ceb.cam.ac.uk/research/groups/rg-eme/teaching-notes/linear-sweep-and-cyclic-voltametry-the-principles

12. www.gamry.com/application-notes/EIS/basics-of-electrochemical-impedance-spectroscopy.
13. Sun, T.; Xu, L.; Yan, Y.; Zakhidov, A. A.; Baughman, R. H.; Chen, J., *ACS Catal.* **2016**, *6*, 1446-1450.
14. Yin, H.; Zhao, S.; Zhao, K.; Muqsit, A.; Tang, H.; Chang, L.; Zhao, H.; Gao, Y.; Tang, Z. *Nat. Commun.* **2015**, *6*, 6430.
15. Zheng, J.; Sheng, W.; Zhuang, Z.; Xu, B.; Yan, Y. *Sci. Adv.* **2016**, *2*, e1501602.

CHAPTER 3

Gold Aerogel Supported on Graphitic Carbon Nitride: Synthesis, Characterisation and Applications in Oxygen Reduction Reaction and Hydrogen Evolution Reaction

3.1 ABSTRACT

Fabrication of high surface area interconnected porous network of metallic nanomaterials is important for their applications in various fields such as catalysis, sensors, and electrochemistry. In this chapter we have shown a facile bottom up synthesis of high surface area and porous gold aerogel supported on carbon nitride sheets (CN_x). The reduction of HAuCl_4 in presence of carbon nitride nanosheets using sodium borohydride and ultrasonic treatment produces gold aerogel supported on carbon nitride (Au-aerogel- CN_x). When the reduction of HAuCl_4 in presence CN_x nanosheets was done only with ultrasonication, highly dispersed ultra-small (~ 2 nm) gold nanoparticles on CN_x sheets (AuNPs- CN_x) were formed. The Au-aerogel- CN_x and AuNPs- CN_x composites exhibited superior electro catalytic activity towards oxygen reduction reaction (ORR) in alkaline and acidic media. The Au-aerogel- CN_x composite show ORR onset potentials at 0.92 V and 0.43 V (Vs RHE) in 0.5 M KOH and H_2SO_4 solution. The four electron oxygen reduction process occurs at these supported catalysts in both alkaline and acidic media. In alkaline (KOH) medium the onset potential at Au-aerogel- CN_x is more positive (~ 30 mV) than that of commercial Pt/C catalyst. The composites display excellent methanol tolerance and comparable durability with commercial Pt/C. Furthermore, the Au-aerogel- CN_x composites exhibited high catalytic activity for hydrogen reduction reaction (HER) with small onset potential of -30 mV and a

Tafel slope of 53 mV dec^{-1} in acidic medium. At a small Au loading of 0.130 mg cm^{-2} , this catalyst also exhibit a current density of 10 mA cm^{-2} at a low overpotential of -185 mV with an excellent stability. The ORR and HER performances on porous, Au-aerogel- CN_x composites is better than that of AuNPs- CN_x catalyst and commercial flat gold electrode. The superior ORR and HER activity at Au-aerogel- CN_x composite are originated from the unique synergistic effects between porous Au network and carbon nitride (CN_x) support.

3.2 INTRODUCTION

Porous materials have attracted a tremendous attention in last few years due to their exceptionally high catalytic activity¹⁻³, electrical conductivity⁴ and mechanical properties⁵. These properties arise due to their ability to interact with the atoms or ions or molecules throughout the bulk of the materials, not only by their surfaces. In last decade porous metallic network structures have gained a tremendous attention for their various kinds of biological sensing applications^{6,7} and catalytic³ or electrocatalytic applications⁸. Metal aerogels is a new type of porous solid materials that have extremely low density, high porosity, high surface area, high electrical conductivity and catalytic properties. The properties of nanoparticles such as catalytic activities retain in the metal aerogel and it may thus bridge the gap between nanomaterials and macromaterials. It was reported that the properties of some of metal aerogels are superior to that of metal nanoparticles because of combined effects of nanoparticles in the aerogel⁹. Since the discovery of aerogel in 1963 by Kistler¹⁰, enormous efforts have been paid to synthesis various aerogels. Several approaches are available in literature for synthesis of different non-metal aerogel such as carbon aerogel¹¹, silica aerogel¹², organic-inorganic hybrid¹³, metal oxide¹⁴, and metal chalcogenides¹⁵. But only few methods are available for the production of metal aerogel^{18,16}.

¹⁸. For example, Eychmüller and coworkers^{8,16} have reported synthesis for monometallic, bi-metallic and composite aerogels based on controlled aggregation of metal nanoparticles using controllable destabilization and spontaneous gelation methods. Leventis and his coworkers^{17,18} developed methods for synthesis of different metallic (Fe, Cu, Ni, Co) aerogels by nanosmelting (sol-gel method) of hybrid polymer-metal oxide composites. A combustion method for synthesis of porous metallic aerogel was also reported by Tappan *et al.*¹⁹. The synthesis metallic aerogel supported on a two dimensional conducting support and their catalytic applications so far is not reported.

The synthesis of supported nanostructured compounds and studies on their catalytic properties has attracted so much attention to the scientific community recently since catalytic support is not only stabilize the nanoparticles, but also enhances their catalytic activities in some cases. For example, supported gold nanoparticles, display superior catalytic activity for various chemical reactions²⁰, such as low temperature catalytic combustion, partial oxidation of organic molecules, reduction of oxygen and hydrogen peroxide. It is also well known that the catalytic activity of gold catalyst depend not only size of nanoparticles, but, the nature of the support materials, preparation methods of the catalysts are also important for their superior catalytic activity. The remarkably high catalytic oxidation of CO over gold nanoparticles dispersed on various metal oxides catalyst was explained due to the synergic effect between gold nanoparticles and metal oxides²¹⁻²³. Graphene has already become a promising candidate as a two dimensional support for different nanoparticles due to its unique properties²⁴. Another 2D material, graphitic carbon nitride (g-C₃N₄) which has similar structure like graphene is a promising support for various nanomaterials. The graphene/ g-C₃N₄ supported metal or semiconductor nanoparticles have confirmed to be

effective materials for photocatalysis²⁵⁻²⁷, catalysis^{2,28} and biosensor applications^{29,30}. Though C₃N₄ supported nanoparticles were reported by several groups^{26,27,30} but C₃N₄ or any other 2D material supported metal Au aerogel is not reported so far. However few self-supported metal aerogel and their applications are available in literature. For example synthesis of Pt-aerogel and Pt based bi-metallic was reported for ORR³¹. Pd-aerogel was reported for formic acid oxidation³², ethanol oxidation³³.

The concern about the energy shortage and environmental pollution is rising due to use of fossil fuel; there are thus always need of alternate renewable green sources of energy^{34,35}. The electrochemical energy generation such as fuel cell and electrochemical water splitting is one of the most viable green approaches for energy generation. The oxygen reduction reaction (ORR) and hydrogen evolution reaction (HER) are the two important processes that are involved in fuel cell and electrochemical water splitting. Without any suitable catalyst, both these reactions (HER and ORR) show a sluggish kinetics. Platinum is the best known catalyst for the both processes. But, the high cost and scarcity of platinum prevent its wide spread commercialization. It is important to develop non platinum based ORR active cathode for commercialization of fuel cell. Enormous efforts have been spent during the past decades on finding an economically viable novel and better catalyst for this purpose. Recently noble metal nanoparticles were found to be most promising electrocatalyst due to their high surface area and their cost effective of production since small amount of metal are used in their synthesis. Bulk gold metal shows moderate ORR activity and its activity depends on the size in nanoparticles. For example Crompton and co-workers³⁶ showed that ultra-small (1.5-2 nm) citrate capped gold nanoparticles acts as negative catalyst for ORR in compare to Au macro-electrode. It is also reported by them³⁷

that the 17-40 nm AuNPs showed comparable ORR properties with Au electrode and H_2O_2 was the final product due to two electron reduction of oxygen. M. Bron³⁸ has claimed that surface specific activity and number of transferred e in ORR process of carbon black stabilized AuNPs are independent with different sizes (2.2-42.3nm). T. Inasaki *et al.*³⁹ reported that SA increases with decreasing particle size and number of electron transferred per O_2 molecule also increases. S. Guerin *et al.*⁴⁰ found that the specific activity towards ORR decays rapidly with decreasing particle size below 3 nm. Although several reports on ORR activity Au nanoparticles are available, they are still inferior in compared to platinum.

Electrolysis of water to generate hydrogen through HER process in acidic medium i.e electro-catalytic reduction of proton to molecular hydrogen shows a promising approach to produce a clean energy^{34,35}. An efficient HER catalyst is required to produce a large cathodic current densities at low overpotential⁴¹. The research efforts are going to find suitable hydrogen evolution catalyst based on more economical materials such as Ni Based catalyst⁴²⁻⁴³, Mo based catalyst^{41,44-46}, other transition metal phosphides^{47,48} *etc.*, which may replace the expensive Pt catalysts. The gold surface shows moderate HER activity. Although some reports of HER on gold are available, but, these are mostly dedicated to either influence of surface structure⁴⁹ on the HER rates or effects of organic molecules on HER performances⁵⁰. J. Perez *et al.*⁵¹ reported pronounced structural sensitivity of Au crystal face and they have shown the catalytic activity decreases in this sequence $Au(111) < Au(100) < Au(110)$. Negative HER activity of small (1-2 nm) AuNPs was also reported recently³⁶.

Herein, we report here facile synthesis of gold aerogel supported on thin carbon nitride sheets (Au-aerogel-CN_x) and their applications in oxygen reduction (ORR) and

hydrogen evolution (HER) reactions. Highly porous interconnected metal nanoparticles network are formed on CN_x support due to reduction $HAuCl_4$ in presence of g- CN_x nanosheets with $NaBH_4$ and ultrasound treatment; whereas only ultrasonic reduction (without $NaBH_4$) produces highly dispersed ultra-small (~2nm) gold nanoparticles supported on CN_x sheets (AuNPs- CN_x). The Au-aerogel- CN_x and AuNPs- CN_x , composites exhibited superior electrocatalytic activities towards ORR in acidic and basic medium. The ORR activity of Au aerogel composite in basic medium is better than that of commercial Pt/C whereas it is lower than Pt/C in acidic medium; but, better than that of reported gold metal based electrocatalysts. The oxygen reduction in acidic and basic media occurs via 4 electron pathways at both AuNPs and Au aerogel supported CN_x catalysts. Furthermore, these two composite also showed superior hydrogen evolution activity in acidic medium. The morphology dependent HER behaviour of Au composites was observed in acidic media; Au-aerogel- CN_x composite showed best performance and flat gold electrode displayed poorest performance. The Au-aerogel CN_x catalyst exhibited an onset potential of -30 mV, current density of 10 mA cm^{-2} at small HER overpotential of -185 mV and a Tafel slope of 53 mV dec^{-1} with excellent durability. The superior HER and ORR activities at Au-aerogel supported CN_x composite was explained based on synergetic effects of CN_x support and porous gold and strong catalyst-support interaction.

3.3 EXPERIMENTAL SECTION

Preparation of Graphitic Carbon Nitride (g- CN_x):

The synthesis of carbon nitride (g- CN_x) from formamide was done by a microwave-mediated method^{51,52} reported by our group previously. In brief, 30 mL of formamide was heated using a microwave synthesizer for 2 h at 180 °C. The resulting brown solution was

evaporated at 180 °C in a rotary evaporator to obtain a bulk amount of black product. This product was washed with water, filtered and vacuum-dried to give a dry solid of g-CN_x.

Preparation of Au-aerogel-CN_x composite:

The 5 mg of as prepared g-CN_x was dispersed in 3 ml of water by sonication for 10 min. The aqueous solution of HAuCl₄ was also prepared in a separate vial. These two solutions were mixed together followed by sonication for 10 minute. Then solid NaBH₄ was added and the mixture was ultra-sounded with 28 kHz frequency for 3 hours at 400 watt. After ultrasound treatment the freshly formed solid product was separated by centrifugation at 8000 rpm for 10 minutes. After washing with water, Au aerogel supported CN_x products were dried under vacuum. The 0.162 mmol HAuCl₄ and 0.53 mmol NaBH₄ solutions were used for the synthesis of 88 wt% Au-aerogel-CN_x whereas 0.235 mmol of HAuCl₄ and 0.79 mmol NaBH₄ solutions were used for 92 wt% Au-aerogel-CN_x. The gold nanoparticles supported on CN_x were produced by only ultrasonic treatment of HAuCl₄ (0.147 mmol) in presence of CN_x sheets (5 mg) without any reducing agent²⁶.

Preparation of Au-aerogel-CN_x/GC and AuNPs-CN_x/GC electrodes:

Glassy carbon electrode (GCE) was polished with 1.0, 0.1 and 0.05 mm alumina slurry on Buehler micro cloth polishing cloth. After rinsing, the electrode was sonicated in distilled water about 10 min. 1 mg synthesized composite was dissolved in 1 ml water to make a stock solution. 15, 11, 10 µl of aqueous stock solution was evaporated on cleaned glassy carbon electrode to prepare AuNPs-CN_x, Au-aerogel-CN_x/GC Electrode to maintain constant amount of Au in every electrode. ORR was done in both alkaline and acidic medium with the help of linear sweep voltammetry (LSV) and cyclic voltammetry (CV) measurement by using oxygen saturated 0.5 M H₂SO₄ and KOH with 100 mV sec⁻¹ scan

rate. For HER analysis LSV measurement was done using nitrogen saturated 0.5 M H₂SO₄ with 10 mV sec⁻¹ scan rate.

3.4 RESULTS AND DISCUSSIONS

3.4.1 Characterization of Au composites:

The powder x-ray diffraction (p-XRD) patterns of g-CN_x, AuNPs-CN_x, Au-aerogel-CN_x nanocomposites are shown in Figure 3.1. Peak positioned at 2θ value of 27.30 corresponds to (002) plane of g-CN_x with interlayer d-spacing 3.27Å which was reported previously by our group^{52,53}. The additional four well resolved peaks of Au composites located at 2θ values 38.20⁰, 44.40⁰, 64.50⁰, 77.54⁰ and 81.80⁰ can be indexed as (111), (200), (220), (311) and (222) reflection planes respectively for pure face centered cubic (f.c.c.) Au nanoparticles (JCPDS No. 04-0784)⁵⁴. The p-XRD pattern of Au-aerogel-CN_x composite is further studied by Scherrer analysis (see appendix). The most intense peak positioned (2θ) at 38.20⁰ was used to calculate the size of Au-aerogel in the composite and the size of ~8 nm gold nanoparticle was obtained from the Scherrer analysis.

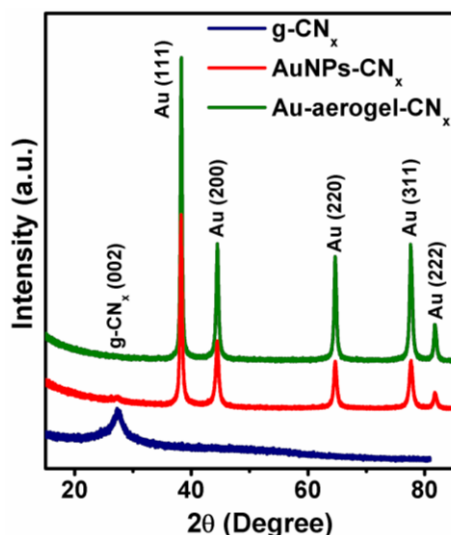


Figure 3.1. p-XRD of g-CN_x, AuNPs-CN_x and Au-aerogel-CN_x composite.

The tunneling electron microscopy (TEM) and field emission scanning electron microscopy (FESEM) were used to study the morphology of Au-aerogel network supported on CN_x sheets. TEM samples were prepared by evaporation of 10 μl aqueous solution of Au aerogel-CN_x composite on TEM grid. Figure 3.2a shows the TEM image two dimensional thin CN_x sheets which were formed on evaporation of g-CN_x. The Ultrasound treatment of HAuCl₄ and CN_x sheets produces AuNPs-CN_x composite. As shown in Figure 3.2b and Figure 3.5a, nice nearly ordered distribution of 1.0 - 2.5 nm sized gold nanoparticles on CN_x sheets were produced after ultrasound treatment. The formation of noble metal particles on the surface of CN_x sheets resulting from ultrasound treatment without reducing agent was reported by our group recently²⁶. When the reduction of HAuCl₄ in presence of CN_x sheets was done along with NaBH₄ and ultrasound treatment, the Au-aerogel supported on CN_x sheets is produced. Some representatives TEM images of Au-aerogel supported on CN_x sheets are shown in Figure 3.2 (c-f) and Figure 3.5 (d-i). In all these images, the ultra-thin Au nanowires are interconnected to form three dimensional networks like structure with large number of open pores. The Au aerogel with porous structure are supported on CN_x sheets, which are clearly visible in Figure 3.2d and Figure 3.5h. The nano-chains has uniform diameter of about 8-10 nm. The coalescence of initial spherical particles into chains structure is quite obvious in the TEM images. The assembly of 6-8 nm sized nanoparticles of supported on CN_x sheets is also seen (Figure 3.5f), but their abundance are low. Since the size of independent nanoparticles and diameter of nanochains are quite similar / less, it can be concluded that the aerogel are directly from the colloidal particles with fusion of nanoparticles, no pre-agglomeration occurs.

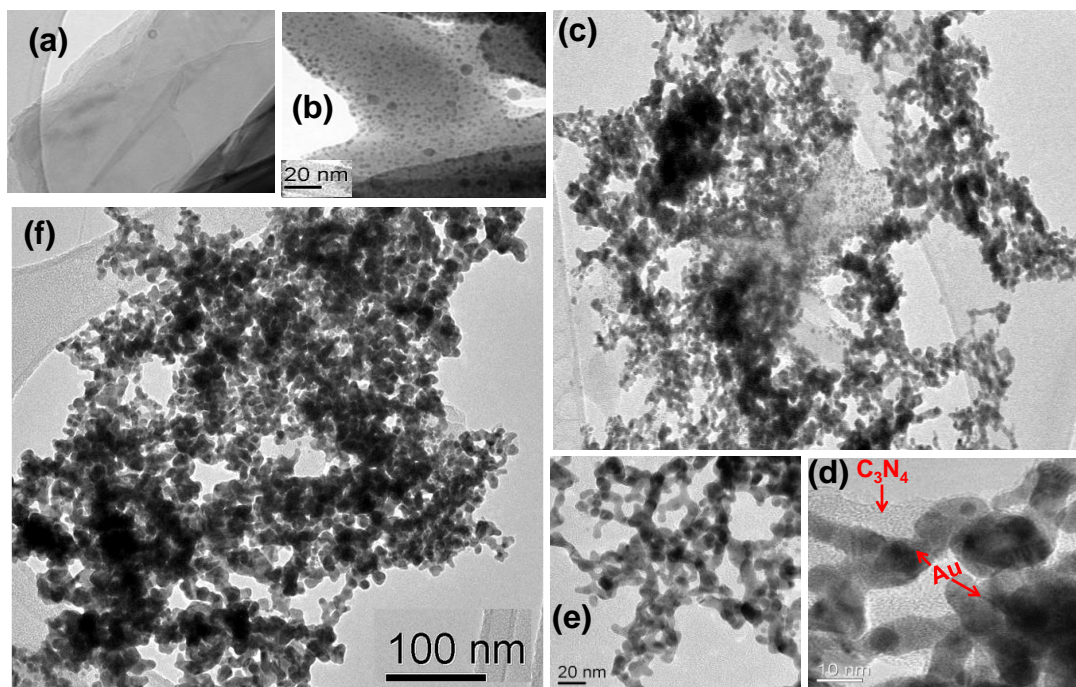


Figure 3.2. TEM images of (a) g-CN_x sheet (b) AuNPs on CN_x (AuNPs-CN_x composite) showing highly dispersed ultra-small AuNPs on the CN_x sheets (c, f) Low resolution TEM images of Au-aerogel supported on CN_x showing porous morphology. (d, e) Mid resolution TEM images of Au-aerogel showing interconnected Au nanochains and CN_x support.

The SAED image of Au aerogel is shown in Figure 3.3a suggesting a polycrystalline structure. The interlayer spacing calculated from SAED image are 2.36, 2.03, 1.22, 0.946 Å which corresponds to (111), (200), (220), (311) and (331) planes of f.c.c gold lattice. This is in good agreement with p- XRD studies (see Figure 3.1) of Au-composites. The HRTEM images as shown in Figure 3.3b and Figure 3.5i clearly show the lattice fringes with the d spacing of 2.36 Å corresponding to the (111) plane of face centered cubic gold suggests the gold aerogel are generally growing along the Au (111) planes. The orientations of these lattice fringes are same. This From TEM analysis it can be concluded that interconnected Au network was formed due to ultrasound treatment in the mixture of HAuCl₄, CN_x and NaBH₄.

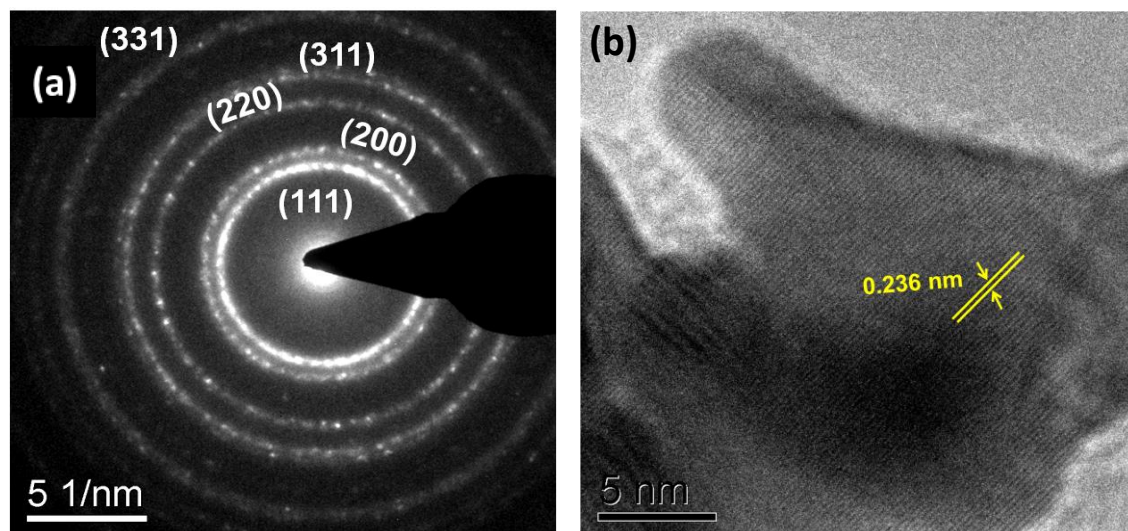


Figure 3.3. (a) SAED images of Au-aerogel-CN_x (b) HRTEM images of Au-aerogel-CN_x showing preferential growth along Au (111) plane.

FESEM images (Figure 3.4 a, b, c) also have been taken also to study the surface morphology of the composite on silicon substrate. FESEM samples were prepared by evaporation of 30 μ l stock solution with 0.5 mg/ml concentration on Si wafer. In FESEM images it is clearly visible of the interconnected porous network with ultrathin wire like structure with many bifurcations.

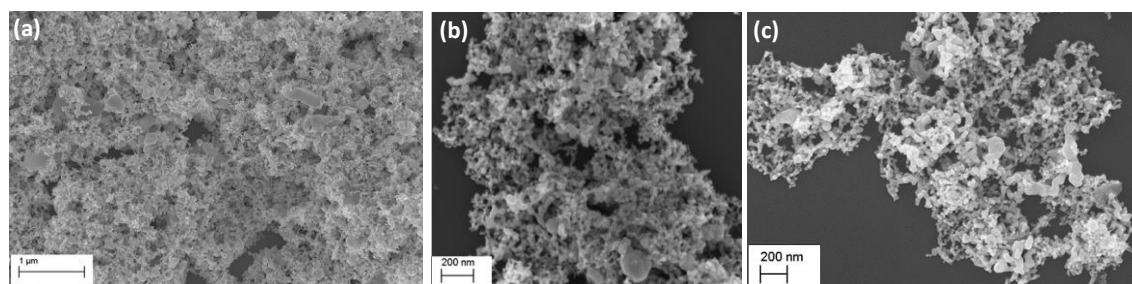


Figure 3.4. FESEM images of Au-aerogel-CN_x shows highly porous morphologies of interconnected nanoparticles

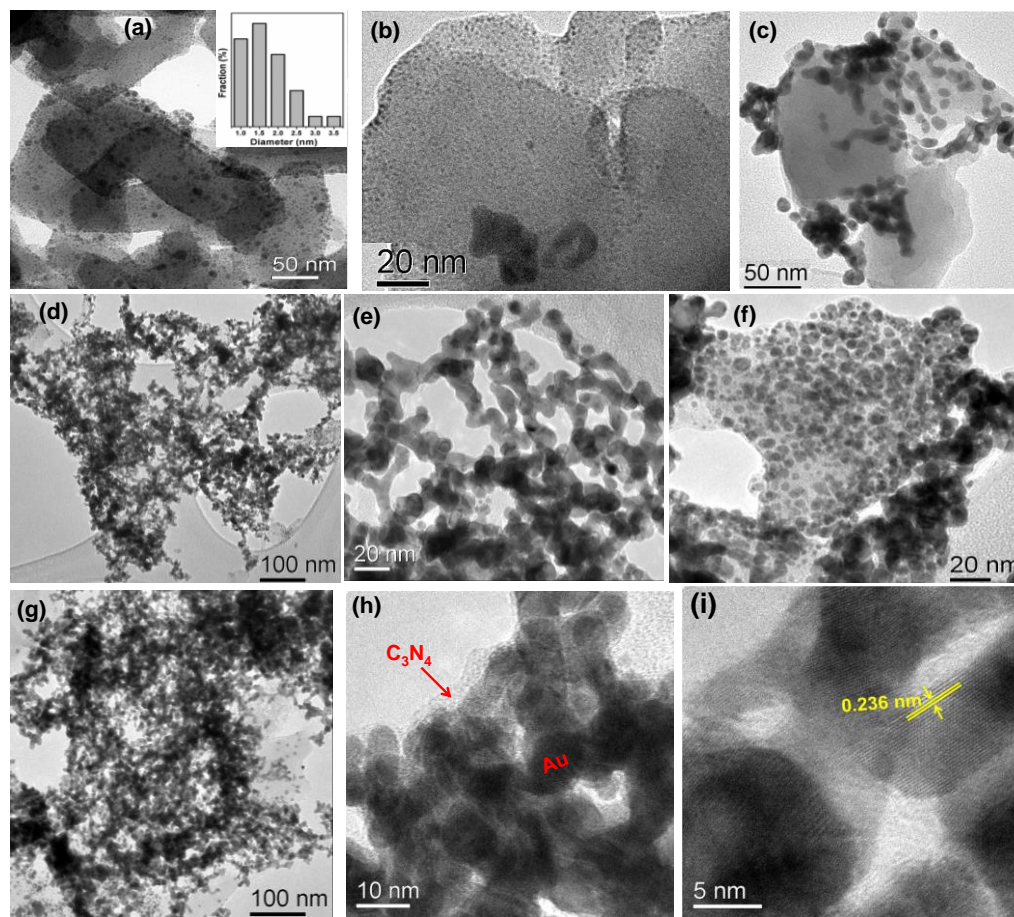


Figure 3.5. (a) TEM images of AuNPs-CN_x formed from ultrasound treatment of HAuCl₄ with CN_x (inset: particle size distribution graph, particle size are in the range of 1 nm - 2.5 nm). (b, c) TEM images of Au-CN_x composite (formed from ultrasonic treatment on 0.162 mmol of HAuCl₄ and 0.10 mmol of NaBH₄) showing highly dispersed AuNPs of less than 1 nm on CN_x sheet in Figure 3.5b and few nano chains on S1c. (d, e) TEM images of Au-aerogel-CN_x formed when 0.162 mmol HAuCl₄ and 0.53 mmol NaBH₄ was used and (f) TEM images showing 6-8 nm AuNPs distributed on CN_x sheet. (g, h) TEM images of Au-aerogel-CN_x formed when 0.235 mmol of HAuCl₄ and 0.79 mmol of NaBH₄ was used. (i) HRTEM image of Au-aerogel-CN_x.

To understand the formation mechanism of Au-aerogel on CN_x sheets, the structural morphologies of several compounds, prepared by varying amount of NaBH₄, were examined using TEM. When no NaBH₄ used, only ultrasonic treatment of HAuCl₄ and CN_x yields nearly ordered, highly dispersed AuNPs of size~2nm on CN_x sheets are formed as shown in Figure 3.2b and Figure 3.5a. The size of these particles is in between 1.0 – 2.5 nm with mean diameter of 2 nm. Addition of small amount of NaBH₄ (0.10 mmol) during synthesis

process, highly dispersed gold nano-dots of size less than 1 nm on CN_x are formed and some nanochains with single or few branches are also visible indicating initiation of aerogel formation (Figure 3.5b, c).

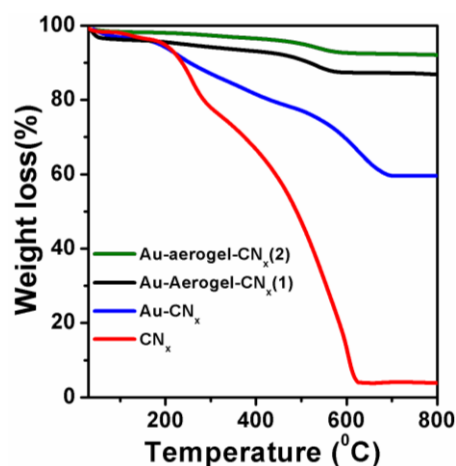


Figure 3.6. TGA curves of Au-aerogel(1)- CN_x , Au-aerogel(2)- CN_x , AuNPs- CN_x and CN_x .

Since the amount of CN_x nano-sheets and HAuCl_4 were taken same with varying in amount NaBH_4 in synthesis of these two Au-aerogel composites, same amount of Au atoms is produced due to ultrasonication with or without NaBH_4 . Some of gold atoms are utilized for the formation of gold nanochains when synthesis was done in presence of small amount of NaBH_4 . This explains why gold nanoparticles (less than 1nm) produced with small amount NaBH_4 are smaller than that of (2nm) when ultrasonication was done without any reducing agent. On the other hand, as shown in Figure 3.2 (d-f) and 3.3 (d-i), highly porous, interconnected gold nano chain network structure (aerogel) supported on CN_x sheets are formed when sufficient NaBH_4 (0.53 or 0.79 mmol solution) was added during synthesis process. These TEM images clearly show the aerogels are composed of ultrathin gold nanochains with a diameter of 8-10 nm.

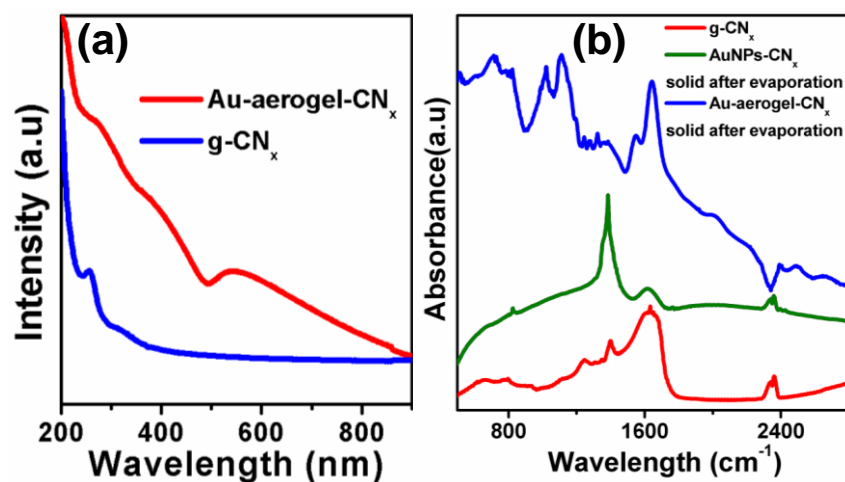


Figure 3.7. (a) UV-Visible spectrum of g-CN_x and Au-aerogel-CN_x. (b) FT-IR spectra of CN_x (red line), AuNPs-CN_x (green line) and Au-aerogel-CN_x (blue line).

Freshly prepared g-CN_x and solid, obtained from evaporation of aqueous dispersion of Au-aerogel-CN_x and AuNPs-CN_x were used for FT-IR measurement. The ultrasonication of HAuCl₄ without NaBH₄ produces gold atoms (nanoparticles) slowly due to slow reduction of HAuCl₄, and AuNPs are physically adsorbed on the surface of CN_x sheets. Since the fast reduction of HAuCl₄ with NaBH₄ produce large number gold atoms in a very short time, nucleation and uncontrolled growth of nanoparticles occurs on CN_x sheets to form porous network of gold on CN_x support. The exact amount of gold loading in Au-aerogel-CN_x was determined by Thermo Gravimetric Analysis (TGA) method also. TGA curves (Figure 3.6) shows 82 wt% loading of Au on Au-Aerogel supported CN_x whereas Au loading is 58% in AuNPs-CN_x composite. In order to achieve higher Au loading samples were also prepared with higher amount of HAuCl₄ and NaBH₄ taking constant amount of CN_x sheets. The highest loading we could achieve is 92 wt% gold when 0.235 mmol HAuCl₄, 0.79 mmol NaBH₄ were used for synthesis.

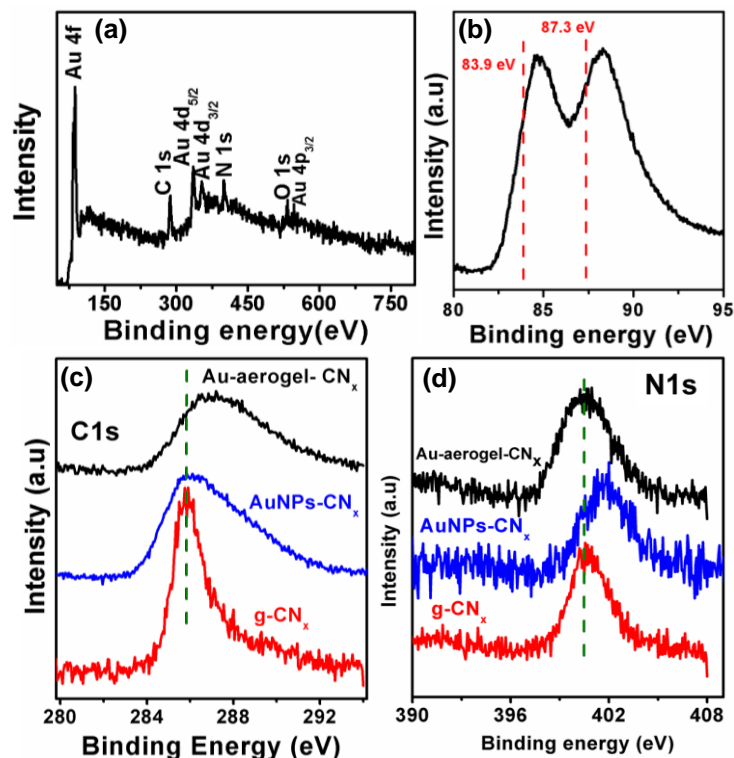
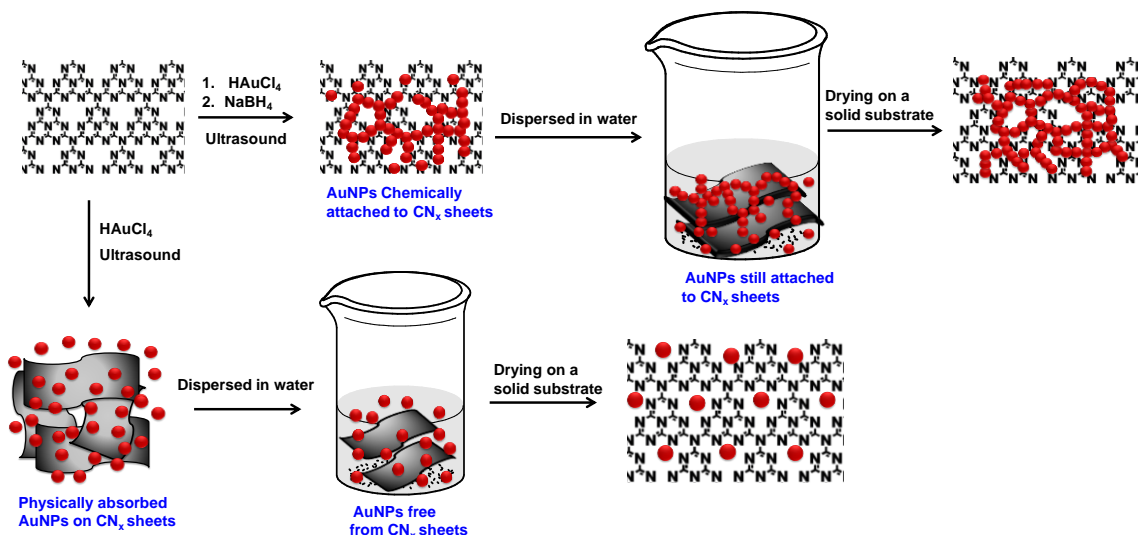


Figure 3.8. (a) XPS survey scan of Au-aerogel-CN_x. XPS spectrum of (b) Au 4f orbital and (c) C1s for Au-aerogel-CN_x (black line), AuNPs-CN_x (blue line), g-CN_x (red line). (d) Comparison of N2p XPS spectra of g-CN_x, AuNPs-CN_x, Au-aerogel-CN_x.

The amount of gold loading in these catalysts was also determined by inductively coupled plasma optical emission spectrometry (ICP-OES), measurement and the concentration of carbon and nitrogen was determined by EDX and XPS analysis. The exact wt% of Au present in Au-aerogel-CN_x and AuNPs-CN_x composite was 85.4 and 55.9 respectively. The carbon: nitrogen ratio in Au-aerogel-CN_x and AuNPs-CN_x was 1.25:1 and 1:1.1 respectively. Figure 3.2f and Figure 3.5g represent the Au-aerogel-CN_x composite with 92 wt% Au loading. Width of nano chains is almost same as 82 wt% loading sample but, pores size become small due to large number of interconnections between nano chains forming highly porous Au network on CN_x support and nanoparticles are clearly visible in the nanochains since large amount of Au precursor were used. The 82 wt% and 92 wt% Au

loading in Au-aerogel supported CN_x composite is abbreviated as Au-aerogel(1)- CN_x and Au-aerogel(2)- CN_x respectively.



Scheme 3.1. Schematic representations of formation of Au-aerogel and AuNPs on CN_x sheet.

Figure 3.7a shows the UV-Visible spectrum of aqueous solution of g- CN_x and Au-aerogel- CN_x . The strong surface plasmon peak at 540 nm for Au-aerogel- CN_x compound suggests the presence of Au nanostructure. X-ray photoelectron spectroscopy (XPS) and FT-IR spectroscopy were used to examine the change of electronic structure of CN_x framework in presence of AuNPs and Au-aerogels. The FT-IR spectra of g- CN_x as shown in Figure 3.7b, two peaks, at 1230 cm^{-1} and 1400 cm^{-1} , are due to aromatic C=N stretch and 1600 cm^{-1} can be assigned as C=N stretching^{51,52}. These three peaks disappeared and a new intense peak at 1380 cm^{-1} appeared when AuNPs are dispersed on CN_x matrix. The FT-IR spectrum of Au-aerogel- CN_x compound is also completely different from that free CN_x and AuNPs- CN_x compound. The peaks at 1116 and 1024 cm^{-1} can be assigned C-N single bond and peak at 1636 cm^{-1} is attributed to C=N double bond. The aqueous solutions of AuNPs- CN_x and

Au-Aerogel-CN_x compounds were evaporated separately and solid products were used for FT-IR measurements. However, FT-IR spectra of freshly prepared powder sample were also taken. The IR spectrum of freshly prepared powder AuNPs-CN_x compounds is similar to free CN_x compound whereas spectra of freshly prepared Au-aerogel-CN_x is completely different from free CN_x compound (Figure 3.7b and S3.1 a, b). This indicates that Au aerogel is chemically attached to CN_x sheets and AuNPs are physically adsorbed in freshly prepared AuNPs-CN_x powder sample. Figure 3.8a shows the survey scan of the XPS spectrum which clearly indicates the presence of gold, carbon, nitrogen and oxygen atoms in AuNPs-CN_x composite. It is well known that the binding energy spectra of Au 4f of metallic AuNPs is appeared as doublet with binding energy 83.9 eV for 4f_{7/2} and 87.3 for 4f_{5/2} peak⁵⁵. Figure 3.8b display the Au 4f spectrum for Au-aerogel-CN_x and two peaks appeared at 84.7 and 88.4 eV. The peaks at 84.7 and 88.4 eV can be assigned to Au 4f_{7/2} and 4f_{5/2} photoelectron. This binding energy shift suggests the strong interaction between Au aerogel and the CN_x support. The carbon 1s (C1s) and nitrogen 1s (N1s) XPS spectra of the CN_x were deconvoluted to three and two main Gaussian peaks, respectively (Figure S3.2 a, b). The peaks at 285.45 (C1s) and 286.35 eV (C1s) were assigned to the presence of (sp²) N-C-N (carbon bonded to two nitrogen atom) and C(-N)₃ (planar trigonal carbon geometry), respectively whereas the peaks at 400.3 and 401.4 eV suggest the presence of (sp²) C-N(sp²) or a pyridine moiety and quaternary nitrogen, respectively. The comparison of C1s and N1s XPS spectra of CN_x, AuNPs-CN_x and Au-aerogel-CN_x are shown in Figure 3.8c and 3.8d respectively. This shows the positions as well as the shapes of the C1s XPS spectrums of CN_x in the presence of Au-aerogel-CN_x are significantly different than that of free CN_x. The C1s peaks became broad and shift of 1.6 eV towards higher binding energy was observed when Au-aerogel is supported on CN_x framework, but the position of N1s

peaks remain unaffected. Therefore, the change of binding energy of carbon and Au confirm there is strong interaction between carbon and Au in Au-aerogel-CN_x composite. As shown in Figure 3.8d binding energy of 1s nitrogen in AuNPs-CN_x is 1 eV higher than that of free CN_x whereas position of C binding energy is almost remain same, only broadening of the peak is observed (Figure 3.8c). Thus, it can be concluded that nucleation of Au nanoparticles occurs at carbon site in case of Au-aerogel-CN_x whereas nucleation occurs at nitrogen site for AuNPs-CN_x. Based on TEM, SEM, XPS, FT-IR spectroscopic studied, formation mechanism of Au metal aerogel supported on CN_x sheets was proposed (Scheme 1). Since, during the synthesis of Au-aerogel-CN_x composite, large number Au atoms are produced in very short time due to fast reduction of HAuCl₄ by NaBH₄, nucleation of AuNPs carbon center in CN_x sheets and finally growth takes place to form Au-aerogel on CN_x sheets. However, when there is no NaBH₄ used reduction of HAuCl₄ due to ultrasonication, produces gold atoms slowly, and gold particles are physically adsorbed on the surface of CN_x sheets leading to precipitation of AuNPs-CN_x composite. On evaporation of aqueous solution of AuNPs-CN_x composite on a solid substrate, first 2D sheets of CN_x sheets are formed and nucleation at nitrogen atom, followed by growth occurs to form assembly of gold nanoparticles on CN_x sheets. Formation and evaporation induced ordered assembly of silver nanoparticles on CN_x sheets was also reported by our group recently³⁰.

3.4.2 Electrochemical Characterization

The electrochemical activity of freshly prepared Au-aerogel-CN_x composite modified GC electrode was first investigated using Cyclic voltammetry (CV) with the [Fe(CN)₆]^{3-/4-} redox couple.

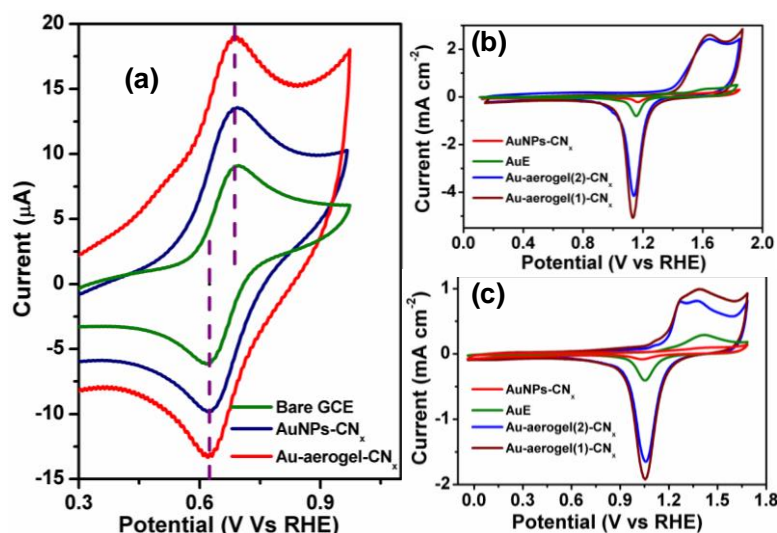


Figure 3.9. (a) CVs of 0.5 mM $[\text{Fe}(\text{CN})_6]^{3-/4-}$ solution at GCE, AuNPs- CN_x and Au-aerogel- CN_x modified GC electrode. Electrolyte: 0.05 M H_2SO_4 solution. (b) CVs of AuNPs- CN_x , commercial flat Au electrode, Au-aerogel(1)- CN_x , Au-aerogel(2)- CN_x in N_2 saturated 0.5 M H_2SO_4 solution and (c) CVs of AuNPs- CN_x , commercial flat Au electrode, Au-aerogel(1)- CN_x , Au-aerogel(2)- CN_x in N_2 saturated 0.5 M KOH solution. Scan rate 100 mV sec^{-1} .

Figure 3.9a represent the CVs of GC electrode and Au-aerogel- CN_x as well as AuNPs- CN_x modified GC electrode recorded in 0.05 M H_2SO_4 solution containing 0.5 mM $\text{K}_4[\text{Fe}(\text{CN})_6]$. This shows the significant improvement of catalytic activity at Au-aerogel- CN_x/GC electrode in compared to bare GC. It is well known that the electrochemical reaction of $[\text{Fe}(\text{CN})_6]^{3-/4-}$ is sensitive to surface, but less significant effect on oxygen functionalities in carbon based electrode^{56,57}. The CV at GC electrode showed a redox peak with a peak potential difference (ΔE_p) of 75 mV indicating a quasi-reversible redox reaction. For Au-aerogel- CN_x modified GC electrode, both anodic and cathodic current densities were increased significantly and 13 mV decrease of ΔE_p was observed in comparison to bare GC electrode. The observed ΔE_p values at Au-aerogel- CN_x/GC and AuNPs- CN_x/GC are 62 mV and 66 mV respectively.

Table 3.1. Electrochemical parameters deduced from Figure S3.3 such as ΔE_p and slope of cathodic and anodic current of Au-aerogel-CN_x, AuNPs-CN_x and bare GCE.

Catalyst	ΔE_p (mV)	Slope (i_a) ($\mu\text{A}/\text{Vsec}^{-1/2}$)	Slope (i_c) ($\mu\text{A}/(\text{Vsec}^{-1/2})$)
Au-aerogel-CN_x	62	94 ($R^2 = 0.985$)	-68 ($R^2 = 0.990$)
AuNPs-CN_x	66	64 ($R^2 = 0.993$)	-32 ($R^2 = 0.997$)
GCE	75	28 ($R^2 = 0.999$)	-20 ($R^2 = 0.997$)

The decrease of ΔE_p value with enhancement of peak currents at Au-aerogel-CN_x-GC suggests facile fast electron-transfer kinetics for this redox couple. As shown in Figure S3.3, both the oxidation and reduction peak of currents at these three Au-aerogel-CN_x/GC, AuNPs-CN_x/GC and GC electrodes increased linearly with square root of the scan rate, indicating that the reaction is controlled by a semi-infinite linear diffusion. The larger slope values of the linear regression equation (Table 3.1) and low ΔE_p suggest that⁵⁷ the unique electron structure and requisite surface structure endows Au-aerogel-CN_x film with fast electron and mass transfer. Voltammetry method was used to further electrochemical characterization of synthesized composite. CV was done in both 0.5 M H₂SO₄ and 0.5 M KOH medium in N₂ saturated atmosphere. Representative voltammograms are shown in Figure 3.9(b, c). In acidic solution the anodic peak at $E > 1.4$ V can be attributed as the formation of Au surface oxides and the cathodic peak at 1.1 V to the reduction of these surface oxides⁵⁸. The large back ground mainly due to the high surface area of Au-aerogel on CN_x support. In alkaline (KOH) medium Au surface oxidation and reduction are also visible.

Table 3.2 ECSA of different catalysts in acidic and basic medium.

Catalyst	A_r cm ² (Acidic)	A_r cm ² (Basic)
AuNPs-CN _x	0.14	0.07
Au-aerogel(1)-CN _x	1.17	0.6
Au-aerogel(2)-CN _x	1.05	0.5
AuE	0.17	0.1

Au oxidation peak is observed at $E > 1.2$ V and reduction peak at 1.0 V. The real electrochemical surface area of samples (ECSA) was determined by using cyclic voltammograms by using charge integration of reduction of gold oxide peak and reduction value of monolayer is assumed $400 \mu\text{C cm}^{-2}$. From CV it is evident that ECSA is increasing as we entering in porous network structure. The ESCA values of AuNPs-CN_x, commercial flat Au electrode, Au-aerogel(1)-CN_x, Au-aerogel(2)-CN_x are 0.14, 0.17, 1.17 and 1.05 per cm² (Table 3.2) in acidic medium. The surface areas of porous Au-aerogel-CN_x samples are much higher than that of AuNPs-CN_x and commercial flat Au electrode. In alkaline medium also Au-aerogel-CN_x has high ECSA value than AuNPs-CN_x and commercial flat Au electrode (Table 3.2).

3.4.3 ORR studies on Au-aerogel-CN_x catalysts in alkaline medium:

The electrochemical behavior of Au-aerogel-CN_x samples was measured towards oxygen reduction reaction (ORR). ORR is a complex multi electron reaction with involving different elementary steps with different intermediates⁵⁹. Oxygen can electrochemically reduce either directly to water (direct 4e reduction) or through the formation of H₂O₂ (2e reduction) and then this peroxide can be reduced to water (series 4e pathway) or chemically decomposed on electrode or desorbed in bulk.

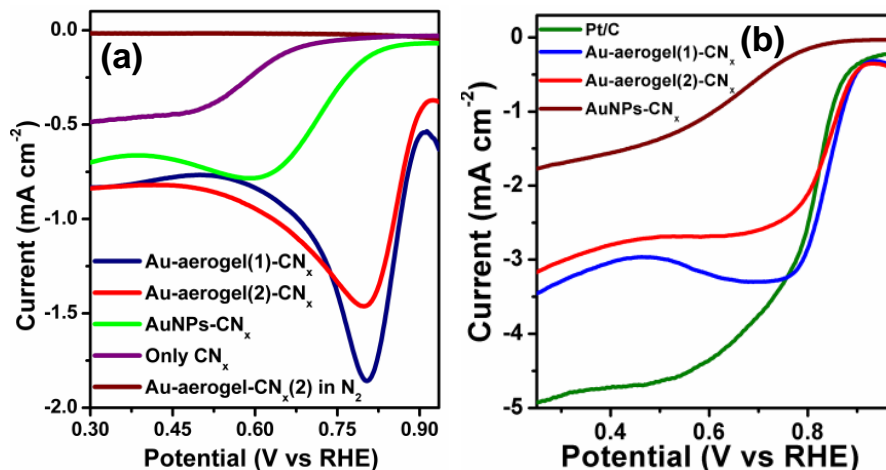


Figure 3.10. electrodes (a) LSV curves at Au-aerogel(1)-CN_x/GCE, Au-aerogel(2)-CN_x, AuNPs-CN_x, CN_x modified GC electrode in presence of oxygen saturated KOH medium and Au-aerogel(2)-CN_x in presence of nitrogen saturated solution. (b) Comparison of LSV polarization curve of Au-aerogel-CN_x, Pt/C-GCE with 1000 rpm rotation speed.

Production of H₂O₂ in fuel cell is never desirable at all as it can corrode the membrane electrode assembly. Therefore, many efforts have been made for preparation of Pt, Pd, Au based catalysts to decrease the overpotential and the H₂O₂ formation. To examine the catalyst activity we performed the ORR in alkaline medium. Figure 3.10a shows the typical linear sweep voltammetric (LSV) curves for ORR at CN_x, AuNPs-CN_x, porous-Au-aerogel(1)-CN_x and Au-aerogel(2)-CN_x modified GC electrodes in O₂ saturated 0.5 M KOH medium with each Au loading of 0.130 mg cm⁻². All the modified electrodes show a LSV peak in O₂ saturated KOH solution and the Au-aerogel-CN_x modified electrode doesn't show any peak in nitrogen saturated KOH medium suggesting the ORR activity of these electrodes. The CN_x modified GC shows a weak peak at 0.48 V (vs. RHE). When GC electrode was modified with AuNPs-CN_x and Au-Aerogel-CN_x, a stronger peak was appeared at 0.61 V and 0.8 V respectively.

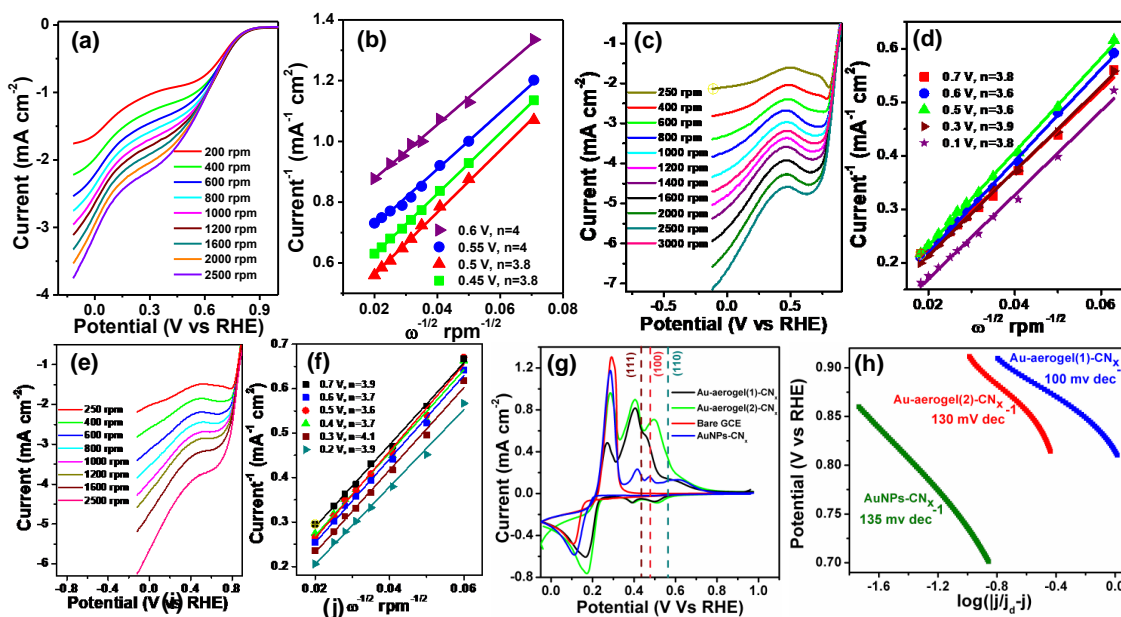


Figure 3.11. (a) ORR polarisation curves of AuNPs-CN_x/GCE. (b) K-L plot of the ORR of AuNPs-CN_x/GCE. (c) ORR polarisation curves of Au-aerogel(1)-CN_x/GCE. (d) K-L plot of the ORR of Au-aerogel(1)-CN_x/GCE. (e) Au-aerogel(2)-CN_x/GCE at different rotation speed at 0.5 M oxygen saturated KOH solution at a scan speed 100 mV sec⁻¹ with Au loading of 0.130 mg cm⁻². (f) K-L plot of the ORR of Au-aerogel(2)-CN_x/GCE. (g) Voltammetric profile of Au-aerogel-CN_x, AuNPs-CN_x and GCE in 0.1 M KOH solution containing 2mM Pb(NO₃)₂ solution at a scan rate 10 mV sec⁻¹. The main Pb desorption peaks from Au surfaces are marked. (h) Mass transfer corrected Tafel slope of different catalyst was shown. All ORR experiments were done at oxygen saturated 0.5 M KOH solution by at a scan speed 100 mV sec⁻¹. Au loading: 0.130 mg cm⁻².

The porous-Au-aerogel(1)-CN_x and porous-Au-aerogel(2)-CN_x modified GC electrode showed better ORR activity in compared to AuNPs- CN_x electrode, with a much stronger cathodic peak and more positive onset potential at ~0.92 V with E_{1/2} of ~0.855 V. The comparison ORR activity at Au aerogel-CN_x catalyst with Pt/C catalyst is presented in the Figure 3.10b. This shows that half-wave potential (E_{1/2}) for O₂ reduction on Au-aerogel-CN_x is more positive potential than the commercial Pt/C catalyst. E_{1/2} on Au-aerogel-CN_x is 30 mV more positive than that of Pt/C. The E_{1/2} value for AuNPs-CN_x was found higher than Au-aerogel-CN_x.

Table 3.3. Different parameter of synthesized catalyst at 0.5 M KOH.

Catalyst	A_r	$E_{1/2}$	SA at 0.6V (mA cm ⁻²)	MA at 0.6V (Ag ⁻¹)	Tafel slope (mV dec ⁻¹)
AuNPs-CN _x	0.07	+0.6	1.42	12	135
Au-aerogel(1)-CN _x	0.6	+0.854	2.91	190	100
Au-aerogel(2)-CN _x	0.5	+0.860	2.12	115	130

This suggests that the porous Au-aerogel-CN_x can able to reduce oxygen more easily than AuNPs-CN_x. The kinetics of ORR at the modified electrode is carried out by rotating disk electrode (RDE) at oxygen saturated 0.5 M KOH solution. Figure 3.11a shows LSV polarization (current density vs applied potential) curve for ORR on AuNPs-CN_x electrode at different rotation speed varying from 200 rpm to 2500 rpm. From this Figure it is obvious that current density increases with increasing rotation speed. The number of electron involved per O₂ in ORR can be determined from the Koutecky-Levich (K-L) equation (see appendix). Figure 3.11b shows that K-L plot of ORR on AuNPs-CN_x electrode at different voltage, ranging from 0.45 to 0.6V constructed from Figure 3.11a. The linearity of K-L plots and near parallelism of K-L plots suggests first order reaction kinetics towards the concentration of dissolved oxygen. From K-L plot it can be concluded that mainly a 4e transfer ORR process predominates over AuNPs-CN_x surface. However, a very small amount of 2e process also occurs in the foot of polarization curve. Figures 3.11c, e show LSV polarisation curve for ORR on Au-aerogel(1)-CN_x, Au-aerogel(2)-CN_x modified electrode at different rotation speeds. The corresponding K-L plot constructed from Figures 3.11c and 3.11e are shown in Figures 3.11d and 3.11f respectively. The n value is 3.5 at 0.7 V for Au-aerogel(2)-CN_x electrode and increases with decreasing voltage, reaches 4 at 0.6 V (Figure 3.11f). Similar 4e reduction and some 2e along with 4e reduction process in the

foot of curve are also observed for Au-aerogel(1)-CN_x electrode (Figure 3.11d). Thus, these results indicate that gold-carbon nitride hybrids favour a 4e oxygen reduction processes. It is known that the reduction of oxygen at gold surface can occur via either 2e pathway producing hydrogen peroxide or 4e pathways forming water⁵⁸. It is also reported that the surface structure of the gold nanoparticles can influence the electrochemical ORR behavior of gold nanoparticles⁶⁰⁻⁶¹. The 4e reduction mechanism takes place on the Au (100) crystal surface whereas 2e reduction of oxygen occurs on Au (111) and Au (110) crystal surfaces. In addition, it is also reported⁶² that ORR activity at these crystal planes decreases in the order Au (100)>Au (110)>Au (111). The presence of surface modifier during synthesis of gold nanoparticles can influence the formation of specific surface structure.

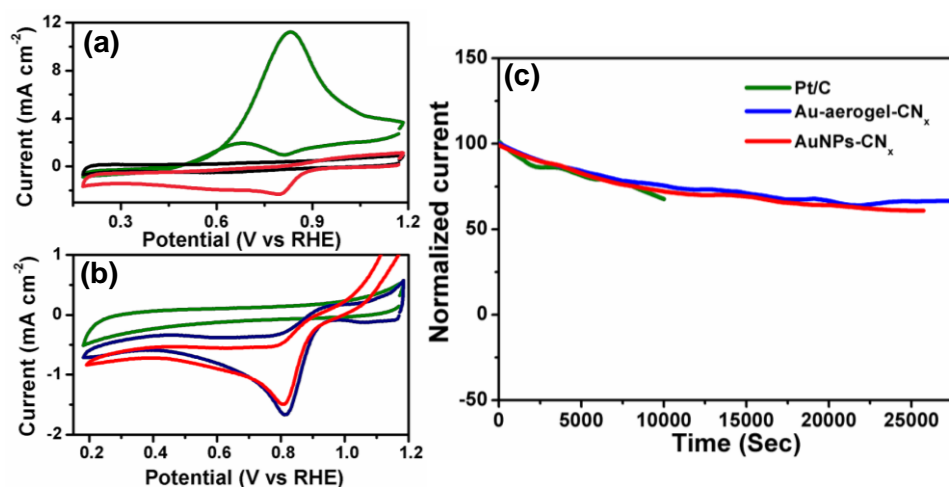


Figure 3.12. (a) CVs of Pt-C in N₂ saturated (green line), O₂ saturated (blue line) and O₂ saturated 2 M methanol (red line) in 0.5 M KOH solution (b) Au-aerogel-CN_x in N₂ saturated (green line), O₂ saturated (blue line), O₂ saturated 2 M methanol (red line) 0.5 M KOH solution. Scan rate 100 mV/sec (c) Chronoamperometric stability in 0.5 M alkaline medium at Au-aerogel-CN_x, AuNPs-CN_x and 10% Pt-C at 0.7 V(RHE).

For example, the (100) or (111) facet of gold formed if gold nanoparticle synthesized in presence of iodide whereas sulphide induces formation of (110) facet of gold⁶⁰. The highest

catalytic activity and 4e reduction of oxygen was reported by Hernandez *et al.*⁶⁰ when gold nanoparticles were synthesized in water-in-oil micro emulsion in presence of iodide. Gold nanoparticles, dispersed in the conducting polymer-poly (aminothiophenol) exhibited 4e reduction of oxygen due to presence of poly (aminothiophenol), surface modifier⁶¹. H Erikson^{58, 62} reported at low potential mainly H₂O₂ (2e) predominates and more negative potential H₂O₂ further reduced (4e) to water. Tokeo Ohsaka *et al.*⁶³ also reported 4e reduction of oxygen to water on crystallo-graphically oriented Au(100)-like gold nanoparticles with at a reasonably lower cathodic over potential. In the case of AuNPs-CN_x, Au-aerogel(1)-CN_x, Au-aerogel(2)-CN_x, n value reaches to 4 at a small overpotential. So it can be concluded that OH⁻ formation is the major pathway rather than OH₂⁻ formation. In order to get an insight view of Au structuration in Au-aerogel-CN_x composites, Pb adsorption-desorption experiment was performed in 2 mM Pb(NO₃)₂ dissolved in 0.1 M KOH solution (Figure 3.11g). The peak potential exhibit here signifies the orientation of Au surfaces. The main Pb desorption peak for Au (111), (100) and (110) facets generally arises at 0.435, 0.475 and 0.56 V respectively. Figure 3.11g represents the complete lead under potential deposition (UPD) curve for AuNPs-CN_x modified GC electrode. The strong peaks at 0.435 and 0.475V suggest that the Au (111) and (100) facets mainly predominate in Au-aerogel-CN_x with a little lower surface area of Au (110) facets. Since the ORR activity of Au (100) facet is much higher than that of Au (110) facet, small portion Au (100) crystalline plane is sufficient to induce 4e reduction of oxygen. It can be concluded that, since synthesis of Au-aerogel was done in presence of CN_x sheets, CN_x acts as surface modifier to form electrochemically active Au (100) crystal plane in Au-aerogel-CN_x composite, oxygen reduction at AuNPs-CN_x composite surface thus probably occurs via 4e reduction pathways to form water. The superior ORR activity at Au-aerogel-CN_x in comparison to others can be

explained by high electrochemical surface area of this catalyst (Table 3.3). The ESCA of AuNPs-CN_x was small and thus E_{1/2} is less positive. As E_{1/2} does not provide the intrinsic property of the catalysts thus the SA and MA values calculated at 0.6 V (RHE) are also given in Table 3.3 (For detailed information see appendix). The SA values for porous Au-aerogel-CN_x catalysts are higher than AuNPs-CN_x. The considerably lower SA value for small AuNPs (2 nm) is due to the particle size effect³⁹ and particular crystallographic orientation of AuNPs⁵⁸. It is reported recently that negative ORR activity of AuNPs when particle size is ~2 nm³⁶, but when particle size was 17- 40 nm³⁷, ORR activity become comparable with bulk gold. So from above observations it can be concluded that higher particle size in porous network structure of Au-aerogel supported on CN_x is responsible for these higher catalytic activity. The MA values for porous Au-aerogel(1)-CN_x is slightly higher than Au-aerogel(2)-CN_x and it is much higher than AuNPs-CN_x catalyst. Mass transport corrected reported Tafel slope values for oxygen reduction over bulk gold and platinum is close to 120 mV dec⁻¹. Tafel slope for Pt based^{64,65} catalysts are in between 60-70 mV dec⁻¹ (at low overpotential) and increases up to ~120 mV dec⁻¹ with increasing overpotential. This low Tafel slope (60-70 mV dec⁻¹) arises due to the formation of clogged oxide species at the surface active sites. The Tafel plots were obtained after the measured currents were corrected for diffusion to give the kinetic currents in the mixed activation-diffusion region, calculated from the equation

$$J_k = j j_d / (j_d - j)$$

where $j / (j_d - j)$ is the mass transfer correction term.

The mass transport correction was made using the limiting

$$\text{current } j_d = B\omega^{1/2}$$

where ω is the rotation rate (rpm) of the electrode.

Mass transfer corrected Tafel plots, constructed from RDE analysis for ORR activities are shown in Figure 3.11h. The Tafel slope for Au-aerogel(1)-CN_x sample is ~ 100 mV dec⁻¹ whereas for other two compounds are 130 and 135 mV dec⁻¹. In all three Au-CN_x composites Tafel slope lies in between 100-140 mV dec⁻¹ which is close to that of bulk Au (120 mV dec⁻¹) and some Au based catalyst, reported in literature earlier⁶². This suggests that the transfer of first electron is the rate determining step for O₂ reduction on gold surface in alkaline medium. The high Tafel slopes of ~ 160 mV dec⁻¹ as well as low Tafel slopes of ~ 60 mV dec⁻¹ were reported by various groups^{58, 62} in the literature for Au/C ORR catalyst. Table 3.4 listed some Au based catalyst activity reported in literature earlier. This catalyst has a comparable and in some case better catalytic activity in terms of onset potential and half wave potential ($E_{1/2}$). To evaluate the properties of a catalyst, methanol crossover effect should be evaluated carefully as fuel molecules (methanol, glucose) from anode sometimes permeate to cathode and seriously affect the activity of cathode material^{34, 66}. Crossover effect is one of the prime problems in methanol fuel cell for Pt/C catalyst. Figure 3.12(a, b) shows the cyclic voltammograms of Pt/C and Au-aerogel-CN_x electrode in oxygen saturated 0.5 M KOH in presence of 2 M methanol. Pt-C shows a very strong methanol oxidation peak (0.83 V) and very weak oxygen reduction peak (0.810 V) but no noticeable response for methanol oxidation was observed in our Au-aerogel-CN_x catalyst at that same experimental condition. In both cases no peak were observed in N₂ atmosphere. So we conclude that our catalyst has high selectivity towards ORR and possess a good tolerance of cross-over effect of methanol. Besides the high catalytic activity, Au-aerogel-CN_x also exhibit considerable stability. In alkaline medium catalyst was stable up to 25,000 second with retention of chronoamperometric current is 65%.

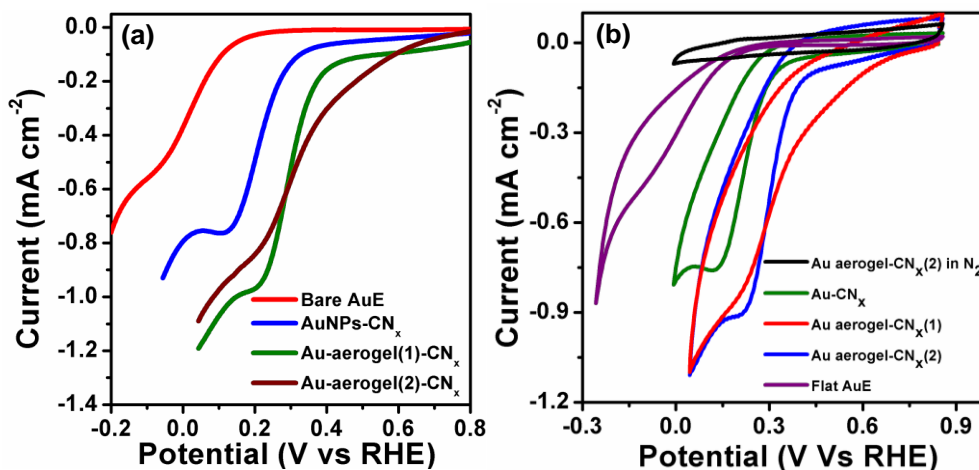


Figure 3.13. (a) LSV curve by AuNPs-CN_x, Au-aerogel(1)-CN_x, Au-aerogel(2)-CN_x, and flat AuE in presence of oxygen saturated 0.5 M H₂SO₄ solution. (b) CVs of different catalyst at O₂ saturated 0.5 M H₂SO₄: Au-aerogel(2)-CN_x (red line), Au-aerogel(1)-CN_x (blue line) AuNPs-CN_x (green line), flat Au electrode (purple line) and Au-aerogel(2)-CN_x in N₂ atmosphere. Scan rate 100 mV sec⁻¹.

The stability of Au-aerogel-CN_x is slightly better than Pt/C where stability of AuNPs-CN_x and Pt/C are comparable. Thus Au-aerogel-CN_x is superior to commercial Pt-C catalyst in terms of ORR peak position, stability and methanol tolerances.

3.4.4 ORR studies on Au-aerogel-CN_x catalysts in acidic medium

The catalytic activity of Au-aerogel-CN_x was further evaluated by ORR in acidic medium. As reported, in acidic medium Au possesses modest catalytic activity; but its catalytic activity is considerably higher than carbon materials. We perform the catalytic activity of porous Au-aerogel to show the versatility of our catalysts. The CV and LSV technique was used to evaluate the catalytic efficiency of Au-aerogel-CN_x. Figure 3.13a show the LSV curves of commercial flat Au electrode, AuNPs-CN_x, Au-aerogel(2)-CN_x, Au-aerogel(1)-CN_x modified GC electrode in 0.5 M H₂SO₄ with each catalyst loading of 0.130 mg cm⁻². For comparison ORR activity of commercial 10% Pt/C was shown. Commercial flat-Au electrode shows ORR activity with a cathodic peak at -0.05 V with onset potential of +0.20 V.

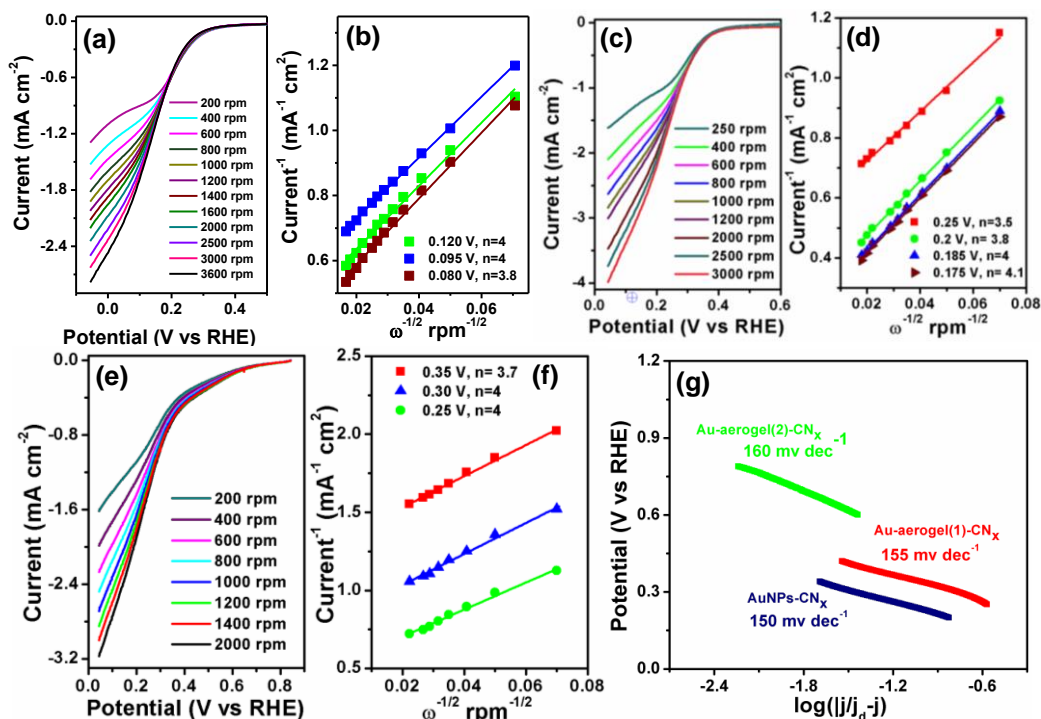


Figure 3.14. (a) ORR polarisation curves of AuNPs-CN_x/GCE. (b) K-L plot of the ORR of AuNPs-CN_x/GCE (c) ORR polarisation curves of Au-aerogel(1)-CN_x/GCE. (d) K-L plot of the ORR of Au-aerogel(1)-CN_x/GCE (e) ORR polarisation curves of Au-aerogel(2)-CN_x/GCE at different rotation speed at 0.5 M O₂ saturated H₂SO₄ solution at a scan speed 100 mV sec⁻¹ with Au loading of 0.130 mg cm⁻². (f) K-L plot of the ORR of Au-aerogel(2)-CN_x/GCE constructed from the polarisation curves. (g) Mass corrected Tafel slope of different catalyst was shown.

The Au-aerogel-CN_x composites are the most active ORR catalyst with much stronger cathodic peak and more positive onset potential. The cathodic peaks were observed at +0.22V (vs.RHE) for Au-aerogel-(2)-CN_x and Au-aerogel(1)-CN_x modified electrode with onset potentials of 0.6V and 0.43V (RHE) respectively. The complete CV scan for these catalysts in O₂ saturated KOH medium was given at Figure 3.13b. The ORR performance of AuNPs-CN_x catalyst is better than of flat Au electrode but inferior than Au-aerogel-CN_x electrode. The RDE method was also used to study the kinetics of oxygen reduction in O₂ saturated 0.5 M H₂SO₄ solution. Figure 3.14a shows LSV polarization curves (current density-potential curves) of ORR for AuNPs-CN_x electrode at different rotation speed. The

corresponding K-L plot for AuNPs-CN_x electrode is shown in Figure 3.14b. As shown in Figure 3.14b, the linearity of the plot and parallelism of fitting curves suggests first order kinetics towards the concentration of O₂. The value of n it can be concluded that ORR is mainly dominated by 4 electron transfer process where O₂ is directly reduced to OH⁻. The LSV polarization curves of Au-aerogel(1)-CN_x and Au-aerogel(2)-CN_x modified electrode are shown in Figure 3.14 (c and e) respectively. The corresponding K-L plots are given in Figure 3.16c and 3.16d. Like previous case, ORR at Au-aerogel-CN_x electrodes in acidic medium is mainly guided by direct 4 electron reduction mechanism. Mass transfer corrected Tafel slopes (Figure 3.14g) were found 160 mV dec⁻¹, 155 mV dec⁻¹ and 150 mV dec⁻¹ for Au-aerogel(2)-CN_x, Au-aerogel(1)-CN_x, AuNPs-CN_x which is slightly higher than the typical value 120 mV dec⁻¹ reported for bulk Au previously^{62, 67}. The similar high value of Tafel slope in acidic medium is also reported for carbon supported gold nanoparticles based catalysts⁵⁸. Moreover catalyst is well stable in acidic medium.

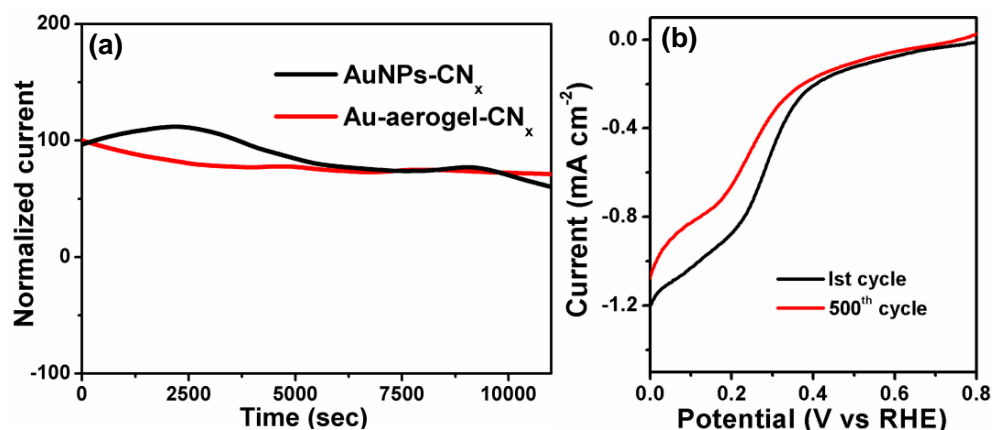


Figure 3.15. (a) Chronoamperometric responses of Au-aerogel-CN_x and AuNPs-CN_x at 0.15 V. (b) Stability of catalyst at up to 10000th cycles. All ORR experiments were done at oxygen saturated 0.5 M H₂SO₄ solution at a scan speed 100 mV sec⁻¹. Au loading: 0.130 mg cm⁻².

A chronoamperometric measurement (Figure 3.15a) was carried out at a fixed potential at 0.15 V (RHE) where it shows 60% current can be retained after 20000 sec. From Figure

3.15b it is also evident that a small current density was decreased after 10000 LSV scan. So Au-aerogel-CN_x catalyst shows enough stability in acidic medium also. A comparison with different Au composite catalyst in this work towards ORR is presented in Table 3.5. From Figure 3.13a and Table 3.5 it may be concluded that ORR activity of these Au composite in acid media depends on morphology of the catalysts. The onset potential for oxygen reduction in acidic medium at commercial flat Au electrode, 2 nm AuNPs supported CN_x, Au-aerogel supported CN_x modified GC electrodes are 0.20 V, 0.37 V and 0.6 V respectively and E_{1/2} values are 0.03 V, 0.21 V and 0.33 V respectively. This suggests that ORR activity on Au-aerogel-CN_x electrode is highest and commercial flat Au electrode is poorest. The high electrochemical surface area of Au-aerogel-CN_x catalyst is due to its porous interconnected network and crystallographic orientation of bigger Au particles.

Table 3.4. Comparison of ORR the activity of different catalysts in acidic and alkaline media.

Catalyst	Medium	E _{1/2} (V) (vs RHE)	Tafel Slope (mV dec ⁻¹)	Ref
5 nm Au sphere	Alkaline	0.78	43	58
30% Au/C	Alkaline	0.725	114	62
Fe _x N-NGA	Alkaline	-0.860	59	68
Au@rGO	Alkaline	~0.763	-	69
C-Mn _x Fe _{3-x} O ₄ NPs	Alkaline	-0.809	-	70
30% Au/C	Acidic	0.218	181	62
5 nm Au sphere	Acidic	0.238	139	58
2 nm Au thin film	Acidic	-	109	67
PtNi-CN ₁	Acidic	0.8	120	64
Pt-dendrimer	acidic	0.9	-	71
Au-aerogel-CN _x	Acidic	0.33	~155	This work
Au-aerogel-CN _x	Alkaline	0.860	~130	This work

This porous structure also helps easy mass transport of reactant or product to catalytically active sites. For better comparison SA and MA (at 0.25 volt vs RHE) are also given in Table 3.5. The SA values of AuNPs-CN_x and Au-aerogel-CN_x are same, but their MA changes for different catalyst morphology. Table 3.4 listed some catalyst activity in alkaline and acidic medium reported in literature earlier. This Au-aerogel-CN_x catalyst has a comparable or better ORR activity with Pt/C catalyst in basic media and its activity in acid media are better than any reported Au based catalysts. The high electrochemical surface area of Au-aerogel-CN_x is probably not only reason for its superior ORR performance. It has been reported recently that AuNPs less than 2 nm acts as a negative electrocatalyst for oxygen reduction. The ORR activities in acidic medium at citrate capped 2 nm AuNPs modified GC electrode is better than bare GC, but is much inferior in comparison to bare gold electrode. But this work report much better performance 2 nm AuNPs, supported on CN_x sheets towards oxygen reduction in compared to bare gold electrode in acidic medium (Figure 3.13a and 3.13b). Thus this shows the CN_x support plays an important role in making 2 nm AuNPs a strong positive electrocatalyst. The shift of C1s or N1s peaks and Au 4f peaks in the XPS spectra of Au composites was observed, suggesting the gold nanoparticles are directly bonded to the CN_x sheets. FT-IR spectra of these also confirm the change of electronic structure of CN_x sheets is due to presence of nanoparticles or Au on CN_x sheets. The strong interaction and the transfer of electrons between them lead to the change of the electronic state of gold and CN_x sheets. The CV studies of K₄[Fe(CN)₆] at modified GC electrode also confirm more facile electron transfer at porous Au-aerogel-CN_x electrode. In addition several groups^{22,72} reported that catalytic activities of supported gold nanoparticles are due to extra negative charge at the periphery of gold nanoparticles resulting from the interaction between nanoparticles and support. It is reported that charged gold nanoparticles

on MgO support²² promote the activation of adsorbed reactant molecule such as O₂. It is also reported that the tolerance of nano-particle loaded C₃N₄ electro-catalysts increases with increasing higher concentration of nitrogen in C₃N₄ support. The conductivity of the support increases and the electrochemical behavior become closer to that of Pt/C catalyst when low nitrogen concentration present in the C₃N₄ support. Recently, V. Di. Noto and his co-workers reported⁷³⁻⁷⁴ relationship between nitrogen concentration, structure morphology, and electrochemical ORR performances of PdCoNi “core-Shell” C₃N₄ electrocatalysts. When concentration of N in carbon nitride shell is low and cell constant of PdCoNi alloy NPs is shortest, best ORR activities were observed⁷³. Various groups reported⁷⁵⁻⁷⁶ that hetero-atom such as nitrogen based ligands can easily coordinate metal nanoparticles and metal-support interaction improves tolerance as well as activity of the electrocatalysts under oxidation condition. Similar behavior was also observed in case of Au-aerogel-CN_x composite. The concentration of N is lower in Au-aerogel-CN_x in compared to AuNPs-CN_x and better activity on Au-aerogel-CN_x was observed. Although support is same (CN_x) for AuNPs-CN_x and Au-aerogel-CN_x catalysts, nature of interaction between CN_x and gold is distinctly different as suggested by FT-IR and XPS studies. This suggests that CN_x support (AuNPs-CN_x interaction) plays important role for enhancement of ORR activity at porous Au-aerogel-CN_x composite. In addition, porous morphology of gold in Au-aerogel-CN_x may help adsorption of reactant such as O₂ and desorption of products from the electrode surface facilitating oxygen reduction. Therefore, we may conclude that the unique synergistic effects of CN_x and Au-aerogel-CN_x, due to strong interaction between CN_x and porous Au/AuNPs, make porous Au-aerogel-CN_x composite a superior electrocatalyst for oxygen reduction.

Table 3.5. Different parameter of synthesized catalysts in acidic media.

Catalyst	A_r (cm^{-2})	$E_{1/2}$ (V)	SA (0.25 V) (mA cm^{-2})	MA (Ag^- ¹) (0.25 V)	Tafel slope (mV)
AuNPs-CN _x	0.14	+0.21	0.14	3	150
Au-aerogel(1) - CN _x	1.17	+0.3	0.15	19	155
Au-aerogel(2) - CN _x	1.05	+0.33	0.13	15	160
Flat Au electrode	0.17	+0.03	-	-	-

3.4.5. HER studies on Au-aerogel-CN_x catalyst in acidic medium

The catalyst activity of AuNPs-CN_x and Au-aerogel-CN_x catalyst was then investigated towards HER process. The HER activity was studied in 0.5 M H₂SO₄ solution in a nitrogen saturated system using a three electrode linear sweep voltammograms at a scan speed of 10 mV sec⁻¹. The representative linear sweep voltammograms curves of geometric current density (mA cm^{-2}) vs applied potential show HER activity of bare GCE, CN_x, commercial flat AuE, AuNPs-CN_x, Au-aerogel-CN_x, and Pt/C in Figure 3.16a. As expected Pt/C exhibit HER activity with a near zero potential. The onset potential of GCE, and CN_x was observed at -0.160, and -0.170 V with very low current density respectively. Thus it is obvious that GCE, CN_x are almost inert catalysts whereas Pt/C is an active catalyst for HER. The commercial flat Au electrode exhibits moderate HER activity with onset potential -150 mV. The base line corrected LSV curves for different morphologies of Au metal in region of low current density are also presented in Figure 3.16b. It clearly shows that morphology of gold metal play an important role in its performance towards HER activity.

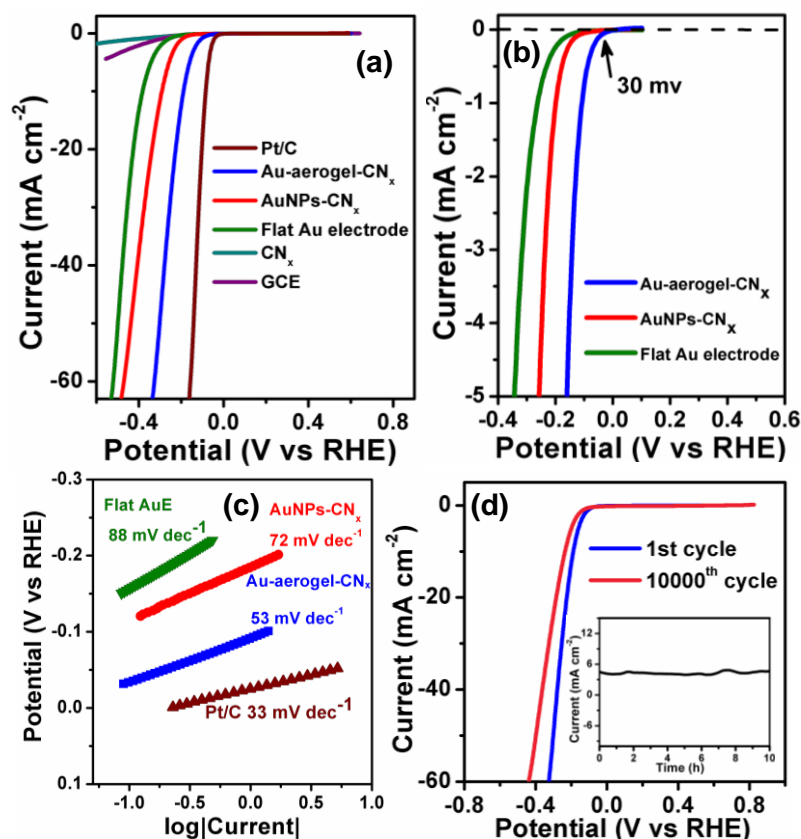


Figure 3.16. HER performance by various electrode (a) LSV polarization curves of Pt/C, Au-aerogel-CN^x, AuNPs-CN_x, Au electrode, CN_x, GCE at N₂ saturated 0.5 M H₂SO₄ solution (scan rate 10 mV Sec⁻¹, rotation speed 1000 rpm) (b) Base line corrected LSV polarization curves of Au-aerogel-CN_x, AuNPs-CN_x, Au electrode. (c) HER Tafel plot (log *j* vs potential) of Pt/C, Au-aerogel-CN_x-GCE, AuNPs-CN_x, Au electrode. (d) HER activity of Au-aerogel-CN_x electrode at first cycle and after 10000 times scan (at scan speed 50 mV sec⁻¹). Inset: chronoamperometric responses of Au-aerogel-CN_x for a long time (10 hrs) at -0.15 V (RHE). Au loading: 0.130 mg cm⁻².

The porous Au-aerogel supported on CN_x sheets exhibit much better activity than that of AuNPs-CN_x and flat commercial gold electrode. The onset potential for HER of Au-aerogel supported CN_x sheets is -30 mV whereas the onset potentials for AuNPs-CN_x and flat Au electrode are -120 mV and -150 mV respectively. In acidic condition, the over potential required for Au-aerogel-CN_x to drive the current density of 10, 20 and 50 mA cm⁻² are 185, 225 and 300 mV whereas overpotentials required for AuNPs-CN_x are 285, 335 and 440 mV

respectively. In contrast, flat gold shows much lower HER performances with large overpotential of 380 and 420 mV for achieving 10 mA cm^{-2} and 20 mA cm^{-2} current density respectively. This clearly demonstrates superior electrocatalytic activity towards HER of Au-aerogel-CN_x. The Tafel slope is considered as an inherent property of the catalyst and used as significant standard for the HER performance. A low Tafel slope means a faster increase of HER rate with increasing potential. The HER Tafel plot showing $\log|j|$ vs applied potential for Pt/C, Au-aerogel-CN_x/GCE, AuNPs-CN_x, AuE are given in Figure 3.16c. The Tafel slope for Pt/C in acidic medium was 33 mV dec^{-1} , which is consistent with reported data. The Tafel analysis for the Au-aerogel-CN_x/GC electrode in $0.5 \text{ M H}_2\text{SO}_4$ gives a slope of 53 mV dec^{-1} . The Tafel slopes of AuNPs-CN_x and commercial flat Au electrode were found to be 72 and 88 mV dec^{-1} . This low Tafel slope value (53 mV dec^{-1}) for Au-aerogel-CN_x indicates that the Volmer-Heyrovsky mechanism is responsible for HER where desorption of hydrogen is the rate limiting step⁷⁷. Thus, Tafel slope of Au-aerogel-CN_x is significantly lower than the flat Au electrode suggesting a better HER activity on Au-aerogel-CN_x electrode. The exchange current density for Au-aerogel-CN_x in $0.5 \text{ M H}_2\text{SO}_4$ medium was 0.03 mA cm^{-2} which is comparable to other related systems. The exchange current densities for flat Au electrode and AuNPs-CN_x were observed and 0.002 mA cm^{-2} respectively. Another important criterion for a good HER catalyst is the good stability. Stability of the catalytic responses was measured by cycling Au-aerogel-CN_x continuously for 10,000 cycles ranging from +0.8 to -0.45 V vs RHE at a scan rate 50 mV sec^{-1} . The comparison of onset-potential, overpotential at 20 mA cm^{-2} current density, catalyst mass loading and Tafel slopes is given in Table 3.6. The onset potential (-30 mV) of Au-aerogel-CN_x electrode is lower or comparable than those other non-platinum based systems such as Mo-based, Ni based, Co based (Table 3.6). The required overpotential to reach a current

density of 10 mA cm^{-2} for porous Au-aerogel-CN_x is lower or Au-aerogel-CN_x catalyst affords very less loss of cathodic current density in time of cycling. Long term stability of the electrode was also performed by chronoamperometry at a fixed overpotential at -150 mV (RHE). It shows catalytic current density remains around 70% of initial current density at the end of at least 10 hour (inset of Figure 3.16d). The mass loading of Au in Au-aerogel-CN_x catalyst (0.130 mg cm^{-2}) is much lower than the previously reported catalysts. This suggests that Au-aerogel-CN_x is one of the most HER active Pt-metal free catalyst comparable to other reported related systems. For examples FeS₂ nanosheet⁸¹ requires 265mV to generate current current density 10 mA cm^{-2} , Co embedded carbon rich CNT⁸⁰ need 260 mV to acquire 10 mA cm^{-2} current density, Co-MoN⁸² require 200 mV for 10 mA cm^{-2} current density, Ni₂P⁴² requires 130 mV for 10 mA cm^{-2} current density and Au-aerogel-CN_x required 10 mA cm^{-2} current density at overpotential 185 mV. The Tafel slope of Au-aerogel-CN_x is slightly lower or comparable to the Tafel slope of many reported non-Pt based system (Table 3.6). From the Table 3.6 it is obvious that catalyst has a comparable catalytic activity in terms of onset potential, Tafel slope, exchange current, catalyst loading on other non Pt based catalyst. In addition, some better HER performance for porous electrocatalysts are also reported in the literature. Such as, Y.H. Chang *et al.*⁸⁶ reported that MoS_x film grown on graphene-protected 3D Ni foam showed highly efficient HER activity due to highly conducting porous catalytic film. Superior catalysis behavior was also reported when MoS₂ nanoparticles on 3D substrate. Several groups also reported recently morphology dependent electrocatalytic activity towards hydrogen evolution. The adhesion of evolved gas on a flat electrode surface is a big problem because adhesion of gas bubbles blocks electrolyte diffusion leading to ohmic drop and decrease performance of the catalyst.

Table 3.6. Comparison of HER activity of different reported catalyst in acidic media.

Catalyst	Catalyst loading (mg cm ⁻²)	Onset potential (mV Vs RHE)	Over potential (mV Vs RHE) vs current density (mA cm ⁻²)	Tafel slope (mV/dec)	Exchange current (mA cm ⁻²)	Ref
MoS ₂ /CoSe ₂	0.28	-11	-68 (10 mA cm ⁻²)	36	0.073	⁷⁸
WPNA _s /CC	2	-50	-130 (10 mA cm ⁻²)	69	0.29	⁴⁷
MoP-CA2	0.36	-40 (IR free)	-125 (10 mA/cm ²)	54	0.086	⁷⁷
MoP	1	-50	-180 (10 mA/cm ²)	54	0.034	⁴⁶
Nano MoP	1	-	-110 (10 mA cm ⁻²)	45	0.12	⁷⁹
(GO 8 wt%) Cu-MOF	0.226	-87	-400 (122.48 mA cm ⁻²)	84	-	³⁴
Ni ₂ NS/CC	4.3	-50	-75 (10 mA cm ⁻²)	51	0.26	⁴³
Co-NRCNT	0.28	-50	-260 (10 mA cm ⁻²)	69	0.01	⁸⁰
CoSe ₂	0.37	-30	-90 (4 mA cm ⁻²)	40	0.037	⁸¹
Co _{0.6} Mo _{1.4} N ₂	0.24	-	-200 (10 mA cm ⁻²)	-	0.23	⁸²
MoS ₂ /RGO	0.28	-100	-	-41	-	⁸³
Ni ₂ P	-	-25	-130 (20 mA cm ⁻²)	-46	0.033	⁴²
CMSNA-8	-	-121	-365 (20 mA cm ⁻²)	43	-	⁸⁴
Ni-Mo-N nanosheets	0.25	-78	~ -200 mV (3.5 mA cm ⁻²)	35.9	0.24	⁸⁵
AuNPs-CN _x	0.127	-120	-330 (20 mA cm ⁻²)	72	0.004	This work
Au-aerogel-CN _x	0.127	-30	-225 (20 mA cm ⁻²)	53	0.03	This work

Sun and his coworkers⁸⁷ demonstrated that nonostructured MoS₂ film showed much higher HER activities (overpotential, stability) than that of flat MoS₂ film due to the low gas adhesion force of nonostructured MoS₂ electrode. Enhanced hydrogen evolution at micro and nonostructured CoS₂ as compared to flat CoS₂ film was also reported by M. S. Faber *et al.*⁸⁸ due to enhanced release of evolved gas from the electrode surface. The high HER activity of Au-aerogel-CN_x catalyst could be attributed to several factors. The enhanced electrochemical surface area could be one of the reasons for superior hydrogen evolution at Au aerogel-CN_x. As discussed in the previous section, electrochemical electrode surface area of Au-aerogel-CN_x is much higher than that of 2 nm AuNPs-CN_x or flat gold electrode.

The porous network structure in Au-aerogel-CN_x is responsible for this high electrochemical surface area. It is also reported that HER activity on gold has strong structural sensitivity; the Au (111) facet is the most active for hydrogen evolution. The strong (111) reflection in p-XRD and SAED patterns (Figure 3.1 and Figure 3.3a) of Au-aerogel-CN_x confirmed the presence large amount of (111) surface sites. The HRTEM studies also suggested the growth of Au-aerogel occurred preferentially in (111) plane directions. The presence of large amount of (111) planes in Au-aerogel-CN_x also suggests its high catalytic activity for HER. The strong catalyst-support interaction at Au-aerogel-CN_x could also be playing an important role for the superior catalytic enhancements. The strong metal-support interaction modifies the electronic structure of Au and carbon nitrides, which leads to fast electron transfer for catalytic reactions. The highly porous morphology of gold may enhances mass transport to catalytic sites. Based on recent reports⁸⁷⁻⁸⁸ on porous HER catalysts, the highly porous morphology of Au aerogel could significantly contribute to HER activity

3.5 CONCLUSION

In conclusion, we have demonstrated a facile synthetic route for the formation of Au aerogel on carbon nitride sheets. The porous network was formed by interconnection of AuNPs on CN_x sheet. The strong interaction between gold aerogel and carbon nitride support, confirmed by XPS and FT-IR studies, leads to the change of electronic properties of Au and CN_x. Au-aerogel-CN_x composites has a high electrochemical surface area and mass activities than that of AuNPs-CN_x and commercial flat Au electrode. This catalyst exhibited superior catalytic activity towards HER and ORR. In alkaline media, ORR activity of Au-aerogel-CN_x catalyst is superior to commercial Pt/C catalyst. The Au-CN_x composites show morphology dependent ORR and HER activities in acidic medium. The catalytic activities of porous composite are superior to that of AuNPs-CN_x composite and flat Au

electrode. The synergistic effects between porous Au-aerogel-CN_x and carbon nitrides lead to an outstanding ORR and HER performances at Au-aerogel supported on CN_x catalysts. The excellent ORR and HER activity of Au-aerogel-CN_x with methanol tolerance, good durability, and low catalyst loading are making them a promising electrocatalyst for fuel cell and water splitting or other electrochemical devices.

3.6 REFERENCES

- (1) Corma, A. *Chem. Rev.* **1997**, *97*, 2373-2420.
- (2) Datta, K. K. R.; Reddy, B. V. S.; Ariga, K.; Vinu, A. *Angew. Chem. Int. Ed.* **2010**, *49*, 5961-5965.
- (3) Xu, C.; Su, J.; Xu, X.; Liu, P.; Zhao, H.; Tian, F.; Ding, Y. *J. Am. Chem. Soc.* **2007**, *129*, 42-43.
- (4) Zhang, R.; Hummelgård, M.; Olin, H. *Physica B* **2010**, *405*, 4517-4522.
- (5) Seker, E.; Gaskins, J. T.; Bart-Smith, H.; Zhu, J.; Reed, M. L.; Zangari, G.; Kelly, R.; Begley, M. R. *Acta mater.* **2007**, *55*, 4593-4602.
- (6) Seo, B.; Kim, J. *Electroanalysis* **2010**, *22*, 939-945.
- (7) Yan, M.; Zhang, M.; Ge, S.; Yu, J.; Li, M.; Huang, J.; Liu, S. *Analyst* **2012**, *137*, 3314-3320.
- (8) Zhu, C.; Wen, D.; Oschatz, M.; Holzschuh, M.; Liu, W.; Herrmann, A.-K.; Simon, F.; Kaskel, S.; Eychmüller, A. *Small* **2015**, *11*, 1430-1434.
- (9) Liu, W.; Herrmann, A.-K.; Geiger, D.; Borchardt, L.; Simon, F.; Kaskel, S.; Gaponik, N.; Eychmüller, A. *Angew. Chem.* **2012**, *124*, 5841-5846.
- (10) S., K. S. *Nature* **1931**, *127*, 741-741

- (11) Sadekar, A. G.; Mahadik, S. S.; Bang, A. N.; Larimore, Z. J.; Wisner, C. A.; Bertino, M. F.; Kalkan, A. K.; Mang, J. T.; Sotiriou-Leventis, C.; Leventis, N. *Chem. Mater.* **2012**, *24*, 26-47.
- (12) Soleimani Dorcheh, A.; Abbasi, M. H. *J. Mater. Process. Tech.* **2008**, *199*, 10-26.
- (13) Hoffmann, F.; Cornelius, M.; Morell, J.; Fröba, M. *Angew. Chem. Int. Ed.* **2006**, *45*, 3216-3251.
- (14) Heiligtag, F. J.; Cheng, W.; de Mendonça, V. R.; Süess, M. J.; Hametner, K.; Günther, D.; Ribeiro, C.; Niederberger, M. *Chem. Mater.* **2014**, *26*, 5576-5584.
- (15) Mohanan, J. L.; Arachchige, I. U.; Brock, S. L. *Science* **2005**, *307*, 397-400.
- (16) Bigall, N. C.; Herrmann, A.-K.; Vogel, M.; Rose, M.; Simon, P.; Carrillo-Cabrera, W.; Dorfs, D.; Kaskel, S.; Gaponik, N.; Eychmüller, A. *Angew. Chem. Int. Ed.* **2009**, *48*, 9731-9734.
- (17) Leventis, N.; Chandrasekaran, N.; Sotiriou-Leventis, C.; Mumtaz, A. *J. Mater. Chem.* **2009**, *19*, 63-65.
- (18) Leventis, N.; Chandrasekaran, N.; Sadekar, A. G.; Mulik, S.; Sotiriou-Leventis, C. *J. Mater. Chem.* **2010**, *20*, 7456-7471.
- (19) Tappan, B. C.; Huynh, M. H.; Hiskey, M. A.; Chavez, D. E.; Luther, E. P.; Mang, J. T.; Son, S. F. *J. Am. Chem. Soc.* **2006**, *128*, 6589-6594.
- (20) Corma, A.; Garcia, H. *Chem. Soc. Rev.* **2008**, *37*, 2096-2126.
- (21) Herzing, A. A.; Kiely, C. J.; Carley, A. F.; Landon, P.; Hutchings, G. J. *Science* **2008**, *321*, 1331-1335.
- (22) Yoon, B.; Häkkinen, H.; Landman, U.; Wörz, A. S.; Antonietti, J.-M.; Abbet, S.; Judai, K.; Heiz, U. *Science* **2005**, *307*, 403-407.

- (23) Hayden, B. E.; Pletcher, D.; Suchsland, J.-P. *Angew. Chem. Int. Ed.* **2007**, *46*, 3530-3532.
- (24) Geim, A. K. *Science* **2009**, *324*, 1530-1534.
- (25) Liu, J.; Bai, H.; Wang, Y.; Liu, Z.; Zhang, X.; Sun, D. D. *Adv. funct. mater.* **2010**, *20*, 4175-4181.
- (26) Bhowmik, T.; Kundu, M. K.; Barman, S. *RSC Adv.* **2015**, *5*, 38760-38773.
- (27) Yao, X.; Liu, X.; Hu, X. *ChemCatChem* **2014**, *6*, 3409-3418.
- (28) Scheuermann, G. M.; Rumi, L.; Steurer, P.; Bannwarth, W.; Mülhaupt, R. *J. Am. Chem. Soc.* **2009**, *131*, 8262-8270.
- (29) Guo, S.; Wen, D.; Zhai, Y.; Dong, S.; Wang, E. *ACS Nano* **2010**, *4*, 3959-3968.
- (30) Kundu, M. K.; Sadhukhan, M.; Barman, S. *J. Mater. Chem. B* **2015**, *3*, 1289-1300.
- (31) Liu, W.; Rodriguez, P.; Borchardt, L.; Foelske, A.; Yuan, J.; Herrmann, A.-K.; Geiger, D.; Zheng, Z.; Kaskel, S.; Gaponik, N.; Kötz, R.; Schmidt, T. J.; Eychmüller, A. *Angew. Chem. Int. Ed.* **2013**, *52*, 9849-9852.
- (32) Zhang, J.; Xu, Y.; Zhang, B. *Chem. Commun.* **2014**, *50*, 13451-13453.
- (33) Liu, W.; Herrmann, A.-K.; Geiger, D.; Borchardt, L.; Simon, F.; Kaskel, S.; Gaponik, N.; Eychmüller, A. *Angew. Chem. Int. Ed.* **2012**, *51*, 5743-5747.
- (34) Jahan, M.; Liu, Z.; Loh, K. P. *Adv. funct. mater.* **2013**, *23*, 5363-5372.
- (35) Sheng, W.; Myint, M.; Chen, J. G.; Yan, Y. *Energy Environ. Sci.* **2013**, *6*, 1509-1512.
- (36) Wang, Y.; Laborda, E.; Tschulik, K.; Damm, C.; Molina, A.; Compton, R. G. *Nanoscale* **2014**, *6*, 11024-11030.
- (37) Wang, Y.; Laborda, E.; Ward, K. R.; Tschulik, K.; Compton, R. G. *Nanoscale* **2013**, *5*, 9699-9708.
- (38) Bron, M. J. *Electroanal. Chem.* **2008**, *624*, 64-68.

- (39) Inasaki, T.; Kobayashi, S. *Electrochimica Acta* **2009**, *54*, 4893-4897.
- (40) Guerin, S.; Hayden, B. E.; Pletcher, D.; Rendall, M. E.; Suchsland, J.-P. *J. Comb. Chem.* **2006**, *8*, 679-686.
- (41) Liao, L.; Zhu, J.; Bian, X.; Zhu, L.; Scanlon, M. D.; Girault, H. H.; Liu, B. *Adv. funct. mater.* **2013**, *23*, 5326-5333.
- (42) Popczun, E. J.; McKone, J. R.; Read, C. G.; Biacchi, A. J.; Wiltrout, A. M.; Lewis, N. S.; Schaak, R. E. *J. Am. Chem. Soc.* **2013**, *135*, 9267-9270.
- (43) Jiang, P.; Liu, Q.; Sun, X. *Nanoscale* **2014**, *6*, 13440-13445.
- (44) Chen, W. F.; Wang, C. H.; Sasaki, K.; Marinkovic, N.; Xu, W.; Muckerman, J. T.; Zhu, Y.; Adzic, R. R. *Energy Environ. Sci.* **2013**, *6*, 943-951.
- (45) Vrubel, H.; Hu, X. *Angew. Chem. Int. Ed.* **2012**, *51*, 12703-12706.
- (46) Xiao, P.; Sk, M. A.; Thia, L.; Ge, X.; Lim, R. J.; Wang, J.-Y.; Lim, K. H.; Wang, X. *Energy Environ. Sci.* **2014**, *7*, 2624-2629.
- (47) Pu, Z.; Liu, Q.; Asiri, A. M.; Sun, X. *ACS Appl. Mater. Interfaces* **2014**, *6*, 21874-9.
- (48) Lukowski, M. A.; Daniel, A. S.; English, C. R.; Meng, F.; Forticaux, A.; Hamers, R. J.; Jin, S. *Energy Environ. Sci.* **2014**, *7*, 2608-2613.
- (49) Xu, Y. *Int. J. Electrochem. Sci.* **2009**, *34*, 77-83.
- (50) Creu, R. K., A.; Medeleanu, M.; Vaszilcsin, N.;. *Int. J. Electrochem. Sci.* **2014**, *9*, 4465-4467.
- (51) Perez, J. G., R. E. *J. Phys. Chem. B* **102**, 10931-10935.
- (52) Barman, S.; Sadhukhan, M. *J. Mater. Chem.* **2012**, *22*, 21832-21837.
- (53) Sadhukhan, M.; Barman, S. *J. Mater. Chem. A* **2013**, *1*, 2752-2756.
- (54) Cheng, N.; Tian, J.; Liu, Q.; Ge, C.; Qusti, A. H.; Asiri, A. M.; Al-Youbi, A. O.; Sun, X. *ACS Appl. Mater. Interfaces* **2013**, *5*, 6815-6819.

- (55) Hareesh, K.; Williams, J. F.; Dhole, N. A.; Kodam, K. M.; Bhoraskar, V. N.; Dhole, S. *D. Mater. Research Exp.* **2016**, *3*, 075010.
- (56) Sadhukhan, M.; Bhowmik, T.; Kundu, M. K.; Barman, S. *RSC Adv.* **2014**, *4*, 4998-5005.
- (57) Tang, L.; Wang, Y.; Li, Y.; Feng, H.; Lu, J.; Li, J. *Adv. funct. mater.* **2009**, *19*, 2782-2789.
- (58) Erikson, H.; Sarapuu, A.; Tammeveski, K.; Solla-Gullón, J.; Feliu, J. M. *ChemElectroChem* **2014**, *1*, 1338-1347.
- (59) Ge, X.; Sumboja, A.; Wu, D.; An, T.; Li, B.; Goh, F. W. T.; Hor, T. S. A.; Zong, Y.; Liu, Z. *ACS Catal.* **2015**, *5*, 4643-4667.
- (60) Hernández, J.; Solla-Gullón, J.; Herrero, E. *J. Electroanal. Chem.* **2004**, *574*, 185-196.
- (61) Gopalan, A. I.; Lee, K.-P.; Manesh, K. M.; Santhosh, P.; Kim, J. H. *J. Mol. Catal A: Chem.* **2006**, *256*, 335-345.
- (62) Erikson, H.; Jürmann, G.; Sarapuu, A.; Potter, R. J.; Tammeveski, K. *Electrochim. Acta* **2009**, *54*, 7483-7489.
- (63) El-Deab, M. S.; Sotomura, T.; Ohsaka, T. *Electrochem. Commun.* **2005**, *7*, 29-34.
- (64) Negro, E.; Polizzi, S.; Vezzù, K.; Toniolo, L.; Cavinato, G.; Di Noto, V. *Int. J. Hydrogen Energy* **2014**, *39*, 2828-2841.
- (65) Di Noto, V.; Negro, E.; Polizzi, S.; Riello, P.; Atanassov, P. *Appl. Catal. B: Environ.* **2012**, *111-112*, 185-199.
- (66) Yang, S.; Feng, X.; Wang, X.; Müllen, K. *Angew. Chem. Int. Ed.* **2011**, *50*, 5339-5343.
- (67) Sarapuu, A.; Tammeveski, K.; Tenno, T. T.; Sammelselg, V.; Kontturi, K.; Schiffrin, D. *J. Electrochem. Commun.* **2001**, *3*, 446-450.
- (68) Yin, H.; Zhang, C.; Liu, F.; Hou, Y. *Adv. funct. mater.* **2014**, *24*, 2930-2937.

- (69) Barman, B. K.; Nanda, K. K. *Chem. Commun.* **2013**, *49*, 8949-8951.
- (70) Zhu, H.; Zhang, S.; Huang, Y.-X.; Wu, L.; Sun, S. *Nano Lett.* **2013**, *13*, 2947-2951.
- (71) Zhang, G.; Sun, S.; Cai, M.; Zhang, Y.; Li, R.; Sun, X. *Sci. Rep.* **2013**, *3*, 1526.
- (72) Haruta, M. *Faraday Discuss.* **2011**, *152*, 11-32.
- (73) Negro, E.; Vezzù, K.; Bertasi, F.; Schiavuta, P.; Toniolo, L.; Polizzi, S.; Di Noto, V. *ChemElectroChem* **2014**, *1*, 1359-1369.
- (74) Di Noto, V.; Negro, E.; Polizzi, S.; Agresti, F.; Giffin, G. A. *ChemSusChem* **2012**, *5*, 2451-2459.
- (75) Di Noto, V.; Negro, E. *Fuel Cells* **2010**, *10*, 234-244.
- (76) Perini, L.; Durante, C.; Favaro, M.; Perazzolo, V.; Agnoli, S.; Schneider, O.; Granozzi, G.; Gennaro, A. *ACS Appl. Mater. Interfaces* **2015**, *7*, 1170-1179.
- (77) Xing, Z.; Liu, Q.; Asiri, A. M.; Sun, X. *Adv. Mater.* **2014**, *26*, 5702-5707.
- (78) Gao, M.-R.; Liang, J.-X.; Zheng, Y.-R.; Xu, Y.-F.; Jiang, J.; Gao, Q.; Li, J.; Yu, S.-H. *Nat. Commun.* **2015**, *6*.
- (79) McEnaney, J. M.; Crompton, J. C.; Callejas, J. F.; Popczun, E. J.; Biacchi, A. J.; Lewis, N. S.; Schaak, R. E. *Chem. Mater.* **2014**, *26*, 4826-4831.
- (80) Zou, X.; Huang, X.; Goswami, A.; Silva, R.; Sathe, B. R.; Mikmeková, E.; Asefa, T. *Angew. Chem. Int. Ed.* **2014**, *126*, 4461-4465.
- (81) Kong, D.; Cha, J. J.; Wang, H.; Lee, H. R.; Cui, Y. *Energy Environ. Sci.* **2013**, *6*, 3553-3558.
- (82) Cao, B.; Veith, G. M.; Neuefeind, J. C.; Adzic, R. R.; Khalifah, P. G. *J. Am. Chem. Soc.* **2013**, *135*, 19186-19192.
- (83) Li, Y.; Wang, H.; Xie, L.; Liang, Y.; Hong, G.; Dai, H. *J. Am. Chem. Soc.* **2011**, *133*, 7296-7299.

- (84) Yu, H.; Yu, X.; Chen, Y.; Zhang, S.; Gao, P.; Li, C. *Nanoscale* **2015**, *7*, 8731-8738.
- (85) Chen, W.-F.; Sasaki, K.; Ma, C.; Frenkel, A. I.; Marinkovic, N.; Muckerman, J. T.; Zhu, Y.; Adzic, R. R. *Angew. Chem. Int. Ed.* **2012**, *51*, 6131-6135.
- (86) Chang, Y.-H.; Lin, C.-T.; Chen, T.-Y.; Hsu, C.-L.; Lee, Y.-H.; Zhang, W.; Wei, K.-H.; Li, L.-J. *Adv. Mater.* **2013**, *25*, 756-760.
- (87) Lu, Z.; Zhu, W.; Yu, X.; Zhang, H.; Li, Y.; Sun, X.; Wang, X.; Wang, H.; Wang, J.; Luo, J.; Lei, X.; Jiang, L. *Adv. Mater.* **2014**, *26*, 2683-2687.
- (88) Tian, J.; Liu, Q.; Asiri, A. M.; Sun, X. *J. Am. Chem. Soc.* **2014**, *136*, 7587-7590.

Appendix A

Determination of nanoparticle size from p-XRD pattern:

The size of AuNPs in the composite could be determined from the following Debye–Scherrer Equation by determining the width of the (111) Bragg reflection.

$$B(2\theta) = \frac{K\lambda}{L \cos \theta}$$

Where L is the mean size of the ordered (crystalline) domains, K is a dimensionless shape factor, with a value close to unity. The shape factor has a typical value of about 0.9, but varies with the actual shape of the crystallite, λ is the X-ray wavelength (0.154 nm), B is the line broadening at half the maximum intensity (FWHM) in radians.

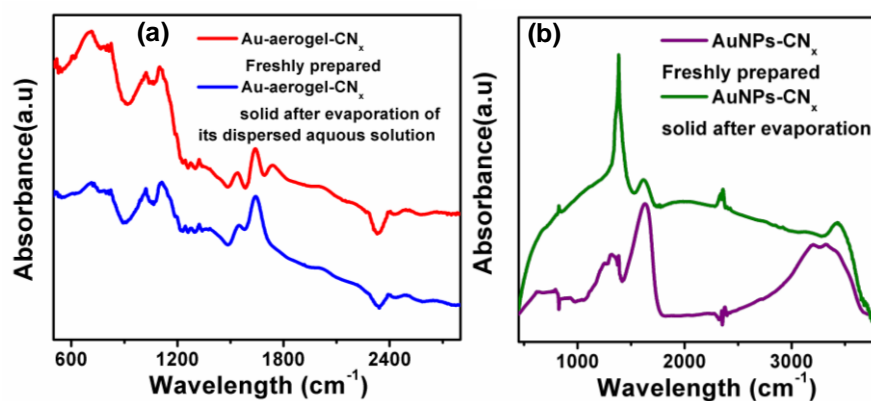


Figure S3.1. FT-IR spectra of (a) freshly prepared Au-aerogel-CN_x (blue line) and solid obtained from evaporation of water dispersion of Au-aerogel-CN_x (red line). (b) Freshly prepared AuNPs -CN_x (purple line) and solid, obtained from evaporation of water dispersion of AuNPs -CN_x (green line).

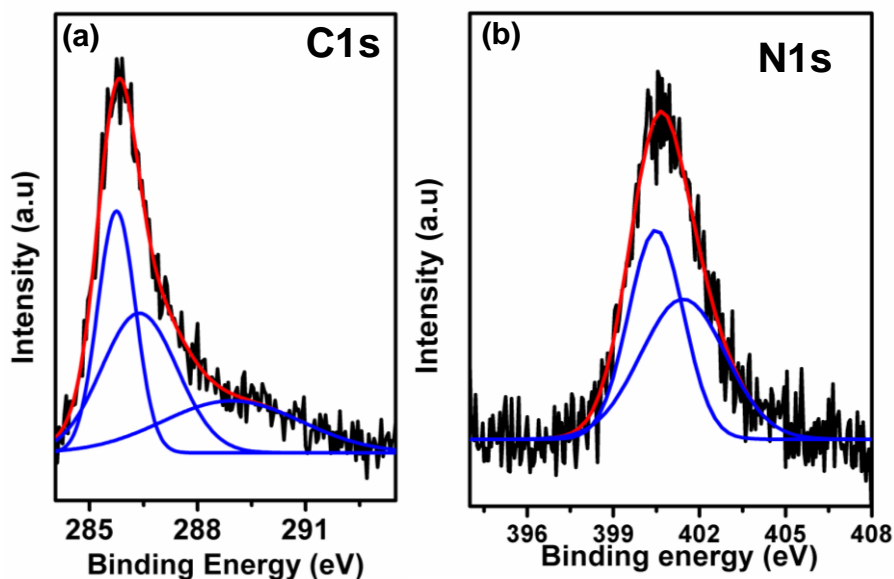


Figure S3.2. (a, b) The deconvoluted spectra of C1s and N1s XPS spectra of CN_x. (c) Comparison of N1s XPS spectra of g-CN_x, AuNPs-CN_x, Au-aerogel-CN_x.

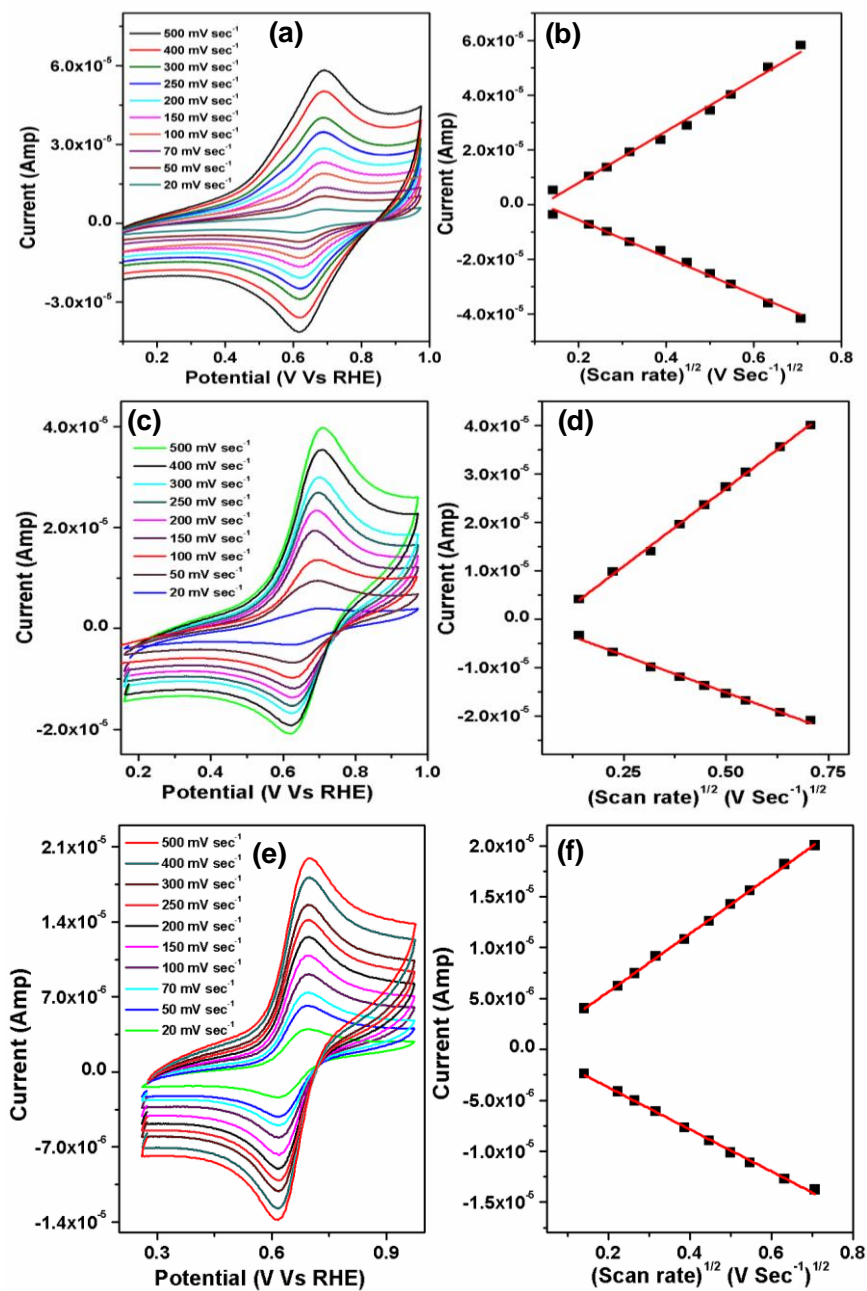


Figure S3.3. CVs curve for 0.5 mM $[\text{Fe}(\text{CN})_6]^{3-/4-}$ redox couple in 0.05 M H_2SO_4 at different scan rate and corresponding current vs square root of scan rate plot of (a, b) Au-aerogel- CN_x (c, d) AuNPs- CN_x and (e, f) bare GCE.

Koutecky-Levich (K-L) equation:

$$1/j = 1/j_k + 1/j_d = -1/nFkCo_2 - 1/B\omega^{1/2}$$

Where j is the measured current density, j_k , j_d is the kinetic and diffusion limited current density. ω is the electrode rotating rate. B can be determined from the slope of K-L plot and theoretically can be obtained from the following equation

$$B = 0.62 nF(DO_2)^{2/3}v^{-1/6}Co_2$$

where Faraday constant ($F= 96485 \text{ C mol}^{-1}$) and n is the number of electron transferred per O_2 molecule, in 0.5 M KOH diffusion coefficient (DO_2) of O_2 ($1.9 \times 10^{-5} \text{ cm}^2 \text{ s}^{-1}$), kinetic viscosity ($v = 0.01 \text{ cm}^2 \text{ s}^{-1}$) and Co_2 is the bulk concentration of O_2 ($1.2 \times 10^{-6} \text{ mol cm}^{-3}$).

For 0.5 M H_2SO_4 diffusion coefficient (DO_2) is $1.8 \times 10^{-5} \text{ cm}^2 \text{ s}^{-1}$, $v = 0.01 \text{ cm}^2 \text{ s}^{-1}$ and $Co_2 = 1.13 \times 10^{-6} \text{ mol cm}^{-3}$.

Specific activity and Mass activity determination

The specific activity (SA) and MA (mass activity) were calculated using these equations

$$SA = I_k / ECSA$$

Here I_k is the kinetic current.

Mass activity of the electrode were evaluated from equation below

$$MA = I_k / m_{Au}$$

Here m_{Au} is the mass of Au on the electrode.

CHAPTER 4

One dimensional Pt Nanostructures/Carbon Nitride hybrid: Synthesis and its Applications as Highly Efficient Catalyst in Hydrogen Evolution/Oxidation Reactions at Different pH Values

4.1 ABSTRACT

Design and synthesis of active catalyst for HER/HOR are important for the development of hydrogen based renewable technologies. The sluggish HER/HOR kinetic of Pt/C in base and poor HER/HOR stability of Pt/C catalyst in strong acid are the main obstacles for commercialization of anion and proton exchange membrane fuel cells. In this chapter we have shown synthesis of Pt nanostructures-N-doped carbon hybrid (Pt-(PtO_x)-NSs/C) for HER/HOR applications. The HER activity of this Pt-(PtO_x)-NSs/C catalyst is 4 and 6.5 times better than commercial Pt/C in acid and base. The catalyst exhibits a current density of 10 mA/cm² at overpotentials of 5 and 51 mV with Tafel slopes of 29 and 64 mV/dec in 0.5 M H₂SO₄ and 0.5 M KOH. The stability test confirmed extraordinary HER stability of the Pt-(PtO₂)-NWs/C catalyst in both medium. This catalyst also showed superior HOR activity at all pH values. This catalyst also showed superior HOR activity at all pH values. The HER/HOR activity of Pt-(PtO_x)-NSs/C and PtO_x-free Pt-Nanostructures/C (PtNSs/C) catalysts are comparable in acid with exchange current, i_0 values of 7.2 and 6.1 mA/cm². The presence of PtO_x in Pt-(PtO_x)-NSs/C makes this Pt-catalyst more HER/HOR active in basic media. The activity of Pt-(PtO_x)-NSs/C catalyst is 5 fold higher than that of PtNSs/C catalyst in basic medium although their activity is comparable in acid. Hydrogen binding energy and oxophilicity are the two equivalent descriptors for HER/HOR in basic media. We propose a

bi-functional mechanism for the enhanced alkaline HER/HOR activity of Pt-(PtO_x)-NSs/C catalyst. In bi-functional Pt-(PtO_x)-NWs/C catalyst, PtO_x provide an active site for OH⁻ adsorption to form OH_{ads} which reacts with hydrogen intermediate (H_{ads}), present at neighbouring Pt sites to form H₂O leading to enhancement of HOR activity in basic medium. For HER in the base, PtO_x favours the adsorptive dissociation of water to form H_{ads} on adjacent Pt sites and then recombination of H_{ads} results to the formation of the hydrogen molecule. This work may provide new opportunity to design and develop bi-functional HER/HOR electro-catalyst for development of various renewable energy technologies.

4.2 INTRODUCTION

The rapid rise of global energy demand and environmental problems associated with the use of fossil fuels are the driving force for exploring the renewable energy sources and energy storage^{1,2}. Water electrolyzers and fuel cells are the two important renewable techniques for energy storage and conversion²⁻⁴. Hydrogen is considered as one of the best clean energy carriers with high mass density and hydrogen evolution reaction (HER) is featured in water electrolyzers that store the energy in chemical form by generating molecular hydrogen⁵. Hydrogen oxidation reaction (HOR) is mainly used in fuel cells where chemical energy of hydrogen is converted into electrical energy⁶. The hydrogen fuel cell consists two half-cell reactions such as HOR at anode and oxygen reduction reaction (ORR) at cathode whereas water electrolyzers are based on two reactions: HER at cathode and oxygen evolution reaction (OER) at anode⁷. Among the various fuel cells, proton exchange membrane fuel cells (PEMFCs) is one best renewable energy sources due to its better environmental friendliness, high energy conversion efficiency, high energy and power density². The platinum (Pt) is the most active catalyst for both HER/HOR processes in acid media⁸, but poor stability of commercial Pt/C under the strong acidic condition is one of the main obstacles for the commercialization of PEMFCs⁹. Thus, it is highly desirable to find

new highly active and highly durable HER/HOR catalyst. In recent years, Alkali membrane fuel cells (AMFCs) and alkaline electrolyzers are considered as a suitable alternative to PEMFCs and water electrolyzer respectively since earth abundant transition metal based non-precious catalysts are available for ORR and OER in alkaline media¹⁰⁻¹³. Another advantage of AMFCs over PEMFCs is the high stability of electrocatalyst in alkaline medium. Although Pt is also the best catalyst for HER, HOR in alkaline medium, but the HER/HOR activity of commercial Pt/C in base media is 2 orders of magnitude lower than that of acid^{14,15}. Because of sluggish HER/HOR kinetics at commercial Pt/C catalyst in alkaline media, a very large amount of Pt loading ($\sim 0.5 \text{ mg cm}^{-2}$) is required at anode for AMFCs in comparison to low Pt loading ($\sim 0.05 \text{ mg cm}^{-2}$) for PEMFCs¹⁶. Therefore, effective HOR/HER catalyst is highly desirable for the development of AMFCs or alkaline electrolyzers. Understanding the mechanism of HOR/HER in alkaline media is important for designing efficient alkaline HOR/HER electrocatalysts. In acidic media, HOR/HER occurs via either Tafel-Volmer or Heyrovsky-Volmer mechanism^{14, 16,17} :



Therefore, hydrogen binding energy is the dominant descriptor for HOR/HER in acid media^{14,18,19}. However, in alkaline media the role OH^- ion is debatable⁶. In strong basic media, several groups suggested that H_{ads} is desorbed as a proton (H^+) and then quick reaction between H^+ and OH^- ions to form water.



Thus, HBE is a sole descriptor for HOR/HER in alkaline media like acid medium²⁰⁻²³. There is another possibility that OH⁻ ions from solution can adsorb on the catalyst surface to form OH_{ads} species which then react with neighboring H_{abs} to generate water molecule.



If OH⁻ ions is adsorbed on the catalyst surface, followed by reaction between H_{ads} and OH_{ads} occurs through the bi-functional mechanism, then stronger OH adsorption will enhance HOR activity in alkaline media^{24,25}. Durst²⁰ *et al.* and Sheng *et al.*¹⁸ also showed that poor HER/HOR activity was correlated with high HBE of the catalyst in basic media suggesting that HBE is a prime descriptor for HER/HOR in alkaline media. Wang *et al.*²² has reported HOR activity of PtRu alloy catalyst in basic media is double than that of monometallic Pt and concluded that HBE is the main descriptor and oxophilicity of metals doesn't play a major role in HOR activity. Gasteiger and coauthors showed HBE has main influence for HOR in alkaline media²⁶. In contrary, Strmcnik *et al.*²⁴ reported oxophilicity (i.e. ability to absorb (OH⁻) of metals plays a significant role in the oxidation of H₂ in basic medium-the stronger OH adsorption is beneficial for HOR activity in the alkaline medium through the bi-functional mechanism. They also modified the surface of pristine Pt by depositing OH⁻ ion promoter such as Ni(OH)₂ and it was observed that HOR activity in basic media was enhanced in comparison to that of Ni(OH)₂-free Pt surface.

The synthesis of platinum metal nanostructures has attracted a huge attention in recent years since they are often used in catalysis for organic transformations²⁷, fuel cell/electrocatalysis²⁸⁻³¹ and sensors³². The electrocatalytic activities of Pt nanostructures can be improved by modifying size or morphology³³ of Pt nanostructures and sometimes morphology may offer more versatility than size due to the crystal facet effect³⁴. The synthesis of Pt nanomaterial with different morphologies is thus highly attractive for their

electrochemical applications such as HOR and ORR catalyst in PEM fuel cells³⁵⁻³⁷. Pt-octahedra³⁸ and tetrahedral platinum³⁵ nanocrystals with high-index facets showed an enormous high electrocatalytic activity towards ORR and formic acid oxidation than commercial Pt/C. One-dimensional (1-D) metal nanostructures have received considerable interest for its various applications. The 1-D noble metal nanostructures were found to be suitable electro-catalyst especially for ORR in PEM fuel cell because of unique anisotropic nature of 1-D materials, extended smooth defect-free facets, fewer lattice boundaries and surface to volume ratio^{39,40}. All these properties are desirable for fuel cell catalysts. 1-D noble metal electro-catalysts were reported for better activity than that of commercial Pt/C for ORR and alcohol oxidation reactions. Recently branched Pt-nanostructures³³ with structural anisotropy has drawn a great interest because of their enhanced catalytic activity. Decreasing the diameter and increasing branched structure enhances the surface area and higher porosity, and activities³³. Pt tripods³⁶, Pt octapods⁴¹, Pt dendrites⁴², star-like Pt nanowires⁴³ structure are known as catalytically more active than commercially available Pt/C. Although several reports available for ORR applications of 1-D Pt nanostructures but, the report of hydrogen evolution and oxidation of one dimensional Pt nanostructures are few^{15,28}.

Herein, we have shown a facile synthesis of one-dimensional platinum nanostructures, nitrogen-doped carbon composite (Pt-(PtO_x)-NSs/C). This catalyst exhibited superior HER and HOR activity in the acidic and alkaline medium. The HER activity of this Pt(PtO_x)-NSs in acid media is 3.2 times higher than that of commercial Pt/C whereas in the base it is 4.9 times more active than commercial Pt/C. Understanding the role of OH⁻ ions in the basic medium of HOR/HER mechanism is important for the development of new catalysts. It was found that both hydrogen binding energy and oxophilicity play an important role in enhancing the HOR and HER activity in the base. The Pt-(PtO_x)-NSs/C catalyst

behaves as a bi-functional catalyst in basic media. The Pt site provides an active site for hydrogen intermediate (H_{ads}) and PtO_2 site offer adsorption site for OH^- , the presence of OH^- species in Pt-(PtO_x)-NSs/C enhances the reactivity of H_{ads} leading to improvement of HOR activity in basic media. In the bi-functional mechanism of HER in basic media, the dissociation of water occurs on PtO_2 sites, leading to the formation of hydrogen intermediate (H_{ads}) on neighboring Pt site and then recombination of H_{ads} to form the H_2 molecule. The Hydrogen binding energy (HBE) and oxophilicity are the two descriptors for HER/HOR in basic media.

4.3 EXPERIMENTAL SECTION

Preparation of the PtNSs/C composite:

PtNSs/C composite was synthesized via reduction of H_2PtCl_6 by $NaBH_4$ followed by ultrasonic treatment in presence of g-CN_x. Briefly, 0.0965 mmol of H_2PtCl_6 , 6H₂O was taken in 5 ml water & and dissolve it well. Then 0.449 mmol of $NaBH_4$ was directly added to the solution and again sonicated properly. In another vial, 5 mg of as prepared of g-CN_x⁴⁴ was dispersed in 2 ml water by sonication for few minutes. Then two solutions are mixed together by using a bath-sonicator for 10 minutes. Finally, the resultant solution was sonicated by ultrasound operating at 28 kHz frequency (power 700 watts) for 90 minutes. The black colored mass was recovered by centrifugation at 16,000 rpm for 20 minutes and washed repeatedly with deionized water & ethanol. Finally, the product was kept in vacuum for drying

Synthesis of the Pt-(PtO_x)-NSs/C composite:

Pt-(PtO_x)-NSs/C composite was synthesized by two steps process. The first step, synthesis of PtNSs/C from $NaBH_4$ reduction of H_2PtCl_6 , 6H₂O salt in the presence of g-CN_x and second step PtNSs/C was heated at 400 °C for 1h. Briefly, 0.116 mmol of H_2PtCl_6 , 6H₂O was dissolved in 5 ml water and 0.528 mmol of $NaBH_4$ was directly added

into the solution and again sonicated properly. Water dispersed 20 mg of CN_x was mixed together by using a bath-sonicator for 10 minutes. Finally, the resultant solution was sonicated by ultrasound operating at 28 kHz frequency (power 700 watt) for 90 minutes. The black colored solid was recovered by centrifugation at 16,000 rpm. This composite was taken in an alumina crucible and calcinated at $400^\circ C$ in a tube furnace with a temperature accuracy $\pm 2^\circ C$ for 1 h. After that, it was cooled down to room temperature normally & collected carefully black solid product. In addition, we have also synthesized this composite at different temperature as 300, 350, 400, 450, 500, $600^\circ C$. Higher catalytic activity was observed for the catalyst synthesized at $400^\circ C$ composite. Therefore, Pt-(PtO_x)-NSs/C composite synthesized at $400^\circ C$ was optimized and further studies were performed with this catalyst.

For comparison purpose, we have synthesized Pt sample without using any carbon support, following the same synthesis procedure. This composite is termed as Pt- PtO_x .

Electrochemical measurements:

All the electrochemical measurements were done in a conventional three-electrode system at an Autolab 302N electrochemical station using Ag/AgCl (3 M KCl) as reference electrode, Pt mesh as counter electrode and GC as a working electrode. Glassy carbon electrode was polished with 1.0, 0.1 and 0.05 mm alumina slurry on Buehler micro cloth polishing cloth. After rinsing, the electrode was sonicated in distilled water about 10 min. 1 mg of the synthesized composite was dissolved in 1 ml water to make a stock solution. 2.5 μl of the aqueous stock solution was evaporated on cleaned glassy carbon electrode to prepare Pt-(PtO_x)-NSs/C electrode. Thus amount of Pt on the electrode was 2 μg ($28.5 \mu g/cm^2$). For stability measurement 20 μl 5 wt% nafion solution was used to make the stock solution and only the potentiometric study in KOH medium, 5 μl of aqueous stock solution (i.e 4 μg of Pt) was drop-casted on GC. The amount of comm. Pt/C was also kept same for

comparison for all the experiment. 10 μl 5% nafion and 10 μl ethanol was used to make the stock solution of comm. Pt/C. Thus the HER measurements were carried out in both acidic and basic medium degassed with nitrogen using LSV at a scan rate 10 mV/sec. HOR was done in alkaline and acidic and buffer medium with the help of linear sweep voltammetry (LSV) by using hydrogen 10 mV sec^{-1} scan rate in an H_2 saturated environment. CV was done in different pH with 30 mv/sec scan rate with N_2 saturated medium. The stability of the electrode was measured by both repeated LSV and chronoamperometric at constant potential and current method. AC impedance measurements were performed in the identical system in the frequency range 10^5 Hz to 10^{-1} Hz with a constant AC voltage. Cell resistance was calculated for iR correction in HOR polarization curves. In impedance spectra linearly extrapolated intercept with real axis was taken as resistance of cell.

4.4 RESULTS AND DISCUSSIONS:

4.4.1 Characterization of Pt-(PtO_x)-NSs/C composite:

The powder X-ray diffraction (p-XRD) of as-synthesized Pt-(PtO_x)-NSs/C composite was shown in Figure 4.1. The five well resolved, highly instanced diffraction peaks positioned at 39.71, 46.07, 67.53, 81.28, 85.57 in Pt-(PtO_x)-NSs/C composite corresponds to the (111), (200), (220), (311), (222) reflection planes of f.c.c platinum (JCPDS No 04-0802)²⁷. This suggests the presence of Pt nanostructure in the composite. The peak positioned at $2\theta = 39.71$ for Pt (111) plane was chosen to calculate the size of Pt nanowires by using well define Debye–Scherrer Equation⁴². The size of Pt-(PtO_x)-NSs/C in the composite could be determined from the following Debye–Scherrer Equation described bellow

$$B(2\theta) = \frac{K\lambda}{L \cos \theta}$$

Where L is the mean size of the ordered (crystalline) domains, K is a dimensionless shape factor, with a value close to unity.

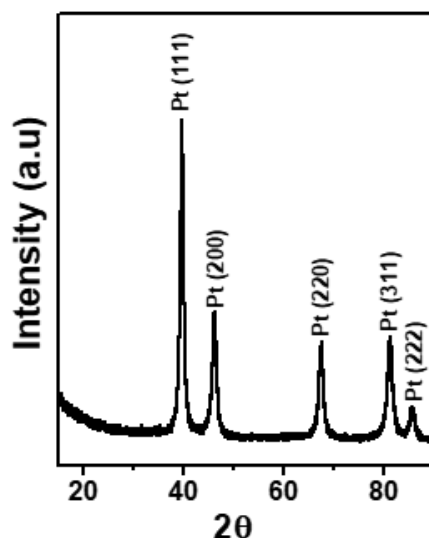


Figure 4.1. p-XRD of Pt-(PtO_x)-NSs/C composite.

The shape factor has a typical value of about 0.9, but varies with the actual shape of the crystallite, λ is the X-ray wavelength (0.154 nm), B is the line broadening at half the maximum intensity (FWHM) in radians. The most intense peak positioned (2θ) at 39.83° was used to calculate the size of Pt-(PtO_x)-NSs/C in the composite using this equation and obtained as ~11 nm. The average size of Pt-(PtO_x)-NSs/C composite was calculated and it was ~ 11 nm.

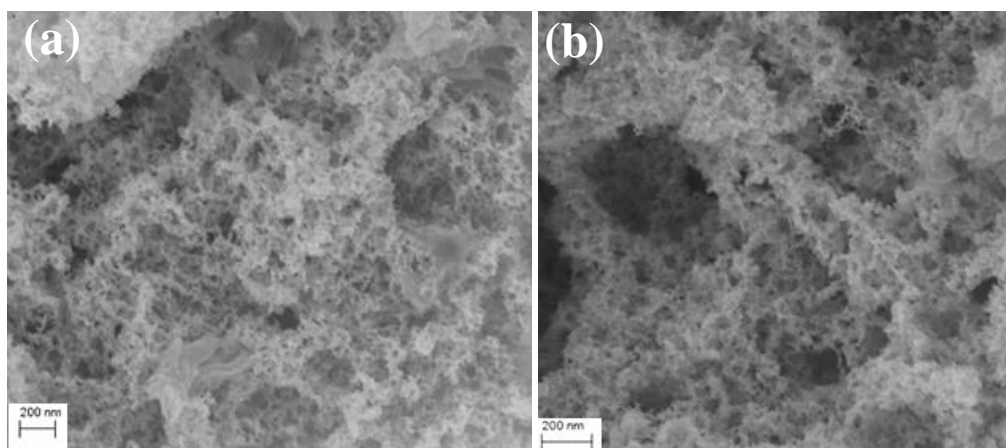


Figure 4.2. (a, b) FESEM images of Pt-(PtO_x)-NSs/C composite.

The p-XRD pattern of PtNSs/C is shown in Figure S4.1, indicates the presence of f.c.c platinum. Field Emission Scanning Electron Microscopy (FESEM) and Transmission

Electron Microscopy (TEM) measurements were done to investigate the surface morphology Pt nanowires. The representative FESEM images of the composite Pt-(PtO_x)-NSs/C are shown in Figure 4.2a and b. The nanowires are clearly visible in the FESEM images also. These Pt-nanowires are assembled together to form highly porous morphology. The FESEM images of PtNSs/C composite are also shown in Figure S4.2 These images show wire-like morphology and connected Pt nanoparticles are clearly visible. When PtNSs/C composite was heated at 400 °C the growth and coalescence of Pt nanoparticles lead to the formation of Pt-nanowires. TEM images of Pt-(PtO_x)-NSs/C are shown in Figure 4.3a, b and Figure S4.3a, b. In all these images, the thin Pt nanowires are interconnected to form interconnected networks like structure with a large number of open pores. The nanowires have an almost uniform diameter of about 11-15 nm. In some wires, the coalescence of initial spherical particles is quite obvious in the TEM images. The SAED image of Pt-(PtO_x)-NSs/C is shown in Figure 4.3c suggesting a polycrystalline structure. The interlayer spacing calculated from SAED image are 2.28, 1.98, 1.4, 1.2, 1.13 Å which corresponds to (111), (200), (220), (311) and (222) planes of f.c.c Pt(0)⁴⁵. HRTEM image of Pt-(PtO_x)-NSs/C composite was shown in Figure 4.3d. The lattice fringes with d spacing of 2.28 and 1.98 Å corresponds to the (111) and (200) lattice plane of Pt(0). In addition, lattice fringes of d spacing 2.6 Å corresponds to (011) plane of PtO₂ suggesting the presence of PtO₂ in the composite. The XPS survey scan spectra of porous Pt-(PtO_x)-NSs/C composite was given in Figure 4.4a, showing the presence of platinum (Pt), carbon(C), oxygen (O) and very small amount of nitrogen (N) atom. The XPS survey scan spectrum of PtNSs/C composite is also shown in Figure 4.4b. This spectrum clearly indicates the presence of C, N, Pt and a smaller amount of O. The high-resolution Pt4f XPS spectra of both the composite PtNSs/C and Pt-(PtO_x)-NSs/C are shown in Figure 4.4c.

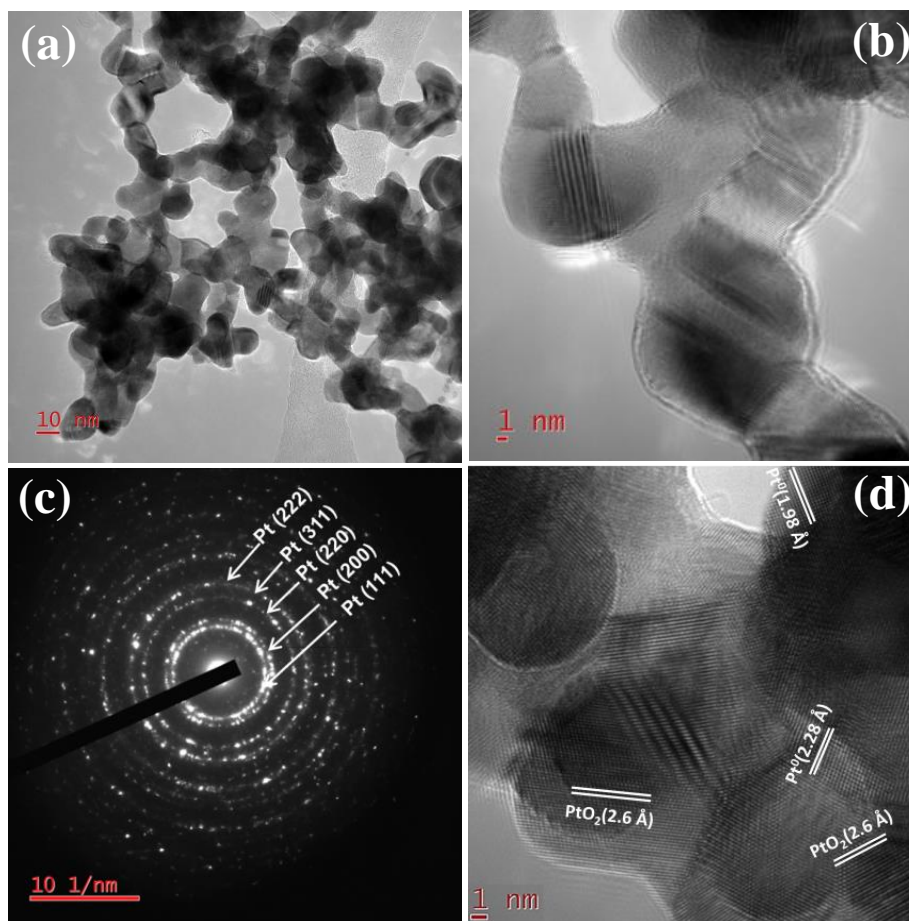


Figure 4.3. (a,b) TEM images of Pt-(PtO_x)-NSs/C composite showing the nanowires morphology. (c) SAED image (d) HRTEM image.

The Pt4f XPS spectra of Pt NSs/C was appeared⁴⁶ as doublet with peak centered at 71.5 and 74.9 eV corresponding to 4f_{7/2} and 4f_{5/2} component of Pt(0) whereas the Pt4f XPS spectra of Pt-(PtO_x)-NSs/C composite also appeared as doublet with an additional peak centered at 78.1eV due to Pt(IV) species^{46,47}. We have deconvoluted the high-resolution Pt 4f spectra of Pt-(PtO_x)-NSs/C composite into six components as shown in Figure 4.4d. The peak position at 71.4, 74.9 eV; 72.1, 75.9 eV; 73.8, 78.1eV are assigned to 4f_{7/2} and 4f_{5/2} of Pt(0), Pt(II) and Pt(IV) species respectively. This suggested the presence of platinum oxide species (PtO, PtO₂) in the composite. The high-resolution C1s spectra of Pt-(PtO_x)-NSs/C and Pt NSs/C were shown in Figure S4.4a.

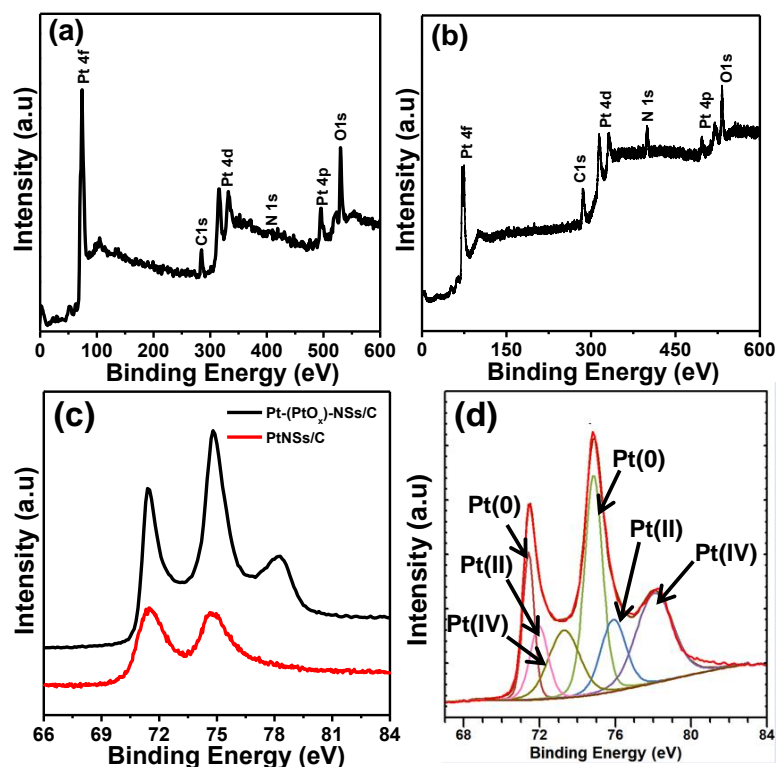


Figure 4.4. XPS survey scan of (a) Pt-(PtO_x)-NSs/C (b) PtNSs/C composite. (c) Comparison of Pt4f XPS spectra of Pt-(PtO_x)-NSs/C and PtNSs/C composite. (d) Deconvoluted Pt4f XPS spectra of Pt-(PtO_x)-NSs/C composite.

The C1s peak for both the compound appeared at 285.1 eV was assigned to sp² hybridized graphitic carbon^{48,49}. O1s XPS spectrum of Pt-(PtO_x)-NSs/C and PtNSs/C composite was compared in the Figure S4.4b. The O1s peak of Pt-(PtO_x)-NSs/C and PtNSs/C composite appeared at 530.8 and 532.2 eV. A lower binding energy of O1s spectra for Pt-(PtO_x)-NSs/C composite indicate the presence of Pt bonded O (Pt-O)⁴⁷. Moreover, the N 1s XPS spectra of Pt-(PtO_x)-NSs/C and PtNSs/C composite appeared at 399.1 eV was assigned to the pyridine N atom⁵⁰ as shown in Figure S4.4c. The low intensity of high-resolution N1s peak in survey scan, as well as high-resolution spectra, suggested the presence of small amount of nitrogen in Pt-(PtO_x)-NSs/C composite. We have also performed the EDS measurement of Pt-(PtO_x)-NSs/C and PtNSs/C composite as shown in Figure S4.5 and S4.6. This clearly showed the very less amount of N atom presence in Pt-(PtO_x)-NSs/C composite.

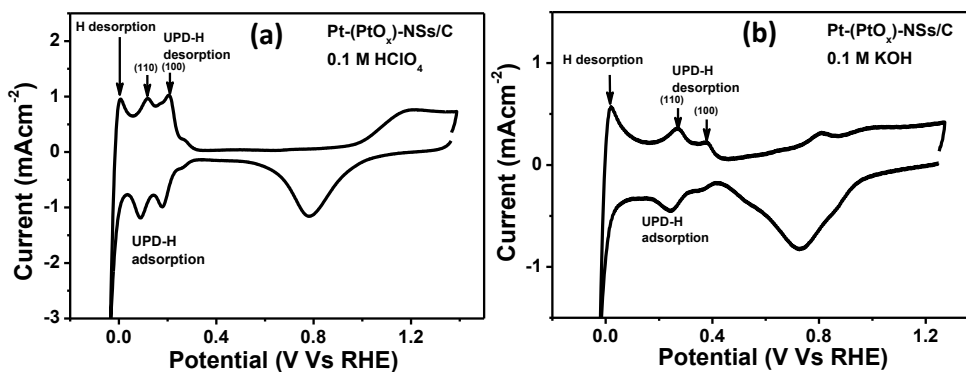


Figure 4.5. Cyclic voltammograms of porous Pt-(PtO_x)-NSs/C (a) 0.1 M HClO₄ and (b) 0.1 M KOH electrolyte was showing H adsorption and desorption peaks clearly. (Scan rate 30 mV/sec, N₂ atmosphere, Pt loading 8 μg).

The exact amount of Pt loading in Pt-(PtO_x)-NSs/C was determined by inductively coupled plasma optical emission spectrometry (ICP-OES) measurement. The exact wt% of Pt presents in Pt-(PtO_x)-NSs/C and PtNSs/C composite was 80.1% and 74% respectively. Cyclic voltammetry was used to investigate the electrochemical property of Pt-(PtO_x)-NSs/C composite in both acidic and alkaline medium to explore hydrogen absorption (H_{abs}), desorption (H_{des}) and surface oxide formation property. Chemisorbed-H species is important as it serves as an intermediate for HOR/HER reaction and has withdrawn a great attention. The noble metal has two types of electrodeposited H intermediate: one is under potential deposited hydrogen (UPD-H), occurred at a little positive potential of H⁺/H₂ potential and other is over potential deposited hydrogen (OPD-H) occurred at very close to H⁺/H₂ potential. UPD process can be depicted by as follows

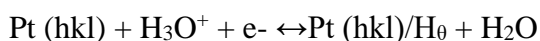


Figure 4.5a shows the CV of Pt-(PtO_x)-NSs/C in 0.1 M HClO₄ solution. Pt-(PtO_x)-NSs/C shows strong proton adsorption–desorption peaks occurred at < 0.4 V. A broad anodic peak appeared at E > 1.0 V suggested the formation of Pt–O and its corresponding cathodic peak at 0.8 V for the reduction of Pt–O. Two distinctive H-desorption peaks corresponding to Pt(110) located at lower overpotential and Pt(100) located at higher overpotential are clearly

visible¹⁴. The symmetrical anodic and cathodic peaks at 0.088 and 0.117 V are assigned to UPD hydrogen adsorption (UPD-H_{ads}) and desorption (UPD-H_{des}) from Pt-(PtO_x)-NSs/C surfaces, respectively. Difference between two coupled UPD-H_{ads} and UPD-H_{des} (ΔE_p) peak of Pt-(PtO_x)-NSs/C composite was ~29 mV, which is lower than the reversible value of 60 mV. Recently, Gasteiger and co-workers reported²⁶ that the ΔE_p value for reversible UPD-H on commercial Pt/C was 50 mV. Recently, our group²³ also observed a ΔE_p of 70 mV for Pd-CN_x composite. Thus, porous Pt-(PtO_x)-NSs/C composite was more reversible towards the H_{ads} and H_{des}. It is noteworthy that Pt-(PtO_x)-NSs/C can distinguish all H-absorption and H-desorption peaks clearly. In addition, CV of Pt-(PtO_x)-NSs/C in 0.1 M KOH was also performed and is shown in Figure 4.5b. UPD-H peaks for both the plane Pt (110) and Pt (100) in alkaline medium is also visible from the above-mentioned CV. The electrochemical active surface area (ECSA) of Pt-(PtO_x)-NSs/C and commercial Pt/C catalyst was calculated from H-desorption peak obtained from the CV as shown in Figure S4.7 and S4.8. The ECSA value of Pt-(PtO_x)-NSs/C catalyst was found to be 23 m²/g_{Pt} in 0.5 M KOH and 28 m²/g_{Pt} in H₂SO₄, lower than that of the commercial Pt/C catalyst (47 m²/g_{Pt} and 52 m²/g_{Pt} in 0.5 KOH and 0.5 M H₂SO₄).

4.4.2 HER Activity of Pt-(PtO_x)-NSs/C in Acid and Alkaline medium

The electrocatalytic activity of as-synthesized Pt-(PtO_x)-NSs/C catalyst was evaluated for HER in both acid and alkaline medium in N₂ saturated acid and alkaline solution using a three-electrode linear sweep voltammograms (LSV) with a scan rate of 10 mV/sec at a rotation of 1600 rpm. The LSV polarization curve (current normalized by electrode surface area vs potential) of Pt-(PtO_x)-NSs/C catalyst for HER in 0.5 M H₂SO₄ solution is compared with commercial Pt/C, PtNSs/C, CN_x and GC electrodes as shown in Figure 4.6a.

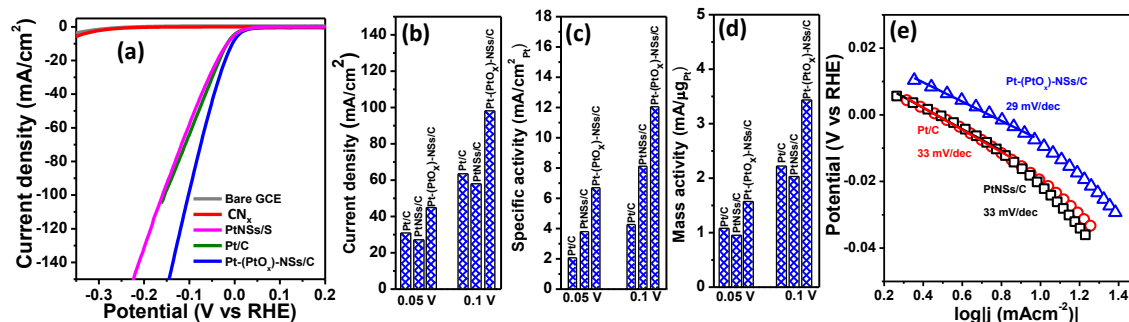


Figure 4.6. HER performance of various electrodes (a) LSV polarization curves of Pt-(PtO_x)-NSs/C, commercial Pt/C, PtNSs/C, CN_x and GCE in 0.5 M H₂SO₄ with scan rate 10 mV/s at 1600 rpm rotation. Comparison of (b) Geometric current density (c) SA (d) MA of Pt-(PtO_x)-NSs/C, PtNSs/C and commercial Pt/C. (e) The HER Tafel plot of Pt-(PtO_x)-NSs/C, commercial Pt/C and PtNSs/C.

It shows Pt-(PtO_x)-NSs/C, commercial Pt/C and PtNSs/C exhibited superior HER activity with a zero volt onset potential and appreciable current densities at low overpotentials; but, GC, CN_x modified GC electrode was almost inert. The Pt-(PtO_x)-NSs/C catalyst requires a significantly lower over-potential to achieve a significant current density in comparison to commercial Pt/C. In acidic 0.5 M H₂SO₄ medium, the overpotential required for Pt-(PtO_x)-NSs/C to drive the current density of 10 mA cm⁻² is 5 mV whereas required over-potential for commercial Pt/C and Pt-NPs is about 17 mV (Figure 4.6. (a) and Table 4.1). In order to investigate the intrinsic properties such as mass activity (MA, current normalized by mass of Pt on electrode) and surface activity (SA, current normalized by electrochemical surface area of Pt) was evaluated at -0.05 and -0.1 V. Figure 4.6 (b), 4.6 (c) and 4.6 (d) showed the current density (disk), SA and MA at a fixed over-potential of -0.05 V of Pt-(PtO_x)-NSs/C is compared with commercial Pt/C and PtNSs/C. The current density of Pt-(PtO_x)-NSs/C at -0.05 V is 45 mA cm⁻² which is 1.45 times higher than the commercial Pt/C. The SA of Pt-(PtO_x)-NSs/C at -0.05 V is 6.7 which is 3.2 times higher than that of commercial Pt/C. The MA at -0.05 V of Pt-(PtO_x)-NSs/C (1.57 mA cm_{Pt}⁻²) is 1.45 times higher than that of commercial Pt/C.

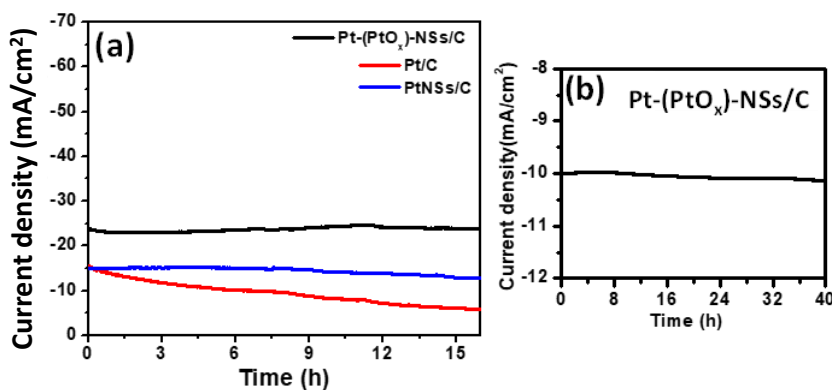


Figure 4.7. (a) Chronoamperometric responses of Pt-(PtO_x)-NSs/C, commercial Pt/C and PtNSs/C catalyst at $\eta = -25$ mV in (RHE). (b) Chronoamperometric stability of Pt-(PtO_x)-NSs/C for 40 h.

The HER Tafel slope is an inherent property of the catalyst and is obtained from Tafel equation ($\eta = a + b \log|j|$) where b is the Tafel slope). The HER Tafel plot showing $\log|j|$ vs applied potential for commercial Pt/C, Pt-(PtO_x)-NSs/C and PtNSs/C is presented in Figure 4.6 (e). The Tafel slope values of Pt-(PtO_x)-NSs/C, PtNSs/C and commercial Pt/C are found to be 29, 33, 33 mV dec⁻¹ respectively. This Tafel slope value suggests that Tafel-Volmer mechanism in the acidic medium where desorption of hydrogen is the rate-determining step (Tafel step).

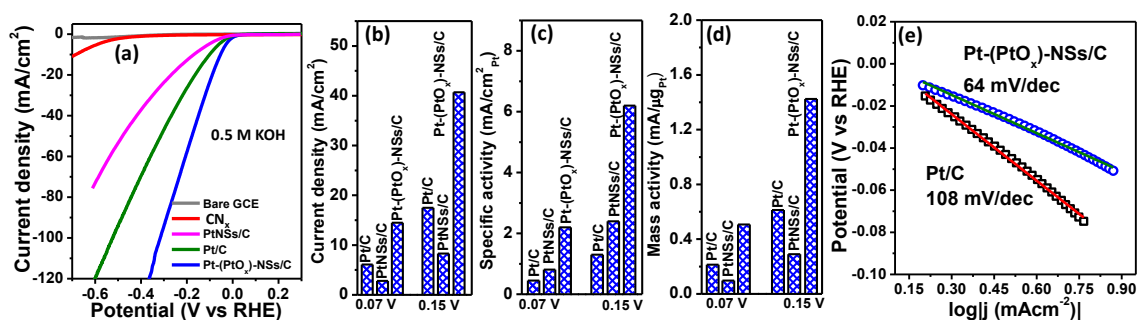


Figure 4.8. (a) LSV polarization curves of Pt-(PtO_x)-NSs/C, commercial Pt/C, PtNSs/C and CN_x in 0.5 M KOH. Comparison of (b) Geometric current density (c) SA (d) MA of Pt-(PtO_x)-NSs/C, PtNSs/C and commercial Pt/C. (e) The HER Tafel plot of Pt-(PtO_x)-NSs/C, commercial Pt/C.

The exchange current density (j_0) is also an important kinetic parameter that explores the rate of electron transfer at the reversible condition. The exchange current density for Pt-

(PtO_x)-NSs/C in 0.5 M H₂SO₄ medium was 5.0 mAcm⁻² which is higher than that of commercial Pt/C electrode (2.8 mA cm⁻²) and is also higher or comparable to other related systems^{23, 51-54}. The long-term HER durability of a catalyst in acid media is important for its commercialization of PEMFCs. The stability of Pt-(PtO_x)-NSs/C was investigated by chronoamperometric studies. As shown in Figure 4.7a, Pt-(PtO_x)-NSs/C and PtNSs/C possesses superior stability in a long-term operation over commercial Pt/C. It can sustain almost same current density for 16 hours whereas 40% current was decreased for commercial Pt/C in the same time chronoamperometric operation. A stability test for 40 h was carried out for Pt-(PtO_x)-NSs/C catalyst in same experimental conditions as shown in Figure 4.7b. The Pt-(PtO_x)-NSs/C catalyst maintains almost same current density up-to 40 h suggesting remarkable stability of the composite in acid media. Furthermore, we have also performed the XPS and TEM experiment of the catalyst after 40 h HER stability and shown in Figure S4.9 (a, b, c).

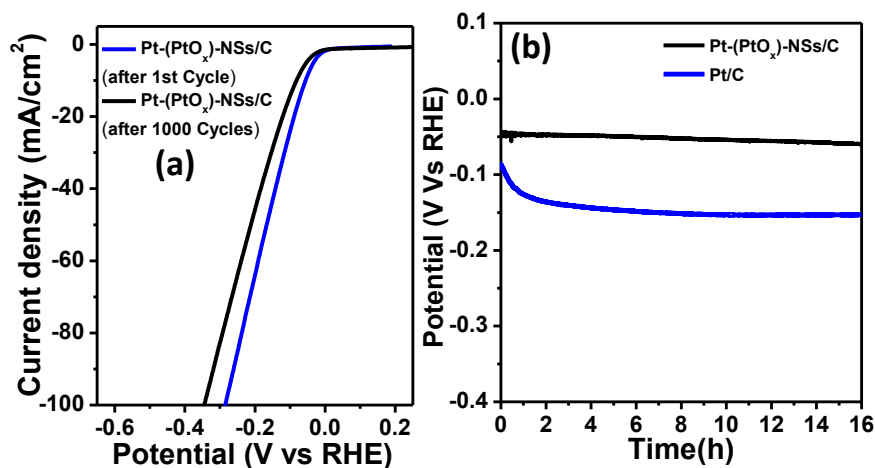


Figure 4.9. (a) LSV curves on the Pt-(PtO_x)-NSs/C catalyst at the first cycle and after 1000 cycles (scan rate 50 mV/s). (b) Chronopotentiometric stability of Pt-(PtO_x)-NSs/C, commercial Pt/C at 10 mA cm⁻².

The HER performance (onset potential, over potential, Tafel slope, exchange current density and MA) of Pt-(PtO_x)-NSs/C catalyst is compared with recent reported noble metal-based

catalysts^{23, 51, 55, 56, 36 57-60}, other non-noble metal catalysts⁶¹⁻⁶³ and shown in Table S4.1. This shows that this Pt-(PtO_x)-NSs/C catalyst is better or comparable than most of the recently reported catalysts. The HER activity of Pt-(PtO_x)-NSs/C catalyst was also studied in alkaline media. The comparison of representative LSV curves of Pt-(PtO_x)-NSs/C, commercial Pt/C, CN_x and GC electrode in 0.5 M KOH solution is shown in Figure 4.8a. This Figure shows that the Pt-(PtO_x)-NSs/C showed much better electrocatalytic activity towards HER than that of commercial Pt/C and PtNSs/C. Though Pt-(PtO_x)-NSs/C shows commercial Pt/C-like activity in the acidic medium, in alkaline medium, its activity is much lower than that of commercial Pt/C and Pt-(PtO_x)-NSs/C (Figure 4.8b). The Pt-(PtO_x)-NSs/C catalyst showed the 10 mA cm⁻² current density at overpotential of -0.051 V which is much lower than that of commercial Pt/C (0.098 V).

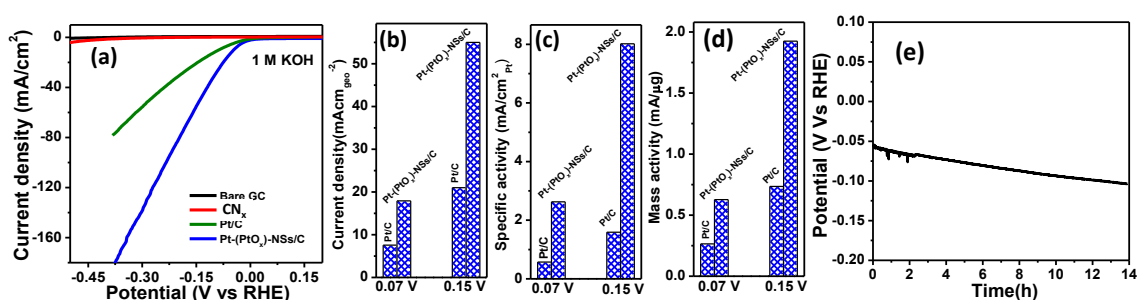


Figure 4.10. (a) LSV polarization curves of Pt-(PtO_x)-NSs/C, commercial Pt/C, CN_x and GCE in 1 M KOH with scan rate 10 mV/s at 1600 rpm rotation. Comparison of (b) Geometric current density (c) SA (d) MA of Pt-(PtO_x)-NSs/C, and commercial Pt/C in 1 M KOH. (e) Chronoamperometric study of Pt-(PtO_x)-NSs/C in 1 M KOH at constant current density of 10 mA/cm².

The SA and MA values at -0.07 V for Pt-(PtO_x)-NSs/C are 4.9 and 2.5 times higher than commercial Pt/C (Figure 4.8 c, d). As shown in Figure 4.8e, the Tafel slope for commercial Pt/C in 0.5 M KOH medium was 110 mV/dec, which is consistent with the previously reported data⁶⁴. The Tafel slope of the Pt-(PtO_x)-NSs/C in 0.5 M KOH was found 64 mV/dec, lower than other reported values^{23, 65}. This Tafel slope value suggests that HER follows Volmer-Heyrovsky pathway the basic medium where Heyrovsky or Volmer is the

rate-determining step. The exchange current density of Pt-(PtO_x)-NSs/C and commercial Pt/C was 1.25 mA cm⁻² and 1.1 mA cm⁻² in 0.5 M KOH medium. The exchange current density of Pt-(PtO_x)-NSs/C is higher or comparable than noble metal-based composite^{23, 51} and more than 10 times higher than other non-noble, transition metal catalysts⁶⁶⁻⁶⁸. The stability of Pt-(PtO_x)-NSs/C was investigated by continuous LSV cycling at 50 mV/s scan rate and chronopotentiometric studies at a constant current density (10 mA cm⁻²). A small current density was decreased after 1000 cycles of LSV scan as shown in Figure 4.9a. The chronopotentiometric study at constant current of 10 mA/cm² proved that this catalyst is highly stable in alkaline medium as compared to commercial Pt/C (Figure 4.9b). We also calculated Tafel slope from electrochemical impedance spectroscopy (EIS) in 0.5 M KOH solution. EIS of Pt-(PtO_x)-NSs/C composite at different overpotentials in 0.5 M KOH solution is shown in Figure 4.11a. The experimental data of impedance spectra have been fitted with an electrical equivalent circuit as shown in the insets of Figure 4.11a.

Table 4.1. Different HER parameter in acidic and alkaline medium.

Solution	Catalyst	Overpotential (mV) At (10 mA cm ⁻²)	Current density (mA cm ⁻²)	SA (mAcm ⁻² _{Pt})	MA (A/mg _{Pt})	Tafel slope (mV/dec)	Exchange Current (i ₀) (mAcm ⁻²)
0.5 M H ₂ SO ₄	Commercial Pt/C	17	30.9*	2.07*	1.08*	33	2.28
	Pt-(PtO _x)-NSs/C	5	44.9*	6.7*	1.5*	30	3.6
0.5 M KOH	Commercial Pt/C	105	6.1 [§]	0.45 [§]	0.21 [§]	108	1.3
	Pt-(PtO _x)-NSs/C	50	14.5 [§]	2.2 [§]	0.5 [§]	64	1.5

*at η= -0.05 V, § at η = -0.07 V.

In the equivalent circuit diagram, R_s is the solution resistance, R_{ct} is the overpotential dependence charge transfer resistance and CPE is the constant phase element. As we increase the overpotential value R_{ct} decreases gradually from 800 ohm at 0 mv to 30 ohm at -50 mV. The plot of log R_{ct}⁻¹ vs overpotential (Figure 4.11b) of Pt-(PtO_x)-NSs/C gives rise

to a Tafel slope of 61 mV/dec, which is good agreement with the Tafel slope obtained from the HER polarization curve. We have also studied HER activity of the catalyst in 1 M KOH as well as 0.1 M KOH solution and shown in Figure 4.10 (a-d) and Figure S4.10 respectively. This showed that HER activity of Pt-(PtO_x)-NSs/C in 1M KOH solution is higher than that of 0.1 M and 0.5 M KOH media with comparable stability (Figure 4.10e). As shown in Figure 4.11c and d, the activity enhancement is more prominent for iR-corrected as well as without iR-corrected HER activity in 1 M KOH solution.

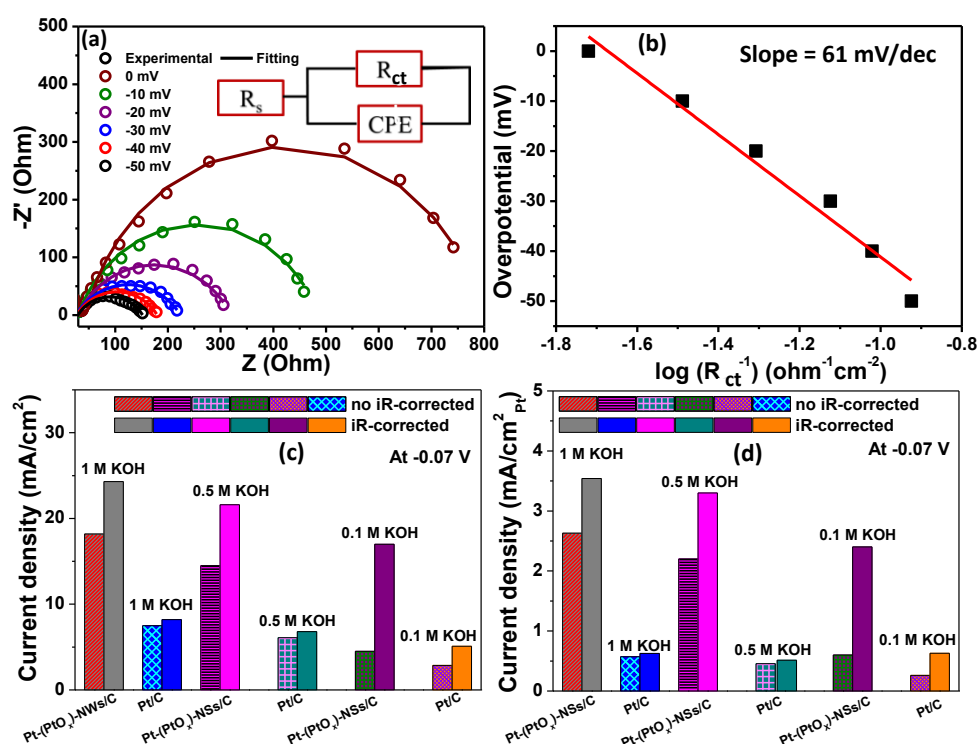


Figure 4.11. (a) Nyquist plot of Pt-(PtO_x)-NSs/C at different overpotentials and its corresponding semicircle fit. Inset: an equivalent circuit for the fitting of the EIS spectra. (b) $\log R_{ct}^{-1}$ vs overpotential plot of Pt-(PtO_x)-NSs/C composite. iR-corrected and non iR-corrected comparison of (c) geometric current density and (d) SA for Pt-(PtO_x)-NSs/C and commercial Pt/C at different base concentrations.

In 1 M KOH solution, the iR-free current density at -0.07 V is 24.3 mA/cm² which is 3 times higher than commercial Pt/C whereas, SA of Pt-(PtO_x)-NSs/C is 5.7 times higher than commercial Pt/C. In both iR free and without iR-free cases HER of this catalyst is increasing with increasing KOH concentration. This proves the HER activity is more susceptible

towards OH^- concentration. It is worth mentioning that Pt-(PtO_x)-NSs/C catalyst outperforms most of the recently reported catalyst with respect to the important parameters^{28, 30, 69-70}. A comparison of HER activity of Pt-(PtO_x)-NSs/C and other reported catalysts are given in Table S4.2. We have also compared iR-corrected HER activity C in 0.5 M H₂SO₄ medium of this Pt-(PtO_x)-NSs/C catalyst with commercial Pt/C. The iR-corrected SA, MA values of Pt-(PtO_x)-NSs/C in acid are found to be are ~4 and ~2.5 times higher than that of commercial Pt/C.

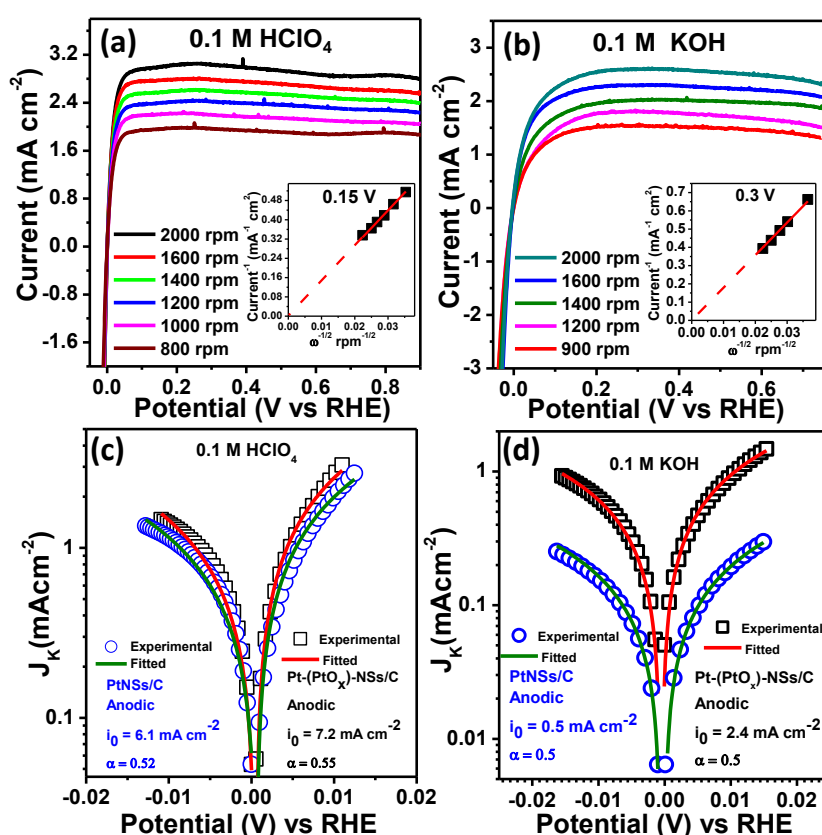


Figure 4.12. (a, b) HER/HOR polarization curves (going positive direction) of Pt-(PtO_x)-NSs/C in 0.1 M HClO₄ and 0.1 M KOH solution saturated with H₂ (~1 atm) with different rotation speeds at a scan rate of 10 mV/s (inset: Koutecky–Levich plot at 0.15 V and 0.3 V in RHE). (c-d) Kinetic current vs potential plot (Butler-Volmer plot) of Pt-(PtO_x)-NSs/C and PtNSs/C at 0.1 M HClO₄ and 0.1 M KOH

4.4.3 HOR Study on Pt-(PtO_x)-NSs/C Surfaces over a Broad pH Range.

With increasing importance for the development of hydrogen fuel cell, active catalysts for HOR in acid and base are essential. The HOR catalysts in PEMFCs and AMFCs are employed in the acidic and alkaline environment. The HOR activity of the Pt-(PtO_x)-NSs/C catalyst was studied by using rotating disk electrode (RDE) method. Figure 4.12 a and b represent the HOR polarization (going to positive direction) curves of Pt-(PtO_x)-NSs/C catalyst in H₂-saturated 0.1 M HClO₄ and 0.1 M KOH solution at 298 K as a function of rotation speeds. Both Figures show the well-defined hydrogen mass transport controlled limiting current densities above a particular potential and the gradual increase of limiting current densities (j_l) are observed with increasing of the rotation speeds. The observed limiting current density (j_l) obtained from RDE method is a summation of two currents: the kinetic current density (j_k) and the diffusion current density (j_d). The kinetic current can be derived using following Koutecky–Levich (K-L) equation¹⁶.

$$\frac{1}{j_l} = \frac{1}{j_k} + \frac{1}{j_d} = \frac{1}{j_k} + \frac{1}{BC_0 \omega^{1/2}}$$

Where j_d obey the Levich equation:

$$j_d = 0.62nFD^{2/3}\nu^{-1/6}C_0\omega^{1/2} = BC_0\omega^{1/2}$$

where F is the Faraday constant (96,485 C mol⁻¹), n is the number of electrons involved in the oxidation reaction, C₀ is the H₂ concentration in the solution, D is the diffusion coefficient of the reactant (cm² s⁻¹), ν is the viscosity of the electrolyte (cm² s⁻¹), and ω is the rotation speed (rpm). BC₀ is a constant related to the concentration and diffusivity of the gas, the number of electron transfers in the reaction, and the kinetic velocity of the electrolyte. The K-L plot (inverse of J_l with $\omega^{-1/2}$) constructed at 0.15 V in acid and 0.3 V in alkaline medium (the inset of Figure 4.12 a and b) give straight line passing through origin suggesting that the HOR reaction kinetics in both the medium are fully controlled by diffusion of H₂ mass.

The BC_0 value of Pt-(PtO_x)-NSs/C catalyst obtained from K-L plot in 0.1 M HClO₄ was 0.0717 mA/ (cm²(disk rpm)^{1/2}) and 0.057 in 0.1 M KOH which are in good agreement with calculated value (0.0678 mA/(cm²(disk rpm)^{1/2})) and other reported results¹⁸. The limiting current densities of Pt-(PtO_x)-NSs/C composite at a rotation speed of 1600 rpm in 0.1 M HClO₄ and in 0.1 M KOH solution are found to be 2.78 and 2.28 mA cm⁻².

Table 4.2. Kinetic parameter of Pt-(PtO_x)-NSs/C extracted from Butler-Volmer fitting at 0.1 M H₂SO₄ and KOH.

	Solution	Exchange Current density (i ₀) (mAcm ⁻²)	Specific exchange Current (mAcm _{Pt} ⁻¹)	Anodic transfer coefficient (α)	Cathodic transfer coefficient (α)
Pt-(PtO _x)-NSs/C	0.1 M HClO ₄	7.2	252	0.55	0.45
	0.1 M KOH	2.4	84	0.5	0.5
PtNSs/C	0.1 M HClO ₄	6.1	213	0.52	0.48
	0.1 M KOH	0.5	17.5	0.5	0.5

The HOR branch of HOR/ HER curves follow Nernstian diffusion potential and potential shift due to the hydrogen surface concentration are corrected by using the following equation¹⁶

$$\eta_{\text{diffusion}} = -RT/F \ln(1-j/j_i)$$

The HOR/HER diffusion overpotential express the maximum HOR current (j_d) under pure diffusion condition, can be rewritten as¹⁶

$$j_d = j_i(1-\exp(-2F\eta/RT))$$

For RDE experiments this implies that the kinetic currents free from diffusion contributions must be plotted versus the potential corrected for both the iR-drop and for j_d in the HOR branch. The iR corrected and diffusion corrected curves of Pt-(PtO_x)-NSs/C in both alkaline and acid medium are shown in Figure S4.11 a and b . The kinetics current density was obtained from the LSV polarization curve at 1600 rpm by using the first-order Koutecky–Levich correction

$$J_k = j (j_{lim}/(j_{lim} - j))$$

Where j_k is the kinetics current density (mA cm^{-2}), j is the measured current density (mA cm^{-2}) at 1600 rpm, and j_{lim} is the diffusion limiting current.

The different kinetic parameters such as transfer coefficient (α), Tafel slope and exchange current density of the HOR/HER can easily be obtained from the plot of j_k vs overpotential.

These parameters are obtained by fitting the Butler–Volmer equation⁷¹

$$j_k = i_0 [e^{[\frac{\alpha F}{RT}] \eta} - e^{-[\frac{(\alpha-1)F}{RT}] \eta}]$$

Where j_k is the kinetics current density (mA cm^{-2}), i_0 is the exchange current density (mA cm^{-2}), α represents the transfer coefficient, F is the Faraday constant (96,485 C/mol), R is the universal gas constant (8.314 J/(mol K)), and T is the temperature in Kelvin. The j_k vs potential plot and their Butler–Volmer fitting for LSV polarization curve at 1600 rpm of PtNSs/C and Pt-(PtO_x)-NSs/C in 0.1 M HClO₄ medium have shown in Figure 4.12c. The experimental plot of Pt-(PtO_x)-NSs/C was well fitted with Butler–Volmer fitting with $\alpha_c = 0.45$ and $\alpha_a = 0.55$ whereas PtNSs/C also well fitted with $\alpha_c = 0.48$ and $\alpha_a = 0.52$. The exchange current density (i_0) of Pt-(PtO_x)-NSs/C was calculated from the Butler–Volmer fitting and it is found to be 7.2 mA/cm² (0.9 mA cm⁻²_{Pt}). The reported exchange currents of Pt-based catalyst (polycrystalline or single crystal Pt electrode Pt electrode) measured in acidic medium by RDE method, ranged from 0.1 mA to 1 mA cm⁻²_{Pt}¹⁶. The i_0 of PtNSs/C is 6.1 mA cm⁻² in 0.1 M HClO₄ medium. The j_k vs potentials plot and their corresponding Butler–Volmer fitting of PtNSs/C and Pt-(PtO_x)-NSs/C catalyst in 0.1 M KOH medium was shown in Figure 4.12d. The details description of the fitting parameter was provided in Table 4.2. The calculated i_0 value for Pt-(PtO_x)-NSs/C is found to be 2.4 mA cm⁻² (0.37 mA cm_{Pt}⁻²) which is comparable to the Pt-based catalysts^{15,71}.

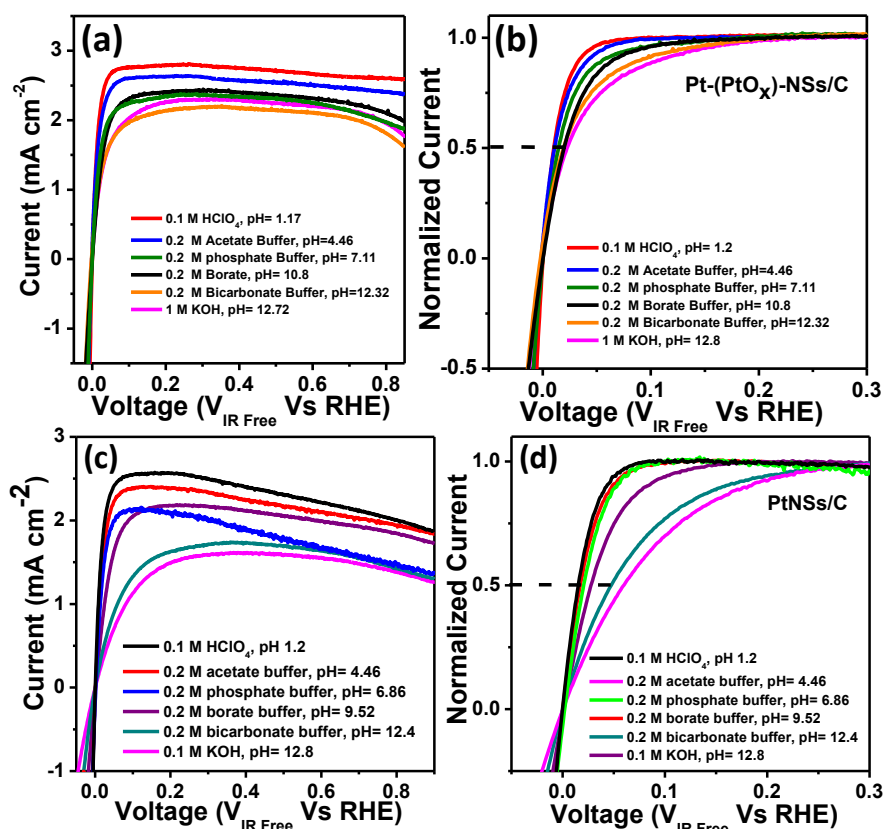


Figure 4.13. (a) HOR polarization curves of Pt-(PtO_x)-NSs/C. (b) Normalized HOR polarization curve in different buffer solutions for Pt-(PtO_x)-NSs/C. (c) HOR polarization curves of PtNSs/C. (d) Normalized HOR polarization curve in different buffer solutions for PtNSs/C. All experiments were done in H₂ saturated different buffer solutions at 10 mV/sec scan rate with 1600 rpm.

J. Zheng *et al.*⁷¹ reported i_0 value for Pt disk electrode are found to be 0.21 mA/cm² in 0.1 M KOH. The i_0 of PtNSs/C is 0.5 mA cm⁻² in 0.1 M KOH. The specific exchange current densities of Pt-(PtO_x)-NSs/C were 252 and 84 mA mg_{Pt}⁻¹ in 0.1 M H₂SO₄ and KOH respectively (Table 4.2). It is noticeable that the HOR activity of the two catalysts in acidic medium is almost equal, but the HOR activity of PtNSs/C in base media is 5 times lower than that of Pt-(PtO_x)-NSs/C. However, HOR activity in basic media of both catalysts is lower than that of acidic media. In order to understand the effect of pH of solutions on HOR activity of the catalysts, we have done the systematic study by measuring HOR activity at different pH buffer solutions for both the catalysts.

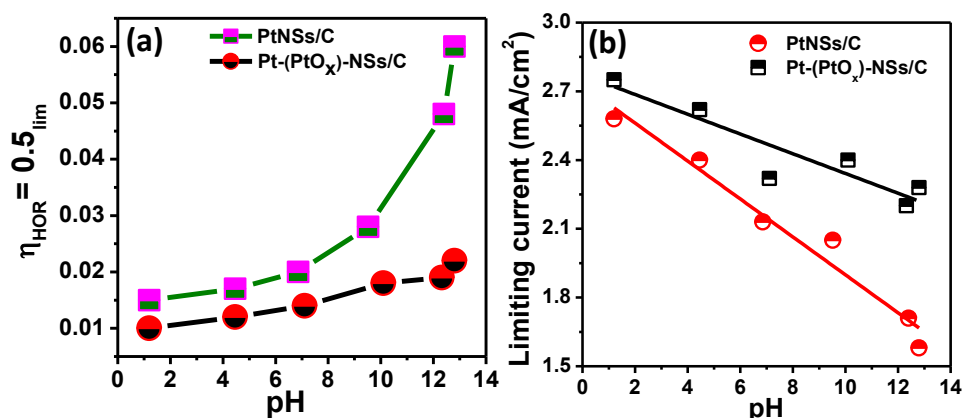


Figure 4.14. (a) Required HOR overpotential for both the catalysts at half of the normalized current density ($0.5i_{\text{lim}}$) at different pH. (b) The limiting HOR current density for both the catalysts at different pH solutions. All polarization curves are iR corrected accordingly.

The HOR polarization curves at a rotation speed of 1600 rpm in different H₂-saturated pHs solutions are presented in Figure 4.13a, c and polarization curves normalized by their corresponding maximum limiting current (j_l) at different pH solutions are shown in Figure 4.13 (b and d). The overpotential at which current density is half of the normalized current density ($\eta_{\text{HOR}}=0.5i_{\text{lim}}$) is known as half-wave potential. The comparison of $0.5i_{\text{lim}}$ of these two catalysts at different pH is compared in Figure 4.14a.

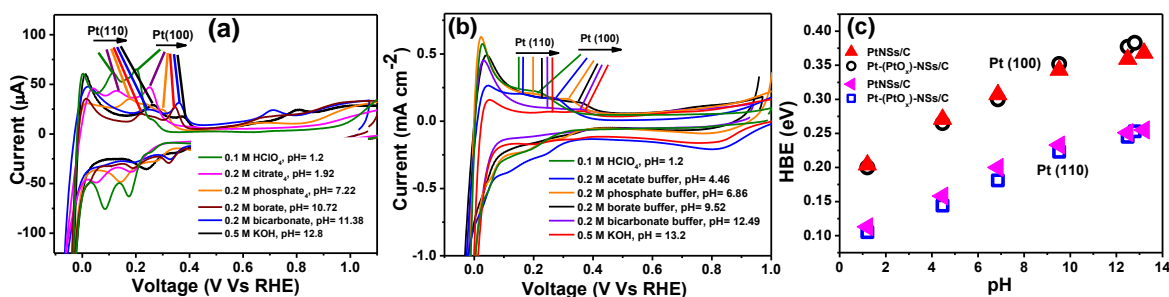


Figure 4.15. CVs of (a) Pt-(PtO_x)-NSs/C and (b) PtNSs/C in different pH for Pt (110) and Pt (100) in N₂ saturated medium at 30 mV/sec. (c) The plot of HBE vs pH of Pt-(PtO_x)-NSs/C and PtNSs/C.

The change of $0.5 i_{\text{lim}}$ for both the catalyst is almost negligible below pH 7 and above pH 7 a large increase of half-wave potentials with pH was observed for PtNSs/c catalyst, but Pt-(PtO_x)-NSs/C catalyst showed a small increase of $0.5i_{\text{lim}}$ value with increasing pH. The half-

wave potential of PtNSs/C were shifted by 50 mV toward the positive side where only 20 mV positive shift of overpotential for Pt-(PtO_x)-NSs/C were observed as the solution pH was changed from 1.2 to 12.8. The comparison of limiting current density of the two catalysts at different pHs is also shown in Figure 4.14 b. This also showed the decrease of i_{lim} for Pt-(PtO_x)-NSs/C catalyst with pH is less in comparison to that of PtNSs/C. Based on the above measurements it may be concluded that HOR performance of PtNSs/C is more sensitive towards pH of solutions than that of Pt-(PtO_x)-NSs/C and its HOR activity in 0.1 M KOH solution is 5 times lower in comparison to that of Pt-(PtO_x)-NSs/C catalyst. In acid media, the HOR occurs via two steps – Tafel (dissociative hydrogen adsorption into H_{ads}) step followed by oxidation of H_{ads} into proton (2nd step).

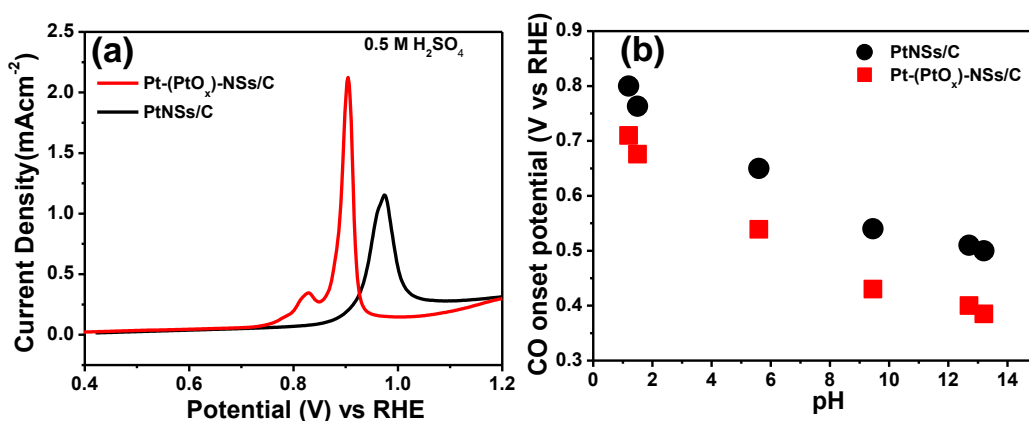


Figure 4.16. (a) CO stripping voltammetry of Pt-(PtO_x)-NSs/C and PtNSs/C catalyst in acid medium (b) Comparison of onset potential of CO stripping with different pH of Pt-(PtO_x)-NSs/C and PtNSs/C.

But in base media the 2nd step is that either H_{ads} can react with OH⁻ ions from solution or H_{ads} can react with adsorbed OH⁻ ions (OH_{ads}) to form water. The role of OH⁻ ions is still not clear yet and two contrasting mechanisms were proposed to explain sluggish HOR/HER kinetics in base media - (1) hydrogen binding energy theory^{17-19,22} and (2) reactive OH_{ads} theory^{23,72}. Durst *et al.*²⁰ showed that after Heyvoskey or Volmer step, quick recombination between proton and OH⁻ from solution occurs and HBE is a sole descriptor for HOR/HER

in strong base. Several reports^{14,18} also suggested that HBE is the prime descriptor for HOR/HER in alkaline media. On the other hand, N. Markovic *et al.*²⁴ showed that the presence of oxophilic metal or Ni(OH)₂ is beneficial for HOR/HER in basic media. Some groups also showed a bi-functional mechanism for enhancing HER activity in basic media when Pt-modified with Ni(OH)₂^{24,31,73}.

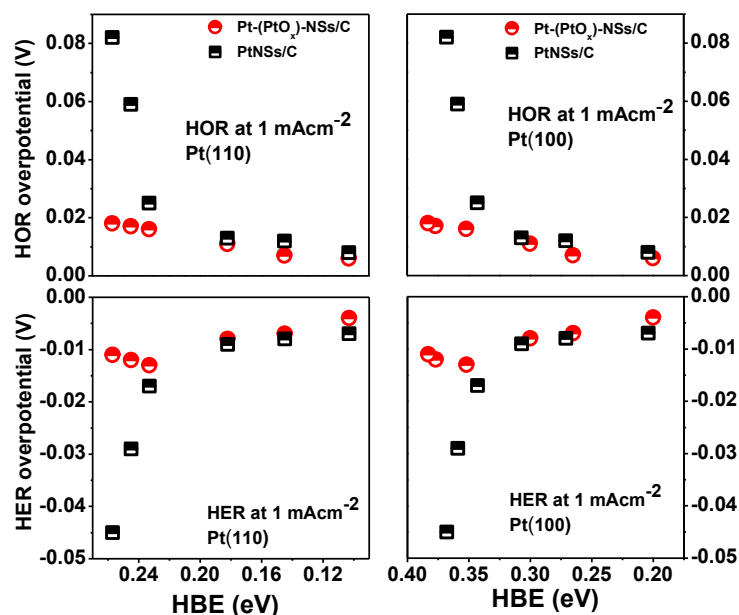


Figure 4.17. HER/HOR overpotential required for 1mA/cm² current density for Pt (110) and Pt (100) plane of Pt-(PtO_x)-NSs/C and PtNSs/C composite.

We have studied the UPD-H_{des} activities properties of both Pt-(PtO_x)-NSs/C and PtNSs/C composites in different pH solutions to understand the insight of the mechanism. It is reported¹⁸ that the UPD-H desorption peak position in CV can easily correlate with the HBE of the corresponding active site. The peak potential of UPD-H_{des} in CV is directly related the HBE with the following equation

$$\Delta G (M-H) = - FE_{\text{peak}}$$

Where F=Faraday constant (96,485 C/mol), ΔG = hydrogen binding energy and E_{peak} is directly taken from the peak position in the CVs. The CV curves of Pt-(PtO_x)-NSs/C and

PtNSs/C composites at different buffer solutions (pH 0-13) are shown in Figure 4.15a and Figure 4.15b. In the CV curves for both composites, the UPD-H adsorption region is cathodic peak appearing below the potential 0.5 V (RHE). In the UPD-H region, the peak appeared at low potential corresponds to the H adsorption/desorption at Pt (110) plane (weakly bonded H) whereas peak at the higher potential in this region is assigned as H adsorption/desorption at Pt (100) (strongly bonded H). Figure 4.15c shows the change of HBE on Pt (110) and Pt (100) surfaces of Pt-(PtO_x)-NSs/C and PtNSs/C two catalysts with solution pH.

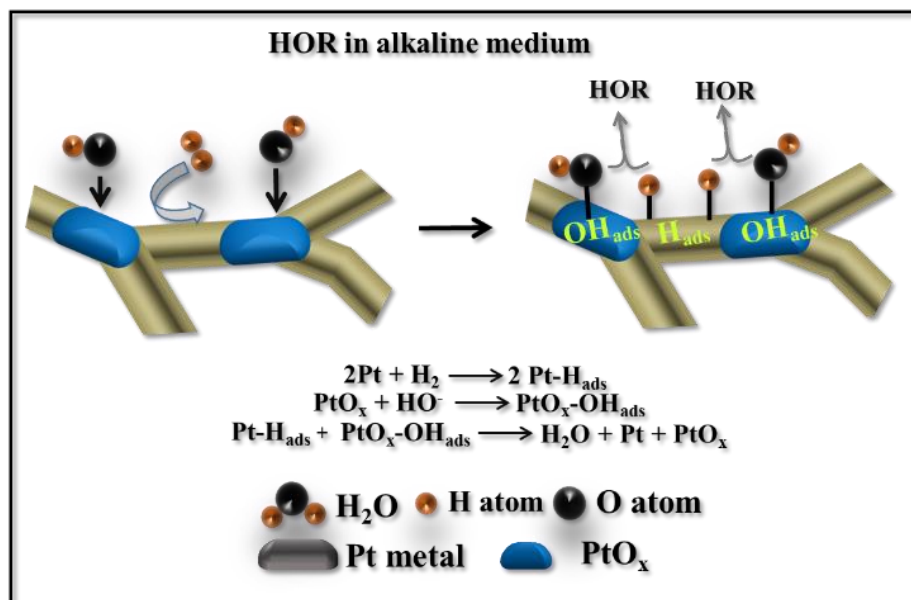


Figure 4.18. Schematic diagram of bi-functional mechanism of HOR on Pt-(PtO_x)-NSs/C catalyst in basic medium.

For both the catalysts, the UPD-H peaks are shifted towards positive potentials with increasing the pH of the buffer solutions. UPD-H peak for Pt (110) and (100) rise linearly with a slope 11 meV/pH and 13 meV/pH respectively. The HBE of Pt (110) and Pt (100) of these two catalysts are same at all pH values¹⁴. It was observed that HOR activity of these two catalysts is same in acid medium and activity decreases with increasing solution pH. This can be easily explained by increased HBE of the catalyst with pH, but, increased HBE

can't explain why HOR activity of Pt-(PtO_x)-NSs/C is 5 higher than that of PtNSs/C although their acid medium activities are same. In order to understand the role OH⁻ ions in HOR mechanism for basic media, we have performed CO stripping voltammetry measurements for both the catalysts. The CO stripping voltammetry actually represent the -OH absorption potentials on the catalyst surface. The comparisons of CO stripping curves of PtNSs/C and Pt-(PtO_x)-NSs/C catalyst in 0.5 M H₂SO₄ solution is shown in Figure 4.16 a. For Pt-(PtO_x)-NSs/C catalyst, two oxidation peaks are observed at + 0.82 and +0.9 V (RHE) due to CO oxidation of different lattice site of Pt-nanowires with onset potential of +0.72 V whereas PtNSs/C catalyst showed a CO stripping peak at +0.98 V with a onset potential of +0.82 V. We have also performed CO stripping measurements in different pH solution and are shown in Figure S4.12 and S4.13. The corresponding CO stripping onset potential at different pH is presented in Figure 4.16b. The onset potentials of CO stripping decreases i.e. OH⁻ adsorption on both the catalyst surfaces increases with increasing solution pH, but all pH solution, Pt-(PtO_x)-NSs/C has stronger OH⁻ absorption than that of PtNSs/C. This suggests that Pt-(PtO_x)-NSs/C catalyst has higher oxophilic character than that of oxide-free PtNSs/C catalyst in alkaline medium. This is probably due to the presence of surface oxide (PtO_x) in the catalyst Pt-(PtO_x)-NSs/C. The surface oxide can act as OH⁻ adsorption site suggesting that Pt-(PtO_x)-NSs/C may be considered as a bi-functional catalyst. As shown in Figure 4.17, we have compared the HOR over-potential at 1mAcm⁻² with changing HBE for the two catalysts (PtNSs/C and Pt-(PtO_x)-NSs/C) whereas HER overpotential at -1 mA cm⁻² as a function of HBE are presented in Figure 4.17. Below pH 7, HER and HOR overpotentials for both the catalysts increases slowly with increase of HBE, but, above pH7, the behavior of HOR and HER activity of two catalysts at high HBE are significantly different – the change of HOR and HER overpotential of Pt-(PtO_x)-NSs/C is very small as compare to PtNSs/C. In the previous section, we have discussed that Pt-(PtO_x)-

NSs/C is 5 times more HOR active than that of PtNSs/C although both catalysts have the same HBE. Thus HBE is not a sole descriptor for HOR/HER in basic media. The benefit of the presence of PtO_2 in Pt-(PtO_x)-NSs/C is that catalyst has stronger OH adsorption i.e. higher oxophilic character than that of oxide-free Pt catalyst (PtNSs/C) in alkaline medium.

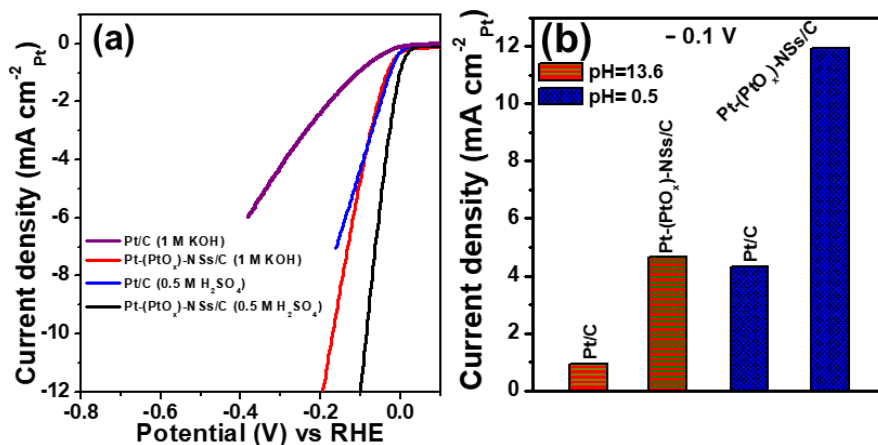


Figure 4.19. (a) HER activity of (current normalized by surface area of the catalyst) of Pt-(PtO_x)-NSs/C and Pt/C in acid and alkaline medium and (b) corresponding SA plot of both the catalysts at $\eta = 0.1$ V.

With increasing the pH values, OH^- adsorption increases with pH. The improvement of HOR activity of Pt-(PtO_x)-NSs/C can be attributed to the enhanced OH^- adsorption of Pt-(PtO_x)-NSs/C relative to PtNSs/C suggesting that OH_{ads} is the key intermediate species for HOR in basic media. Based on these observations we propose a bi-functional mechanism for HOR in strongly basic media. The PtO_x acts as OH^- adsorption site while Pt plays a role of H adsorption (Pt-H_{ads}) site. As shown in schematic diagram (Figure 4.18) dissociation of H_2 occurs at Pt site first then adsorbed at Pt site to form Pt-H_{ads} intermediate. Another active site PtO_x offers the OH^- adsorption and consecutively formed $\text{Pt-OH}_{\text{ads}}$. In the next step both these intermediate species (H_{ads} and OH_{ads}) reacts to form H_2O . The presence of oxide, in the Pt-(PtO_x)-NSs/C catalyst enhances not only HOR activity; it's HER activity in the base is also enhanced drastically. The Pt-(PtO_x)-NSs/C composite is 5 times more HER active

than oxide-free PtNSs/C catalyst in alkaline media. The comparison of HER LSV curves (current normalized by surface area) of this Pt-(PtO_x)-NSs/C in 1 M KOH and commercial Pt/C in 0.5 M H₂SO₄ solutions are shown in Figure 4.19 a and b. The SA in basic media of Pt-(PtO_x)-NSs/C catalyst is almost same with the SA of commercial Pt/C in acid media suggesting that oxide surface makes this Pt-(PtO_x)-NSs/C catalyst highly active towards hydrogen evolution in basic solution.

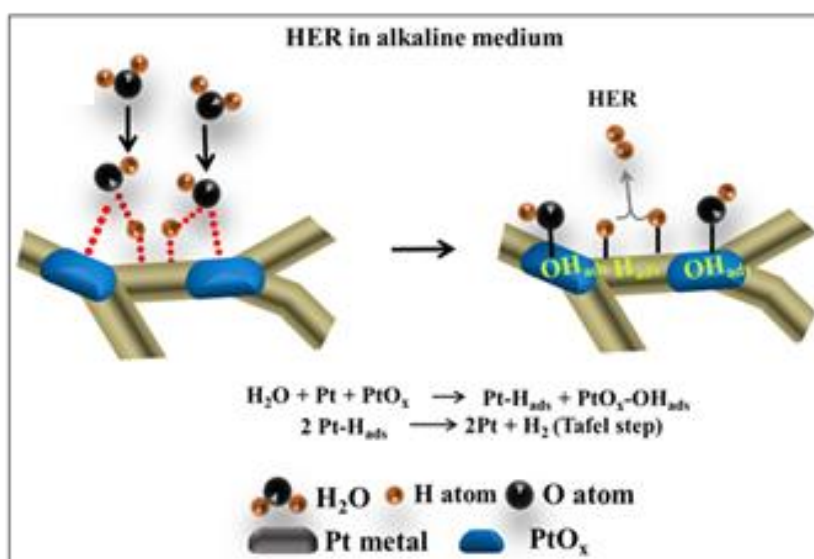


Figure 4.20. Schematic representation of bi-functional mechanism of HER on Pt-(PtO_x)-NSs/C catalyst in basic medium.

Based on above observation, we proposed a bi-functional mechanism of Pt-(PtO_x)-NSs/C for enhanced HER performance in basic media as shown in Figure 4.20. The dissociative water adsorption is facilitated by PtO_x, leading to adsorption of OH⁻ on PtO_x surface and adsorption of H occurs on neighboring Pt sites⁷². The two neighbor H_{ads} on Pt metal sites are recombined then to form the H₂ molecules. The best catalyst can be developed by combining the properties of metal and metal oxide (growing metal oxide on metal nanostructures). This result thus provides an opportunity to develop new bi-functional HOR/HER catalyst for basic media by growing metal oxide on the metal nanostructure.

4.4.4 Factors responsible for the high catalytic activity

The Pt-(PtO_x)-NSs/C catalyst showed superior activity and stability towards HER/HOR in both acidic and basic media. The superior activity and stability of this catalyst could be attributed to several following reasons.

(a) The Pt-(PtO_x)-NSs/C composite is a three-component hybrid where each component play three different roles: Pt metal sites offer as active sites for hydrogen intermediate and PtO_x as active sites for OH⁻ adsorption whereas nitrogen-doped carbon material acts as a high electrical conductive support that is required for electrocatalysis. This high activity could be due to the strong synergistic interaction between three components. If anyone of them is missing then poor HER/HOR activity is observed. In order to understand this, we have performed electrochemical impedance measurements of Pt-(PtO_x)-NSs/C. The Nyquist plot of the EIS analysis for Pt-(PtO_x)-NSs/C, Pt-PtO_x (without support), physical mixture of Pt-PtO_x with CN_x and commercial Pt/C was found a semicircle as shown in Figure S4.14a. EIS spectra of CN_x are also provided in Figure S4.14b. The charge transfer resistance (R_{ct}) of Pt-(PtO_x)-NSs/C, Pt-PtO_x (without support), commercial Pt/C is 280, 460, 390,480 ohm respectively. This Pt-(PtO_x)-NSs/C has much lower R_{ct} compared to Pt-PtO_x and nitrogen doped carbon support alone. This suggests that there is strong metal (Pt-(PtO_x)-NSs)-support (CN_x) interaction. The interaction is also confirmed by electrochemical measurements of these three compounds. Figure S4.14 c shows the comparison of HER LSV curves of commercial Pt/C, Pt-(PtO_x)-NSs/C and Pt-PtO_x (without support). The much lower HER activity and stability (Figure S4.14 d) of Pt-PtO_x (without support), physical mixture of Pt-PtO_x with CN_x in comparison to that of Pt-(PtO_x)-NSs/C (with support) confirmed that strong interaction between them enhancing the electrochemical activities.

(b) The one dimensional Pt nanowires structures of the composite could one of the reasons for its higher activity and higher stability. One dimensional catalyst has several properties

such as smooth defect-free crystalline planes, fewer lattice boundaries, low number of surface defects, and surface to volume ratio etc^{34, 42, 74,75}. All these properties are highly desirable for fuel cell applications. Microscopic measurements of this Pt-(PtO_x)-NSs/C compound are interconnected to form a porous morphology. This porous morphology helps to enhance its activity by allowing easy transport of reactant and products.

(c) The presence of nitrogen in this Pt-(PtO_x)-NSs/C catalyst improves charge transfer kinetics due to the interaction between proton and N atoms leading to enhance the electrocatalytic activity of the catalyst.

4.5 CONCLUSION

In conclusion, we have demonstrated a facile synthesis of one dimensional Pt wire nanostructures/N-doped carbon composite. This Pt-(PtO_x)-NSs/C composite exhibits superior electrocatalytic activity towards HER/HOR in both acid and basic medium. The HER activity of the composite is much better than that of commercial Pt/C in both acid and alkaline media. The HOR activity of the catalyst was studied using RDE method in a wide range of pH from 0 to 14. We demonstrated that PtO₂ offer stronger OH⁻ adsorption and the presence of PtO₂ in Pt-(PtO_x)-NSs/C composite makes dramatic enhancement of its HER/HOR activity in alkaline media through the bi-functional mechanism. The HBE and oxophilicity are equally important two descriptors for HER and HOR in alkaline media. The excellent HER and HOR activity of Pt(PtO_x)-NSs/C with good durability and low catalyst loading are making them a promising future electrocatalyst for fuel cell and water splitting or other electrochemical devices.

4.6 REFERENCES

- (1) Cao, M.; Wu, D.; Cao, R. *ChemCatChem* **2014**, *6*, 26-45.
- (2) Peighambardoust, S. J.; Rowshanzamir, S.; Amjadi, M. *Int. J. Hydrogen Energy* **2010**, *35*, 9349-9384.
- (3) Wilberforce, T.; Alaswad, A.; Palumbo, A.; Dassisti, M.; Olabi, A. G. *Int. J. Hydrogen Energy* **2016**, *41*, 16509-16522.
- (4) Gasteiger, H. A.; Marković, N. M. *Science* **2009**, *324*, 48-49.
- (5) Vesborg, P. C. K.; Seger, B.; Chorkendorff, I. *J. Phys. Chem. Lett.* **2015**, *6*, 951-957.
- (6) Cong, Y.; Yi, B.; Song, Y. *Nano Energy* **2018**, *44*, 288-303.
- (7) Zou, R.; Wen, S.; Zhang, L.; Liu, L.; Yue, D. *RSC Adv.* **2015**, *5*, 99884-99891.
- (8) Seh, Z. W.; Kibsgaard, J.; Dickens, C. F.; Chorkendorff, I.; Nørskov, J. K.; Jaramillo, T. F. *Science* **2017**, *355*.
- (9) Kraysberg, A.; Ein-Eli, Y. *Energy & Fuels* **2014**, *28*, 7303-7330.
- (10) Jin, H.; Wang, J.; Su, D.; Wei, Z.; Pang, Z.; Wang, Y. *J. Am. Chem. Soc.* **2015**, *137*, 2688-2694.
- (11) Ge, X.; Sumboja, A.; Wu, D.; An, T.; Li, B.; Goh, F. W. T.; Hor, T. S. A.; Zong, Y.; Liu, Z. *ACS Catal.* **2015**, *5*, 4643-4667.
- (12) Lu, F.; Zhou, M.; Zhou, Y.; Zeng, X. *Small* **2017**, *13*, 1701931-n/a.
- (13) Wang, J.; Cui, W.; Liu, Q.; Xing, Z.; Asiri, A. M.; Sun, X. *Adv. Mater.* **2016**, *28*, 215-230.
- (14) Zheng, J.; Sheng, W.; Zhuang, Z.; Xu, B.; Yan, Y. *Sci. Adv.* **2016**, *2*, e1501602.
- (15) Scofield, M. E.; Zhou, Y.; Yue, S.; Wang, L.; Su, D.; Tong, X.; Vukmirovic, M. B.; Adzic, R. R.; Wong, S. S. *ACS Catal.* **2016**, *6*, 3895-3908.
- (16) Sheng, W.; Gasteiger, H. A.; Shao-Horn, Y. *J. Electrochem. Soc.* **2010**, *157*, B1529-B1536.

- (17) Durst, J.; Simon, C.; Hasché, F.; Gasteiger, H. A. *J. Electrochem. Soc.* **2015**, *162*, F190-F203.
- (18) Sheng, W.; Zhuang, Z.; Gao, M.; Zheng, J.; Chen, J. G.; Yan, Y. *Nat. Commun.* **2015**, *6*, 5848-5854.
- (19) Lu, S.; Zhuang, Z. *J. Am. Chem. Soc.* **2017**, *139*, 5156-5163.
- (20) Durst, J.; Siebel, A.; Simon, C.; Hasche, F.; Herranz, J.; Gasteiger, H. A. *Energy Environ. Sci.* **2014**, *7*, 2255-2260.
- (21) Sheng, W.; Myint, M.; Chen, J. G.; Yan, Y. *Energy Environ. Sci.* **2013**, *6*, 1509-1512.
- (22) Wang, Y.; Wang, G.; Li, G.; Huang, B.; Pan, J.; Liu, Q.; Han, J.; Xiao, L.; Lu, J.; Zhuang, L. *Energy Environ. Sci.* **2015**, *8*, 177-181.
- (23) Bhowmik, T.; Kundu, M. K.; Barman, S. *ACS Catal.* **2016**, *6*, 1929-1941.
- (24) Strmcnik, D.; Uchimura, M.; Wang, C.; Subbaraman, R.; Danilovic, N.; van der, V.; Paulikas, A. P.; Stamenkovic, V. R.; Markovic, N. M. *Nat. Chem.* **2013**, *5*, 300-306.
- (25) Wang, G.; Parrondo, J.; He, C.; Li, Y.; Ramani, V. *J. Electrochem. Soc.* **2017**, *164*, F1307-F1315.
- (26) Chen, D.; Ye, F.; Liu, H.; Yang, J. *Sci. Rep.* **2016**, *6*, 24600.
- (27) He, L.; Natte, K.; Rabeah, J.; Taeschler, C.; Neumann, H.; Brückner, A.; Beller, M. *Angew. Chem. Int. Ed.* **2015**, *54*, 4320-4324.
- (28) Yin, H.; Zhao, S.; Zhao, K.; Muqsit, A.; Tang, H.; Chang, L.; Zhao, H.; Gao, Y.; Tang, Z. *Nat. Commun.* **2015**, *6*, 6430.
- (29) Sadhukhan, M.; Kundu, M. K.; Bhowmik, T.; Barman, S. *Int. J. Hydrogen Energy* **2017**, *42*, 9371-9383.
- (30) Wang, P.; Zhang, X.; Zhang, J.; Wan, S.; Guo, S.; Lu, G.; Yao, J.; Huang, X. *Nat. Commun.* **2017**, *8*, 14580-14589.

- (31) Cheng, N.; Stambula, S.; Wang, D.; Banis, M. N.; Liu, J.; Riese, A.; Xiao, B.; Li, R.; Sham, T.-K.; Liu, L.-M.; Botton, G. A.; Sun, X. *Nat. Chem.* **2016**, *7*, 13638-13647.
- (32) Badhulika, S.; Paul, R. K.; Rajesh; Terse, T.; Mulchandani, A. *Electroanal.* **2014**, *26*, 103-108.
- (33) Ye, E.; Regulacio, M. D.; Zhang, S.-Y.; Loh, X. J.; Han, M.-Y. *Chem. Soc. Rev.* **2015**, *44*, 6001-6017.
- (34) Koenigsmann, C.; Scofield, M. E.; Liu, H.; Wong, S. S. *J. Phys. Chem. Lett.* **2012**, *3*, 3385-3398.
- (35) Tian, N.; Zhou, Z.-Y.; Sun, S.-G.; Ding, Y.; Wang, Z. L. *Science* **2007**, *316*, 732-735.
- (36) Xu, G.-R.; Bai, J.; Yao, L.; Xue, Q.; Jiang, J.-X.; Zeng, J.-H.; Chen, Y.; Lee, J.-M. *ACS Catal.* **2017**, *7*, 452-458.
- (37) Ma, L.; Wang, C.; Gong, M.; Liao, L.; Long, R.; Wang, J.; Wu, D.; Zhong, W.; Kim, M. J.; Chen, Y.; Xie, Y.; Xiong, Y. *ACS Nano* **2012**, *6*, 9797-9806.
- (38) Park, J.; Zhang, L.; Choi, S.-I.; Roling, L. T.; Lu, N.; Herron, J. A.; Xie, S.; Wang, J.; Kim, M. J.; Mavrikakis, M.; Xia, Y. *ACS Nano* **2015**, *9*, 2635-2647.
- (39) Liu, H.; Koenigsmann, C.; Adzic, R. R.; Wong, S. S. *ACS Catal.* **2014**, *4*, 2544-2555.
- (40) Liu, H.; Adzic, R. R.; Wong, S. S. *ACS Appl. Mater. Interfaces* **2015**, *7*, 26145-26157.
- (41) Yin, J.; Wang, J.; Zhang, Y.; Li, H.; Song, Y.; Jin, C.; Lu, T.; Zhang, T. *Chem. Commun.* **2011**, *47*, 11966-11968.
- (42) Mourdikoudis, S.; Chirea, M.; Altantzis, T.; Pastoriza-Santos, I.; Perez-Juste, J.; Silva, F.; Bals, S.; Liz-Marzan, L. M. *Nanoscale* **2013**, *5*, 4776-4784.
- (43) Sun, S.; Zhang, G.; Geng, D.; Chen, Y.; Li, R.; Cai, M.; Sun, X. *Angew. Chem.* **2011**, *123*, 341-341.
- (44) Barman, S.; Sadhukhan, M. *J. Mater. Chem.* **2012**, *22*, 21832-21837.

- (45) Du, S.; Lu, Y.; Malladi, S. K.; Xu, Q.; Steinberger-Wilckens, R. *J. Mater. Chem. A* **2014**, *2*, 692-698.
- (46) Xu, J.; Liu, X.; Chen, Y.; Zhou, Y.; Lu, T.; Tang, Y. *J. Mater. Chem.* **2012**, *22*, 23659-23667.
- (47) Xie, L.; Ren, X.; Liu, Q.; Cui, G.; Ge, R.; Asiri, A. M.; Sun, X.; Zhang, Q.; Chen, L. *J. Mater. Chem. A* **2018**, *6*, 1967-1970.
- (48) Sadhukhan, M.; Bhowmik, T.; Kundu, M. K.; Barman, S. *RSC Adv.* **2014**, *4*, 4998-5005.
- (49) Xing, Z.; Ju, Z.; Zhao, Y.; Wan, J.; Zhu, Y.; Qiang, Y.; Qian, Y. *Sci. Rep.* **2016**, *6*, 26146.
- (50) Sadhukhan, M.; Barman, S. *J. Mater. Chem. A* **2013**, *1*, 2752-2756.
- (51) Bhowmik, T.; Kundu, M. K.; Barman, S. *ACS Appl. Mater. Interfaces* **2016**, *8*, 28678-28688.
- (52) Zhu, C.; Wen, D.; Oschatz, M.; Holzschuh, M.; Liu, W.; Herrmann, A.-K.; Simon, F.; Kaskel, S.; Eychmüller, A. *Small* **2015**, *11*, 1430-1434.
- (53) Tavakkoli, M.; Holmberg, N.; Kronberg, R.; Jiang, H.; Sainio, J.; Kauppinen, E. I.; Kallio, T.; Laasonen, K. *ACS Catal.* **2017**, *7*, 3121-3130.
- (54) Ji, L.; Wang, J.; Zuo, S.; Chen, Z. *J. Phys. Chem. C* **2017**, *121*, 8923-8930.
- (55) Kundu, M. K.; Bhowmik, T.; Barman, S. *J. Mater. Chem. A* **2015**, *3*, 23120-23135.
- (56) Zhu, L.; Lin, H.; Li, Y.; Liao, F.; Lifshitz, Y.; Sheng, M.; Lee, S.-T.; Shao, M. *Nat. Commun.* **2016**, *7*, 12272-12279.
- (57) Xu, G.-R.; Bai, J.; Jiang, J.-X.; Lee, J.-M.; Chen, Y. *Chem. Sci.* **2017**, *8*, 8411-8418.
- (58) Liang, H.-W.; Brüller, S.; Dong, R.; Zhang, J.; Feng, X.; Müllen, K. *Nat. Commun.* **2015**, *6*, 7992.

- (59) Ji, X.; Liu, B.; Ren, X.; Shi, X.; Asiri, A. M.; Sun, X. *ACS Sustainable Chem. Eng.* **2018**, *6*, 4499-4503.
- (60) Xie, L.; Liu, Q.; Shi, X.; Asiri, A. M.; Luo, Y.; Sun, X. *Inorg. Chem. Front.* **2018**.
- (61) Pu, Z.; Liu, Q.; Asiri, A. M.; Sun, X. *ACS Appl. Mater. Interfaces* **2014**, *6*, 21874-9.
- (62) Jahan, M.; Liu, Z.; Loh, K. P. *Adv. Funct. Mater.* **2013**, *23*, 5363-5372.
- (63) Liao, L.; Zhu, J.; Bian, X.; Zhu, L.; Scanlon, M. D.; Girault, H. H.; Liu, B. *Adv. Funct. Mater.* **2013**, *23*, 5326-5333.
- (64) Wu, H. B.; Xia, B. Y.; Yu, L.; Yu, X.-Y.; Lou, X. W. *Nat. Commun.* **2015**, *6*, 6512-6520.
- (65) Feng, L.; Vrubel, H.; Bensimon, M.; Hu, X. *Phys. Chem. Chem. Phys.* **2014**, *16*, 5917-5921.
- (66) Vrubel, H.; Hu, X. *Angew. Chem. Int. Ed.* **2012**, *51*, 12703-12706.
- (67) Hao, J.; Yang, W.; Zhang, Z.; Tang, J. *Nanoscale* **2015**, *7*, 11055-11062.
- (68) Bhowmik, T.; Kundu, M. K.; Barman, S. *ACS Appl. Energy Mater.* **2018**.
- (69) Tang, C.; Zhang, R.; Lu, W.; He, L.; Jiang, X.; Asiri, A. M.; Sun, X. *Adv. Mater.* **2017**, *29*, 1602441.
- (70) Tian, J.; Liu, Q.; Asiri, A. M.; Sun, X. *J. Am. Chem. Soc.* **2014**, *136*, 7587-7590.
- (71) Zheng, J.; Yan, Y.; Xu, B. *J. Electrochem. Soc.* **2015**, *162*, F1470-F1481.
- (72) Strmcnik, D.; Lopes, P. P.; Genorio, B.; Stamenkovic, V. R.; Markovic, N. M. *Nano Energy* **2016**, *29*, 29-36.
- (73) Danilovic, N.; Subbaraman, R.; Strmcnik, D.; Chang, K.-C.; Paulikas, A. P.; Stamenkovic, V. R.; Markovic, N. M. *Angew. Chem. Int. Ed.* **2012**, *51*, 12495-12498.
- (74) Cademartiri, L.; Ozin, G. A. *Adv. Mater.* **2009**, *21*, 1013-1020.
- (75) Lu, Y.; Du, S.; Steinberger-Wilckens, R. *Appl. Catal. B Environ.* **2016**, *199*, 292-314.

Appendix B

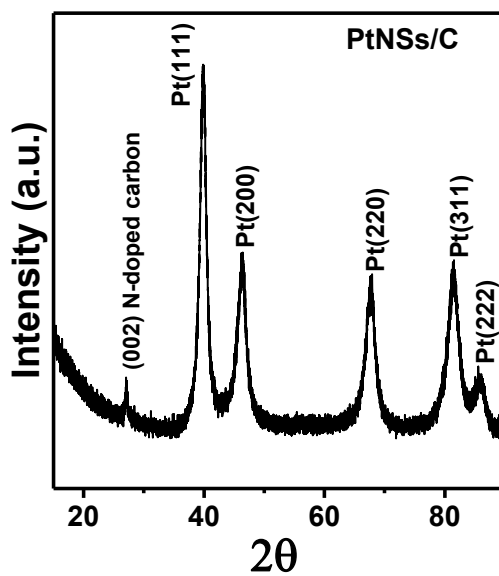


Figure S4.1. p-XRD of PtNSs/C composite.

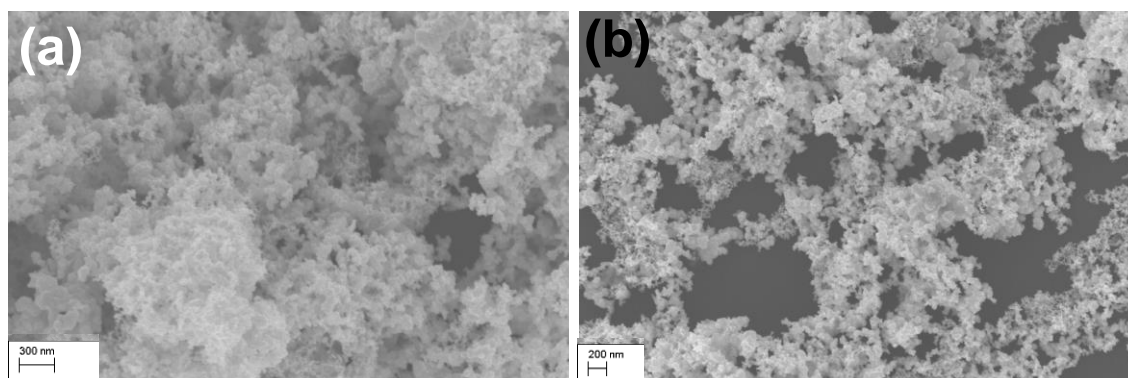


Figure S4.2. (a,b) FESEM images of PtNSs/C composite showing the interconnected PtNPs.

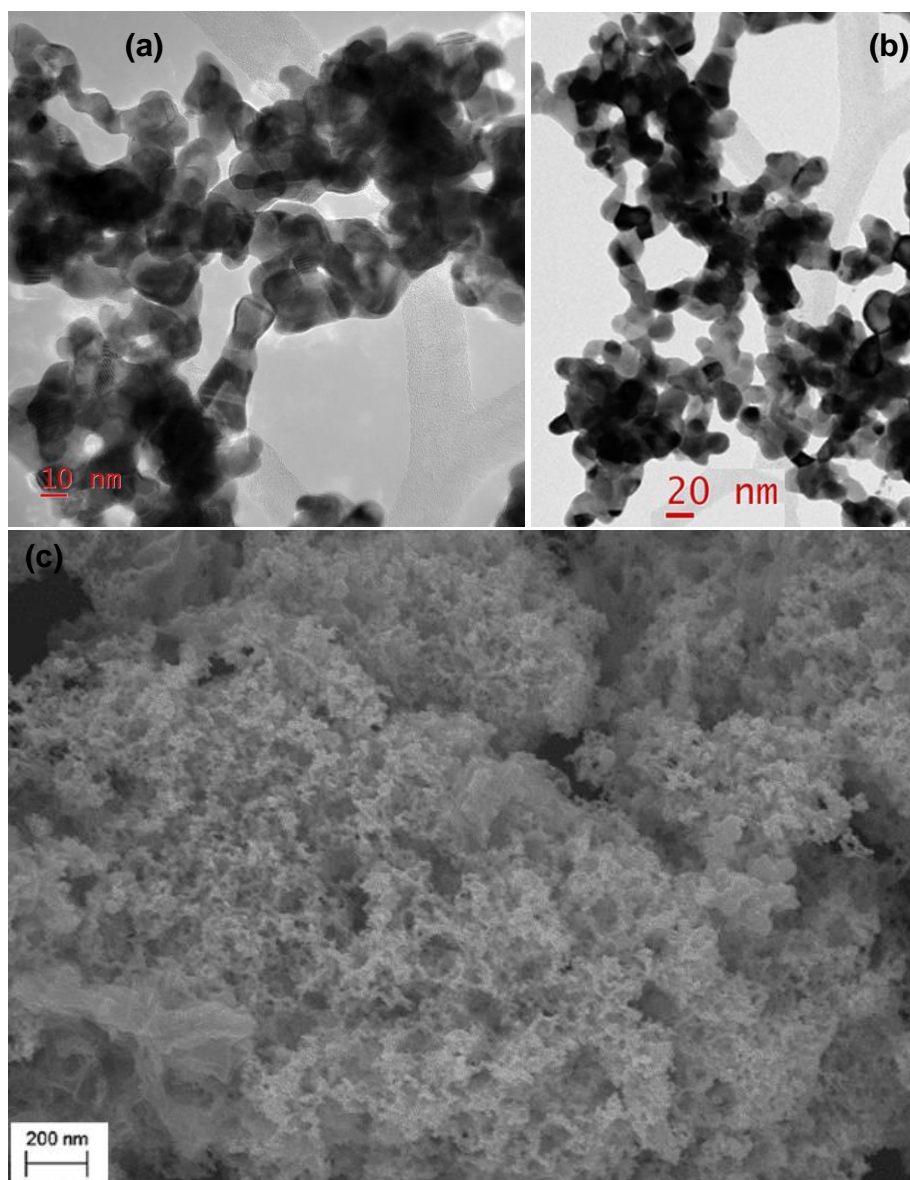


Figure S4.3. (a, b) TEM images(c) FESEM images of Pt-(PtO_x)-NSs/C composite.

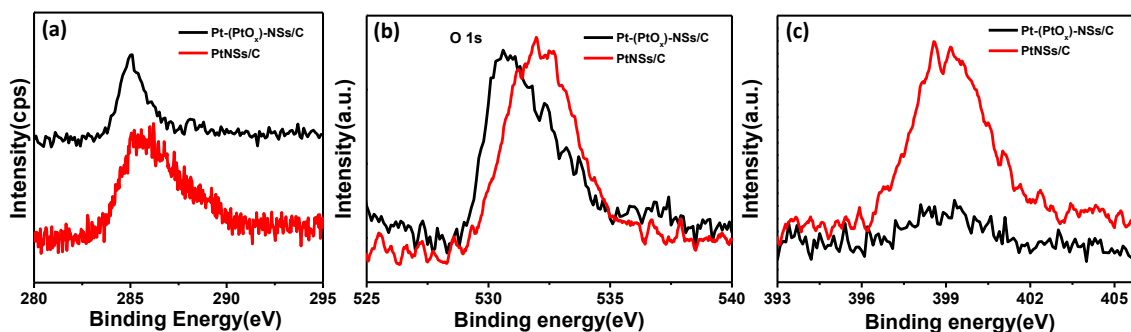


Figure S4.4. Comparison of high resolution XPS spectra of (a) C1s (b) O1s (c) N1s of Pt-(PtO_x)-NSs/C and PtNSs/C composite.

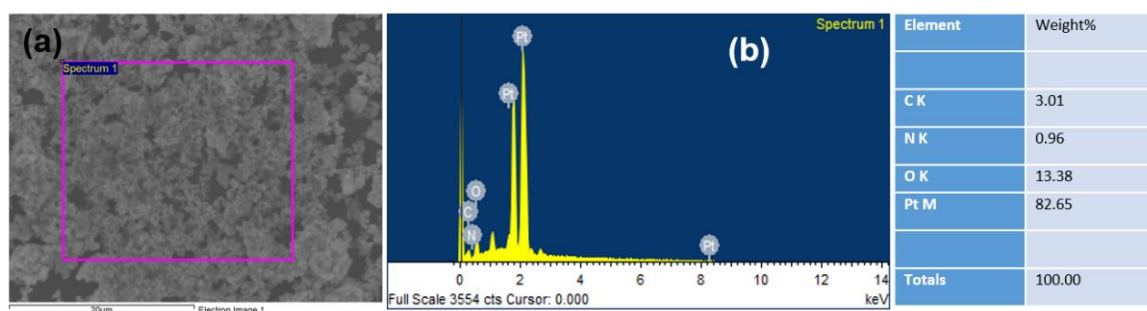


Figure S4.5. (a,b) EDS spectrum of Pt-(PtO_x)-NSs/C where it clearly confirms the presence of carbon, nitrogen, oxygen and platinum.

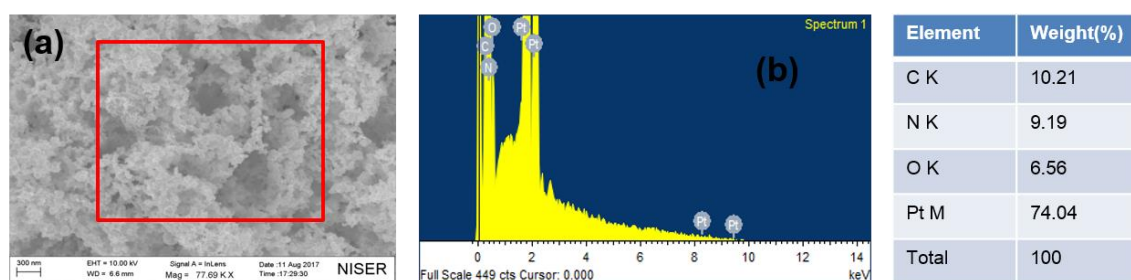


Figure S4.6. (a, b) EDS spectrum was taken on PtNSs/C where it clearly confirms the presence of carbon, nitrogen, oxygen and platinum.

ECSA calculation by UPD-H method:

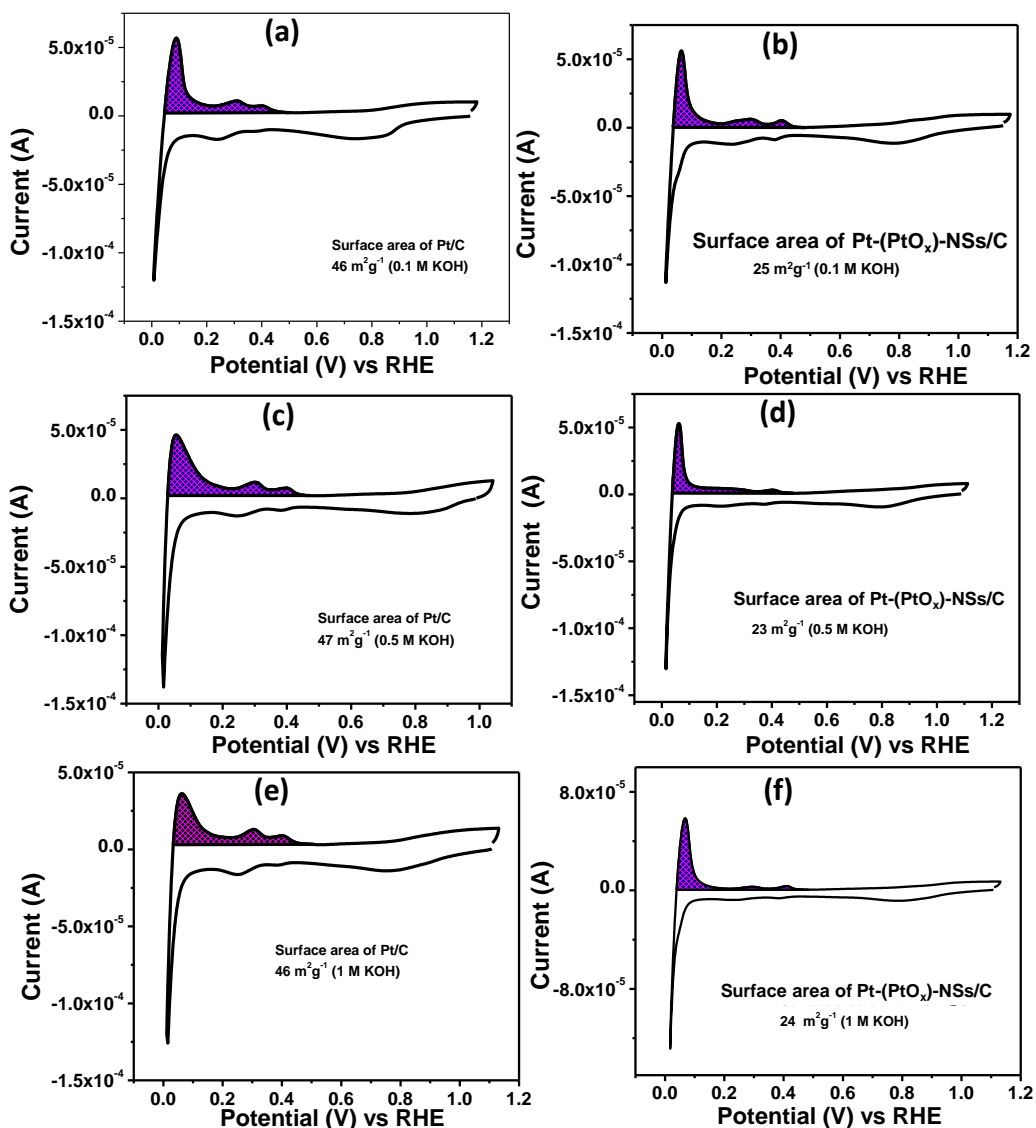


Figure S4.7. CV curves of Pt-(PtO_x)-NSs/C, Pt/C in KOH electrolyte of different concentrations. All CV experiments were performed with 30 mV/s scan rate with a constant Pt loading of 28.57 μg/cm².

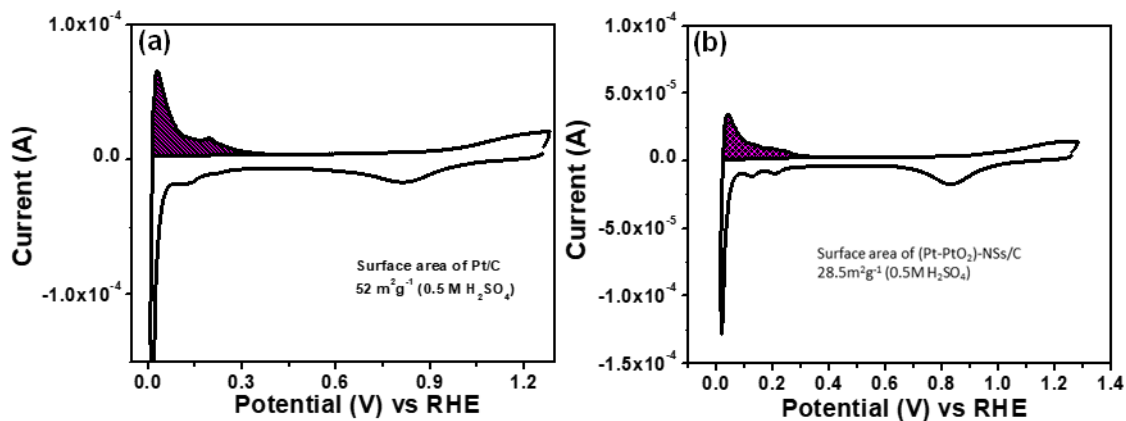


Figure S4.8. CV curves of (a) Pt/C and (b) Pt-(PtO_x)-NSs/C in 0.5 M H₂SO₄. ECSA was calculated from the shaded UPD-H_{des} region. All CV experiments were performed with 30 mV/s scan rate with a constant Pt loading of 28.57 μg/cm².

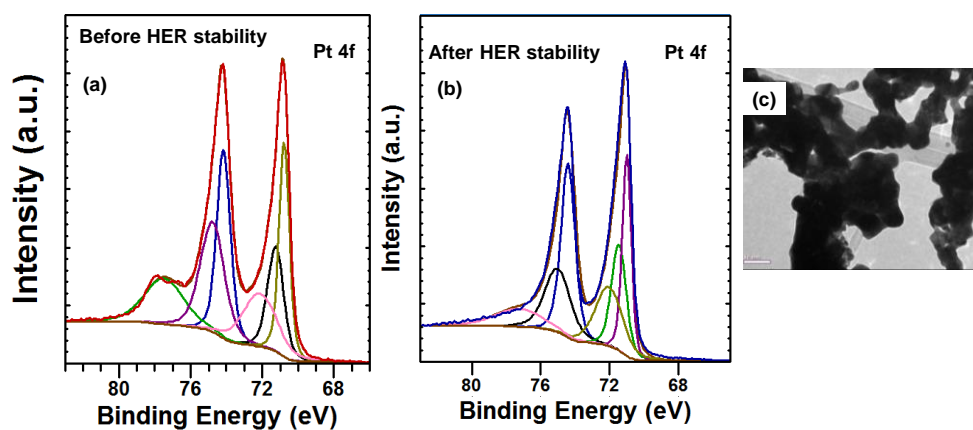


Figure S4.9. Pt 4f XPS spectra of Pt-(PtO_x)-NSs/C (a) before and (b) after HER study. (c) TEM image of Pt-(PtO_x)-NSs/C after HER stability.

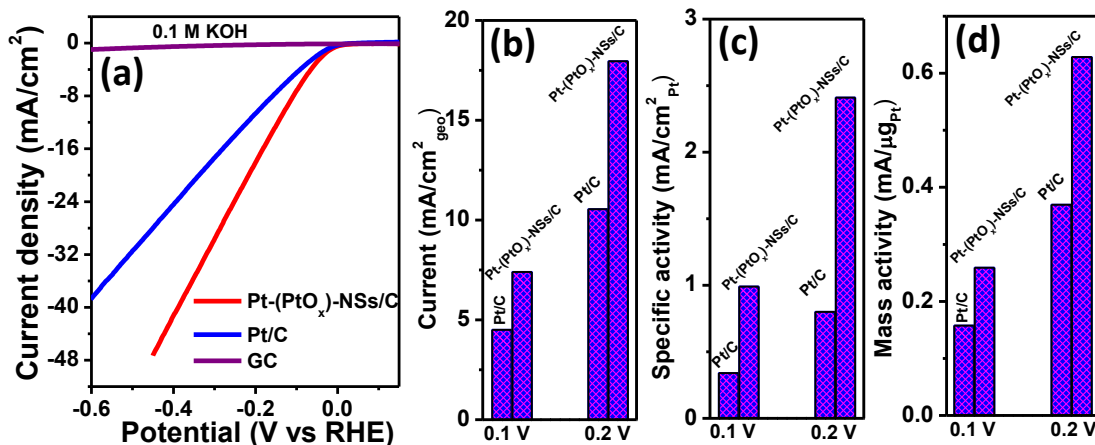


Figure S4.10. (a) HER LSV curves of Pt-(PtO_x)-NSs/C, Pt/C, CN_x and GCE in 0.1 M KOH with scan rate 10 mV/s. Comparison of (b) geometric current density (c) SA (d) MA at -0.1 and -0.2 V of Pt/C and Pt-(PtO_x)-NSs/C.

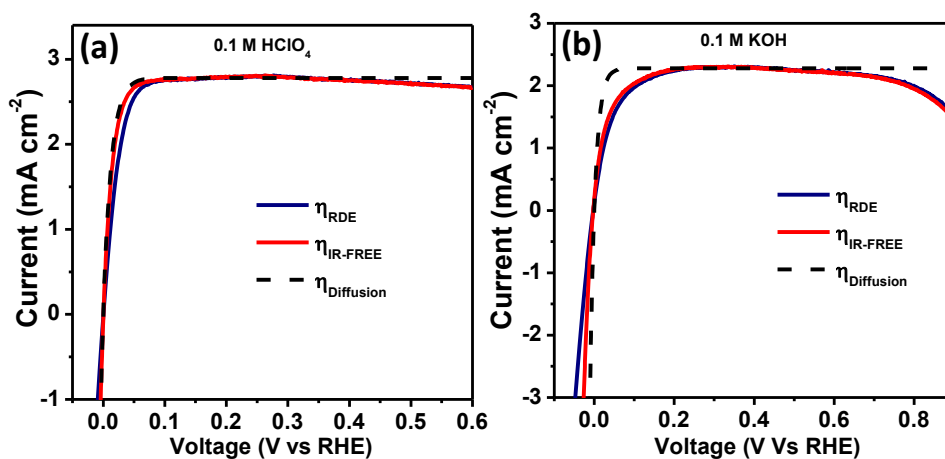


Figure S4.11. iR and diffusion corrected polarization curve at 1600 rpm in (a) 0.1 M HClO₄ (b) 0.1 M KOH.

CO stripping measurement:

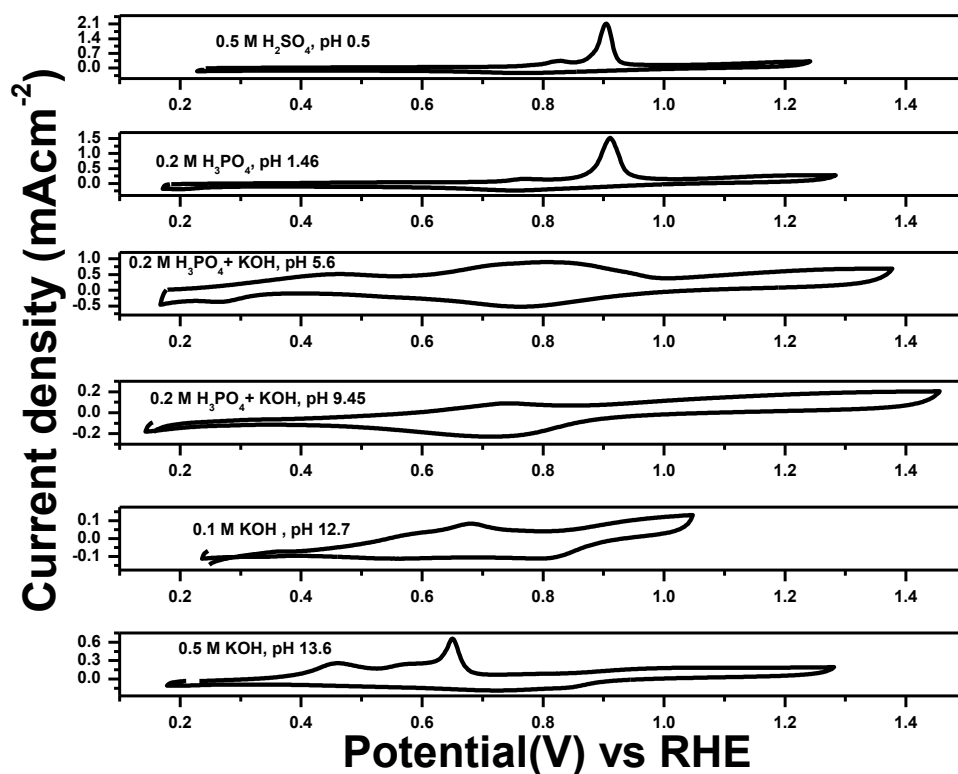


Figure S4.12. CO stripping voltammograms of Pt-(PtO_x)-NSs/C at different pH solutions.

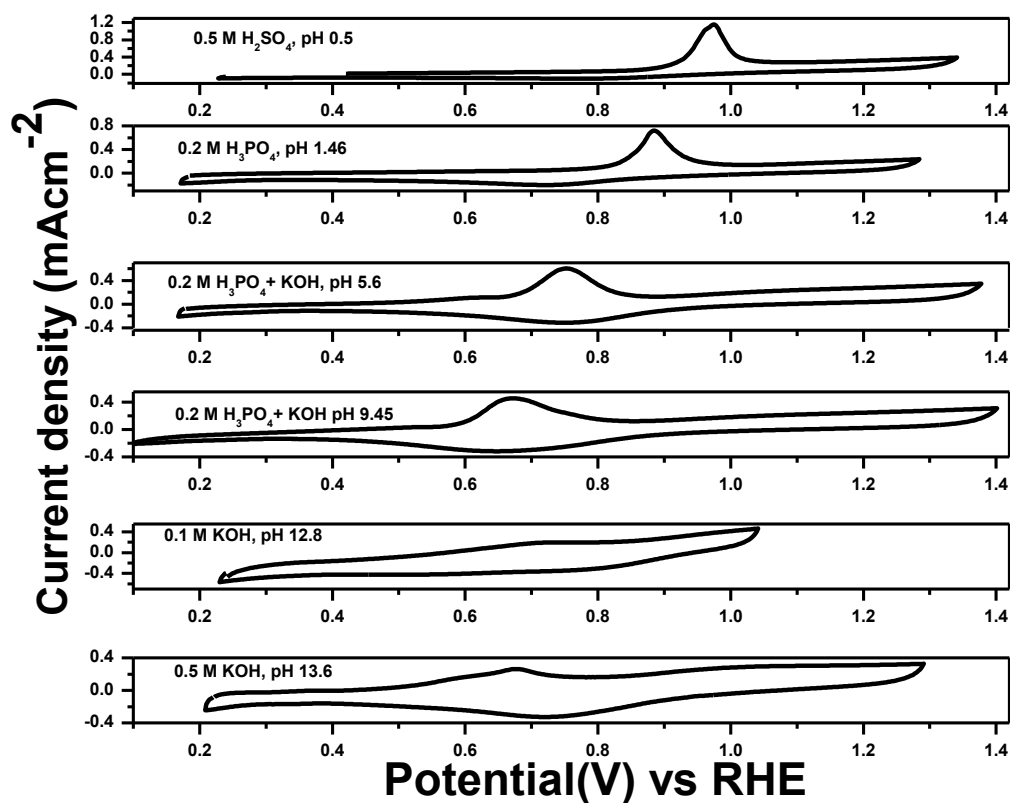


Figure S4.13. CO stripping voltammograms of PtNSs/C at different pH.

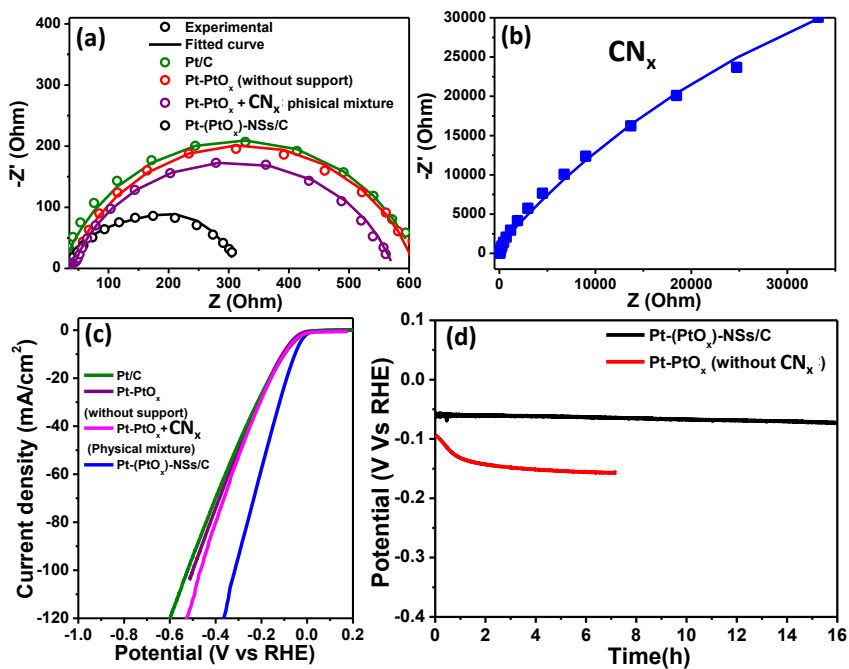


Figure S4.14. Nyquist plot of different catalysts (a) Pt-PtO₂ (without support), Pt-PtO₂ + CN_x physical mixture, Pt/C, Pt-(PtO_x)-NSs/C and (b) CN_x in 0.5 M KOH at a constant voltage -20 mV (RHE). (c) HER activity of different catalysts Pt-PtO₂ (without support), Pt-PtO₂ + CN_x physical mixture, Pt/C, Pt-(PtO_x)-NSs/C in 0.5 M KOH and (d) Chronopotentiometric HER stability of Pt-PtO_x (without support), Pt-(PtO_x)-NSs/C in 0.5 M KOH.

Table S4.1. Comparison of HER activity of Pt-(PtO_x)-NSs/C in 0.5 M H₂SO₄ with other reported catalysts.

Catalyst	Catalyst loading (mg cm ⁻²)	Onset potential (mV Vs RHE)	Over potential (mV Vs RHE) vs current density (mA cm ⁻²)	Tafel slope (mV/dec)	Exchange current (mA cm ⁻²)	Ref
Au-aerogel-CN _x	0.127	-30	-225 (20 mA cm ⁻²)	53	0.03	J. Mater. Chem. A 2015 , <i>3</i> , 23120
Pd-CN _x	0.043	12	55	35	0.40	ACS Catal. 2016 , <i>6</i> , 1929
1-D-RuO ₂ -CN _x	93	-14	-93 (10 mA cm ⁻²)	40	0.22	ACS appl. Mater. interfaces 2016 , <i>8</i> , 28678.
Pt _{tripods} @PA	~0.081	+19.6	-25 (90 mA cm ⁻²)	-	-	ACS Catal. 2017 , <i>7</i> , 452
PtNSSs@PEI	0.089	+64.6	-25 (143 mA cm ⁻²)	28		Chem. Sci. 2017 , <i>8</i> , 8411-8418
PtNiCu	0.06	0	-50 (143 mA cm ⁻²)	28		Chem. Sci. 2017 , <i>8</i> , 8411
Pt ₁₃ Cu ₇₃ Ni ₁₄ /CNF @CF		+5	70	38		ACS Appl. Mater. Interfaces 2016 , <i>8</i> , 3464
Pt _{tripods} @PA	~0.081	+19.6	-25 (90 mA cm ⁻²)	-	-	ACS Catal. 2017 , <i>7</i> , 452
WPNA/CC	2	-50	-130 (10 mA cm ⁻²)	69	0.29	ACS Appl. Mater. Interfaces 2014 , <i>6</i> , 21874
MoP-CA2	0.36	-40 (IR free)	-125 (10 mA/cm ²)	54	0.086	Adv. Mater. 2014 , <i>26</i> , 5702.
Nano MoP	1	-	-110 (10 mA cm ⁻²)	45	0.12	Chem. Mater. 2014 , <i>26</i> , 4826
NiAu/Au	-	-7	-	36	-	J. Am. Chem. Soc. 2015 , <i>137</i> , 5859
A-Ni-C		-	-34 (10 mA cm ⁻²)	41	1.2	Nat. Commun. 2016 , <i>7</i> , 10667
(GO 8 wt%) Cu-MOF	0.226	-87	-400 (122.48 mA cm ⁻²)	84	-	Adv. funct. mater. 2013 , <i>23</i> , 5363
CoP/CC	0.92	-38	67 (10 mA cm ⁻²)	51	0.288	J. Am. Chem. Soc. 2014 , <i>136</i> , 7587
CoN _x /C	2	-20	133	57	0.07	Nat. Commun. 2015 , <i>6</i> , 7992
NiP ₂ NS/CC	4.3	-50	-75 (10 mA cm ⁻²)	51	0.26	Nanoscale 2014 , <i>6</i> , 13440
Co-NRCNT	0.28	-50	-260 (10 mA cm ⁻²)	69	0.01	Angew. Chem. Int. Ed. 2014 , <i>126</i> , 4461
CoSe ₂	0.37	-30	-90 (4 mA cm ⁻²)	40	0.037	Energy Environ. Sci. 2013 , <i>6</i> , 3553
MoS ₂ /CoSe ₂	0.28	-11	-68 (10 mA cm ⁻²)	36	0.073	Nat. Commun. 2015 , <i>6</i> , 5982
Ni ₂ P		-25	-130 (20 mA cm ⁻²)	-46	0.033	J. Am. Chem. Soc. 2013 , <i>135</i> , 9267
Ni-Mo-N nanosheets	0.25	-78	~ -200 mV (3.5 mA cm ⁻²)	35.9	0.24	Angew. Chem. Int. Ed. 2012 , <i>51</i> , 6131
Pt-(PtO _x)-NSs/C	0.0285	+10	-9 (10 mA cm ⁻²)	32	0.5	This Paper

Table S4.2. Comparison of HER activity of Pt-(PtO_x)-NSs/C in 0.5 M KOH with other reported catalysts.

Catalyst	Catalyst loading (mg cm ⁻²)	Onset potential (mV Vs RHE)	Over potential (mV Vs RHE) vs current density (mA cm ⁻²)	Tafel slope (mV/dec)	Exchange current (mAcm ⁻²)	Ref
Ni/MWCNT	-	-	220 (20 mA cm ⁻²)	102	0.011	J. Power Sources 2014 ,266, 365
Co-NRCNTs		-50-100	370 (10 mA cm ⁻²)			Angew. Chem. Int. Ed. 2014 ,53, 4372.
NiP ₂ NS/CC		-74	102 (10 mA cm ⁻²)	64		Nanoscale 2014 ,6, 13440
Co _{0.59} Fe _{0.62} P	0.35	-39	92 (10 mA cm ⁻²)	72	0.568	Nanoscale 2015 ,7,1 1055.
Pt NWs/SLNi(OH) ₂	0.016	0	65 (10 mA cm ⁻²)			Nat. Commun. 2015 ,6, 6430
Pt ₃ Ni ₂ NWs-S/C	0.0153	-	50 (10 mA cm ⁻²)	-	-	Nat. Commun. 2015 ,6,64 30
NiONi-CNT			100 (10 mA cm ⁻²)			Nat. Commun. 2014 ,5, 4695
CoO _x @CN			232 (10 mA cm ⁻²)			J. Am. Chem. Soc. 2015 ,137,2688
CoP/CC			209 (10 mA cm ⁻²)	129		J. Am. Chem. Soc. 2014 ,136, 7587.
CoN _x /C	2.0	-30	170 (10 mA cm ⁻²)	75	-	Nat. Commun. 2015 ,6,79 92.
Porous Pd-CN _x	0.043	-75	180 (5 mA cm ⁻²)	150	0.037	ACS Catal. 2016 ,6,1929
Mo ₂ C	0.8	-110	190 (10 mA cm ⁻²)	54	0.0038	Angew. Chem. Int. Ed. 2012 ,51,12703.
1-D-RuO ₂ -CN _x	0.012	-16	95 (10 mA cm ⁻²)	70	0.28	ACS appl. Mater. interfaces 2016 ,8, 28678.
NiO/Ni-CNT	0.28	-	80 (10 mA cm ⁻²)	82	-	Nat. Commun. 2014 , 5, 4695.
Ni-Mo nanopowders	1	0	80 (10 mA cm ⁻²)			ACS Catalysis 2013 , 3, 166.
Pt-(PtO _x)-NSs/C	0.021	0	53 (10 mA cm ⁻²) 81 (20 mA cm ⁻²)	65	1.25	This work.

CHAPTER 5

Three-dimensional Hierarchically Porous Iridium Oxide-Carbon Nitride Hybrid: Synthesis and their Applications in Overall Water Splitting

5.1. ABSTRACT

Active and durable acid medium electrocatalysts for HER and OER are of critical importance for the development of proton exchange membrane (PEM) water electrolyzer or PEM-Fuel cells. In this chapter, we have revealed a facile synthesis of 3D-hierarchical porous iridium oxide/N-doped carbon hybrid (3D-IrO₂/N@C) for superior OER and HER activity in acid. In 0.5 M HClO₄, this catalyst exhibited superior activity towards OER with a low overpotential of 280 mV at 10 mA/cm², a low Tafel slope of 45 mV/dec and ~98% faradic efficiency. The mass activity and turnover frequency (TOF) at an overpotential of 350 mV are found to be 833 A/g and 0.432 s⁻¹ which are ~32 times higher than that of commercial (comm.) IrO₂. The HER performance of this 3D-IrO₂/N@C is comparable to that of commercial Pt/C catalyst in acid. This 3D-IrO₂/N@C catalyst requires only 35 mV overpotential to reach 10 mA/cm² current density with Tafel slope of 31 mV/dec in acid. Most importantly, stability test confirmed superior HER and OER stability of this catalyst in acid. This 3D-IrO₂/N@C catalyst was applied as cathode and anode for overall water splitting and required only 1.55 V to achieve a current density of 10 mA/cm² in acid. The outstanding activity of the 3D-IrO₂/N@C catalyst can be attributed to a unique hierarchical porous network, high surface area, higher electron and mass transportation, synergistic interaction between IrO₂ and carbon support.

5.2. INTRODUCTION

With the ever-growing energy demand and environmental problems, rapid depletion of fossil fuel owing to the excessive use of fossil fuel, the searching for the sustainable and renewable sources of energy has been a major trend globally in past few decades^{1,2}. The electrochemical water splitting is a most promising method to store the electrical energy into chemical fuel^{3,4} i.e. H₂ and it consists of two half-cell reactions such as hydrogen and oxygen evolution reactions. The electrochemical/photochemical water splitting has attracted tremendous attention to the scientific community in recent years since HER and OER play a significant role in various energy storage and conversion devices such as water electrolyzers, fuel cells, metal-air batteries etc^{5,6}. The OER process is a bottleneck of water splitting due to its slow multi-electron process^{7,8}. In recent years, earth-abundant transition metal materials are studied as OER catalyst⁷⁻¹¹. The main problem of these transition metal based OER catalysts is their stability in acid - although they are active and stable in basic media, they are generally not active and stable in strong acidic condition^{12,13}. The proton exchange membrane (PEM) water electrolyzer or PEM fuel cells require strong acidic corrosive environment and it has several advantages over its alkaline counterpart such as fast response, high efficiency, high power density, simple cell structures etc¹³⁻¹⁵. The IrO₂ and RuO₂ are a highly active catalyst for OER in acid^{13,16}. Although RuO₂ is more active than IrO₂, poor stability of RuO₂ makes IrO₂ a preferred state-of-art catalyst for OER in acid^{17,18}. The state-of-art catalyst still requires large overpotential as compared to theoretical value 1.23 V. Thus, development of an efficient catalyst which can deliver appreciable current density at low overpotential is essential for the commercialization of PEM-electrolyzer/Fuel cells. Since Ir is a precious expensive metal, it is also important to reduce loading these Ir metal at the anode of the electrolyzer. In order to decrease the amount of

precious metal loading, bimetallic nanostructures and the Iridium-transition metals hybrid such as IrNi, IrCu, IrTe, etc and an alloy of IrO₂ with cheap transition metal oxide (ZnO₂, TiO₂, Fe₂O₃, MoO₃ etc) has been investigated by several groups^{15, 17, 19-23}. This two strategy were not beneficial since leaching of Ni or Cu under the strong corrosive condition and low conductivity of transition metal oxide leading to the poor activity of the catalyst²⁴. The properties of nanostructures can easily be tuned by tailoring the size, shape and morphology of nanostructures^{25,26}. The different nanostructures of Ir such as IrO₂ ultrathin nano needles¹⁸, ultrathin laminar superstructure²⁷, nonporous IrO₂²⁸, IrO₂ films^{29,30} can easily be synthesized. The synthesis of three-dimensional porous hybrids of IrO₂ and conducting carbon or IrO₂ nanostructures supported on 3D conducting carbon support could be a good strategy to develop active catalyst since porous electrode allows easy mass transport and conducting support provides effective electron transport.

For hydrogen evolution at cathode, Pt is generally used as HER catalyst^{5,31}. But the poor durability of Pt/C under the strong acid condition is the main obstacle for the commercialization of PEM-based technologies^{3,32}. It is desirable to find highly stable HER catalysts. The HER activity of Ir metal is lower³³ than Pt and activity of IrO₂ is even lower. The comm. Pt/C is highly active for HER whereas comm. IrO₂ is used as OER catalyst⁷. For PEMFC electrolyzers two different catalysts are generally used as cathode and anode in acid media. The designing of a bi-functional catalyst where a single catalyst is able to catalyze HER and OER in the same electrolyte and the same electrochemical device is very attractive because this can simplify fabrication procedure and lower the cost of water electrolyzer^{11, 34-36}.

In the present work, we report a facile synthesis method for 3D-hierarchical porous iridium oxide/N-doped carbon hybrid (3D-IrO₂/N@C) for electrochemical overall water splitting in acidic medium. The OER and HER activity, as well as stability in strong acid

media, were evaluated for 3D-IrO₂/N@C and then compared with the state-of-the-art catalysts. This 3D-IrO₂/N@C electrocatalyst exhibits superior OER activity in acid with low over-potential 280 mV to achieve 10 mA cm⁻² current density, high mass activity and TOF values (0.432 s⁻¹ at η = 350 mV). The HER performance of this catalyst is comparable to commercial Pt/C in acid. This 3D-IrO₂/N@C hybrid also showed outstanding stability for HER and OER in acid media. The N@C functionalized 3D-hierarchical porous iridium oxide hybrid were also applied as cathode and anode in 0.5 M HClO₄ solution for overall splitting. To the best of our knowledge, this 3D-IrO₂/N@C hybrid is one of the best bi-functional electrocatalysts for overall water splitting in strong acid environment.

5.3. EXPERIMENTAL SECTION

Preparation of 3D-IrO₂/N@C hybrid

20 mg of H₂IrCl₆·6H₂O was dissolved in 5 ml of water. Then 5 mg of g-CN_x was added and sonicated in a bath sonicator for dispersed well. Then the mixture was stirred at room temperature for 48 h. A Ti foil of 0.25 cm² (0.5 cm x 0.5 cm) area was taken and cleaned it well by sonicating it 10 % HCl solution and then washed it by copious water. 10 μl of this solution was coated on a Ti foil, then evaporated and annealed at atmosphere at 100, 200, 300, 400, 500, 600 °C for 3 h. Sample prepared at 400 °C (3D-IrO₂/N@C) shows the best catalytic activity. This 3D-IrO₂/N@C modified Ti foil was further characterized and used for electrocatalytic activity.

Calculation of Iridium loading on the electrode:

The amount of Ir on the electrode was calculated from the stock solution concentration and amount of drop casted Ir-precursor on the electrode. The calculation is as follows.

Molecular weight of $\text{H}_2\text{IrCl}_6 \cdot 6\text{H}_2\text{O} = 532.948 \text{ gm}$

Atomic weight of Ir = 192.217 gm

Stock solution contains Iridium salt contained 8 mg/ml.

10 μl stock solution was drop casted on the Ti foil that contained 80 μg of Ir-salt.

So contained of only Ir = $\frac{80 \times 192.217}{532.948} \mu\text{g} = \sim 30 \mu\text{g}$ of Iridium.

5.4 RESULTS AND DISCUSSIONS

5.4.1 Characterization of 3D-IrO₂/N@C composite:

The 3D-hierarchical porous iridium oxide/N-doped carbon (3D-IrO₂/N@C) hybrid was synthesized by facile heating method as discussed in the experimental section.

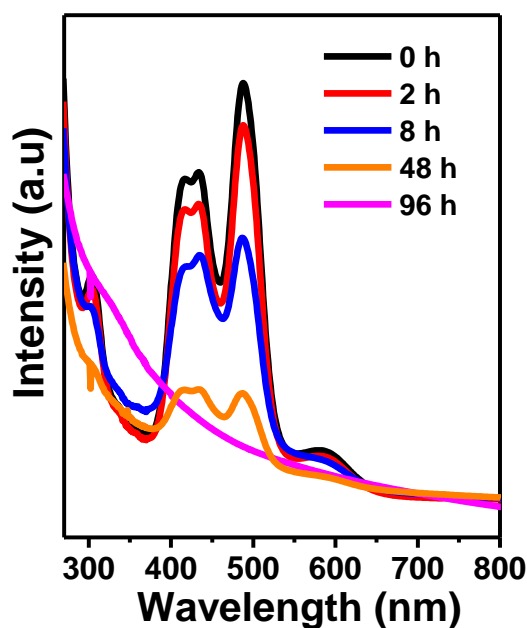


Figure 5.1. UV-Visible spectra of H_2IrCl_6 and g-CN_x mixture in different time.

The synthesis of carbon nitride^{37,39} (g-CN_x) is discussed previously. When an aqueous solution of $[\text{IrCl}_6]^{2-}$ is mixed with g-CN_x material, water soluble or water dispersed Ir^{4+} -

N@C complex is formed. The interaction between Ir^{4+} and g-CN_x was studied by UV-Visible spectroscopy (Figure 5.1). The aqueous solution $[\text{IrCl}_6]^{2-}$ complex showed a strong absorption band in the region 400-500 nm due to d-d transition²⁸ of iridium electrons within the $[\text{IrCl}_6]^{2-}$. The gradual decrease of absorption on the addition of g-CN_x suggested a strong interaction between Ir^{4+} and g-CN_x materials. When an aqueous solution of Ir^{4+} - g-CN_x complex is evaporated and heated at high temperature on Ti-foil, the 3D- $\text{IrO}_2/\text{N@C}$ hybrid is formed. The $\text{IrO}_2/\text{N@C}$ hybrid was also prepared by calcinated at different temperatures such as 100, 200, 300, 400, 500 and 600 °C. The best electrochemical activity was obtained when the preparation temperature was between 300 °C to 500 °C.

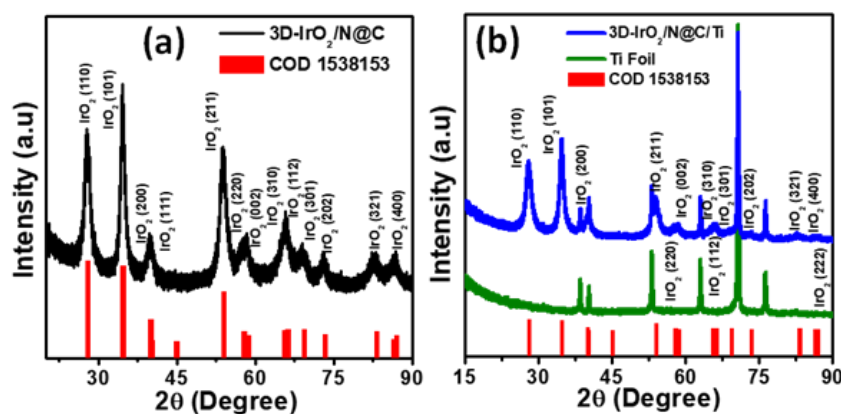


Figure 5.2. (a) p-XRD of 3D- $\text{IrO}_2/\text{N@C}$ hybrid. (b) p-XRD of 3D- $\text{IrO}_2/\text{N@C}$ on Ti foil (blue line) and only Ti foil heated at 400 °C.

The 3D- $\text{IrO}_2/\text{N@C}$ hybrid was easily removed by scratching or sonication in water from Ti foil. The powder X-ray diffraction (p-XRD) patterns of the 3D- $\text{IrO}_2/\text{N@C}$ hybrid are shown in Figure 5.2 a. The different diffraction peaks observed at 2θ values of 27.6, 34.3, 39.99, 53.6, 57.8, 65.7, 77.25, 82.1 corresponds to (110), (101), (200), (211), (002), (212), (221), (321) plane of IrO_2 . The XRD pattern was compared with standard data of IrO_2 (lattice space group P42/mmm with COD no 1538153)^{19,40}. The XRD patterns of 3D- $\text{IrO}_2/\text{N@C}$ on Ti foil is also provided Figure 5.2b. It shows the presence of diffraction peaks for Ti along with the

diffraction peaks for IrO_2 . The scanning electron (SEM) and transmission (TEM) techniques were used to study the morphology of 3D- $\text{IrO}_2/\text{N}@C$ hybrid. The typical morphology of 3D- $\text{IrO}_2/\text{N}@C$ hybrid, grown on Ti foil at 400 °C and 500 °C are shown in Figure 5.3a and 5.3 (b, c). These images show that thin folded nanosheets are uniformly grown on the surface of Ti-foil.

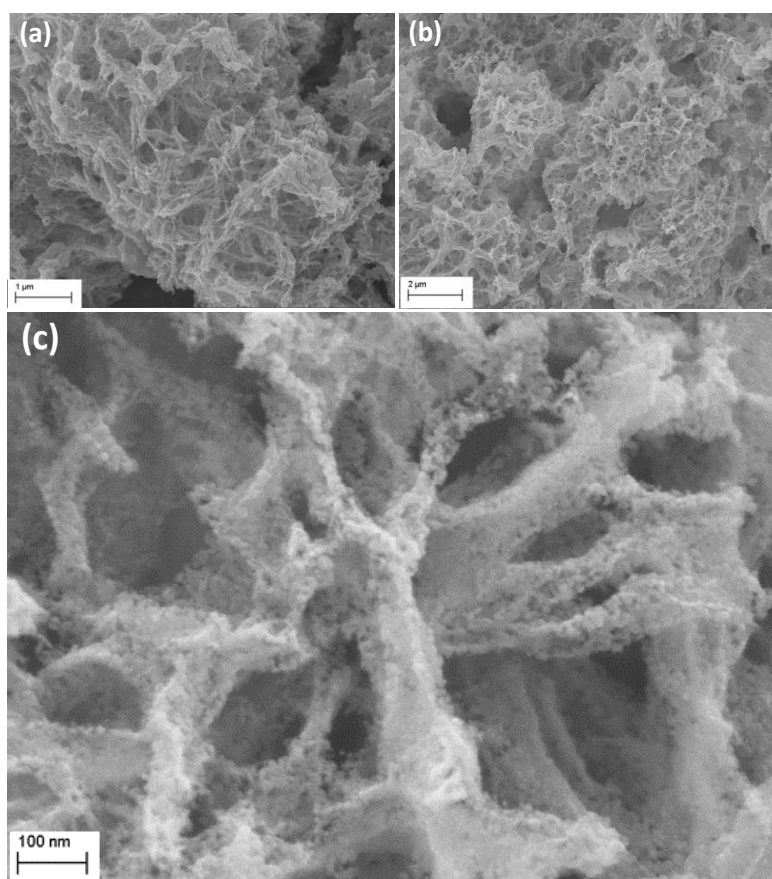


Figure 5.3. FESEM images of 3D- $\text{IrO}_2/\text{N}@C$ prepared at (a) 400 °C (b, c) 500 °C.

As shown in Figure 5.3a and 5.3b, c. these nanosheets are rippled silk-like shape structure and they are interconnected with each other to form free-standing porous network morphology. Notably, the nanosheets are strongly attached to each other forming a lots of 3D porous structure. In the high magnification SEM image (Figure 5.3c) of the hybrid prepared at 500 °C, pores are clearly visible and small IrO_2 nanoparticles are highly dispersed in the 3D porous $\text{N}@C$ network.

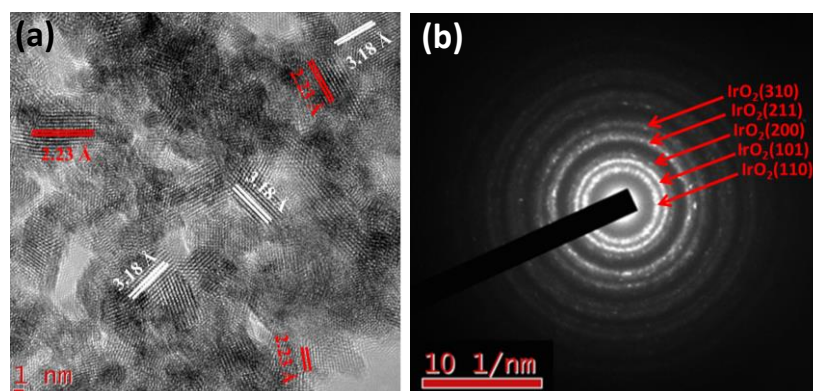


Figure 5.4. (a) HRTEM image of 3D-IrO₂/N@C (b) SAED image of 3D-IrO₂/N@C hybrid.

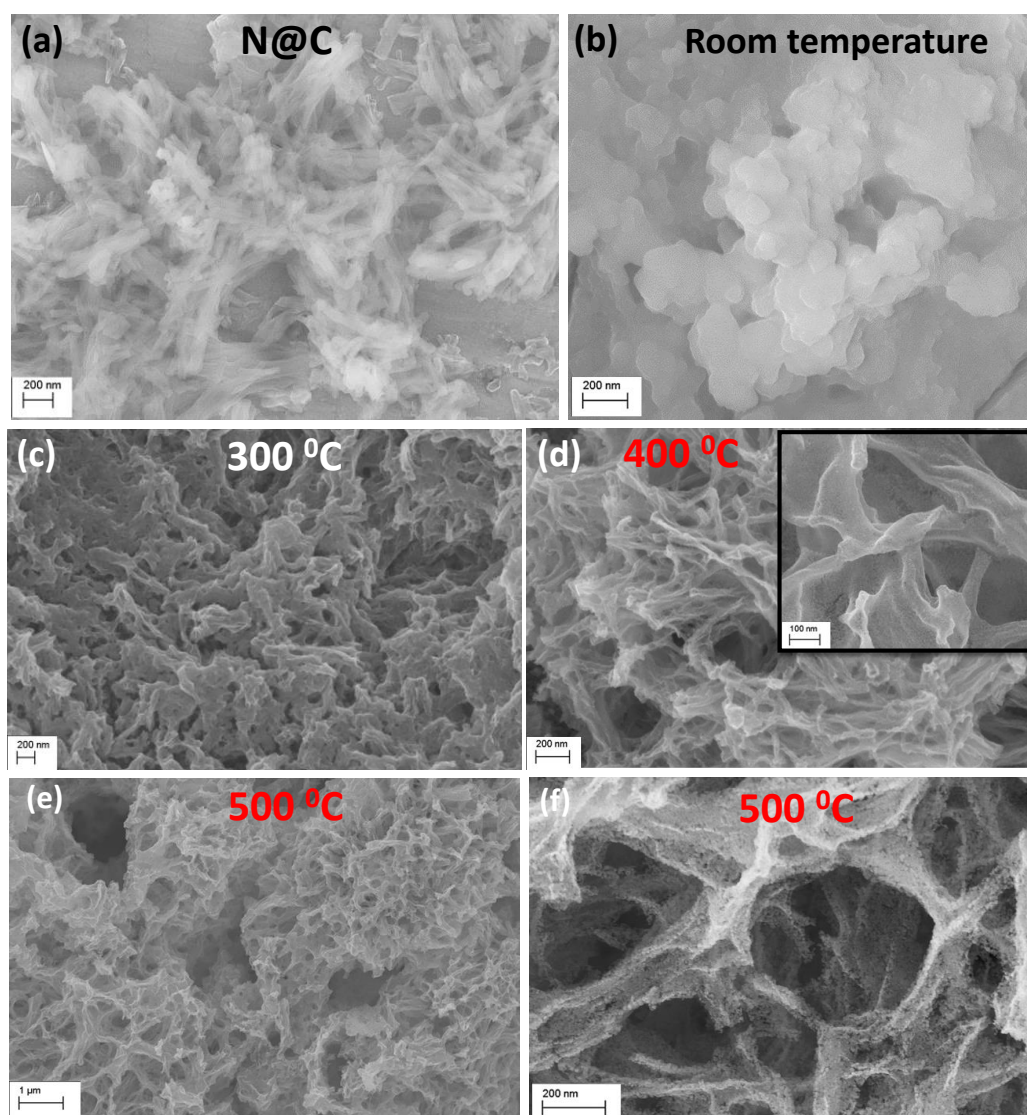


Figure 5.5. FESEM image of (a) N@C (b) N@C-Ir⁴⁺ complex before heating. The FESEM image 3D-IrO₂/N@C prepared at (c) 300 °C (d) 400 °C (inset: high magnification image) (e, f) 500 °C.

It is also observed that size of IrO₂ nanoparticles decreases with decreasing calcination temperature (inset of Figure 5.5 d and Figure 5.5 f). The high-resolution TEM (HR-TEM) image of the 3D-IrO₂/N@C hybrid and corresponding selected area electron diffraction (SAED) are shown in Figure 5.4a and Figure 5.4b respectively. The SAED image show polycrystalline nature of the hybrid and calculated d-spacing of 3.18, 2.58, 2.23, 1.69, 1.42 Å corresponds to (110), (101), (111), (211), (310) of IrO₂.

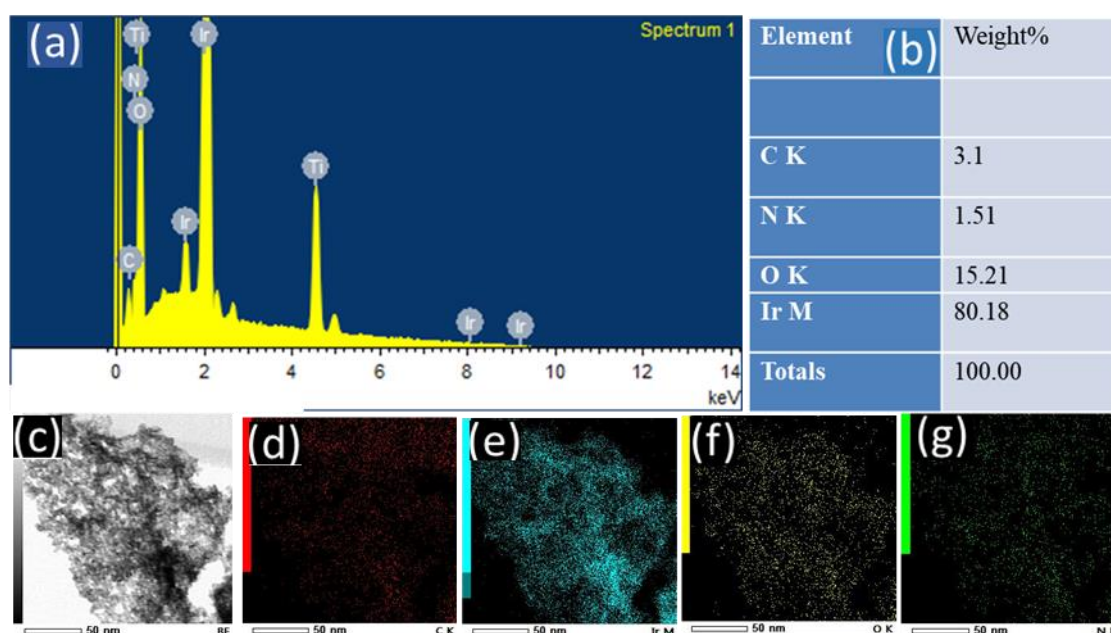


Figure 5.6. (a, b) EDS line profile and elemental weight percentage of the 3D-IrO₂/N@C hybrid (heated at 400 °C). (c-g) STEM image and TEM-EDS elemental mapping of 3D-IrO₂/N@C.

In the HR-TEM image the measured lattice spacing were found to be 2.23 and 3.18 Å. The presence lattice spacing 2.23 Å corresponding to the (111) plane of IrO₂ confirmed the presence IrO₂ in the 3D-IrO₂/N@C hybrid. The d-spacing of 3.18 Å is due to the (002) plane of graphene. Energy dispersive X-ray spectroscopy (EDS) of 3D-IrO₂/N@C hybrid shows the presence of C, N, O and Ir (Figure 5.6 a, b) in the hybrid. The TEM-EDS mapping of a single sheet of 3D-IrO₂/N@C hybrid was presented in Figure 5.6 c-g. These images

show the uniform distribution of C, N, O and Ir. The SEM images of free N@C and N@C after Ir^{+4} ions adsorption are shown in Figure 5.5 a and b showing their flat sheet-like morphology whereas SEM images of 3D- $\text{IrO}_2/\text{N@C}$ hybrids prepared at 300, 400 and 500 $^\circ\text{C}$ are given in Figure 5.5 c-f. These images show that with increase of calcination temperature, thickness of layers reduced and hybrid became more porous. These suggest that Ir^{+4} ions first adsorption on the surface of two dimension sheets of N@C. Then, on heating at high temperature, nucleation of IrO_2 and growth occurs on the surface of N@C sheets that leads to the formation of folded thin nanosheets of the $\text{IrO}_2/\text{N@C}$ hybrid.

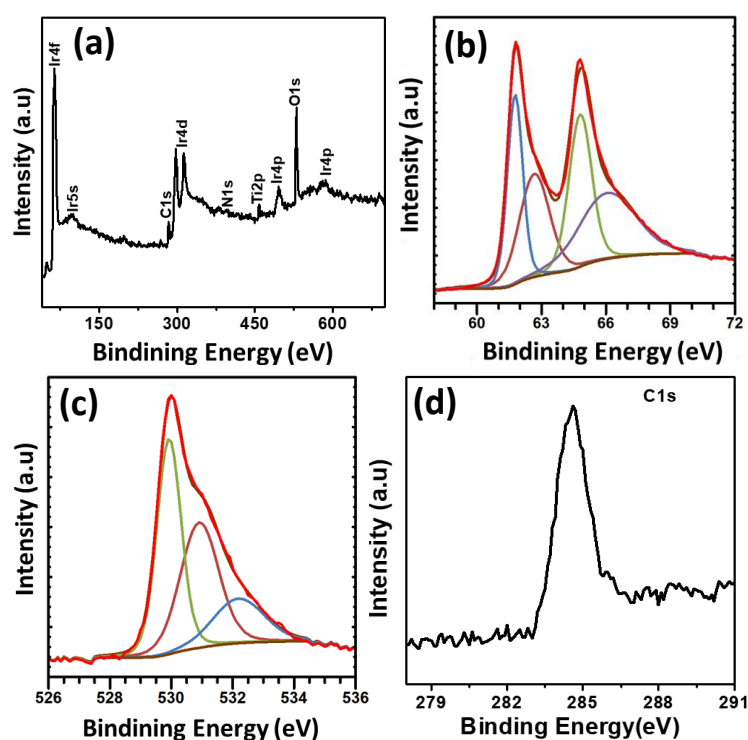


Figure 5.7. (a) XPS survey scan of 3D- $\text{IrO}_2/\text{N@C}$ hybrid. High-resolution XPS spectra of (b) Ir4f (c) O1s (d) C1s of 3D- $\text{IrO}_2/\text{N@C}$ hybrid.

The X-ray photoelectron spectroscopy (XPS) measurement of the (3D- $\text{IrO}_2/\text{N@C}$) hybrid was carried out to find the electronic structure of the hybrid. The XPS survey scan in Figure 5.7 (a) clearly indicates the presence of C, N, O and Ir. In literature, it is reported that Ir4f-XPS peak of the metallic iridium (Ir^0) appeared as a doublet at 60.8 and 63.8 eV for Ir 4f7/2

and Ir5/2, but for the Ir⁴⁺ (for example IrO₂) these two peaks generally appeared at 61.7 and 64.7 eV^{29, 40, 41}. The Ir4f-XPS spectrum of 3D-IrO₂/N@C is deconvoluted into two gaussian peaks. As shown in Figure 5.7b the peak appeared at 61.8 and 64.8 eV are assigned to the 4f7/2 and 4f5/2 peaks of Ir⁴⁺ species and these BE values are matched well with the single crystal IrO₂. Another two broader peaks^{42, 43} also appeared at 62.7 and 66.1 eV, almost 1 eV higher than that of [Ir⁴⁺] species. Figure 5.7 (c) shows the O1s XPS spectrum of 3D-IrO₂/N@C. This O1s XPS spectrum is deconvoluted to three main gaussian peaks. The peak appeared at 529.91 is referred to the Ir bonded oxygen in IrO₂ lattice and the peak appeared at 530.93 is assigned to the absorbed O₂ or OH⁻ in the hybrid^{41, 44}. The peak appeared at 532.21 eV originates from the absorbed water in the hybrid. The C1s XPS spectra is shown in Figure 5.7d. The peak appeared at 284.6 is assigned to the sp² hybridized carbon of graphitic carbon⁴⁵. The EDS spectrum of 3D-IrO₂/N@C hybrid is shown in Figure 5.6 (b) and amount of Ir present in the hybrid (3D-IrO₂/N@C) was found to be nearly 80 wt%.

5.4.2 Oxygen Evolution Reaction (OER) Activity of 3D-IrO₂/N@C hybrid in acidic medium:

The electrocatalytic activity of the as-synthesized 3D-IrO₂/N@C was first evaluated in 0.5 M HClO₄ medium. The electrochemical analysis was done in a three-electrode system where the 3D-IrO₂/N@C, grown on Ti foil was directly used as a working electrode. The OER activities were assessed in O₂ saturated 0.5 M HClO₄ electrolyte solution with a scan rate of 10 mV/sec. As shown in Figure 5.8a, the LSV polarization curve (geometric current density vs. potential) for oxygen evolution of 3D-IrO₂/N@C in 0.5 M HClO₄ solution was compared with that of comm. IrO₂ and Pt/C. The LSV curve of Ti foil was also measured under the same condition and plotted in Figure 5.8 (a). The bare Ti foil exhibits negligible OER activity with large onset potential.

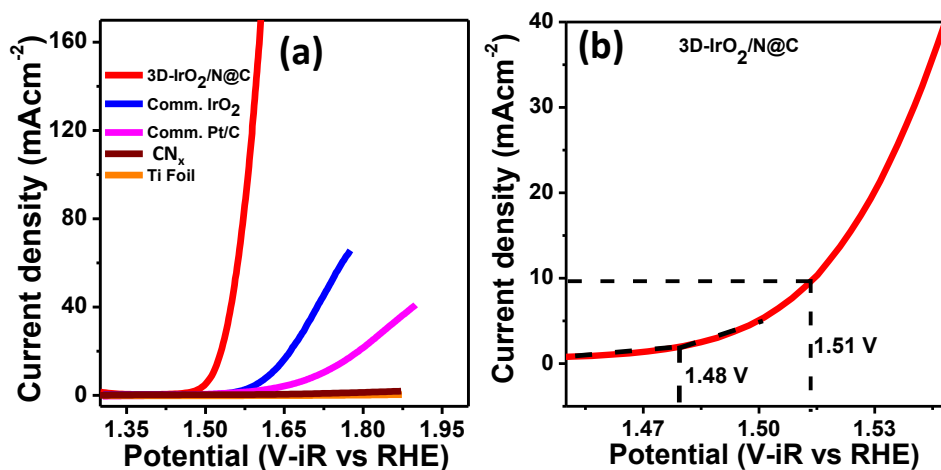


Figure 5.8. (a) LSV polarisation curves of 3D-IrO₂/N@C, comm. IrO₂, comm. Pt/C in 0.5 M HClO₄ with scan rate 10 mV/s (b) Required overpotential required for achieving 10 mA/cm² current density for of 3D-IrO₂/N@C catalyst.

The onset overpotentials of comm. IrO₂ and comm. Pt/C are 300 mV and 320 mV whereas 3D-IrO₂/N@C catalyst shows a low onset potential of 250 mV (Figure 5.8 (b)). The overpotentials required to reach a current density of 10 mAcm⁻² is an important parameter for solar fuel synthesis⁴⁶. Comm. IrO₂ catalyst needs overpotentials of 400 mV to reach a current density of 10 mAcm⁻² which is consistent with the previous reported literature values^{19, 47}. But 3D-IrO₂/N@C affords only 280 mV overpotential to reach a current density of 10 mAcm⁻² (Figure 5.8b and Table 5.1). This required overpotential for 10 mA/cm² current density is lower or comparable to the recently reported noble metal nanostructures in acid such as IrO₂ nanoneedles¹⁸, IrO₂-RuO₂@Ru⁴⁸, RuO₂ nanowires¹⁶ 3D macroporous IrO₂²⁴ etc. The fundamental origin of the activity can be obtained from the mass activity (MA) and turn over frequency (TOF) (see detail calculations of TOF in Chapter 2). The OER activity of 3D-IrO₂/N@C was further compared by comparing mass activity (MA) and TOF value of this catalyst with state-of-art-catalyst (Figure 5.9 a, b and c).

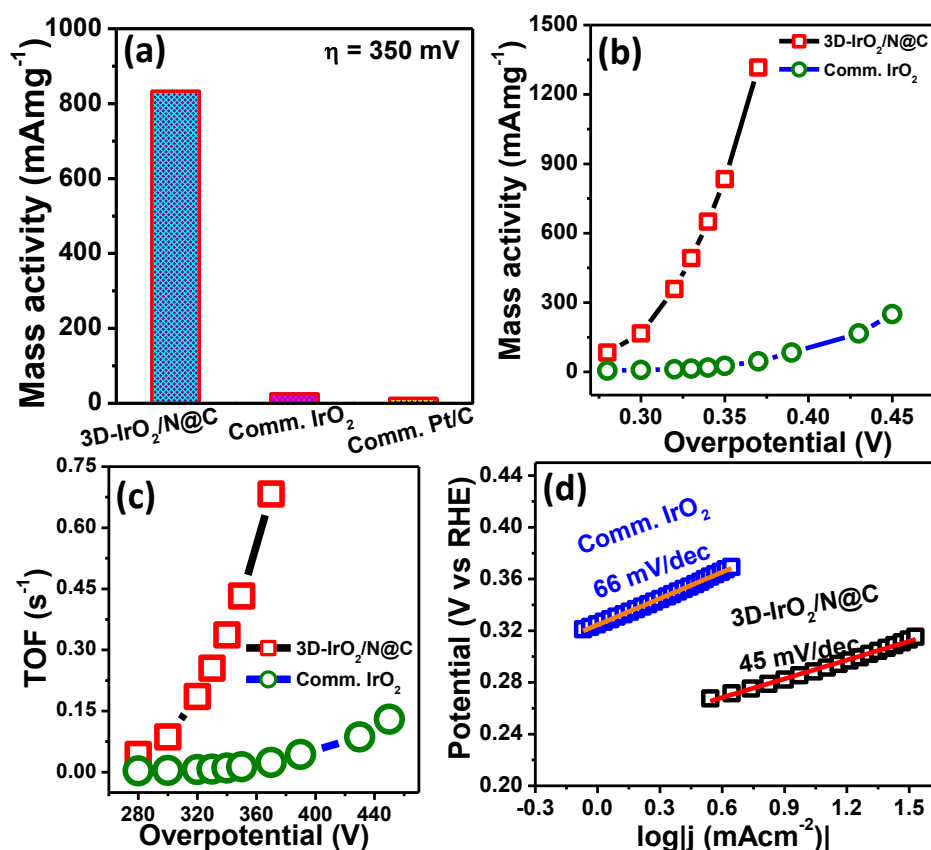


Figure 5.9. (a) MA of 3D-IrO₂/N@C, comm. IrO₂, comm. Pt/C at 1.58 V. (b) MA of 3D-IrO₂/N@C and comm. IrO₂ at different overpotentials (c) TOF of 3D-IrO₂/N@C and comm. IrO₂ at different overpotentials. (d) Tafel slope of 3D-IrO₂/N@C and comm. IrO₂.

The mass activity of this 3D-IrO₂/N@C catalyst was ~ 833 mA mg⁻¹ at 350 mV, which is ~33 times higher than that of comm. IrO₂ (25 mA/mg) (Figure 5.9a). Figure 5.9b shows the increase of MA with overpotential and a very rapid increase of MA value with the increase of overpotentials is observed as compared to the comm. IrO₂ catalyst. This 3D-IrO₂/N@C catalyst showed very high TOF value at η = 350 mV and TOF value of 3D-IrO₂/N@C was 0.432 s⁻¹ which is 32 times higher than comm. IrO₂ (0.0133 s⁻¹) and much higher than comm. Pt/C (Figure 5.9c and Table 5.1). As shown in Figure 5.9c the TOF value of this 3D-IrO₂/N@C catalyst increased drastically at higher overpotentials as compared to comm. IrO₂ catalyst suggesting very high OER activity of this catalyst in acid media.

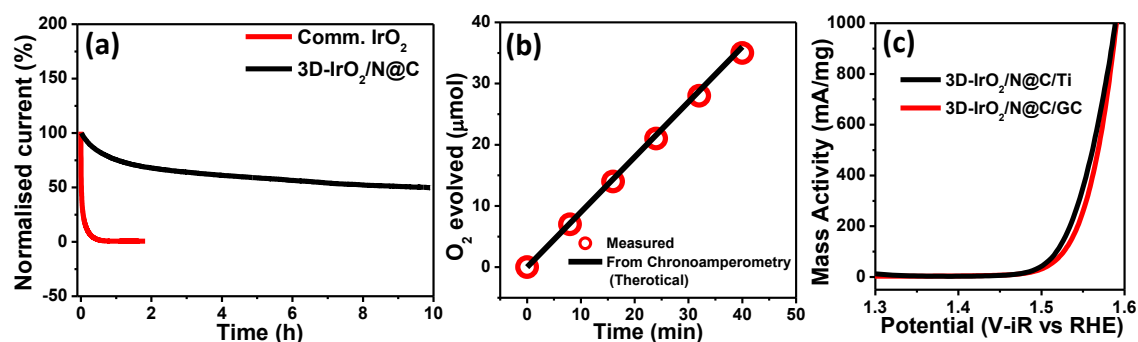


Figure 5.10. (a) Steady-state chronoamperometric stability of 3D-IrO₂/N@C and comm. IrO₂ in 0.5 M HClO₄ at a constant potential of 1.51 V. (b) Theoretical and experimental measured O₂ by the 3D-IrO₂/N@C electrode at 25 mA/cm² current density. (c) LSV polarization curve normalized by mass of the catalyst of 3D-IrO₂/N@C on Ti foil and GC surface.

The Tafel slope generally helps to understand the OER mechanism. In order to investigate the mechanism of OER and the insight of the catalyst Tafel analysis was performed. Several groups reported the mechanism of OER on IrO₂ surface that was described in the following^{20,28}. In the first step of OER, absorption of water followed by the formation of OH*_{ads} intermediate occurs on the active site (S).



The next step is the conversion of OH*_{ads} to another active species OH. Although this active OH species is chemically same but energetically it is different from OH*_{ads}



Then proton and electron transfer takes place to form oxide intermediate



In the final step, two oxide intermediates are recombined to form molecular oxygen.



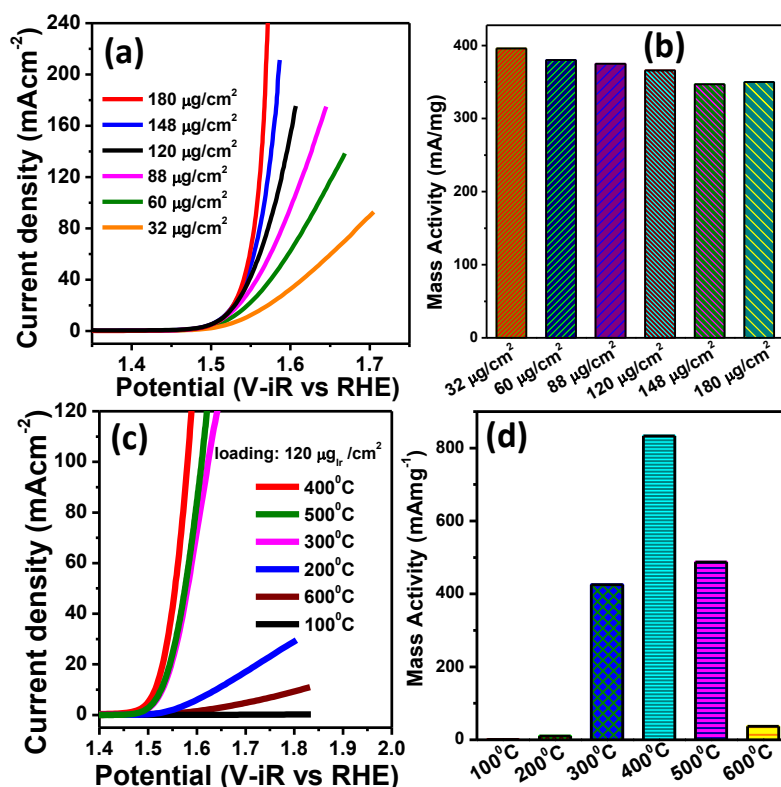


Figure 5.11. (a) OER activity of 3D-IrO₂/N@C at different metal loading in the electrode. (b) Mass activity (with respect to Ir) of 3D-IrO₂/N@C with different Ir loading in the 3D-IrO₂/N@C catalyst. (c) LSV curves (b) Mass activity of 3D-IrO₂/N@C catalysts prepared at different calcination temperature ranging from 100 to 600 °C. Amount of Ir loading kept same (120 μg_{Ir} cm⁻²)

It is reported^{28,47} when Tafel slope value is 60 mV/dec, then step 1 and step 2 is the rate determining steps whereas Tafel slope value of 120, suggest step 1 is the sole rate-determining step. For the Tafel slope value are 40 and 15 mV/dec^{20,22} when the rate determining step is step 3 and step 4 respectively. The Tafel plot of 3D-IrO₂/N@C and comm. IrO₂ is shown in Figure 5.9d. The Tafel slope value in the linear region of Tafel plot for comm. IrO₂ was obtained 65 mV/dec in 0.5 M HClO₄ medium which is comparable to the previously reported IrO₂ catalyst^{28,47}. The Tafel slope value of 45 mV/dec for 3D-IrO₂/N@C suggests the faster rate of OER with step 3 is the rate-determining step. The activity of the 3D-IrO₂/N@C and the comm. IrO₂ catalyst is summarized in Table 5.1.

Table 5.1. Comparison of OER activity of different catalysts in 0.5 M HClO₄.

Catalyst	Onset potential (V, RHE)	$\eta_{10 \text{ mAcm}^{-2}}$ (V)	$J_{\eta=0.35 \text{ V}}$ mAcm ⁻²	Tafel slope (mV/dec)	TOF at $\eta = 0.35 \text{ V}$ (s ⁻¹)
3D-IrO ₂ /N@C	1.48	1.51	100	45	0.432
Comm. IrO ₂	1.53	1.63	3.1	66	0.0133

The high stability of OER catalyst in the strong corrosive environment is important for the commercialization of PEM-electrolyzer. The comparison of the chronoamperometric stability of 3D-IrO₂/N@C and comm. IrO₂ at constant potentials of 1.51 V in 0.5 M HClO₄ is shown in Figure 5.10a. This shows that the current density of comm. IrO₂ decreases very rapidly whereas 3D-IrO₂/N@C catalyst is stable at least for 10 hrs. The comm. IrO₂ showed very poor stability whereas 3D-IrO₂/N@C showed very good stability in strong acid media. We also quantified the amount of O₂ evolved (see details in ESI) in the OER experiment and compared with the amount expected during 100% faradic efficiency. The theoretically amount of O₂ was calculated from accumulated charge during electrolysis by assuming 100% efficiency. The amount of experimentally evolved O₂ was matched well with the ~98 % faradic efficiency during the experimental period of 40 min (Figure 5.10b). This 3D-IrO₂/N@C hybrid was removed from Ti foil and then its catalytic activity was studied. The GC modified 3D-IrO₂/N@C hybrid was applied as an anode for OER under similar experimental condition. The comparison of OER polarization curves of 3D-IrO₂/N@C/GC (sample scratched from Ti foil) and 3D-IrO₂/N@C /Ti. This shows that the catalytic activity of 3D-IrO₂/N@C remains almost unchanged even after removing from Ti-foil (Figure 5.10c).

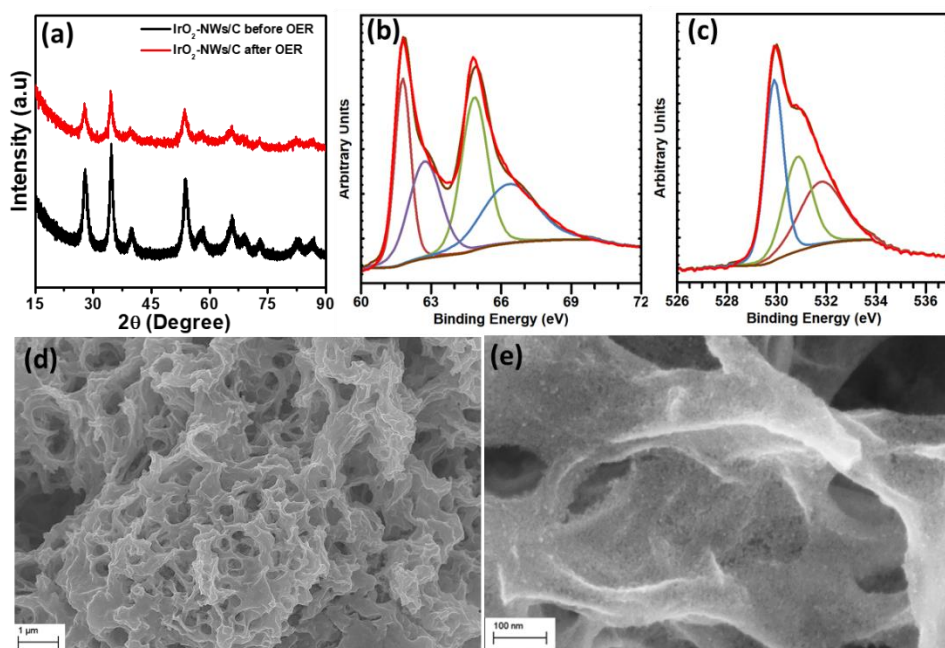


Figure 5.12. (a) p-XRD of 3D-IrO₂/N@C before and after 10 hrs of OER stability. High resolution 4f XPS spectra of (b) Ir (c) O1s (d-e) FESEM images of 3D-IrO₂/N@C after 10h OER stability.

We have grown the 3D-IrO₂/N@C hybrid with different loading of Ir and the effect of catalyst loading on the electrode towards OER was studied as shown in Figure 5.11a. Although with increasing Ir-mass loading on Ti-foil, geometric current density was increased linearly, but MA values of the electrodes remain almost same (Figure 5.11b). We have also synthesized the catalyst at different temperatures and good catalytic activity was obtained when calcination temperature was between 300 °C to 500 °C (Figure 5.11c,d) and best activity and best activity was obtained at 400 °C temperature. The characterization of the OER catalyst after the stability test is important as it gives the information about phase-decomposition, surface oxidation state, morphology, electronic state after the OER stability. We have characterized the 3D-IrO₂/N@C hybrid after 10h chronoamperometric OER stability test. The comparison of the p-XRD patterns of the 3D-IrO₂/N@C before and after stability test is provided in Figure 5.12a. This shows that peak positions in both the XRD patterns are same, suggesting there is no phase change of the catalyst after stability (Figure

5.12a). The Ir 4f XPS and O_{1s} spectra of the 3D-IrO₂/N@C hybrid after stability were deconvoluted in Figure 5.12b, c. The presence of peaks at 61.8, 62.4 eV (4f_{7/2}, 4f_{5/2} of Ir⁺⁴ species) and 529.9 eV for (Ir bonded oxygen) which are similar to XPS spectra of freshly prepared compound (Figure 5.7 b, c and d) suggests electronic structure and phase of IrO₂ remains same after stability. The FESEM images after OER shows the same porous 3D hierarchical morphology of the catalyst as shown in the Figure 5.12d, e. The post characterization of catalyst, 3D-IrO₂/N@C suggests that it retains the same structure and morphology even after 10h of stability test. The 3D-IrO₂/N@C hybrid showed superior catalytic activity towards OER in acid medium and its OER activity was compared with different other catalysts reported in the literature^{16,17,49,50} in Table S5.1. Based on the above results and Table S5.1, this 3D-IrO₂/N@C catalyst is one of the best OER catalysts in acid^{14,15, 44,45}.

5.4.3 Hydrogen Evolution Reaction (HER) by 3D-IrO₂/N@C hybrid in acidic

medium:

The HER activity of 3D-IrO₂/N@C catalyst was then evaluated for HER in an acid medium in N₂ saturated acid solution using LSV with a scan rate of 10 mV/sec. The LSV polarization curves current density vs. potential of 3D-IrO₂/N@C catalyst, comm. Pt/C, comm. IrO₂, N@C and Ti foil for HER in 0.5 M HClO₄ solution is shown in Figure 5.13a. It exhibits that comm. Pt/C and 3D-IrO₂/N@C show the superior HER activity with a zero volt onset potential but, Ti foil, N@C modified Ti electrode was almost inert as these two shows a high onset potential and overpotential for an appreciable amount of current density.

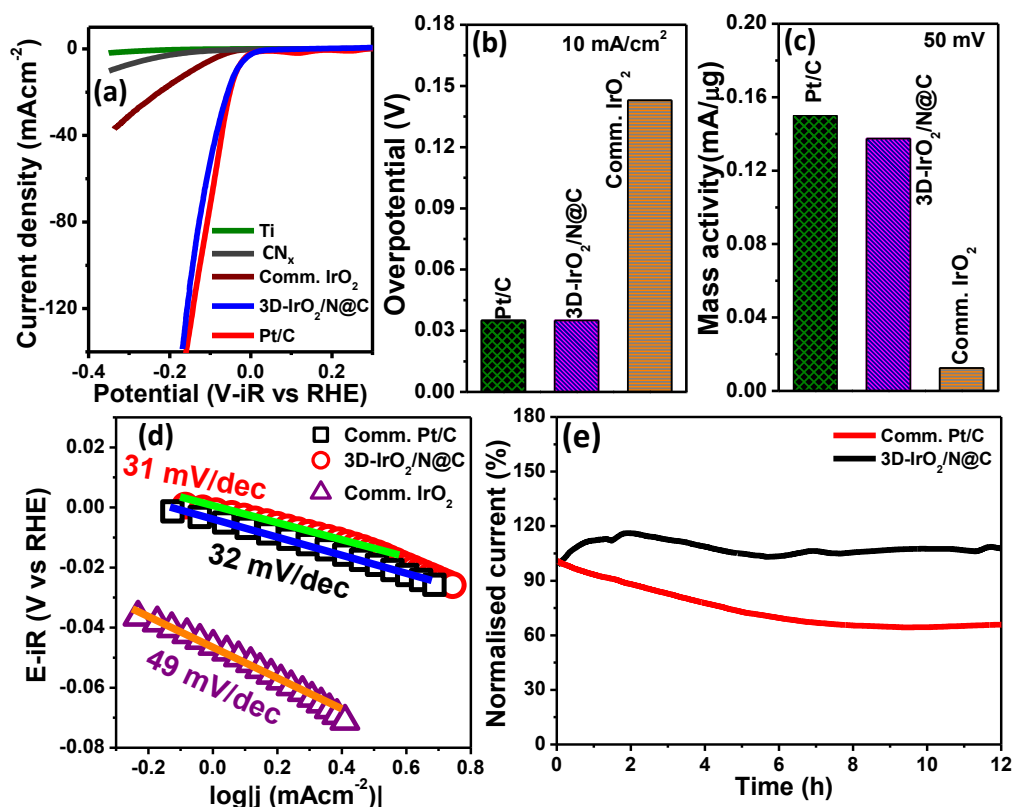


Figure 5.13. HER performance of various electrodes: (a) LSV polarization curves of 3D-IrO₂/N@C, comm. IrO₂, comm. Pt/C in 0.5 M HClO₄ with scan rate of 10 mV/s in N₂ saturated medium. (b) Overpotential required to achieve 10 mA/cm² current density for 3D-IrO₂/N@C, comm. Pt/C and comm. IrO₂ catalyst. (c) MA of 3D-IrO₂/N@C, comm. Pt/C and comm. IrO₂ at -50 mV. (d) Tafel slope of 3D-IrO₂/N@C, comm. Pt/C and comm. IrO₂ (e) Steady-state chronoamperometric stability (at 35 mV) of 3D-IrO₂/N@C and comm. Pt/C in 0.5 M HClO₄.

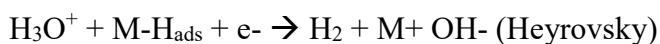
The 3D-IrO₂/N@C and comm. Pt/C catalyst requires a significantly lower over-potential to achieve a significant current density. In 0.5 M HClO₄ medium, the overpotential required for both 3D-IrO₂/N@C and comm. Pt/C catalyst to drive the current density of 10 mAcm⁻² is 35 mV (Figure 5.13b and Table 5.2). Comm. IrO₂ requires a large overpotential (145 mV) to acquire 10 mA cm⁻² current density. In order to investigate the intrinsic properties such as mass activity (MA, current normalized by mass of Ir and Pt on the electrode) was evaluated at 50 mV (Figure 5.13 c).

Table 5.2. Comparison of HER activity of different catalysts in 0.5 M HClO₄.

Catalyst	Onset potential (V _{RHE})	η ₁₀ (mV)	J _{η=0.05V} (mAcm ⁻²)	Tafel slope (mV/dec)	Exchange current (mA/cm ²)
3D-IrO ₂ /N@C	0	-35	-16.5	31	0.996
Pt/C	0	-35	-18	32	0.90

The MA at 50 mV of 3D-IrO₂/N@C is ~0.14 mA/μg_{Ir}, slightly lower than the comm. Pt/C (~0.155 mA/μg_{Pt}) (Figure 5.13 c and Table 5.2). The HER Tafel slope is an inherent property of the catalyst and can be obtained from Tafel equation ($\eta = a + b \log|J|$) where b is the Tafel slope). It is well known that HER in acidic medium undergoes in two steps in acidic medium^{31,51}:

Step 1



Step 2



The HER Tafel slope value is 118, 39 and 30 mV/dec when the rate determining step is Volmer, Heyrovsky and Tafel respectively. The HER Tafel plot showing log|j| vs. applied potential for Pt/C, 3D-IrO₂/N@C is presented in Figure 5.13d. The Tafel slope values of 3D-IrO₂/N@C and comm. Pt/C are found to be 31 and 32 mV/dec respectively. This Tafel slope value suggests that HER follows the Tafel-Volmer mechanism in the acidic medium where desorption of hydrogen is the rate-determining step (Tafel step). The exchange current density (j₀) is also an important kinetic parameter that explores the rate of electron transfer at the reversible condition. The exchange current density for 3D-IrO₂/N@C in 0.5 M HClO₄ medium was 0.996 mAcm⁻² which are comparable to comm. Pt/C electrode (0.9 mA cm⁻²)

and is also higher or comparable to other related systems^{16, 52-54} (Table S5.2). The long-term HER durability of a catalyst in acid media is important for its commercialization of PEMFCs. The main problem associated with the Pt/C is the stability of the catalyst. The aggregation of Pt nanoparticles due to the degradation of carbon support is the main reason for the decrease in stability of the comm. Pt/C in strong oxidizing condition. The long-term stability by chronoamperometric measurement (at 35 mV) shows the decrease of 50 % current density of comm. Pt/C at the end of the 12 h (Figure 5.13 e). But in the same experimental condition 3D-IrO₂/N@C shows an initial increase in current density and after 6h it delivers a constant current density. Thus 3D-IrO₂/N@C is extremely stable at long-term chronoamperometric operation. The HER activity of the 3D-IrO₂/N@C catalyst and other reported catalyst was compared in Table S5.2. The 3D-IrO₂/N@C shows better or similar activity with respect to onset potential, over potential (at 10 mA/cm²), Tafel slope, MA, compared to noble and non-noble metal based catalyst^{16,52,53,55-59}. Though few reports are available for HER in basic medium^{41,60} of IrO₂, there is no such good report of HER catalyst in an acid medium in the literature.

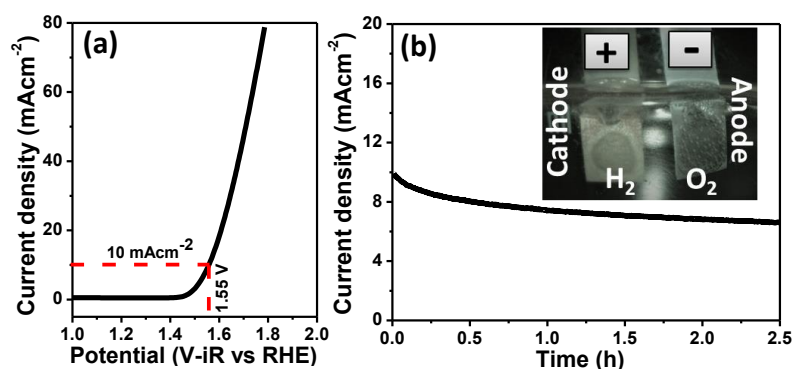


Figure 5.14. (a) LSV polarization curve of overall water splitting using 3D-IrO₂/N@C as a cathode as well as an anode in 0.5 M HClO₄ at 10 mV/s scan rate. (b) The chronoamperometric response of 3D-IrO₂/N@C at 1.55 V. Inset: Photograph of cathode and anode.

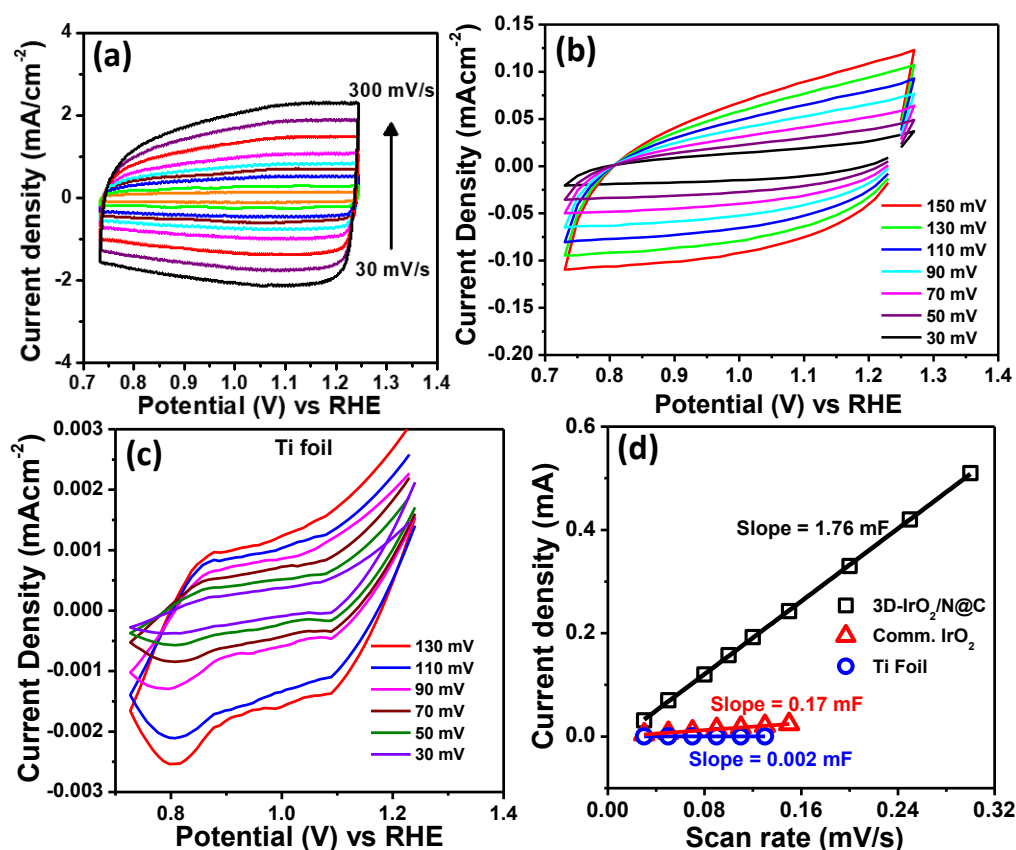


Figure 5.15. (a) CV curves of 3D-IrO₂/N@C hybrid with a different scan rate starting from 30 to 300 mV/s. CV curves of (b) comm. IrO₂ (c) Ti foil in a potential range 0.75-1.25 V (vs. RHE) with different scan rate in 0.5 M HClO₄. (d) Linear plot of double layer current vs. scan rate 3D-IrO₂/N@C comm. IrO₂ and Ti foil in 0.5 M HClO₄ at a potential of 1.1 V in RHE.

Based on the above result of OER and HER of 3D-IrO₂/N@C catalyst in the acidic medium we believed that this catalyst should work well as a bifunctional catalyst for overall water splitting in acidic medium. Bi-functionality of the 3D-IrO₂/N@C catalyst was studied by applying a two-electrode configuration where 3D-IrO₂/N@C catalyst was used as both cathode and anode (see SI for details). The LSV curve in 0.5 M HClO₄ is shown in Figure 5.14a. The overall water splitting shows the catalyst requires onset potential of 1.48 V and shows overpotential of 320 mV for achieving a current density of 10 mA/cm² as shown in Figure 5.14a. The long-term stability measurement (Figure 5.14 b) also confirmed the extraordinary stability of the catalyst in two electrode configuration. Although good overall

water splitting catalysts in basic medium is available^{11,34-36} in the literature, however catalysts for overall water splitting in acid medium is rare^{11,34-36}. This proves that this catalyst can be used as a bifunctional catalyst for overall water splitting in acidic medium.

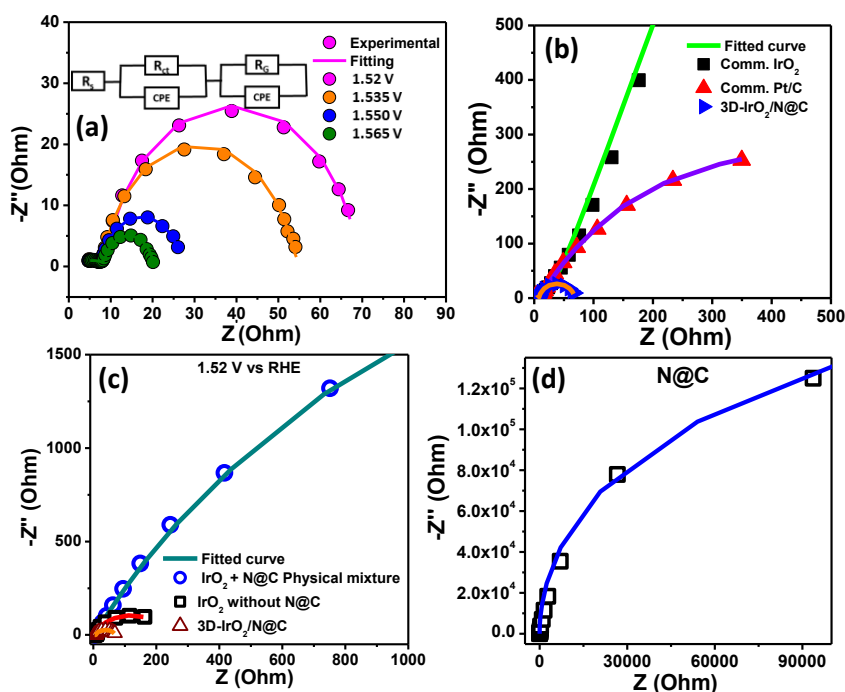


Figure 5.16. (a) EIS spectra of 3D-IrO₂/N@C in 0.5 M HClO₄ at different voltages. Inset: Equivalent circuit for the fitting of the EIS curves. (b) Comparison of EIS spectra of the different catalysts at 1.52 V. (c) Comparison of EIS spectra of 3D-IrO₂/N@C, a physical mixture of IrO₂ and N@C, IrO₂ (IrO₂ was synthesized by heating Ir salt at 400°C) and (d) N@C at 1.52 V (RHE).

5.4.4 Factors responsible for the high catalytic activity of 3D-IrO₂/N@C:

The superior catalytic activity and excellent stability of 3D-IrO₂/N@C for HER and OER in the acidic medium could be attributed to following several factors:

- (1) The large active surface area is one of the important factors required for a good electrocatalyst. It helps in the enhancement of the catalytic activity of the catalyst with increasing number of the active site. The active surface area of 3D-IrO₂/N@C catalyst was evaluated by measuring the double layer capacitance (C_{dl}) as these are directly proportional to active surface area (see details of the procedure for calculation of C_{dl} in SI). Figure 5.15 (a-c) show the CV curves of the different catalysts in non-faradic regions. The linear plot of

current vs. scan rate of corresponding CV curves was given in Figure 5.15d. The C_{dl} were 1.78 mF which are much higher than the comm. IrO_2 (0.17 mF). These results demonstrated that the catalytically active surface area increased due to the porous hierarchical 3D morphology of the 3D- $\text{IrO}_2/\text{N}@C$ catalyst.

(2) The superior HER/OER activity and stability could be originated from unique three-dimensional hierarchical porous nanostructures hybrid. The 3D interconnected continuous porous 3D- $\text{IrO}_2/\text{N}@C$ electrode gives continuous electron transport and it has low charge-transfer resistance³⁵⁻³⁶. Figure 5.16a the electrochemical impedance spectra (EIS) of this 3D- $\text{IrO}_2/\text{N}@C$ hybrid at a different voltage (in-set of this Figure 5.16a is equivalent circuit). The EIS spectra of the 3D- $\text{IrO}_2/\text{N}@C$ hybrid were compared with comm. IrO_2 and comm. Pt/C in Figure 5.16d. The charge transfer resistance of 3D- $\text{IrO}_2/\text{N}@C$ hybrid is found to be 57 ohm which is much lower than that of comm. IrO_2 (53 k Ω) and Pt/C (997 Ω).

(3) The porous morphology of 3D- $\text{IrO}_2/\text{N}@C$ hybrid /electrode facilitates easies mass transport through the electrode. The reactant or electrolyte can easily reach to active sites and products can easily come out from the sites through porous structure⁶¹⁻⁶². In addition, adhesion of evolved gas such as H_2 or O_2 on the flat surface forms bubbles which block electrolytic diffusion, Ohmic drops leading to reduce performances of flat catalyst in compared to porous structure⁶³. The porous morphology of 3D- $\text{IrO}_2/\text{N}@C$ hybrid may increases mass-transport to the active catalytic sites and thereby enhances HER and OER activity of the catalyst.

(4) The in-situ growth of 3D- $\text{IrO}_2/\text{N}@C$ on N-doped carbon to form 3D- $\text{IrO}_2/\text{N}@C$ hybrid suggests there may be strong interaction between IrO_2 and carbon. The synergistic strong interaction between IrO_2 and N-doped carbon could be one of the reasons for their high HER/OER activity^{16,52,53}. It was found that HER/OER activity of 3D- $\text{IrO}_2/\text{N}@C$ is

better than that of carbon-free- IrO₂ catalyst and physical mixture of IrO₂ and N-doped carbon suggesting a catalyst-support interaction. As discussed in the previous section, the decrease of UV-Visible peak of a mixture of N-doped C and [IrCl₆]²⁻ also suggest an interaction between Ir⁴⁺ and N-doped C material. The comparison of EIS spectra of 3D-IrO₂/N@C, IrO₂ (without N@C) and physical mixture (IrO₂ and N@C) is provided in Figure 5.16 (c, d). The R_{ct} value of this porous hybrid is also much lower than that of physical mixture and free IrO₂ or only N@C. This proves that there is a strong synergistic interaction between IrO₂ and N@C in the 3D-IrO₂/N@C hybrid. The presence of nitrogen in N-doped carbon support also helps to enhance the OER/HER activity of the 3D-IrO₂/N@C catalyst^{52, 64}.

(5) The direct growth of 3D-IrO₂/N@C in conducting Ti-foil enhances electron transport and strong bonding between 3D-IrO₂/N@C and Ti-foil gives strong structural stability for long-term stability. Generally for electrochemical studies, polymer binders such as nafion, PTFE *etc.* are used for immobilization of catalyst on the electrode surface. The polymer binder may block active catalytic sites, reduce diffusion and also increases series resistance – the catalytic activity of the catalyst is thus reduced due to use of polymer binder⁶⁵. In this case, no-polymer or conductive additives were used. Therefore, in-situ growth on conducting Ti-foil also helped to enhance OER and HER activity and stability of the catalyst, 3D-IrO₂/N@C.

5.5 CONCLUSION

In conclusion, we have demonstrated a method for the development of three-dimensional hierarchical N@C porous network electrode incorporating IrO₂ as active and stable bifunctional electrode for over-all water splitting in acid media. This 3D interconnected continuous porous network show high surface area, allow easy electron and mass transport

through the electrode. When this hybrid was applied as OER catalyst in acid, it exhibited low overpotential (10 mA/cm² at 280 mV), low Tafel slope (45 mV/dec) and high mass activity and TOF values. Moreover, this 3D-IrO₂/N@C hybrid showed superior HER activity in acid. The HER activity of 3D-IrO₂/N@C hybrid in acid media is better than comm. Pt/C. This hybrid also showed out-standing OER and HER stability in strong acid media. When applied for overall water splitting as a bifunctional electrocatalyst, 3D-IrO₂/N@C hybrid required a small overpotential of 1.55 V for a current density of 10 mA/cm². To best of our knowledge, this is the best bifunctional catalyst for over-all water splitting in acid media. The superior activity of this hybrid is due to the unique porous structure of the hybrid, high surface area, easy electron/ mass transport and strong synergistic interaction between IrO₂ and N@C support. The excellent HER and OER performance in acid media indicates the promising application of this unique 3D hierarchical interconnected porous IrO₂/N@C hybrid for PEM-devices and other electrochemical energy conversion and storage devices.

5.6. REFERENCES

- (1) Wang, Y.-J.; Long, W.; Wang, L.; Yuan, R.; Ignaszak, A.; Fang, B.; Wilkinson, D. P. *Energy Environ. Sci.* **2018**, *11*, 258-275.
- (2) Aneke, M.; Wang, M. *Applied Energy* **2016**, *179*, 350-377.
- (3) Kraytsberg, A.; Ein-Eli, Y. *Energy & Fuels* **2014**, *28*, 7303-7330.
- (4) Sapountzi, F. M.; Gracia, J. M.; Weststrate, C. J.; Fredriksson, H. O. A.; Niemantsverdriet, J. W. *Progress in Energy and Combustion Science* **2017**, *58*, 1-35.
- (5) You, B.; Sun, Y. *Acc. Chem. Res.* **2018**.
- (6) Pan, J.; Xu, Y. Y.; Yang, H.; Dong, Z.; Liu, H.; Xia, B. Y. *Adv. Sci.* **2018**, *5*, 1700691.

- (7) McCrory, C. C. L.; Jung, S.; Ferrer, I. M.; Chatman, S. M.; Peters, J. C.; Jaramillo, T. F. *J. Am. Chem. Soc.* **2015**, *137*, 4347-4357.
- (8) McCrory, C. C. L.; Jung, S.; Peters, J. C.; Jaramillo, T. F. *J. Am. Chem. Soc.* **2013**, *135*, 16977-16987.
- (9) Roger, I.; Shipman, M. A.; Symes, M. D. *Nat. Rev. Chem.* **2017**, *1*, 0003.
- (10) Burke, M. S.; Enman, L. J.; Batchellor, A. S.; Zou, S.; Boettcher, S. W. *Chem. Mater.* **2015**, *27*, 7549-7558.
- (11) Bhowmik, T.; Kundu, M. K.; Barman, S. *ACS Appl. Energy Mater.* **2018**.
- (12) Cheng, Y.; Jiang, S. P. *Progress in Natural Science: Materials International* **2015**, *25*, 545-553.
- (13) Tobias, R.; Nhan, N. H.; Detre, T.; Robert, S.; Peter, S. *Adv. Energy Mater.* **2017**, *7*, 1601275.
- (14) Chen, S.; Thind, S. S.; Chen, A. *Electrochem. Commun.* **2016**, *63*, 10-17.
- (15) Nong, H. N.; Gan, L.; Willinger, E.; Teschner, D.; Strasser, P. *Chem. Sci.* **2014**, *5*, 2955-2963.
- (16) Bhowmik, T.; Kundu, M. K.; Barman, S. *ACS Appl. Mater. Interfaces* **2016**, *8*, 28678-28688.
- (17) Audichon, T.; Napporn, T. W.; Canaff, C.; Morais, C.; Comminges, C.; Kokoh, K. B. *J. Phys. Chem. C* **2016**, *120*, 2562-2573.
- (18) Jinkyu, L.; Dongmin, P.; Seo, J. S.; Chi-Woo, R.; Juhyuk, C.; Daejin, Y.; Minju, P.; Hyeyoung, J.; Hyunjoo, L. *Adv. Funct. Mater.* **2018**, *28*, 1704796.
- (19) Tariq, M.; Zaman, W. Q.; Sun, W.; Zhou, Z.; Wu, Y.; Cao, L.-m.; Yang, J. *ACS Sustainable Chem. Eng.* **2018**, *6*, 4854-4862.
- (20) Shi, Q.; Zhu, C.; Du, D.; Wang, J.; Xia, H.; Engelhard, M. H.; Feng, S.; Lin, Y. *J. Mater. Chem. A* **2018**, *6*, 8855-8859.

- (21) Yang, X.; Li, Y.; Deng, L.; Li, W.; Ren, Z.; Yang, M.; Yang, X.; Zhu, Y. *RSC Adv.* **2017**, *7*, 20252-20258.
- (22) Park, J.; Sa, Y. J.; Baik, H.; Kwon, T.; Joo, S. H.; Lee, K. *ACS Nano* **2017**, *11*, 5500-5509.
- (23) Oakton, E.; Lebedev, D.; Povia, M.; Abbott, D. F.; Fabbri, E.; Fedorov, A.; Nachtegaal, M.; Copéret, C.; Schmidt, T. J. *ACS Catalysis* **2017**, *7*, 2346-2352.
- (24) Hu, W.; Wang, Y.; Hu, X.; Zhou, Y.; Chen, S. *J. mater. Chem.* **2012**, *22*, 6010-6016.
- (25) Ye, E.; Regulacio, M. D.; Zhang, S.-Y.; Loh, X. J.; Han, M.-Y. *Chem. Soc. Rev.* **2015**, *44*, 6001-6017.
- (26) Xu, G.-R.; Bai, J.; Yao, L.; Xue, Q.; Jiang, J.-X.; Zeng, J.-H.; Chen, Y.; Lee, J.-M. *ACS Catal.* **2017**, *7*, 452-458.
- (27) Scofield, M. E.; Koenigsmann, C.; Wang, L.; Liu, H.; Wong, S. S. *Energy Environ. Sci.* **2015**, *8*, 350-363.
- (28) Li, G.; Li, S.; Xiao, M.; Ge, J.; Liu, C.; Xing, W. *Nanoscale* **2017**, *9*, 9291-9298.
- (29) Smith, R. D. L.; Spornova, B.; Fagan, R. D.; Trudel, S.; Berlinguette, C. P. *Chem. Mater.* **2014**, *26*, 1654-1659.
- (30) Jürgensen, L.; Frank, M.; Pyeon, M.; Czypiel, L.; Mathur, S. *Organometallics* **2017**, *36*, 2331-2337.
- (31) Sudip, B.; Manas, K.; Tanmay, B.; Ranjit, M. *ChemSusChem* **2018**, *11*, 2388-2401.
- (32) Cao, M.; Wu, D.; Cao, R. *ChemCatChem* **2014**, *6*, 26-45.
- (33) Durst, J.; Simon, C.; Hasché, F.; Gasteiger, H. A. *J. Electrochem. Soc.* **2015**, *162*, F190-F203.
- (34) Wang, J.; Cui, W.; Liu, Q.; Xing, Z.; Asiri, A. M.; Sun, X. *Adv. Mater.* **2016**, *28*, 215-230.

- (35) Gao-Feng, C.; Yi, M. T.; Zhao-Qing, L.; Nan, L.; Yu-Zhi, S.; Kenneth, D.; Shi-Zhang, Q. *Adv. Funct. Mater.* **2016**, *26*, 3314-3323.
- (36) Kim, H.; Oh, S.; Cho, E.; Kwon, H. *ACS Sustainable Chem. Eng.* **2018**, *6*, 6305-6311.
- (37) Barman, S.; Sadhukhan, M. *J. Mater. Chem.* **2012**, *22*, 21832-21837.
- (38) Bhowmik, T.; Kundu, M. K.; Barman, S. *Int. J. Hydrogen Energy* **2016**, *41*, 14768-14777.
- (39) Sadhukhan, M.; Barman, S. *J. Mater. Chem. A* **2013**, *1*, 2752-2756.
- (40) Anantharaj, S.; Karthik, P. E.; Kundu, S. *J. Mater. Chem. A* **2015**, *3*, 24463-24478.
- (41) Kwak, I.; Kwon, I. S.; Kim, J.; Park, K.; Ahn, J.-P.; Yoo, S. J.; Kim, J.-G.; Park, J. *J. Phys. Chem. C* **2017**, *121*, 14899-14906.
- (42) Sun, W.; Liu, J.-Y.; Gong, X.-Q.; Zaman, W.-Q.; Cao, L.-M.; Yang, J. *Sci. Rep.* **2016**, *6*, 38429.
- (43) Kahk, J. M.; Poll, C. G.; Oropeza, F. E.; Ablett, J. M.; Céolin, D.; Rueff, J. P.; Agrestini, S.; Utsumi, Y.; Tsuei, K. D.; Liao, Y. F.; Borgatti, F.; Panaccione, G.; Regoutz, A.; Egdell, R. G.; Morgan, B. J.; Scanlon, D. O.; Payne, D. J. *Phys. Rev. Lett.* **2014**, *112*, 117601.
- (44) Kim, S.; Cho, M.; Lee, Y. *J. Electrochem. Soc.* **2017**, *164*, B3029-B3035.
- (45) Jerng, S.-K.; Seong Yu, D.; Hong Lee, J.; Kim, C.; Yoon, S.; Chun, S.-H. *Nanoscale Research Letters* **2011**, *6*, 565-565.
- (46) Suen, N.-T.; Hung, S.-F.; Quan, Q.; Zhang, N.; Xu, Y.-J.; Chen, H. M. *Chem. Soc. Rev.* **2017**, *46*, 337-365.
- (47) Nhan, N. H.; Hyung-Suk, O.; Tobias, R.; Elena, W.; Marc-Georg, W.; Valeri, P.; Detre, T.; Peter, S. *Angew. Chem. Int. Ed.* **2015**, *54*, 2975-2979.
- (48) Li, G.; Li, S.; Ge, J.; Liu, C.; Xing, W. *J. Mater. Chem. A* **2017**, *5*, 17221-17229.
- (49) Lee, Y.; Suntivich, J.; May, K. J.; Perry, E. E.; Shao-Horn, Y. *J. Phys. Chem. Lett.* **2012**, *3*, 399-404.

- (50) Pi, Y.; Zhang, N.; Guo, S.; Guo, J.; Huang, X. *Nano Lett.* **2016**, *16*, 4424-4430.
- (51) Morozan, A.; Goellner, V.; Zitolo, A.; Fonda, E.; Donnadieu, B.; Jones, D.; Jaouen, F. *Phys. Chem. Chem. Phys.* **2015**, *17*, 4047-4053.
- (52) Bhowmik, T.; Kundu, M. K.; Barman, S. *ACS Catal.* **2016**, *6*, 1929-1941.
- (53) Kundu, M. K.; Bhowmik, T.; Barman, S. *J. Mater. Chem. A* **2015**, *3*, 23120-23135.
- (54) Roy, N.; Leung, K. T.; Pradhan, D. *J. Phys. Chem. C* **2015**, *119*, 19117-19125.
- (55) Cheng, Y.; Lu, S.; Liao, F.; Liu, L.; Li, Y.; Shao, M. *Adv. Funct. Mater.* **2017**, *27*, 1700359-n/a.
- (56) Voiry, D.; Salehi, M.; Silva, R.; Fujita, T.; Chen, M.; Asefa, T.; Shenoy, V. B.; Eda, G.; Chhowalla, M. *Nano Lett.* **2013**, *13*, 6222-6227.
- (57) Lv, H.; Xi, Z.; Chen, Z.; Guo, S.; Yu, Y.; Zhu, W.; Li, Q.; Zhang, X.; Pan, M.; Lu, G.; Mu, S.; Sun, S. *J. Am. Chem. Soc.* **2015**, *137*, 5859-5862.
- (58) Jahan, M.; Liu, Z.; Loh, K. P. *Adv. Funct. Mater.* **2013**, *23*, 5363-5372.
- (59) Jiang, P.; Liu, Q.; Sun, X. *Nanoscale* **2014**, *6*, 13440-13445.
- (60) Yan, Y.; Xia, B. Y.; Zhao, B.; Wang, X. *J. Mater. Chem. A* **2016**, *4*, 17587-17603.
- (61) Wenxin, Z.; Rong, Z.; Fengli, Q.; M., A. A.; Xuping, S. *ChemCatChem* **2017**, *9*, 1721-1743.
- (62) Dao-Jun, G.; Yi, D. *Electroanalysis* **2012**, *24*, 2035-2043.
- (63) Zhiyi, L.; Wei, Z.; Xiaoyou, Y.; Haichuan, Z.; Yingjie, L.; Xiaoming, S.; Xinwei, W.; Hao, W.; Jingming, W.; Jun, L.; Xiaodong, L.; Lei, J. *Adv. Mater.* **2014**, *26*, 2683-2687.
- (64) Negro, E.; Polizzi, S.; Vezzù, K.; Toniolo, L.; Cavinato, G.; Di Noto, V. *Int. J. Hydrogen Energy* **2014**, *39*, 2828-2841.
- (65) Roy-Mayhew, J. D.; Boschloo, G.; Hagfeldt, A.; Aksay, I. A. *ACS Appl. Mater. Interfaces* **2012**, *4*, 2794-2800.

Appendix C

Table S5.1. Comparison of OER activity of 3D-IrO₂/N@C in acidic medium with other reported catalysts.

Catalyst	Catalyst loading (mg cm ⁻²)	Onset potential (V vs. RHE)	Over potential (mV RHE) vs. current density (mA cm ⁻²)	Tafel slope (mV/dec)	MA A/g	References
IrO₂ (350 °C)	0.05	1.40	430 (10 mA cm ⁻²)	-	3 at η= 0.25 V	J. Phys. Chem. Lett. 2012, 3, 399-404.
RuO₂	0.05	1.40	450 (10 mA cm ⁻²)	-	11 at η= 0.25 V	J. Phys. Chem. Lett. 2012, 3, 399-404.
IrO₂-RuO₂@Ru (3:1)	0.379	~1.46	281 (10 mA cm ⁻²)	53.1	-	J. Mater. Chem. A, 2017, 5, 17221
IrO₂@RuO₂	0.38	~1.40	270 (10.8 mA cm ⁻²)	57.8	-	J. Phys. Chem. C 2016, 120, 2562-2573.
Ru_{0.7}Ir_{0.3}O₂	1	~1.40	270	48	-	Int. J. Hydrogen Energy. 2014, 39, 16785-16796.
1D-RuO₂-CN_x	0.012		250 (10 mA cm ⁻²)	52	-	ACS Appl. Mater. Interfaces 2016 , 8 (42), 28678-28688
Surface clean 3D Ir superstructure	0.0115	1.47	270 (10 mA cm ⁻²)	40.8	-	Nano Lett. 2016, 16, 4424-4430
Ru_{0.8}Ir_{0.2}O₂	0.38	-	> 320 (10 mA cm ⁻²)	-	-	Appl. Catal. B, 2012, 111-112, 376-380
IrO₂/Nb-TiO₂	0.23	~1.475	~310 (10 mA cm ⁻²)	-	-	ACS. Sustainable Chem. Eng., 2016, 4, 746-756.
Ir_{0.5}Ru_{0.5}O₂/ATO	0.8	-	240 (1 mA cm ⁻²)	~60	-	Electrochim. Acta, 2010, 55, 1978-1984.
Ir_{0.7}Co_{0.3}O_x	0.102	~1.52	~260 (0.5 mA cm ⁻²)	40	-	ACS Appl. Mater. Interfaces, 2014, 6, 12729-12736.
3D-IrO₂/N@C	0.12	1.48	280 (10 mA cm ⁻²)	45	833 at η= 0.35 V	This Paper

Table S5.2. Comparison of HER activity of 3D-IrO₂/N@C in 0.5 M HClO₄ with other reported catalysts.

Catalyst	Catalyst loading (mg cm ⁻²)	Onset potential (mV vs. RHE)	Over potential (mV RHE) vs. current density (mA cm ⁻²)	Tafel slope (mV/dec)	Exchange current (mAcm ⁻²)	Ref
Au-aerogel-CN _x	0.127	-30	-225 (20 mA cm ⁻²)	53	0.03	J. Mater. Chem.A 2015 , 3 , 23120
Pd-CN _x	0.043	12	55	35	0.40	ACS Catal. 2016 , 6 , 1929
1D-RuO ₂ -CN _x	93	-14	-93 (10 mA cm ⁻²)	40	0.22	ACS appl. Mater. interfaces 2016 , 8 , 28678.
Pt _{tripods} @PAA	-0.081	+19.6	-25(90 mA cm ⁻²)	-	-	ACS Catal. 2017 , 7 , 452
PtNSSs@PEI	0.089	+64.6	-25 (143 mA cm ⁻²)	28	-	Chem. Sci. 2017 , 8 , 8411-8418
PtNiCu	0.06	0	-50 (143 mA cm ⁻²)	28	-	Chem. Sci. 2017 , 8 , 8411
Pt ₁₃ Cu ₇₃ Ni ₁₄ /CN F @CF	-	+5	70	38	-	ACS Appl. Mater. Interfaces 2016 , 8 , 3464
Pt _{tripods} @PAA	-0.081	+19.6	-25(90 mA cm ⁻²)	-	-	ACS Catal. 2017 , 7 , 452
WPNA _s /CC	2	-50	-130 (10 mA cm ⁻²)	69	0.29	ACS Appl. Mater. Interfaces 2014 , 6 , 21874
MoP-CA2	0.36	-40 (IR free)	-125 (10 mA/cm ²)	54	0.086	Adv. Mater. 2014 , 26 , 5702.
Nano MoP	1	-	-110 (10 mA cm ⁻²)	45	0.12	Chem. Mater. 2014 , 26 , 4826
NiAu/Au	-	-7	-	36	-	J. Am. Chem. Soc. 2015 , 137 , 5859
A-Ni-C	-	-	-34 (10 mA cm ⁻²)	41	1.2	Nat. Commun. 2016 , 7 , 10667
(GO 8 wt%) Cu-MOF	0.226	-87	-400 (122.48 mA cm ⁻²)	84	-	Adv. funct. mater. 2013 , 23 , 5363
CoP/CC	0.92	-38	67 (10 mA cm ⁻²)	51	0.288	J. Am. Chem. Soc. 2014 , 136 , 7587
CoN _x /C	2	-20	133	57	0.07	Nat. Commun. 2015 , 6 , 7992
NiP ₂ NS/CC	4.3	-50	-75 (10 mA cm ⁻²)	51	0.26	Nanoscale 2014 , 6 , 13440
Co-NRCNT	0.28	-50	-260 (10 mA cm ⁻²)	69	0.01	Angew. Chem. Int. Ed. 2014 , 126 , 4461
CoSe ₂	0.37	-30	-90 (4 mA cm ⁻²)	40	0.037	Energy Environ. Sci. 2013 , 6 , 3553
MoS ₂ /CoSe ₂	0.28	-11	-68 (10 mA cm ⁻²)	36	0.073	Nat. Commun. 2015 , 6 , 5982
Ni ₂ P	-	-25	-130 (20 mA cm ⁻²)	-46	0.033	J. Am. Chem. Soc. 2013 , 135 , 9267
Ni-Mo-N nanosheets	0.25	-78	~ -200 mV (3.5 mA cm ⁻²)	35.9	0.24	Angew. Chem. Int. Ed. 2012 , 51 , 6131
Pt-SiO ₂	0.168	-0.225(SHE)	-500 (200mAcm-2)	32	-	RSC. Adv. 2014, 4 , 50114-50122.
Pt-TiO ₂	0.04	-	-300 (97mAcm-2)	32	0.19	J. Phys. Chem. C 2015 , 119 , 19117-19125.
Pt-W ₂ C	2	-	-10 (16 mAcm-2)	103	2.08	Int. J. Hydrogen Energy. 2008, 33 , 6865-6872.
Pt-SnO ₂	0.13	-	-300 (40 mAcm-2)	111	0.46	Catal. Lett. 2012, 142 , 809-815.
Pt-TiO ₂ - N-rGO	0.04	-	-300 (126mAcm-2)	32	0.22	J. Phys. Chem. C 2015 , 119 , 19117-19125.
3D-IrO ₂ /N@C	0.12	0	-35 (10 mA cm ⁻²)	31	0.996	This Paper

Chapter 6

Interconnected One-dimensional Silver Nanowires Supported on Carbon Nitride: A Stable and Highly Efficient Electrocatalyst for Hydrogen Evolution Reaction and Oxygen Reduction Reaction

6.1 ABSTRACT

The electrochemical HER and ORR are two important processes for the development of renewable energy technologies such as water splitting, FCs, batteries etc. Developing low-cost (precious metal free), highly active and stable electro-catalyst is essential for the practical commercialization of these technologies. In this chapter, a highly active and durable carbon nitride supported interconnected silver nano-wires (AgNWs-CN_x) electrocatalyst for HER and ORR applications was demonstrated. This catalyst exhibited superior HER activity that out-performs commercial Pt/C in both acid and base medium. Like Pt/C, on-set potential of this AgNWs-CN_x electro-catalyst is 0 mV in both medium and the Tafel slopes of this catalyst are 32 mV/dec and 65 mV/dec in acid and base respectively. It requires over-potentials of 25 mV and 85 mV to achieve the current densities of 10 and 50 mA/cm² respectively in acid whereas 110 mV and 290 mV needed to attain the same current densities in base. Most importantly this catalyst showed excellent durability in repeated cycling and long term chronoamperometric studies that confirmed its extraordinary stability in the acid medium. Furthermore, this AgNWs-CN_x catalyst showed superior activity towards ORR in base medium as the one-set potential and half wave potential ($E_{1/2}$) of this Ag catalyst are comparable to that of Pt/C in base. This catalyst also showed excellent

methanol tolerance and superior durability in ORR. The superior electro-catalytic activity of the interconnected AgNWs-CN_x are likely due to its hierarchical 3D porous morphology, presence of hetero atoms and 1-D wires like structure. This work may provide new opportunity to design and develop hierarchical porous electro-catalyst for development of PEMFCs, alkaline fuel cells and other renewable energy technologies.

6.2 INTRODUCTION

Since the concerns for the energy shortage and environmental pollution due to use of fossil fuel are rising, there is urgent demand for renewable energy sources alternative to fossil fuels¹⁻². The electrochemical energy generation is considered as one of the best viable green approaches for energy production³. Molecular hydrogen is considered as a clean fuel (energy carrier) alternative to fossil fuel due to its high storage density and environmental friendliness⁴. The electrochemical water splitting via hydrogen evolution reaction (HER) offers easy method for hydrogen production on a large scale⁵. The oxygen reduction reactions (ORR) is another important critical process for cathodes of electrochemical energy applications such as fuel cells, metal-air batteries^{1,6}. Owing to sluggish kinetics of these processes electro catalyst is required for practical applications. Platinum supported carbon (Pt/C) is the best known HER catalyst in both acid and base medium. But, the high cost and scarcity of platinum limits its wide spread commercialization⁷. Another major disadvantage of Pt based electro-catalysts is its poor stability in strong acidic medium. The most popular proton exchange membrane (PEM) technology and many solar water splitting devices operate under strong acidic conditions. The dissolution of carbon support in strong oxidizing medium of Pt/C leading to agglomeration of small Pt particles made it unstable in this acidic working condition. The stability of HER catalyst in acid medium is critical for the development of PEM based technology. Although enormous efforts have been given in recent years to find suitable acid medium HER catalyst, all efficient catalysts based transition

metals such as Ni⁸, Co⁹, Fe¹⁰, Mo¹¹⁻¹² *etc.* are generally susceptible to dissolution in acidic conditions. It is thus highly desirable to find noble metal free HER catalyst for the replacement Pt/C in acidic conditions. The water electrolysis in alkaline media has also received special attention due to its several advantages such as good manufacturing safety, high product purity, unlimited reactant availability *etc.* Although Pt is best catalyst but its activity in basic solution is two times lower than that of acidic medium^{13,14,10}. The high over-potential and large energy consumption in basic medium are the main obstacles for the practical applications of alkaline electrolysis. The nickel alloys based HER catalysts are active in basic medium^{15,8}. Non-noble metal materials such as MoS₂ nanosheet¹⁶, molybdenum phosphide¹⁷, cobalt/ nickel tungsten sulfide¹⁸, iron-nickel sulphide¹⁹, cobalt selenide²⁰, tungsten thin film²¹ *etc.* are recently reported as active catalyst in acidic medium. Very few catalyst such as Co_xFe_(1-x)P²², MoP¹⁷, NiP²³, Tungsten phosphide²⁴ Co embedded nitrogen rich carbon nanotube²⁵ *etc.* are reported recently for active in both acidic and basic medium. But their activity and stability is still inferior as compared to the platinum in both acid and base media. Therefore, it is highly desirable to develop highly active and durable HER catalyst for both acid and base electrolysis. In case of ORR, Pt/C is also best catalyst, but its cost and stability are the main obstacles for its practical applications²⁶. The methanol cross-over effect of Pt based catalyst leading to reduce fuel efficiency significantly in the direct methanol fuel cells (DMFCs) is another major problem²⁷. Despite enormous efforts it still remain a challenge to develop a cost-effective robust ORR catalyst for practical applications. Silver is generally considered as a viable alternative to Pt for ORR in alkaline fuel cells since silver is less expensive and oxygen reduction on silver surface occurs via 4e- electron reduction pathway²⁸⁻³¹. But, overall catalytic activity of the reported Ag catalysts for ORR is inferior to that of Pt.

In recent years, one-dimensional (1-D) metal nano-structures have received considerable interest for its various applications^{32,33}. The 1-D noble metal nanostructures were found to be suitable electro-catalyst especially for ORR in PEM fuel cell because of unique anisotropic nature of 1-D materials, extended smooth defect free facets, fewer lattice boundaries and surface to volume ratio^{34,35}. All these properties are desirable for fuel cell catalysts. 1-D noble metal electro-catalysts were reported for better activity than that of commercial Pt/C for ORR³⁵ and alcohol oxidation³⁶ reactions. Three dimensional hierarchical porous materials^{37,38} have drawn a tremendous attention due to their exceptionally high potential applications in catalyst support, electrodes, sensors, absorbents. These properties arise due to their ability to interact with the atoms or ions or molecules throughout the bulk of the materials, not only by their surfaces. It was reported by several groups³⁸ that hierarchical porous structure enhanced durability as well as stability of an electro-catalyst.

Herein, ultrasound assisted surfactant-free in-situ growth of interconnected AgNWs on carbon nitride for their applications in HER and oxygen reduction (ORR) reaction in both acid and base media was demonstrated. These interconnected AgNWs are used as building blocks for the formation of 3-D hierarchical porous structures. The hierarchical structure of AgNWs is catalytically activated by repeated cycling scans (ac-AgNWs-CN_x). These ac-AgNWs-CN_x catalyst showed superior activity towards hydrogen evolution in both acid and base medium. In the both medium activity of this Ag catalyst out-performed commercial Pt/C catalyst. Most importantly, stability tests confirmed it has remarkably high long term durability in acid media. In addition, this Ag catalyst also exhibited superior activity for ORR in acid and base media. The oxygen reduction occurs via 4-electron reduction pathway at this ac-AgNWs-CN_x catalyst and its activity and durability in basic medium is comparable to commercial Pt/C. This catalyst is also highly active for ORR in acid media. The superior

electro-catalytic activity of ac-AgNWs-CN_x catalyst can be attributed to its hierarchical 3D porous morphology, presence of hetero atoms and one-dimensional highly crystalline Ag wire-nanostructures.

6.3 EXPERIMENTAL SECTION

Preparation of AgNWs-CN_x composite

The 10 mg of as prepared g-CN_x was dispersed in 5 ml of water by sonication for 10 min. The aqueous solution of 120 mg of AgNO₃ was also prepared in a separate vial. These two solutions were mixed together followed by sonication for 10 minute. Then solid NaBH₄ was added and the mixture was ultra-sounded with ~28 kHz frequency for two and half hours at 400 watt. After ultrasound treatment the freshly formed solid product was separated by centrifugation at 12,000 rpm for 30 minutes. After washing with water, Ag nanowires supported CN_x products were dried under vacuum.

Electrochemical measurements.

All the electrochemical measurements were done in a conventional three electrode system at an Autolab 302N electrochemical station using Ag/AgCl (3 M KCl) as reference electrode, Pt mesh as counter electrode and GC as a working electrode. GC electrode was polished with 1.0, 0.1 and 0.05 mm alumina slurry on Buehler micro cloth polishing cloth. After rinsing, the electrode was sonicated in distilled water about 10 min. 2 mg of synthesized composite was dissolved in 1 ml water to make a stock solution. 15 μl of aqueous stock solution was evaporated on cleaned GC electrode to prepare AGNWs-CN_x/GC electrode. The reference electrode (Ag/AgCl/3 M KCl) was calibrated with respect to RHE using the equation $E_{RHE} = E_{Ag/AgCl} + (0.059 \times \text{pH})$. pH was also measured for all electrolyte before experiment. Thus the HER measurements were carried out in both acidic and basic

medium degassed with nitrogen using LSV at a scan rate 10 mV/sec. ORR was done in both alkaline and acidic medium with the help of linear sweep voltammetry (LSV) and cyclic voltammetry (CV) measurement by using oxygen saturated 0.5 M H₂SO₄ and KOH with 100 mV sec⁻¹ scan rate. The stability of the electrode was measured by both repeated LSV and chronoamperometric at constant potential method. AC impedance measurements were performed in the identical system in the frequency range 10⁵ Hz to 10⁻¹ Hz with a constant AC voltage. AgNWs-CN_x decorated GC was activated by continuous 2000 LSV cycling in acidic medium and all electrochemical performance were tested by this activated AgNWs-CN_x electrode. After activation this ac-AgNWs-CN_x electrode was rinse thoroughly by water and a fresh electrolyte solution was used for the measuring HER and ORR performance.

6.4 RESULTS AND DISCUSSIONS

6.4.1 Characterization of AgNWs-CN_x composite

The microstructure and surface morphology of AgNWs was investigated by powder x-ray diffraction (p-XRD), transmission electron microscopy (TEM) and field emission scanning electron microscopy (FESEM). The p-XRD patterns of AgNWs-CN_x nanocomposites are shown in Figure 6.1. p-XRD shows five intense well defined peaks at 38.19°, 44.35°, 64.54°, 77.47°, 81.6° corresponds to (111), (200), (220), (311), (222) reflections of silver are observed in nano composites. The calculated diffraction pattern for cubic AgNPs (JCPDS card No. 4-783)^{39,31} was also shown in Figure 6.1 for comparison. This also confirms that silver nanowires are formed due to ultrasound treatment in presence of NaBH₄. Peak positioned at 2θ value of 27.30° corresponds to (002) plane of g-CN_x with interlayer d-spacing 3.27Å which was reported previously by our group^{40,41} The p-XRD pattern of AgNWs-CN_x composite is further studied by Scherrer analysis. The size of Ag nanowires was obtained ~18 nm from the Scherrer analysis.

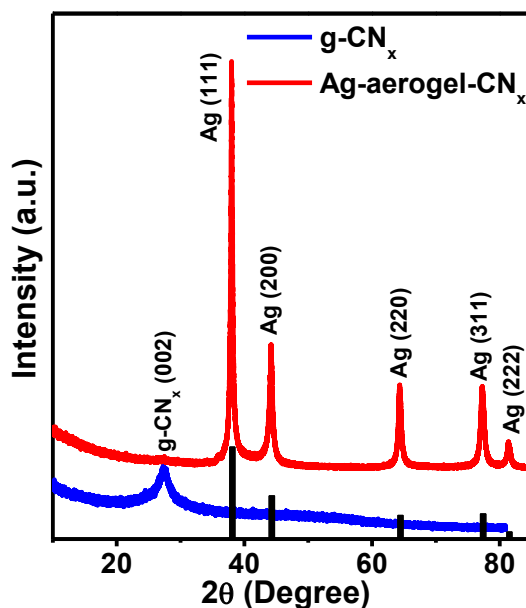


Figure 6.1. p-XRD of AgNWs-CN_x composite.

First, the morphology of AgNWs-CN_x was characterized by TEM. 10 μ l aqueous solution of AgNWs composite was drop casted and evaporated on TEM grid for TEM sample preparation. Some representatives TEM images of AgNWs-CN_x are shown in Figure 6.2 (a-d) and Figure S6.1 (a-c). In all these images, the thin Ag nanowires are interconnected to form three dimensional networks like structure with large number of open pores. The nano chains has almost uniform diameter of about 16-20 nm. The coalescence of initial spherical particles into chains structure is quite obvious in the TEM images. The SAED image of AgNWs-CN_x is shown in Figure 6.2e suggesting a polycrystalline structure, taken from Figure 6.2c. The interlayer spacing calculated from SAED image are 2.33, 2.04, 1.44, 1.22, 0.95 \AA which corresponds to (111), (200), (220), (311) and (331) planes of f.c.c silver lattice. This is in good agreement with p-XRD studies (see Figure 6.1) of Ag-composites. The HRTEM images as shown in Figure 6.2f and Figure S6.1d clearly show the lattice fringes with the d spacing of 2.34 \AA corresponding to the (111) plane of face centered cubic silver.

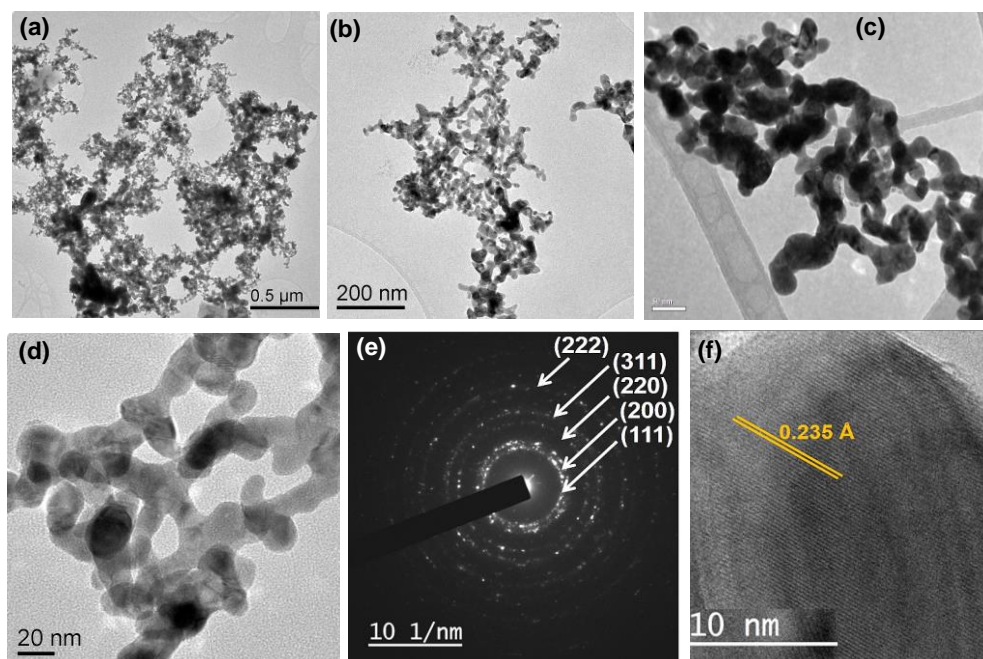


Figure 6.2. (a-d) TEM images of AgNWs-CN_x composite in low and high magnification showing interconnected nanochains of Ag. (e) SAED profile of corresponding AgNWs-CN_x composite. (f) HRTEM images of Ag in AgNWs shows preferential growth on Ag(111) surface.

The orientations of these lattice fringes are same. This suggests the AgNWs are generally growing along the Ag (111) planes. From TEM analysis it can be concluded that interconnected Ag network was formed due to ultrasound treatment in the mixture of AgNO₃, CN_x and NaBH₄. FESEM images (Figure 6.3 a-c) also have been taken also to study the surface structure of the composite on silicon substrate. FESEM samples were prepared by drop casting of 30 μl stock solution on Si wafer and dried in 60°C. In FESEM images of as formed products, it is clearly visible of the interconnected porous network with thin wire like structure with many bifurcations. The diameter of these isolated AgNWs was also obtained 16-20 nm.

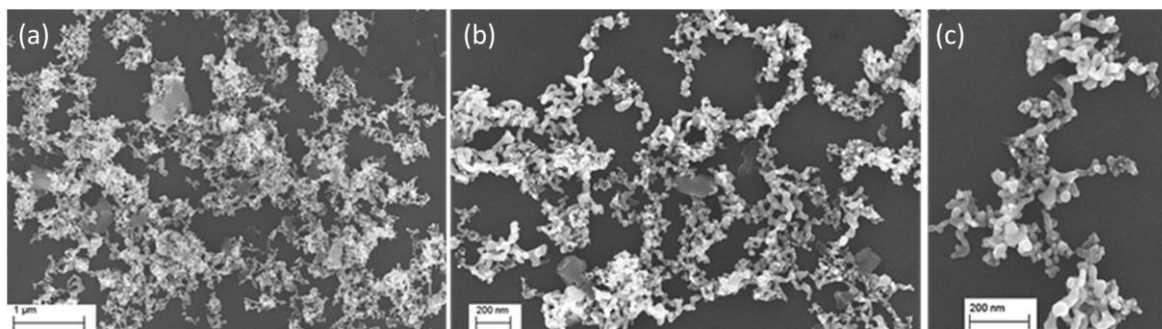


Figure 6.3. (a-c) FESEM images of interconnected AgNWs-CN_x.

The formation of silver nanoparticles (5-8 nm) on the surface of CN_x sheets resulting from ultrasound treatment without reducing agent (NaBH₄) was reported by our group³⁹. Nanowire structure cannot be formed if same amount of NaBH₄ solution added slowly, rather a nanoparticle on CN_x was formed. When fast reduction of AgNO₃ in the presence of CN_x sheets was done along with NaBH₄ and ultrasound treatment, the AgNWs supported on CN_x sheets is produced. Hence NaBH₄ added as solid into the mixture of AgNO₃ and g-CN_x (CN_x: AgNO₃: NaBH₄ = 1:12:4). If lower amount of silver precursor (CN_x: AgNO₃: NaBH₄ = 1:5:4) or reducing agent (CN_x: AgNO₃: NaBH₄ = 1:12:2) is used then we observed similar kind of AgNWs but higher amount of free CN_x sheet was observed. Before ultrasound treatment an agglomeration of NPs was observed. Thus ultrasound treatment helps to well dispersed of NPs and CN_x, connected them and shaped them a nanowire like structure. EDS analysis from TEM and FESEM was carried out to investigate the elements present in the nanocomposite and shown in Figure 6.4 (b-e) and S6.1e. EDS analysis confirmed the presence of carbon, nitrogen, oxygen and silver in the composite. The EDS mapping of AgNWs-CN_x composite also confirmed the presence of the same. XPS was used to examine the change of electronic structure of CN_x framework in presence of Ag-nanowires. Figure 6.5a shows the survey scan of the XPS spectrum which clearly indicates the presence of silver, carbon, nitrogen and oxygen atoms in AgNWs-CN_x composite.

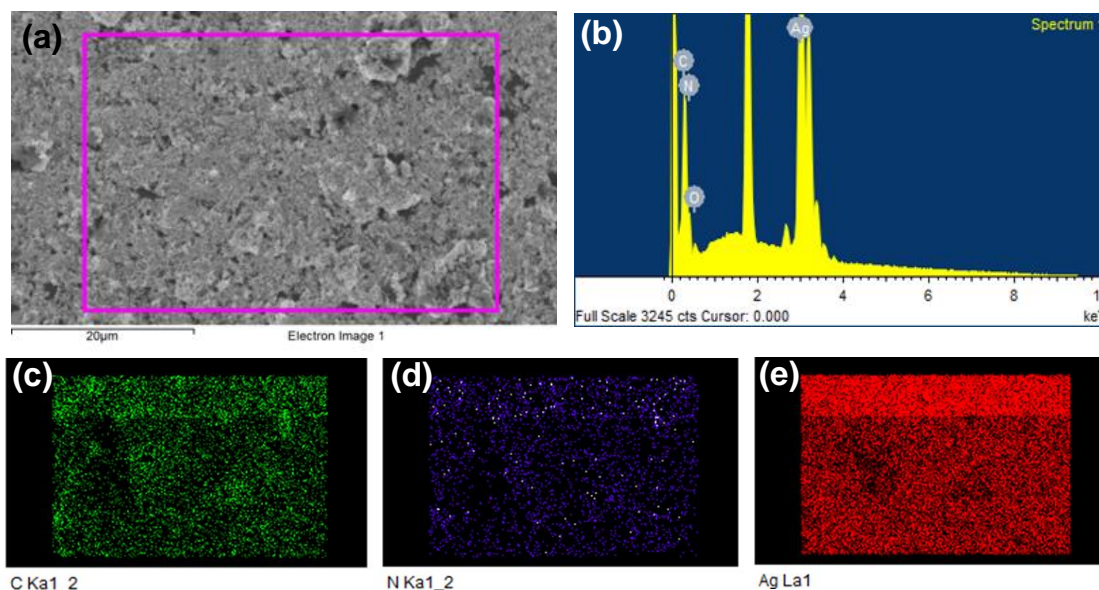


Figure 6.4. (a) FESEM image of interconnected AgNWs. (b) EDS profile of AgNWs-CN_x composite taken from Figure 6.5a. (c, d, e) Corresponding EDS mapping for element Carbon, Nitrogen, Silver respectively.

It is well known that the binding energy spectra of Ag3d of metallic Ag is appeared as doublet with binding energy 368.2 eV for 3d_{5/2} and 374.2 for 3d_{3/2} peak⁴². Figure 6.5 b display the Ag 4f spectrum for Ag3d and two peaks appeared at 368.3 and 373.3 eV. The peaks at 367.3 and 373.2 eV can be assigned to Ag 3d_{5/2} and 3d_{3/2} photoelectron. The carbon 1s (C1s) and N1s XPS spectra of the CN_x were deconvulated to three and two main Gaussian peaks, respectively (Figure 6.5c, d). The peaks at 283.9 (C1), 285.15 eV (C2) and 286.8 (C3) were assigned to the presence of (sp²) N–C=N (sp²) (carbon bonded to two nitrogen atom), C(–N)₃ (planar trigonal carbon geometry) and C=O species respectively whereas the peaks at 397.78 and 398.39 eV suggest the presence of (sp²) C–N(sp²) or a pyridine moiety and quaternary nitrogen, respectively^{40,41}.

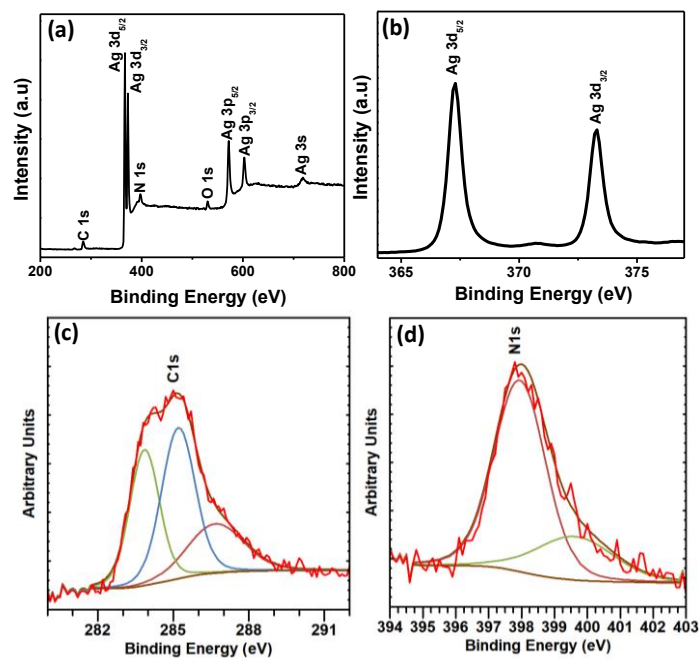


Figure 6.5. (a) XPS survey scan of AgNWs-CN_x and XPS spectra of (b, c, d) Ag3d, C1s, N1s spectra of AgNWs-CN_x.

The amount of exact Ag loading in catalyst was determined by inductively coupled plasma optical emission spectrometry (ICP-OES) measurement and the concentration of carbon and nitrogen was determined by EDS and CHN analysis. The exact wt% of Ag present in the composite is 85.5%. The carbon: nitrogen ratio in AgNWs-CN_x is observed 1:1.1 respectively.

6.4.2 Electrochemical HER process in acidic medium.

Activation of AgNWs (ac-AgNWs-CN_x) was carried out by repeated LSV scanning at a potential window 0.35 to -0.62 V in 0.5 M H₂SO₄ medium as shown in Figure 6.6 a. It shows with increasing LSV cycling the activity of AgNWs-CN_x increases and after 4000 cycles it shows a constant HER activity. This activated Ag nano-wires electrode (ac-AgNWs-CN_x) and fresh electrolyte solution were used for different electrochemical measurements.

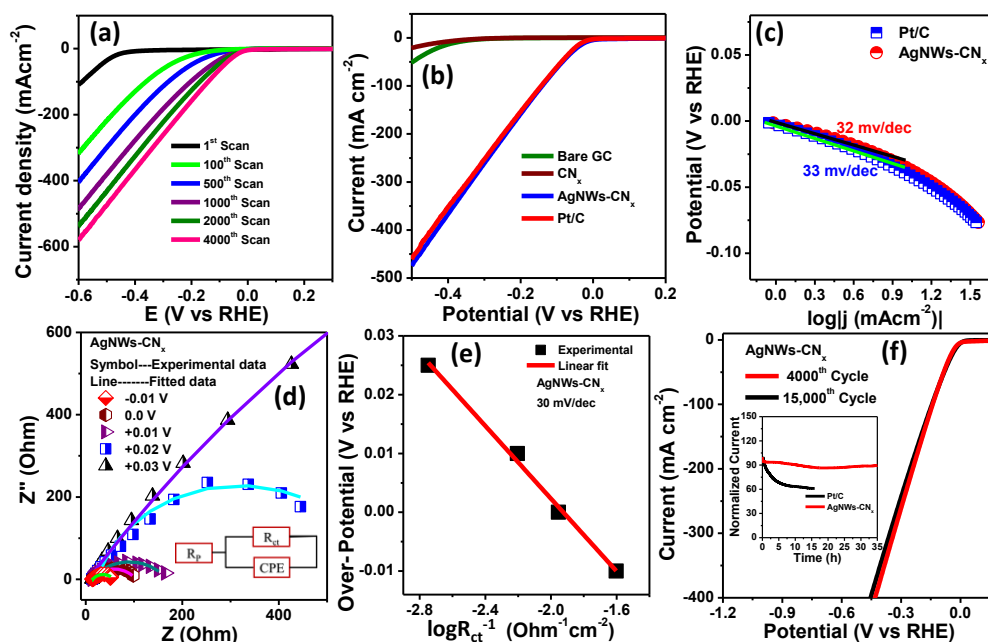


Figure 6.6. (a) HER performance of AgNWs-CN_x with repeated LSV polarization scan at 50 mv/sec scan rate. (b) LSV polarization of Pt/C, ac-AgNWs-CN_x, CN_x and GC at 10 mv/sec scan rate. (c) HER Tafel plot ($\log |j|$ vs. potential) of ac-AgNWs-CN_x and Pt/C. (d) EIS study of ac-AgNWs-CN_x at different overpotential at onset of HER (-0.01 to 0.03). (e) $\log R_{ct}^{-1}$ vs. Potential plot shows the Tafel slope value is 30 mV dec⁻¹. (f) HER activity of ac-AgNWs-CN_x at 1st cycle and 15,000th cycle. Inset: Chronoamperometric study of ac-AgNWs-CN_x and Pt/C electrode for long time (>35 hr). Experimental condition: 0.5 M H₂SO₄, N₂ atmosphere, 1600 rpm rotation.

Figure 6.6b shows the LSV hydrogen evolution polarization curves of ac-AgNWs-CN_x catalyst and commercial 40 wt % Pt/C in H₂SO₄ solution. The HER activities of GC and CN_x modified GC were also compared. It shows Pt/C exhibited superior HER activity with a near zero volt onset potential which is consistent with reported literature value. The GC, CN_x electrode are almost inert catalysts as large values of on-set and over-potentials. The ac-AgNWs-CN_x catalyst showed onset potential of zero volt similar to Pt/C. The over potential required for ac-AgNWs-CN_x to drive the current density of 10, 20 and 50, 100 mA cm⁻² are 25, 42 and 85, 138 mV whereas over-potential required for Pt/C are 30, 50, 87 and 143 mV respectively.

Table 6.1. Summarized HER activity of AgNWs-CN_x and Pt/C in 0.5 M H₂SO₄.

Catalyst	Onset potential (mV)	Over potential			Tafel slope (mV/dec)	exchange current (mA cm ⁻²)
		10 mAcm ⁻²	50 mAcm ⁻²	100 mAcm ⁻²		
ac-AgNWs-CN _x	0	25	85	138	32	0.51
Pt/C	0	30	87	143	33	0.49

his clearly demonstrated superior electrocatalytic activity of ac-AgNWs-CN_x catalyst towards HER in acid media. The HER process generally occurs either Volmer-Heyrovsky mechanism ($\text{H}_3\text{O}^+ + \text{e}^- = \text{H}_{\text{ads}} + \text{H}_2\text{O}$ and $\text{H}_{\text{ads}} + \text{H}_3\text{O}^+ + \text{e}^- = \text{H}_2 + \text{H}_2\text{O}$) or via a Tafel mechanism ($\text{H}_{\text{ads}} + \text{H}_{\text{ads}} = \text{H}_2$)¹⁰. These two methods described that H₂ adsorption- desorption is a competitive way and must have to balance each other to facilitate H₂ production. The Tafel equation ($\eta = a + b \log|j|$, where j is the current density and b is the Tafel slope) can be used to investigate the rate limiting step of HER. A low Tafel slope (Volmer-Tafel pathway) means a faster increase of HER rate with increasing potential but Volmer-Heyvorsky mechanism can have a higher Tafel slope and a significant over-potential². The HER Tafel plot showing $\log|j|$ vs. applied potential for Pt/C, ac-AgNWs-CN_x are presented in Figure 6.6c. The Tafel slope for Pt/C in acidic medium was 32 mV/dec, which is consistent with reported literature data. The Tafel analysis for the ac-AgNWs-CN_x in acid solution gives a Tafel slope of 33 mV/dec. The electrochemical flow of electrons was investigated with EIS and studying the heterogeneous charge transfer resistance (R_{ct}). The R_{ct} was determined from the semicircle diameter of Nyquist plots and calculated from the Randles

equivalent circuit (Figure 6.6d). Smaller semicircle signifies a smaller charge transfer resistance (R_{ct}) value at the electrolyte/electrode interface, hence favors faster ion transfer. Nyquist plots (Z vs. Z'') at different potential at onset of HER was shown in Figure 6.6d. The R_{ct} value was obtained very small, only 38 ohm at zero volt (RHE).

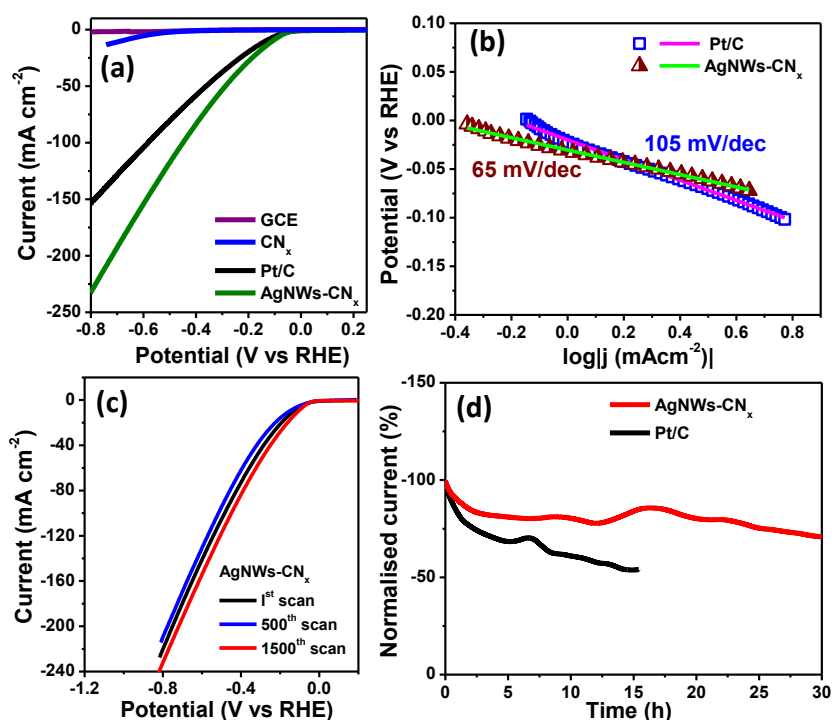


Figure 6.7. (a) LSV polarization curve of Pt/C, ac-AgNWs-CN_x, CN_x and GC at 10 mV/sec scan rate. (b) HER Tafel plot ($\log |j|$ vs. potential) of ac-AgNWs-CN_x and Pt/C. (c) HER activity of ac-AgNWs-CN_x at 1st cycle and 1500th cycle. (d) Chronoamperometric study of ac-AgNWs-CN_x electrode and Pt/C for long time (30 hr). Experimental condition: 0.5 M KOH, N₂ atmosphere, 1000 rpm rotation. ac-AgNWs-CN_x was used after 4000 LSV scan in H₂SO₄.

The plot of $\log R_{ct}^{-1}$ vs. overpotential (Figure 6.6e) also gives rise to a Tafel slope of 31 mV/dec for ac-AgNWs-CN_x. Both these experiment suggests that recombination of two adsorbed hydrogen is the rate determining step. The exchange current density (J_0) is also an important kinetic parameter that explores the rate of electron transfer at reversible condition. The exchange current density of ac-AgNWs-CN_x and Pt/C was 0.50 mA cm⁻² and 0.51 mA cm⁻² in 0.5 M H₂SO₄ medium. The exchange current density of ac-AgNWs-CN_x is

comparable with Pt/C and higher than other reported HER catalysts. As shown in Table 6.1, the HER activity performance of ac-AgNWs-CN_x and commercial Pt/C catalysts suggest that Pt-like hydrogen evolution activity of ac-AgNWs-CN_x. A comparison study of HER activity was also shown with ac-AgNWs-CN_x and other reported catalyst in Table 6.1 and S6.1. The catalytic activity of ac-AgNWs-CN_x is promising catalyst than other reported catalyst. For instance, ac-AgNWs-CN_x shows better or comparable onset potential, overpotential, Tafel slope, exchange current density than Au⁴³, Pd¹³, Ru¹⁴, Pt⁴⁴ based noble metal reported catalysts. This activated Ag-catalyst is also much better (in terms onset, overpotential to reach appreciable current densities) than bi-metallic Bimetallic catalyst such as NiAu/Au, NiMoN_x/C, A-Ni-C, Co_{0.6}Mo_{0.4}N₂, MoS₂/CoSe₂ and other Non-noble metal catalyst like NiP₂NS/CC, MoP, MoS₂/RGO Co-NRCNT, CoSe₂, (GO 8 wt%) Cu-MOF etc. Therefore, ac-AgNWs-CN_x is one of best catalyst in acid media. Another important aspect of a good HER catalyst should have a very good stability in experimental condition. Though Pt/C became a benchmark for its activity but the degradation of carbon support in strong oxidizing acidic condition causes agglomeration of Pt which has made a major drawback for successfully commercialization of PEM fuel cell. Thus the stability of ac-AgNWs-CN_x was investigated by continuous LSV cycles as well as constant voltage chronoamperometric studies. Figure 6.6f show the repeated LSV cycling stability of the catalyst ac-AgNWs-CN_x whereas long term chronoamperometric studies of the catalyst was given in inset of Figure 6.6f. This showed that even after 11,000 potential (between 0.45 to-0.65 V) scans (total 15000 scan) the HER activity of ac-AgNWs-CN_x almost remain same. High stability of ac-AgNWs-CN_x was also observed in the constant potential (-0.03 V) chronoamperometric studies (inset of Figure 6.6f). Most importantly, same ac-AgNWs-CN_x electrode was used to study cycling stability and chronoamperometric studies. The 30h chronoamperometric study was performed after 15,000 LSV cycles. This proves that extra-ordinary stability of

the catalyst in acidic media. The HER stability of this ac-AgNWs-CN_x catalyst is even better than that commercial Pt/C catalyst (inset of Figure 6.7f).

Table 6.2. Summarized HER activity of ac-AgNWs-CN_x and Pt/C in 0.5 M KOH.

Catalyst	Onset potential (mV)	Over potential (mV)		Tafel slope (mV/dec)	exchange current (mA cm ⁻²)
		10 mAcm ⁻²	50 mAcm ⁻²		
ac-AgNWs-CN _x	0	110	290	65	0.3
Pt/C	0	135	360	105	0.6

The chronoamperometric studies showed 30% degradation of Pt/C activity was occurred after 15h of chronoamperometric whereas the 10 % activity loss of this ac-AgNWs-CN_x catalyst in chronoamperometric run.

6.4.3 HER activity of ac-AgNWs-CN_x catalyst in Basic Medium

The HER activity of this ac-AgNWs-CN_x catalyst was also studied in basic media. It is highly desirable to find high HER active in base since Pt/C shows 2-3 time activity in basic media than acid. The AgNWs-CN_x was activated in acid media as discussed in the previous section, before it was used in base media for carrying out HER performance. The representative LSV curves of geometric current density (mA cm⁻²) vs. applied potential in basic KOH media showing HER activity for ac-AgNWs-CN_x, Pt/C and GC electrode in Figure 6.7a. The GC electrode is almost inert whereas both this ac-AgNWs-CN_x and Pt/C showed very good HER activity with same onset potential of zero Volts. Although onset potential of both the catalysts are same but, HER performance of ac this ac-AgNWs-CN_x outperforms the activity of Pt/C. The ac-AgNWs-CN_x catalyst requires much lower overpotential to reach any appreciable current density than that of Pt/C. The over potential required for this ac-AgNWs-CN_x to drive the current density of 10, 20 and 50, 100 mA cm⁻² are 110, 170, 290, 447 mV whereas overpotential required for Pt/C are 135, 203, 360 and

590 mV respectively. As shown in Figure 6.7b, the Tafel slope for Pt/C in basic medium was 105 mV dec⁻¹, which is consistent with reported data. The Tafel slope of the ac-AgNWs-CN_x in 0.5M KOH was found to 65 mV dec⁻¹. This suggests that HER follows Volmer-Heyrovsky in the alkaline medium where Heyrovsky is the rate determination step. The exchange current density for this ac-AgNWs-CN_x in 0.5 M KOH medium was 0.35 mA cm⁻² which is higher or comparable too for related systems. A summarized result towards HER activity in alkaline medium was shown in Table 6.2 for this ac-AgNWs-CN_x and commercial Pt/C. From the Table S6.2 it is clear that catalyst has a better or comparable catalytic activity in terms of onset potential, over potential, Tafel slope, exchange current compared to other Mo, Ni, Co, Ru, Pd based catalyst. The stability of this ac-AgNWs-CN_x was investigated by continuous LSV cycles and chronoamperometric studies. As shown in Figure 6.7 (c and d), this ac-AgNWs-CN_x possesses superior stability in a long-term operation over commercial Pt/C.

6.4.4 ORR studies on ac-AgNWs-CN_x catalysts in alkaline medium

The electrochemical oxygen reduction reaction (ORR) is a fundamental cathodic process occurred in fuel cells. The ORR is a complex multi electron transfer reaction with involving different elementary steps with different intermediates. Oxygen can electrochemically reduce either directly to water via (direct 4e reduction, $O_2 + 2H_2O + 4e \rightarrow 4OH^-$) or through the formation of H₂O₂ (2e reduction, $O_2 + 2H_2O + 2e \rightarrow OH_2^- + OH^-$) and then this peroxide can be reduced to water (series 4e pathway, $OH_2^- + H_2O + 2e \rightarrow 3OH^-$) or chemically decomposed on electrode⁴⁵. In this regard production of H₂O₂ is not desirable for fuel cell as it corrode the membranes in cell assembly. Several efforts have been made for preparation of noble metal based catalysts to reduce the ORR over-potential as well as the

H_2O_2 formation. Since Ag is one of the cheapest metal and 4e reduction of oxygen occur on Ag surface²⁹, thus, Ag is considered as alternative to Pt/C for alkaline fuel cells.

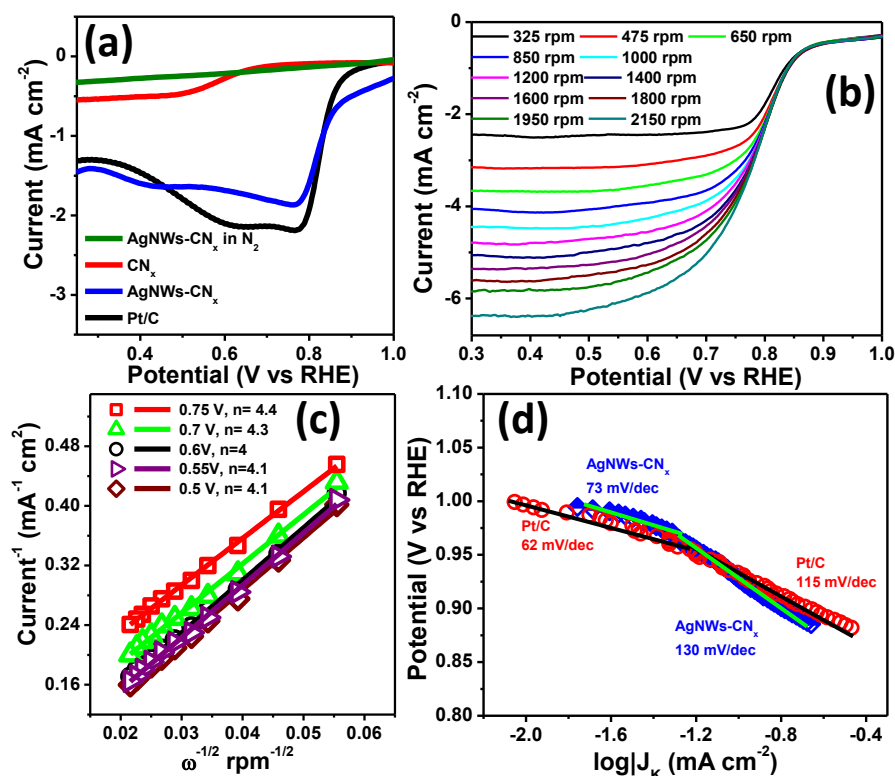


Figure 6.8. (a) LSV polarisation curve of Pt/C, ac-AgNWs-CN_x, CN_x and GC in O₂ saturated 0.5 M KOH at 100 mV/sec scan rate. ac-AgNWs-CN_x was used for ORR studies.

(b) LSV polarisation curve of ac-AgNWs-CN_x at different rotation varied from 200 to 2150 rpm. (c) K-L plot of ac-AgNWs-CN_x electrode constructed from Figure b (d) ORR Tafel plot (log |j| vs. potential) of ac-AgNWs-CN_x and Pt/C.

In order to find ORR activity of ac-AgNWs-CN_x catalyst the LSV and CV measurements in N₂ and O₂ saturated 0.5 M KOH medium were performed. Note that before ORR measurements, ac-AgNWs-CN_x modified GC was activated by repeated cycling in acid media, mentioned in the previous section. The comparison of LSV curves of ac-AgNWs-CN_x, Pt/C was presented in Figure 6.8a. The LSV curve of CN_x modified GC is also compared and it shows a weak peak at 0.50 V (vs. RHE) whereas the ac-AgNWs-CN_x showed a stronger peak at more positive voltage with high limiting current in O₂ saturated KOH solution, but no peak was observed in N₂ saturated KOH medium. The ORR onset

potential of ac-AgNWs-CN_x electrode is 0.885 V, E_{1/2} of 0.818 V. The ORR activity of ac-AgNWs-CN_x is thus comparable to Pt/C which shows slightly more positive onset potential at ~0.9 V, E_{1/2} of ~0.825 V and peak potential of 0.775 V. This suggests a superior activity of ac-AgNWs-CN_x towards ORR in base media. The ORR kinetics on different catalysts was performed through rotating disk electrode (RDE) experiment. The rotation speed dependent ORR LSV polarization curves on ac-AgNWs-CN_x modified GC was shown in Figure 6.8b. The LSV polarization current gradually increases with increasing the rotation speed (varying from 325 rpm to 2150 rpm). Koutecky-Levich (K-L) equation⁴³ can be used to determine the number of electron involved per O₂ in ORR by following the equation

$$1/j = 1/j_k + 1/j_d = -1/nFk C_{O_2} - 1/B\omega^{1/2}$$

Where j is the measured current density, j_k, j_d is the kinetic and diffusion limited current density and ω is the electrode rotating rate. B can be determined from the slope of K-L plot and theoretically can be obtained from the following equation

$$B = 0.62 nF(D_{O_2})^{2/3}\nu^{-1/6}C_{O_2}$$

where Faraday constant (F= 96485 C mol⁻¹) and n is the number of electron transferred per O₂ molecule, in 0.5 M KOH diffusion coefficient D_{O₂} of O₂ (1.9 x 10⁻⁵ cm² s⁻¹), kinetic viscosity (ν = 0.01 cm² s⁻¹) and C_{O₂} is the bulk concentration of O₂ (1.2 x 10⁻⁶ mol cm⁻³). The number of electrons involved in ORR reaction on ac-AgNWs-CN_x electrode was calculated from the slope of the K-L plots at different potentials. Figure 6.8c shows that K-L plot of ORR on ac-AgNWs-CN_x electrode at different voltage, ranging from 0.5 to 0.75V constructed from Figure 6.8b. The linearity and near parallelism of I⁻¹ versus ω^{-1/2} suggests first order reaction kinetics with respect dissolved oxygen. From K-L plot it can be concluded that mainly a 4e transfer ORR process predominates ac-AgNWs-CN_x surface.

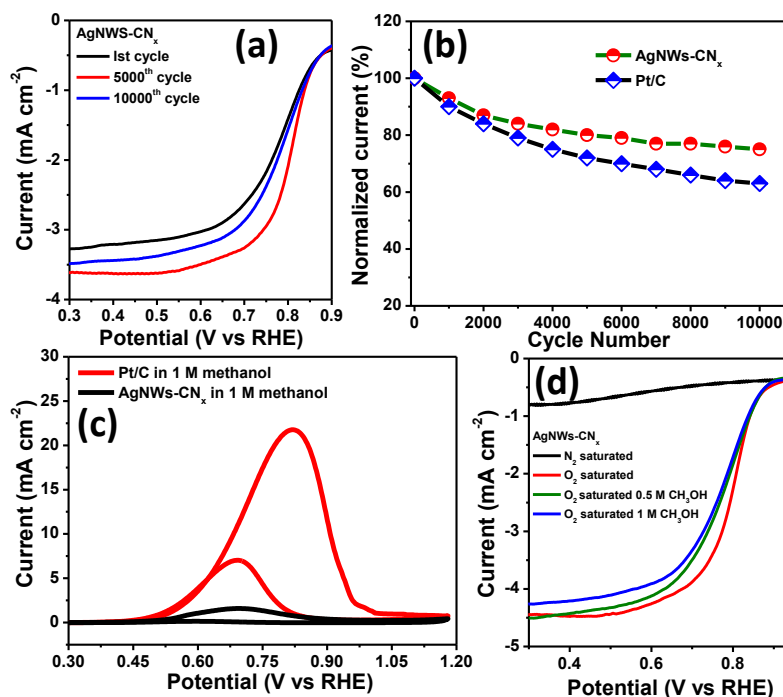


Figure 6.9. (a) ORR activity of ac-AgNWs-CN_x at 1st cycle and 1000th cycle in a O₂ saturated 0.5 M KOH. (b) Comparison of ORR LSV cycling stability between Pt/C and ac-AgNWs-CN_x. (c) CV of ac-AgNWs-CN_x and Pt/C in a N₂ saturated 0.5 M KOH contain 1 M methanol. (d) LSV curve of ac-AgNWs-CN_x in an O₂ saturated 0.5 M KOH contain 1 M methanol shows methanol tolerance of the electrode.

The comparison of Tafel plots of different Pt/C and ac-AgNWs-CN_x are shown in Figure 6.8d. It was reported that Tafel slope of Pt lies between 60-70 mV dec⁻¹ at low over-potential region and the values goes up to ~120 mV dec⁻¹ at high over-potential region. The former Tafel slope suggests that pseudo 2e reaction as the rate determining step but later one implies first electron reduction is the rate determining step where O₂ reduction and O-O bond breaking steps are facile⁴⁶. The Tafel plots were obtained after the measured currents were corrected for diffusion to give the kinetic currents in the mixed activation-diffusion region, obtained from K-L equation $J_k = j_d / (j_d - j)$ where $j / (j_d - j)$ is the mass transfer correction term. The mass transport correction was made using the limiting current $j_d = B\omega^{1/2}$.

Table 6.3. Different parameter of ac ac-AgNWs-CN_x in ORR.

Catalyst	Electrolyte	E _{1/2} (V vs. RHE)	Tafel slope (mV/dec)
ac-AgNWs-CN _x	0.5 M KOH	0.818	73
			130
	0.5 M H ₂ SO ₄	0.510	65
			122

The Tafel slopes of ac-AgNWs-CN_x catalyst is found to be ~73 mV dec⁻¹ in low over-potential region and 130 mV dec⁻¹ at higher over potential region. These values are lower than some Ag based reported catalysts and is close or slightly high to the Tafel values of Pt/C. This suggests that the transfer of first electron is the rate determining step for O₂ reduction on Ag surface in alkaline medium. Table 6.3 listed the several parameters of ac-AgNWs-CN_x in basic medium. The stability of the ac-AgNWs-CN_x electrode was shown in Figure 6.9 a. A significant catalytic activity is retained after 10000 potential cycling from 1 to 0.3 V (RHE). ac-AgNWs-CN_x scan retained 76% current density at E_{1/2} after 5000 potential scanning and 70 % after 10000 scan. In Figure 6.9b, a comparison study of number of cycle vs. normalized current density at E_{1/2} of ac-AgNWs-CN_x and Pt/C was shown. More than 15% current density was decreased for Pt/C compared ac-AgNWs-CN_x. The stability of ac-AgNWs-CN_x is slightly better than Pt/C. Methanol crossover effect is one of the prime problems in methanol fuel cell for Pt/C catalyst as fuel molecules (methanol, ethanol, glucose) from anode sometimes permeate to cathode and seriously affect the activity of Pt material³⁴. Figure 6.9c shows the cyclic voltammograms of Pt/C and ac-AgNWs-CN_x electrode in nitrogen saturated 0.5 M KOH in presence of 1 M methanol. Pt-C shows a very strong methanol oxidation peak (0.83 V) but no noticeable response for methanol oxidation was observed in our ac-AgNWs-CN_x catalyst at that same experimental condition. Moreover ORR polarization graph is hardly affected by methanol as shown in Figure 6.9 d. ac-AgNWs-

CN_x can retain 96% and 95 % E_{1/2} potential after addition of 0.5 M and 1 M of methanol. So we conclude that our catalyst has high selectivity towards ORR and possess a good tolerance of cross-over effect of methanol. Thus Ag-aerogel-CN_x is superior to commercial Pt-C catalyst in terms of ORR peak position, stability and methanol tolerances.

6.4.5 ORR studies on ac-AgNWs-CN_x catalysts in acidic medium

The catalytic activity of AgNWs was further evaluated by ORR in acidic medium. Figure 6.10a show the LSV curves of commercial Pt/C, ac-AgNWs-CN_x, CN_x modified GC electrode and bare GCE in 0.5 M H₂SO₄. GCE and CN_x-GCE has a very little ORR activity with a very high onset potential. The ac-AgNWs-CN_x composites are the most active ORR catalyst with much stronger cathodic peak and more positive onset potential. The cathodic peaks were observed at +0.43V (vs. RHE) for ac-AgNWs-CN_x modified electrode. The complete CV scan for these catalysts in O₂ saturated H₂SO₄ medium was given at Figure S6.2. The ORR performance of ac-AgNWs-CN_x catalyst is better than of CN_x and GCE but inferior than Pt/C electrode. Figure 6.10b shows LSV polarization curves (current density-potential curves) of ORR for ac-AgNWs-CN_x electrode at different rotation speed. The corresponding K-L plot for AgNWs electrode is shown in inset of Figure 6.10c. The value of n at 0.4 V was ~3.9 and it increased to 4 at 0.3 V. This suggests, ORR is mainly dominated by 4 electron transfer process where O₂ is directly reduced to OH⁻. Moreover catalyst is well stable in acidic medium. From Figure 6.10d it is also evident that a small current density was decreased after 10000 LSV scan. So ac-AgNWs-CN_x catalyst shows enough stability in acidic medium also.

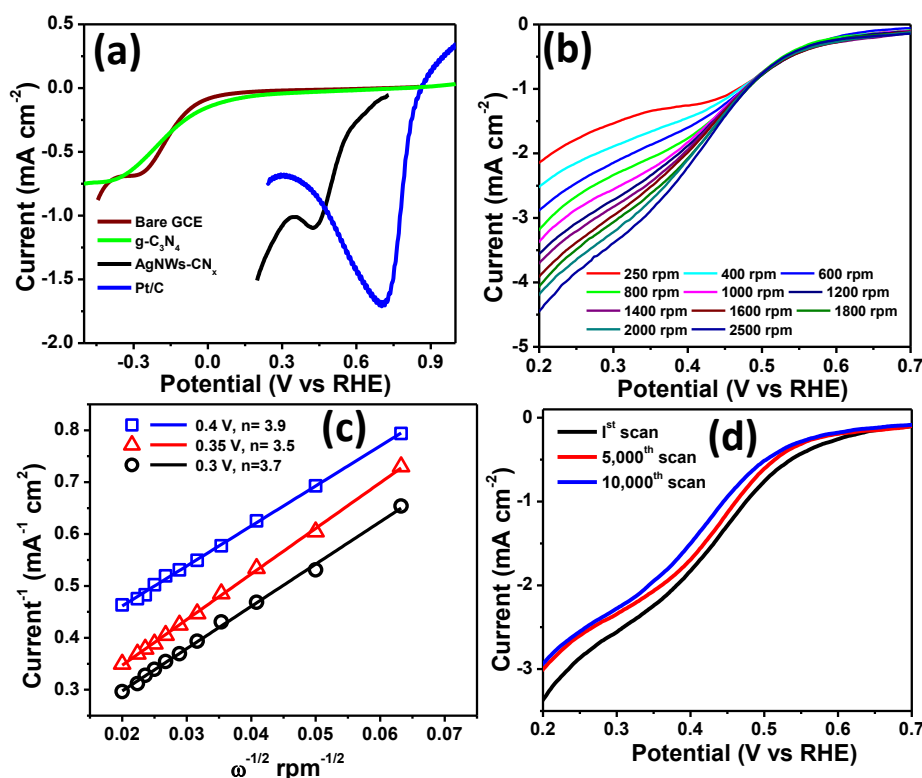


Figure 6.10. (a) LSV polarisation curve of Pt/C, ac-AgNWs-CN_x, CN_x and GC in O₂ saturated 0.5 M H₂SO₄ at 100 mV/sec scan rate (b) LSV polarisation curve of ac-AgNWs-CN_x at different rotation varied from 250 to 2500 rpm. (c) K-L plot of ac-AgNWs-CN_x electrode. (d) ORR activity of AgNWs at 1st cycle and 10,000th cycle in an O₂ saturated 0.5 M H₂SO₄

6.4.6 Factors responsible for high catalytic activity.

The activated AgNWs-CN_x catalyst showed superior activity and stability towards hydrogen evolution and oxygen reduction reactions in both acid and base media. This ac-AgNWs-CN_x catalyst has better activity and stability than that of other reported catalyst and commercial Pt/C. The superior activity and stability of this catalyst could be attributed to several following reasons.

- (1) Interconnected one dimensional Ag nanowires structures of the composite could one of the reasons for its high activity. In general, anisotropic nature of 1-D materials, extended smooth defect free crystalline planes, fewer lattice boundaries, low number of surface defects, and surface to volume ratio are desirable for a fuel cell catalysts³⁴. The one

dimensional noble metal nano-structures are reported suitable electro-catalyst especially for ORR in PEM fuel cells. The TEM/HRTEM analysis of this AgNWs-CN_x composites (Figure 6.2 a-d) proves interconnected one dimensional structures and preferential growth of Ag along (111) planes. It is also reported in several scientific reports that Ag (111) plane is the most active plane towards HER as the lower, more favorable, adsorption energy for the first step (volmer). W. Schemickler calculated the free energy required to adsorb a proton from the solution to the electrode. They found three fold hollow sites fcc (111) plane has a lower adsorption energy compared to four fold hollow site fcc (100)⁴⁷. The activation energy of electrochemical desorption step are same in both surfaces. The growth AgNWs occurred along (111) plane. The highly crystalline one dimensional Ag wire nanostructures is one of the main reasons for its superior activity.

(2) 1-D interconnected porous morphology is generally suitable for high performance electro-catalysis since porous morphology provide easy path ay for fast electron transport as well as allow to enhance mass transport. In addition, the particle migration, Ostwald ripening and aggregation is greatly reduced in case of 1-D nanostructures in compare to zero dimensional nano-materials, thereby enhancing stability and durability of the 1-D electro-catalyst³⁸. The interconnected AgNWs are used as building block for the porous morphology of the catalyst which was confirmed by the SEM image of AgNWs composite. In order to gain insight into the origin of enhanced catalytic activity of ac-AgNWs-CN_x we discussed CV measurements using [(FeCN₆)]^{3-/4-} redox couple in 0.1 M H₂SO₄ medium. As shown in Figure 6.11a, a significant improvement of current density with reduced gap of ΔE_p at ac-AgNWs-CN_x electrode was observed compared to bare GC. The larger slope values of the linear regression equation in current vs. scan rate^{1/2} (Figure 6.11 b-d and Table 6.4) and low ΔE_p suggest that the unique electronic structure and requisite surface structure which facilitate fast electron and mass transfer through ac-AgNWs-CN_x film.

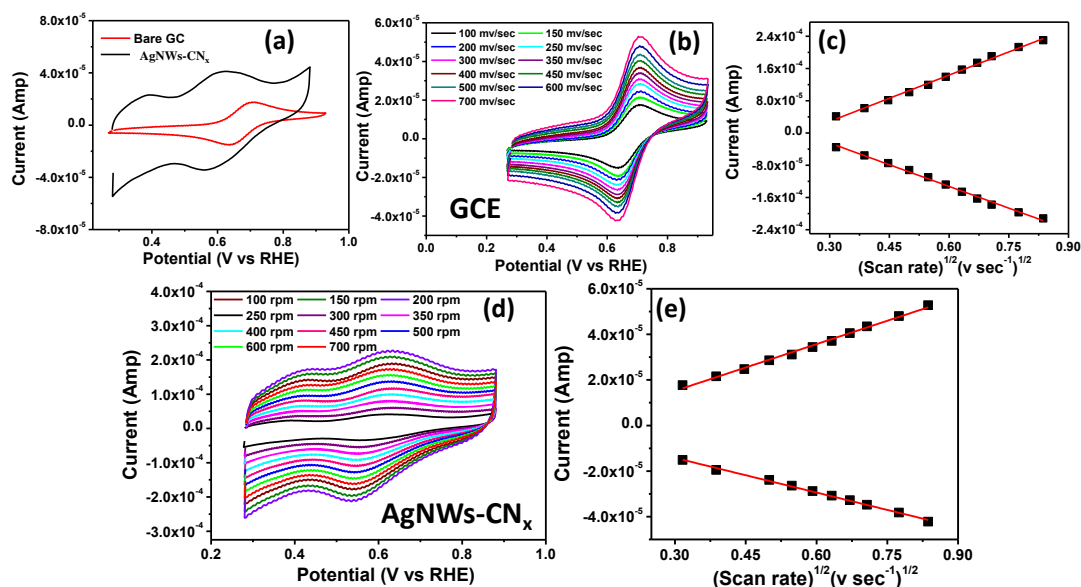


Figure 6.11. (a) CVs of 0.5 M $[\text{FeCN}_6]^{3-/4-}$ solution at GCE and ac-AgNWs-CN_x electrode in N₂ saturated 0.1 M H₂SO₄ solution. (b, d) CVs of GC electrode and ac-AgNWs-CN_x electrode in different scan rate ranging from 100 to 700 mV/sec. (c, e) Cathodic and anodic current vs. (scan rate)^{1/2} plot shows a linear fit in both the electrode.

(3) The presence of pyridinic and graphitic N atom concentrations in ac-AgNWs composite improves the charge transfer kinetics due to the interaction of protons and oxygen with N atoms and enhances the electro-catalytic activities of the catalysts²⁹ also. It is also reported nitrogen doping in carbon support introduces atomic charge density and asymmetry in spin density into carbon networks that facilitates charge transfer from carbon support to the adsorbing molecules. Kim and his co-workers⁴⁸ suggested that presence of the N-species improved the electro-catalytic activity of cobalt doped g-C₃N₄ and also showed that among the different type N-functional groups, graphitic and pyridinic N are known to play more significant role in the improvement of electro-catalytic affects by superior the charge transfer. The presences of large amount of pyridinic and graphitic N-atoms in Ac-AgNWs may be helping to enhance the catalytic activities. Recently V. Di Noto *et al.*⁴⁹ reported “PdCONi” core shell C₃N₄ electrocatalyst where they showed the relationship between nitrogen concentration with structure morphology and electrochemical performance. Based on this work and reported literature it may be concluded that superior electro-catalytic

activity of ac-AgNWs-CN_x is probably due to synergistic effect between AgNWs and porous CN_x supports.

Table 6.4. Different parameters obtained from the CV of [FeCN₆]^{3-/4-} by the ac-AgNWs-CN_x and GCE electrode.

Catalyst	ΔE_p (mV)	Slope (i_a) ($\mu\text{A}/\text{Vsec}^{-1}$) ^{1/2}	Slope (i_c) ($\mu\text{A}/(\text{Vsec}^{-1})^{1/2}$)
ac-AgNWs-CN _x	62	380 ($R^2 = 0.995$)	-355 ($R^2 = 0.994$)
GCE	70	68 ($R^2 = 0.994$)	-50 ($R^2 = 0.996$)

6.5 CONCLUSION

In conclusion, a facile synthetic route for the formation of Ag nanowires on carbon nitride sheets by reduction and ultrasound method have demonstrated. Activation of AgNWs-CN_x was observed by continuous LSV scanning in 0.5 M H₂SO₄. Activated AgNWs-CN_x composites has low charge transfer resistance. This catalyst exhibited superior catalytic activity towards HER and ORR. The ac-AgNWs-CN_x composite shows high HER activities in both acidic and basic medium with exceptionally high stability in acid medium. In alkaline media, ORR activity of ac-AgNWs-CN_x catalyst is comparable to commercial Pt/C catalyst. The synergistic effects between porous AgNWs and CN_x lead to an outstanding ORR and HER performances at ac-AgNWs-CN_x catalysts. The excellent HER and ORR activity of ac-AgNWs-CN_x with methanol tolerance, good durability and low catalyst loading are making them a promising future electrocatalyst for fuel cell and water splitting or other electrochemical devices.

6.6 REFERENCES

- (1) Shao, M.; Chang, Q.; Dodelet, J.-P.; Chenitz, R. *Chem. Rev.* **2016**, *116*, 3594-3657.
- (2) Shi, Y.; Zhang, B. *Chem. Soc. Rev.* **2016**, *45*, 1529-1541.

- (3) Pumera, M.; Sofer, Z.; Ambrosi, A. *J. Mater. Chem. A* **2014**, *2*, 8981-8987.
- (4) Cook, T. R.; Dogutan, D. K.; Reece, S. Y.; Surendranath, Y.; Teets, T. S.; Nocera, D. G. *Chem. Rev.* **2010**, *110*, 6474-6502.
- (5) Lu, S.; Pan, J.; Huang, A.; Zhuang, L.; Lu, J. *Proc. Nat. Acad. Sci.* **2008**, *105*, 20611-20614.
- (6) Zhang, W.; Lai, W.; Cao, R. *Chem. Rev.* **2017**, *117*, 3717-3797.
- (7) Dasgupta, N. P.; Liu, C.; Andrews, S.; Prinz, F. B.; Yang, P. *J. Am. Chem. Soc.* **2013**, *135*, 12932-12935.
- (8) Popczun, E. J.; McKone, J. R.; Read, C. G.; Biacchi, A. J.; Wiltrout, A. M.; Lewis, N. S.; Schaak, R. E. *J. Am. Chem. Soc.* **2013**, *135*, 9267-9270.
- (9) Du, H.; Liu, Q.; Cheng, N.; Asiri, A. M.; Sun, X.; Li, C. M. *J. Mater. Chem. A* **2014**, *2*, 14812-14816.
- (10) Son, C. Y.; Kwak, I. H.; Lim, Y. R.; Park, J. *Chem. Commun.* **2016**, *52*, 2819-2822.
- (11) Liao, L.; Zhu, J.; Bian, X.; Zhu, L.; Scanlon, M. D.; Girault, H. H.; Liu, B. *Adv. Funct. Mater.* **2013**, *23*, 5326-5333.
- (12) Chang, Y.-H.; Lin, C.-T.; Chen, T.-Y.; Hsu, C.-L.; Lee, Y.-H.; Zhang, W.; Wei, K.-H.; Li, L.-J. *Adv. Mater.* **2013**, *25*, 756-760.
- (13) Bhowmik, T.; Kundu, M. K.; Barman, S. *ACS Catal.* **2016**, *6*, 1929-1941.
- (14) Bhowmik, T.; Kundu, M. K.; Barman, S. *ACS Appl. Mater. Interfaces* **2016**, *8*, 28678-28688.
- (15) Gong, M.; Zhou, W.; Tsai, M.-C.; Zhou, J.; Guan, M.; Lin, M.-C.; Zhang, B.; Hu, Y.; Wang, D.-Y.; Yang, J.; Pennycook, S. J.; Hwang, B.-J.; Dai, H. *Nat. Commun.* **2014**, *5*, 4695.
- (16) Voiry, D.; Salehi, M.; Silva, R.; Fujita, T.; Chen, M.; Asefa, T.; Shenoy, V. B.; Eda, G.; Chhowalla, M. *Nano Lett.* **2013**, *13*, 6222-6227.

- (17) Xiao, P.; Sk, M. A.; Thia, L.; Ge, X.; Lim, R. J.; Wang, J.-Y.; Lim, K. H.; Wang, X. *Energy Environ. Sci.* **2014**, *7*, 2624-2629.
- (18) Tran, P. D.; Chiam, S. Y.; Boix, P. P.; Ren, Y.; Pramana, S. S.; Fize, J.; Artero, V.; Barber, J. *Energy Environ. Sci.* **2013**, *6*, 2452-2459.
- (19) Long, X.; Li, G.; Wang, Z.; Zhu, H.; Zhang, T.; Xiao, S.; Guo, W.; Yang, S. *J. Am. Chem. Soc.* **2015**, *137*, 11900-11903.
- (20) Kong, D.; Cha, J. J.; Wang, H.; Lee, H. R.; Cui, Y. *Energy Environ. Sci.* **2013**, *6*, 3553-3558.
- (21) Fei, H.; Yang, Y.; Fan, X.; Wang, G.; Ruan, G.; Tour, J. M. *J. Mater. Chem. A* **2015**, *3*, 5798-5804.
- (22) Hao, J.; Yang, W.; Zhang, Z.; Tang, J. *Nanoscale* **2015**, *7*, 11055-11062.
- (23) Jiang, P.; Liu, Q.; Sun, X. *Nanoscale* **2014**, *6*, 13440-13445.
- (24) Pu, Z.; Liu, Q.; Asiri, A. M.; Sun, X. *ACS Appl. Mater. Interfaces* **2014**, *6*, 21874-9.
- (25) Zou, X.; Huang, X.; Goswami, A.; Silva, R.; Sathe, B. R.; Mikmeková, E.; Asefa, T. *Angew. Chem. Int. Ed.* **2014**, *53*, 4372-4376.
- (26) Holewinski, A.; Idrobo, J.-C.; Linic, S. *Nat. Chem.* **2014**, *6*, 828-834.
- (27) Chen, D.; Ye, F.; Liu, H.; Yang, J. *Sci. Rep.* **2016**, *6*, 24600.
- (28) Yang, X.; Gan, L.; Zhu, C.; Lou, B.; Han, L.; Wang, J.; Wang, E. *Chem. Commun.* **2014**, *50*, 234-236.
- (29) Zhou, R.; Qiao, S. Z. *Chem. Mater.* **2014**, *26*, 5868-5873.
- (30) Tiwari, A.; Nagaiah, T. C. *ChemCatChem* **2016**, *8*, 396-403.
- (31) Xu, L.; Li, H.; Xia, J.; Wang, L.; Xu, H.; Ji, H.; Li, H.; Sun, K. *Mater. Lett.* **2014**, *128*, 349-353.
- (32) Lu, Y.; Du, S.; Steinberger-Wilckens, R. *Appl. Catal. B: Environ.* **2016**, *199*, 292-314.
- (33) Liu, H.; Adzic, R. R.; Wong, S. S. *ACS Appl. Mater. Interfaces* **2015**, *7*, 26145-26157.

- (34) Koenigsmann, C.; Scofield, M. E.; Liu, H.; Wong, S. S. *J. Phys. Chem. Lett.* **2012**, *3*, 3385-3398.
- (35) Liu, H.; Koenigsmann, C.; Adzic, R. R.; Wong, S. S. *ACS Catal.* **2014**, *4*, 2544-2555.
- (36) Scofield, M. E.; Koenigsmann, C.; Wang, L.; Liu, H.; Wong, S. S. *Energy Environ. Sci.* **2015**, *8*, 350-363.
- (37) Zhu, C.; Wen, D.; Oschatz, M.; Holzschuh, M.; Liu, W.; Herrmann, A.-K.; Simon, F.; Kaskel, S.; Eychmüller, A. *Small* **2015**, *11*, 1430-1434.
- (38) Liu, W.; Herrmann, A.-K.; Bigall, N. C.; Rodriguez, P.; Wen, D.; Oezaslan, M.; Schmidt, T. J.; Gaponik, N.; Eychmüller, A. *Acc. Chem. Res.* **2015**, *48*, 154-162.
- (39) Kundu, M. K.; Sadhukhan, M.; Barman, S. *J. Mater. Chem. B* **2015**, *3*, 1289-1300.
- (40) Barman, S.; Sadhukhan, M. *J. Mater. Chem.* **2012**, *22*, 21832-21837.
- (41) Sadhukhan, M.; Barman, S. *J. Mater. Chem. A* **2013**, *1*, 2752-2756.
- (42) Gopiraman, M.; Bang, H.; Yuan, G.; Yin, C.; Song, K.-H.; Lee, J. S.; Chung, I. M.; Karvembu, R.; Kim, I. S. *Carbohydrate Polymers* **2015**, *132*, 554-564.
- (43) Kundu, M. K.; Bhowmik, T.; Barman, S. *J. Mater. Chem. A* **2015**, *3*, 23120-23135.
- (44) Batalovic, K.; Bundaleski, N.; Radakovic, J.; Abazovic, N.; Mitric, M.; Silva, R. A.; Savic, M.; Belosevic-Cavor, J.; Rakocevic, Z.; Rangel, C. M. *Phys. Chem. Chem. Phys.* **2017**, *19*, 7062-7071.
- (45) Markovic, N. M.; Schmidt, T. J.; Stamenkovic, V.; Ross, P. N. *Fuel Cells* **2001**, *1*, 105-116.
- (46) Hu, P.; Song, Y.; Chen, L.; Chen, S. *Nanoscale* **2015**, *7*, 9627-9636.
- (47) Santos, E.; Pötting, K.; Lundin, A.; Quaino, P.; Schmickler, W. *ChemPhysChem* **2010**, *11*, 1491-1495.
- (48) Liang, H.-W.; Wei, W.; Wu, Z.-S.; Feng, X.; Müllen, K. *J. Am. Chem. Soc.* **2013**, *135*, 16002-16005.

(49) Negro, E.; Vezzù, K.; Bertasi, F.; Schiavuta, P.; Toniolo, L.; Polizzi, S.; Di Noto, V. *ChemElectroChem* **2014**, *1*, 1359-1369.

Appendix D

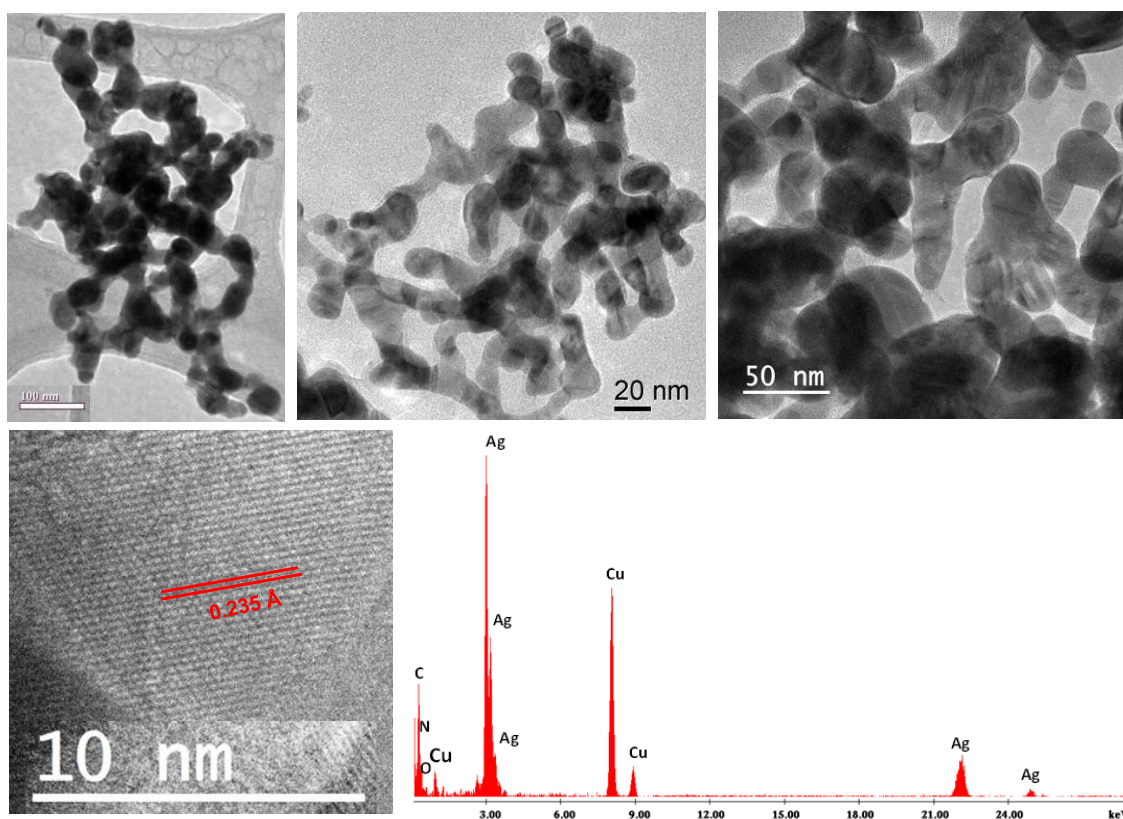


Figure S6.1. (a-c) TEM images of AgNWs composite in low and high magnification showing interconnected nanochains of Ag. (d) HRTEM images of Ag in AgNWs. (e) TEM EDS profile has taken on AgNWs composite.

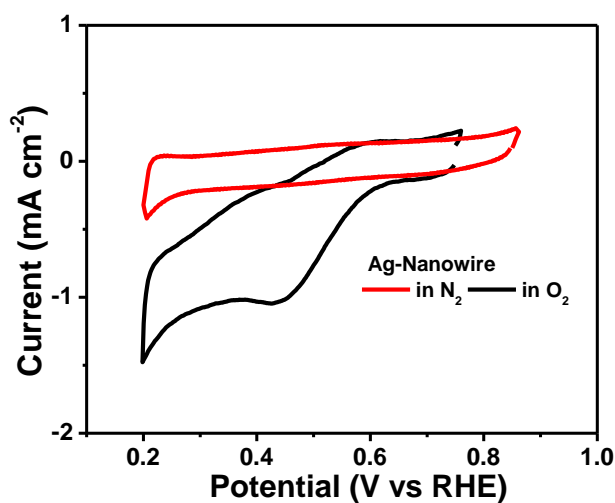


Figure S6.2. CVs of ac-AgNWs-CN_x in O₂ saturated and N₂ saturated 0.5 M H₂SO₄.

Table S6.1. Comparison of HER activity of different catalysts with ac-AgNWs-CN_x on GC electrode in acidic medium.

Catalyst	Catalyst loading (mg cm ⁻²)	Onset potential (mV vs. RHE)	Over potential (mV in RHE) vs. current density (mA cm ⁻²)	Tafel slope (mV/dec)	Exchange current (mA cm ⁻²)	Ref
PtNSSs@PEI	0.089	+64.6	-25 (143 mA cm ⁻²)	28		Chem. Sci. 2017 , <i>8</i> , 8411-8418
Co-NRCNT	0.28	-50	-260 (10 mA cm ⁻²)	69	0.01	Angew. Chem. Int. Ed. 2014 , <i>126</i> , 4461
CoSe ₂	0.37	-30	-90 (4 mA cm ⁻²)	40	0.037	Energy Environ. Sci. 2013 , <i>6</i> , 3553
PtNiCu	0.06	0	-50 (143 mA cm ⁻²)	28		Chem. Sci. 2017 , <i>8</i> , 8411
Pt ₁₃ Cu ₇₃ Ni ₁₄ /CNF @CF		+5	70	38		ACS Appl. Mater. Interfaces 2016 , <i>8</i> , 3464
Pt _{tripods} @PA	~0.081	+19.6	-25(90 mA cm ⁻²)	-	-	ACS Catal. 2017 , <i>7</i> , 452
WPNA _s /CC	2	-50	-130 (10 mA cm ⁻²)	69	0.29	ACS Appl. Mater. Interfaces 2014 , <i>6</i> , 21874
MoP-CA ₂	0.36	-40 (IR free)	-125 (10 mA/cm ²)	54	0.086	Adv. Mater. 2014 , <i>26</i> , 5702.
Nano MoP	1	-	-110 (10 mA cm ⁻²)	45	0.12	Chem. Mater. 2014 , <i>26</i> , 4826
NiAu/Au	-	-7	-	36	-	J. Am. Chem. Soc. 2015 , <i>137</i> , 5859
A-Ni-C		-	-34 (10 mA cm ⁻²)	41	1.2	Nat. Commun. 2016 , <i>7</i> , 10667
Au-aerogel-CN _x	0.127	-30	-225 (20 mA cm ⁻²)	53	0.03	J. Mater. Chem. A 2015 , <i>3</i> , 23120
Pd-CN _x	0.043	12	55	35	0.40	ACS Catal. 2016 , <i>6</i> , 1929
1-D-RuO ₂ -CN _x	93	-14	-93 (10 mA cm ⁻²)	40	0.22	ACS appl. Mater. interfaces 2016 , <i>8</i> , 28678.
Pt _{tripods} @PA	~0.081	+19.6	-25(90 mA cm ⁻²)	-	-	ACS Catal. 2017 , <i>7</i> , 452
MoS ₂ /CoSe ₂	0.28	-11	-68 (10 mA cm ⁻²)	36	0.073	Nat. Commun. 2015 , <i>6</i> , 5982
Ni ₂ P		-25	-130 (20 mA cm ⁻²)	-46	0.033	J. Am. Chem. Soc. 2013 , <i>135</i> , 9267
Ni-Mo-N nanosheets	0.25	-78	~ -200 mV (3.5 mA cm ⁻²)	35.9	0.24	Angew. Chem. Int. Ed. 2012 , <i>51</i> , 6131
Ac-AgNWs-CN _x	0.363	-0	-25 (10 mA cm ⁻²)	32	0.5	This Work

Table S6.2. Comparison of HER activity of different catalysts with ac-AgNWs-CN_x on GC electrode in basic medium.

Catalyst	Catalyst loading (mg cm ⁻²)	Onset potential (mV vs. RHE)	Over potential (mV in RHE) vs. current density (mA cm ⁻²)	Tafel slope (mV/dec)	Exchange current (mA cm ⁻²)	Ref.
Ni/MWCNT	-	-	220 (20 mA cm ⁻²)	102	0.011	J. Power Sources 2014 ,266, 365
Co-NRCNTs		-50-100	370 (10 mA cm ⁻²)			Angew. Chem. Int. Ed. 2014 ,53, 4372.
NiP ₂ NS/CC		-74	102 (10 mA cm ⁻²)	64		Nanoscale 2014 , 6, 13440
Co _{0.59} Fe _{0.62} P	0.35	-39	92 (10 mA cm ⁻²)	72	0.568	Nanoscale 2015 ,7, 11055.
Pt NWs/SLNi(OH) ₂	0.016	0	65 (10 mA cm ⁻²)			Nat. Commun. 2015 ,6, 6430
Pt ₃ Ni ₂ NWs-S/C	0.0153	-	50 (10 mA cm ⁻²)	-	-	Nat. Commun. 2015 ,6, 6430
NiONi-CNT			100 (10 mA cm ⁻²)			Nat. Commun. 2014 ,5, 4695
CoO _x @CN			232 (10 mA cm ⁻²)			J. Am. Chem. Soc. 2015 ,137,2688
CoP/CC			209 (10 mA cm ⁻²)	129		J. Am. Chem. Soc. 2014 ,136, 7587.
CoN _x /C	2.0	-30	170 (10 mA cm ⁻²)	75	-	Nat. Commun. 2015 ,6, 7992.
Porous Pd-CN _x	0.043	-75	180 (5 mA cm ⁻²)	150	0.037	ACS Catal. 2016 ,6,1929
Mo ₂ C	0.8	-110	190 (10 mA cm ⁻²)	54	0.0038	Angew. Chem. Int. Ed. 2012 ,51,12703.
1-D-RuO ₂ -CN _x	0.012	-16	95 (10 mA cm ⁻²)	70	0.28	ACS appl. Mater. Interfaces 2016 ,8, 28678.
NiO/Ni-CNT	0.28	-	80 (10 mA cm ⁻²)	82	-	Nat. Commun. 2014 , 5, 4695.
Ni-Mo nanopowders	1	0	80 (10 mA cm ⁻²)			ACS Catal. 2013 , 3, 166.
Ac-AgNWs-CN _x		0	110 (10 mA cm ⁻²) 160 (20 mA cm ⁻²)	65	0.3	This work

CHAPTER 7

Two-dimensional Assembly of Silver Nanoparticles on Carbon Nitride Sheets and their Applications in Non-enzymatic Sensing of Hydrogen Peroxide and Glucose

7.1 ABSTRACT

Fabrication of ordered assembly of noble metal nanoparticles on a two dimensional (2-D) sheets is a very challenging task. In this chapter, we demonstrated a facile bottom up self-assembly method for the formation of ordered assembly silver nanoparticles on carbon nitride sheets. Ultrasonication of aqueous graphitic carbon nitride quantum dots ($g\text{-CN}_x$) in presence of Ag^+ ion produces silver-carbon nitride (Ag-CN_x) composite. The ordered assemblies of monodispersed silver nanoparticles on thin carbon nitride sheets are produced by evaporation of aqueous solution of Ag-CN_x composites. On evaporation of this solution, first 2-D sheets are formed due to condensation of $g\text{-CN}_x$ on a solid substrate and then silver nanoparticles sit on voids of carbon nitrides on drying. The silver nanoparticles carbon nitride sheets modified glassy carbon electrode can be used highly sensitive electrochemical non enzymatic sensors for hydrogen peroxide (H_2O_2) and glucose. The lowest detection limits for H_2O_2 and glucose were 0.6 nM and 0.6 μM respectively.

7.2. INTRODUCTION

In the past several years, nanostructured materials have attracted significant interests^{1,2} due to their size, shape and composition dependent properties which lead to their unique performance in electronic³, optical⁴, catalytic⁵, sensor⁶ applications. The preparation and organization of monodispersed nanomaterials is important for scientific and technologic developments. Nanoparticles can easily self-assembled into 2-D ordered monolayer and 3-D nanocrystals⁷. The ordered 2-D assemblies of nanomaterials exhibit different properties from individual nanoparticle as well as bulk due to the quantum confinement in individual particles and inter particle coupling. Several bottom up methods are available in the literature for the fabrication 2-D super lattice nanomaterials such as, evaporation induced self-assembly⁸, spin coating⁹, Langmuir-Blodgett method¹⁰, layer by layer assembly¹¹, adsorption on to self-assembled monolayers (SAMs)¹², liquid-liquid interface assembly¹³ *etc.* Although this self-assembled monolayer represents a new class of materials, it suffers serious draw back due to the presence of defects in the film and poor stability of these mono layers. The development of self-assemblies of nanomaterials on two dimensional sheets is important to achieve desired properties for the applications in surface plasmonics¹⁴, photovoltaic¹⁵, photonic devices¹⁶, and sensors¹⁷. Graphene, due to its unique properties¹⁸ such as high specific surface area, excellent electrical conductivity, high charge carrier mobility, high mechanical strength, make it a promising candidate as a two dimensional support for different nanoparticles. The graphene containing metal or semiconductor nanoparticles have confirmed to be effective nano-composite materials for photovoltaic¹⁵, catalysis¹⁹ and biosensor²⁰ applications. Noble metal nanoparticle doped graphene based composite materials has been reported for their potential applications in catalysis for fuel cell²¹, sensors²² and gas storage²³. Semiconductor

nanoparticles-graphene composite have attracted attention for photocatalytic applications²⁴. In most of cases, graphene oxide or functionalized graphene oxide used as 2-D substrate for synthesis metal composite materials. The oxygen containing functional groups and defects in the graphene oxide are the active sites for catalytic reactions and growth of metal nanoparticles. Since uniform distribution of functional groups and defects on graphene are difficult to generate, fabrication of well-ordered metal nanoparticle on 2-D graphene sheets is thus a challenge. Nanoparticles can also be assembled on graphene using a stabilizer²⁵ such as polymer or organic molecules, an indirect attachment of nanoparticles to graphene sheets are present through this organic or polymer molecule. Therefore, effective attachment of nanoparticle to graphene sheets and uniform distribution of monodispersed particle on graphene sheets remain great challenge. Thus, there are needs of new fabrication methods as well as a new supports for the formation of ordered assembly of nanoparticles. Recent years graphitic carbon nitride (g-C₃N₄) which is also a 2-D material, has attracted so much attention for its potential applications in photo catalytic water splitting²⁶, degradation of organic pollutants²⁷, photosynthesis under visible light²⁸, sensors²⁹ and catalysis³⁰ of various important reactions. Although several reports on synthesis of mesoporous carbon nitride metal nanoparticles composites and their applications are reported by various groups^{31,32}. X. Yao *et al.* reported synthesis of Ag/AgCl/g-C₃N₄ composite and their application in photocatalytic degradation of organic dye under visible light irradiation³³. The heterostructured g-C₃N₄/Ag/TiO₂ microspheres with enhanced Photocatalytic performance towards degradation of methyl orange under visible light irradiation was reported³⁴. Y. Yang *et al.* prepared silver deposited carbon nitride plasmonic photocatalysts for the degradation of methyl orange and p-nitrophenol under

visible light³⁵. However ordered assembly of metal nanoparticles on 2-D carbon nitride sheets is not reported in the literature so far.

The development of rapid and reliable methods for highly sensitive, selective glucose³⁶ and hydrogen peroxide³⁷ detection is necessary in many fields such as clinical diagnostics, food industry, sustainable fuel cell, environmental analyses. For example, H₂O₂ is involved in several biological processes and is one of the important products of several biological enzyme-catalysed reactions. It is extensively used as an oxidant for liquid-fuel cell, chemical and food industry. On the other hand, diabetic mellitus is a public health problem worldwide. The reason for this metabolic disorder is due to the insulin deficiency and hyperglycaemia, which leads to several complications such as kidney failure, heart diseases and blindness. Thus, accurate determination of H₂O₂ and glucose is important. Several analytical methods such as titration³⁸, fluorometric³⁷, chemiluminescent³⁹, electrochemical methods³⁷ are available for determination of H₂O₂. Among these methods, the electrochemical methods for determination of glucose and H₂O₂ are the most promising methods because of their low costs, high sensitivity and portability. The conventional enzymatic electrochemical glucose and H₂O₂ biosensors generally suffer several drawbacks such as their short device life and their performances are generally affected on changing pH, temperatures due to the use of enzyme in the conventional biosensors. These limitations can be easily overcome by using non-enzymatic electrochemical sensing of glucose and H₂O₂.

We report here a facile synthesis method of ordered assembly of metal nanoparticles in the size range (1-10 nm). Most importantly, we report here synthesis and ordered 2-D assembly of nearly monodispersed silver nanoparticles in the size range 2-10 nm on carbon nitride sheets. On evaporation of aqueous solution of Ag-CN_x composite on a solid support, thin CN_x sheets were formed first due to condensation of g-CN_x

solution and then silver nanoparticles sit on the voids of CN_x framework leading to formation of 2-D assembly of Ag nanoparticles on CN_x sheets. Silver nanoparticles carbon nitride composites were formed from ultrasonic treatment of AgNO_3 in presence of carbon nitride quantum dots, without reducing agents. Carbon nitride sheets containing Ag nanoparticles can be used as electrochemical biosensors for hydrogen peroxide and glucose. The detection limit for hydrogen peroxide are found to be 0.7 nM and 5 nM with sensitivity of 4.25×10^5 and $1.7 \times 10^4 \mu\text{A cm}^{-2} \text{mM}^{-1}$ respectively.

7.3 EXPERIMENTAL SECTION

Preparation of Ag- CN_x composite.

5 mg of freshly prepared g- C_3N_4 was dissolved in 5 ml water. Then this solution was mixed with 5ml aqueous solution containing 40 mg AgNO_3 . Ultrasonication of this solution at 35°C for 2.5 hrs by probe sonicator operating at 28 kHz frequency (400 watt) produces black precipitate. Finally this solution was centrifuged at 16000 rpm for 30 minutes to collect solid product. Finally, the product was washed with water dried under vacuum.

Preparation of modified Ag- CN_x /GC electrode.

Glassy carbon (GC) electrode was polished with 1.0, 0.1 and 0.05 mm alumina slurry on Buehler micro cloth polishing cloth. After rinsing, the electrode was sonicated in distilled water for about 10 min. 1 mg Ag- CN_x composite was dissolved in 1ml water to make a stock solution. 20 μL of 7 hrs old aqueous stock solution was evaporated on cleaned GC electrode to prepare Ag- CN_x /GC electrode.

7.4 RESULTS AND DISCUSSIONS

When aqueous solution of Ag^+ ion was mixed with g-CN_x then $\text{g-CN}_x\text{-Ag}^+$ complex was formed. Figure 7.1a and 7.1b shows the FT-IR and UV-Visible spectra of the g-CN_x respectively in the presence and the absence of Ag^+ ions.

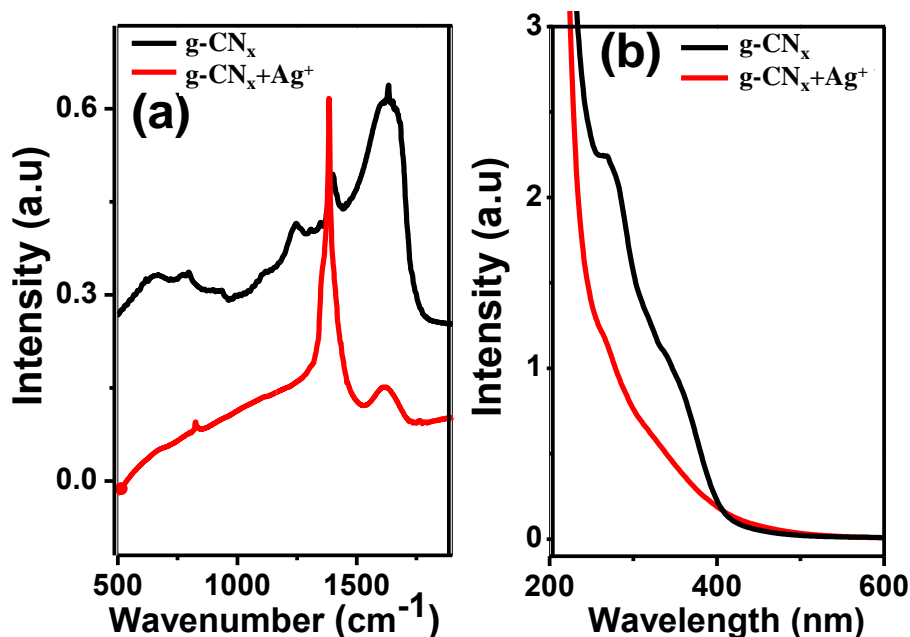


Figure 7.1. (a) FT-IR spectra and (b) UV-Visible spectra of free g-CN_x and in the presence of Ag^+ ions.

The FT-IR spectra of g-CN_x has two peaks, one at 1230 cm^{-1} and the other at 1400 cm^{-1} due to aromatic $\text{C}=\text{N}$ stretch which disappeared on addition of Ag^+ ions with the appearance of a new intense peak at 1380 cm^{-1} (Figure 7.1a). In addition, the $\pi \rightarrow \pi^*$ transition at 260 nm in UV-Visible spectra of the g-CN_x respectively in the presence and the absence of Ag^+ ions. The FT-IR spectra of g-CN_x has two peaks, one at 1230 cm^{-1} and the other at 1400 cm^{-1} due to aromatic $\text{C}=\text{N}$ stretch which disappeared on addition of Ag^+ ions with the appearance of a new intense peak at 1380 cm^{-1} (Figure 7.1a). In addition, the $\pi \rightarrow \pi^*$ transition at 260 nm in UV-Visible spectra disappears completely on addition of Ag^+ ions (Figure 7.1b). The Ag-CN_x composite was prepared by ultrasound method. Powder X-ray diffraction (p-XRD) patterns of $\text{g-C}_3\text{N}_4$ and Ag-

CN_x composite are shown in Figure 7.2. Both the p-XRD patterns exhibit a peak at ~ 27.4° (2θ) with interlayer spacing of 3.3 Å due to (002) reflection of g-C₃N₄. In addition to this peak, five additional peaks at 38.1°, 44.09°, 64.36°, 77.29°, 81.31° corresponds to (111), (200), (220), (311), (222) reflections of silver are observed in nano composites⁴⁰. This also confirms that silver nanoparticles are formed due to ultrasonic treatment. Figure 7.3a and 7.3b shows TEM images of silver nanoparticles highly dispersed on the carbon nitride sheets on evaporation of Ag-CN_x composite solution on TEM grid. The corresponding EDX spectrum (Figure 7.3c) has taken from the carbon nitride in the image of Figure 7.3a shows the presence of carbon, nitrogen and silver confirming deposition of Ag nanoparticle on carbon nitride sheets. The size distribution of nanoparticles as shown in Figure 7.3d indicates dispersed AgNPs in CN_x sheets are in the range 5-8 nm. The SAED image of Ag NPs, taken from Figure 7.3b is shown in Figure S7.1. The interlayer spacing calculated from SAED image are 2.36, 1.44, 1.23, 0.946 Å which corresponds to (111), (220), (311) and (331) planes of face centered cubic silver nanoparticle respectively based on powder X-ray data base (JCPDS No.04-0783). This is in agreement with p-XRD data (Figure 7.2) of Ag-CN_x composites. The X-ray Photo Electron Spectroscopy (XPS) has been widely used to monitor the change of electronic structure of carbon nitride framework in presence of Ag⁺ ion and silver nanoparticles. XPS spectra of CN_x in the carbon 1s and nitrogen 1s region were deconvoluted to three and two main Gaussian peaks respectively (Figure S7.2). The binding energy of 285.45 eV (C1) and 286.35 eV (C2) are assigned to the presence of (sp²) N-C=N (sp²) (carbon bonded to two nitrogen atom) and C(-N)₃ (planar trigonal carbon geometry) respectively⁴¹.

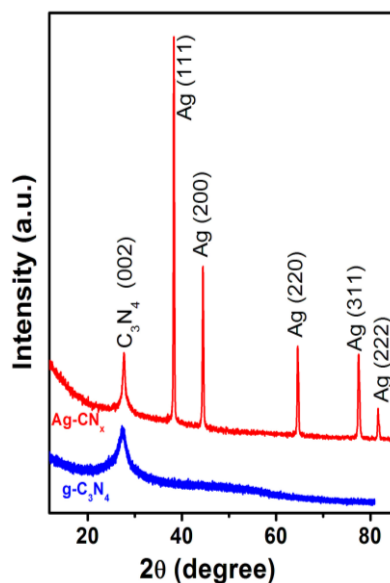


Figure 7.2. p-XRD of g-CN_x and Ag-CN_x composite.

The peaks at 400.3 eV and 401.4 eV refer to the presence of (sp²) C-N1=C (sp²) or pyridine moiety and quaternary nitrogen respectively. The position (Figure 7.4a) and shape of C1s XPS spectrum of CN_x in presence Ag⁺ ions is significantly higher than that of free CN_x, whereas the binding energies of nitrogen atoms in free CN_x and Ag⁺-CN_x are same (Figure 7.4b). It is well known that the binding energy of Ag 3d is very sensitive to the chemical environment around Ag⁺ ions. The peaks due to Ag 3d_{5/2} and 3d_{3/2} were reported to be appeared at 368.21 eV and 374.22 eV respectively for AgNO₃ while these two peaks centred at 369.7 eV and 375.6 eV for metallic Ag(0)⁴². The Ag 3d XPS of Ag⁺ doped CN_x and Ag nanoparticle dispersed on CN_x are shown in Figure 7.4c. It shows that the Ag 3d_{5/2} and 3d_{3/2} peaks for Ag⁺-CN_x appeared at 369.05 and 375.12, which are higher than that of Ag⁺ and lower than metallic silver. Thus, change in carbon and silver binding energies suggest that significant interaction between carbon of CN_x sheets and Ag⁺ ions, which is in accordance with FT-IR and UV-Visible studies.

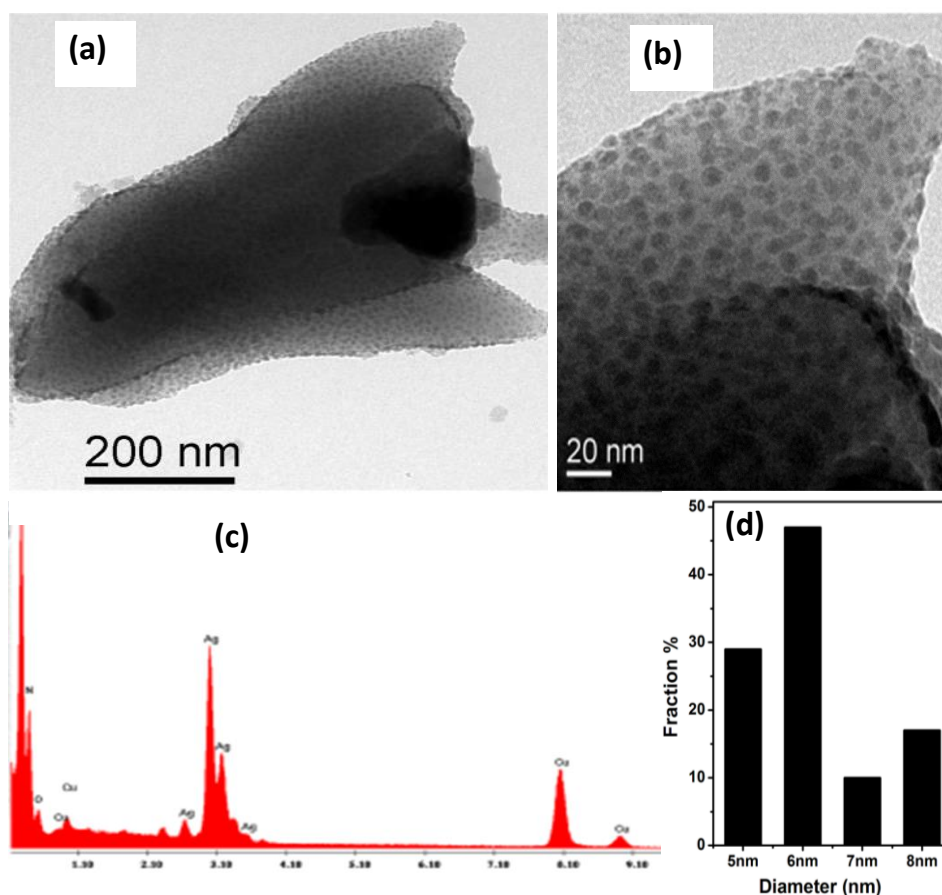


Figure 7.3. Two dimensional self-assembly of silver nanoparticles on CN_x sheets: (a) and (b) TEM images showing AgNPs highly dispersed on CN_x sheet (c) EDX spectrum on this sheet. (d) Size distribution of AgNPs.

The N1s spectrum of free g-CN_x and Ag⁺-CN_x exhibit a peak centered at 400.5eV and the N1s peak is shifted to significant interaction between carbon of CN_x sheets and Ag⁺ ions, which is in accordance with FT-IR and UV-Visible studies. The N1s spectrum of free g-CN_x and Ag⁺-CN_x exhibit a peak centered at 400.5eV and the N1s peak is shifted to higher binding energy at 404.5 eV in presence of Ag nanoparticles in Ag-CN_x (Figure 7.4b). However, C1s binding energy of AgNPs dispersed CN_x and free CN_x are same, which is lower than that of Ag⁺-CN_x (Figure 7.4a). The two peaks centered at 372.5 eV and 378.3 eV can be assigned to Ag 3d_{5/2} and Ag 3d_{3/2} respectively of Ag-CN_x composite. Therefore the shift of 4.0 eV to higher N1s binding energy and 3.0 eV to higher Ag 3d

binding energies of Ag-CN_x compared to metallic Ag suggests that the silver nanoparticles are chemically bonded to CN_x sheets through nitrogen atoms.

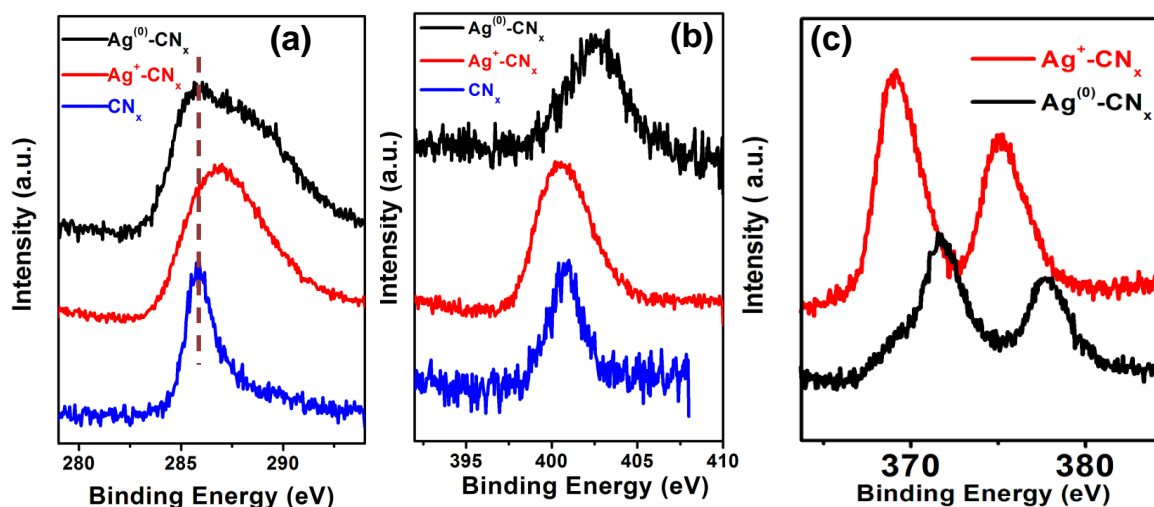


Figure 7.4. Comparison of XPS spectra of (a) C1s, (b) N1s of Ag-CN_x, Ag⁺-CN_x and CN_x, (c) Ag 3d XPS spectra of Ag-CN_x, Ag⁺-CN_x.

7.4.1 Growth and Assembly AgNPs on Carbon Nitride sheets

In order to synthesis of Ag-CN_x composites, ultrasonication of aqueous solution of AgNO₃ in presence of g-CN_x was used. During ultrasound treatment Ag⁺ reduces to form very small silver nanoparticles which are physically adsorbed on the surface of carbon nitride sheets and thereby Ag-CN_x composites precipitated out. The 1.0 mg Ag-CN_x composites were dissolved in 1.0 ml water and used as stock solution for FESEM measurements. Evaporation of this solution on a solid substrate leads to formation of 2-D assembly of Ag nanoparticles on CN_x sheets. It was reported by our group²⁹ recently that two-dimensional (2-D) carbon nitride sheets are formed by evaporation induced self-assembly and condensation of g-CN_x on a solid substrate. As shown in Figure S7.3 and S7.4, TEM and AFM images of CN_x sheets respectively confirm the formation of 2-D CN_x on evaporation of aqueous solution of g-CN_x.

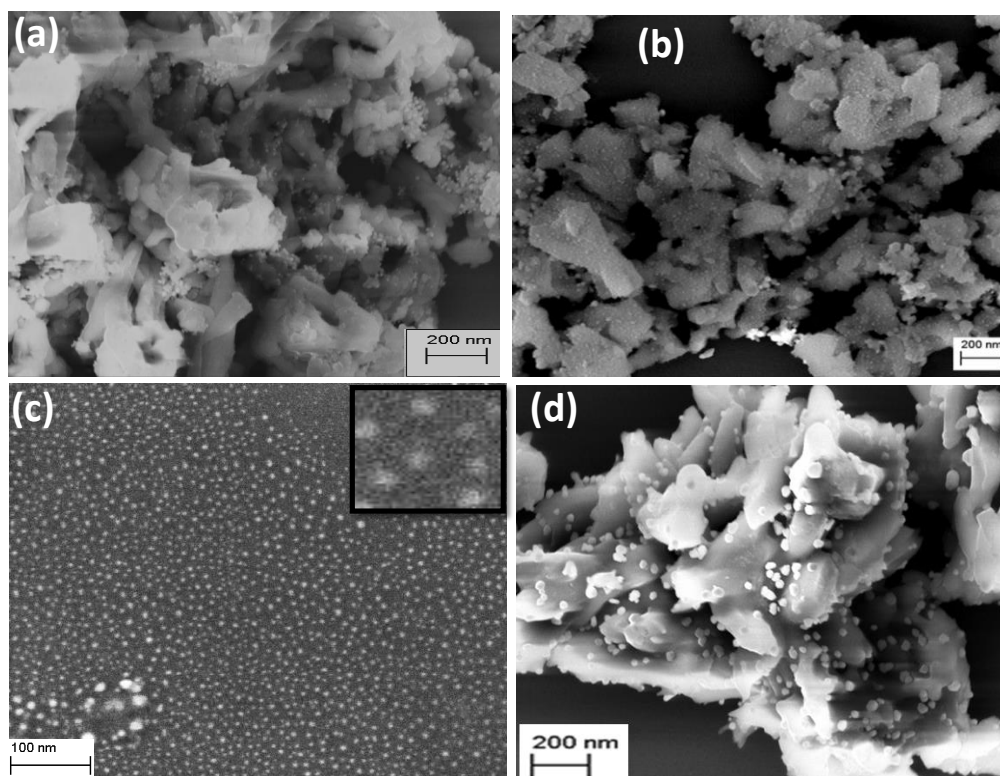
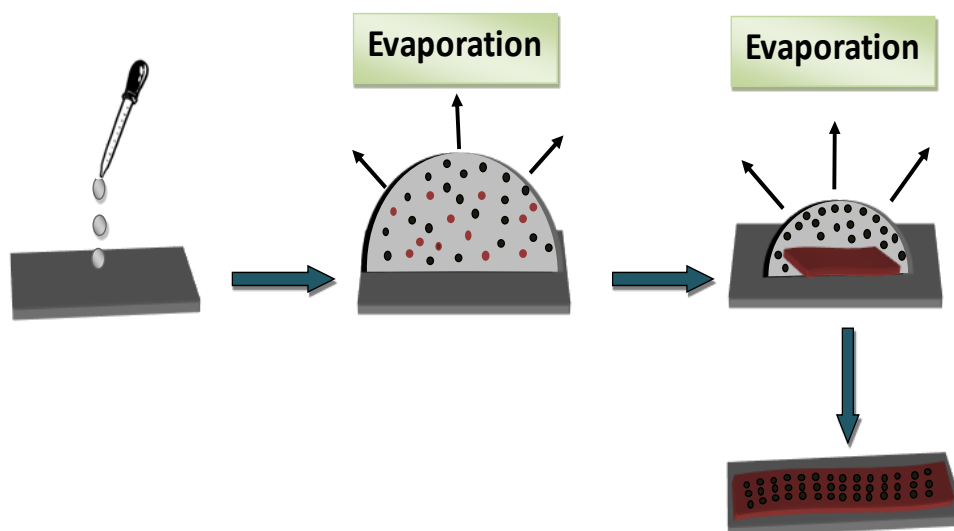


Figure 7.5. FESEM images showing assembly of AgNPs on CN_x sheets prepared from evaporation of (a) zero hrs (b) 7 hrs (d) 14 hrs old stock solution on Si wafer. (c) SEM image of ordered 2-D assembly of AgNPs on a very thin CN_x sheet from 7 hrs old stock solution on Si wafer (inset of (c) showing heptamer arrangement of AgNPs).

SEM measurements were used extensively to understand growth process of silver nanoparticles and their assembly on CN_x sheets. SEM samples were prepared by evaporating this stock solution at different time intervals on silicon substrate. Figure 7.5a, (b, C) and d display the FESEM images of 2-D assembly of AgNPs on CN_x sheets prepared by evaporating from zero hours (zero hrs), seven hours (7 hrs) and fourteen hours (14 hrs) old stock solution respectively. The SEM image, prepared by evaporation from 7 hrs old stock solution as shown in Figure 7.6b and S7.5, indicates that spherical silver nanoparticles in the size range of 5-6 nm are highly dispersed and uniformly distributed on CN_x sheets.



Scheme 7.1. Schematic diagram of evaporation induced ordered self-assembly of AgNPs on CN_x sheet on a solid surface.

In addition, Figure 7.6b and S7.6 clearly show the uniform distribution of Ag nanoparticles (5-6 nm) on very thin CN_x sheets. Although we could not see SEM images of these thin sheets, but the presence of same percentage of carbon, nitrogen in EDX measurements confirms the presence of thin CN_x sheets. The distance between the particles are ~ 3 nm and all individual particles is surrounded by six or five or four particles to form a two dimensional assembly of silver nanoparticles on carbon nitride sheets. From the SEM image of AgNPs-CN_x in Figure 7.5a, it can be seen that very few silver nanoparticles are randomly distributed on CN_x sheets when freshly prepared (zero hrs) stock solution was evaporated. The few particles on CN_x sheets indicate that the silver nuclei which were formed from ultrasonication, did not get time to grow bigger particles in solution since freshly prepared (zero hrs) stock solution was evaporated. The SEM image (Figure S7.7) of a remarkable long range hexagonal ordered assembly of silver nanoparticles on carbon nitride is also observed rarely.

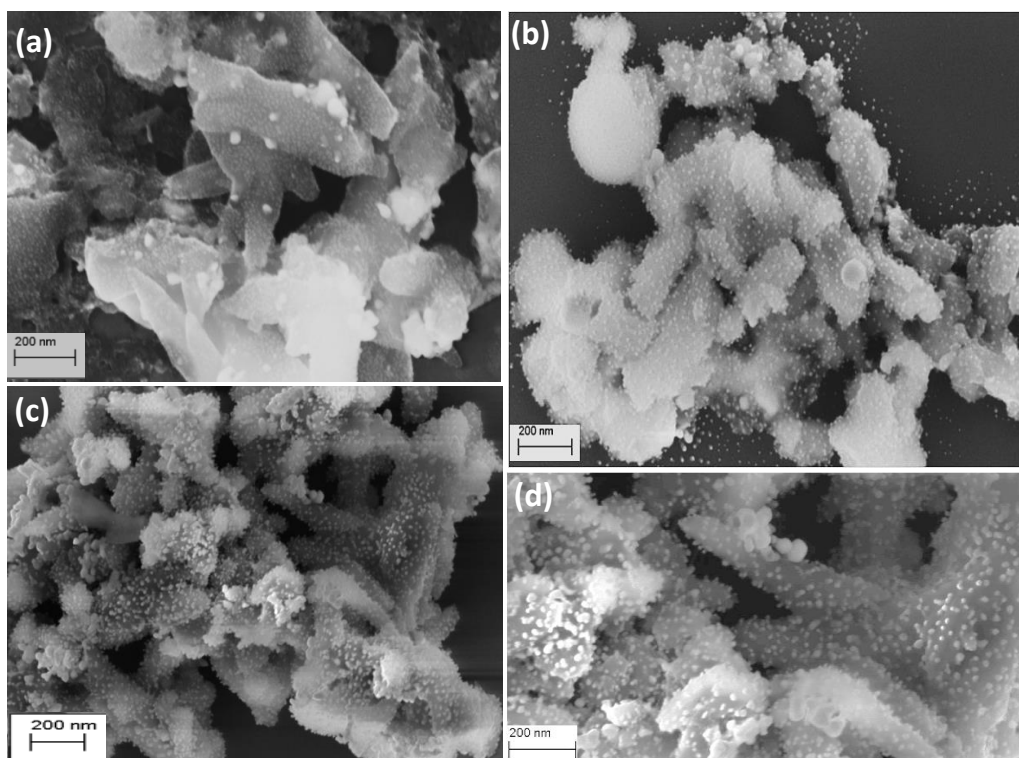


Figure 7.6. SEM images of AgNPs dispersed on CN_x sheets prepared from evaporation of 7 hrs old solution. The average sizes in (a), (b) and (c,d) are 3-4 nm, 5-6 nm and 8-10 nm respectively.

When SEM sample was prepared from drying of 14 hrs old stock solution, aggregated Ag nanoparticles with much greater size are randomly distributed on CN_x sheets, as shown in Figure 7.5d. This behaviour is likely due to the growth and ripening of silver nanoparticles become significant for 14 hrs old stock solutions. The strong chemical bonding between Ag atoms of nanoparticles and nitrogen atoms of CN_x as suggested by XPS, FT-IR analysis (discussed in the previous section), provides anchoring site where nucleation and growth of nanoparticles occurs. For the production of monodispersed nanoparticles, it is important to generate all the nuclei at the same time and all the nuclei should undergo same subsequent growth process. The narrow size distribution of Ag nanoparticles (Figure 7.6b, c) is due to the fact that silver nuclei formed at same time during ultrasonication, and the silver nanoparticles in solution undergo similar growth process before used sample preparation.

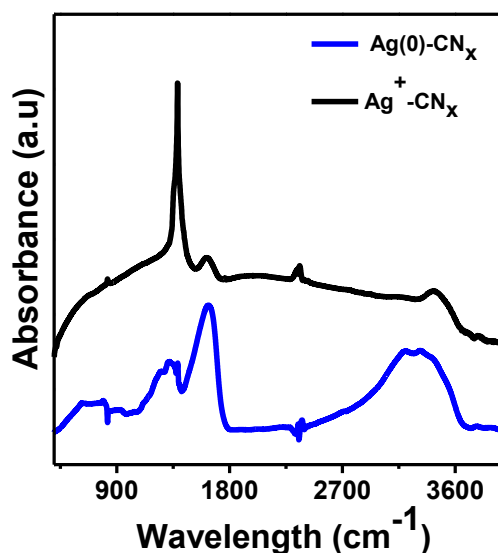


Figure 7.7. Comparison FT-IR spectra of $\text{Ag}^+\text{-CN}_x$ and $\text{Ag}(0)\text{-CN}_x$

Obtaining a small gap between two nanoparticles is always a quite challenging job to achieve due to aggregation of nanoparticles. XPS measurements predicted strong chemical bonding between silver and nitrogen atoms. The reason for small and fixed inter nanoparticles distance of 3 nm without aggregation of nanoparticles is possibly due to nucleation of Ag nanoparticles occurs at voids containing nitrogen atoms of CN_x framework. Figure 7.7 shows FT-IR spectra of the Ag-CN_x composites (product of ultrasonication) and $\text{Ag}^+\text{-CN}_x$. The strong peak in FT-IR spectra at 1400 cm^{-1} of $\text{Ag}^+\text{-CN}_x$ disappears completely and three peaks at $1317, 1400, 1627\text{ cm}^{-1}$ peaks due to C=N , similar to parent CN_x , for Ag-CN_x composites are regenerate due to ultrasonication. This indicates that Ag^+ ions which were bonded to CN_x sheets are also reduce to form silver nuclei (nanoparticles) and adsorbed to CN_x sheets.

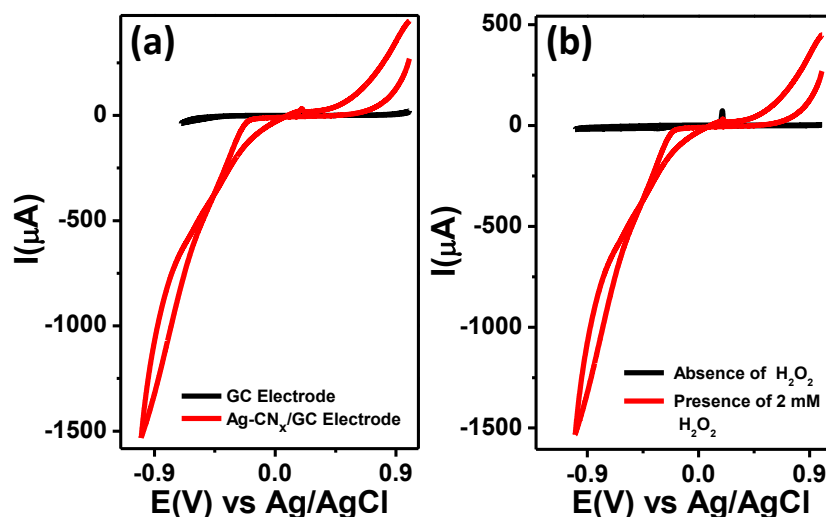


Figure 7.8. (a) CVs of 2 mM H_2O_2 in 0.01M PBS at bare and Ag- CN_x /GC electrode. (b) CVs of Ag- CN_x /GC electrode in absence and presence of 2 mM H_2O_2 in 0.01M PBS (pH=7) solution

In Figure 7.6 a, b and (c, d) silver nanoparticles in the range between 3-4 nm, 5-6 nm and 8-10 nm are formed when 7 hrs old stock solutions of 1.0 mg, 1.2 mg and 1.3 mg Ag- CN_x composites were dissolved in 1.0 ml water respectively and evaporated on silicon substrate. On dissolving of Ag- CN_x composites in water, Ag nuclei and carbon nitride quantum dots goes to solution separately and growth, repining of Ag nanoparticles occurs in solution. The two dimensional CN_x sheets from the condensation of CNQDs are formed first and then directed 2-D assembly of silver nanoparticles on the surface of CN_x sheets takes place. Based on TEM, SEM, XPS, FT-IR measurement a proposed mechanism for 2-D self-assembly of silver nanoparticle on CN_x is shown in Scheme 7.1.

7.4.2 Electrochemical Applications

The electro catalytic property of Ag nanoparticles doped CN_x modified glassy carbon (Ag- CN_x /GC) electrode towards the electrochemical reduction and oxidation of H_2O_2 was examined using cyclic voltammetry measurements.

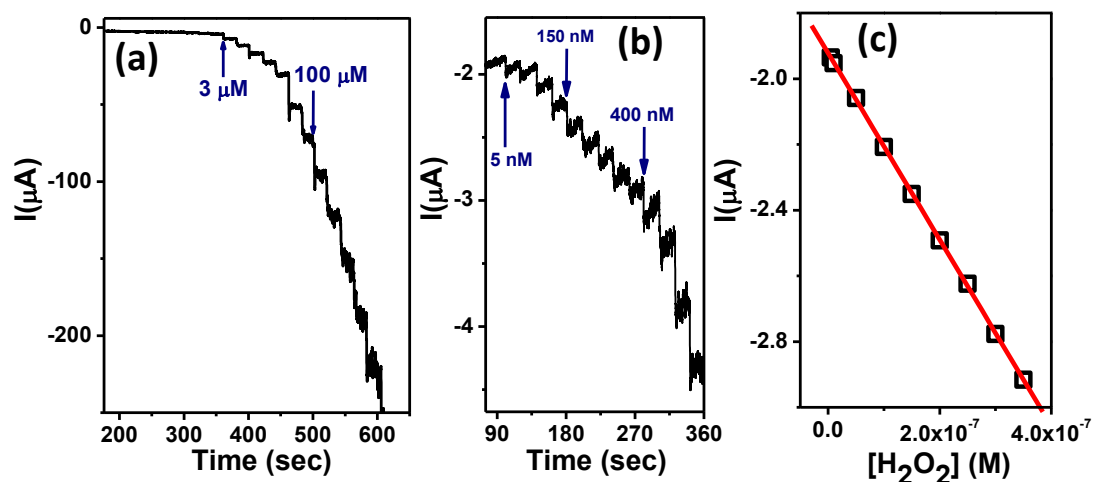


Figure 7.9. (a) Amperometric response of Ag-CN_x/GC electrode on successive addition of H₂O₂ into 0.01M PBS with stirring. Inset: lower concentration regime. (b) Lower concentration regime (c) Calibration curve of current vs. H₂O₂ concentration.

Figure 7.8a represents the comparison of voltammetry response of 2 mM H₂O₂ in 0.01 M PBS solution at bare GC electrode and Ag-CN_x/GC electrode. This suggests the superior electro catalytic activity at Ag-CN_x/GC electrode toward H₂O₂ oxidation. Figure 7.8b shows cyclic voltammograms at Ag-CN_x/GC electrode in absence and presence of 2 mM H₂O₂ in 0.01M PBS buffer solution. A small background current was observed in the blank of 0.01M PBS solution at Ag-CN_x/GC electrode where as a drastic increase of electrocatalytic current was observed in 0.01M PBS solution containing 2 mM H₂O₂. Figure 7.9a, b shows the typical amperometric current-time response at Ag-CN_x/GC electrode for successive addition of H₂O₂ into stirring 0.01M PBS buffer solution at an applied potential of -0.7V. Figure 7.9c shows calibration plot where a linear relation of current with concentration of H₂O₂ was observed in the concentration region ranging 5 nM to 0.35 μM with coefficient 0.999. From the slope of calibration plot as shown in Figure 7.9c, the lower detection limit for H₂O₂ at Ag-CN_x/GC electrode was found to be 4.5 nM at signal-to-noise ratio of 3.

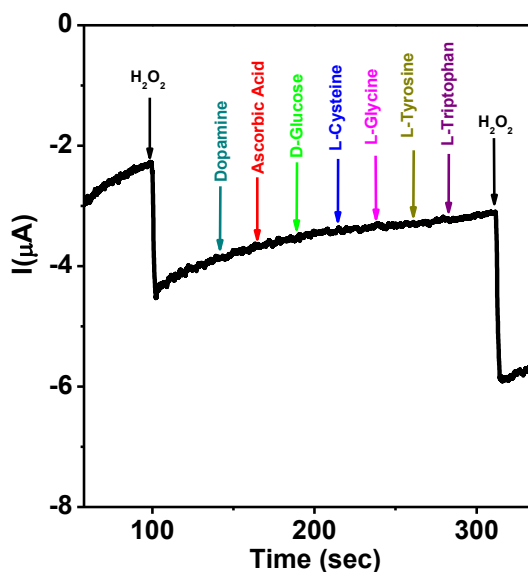


Fig 7.10. Amperometric responses of Ag-CN_x/GC electrode at a potential of -0.7V on subsequent addition of 5 μM dopamine (DA) 5 μM ascorbic acid (AA), 5 μM D-Glucose, 5 μM L-Glycine, 5 μM L-Cysteine, 5 μM L-Tyrosine, 5 μM L-Tryptophan and 5 μM H₂O₂.

The interference of other biomolecules such as dopamine (DA), ascorbic acid (AA), D-Glucose, L-Cysteine, L-Glycine, L-Tyrosine and L-Tryptophan on H₂O₂ detection were examined. As shown in Figure 7.10 the addition of 10 μM of H₂O₂ causes significant increase of amperometric response at the applied potential of -0.7 V, but addition of similar concentration of AA and DA did not cause interference the amperometric response of H₂O₂. We further studied electrochemical oxidation/reduction of H₂O₂ at Ag-CN_x/GC in basic NaOH medium. Figure 7.11a shows cyclic voltammograms at Ag-CN_x/GC electrode in absence and presence of 2 mM H₂O₂ in 0.05M NaOH solution. There is significant increase of current in case of 2 mM H₂O₂ compare to the blank in NaOH medium. The sensitivity of H₂O₂ detection at Ag-CN_x/GC electrode was studied by chronoamperometric current-time (i-t) measurements at +0.7V.

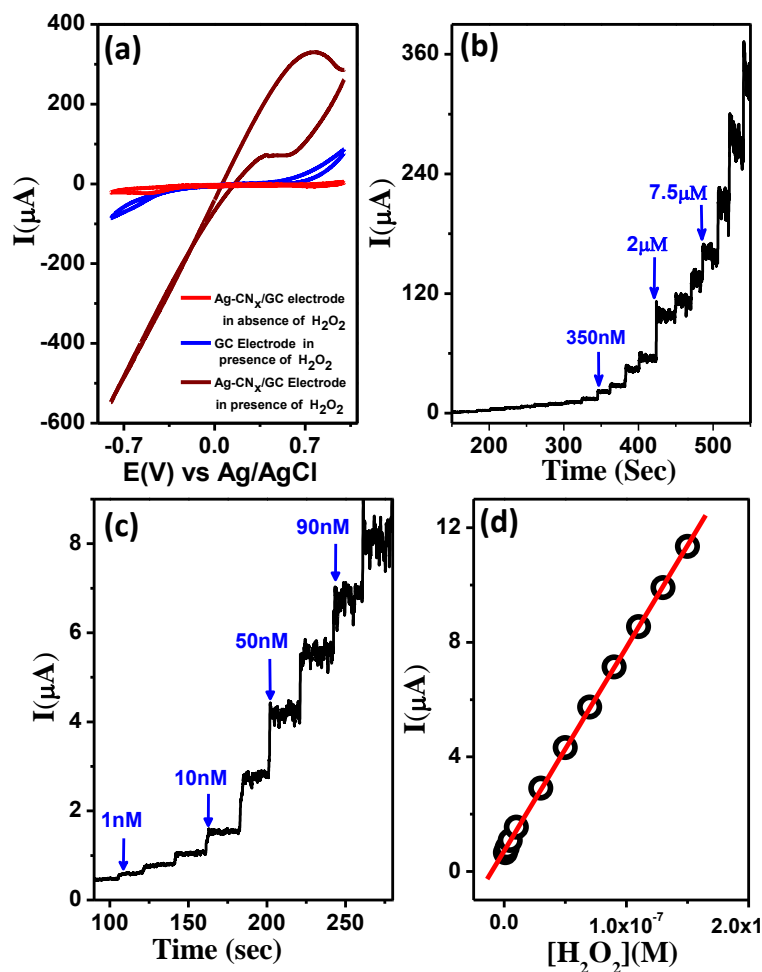


Figure 7.11. (a) CVs of Ag-CN_x/GC and only GC electrode in presence of 2 mM H₂O₂ and Ag-CN_x/GC electrode in absence of H₂O₂ in 0.05 M NaOH solution (b) Amperometric response of Ag-CN_x/GC electrode on successive addition of H₂O₂ into 0.05M NaOH with stirring. (c) Lower concentration regime of amperometric curve. (d) Calibration curve of current vs. H₂O₂ concentration.

The detection limit, calculated from the plot was found to be 0.6 nM. The detection limit, sensitivity of non-enzymatic H₂O₂ detection at Ag-CN_x/GC electrode were compared with the reported results of non-enzymatic H₂O₂ detection, which are summarized in Table 7.1

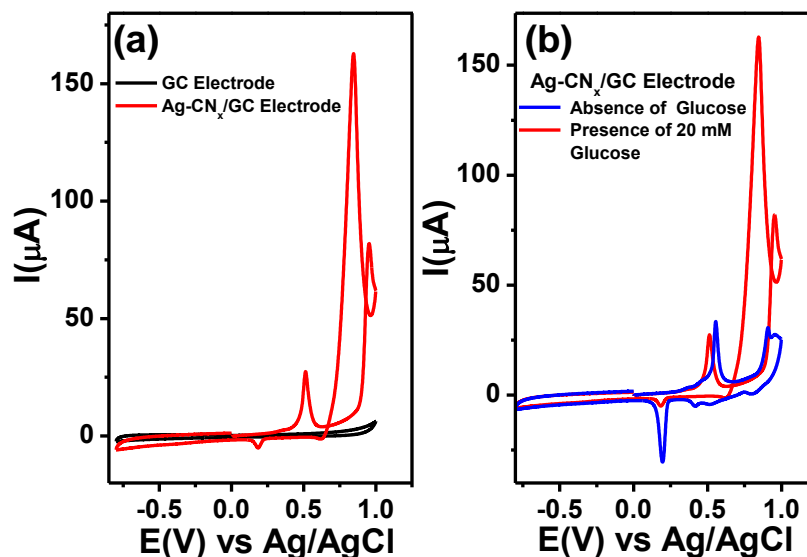


Figure 7.12. (a) CVs of 20mM glucose in 0.05M NaOH at bare GC and Ag-CN_x/GC electrode. (b) CVs of Ag-CN_x/GC electrode in absence and presence of 20 mM glucose in 0.05 (M) NaOH solution.

. From the Table 7.1 it is clear that our Ag-CN_x/GC electrode exhibits lower detection limit and higher sensitivity as compared to that of reported H₂O₂ biosensors. This outstanding performance of Ag-CN_x/GC electrode for non-enzymatic detection of H₂O₂ can be attributed to efficient electrochemical processes of silver nanoparticles and large surface area of two dimensional carbon nitride sheet. The amperometric current-time response at Ag-CN_x/GC electrode upon successive addition of H₂O₂ into stirring 0.05 M NaOH solution at +0.7V is shown in Figure 7.11b and Figure 7.11c. As plotted in Figure 7.11d, the calibration plot was linear over the concentration range of 1 nM - 0.15 μM with a correlation coefficient of 0.999 and a sensitivity of $4.5 \times 10^5 \mu\text{A} \cdot \text{cm}^{-2} \cdot \text{mM}^{-1}$ which was few order higher than reported values. The Cyclic voltammograms measurements were used to investigate the catalytic activity of Ag-CN_x modified GC electrode towards glucose oxidation.

Two Dimensional Assembly of Silver Nanoparticles on Carbon Nitride Sheets and their Application in Non-enzymatic Sensing of Hydrogen Peroxide and Glucose

Table. 7.1. Comparison of detection limit and sensitivity of Ag-CN_x/GC sensor with reported non enzymatic H₂O₂ sensors.

Electrode material	Applied potential	Linear range (μM)	Sensitivity	LOD (μM)	References
AgNP/SnO ₂ /GC	-0.3	10 - 35,000	-	5	<i>Electrochim. Acta</i> , 2013, 99 , 117-123
Ag-PIL-GE/GC	-0.22	0.1 - 2200	38.73 μA mM ⁻¹	0.05	<i>Microchim. Acta</i> , 2013, 180 , 261-268
PDA-Ag/GC	-0.3(SCE)	92 - 20000	6.79 μA mM ⁻¹	1.97	<i>Electrochim. Acta</i> , 2012, 61 , 31-35
SWCNT/AgNPs/C	-0.2(SCE)	10 - 8000	3.23 μA mM ⁻¹	0.2	<i>Microchim. Acta</i> , 2012, 177 , 185-193.
PQ11-AgNPs/GC	-0.3	100 - 180	-	33.9	<i>Electrochim. Acta</i> , 2011, 56 , 2295-2298.
Ag/GN-R/GC	-0.4	100 - 40000	-	28	<i>Macromolecules</i> 2010 , <i>43</i> , 10078-10083.
3D graphene/pDA/TH	-0.25	0.4 - 660	169.7 μA mM ⁻¹	0.08	<i>Electrochem. Commun.</i> , 2013, 26 , 81-84.
CR-GO/GC	-0.2	0.05 - 1500	-	0.05	<i>Anal. Chem.</i> , 2009, 81 , 5603-5613.
3DGN/MWCNT/Pt NP	+0.45	0.025 - 6.3	-	0.0086	<i>Small</i> , 2013, 9 , 1703-1707.
PtNPs-IP6 /GC	+0.4	0.24 - 1300	146.17 μA mM ⁻¹ cm ⁻²	0.2	<i>Nanotechnology</i> , 2013, 24 , 295503.
PDDA/t-MWCNT-Pt/GC	-0.1	1 - 800	481.25 μAmM ⁻¹ cm ⁻²	0.27	<i>Electrochim. Acta</i> , 2012, 65 , 288-293
PVA-MWCNTs-PtNPs/GC	0	2 - 3800	122.63 μAmM ⁻¹ cm ⁻²	0.7	<i>Electrochim. Acta</i> , 2012, 70 , 266 - 271.
GN-Pt/ GC	0	2 - 710	-	0.5	<i>Electrochem. Commun.</i> , 2011, 13 , 1131-1134.
MWCNTs-PANI/GC	-0.25(SCE)	7 - 2500	748.4 μAmM ⁻¹ cm ⁻²	2.0	<i>Microchim. Acta</i> , 2012, 176 , 389-395.
PNEGHNS/GC	0	1 - 500	-	0.08	<i>ACS Nano</i> 2010 , <i>4</i> , 3959-3968.
PDDA/Pt NP/ITO	0.6	0.042 - 160	0.500-0.019 AM ⁻¹ cm ⁻²	0.042	<i>Anal. Chem.</i> , 2008, 80 , 5441-5448.
Pt/CNF electrode	0	1 - 800	-	0.6	<i>Biosens. Bioelectron.</i> , 2011, 26 , 4585-4590
GS/GC	-0.4	0.1 - 10	-	0.3	<i>RSC Adv.</i> , 2014, 4 , 4998-5005

Two Dimensional Assembly of Silver Nanoparticles on Carbon Nitride Sheets and their Application in Non-enzymatic Sensing of Hydrogen Peroxide and Glucose

AgNP/rGO	-0.3	100-100000	-	31.3	<i>Carbon</i> , 2011, 49 , 3158
AgNP/rGO	-0.4	100-80000	-	7.1	-3164.63
AgNP-PMPD-GCE	-0.3	100-30000	-	4.7	<i>Analyst</i> , 2011, 136 , 1806-1809.
AgNP-TBTNB/GCE	-0.3	100-60000	-	2.04	<i>Analyst</i> , 2012, 137 , 939-943.
g-C ₃ N ₄ /GCE	-0.3	100-90000	-	2.0	<i>Nanoscale</i> , 2013, 5 , 8921-8924.
AgNps/GS	-0.3	100-100000	-	0.5	<i>J Nanopart Res</i> , 2011, 13 , 4539-4548.
AgNP-PMPD/GCE	-0.3	100-170000	-	2.5	<i>Catal. Sci. Technol.</i> , 2011, 1 , 1393-1398.
AgNPs/PANINs/GCE	-0.3	100-60000	-	1.7	<i>Catal. Sci. Technol.</i> , 2012, 2 , 800-806.
Chitosan/AgNPs-G/GCE	-0.3	100-10000	-	7	<i>RSC Advances</i> , 2012, 2 , 538-545.
AgNP/F-SiO ₂ /GO/GCE	-0.3	100-260000	-	4	<i>Biosens. Bioelectron.</i> , 2011, 26 , 4791-4797
Ag-CN _x /GC	+0.7	0.001 –	4.5x10 ⁵	0.0006	This work
Ag-CN _x /GC	-0.7	0.15	1.7x10 ⁴	0.0045	This work
		0.005 –	μAmM		
		0.35	cm ⁻²		

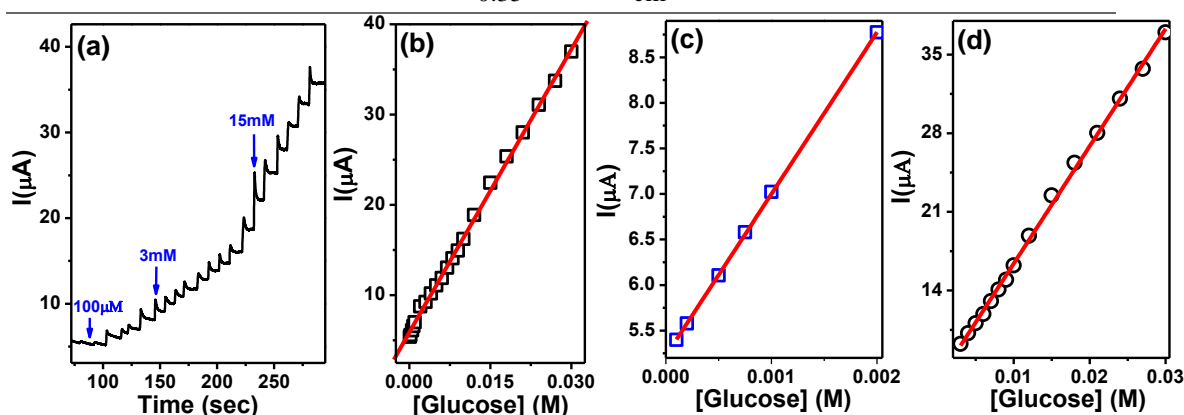


Fig 7.13. (a) Amperometric response of Ag-CN_x/GC electrode on successive addition of glucose into 0.05 M NaOH with stirring at 1.0 V. (b) Calibration curve of current vs. glucose concentration at 1.0 V. (c) Calibration curve of current vs. glucose concentration (100 μM - 2 mM) (d) Calibration curve of current vs. glucose concentration (2 mM - 30 mM).

Figure 7.12a represents the comparison of CV response of 20 mM glucose in 0.05 M NaOH solution at bare GC electrode and Ag-CN_x/GC electrode. This suggests the superior electrocatalytic activity toward glucose oxidation at Ag-CN_x/GC electrode as compared to GC electrode. Figure 7.12b shows cyclic voltammograms at Ag-CN_x/GC electrode in absence and presence of 20 mM Glucose in 0.05 M NaOH solutions at a

Two Dimensional Assembly of Silver Nanoparticles on Carbon Nitride Sheets and their Application in Non-enzymatic Sensing of Hydrogen Peroxide and Glucose

scan rate of 0.1 V Sec^{-1} . In the cathodic scan two redox peaks were obtained of Ag-CN_x/GC electrode in absence of glucose. The anodic peak at 0.5V was due to the formation of Ag⁺ (CN_x-Ag-OH) and second peak at 0.95 V corresponds to Ag²⁺ formation (CN_x-AgO). In the reverse scan (cathodic scan) two peaks at 0.84 V and 0.18 V were observed. However, the position of cathodic and anodic peaks are different from reported oxidation/ reduction peaks at silver disk electrode. A large peak at 0.95 V due to the oxidation of glucose was appeared at Ag-CN_x/GC electrode in presence of 20 mM glucose during the anodic scan.

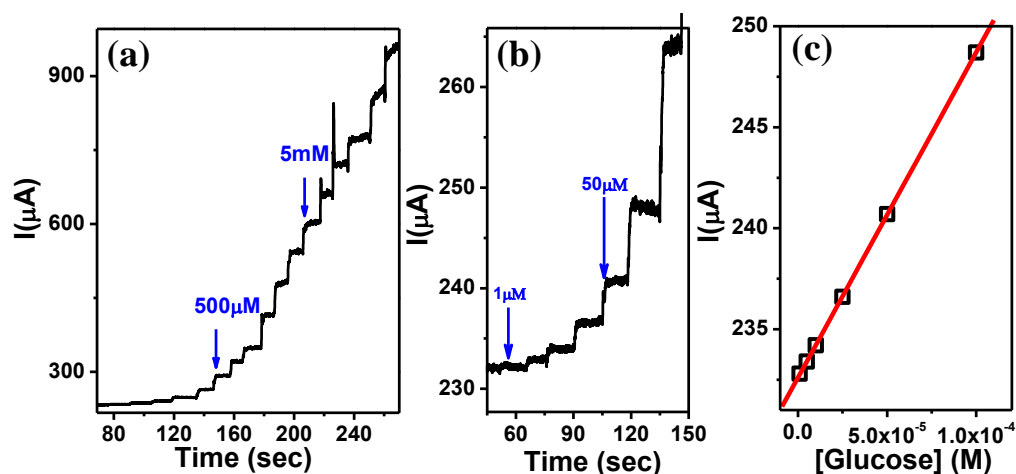


Figure 7.14. (a) Amperometric response of Ag-CN_x/GC electrode on successive addition of glucose into 0.05M NaOH with stirring at 1.5 V. (b) Lower concentration regime of amperometric curve. (c) Calibration curve of current vs. glucose concentration (lower concentration regime)

Table 7.2. Comparison of detection limit and sensitivity of Ag-CN_x/GC sensor with reported non enzymatic glucose sensors.

Electrode material	Linear range (mM)	Sensitivity ($\mu\text{A cm}^{-2} \text{ mM}^{-1}$)	LOD (μM)	References
NiO HSs/GC	0.002–0.01	-	0.3	<i>Electrochim. Acta</i> , 2013, 102 , 104-107
Au nanotube array/Au	1 - 42.5	1.13	10	<i>Electrochem. Commun.</i> , 2009, 11 , 216-219.

Two Dimensional Assembly of Silver Nanoparticles on Carbon Nitride Sheets and their Application in Non-enzymatic Sensing of Hydrogen Peroxide and Glucose

PdNPs-FCNTs-Nafion/ GC	0 - 46	11.4	-	<i>Biosens. Bioelectron.</i> , 2010, 25 , 1803-1808.
Nafion-graphene-PdNPs/GC	0.01- 5	-	1	<i>Biosens. Bioelectron.</i> , 2011, 26 , 3500-3504.
PtNFs-GO-nafion/GC	0.002 -10.3	1.26	2	<i>Talanta</i> , 2013, 105 , 379-385.
Ni(OH)₂-graphene/ GC	0.001- 0.01	494	0.6	<i>Microchim. Acta</i> , 2012, 177 , 103-109.
GNS/NiO/DNA/ GC	0.001–0.2	14.3	2.5	<i>Electrochim. Acta</i> , 2012, 73 , 129-135.
Cu NPs/graphene/ GC	0.005 - 1.4	607 $\mu\text{A mM}^{-1}$	0.2	<i>Microchim. Acta</i> , 2012, 177 , 485-490.
RGO-Ni(OH)₂/GC	0.002 - 3.1	11.43	0.6	<i>Mater. Chem.</i> , 2011, 21 , 16949-16954.
Cu-graphene/GC	Up to 4.5	-	0.5	<i>Anal. Chim. Acta</i> , 2012, 709 , 47-53.
Au nanocoral/Au	0.05 - 30	22.6	10	<i>ACS Appl. Mater. Interfaces</i> , 2010, 2 , 2773-2780.
CHI-GNPs/GC	4.00×10^{-4} mol/L - 1.07×10^{-2} mol/L	-	3.70×10^{-4} mol/L	<i>Sensors and Actuators B: Chemical</i> , 2009, 138 , 539-544.
Pt nanoflower/Au	1 - 16	1.87	48	<i>Electrochim. Acta</i> , 2012, 63 , 1-8.
Macroporous Au-Pt	up to 20	39.53	25	<i>Sensors and Actuators B: Chemical</i> , 2011, 155 , 134-139.
Cu-Ag₂O NWS/ GC	0.2 - 3.2	298.2	10	<i>ACS Appl. Mater. Interfaces</i> , 2009, 1 , 2829-2834.
Nafion-Cu-CuO NWs/GC	0.1-12	-	50	<i>Microchim. Acta</i> , 2010, 168 , 87-92.
MWCNT/NiO/G C	2.0×10^{-4} mol/L - 1.2×10^{-2} mol/L	-	1.6×10^{-4} mol/L	<i>Bioelectrochemistry</i> , 2010, 77 , 120-124.
GOx/PtNP/PAni/ Pt	0.01-8	96.1	0.7	<i>ACS Nano</i> , 2013, 7 , 3540-3546.
AgNP-TBTNB/GCE	3-20	-	190	<i>Analyst</i> , 2012, 137 , 939-943
g-C₃N₄/GCE	1-12	-	11	<i>Nanoscale</i> , 2013, 5 , 8921-8924.
AgNPs/PANINFs /GCE	1-12	-	250	<i>Catal. Sci. Technol.</i> , 2012, 2 , 800-806.
chitosan/AgNPs-G/GCE	2-10	-	100	<i>RSC Advances</i> , 2012, 2 , 538-545.

Two Dimensional Assembly of Silver Nanoparticles on Carbon Nitride Sheets and their Application in Non-enzymatic Sensing of Hydrogen Peroxide and Glucose

AgNP/F-SiO ₂ /GO/GCE	2-12	-	310	<i>Biosens. Bioelectron.</i> , 2011, 26, 4791-4797.
Ag-CN _x /GC	0.001-0.1	97	0.6	This work

In addition, a very large oxidation peak of glucose is observed at 0.84 V during the cathodic reverse scan. Figure 7.13a shows a typical amperometric current-time response at Ag-CN_x/GC upon the successive addition of glucose into a stirring 0.05 M NaOH solution at an applied potential of 1V. Figure 7.13b shows a good linear calibration plot covering the whole range from 100 μM to 30 mM. It can be divided two linear range from 100 μM to 2 mM and 2 mM to 30 mM (Figure 7.13c and 7.13d). The detection limit was calculated from Figure 7.13c, ranging from 100 μM to 2 mM is found to 15 μM with a sensitivity of 20 μA cm⁻² mM⁻¹ at signal to noise ratio of 3 (R²=0.9988). In addition, it was found that oxidation of glucose is found to be sensitive to applied voltage. Figure 7.14a display the current-time responses of Ag-CN_x/GC electrode with successive addition of glucose in 0.05 M NaOH solution at applied potential of 1.5 V. Figure 7.14b shows the amperometric (i-t) response of low concentration of glucose at Ag-CN_x/GC electrode. The lowest detection limit is calculated from the calibration plot (Figure 7.14c) is found to be 615 nM with sensitivity of 97 μA cm⁻² mM⁻¹. In Table 7.2, the lower detection limit, linear range and sensitivity of non-enzymatic electrochemical glucose detection at Ag-CN_x/GC electrode were compared with several typical metal and carbon based biosensors.

7.5 CONCLUSION

In conclusion, we have shown that g-CN_x can play dual role for selective and sensitive sensing of silver ions and cysteine in aqueous media by exploiting the fluorescence properties of g-CN_x. We also demonstrated that two dimensional ordered assemblies of silver nanoparticles on 2-D CN_x sheets is formed on a solid substrate on drying of aqueous solution of Ag-CN_x composites. Nucleation and then growth of silver

nanoparticles takes place at voids on CN_x sheets due the affinity of silver towards nitrogen atoms. CN_x sheets containing ordered assembly of silver nanoparticles can be used as superior electrochemical non enzymatic biosensors for hydrogen peroxide and glucose.

7.6 REFERENCES

1. El-Sayed M. A. *Acc. Chem. Res.*, 2004, **37**, 326-333.
2. Tao A. R.; Habas S.; Yang, P. *Small*, 2008, **4**, 310-325.
3. Talapin D. V.; Lee, J.-S.; Kovalenko M. V.; Shevchenko E. V.; *Chem. Rev.*, 2009, **110**, 389-458.
4. Murphy C. J.; Sau T. K.; Gole A. M.; Orendorff C. J.; Gao J.; Gou L.; Hunyadi S. E.; Li T. *J. Phys. Chem. B*, 2005, **109**, 13857-13870.
5. Yoon B.; Wai C. M.; *J. Am. Chem. Soc.*, 2005, **127**, 17174-17175.
6. Li H.; D. Chen X.; Sun Y.L; Zheng Y. B.; Tan, L.-L.; Weiss P. S.; Yang Y.W.; *J. Am. Chem. Soc.*, 2012, **135**, 1570-1576.
7. Pileni M. P.; *J. Mater. Chem.*, 2011, **21**, 16748-16758.
8. Liu, S.; Zhu, T.; Hu, R.; Liu, Z. *Phys. Chem. Chem. Phys.* **2002**, **4**, 6059-6062.
9. Xia D.; Biswas A.; Li D; Brueck S. R. J.; *Adv. Mater.*, 2004, **16**, 1427-1432.
10. Song, H.; Kim, F.; Connor, S.; Somorjai, G. A.; Yang, P. *J. Phys. Chem. B* **2004**, **109**, 188-193.
11. Kotov N. A.; Dekany I.; Fendler J. H.; *J. Phys. Chem.*, 1995, **99**, 13065-13069.
12. Kalsin, A. M.; Fialkowski, M.; Paszewski, M.; Smoukov, S. K.; Bishop, K. J. M.; Grzybowski, B. A. *Science* **2006**, **312**, 420-424.
13. Duan, H.; Wang, D.; Kurth, D. G.; Mohwald, H. *Angew. Chem. Int. Ed.* **2004**, **43**, 5639-42.

14. Yi, C.; Kim, T.-H.; Jiao, W.; Yang, Y.; Lazarides, A.; Hingerl, K.; Bruno, G.; Brown, A.; Losurdo, M. *Small* **2012**, *8*, 2721-2730.
15. Wu, B.; Oo, T. Z.; Li, X.; Liu, X.; Wu, X.; Yeow, E. K. L.; Fan, H. J.; Mathews, N.; Sum, T. C. *J. Phys. Chem. C* **2012**, *116*, 14820-14825
16. Lee, J. M.; Kim, I. Y.; Han, S. Y.; Kim, T. W.; Hwang, S.-J. *Chem. Eur. J.* **2012**, *18*, 13800-13809.
17. Hong, W.; Bai, H.; Xu, Y.; Yao, Z.; Gu, Z.; Shi, G. *J. Phys. Chem. C* **2010**, *114*, 1822-1826.
18. Geim, A. K. *Science* **2009**, *324*, 1530-1534..
19. Scheuermann, G. M.; Rumi, L.; Steurer, P.; Bannwarth, W.; Mülhaupt, R. *J. Am. Chem. Soc.* **2009**, *131*, 8262-8270.
20. Mao, S.; Lu, G.; Yu, K.; Bo, Z.; Chen, J. *Adv. Mater.* **2010**, *22*, 3521-3526.
21. Xiong, B.; Zhou, Y.; Zhao, Y.; Wang, J.; Chen, X.; O'Hayre, R.; Shao, Z. *Carbon* **2013**, *52*, 181-192.
22. Guo, S.; Wen, D.; Zhai, Y.; Dong, S.; Wang, E. *ACS Nano* **2010**, *4*, 3959-3968.
23. Parambath, V. B.; Nagar, R.; Ramaprabhu, S. *Langmuir* **2012**, *28*, 7826-7833.
24. Liu, L.; Dong, C.; Wu, K.-L.; Ye, Y.; Wei, X.-W. *Mater. Lett.* **2014**, *129*, 170-173.
25. Liu, S.; Tian, J.; Wang, L.; Li, H.; Zhang, Y.; Sun, X. *Macromolecules* **2010**, *43*, 10078-10083.
26. Maeda, K.; Wang, X.; Nishihara, Y.; Lu, D.; Antonietti, M.; Domen, K. *J. Phys. Chem. C* **2009**, *113*, 4940-4947.
27. Cui, Y.; Ding, Z.; Liu, P.; Antonietti, M.; Fu, X.; Wang, X. *Phys. Chem. Chem. Phys.* **2012**, *14*, 1455-1462.

28. Huang, J.; Antonietti, M.; Liu, J. *J. Mater. Chem. A* **2014**, *2*, 7686-7693.
29. Sadhukhan, M.; Barman, S. *J. Mater. Chem. A* **2013**, *1*, 2752-2756.
30. Wang, Y.; Wang, X.; Antonietti, M. *Angew. Chem. Int. Ed.* **2012**, *51*, 68-89.
31. Li, X.-H.; Wang, X.; Antonietti, M. *Chem. Sci.* **2012**, *3*, 2170-2174.
32. Datta, K. K. R.; Reddy, B. V. S.; Ariga, K.; Vinu, A. *Angew. Chem. Int. Ed.* **2010**, *49*, 5961-5965.
33. Yao X.; Liu X.; Hu X.; *ChemCatChem*, 2014, **6**, 3409-3418.
34. Chen Y.; Huang W.; He D.; Situ Y.; Huang H.; *ACS Appl. Mater. Interfaces*, 2014, **6**, 14405-14414.
35. Yang Y.; Guo Y.; Liu F.; Yun X.; Guo Y.; Zhang S.; Guo W.; Huo M. *Appl. Catal. B*, 2014, *142*, 828-837.
36. Park S.; Boo H.; Chung T. D. *Anal. Chim. Acta*, 2006, **556**, 46-57.
37. Sadhukhan M.; Bhowmik T.; Kundu M. K.; Barman S. *RSC Adv.*, 2014, **4**, 4998-5005.
38. Klassen N. V.; Marchington D.; McGowan H. C. E. *Anal. Chem.*, 1994, **66**, 2921-2925.
39. Preuschoff F.; Spohn U.; Blankenstein G.; Mohr K.-H. K.-H.; Kula M.R. *Fresenius J Anal Chem*, 1993, **346**, 924-929.
40. Rupali, S. P.; Mangesh, R. K.; Chitra, L. J.; Sambhaji, M. P.; Sung, H. H.; Sanjay, S. *Adv. Nat. Sci.; Nanosci. Nanotechnol.* **2012**, *3*, 015013.
41. S. Barman and M. Sadhukhan, *J. Mater. Chem.*, 2012, **22**, 21832-21837.
42. Prieto P.; Nistor V.; Nouneh K.; Oyama M.; Abd-Lefdil M.; Díaz R. *Appl. Surf. Sci.*, 2012, **258**, 8807-8813.

Appendix E

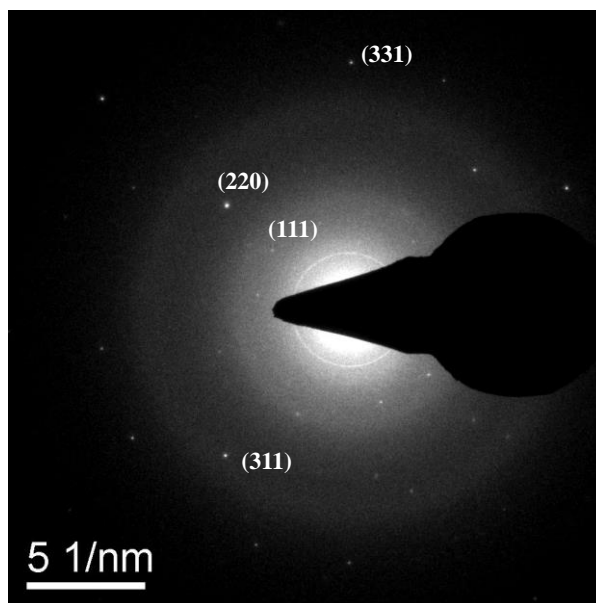


Figure S7.1. SAED image of AgNPs taken from Figure 7.6(b).

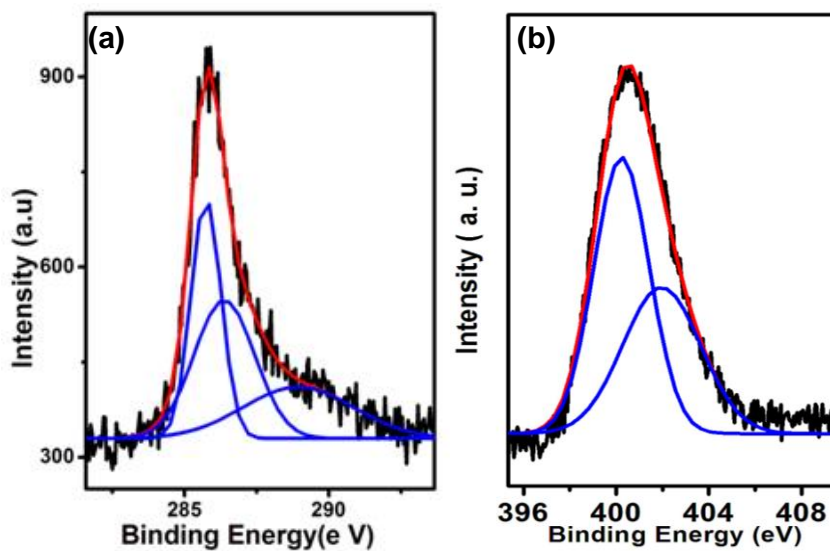


Figure S7.2. (a) C1s and (b) N1s XPS spectra of CN_x .

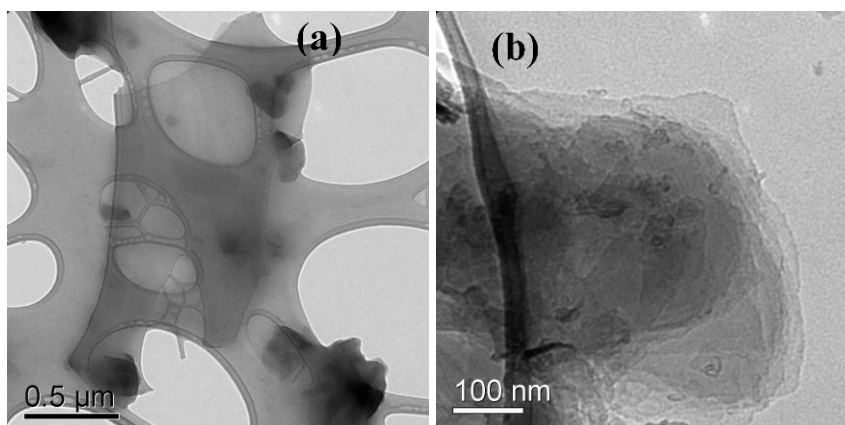


Figure S7.3. (a, b) TEM images of CN_x sheets prepared from g- CN_x .

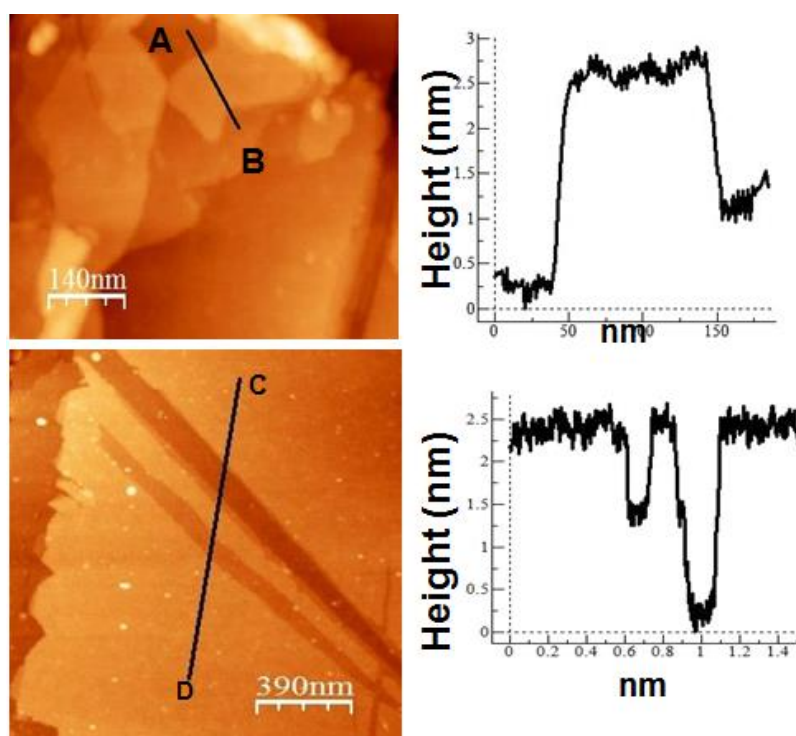


Figure S7.4. AFM images of thin CN_x sheets and its height profile shows thickness 2.0 to 2.5 nm.

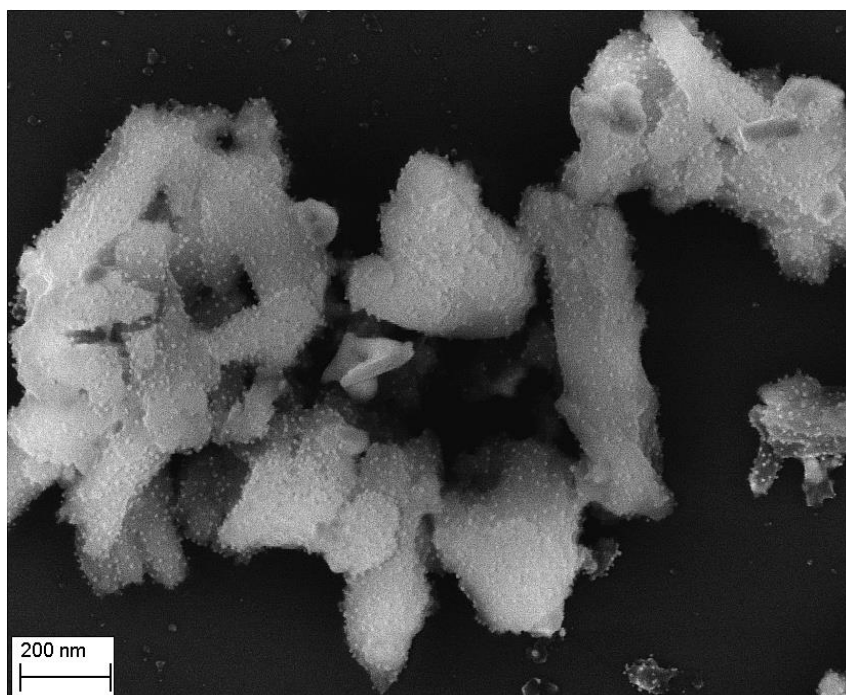


Figure S7.5. SEM image of AgNPs assembly on CN_x sheet.

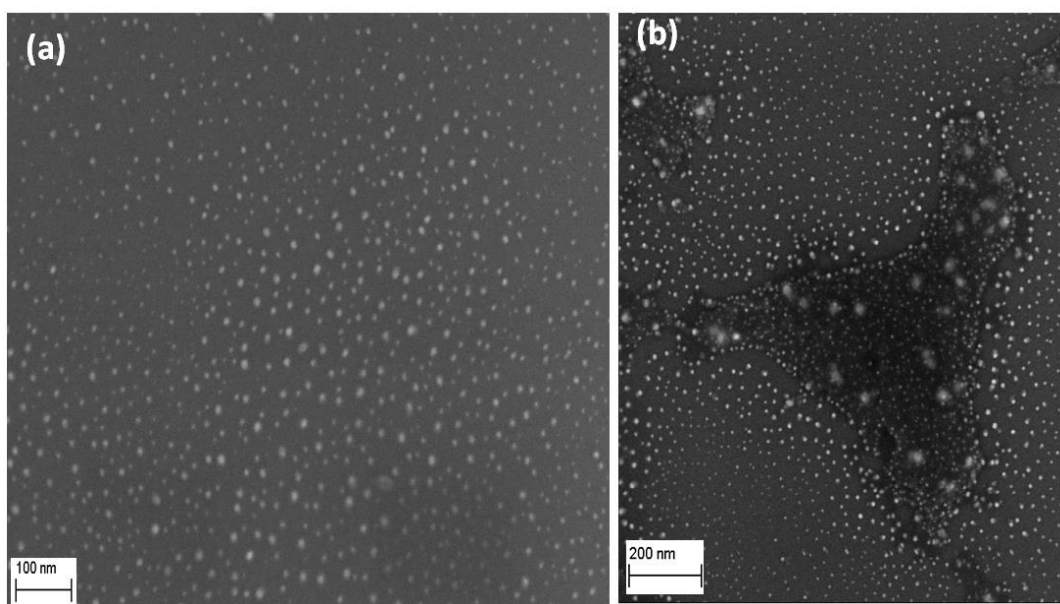


Figure S7.6. (a) and (b) SEM images showing ordered assembly of AgNPs on thin CN_x sheets.

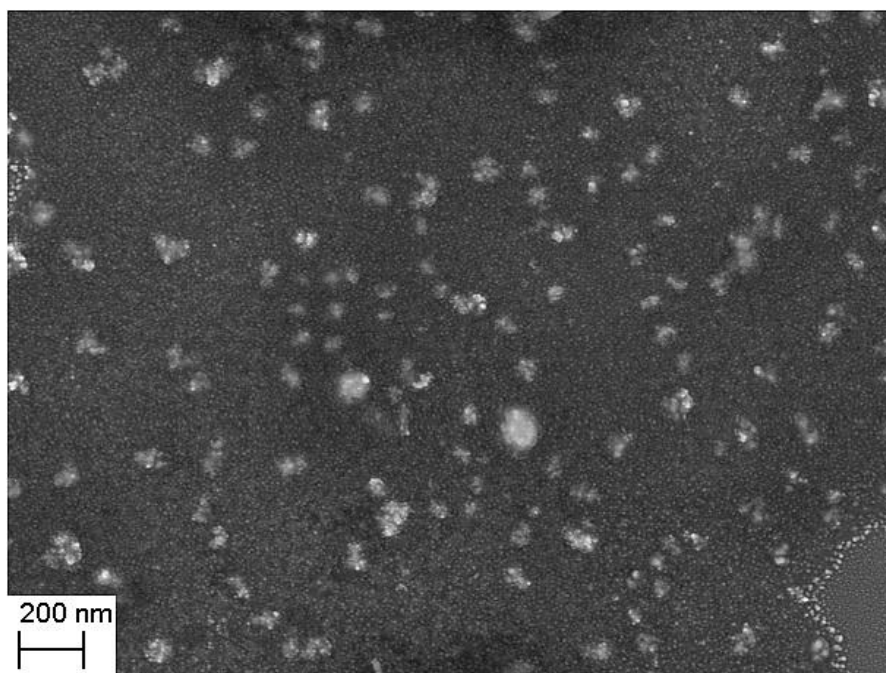


Figure S7.7. SEM image of highly ordered 2-D assembly

Chapter 8

Ultra Small Gold Nanoparticles on Two-dimensional Graphitic Carbon Nitride: An Efficient Catalyst for Ultrafast Reduction of 4-nitrophenol and Removal of Organic Dyes from Water

8.1 ABSTRACT

Synthesis of supported ultra-small gold particles is important for their unusual properties and catalytic applications. We report a facile method for synthesis of ultra-small gold nanoparticles supported on carbon nitride sheets (Au-CN_x). The ultrasonication was used to form Au-CN_x composite from carbon nitride quantum dots and HAuCl₄ without any aid of external reducing agent. The Au-CN_x composite was well characterized by TEM, SAED, EDS, p-XRD, XPS Methods. Electron microscopic measurements confirm that thin graphitic carbon nitride sheets provided two dimensional supports to stabilize ultra-small, 1-3 nm sized gold nanoparticles (AuNPs). The Au-CN_x composite showed excellent catalytic activity towards the reduction of 4-Nitrophenol in aqueous medium in presence of sodium borohydride (NaBH₄) with very fast kinetics and good stability. The Au-CN_x catalyst can be used as an absorbent for the removal of organic dye [Rhodamine B (RhB), methylene blue (MB), and methyl red (MR)] from water. It showed excellent adsorption capacity for RhB and MB due to electrostatic interaction between anionic catalyst and cationic organic dye molecules. The catalyst can easily be reused after removing adsorbed dye from the catalyst simply by changing pH of the solution. In addition, Au-CN_x composite exhibited superior photo catalytic degradation of various dyes (RhB, MB and MR) on irradiation of UV, Visible light and natural sunlight. Excellent photo degradation rate

constants for RhB (0.024 min^{-1}), MB (0.024 min^{-1}) and MR (0.02 min^{-1}) were observed although high concentration of dyes were used for degradation. Au-CN_x is one of the best adsorbent for RhB adsorption with maximum adsorption capacity of 400 mg gm^{-1} and catalyst for nitrophenol reduction. We hope that this Au-CN_x composite will find its application as an effective catalyst for water purification.

8.2 INTRODUCTION

In recent years, noble metal nanoparticles (NPs) have attracted tremendous attention due to their potential applications in various fields such as catalysis¹, sensors²⁻⁶, optics⁶, fuel cell⁷. For example, gold nanoparticles⁸ are being used for a long time in drug delivery, different biological application and catalysis. Silver and platinum nanoparticles show promising capabilities in biosensors⁹ and in fuel cell¹⁰. Very small metal NPs has an interesting size and shape dependent reactivity¹¹ due to the increase of volume to surface ratio. The reduction in size of metal nanoparticles causes a significant change in reduction potential of metal nanoparticles as compared to bulk materials because their Fermi potential becomes more negative. This typical important property helps them in electron transfer in various catalysis reactions. But synthesis of ultra-small metal nanoparticle is a very challenging task due its high agglomeration property, arises from its high surface energy. In order to avoid aggregation, nanoparticles should be stabilized by using organic molecules or polymer as a capping agent. But their catalytic activity greatly reduced due to the presence of organic or polymer molecules around nanoparticles. Another alternative available method is to stabilize them on the surface of a solid support¹². Two dimensional (2-D) Graphene, due to its unique properties¹³ such as high specific surface area, excellent electrical conductivity, high charge carrier mobility, high mechanical strength, became a promising candidate as a support for different nanoparticles. The graphene containing metal or

semiconductor nanoparticles have confirmed to be effective nano-composite materials for photovoltaic¹⁴⁻¹⁵, catalysis and biosensor applications¹⁶. In recent year another 2-D material graphitic carbon nitride (g-C₃N₄), has attracted a significant attention due to its moderate band gap which leads to a potential application in the photocatalysis^{17-18,19}, organic reactions²⁰⁻²¹ and fuel cell^{17, 22-23}. g-C₃N₄ consists of repeating triazine units which has large number of binding sites to stabilize the MNPs making this materials as a promising supports for noble MNPs. But, most of the reports²⁴⁻²⁵ for g-C₃N₄ as supported materials are mesoporous due to the better diffusion and strong binding of metal NPs through the surface pore of the g-C₃N₄. The synthetic procedure of mesoporous compound needs of hazardous materials and also high temperature which is not environmental friendly. Some time it was difficult to remove the template from the products which demises the products purity. Thus, 2-D sheet of carbon nitride can be considered as feasible alternative for stabilizing metal nanoparticles for their unusual catalytic properties.

In 21st century, environmental pollution is increasing due to the fast growth of chemical industries and the release of various types of industrial contaminant into water²⁶. The different industrial contaminants are chlorinated organic compounds, volatile organic compounds, nitro aromatics and fertilizers, dyes etc. Among these toxic threats, dyes and nitro aromatics are more concerned to us because of their high chemical and biological stability which makes difficult to removes from water. In chemical industries 4-NP is generally used to prepare different synthetic dyes, medicines and pesticides. The remediation of aromatic nitro compounds is important, because aromatic nitro moiety is one the most characteristic of anthropogenic contaminants. 4-nitro phenol (4-NP) is toxic pollutant and hazardous compound, declared by U.S. Environmental Protection Agency. 4-NP can causes disorder of our central nervous system, and can damage kidney, liver of

humans as well as animals. So removal of 4-NP is very much important. A conventional water purification treatment is not effective for removal of 4-NP due to its high stability and solubility in water. So reduction of 4-NP to 4-AP is the best idea as 4-AP is a starting material in various industrial synthesis like pharmaceutical, photographic, and corrosion inhibitor. Therefore, recently scientific community has given a lot of attention for inventing new catalyst for the reduction of 4-NP to 4-AP^{27,28}.

The effluents from the pesticides, dying, petrochemical, and pharmaceutical industries contains highly water pollutant dyes which release in environment and cause various problem such as some skin diseases in human health, and also aquatic biota are also adversely affected²⁹. So removal of these type environmental threats is very important. Different methods are used to remove dyes from the environment such as coagulation-flocculation³⁰, photo degradation^{31,32}, electrochemical oxidation³³ and adsorption³⁴. Among them, sorption and degradation process are most effective treatment for cleaning up water. The adsorption property depends on the surface structure of adsorbent whereas photocatalytic activity control by the band gap of the semiconductor material or hetero-junction structure of the metal-semiconductor composite. The adsorption procedure used frequently to remove the dye molecules from water due the simplicity of operation procedure, low cost, and also easy recycling of the adsorbent. Scientific community has given more attention on the porous molecule³⁵ as a good adsorbent due to easy diffusion of the dye molecule through the pore of the adsorbent. Different natural polymers were found to be good adsorbent. Hunt and his co-workers developed polysaccharide based polymer for removal of dyes from water³⁶. The main limitation of the polymer based catalyst is lower thermal stability, poor hydrodynamic volume as well as low surfaces area. Sometime the polymer molecules shows lack of separation selectivity, low adsorbing capacity and

recycling property. Polymeric g-C₃N₄ doesn't have good adsorption property. The adsorption property of C₃N₄ was improved by doping boron into the carbon nitride framework³⁵. Recently Chen and his co-workers synthesized porous BN sheet for effective water cleaning agent³⁵. However there was no report on adsorption of dye using metal nanoparticles deposited carbon nitride as an adsorbent.

Photocatalyst based on heterogeneous semiconductor has created a lot of attention due to its potential application on reducing of global water pollution which was well accepted strategy to solve the environmental problem³⁷. Among different photocatalytic system semiconductor³⁸ TiO₂ explored more but unfortunately TiO₂ is photo catalytically active only under UV-light irradiation³⁹ due to its wide band gap. The quantum yield of this type semiconductor catalyst is very low under solar light, since only 5 % of solar energy is UV light. This is the major limitation of their applications. The photocatalysts, sensitive to visible light, are promising candidate for degradation of dyes, since visible light present in of solar energy is ~ 40 %. Therefore, both visible light as well as UV light driven photocatalysis are significantly important for practical applications. There are several reports on the different photocatalytic system based on their different photo physical properties such as band gap and band position of conduction and valence band, surfaces area, size, shape and morphology of the catalyst. But last few years scientific community are mostly focused on the metal oxide, sulphide and metal nitride based photocatalytic systems which are mostly toxic and costly materials. The enormous efforts has been given to develop the environmental friendly less toxic and cheap materials⁴⁰. Among them, carbon, nitrogen based semiconductor, graphitic carbon nitride (g-C₃N₄) has created more attention in last few years due to their extreme stability under harsh thermal and photochemical condition in compared to other polymeric system and potential photocatalytic activity under

visible light irradiation⁴¹. But the low surface area, high recombination rate of photo excited charge carriers electron-hole, and low quantum efficiency is limiting their practical applications⁴¹. Several methods have been applied to improve the charge separation efficiency of g-C₃N₄, such as designing the porous structure⁴², coupled with different n-type semiconductor⁴⁰ and making hetero-junction composite with noble metals^{37, 43-48}. Among these processes, hetero-junction composites are most widely used⁴⁹⁻⁵⁰. X. Hu and his co-workers reported³⁷ Ag/AgCl/g-C₃N₄ composite for MB degradation under visible light. X. Wang⁵¹ and his co-worker also reported highly efficient visible light induced photocatalytic degradation of various dyes by Ag/AgCl/g-C₃N₄ composite. But there is very few reported on AuNPs deposited g-C₃N₄ based photocatalysis⁴³.

Herein, we demonstrated ultrasonication mediated synthesis of ultra-small AuNPs supported on g-C₃N₄ sheets and their superior catalytic properties. Nearly monodispersed ultra small gold nanoparticles with diameter of 1 -3 nm were formed on carbon nitride sheets (CN_x) by ultrasound mediated reduction of HAuCl₄ in presence of carbon nitride quantum dots. The Au-CN_x composite exhibited superior catalytic activity toward the reduction of 4-NP in presence of NaBH₄. It can reduce 0.1 mM 4-NP solution in 15 sec with NaBH₄. The Au-CN_x composite showed superior adsorption capacity for various dyes. The surface charge of the Au-CN_x sheets is responsible superior adsorption of cationic dyes (RhB, MB) at neutral medium and anionic dye (MR) in acidic medium. In addition, this catalyst showed superior catalytic activity towards the degradation organic dye such as RhB, MB, MR under UV/ Visible/ Sun light. Possible mechanism for degradation of dyes upon Au-CN_x catalyst under UV and visible light irradiation were proposed. The photo-degradation of RhB on the Au-CN_x surface takes place via N-de-ethylation processes and formation of N-de-ethylated products was confirmed by UV-Visible and ESI-MS spectroscopy. The Au-CN_x catalyst is

very efficient for removal of cationic as well as anionic organic dye from aqueous environment by its dual actions with adsorption and photo catalytic degradation of dye.

8.3 EXPERIMENTAL SECTION

Preparation of Au-CN_x composite

5 mg of prepared g-CN_x^{52,53} was dispersed in 3 ml of water by sonication for 10 min (see previous section for synthesis procedure). In another vial 0.032 gm of H₂AuCl₄ · xH₂O was taken in 5 ml of water. Next, the dispersed g-CN_x and gold solution were mixed together and again sonicated for 15 min. Finally, the mixture was ultra-sounded with ~28 kHz frequency for 3 hours at 400 watt. After ultrasound the solid product was separated by centrifugation. After washing this solid product with water and vacuum dried, was taken for further characterization and others experimental procedure.

Catalytic reduction method of 4-Nitrophenol

In this typical reaction procedure, 3.0 ml of 0.1 mM 4-NP was taken in a glass-vial followed by addition of 0.3 mmol of NaBH₄. Here NaBH₄ has taken in excess amount to avoid the concentration change throughout the reaction. As soon as NaBH₄ was added the colour of the reaction solution changed to dark yellow from light yellow. Then 0.005 g of the nanocomposite catalyst was added to it. Within few second the colour of the solution was changed from dark yellow to colourless. After completion of the reaction, a little amount of ammonium chloride was added to neutralize the excess NaBH₄ and the catalyst was recovered after doing centrifugation for 20 min at 16000 rpm. Here we have also studied the regeneration of catalytic activity of our separated catalyst.

Adsorption efficiency measurement

Adsorption activity of the prepared catalyst was measured on two cationic dye [Rhodamine B (RB), methylene blue (MB)] and anionic azo dye [methyl red (MR)]. Adsorption study of RB, MB was done in neutral medium and MR was done in acidic medium (pH 3). Typically 1 ml catalyst was taken and kept in oven at 80°C for half an hour. Then desired concentration of dye was added and kept in a dark place with stirring for 12 hours. After reached in adsorption-desorption equilibrium solution was centrifuged at 1600 rpm and concentration of remaining dye was determined by UV-Vis spectrometer. The percentage of adsorption was calculated using equation (1)

$$\% \text{ dye adsorption} = \frac{C_0 - C_e}{C_0} \times 100 \quad (1)$$

And equilibrium uptake was calculated using equation (2)

$$q_e = (C_0 - C_e) \frac{V}{W} \quad (2)$$

Where C_0 is initial concentration of dye solution (mg L^{-1}) C_e is the equilibrium concentration of dye solution (mg L^{-1}) q_e is the equilibrium capacity of dye on adsorbent (mg gm^{-1}) V is volume of dye solution (L) and W is the weight of adsorbent (gm) used.

Photocatalytic activity measurement

For degradation of RB and MR, UV light was illuminated with 84 watt of 250 nm wavelength light, for visible light 135 watt Xenon lamp with cut off filter 3 ($\lambda \geq 400 \text{ nm}$) and all dye degradation in sunlight was done between 10 am to 3 pm under a clear sky. All photo catalysis experiment was done after complete adsorption of dye and pH was adjusted to 3 by adding 0.1 M H_2SO_4 . The degradation of dye was monitored by UV-Visible

spectroscopy by withdrawn centrifuged (10000 rpm, 5 min) dye solution from reaction mixture.

8.4 RESULTS AND DISCUSSIONS

The powder x-ray diffraction pattern of g-C₃N₄ and Au-CN_x nanocomposite is shown in Figure 8.1. In both p-XRD pattern the peak at 2θ value of 27.3° corresponds to (002) plane of g-C₃N₄ with interlayer d-spacing 3.27 Å⁵². The additional four well resolved peaks of Au-CN_x composite located at 2θ values 38.2°, 44.4°, 64.5°, 77.54° and 81.8° can be indexed as (111), (200), (220), (311) and (222) reflection planes respectively for pure f.c.c. metallic Au nanoparticles⁴³ (JCPDS No. 04-0784). This suggests that the formation of AuNPs on CN_x sheets by ultrasonic treatment. TEM (Figure 8.2 a and b) and AFM (Figure S8.1 a, b Annexure) measurements were extensively used to study morphology of carbon nitride sheets.

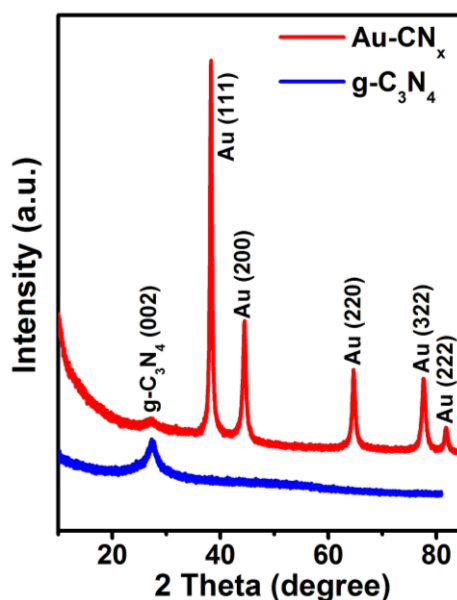


Figure 8.1. p-XRD of g-C₃N₄ and Au-CN_x composite

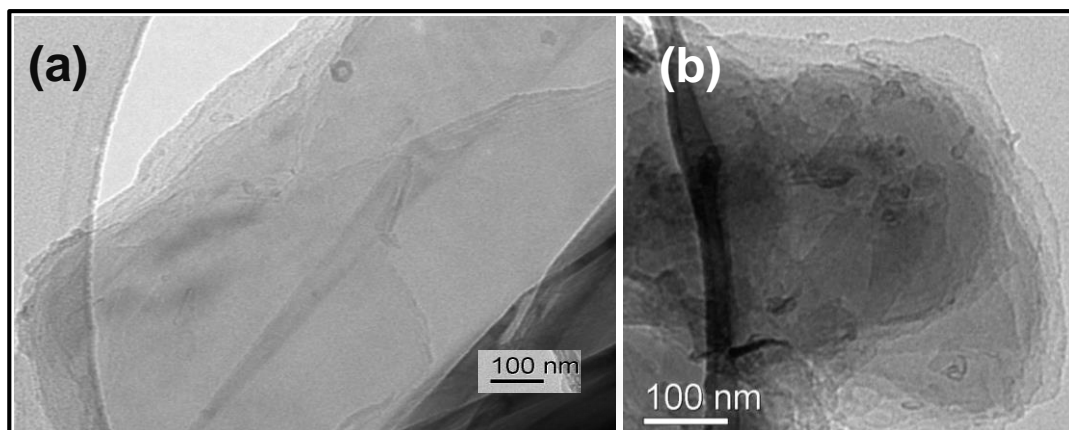


Figure 8.2. (a, b) TEM images of g-carbon nitride

Recently we have reported the formation of 2-D sheets on a solid substrate by evaporation induced self-assembly and condensation of carbon nitride quantum dots⁵². Highly ordered assembly of silver nanoparticles on carbon nitride sheets and their application in non-enzymatic detection of glucose/H₂O₂ was also reported by our group recently³.

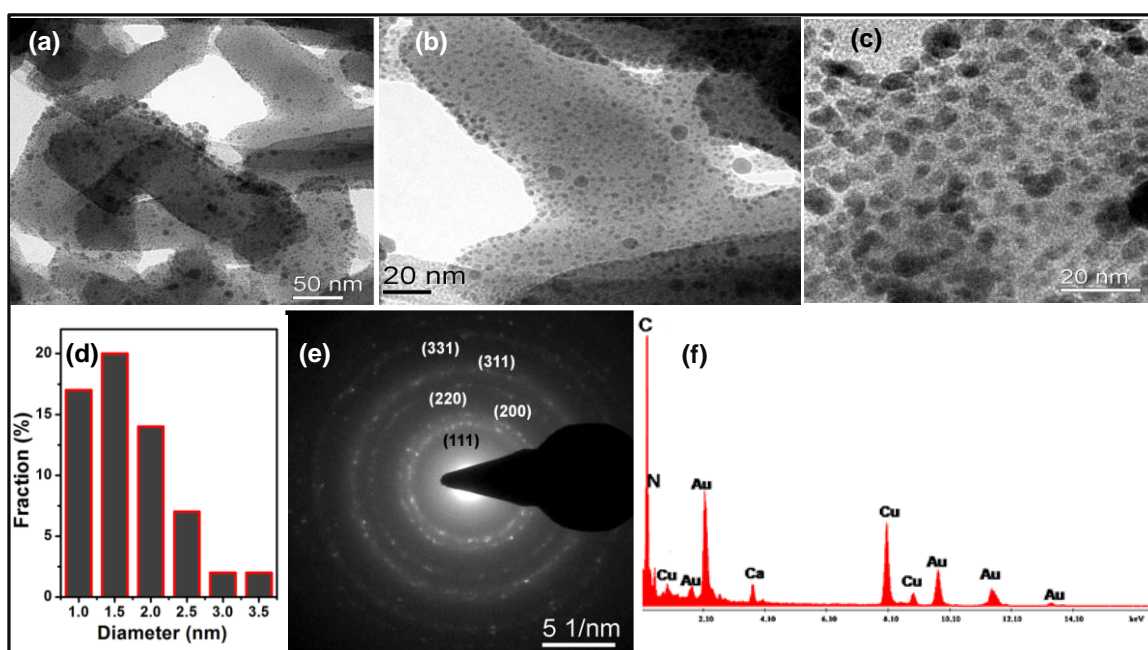


Figure 8.3. (a, b, c) TEM images of Au-CN_x composite shows ultra-small Au NPs are highly dispersed on the CN_x sheets. (d) Size distribution plot of Au NPs taken from Figure 2d. (e, f) SEAD and EDS spectra of Au-CN_x composite respectively, has taken from Figure 8.3a.

TEM samples were prepared by evaporation of aqueous solution of Au-CN_x composite on TEM grid. Figure 8.3(a, b, c) show TEM images of very small gold nanoparticles, highly dispersed on the carbon nitride sheets indicating very high loading of AuNPs on CN_x sheets. The size distribution of AuNPs as shown in Figure 8.3d and the size of dispersed AuNPs in CN_x sheets are in the range 1-3 nm with mean particle size of 1.5 nm. In addition few larger gold particles of 6 -8 nm size are also visible in TEM images. The SAED image of AuNPs, taken from Figure 8.3b is shown in Figure 8.3e. The interlayer spacing calculated from SAED image are 2.36, 2.03, 1.22, 0.946 Å which corresponds to (111), (200), (220), (311) and (331) planes of face centred cubic AuNPs respectively, based on p-XRD data base (JCPDS No. 04-0784). This is in agreement with p- XRD data (Figure 8.1) of Au-CN_x composites. The EDS spectrum (Figure 8.3f) has taken from AuNPs-carbon nitride sheets in the image of Figure 8.3f shows the presence of carbon, nitrogen and gold, also confirming deposition of AuNPs on carbon nitride sheets. In addition, EDS spectrum of Au-CN_x was also done on silicon wafer in order to calculate the amount of Au present in Au-CN_x sheets (Figure 8.4) and it was found ~ 40 weight % Au present in the composite.

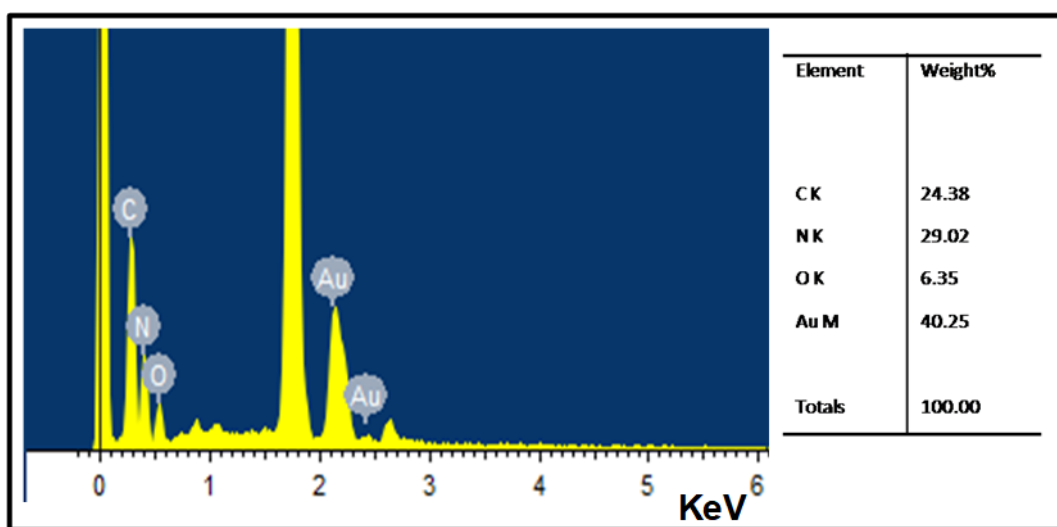


Figure 8.4. EDS spectra Au-CN_x composite prepared on silicon wafer.

The exact amount of gold loading in Au-CN_x composite was determined by Thermo Gravimetric Analysis (TGA) method. TGA curves of Au-CN_x and CN_x were shown in Figure 8.5. It shows that 46 wt% gold present in this Au-CN_x composite. The Au-CN_x composite with different amount of gold loading were prepared by ultrasonic treatment of CN_x sheets and different amount of AuCl₄ salts. The maximum loading of gold in CN_x sheets we could achieve is 50 wt%.

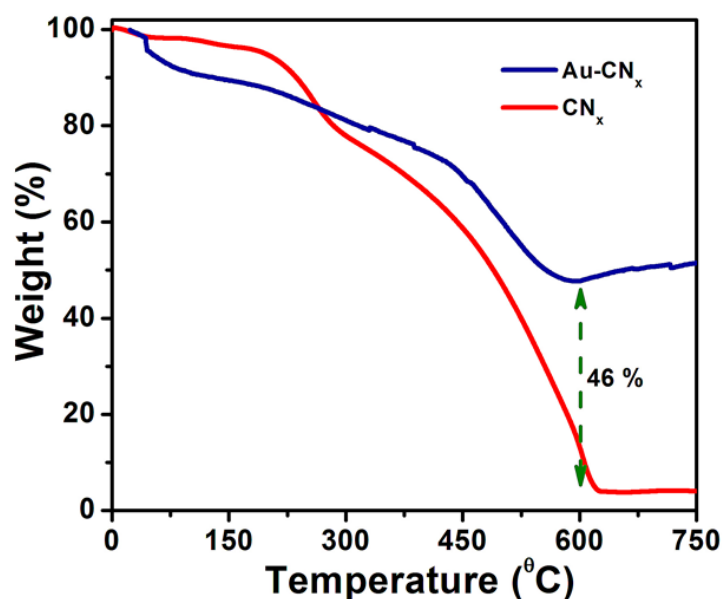


Figure 8.5. TGA spectra of Au-CN_x (blue line) and CN_x (red line) at N₂ atmosphere

X-ray photoelectron spectroscopy (XPS) measurements were carried out to know the oxidation state of gold particle and chemical environment around carbon and nitrogen atoms in Au-CN_x. Figure 8.6a shows the survey scan of the XPS spectrum which clearly indicates the presence of gold, carbon, nitrogen and oxygen atoms in Au-CN_x composite. The binding energy spectra of Au 4f are very sensitive to the chemical environment around the gold surface and size of gold nanoparticles. It is well known that the binding energy spectra of Au 4f of metallic gold NPs is appeared as doublet with binding energy 83.9 eV for 4f_{7/2} and 87.3 for 4f_{5/2} peak⁵⁴. It was reported^{55,56} by various groups that binding energy of Au 4f electron for very small gold cluster shifts towards higher binding energy in compared to the

position of bulk as the size of the nanoparticles is reduced. Recently Mark Turner *et. al.* reported⁵⁷ binding energy of Au 4f_{7/2} electron for very small (1-2 nm) gold nanoparticles was 1.1 eV higher than that of bulk Au. This typical shift in binding energy for ultra-small metal nanoparticles on various supports materials was also reported^{55,56}. The reduced core-hole screening in small metal nanoparticles and temporal charging^{58,59} of nanoparticles during photo emission process is responsible for this shift. The electronic properties are significantly different for these very small particles and unusual catalytic properties were observed due to size dependent alteration of electronic structure. David P. Anderson *et al.* reported⁶⁰ Au 4f_{7/2} peak for Au₈, Au₉, Au₁₁ clusters dispersed on titanium oxide were appeared in the region 85 – 86.2 eV whereas for Au₁₀₁ cluster appeared at 83.9 eV. Figure 8.6b display the Au 4f spectrum for Au-CN_x and two peaks appeared at 85.6 and 88.9 eV. Thus, peaks at 85.6 and 88.9 eV can be assigned to Au 4f_{7/2} and 4f_{5/2} photoelectron. The binding energy of Au 4f electron shifts towards higher value due to very small Au NPs dispersed on CN_x. It is reported⁵² for C1s XPS spectra of CN_x that peaks due to C–N bonding are generally appeared in the range 285–287 eV and the peaks in the range 288–290 eV are attributed to CO_x. Figure 8.6 c and d show the XPS spectrum in the carbon 1s and nitrogen 1s peaks, which was de-convoluted to three and two main Gaussian peaks respectively. The binding energies of 285.3 eV and 286.45 eV are due to the presence of (sp²) N–C–N (sp²) (carbon bonded to two nitrogen atoms) and C(–N)₃ (planar trigonal carbon geometry) respectively, whereas the peak at 288.8 eV is attributed to CO⁵². The peak at 400.1 eV refers to the presence of [(sp²) C–N1]C (sp²), nitrogen bonded to two carbon atoms or pyridone moiety whereas the second peak in this region at 401.6 eV corresponds to quaternary nitrogen which is bonded to three sp² carbon atoms, known as graphitic nitrogen^{52, 61}. Based on p-XRD, TEM, SAED, EDS and XPS measurements it can be concluded that ultra-small (1 - 3 nm), naked gold nanoparticles are highly dispersed on carbon nitride sheets.

8.4.1 Catalytic reduction of 4-Nitrophenol

The catalytic activity of ultra-small AuNPs supported on CN_x sheets was first tested for reduction of 4-NP was monitored by observing the change in UV-Vis absorption spectra as well as colour change of aqueous solution. UV-Vis absorption spectrum of 4-NP solution shows in Figure 8.7a. Aqueous solution of 4-NP shows an absorption maxima at 317 (Figure 8.7a green line) but after addition of $NaBH_4$ the peak shifted to 400nm with increasing the intensity (Figure 8.7a red curve) due to the formation of phenolate ion which is fully conjugated with benzene moiety.

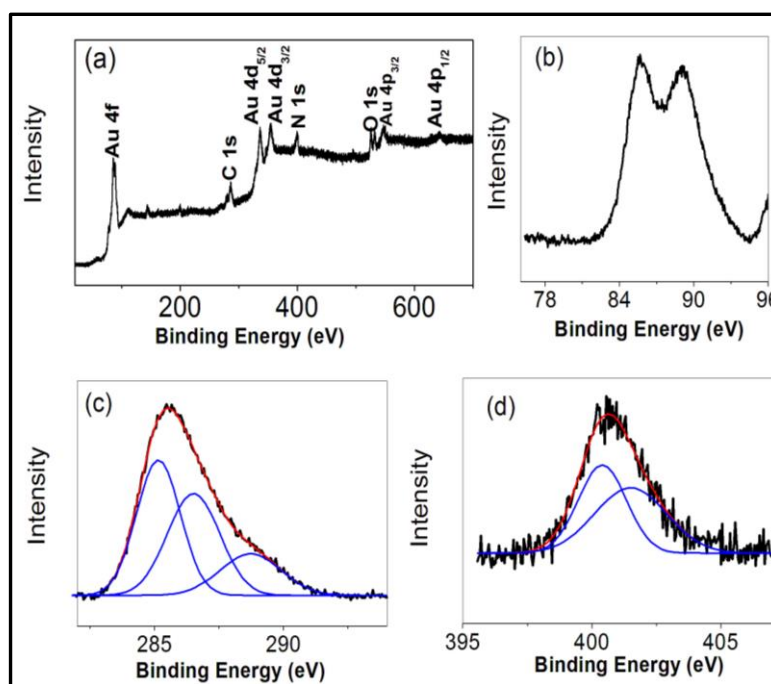


Figure 8.6. (a) XPS spectra of 4f orbital of Au (b, c) The de-convoluted spectra of 1s carbon(C) and nitrogen(N) of Au- CN_x respectively.

The yellow color of 4-nitrophenolate ion immediately bleached to colorless solution on addition of Au- CN_x catalyst and absorption maxima at 400 nm diminished with appearance of a new peak at 298 nm (Figure 8.6a blue curve).

This confirmed the reduction of 4-NP and formation of 4-AP²⁷. Here, Au-CN_x composite reduced 4-NP completely (100%) in 15 sec which is comparable to other reported values, given in Table 8.1.

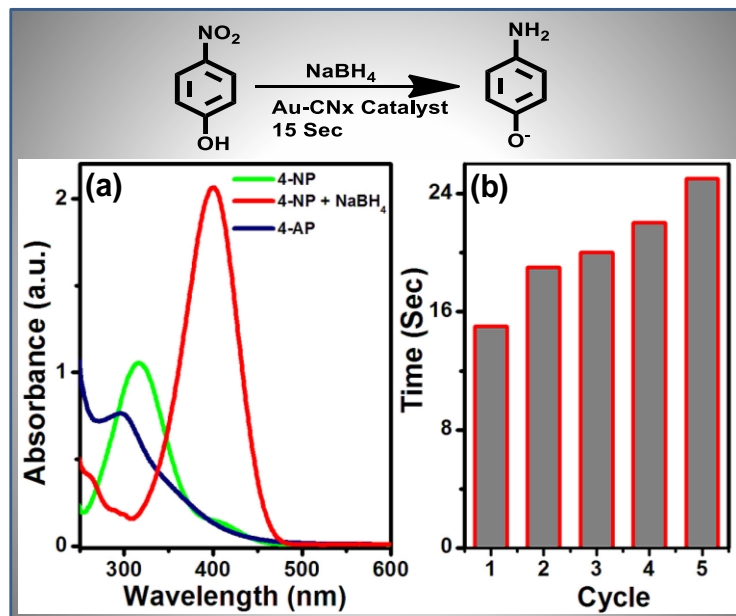


Figure 8.7. (a) UV-Visible spectra for the reduction 4-NP catalysed by Au-CN_x composite. 4-NP is represented by green colour curve, red colour curve is in presence of only NaBH₄ without catalyst and blue colour curve represent reductive product 4-AP. (b) The stability of the Au-CN_x catalyst with 5 successive cycles keeping the conditions same at every cycles.

Recently M. Antonietti and his co-worker reported⁶² reduction of 4-NP with AuNPs doped mesoporous carbon nitride (m-CNR-Au), only 96% conversion was happened with NaBH₄ in 300 sec. But the Au-CN_x catalyst take only 15 sec for full conversion of 4-NP. The superior catalytic activity of this Au-CN_x composite is probably due to the presence of ultra-small; naked gold particle on CN_x sheet. The stability of the catalyst was studied by doing the measurement repeatedly at the same condition. Catalyst can be successfully recycled by centrifugation, followed by washing with water and dried in vacuum. This catalyst can be used for at least 5 successive cycles with high conversion efficiency (Figure 8.7b). This proves that catalyst has good catalytic efficiency and stability.

8.4.2 Adsorption of organic dyes

The cationic dyes (RhB, MB) consider as primary toxic pollutant in water resource. The Au-CN_x can be used as adsorbent to remove these dyes. Change of UV-Vis absorption spectra was used to study the adsorption process on surface of Au-CN_x. Figure 8.8a shows the UV-Vis adsorption of 70 ppm RhB in aqueous solution. The absorption maximum of RhB at 552 nm was monitored for adsorption process on the Au-CN_x. The corresponding decay plot (C/C_0 vs. t) of RhB is shown in Figure 8.8b. It suggests that the Au-CN_x effectively removes 91% RhB dye within 380 min. Another cationic dye, MB also shows good adsorption on the Au-CN_x surface. Figure 8.8d shows the change UV-Visible adsorption spectra of MB solution with adsorption time in presence of Au-CN_x catalyst. This Au-CN_x catalyst can effectively remove 90% dye within 420 minutes. The versatility of the catalyst has been evaluated by measuring the adsorption capacity of textile an anionic dye (MR).

Table 8.1. Comparison of activity of different catalyst on 4-NP reduction.

Catalyst	Amt. Of catalyst (mg)	Amt. Of 4-NP (mmol)	Amt.Of NaBH ₄ (mmol)	Conv. Time (Sec)	Ref.
Au-CN _x	5	3x10 ⁻⁴	3x10 ⁻¹	15	This Work
Porous Au	0.5	5x10 ⁻⁴	2x10 ⁻¹	80	63
Porous Au-PdNPs	0.5	5x10 ⁻⁴	2x10 ⁻¹	12	63
RGO@Pd@C	5	3x10 ⁻⁴	3x10 ⁻²	30	64
Pd-rGO-CNT	5	3x10 ⁻⁴	3x10 ⁻²	20	65
Au-mpg C ₃ N ₄	5	3x10 ⁻⁴	3x10 ⁻¹	300	62

MR has poor adsorption on Au-CN_x composite at neutral pH. However, the adsorption of MR over Au-CN_x was increased significantly at lower pH (pH 3). The change of UV-Visible adsorption spectra of MR in presence of Au-CN_x catalyst with different time is shown in Figure 8.9a and the corresponding decay plot (C/C_0 vs. t) is also shown in 8.9b. Adsorption isotherm demonstrated the actual distribution of dye in equilibrium between liquid and solid adsorbent. The adsorption isotherm model of different dye was established by batch experiment where a known amount of Au-CN_x catalyst was dispersed in different known concentration of dye in dark with contentious stirring for certain time to establish the equilibration between adsorbent and adsorbed. The interactive behaviour of dyes and Au-CN_x was described by the different appropriate adsorption model including Freundlich, Langmuir and Sips isotherms⁶⁶, as described below.

$$\text{Freundlich isotherm} \quad q_e = K_F C_e^{1/n} \quad (\text{a})$$

$$\text{Langmuir isotherm} \quad q_e = q_m b C_e / (1 + K_L C_e) \quad (\text{b})$$

$$\text{Sips isotherm} \quad q_e = q_m b C_e^{1/n} / (1 + K_s C_e^{1/n}) \quad (\text{c})$$

Freundlich isotherm model described the ratio of concentration of solute adsorbed on surface and solute in liquid which is in contact with adsorbent (eqn. (a)). Langmuir model describes the chemisorptions of solute on the surface of adsorbent and only monolayer of solute was formed with maximum limit (eqn. (b)). The Sips model is an improved model of Freundlich and Langmuir. According to sips model solute follow the Freundlich model at lower concentration and Langmuir model at higher concentration (eqn. (c)). The experimental data for adsorption of RhB and MB on Au-CN_x composite were fitted with different adsorption isotherm models (Figure 8.8(c, f)).

Table 8.2. Parameters of different isotherm model of RhB dye.

<i>RhB dye</i>	<i>Isotherm models</i>		
Parameter	Freundlich	Langmuir	sips
K(mg/gm)	31	-	-
n	2.5	-	1.63
q _{max} (mg/gm)	-	250	400
b	-	0.02	0.04
R ²	0.966	0.950	0.971

The fitting parameters of RhB, MB and MR are shown in Table 8.2, Table 8.3 and Table S8.1 respectively. On the basis of R² value, the experimental data of RhB, MB and MR follow the sips isotherm suggesting multi-layered adsorption of RhB, MB and MR. The maximum adsorption capacities for RhB, MB and MR were found to be 400 mg gm⁻¹, 250 mg gm⁻¹ and 130 mg gm⁻¹ respectively.

Table 8.3. Parameters of different isotherm model of MB dye.

MB dye	Isotherm models		
Parameter	Freundlich	Langmuir	sips
K(mg/gm)	20.63	-	-
n	2.72	-	1.30
q_{max}(mg/gm)	-	200	235
b	-	0.01	0.02
R²	0.985	0.993	0.994

There were few reports on the adsorption of RhB dye in literature^{67,68}. Recently K. S. Kim reported⁶⁹ reduced graphene oxide based adsorbent for RhB adsorption with maximum capacity 30 mg gm⁻¹. But our Au-CN_x show comparable adsorption capacity with other reported value. Generally dye molecules are adsorbed on the adsorbent by two ways a) by electrostatic interaction between solute and adsorbent and b) π - π interaction of aromatic ring of dye molecule and the conjugated domain of the adsorbent.

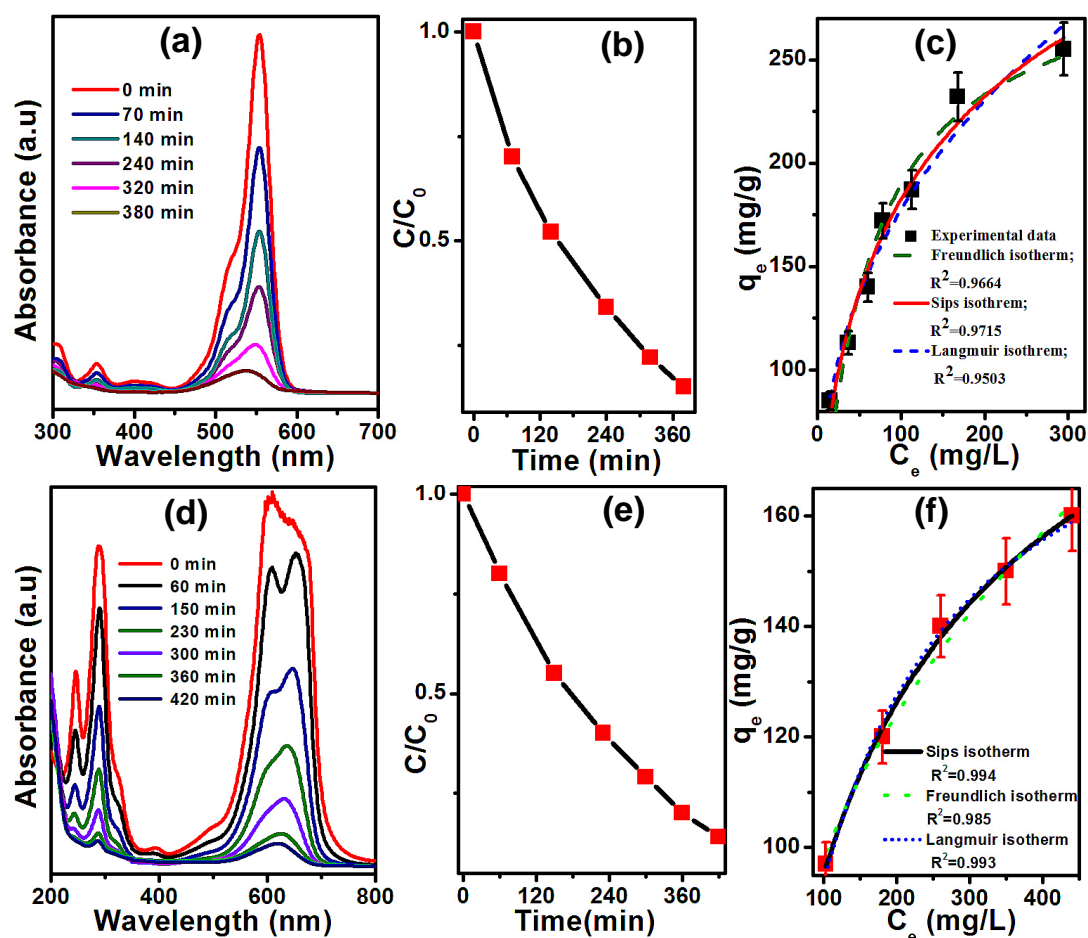


Figure. 8.8. (a,d) UV-Visible absorption spectra of aqueous solution of RhB and MB respectively at different time interval in presence of Au-CN_x catalyst. (b,e) Plot of C/C_0 vs. time for RhB and MB dyes respectively where C_0 is initial concentration of dyes (70 ppm) and C is the concentration at different time interval. (c,f) Fitting of different isotherm model with adsorption of RhB and MB on Au-CN_x surfaces respectively. All the experiment was done with 1 ml of 70 ppm dyes with 1 mg Au-CN_x catalyst.

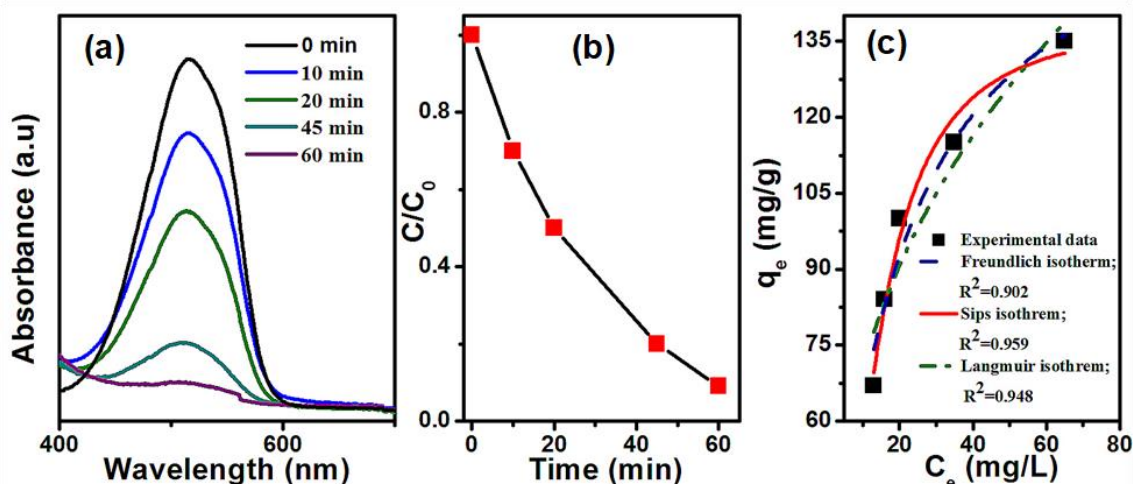


Figure 8.9. (a) UV-Visible absorption spectra of aqueous solution of MR at different time interval in presence of Au-CN_x catalyst. (b) Plot of C/C_0 vs. time for MR dyes respectively where C_0 is initial concentration of dyes (20 ppm) and C is the concentration at different time interval. (c) Fitting of different isotherm model with adsorption of MR on Au-CN_x surfaces. All the experiment was done with 1 ml of 20 ppm dyes with 1 mg Au-CN_x catalyst

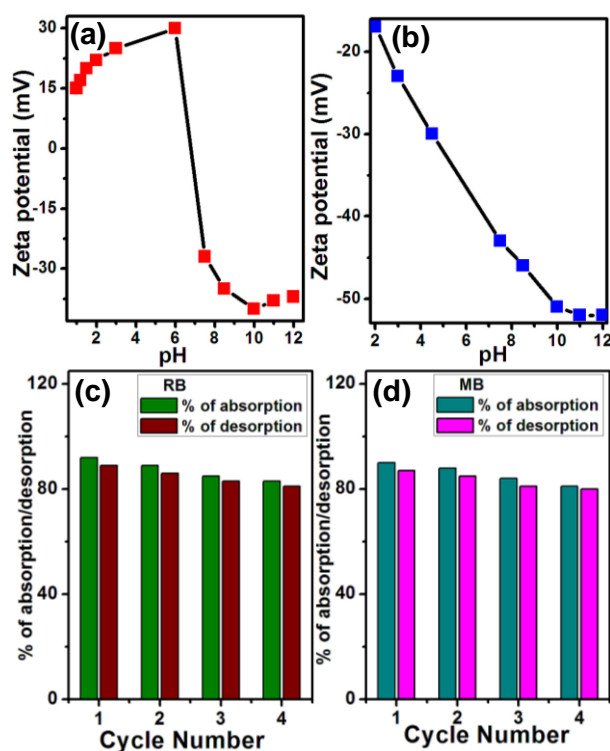


Figure 8.10. (a,b) Change of Zeta potential of g-CN_x and Au- CN_x composite with different pH respectively. (c,d) The adsorption –desorption cycle of RhB and MB respectively.

Graphitic carbon nitride doesn't have good adsorption property where as Au-CN_x shows superior dye adsorption properties. To understand the enhanced adsorption property of Au-CN_x compared to CN_x, zeta potential measurements of aqueous solution of C₃N₄ and Au-CN_x were done as a function of pH, shown in Figure 8.10(a) and (b). The average zeta potential value for CN_x sheets was +30mV at neutral pH whereas value for Au-CN_x was -45mV. RhB and MB are cationic dye at neutral pH and Au-CN_x catalyst has negatively charged at neutral pH. Therefore, Au-CN_x can adsorb RhB and MB at neutral pH due to electrostatic attraction between dye and the catalyst. But g-C₃N₄ has positive charge at neutral pH and these two dyes is also positively charged. The CN_x sheets show poor adsorption due to electrostatic repulsion of same charge. However MR is negatively charged at neutral pH. Thus Au-CN_x doesn't show any adsorption at neutral pH. But at higher pH (pH=3) MR gets positive charge and Au-CN_x is still negatively charged. So it shows significant adsorption at pH 3. Hence, here dye adsorption by Au-CN_x composite was mainly monitor by the electrostatic interaction.

8.4.3 Desorption of adsorbed dyes

Recycling of the catalyst is one of the important properties of a good adsorbent in the economical point of view. In literature, there are several methods are available for desorption of dyes. Q. Wang and his co-workers⁷⁰ reported a method for desorption by annealing the adsorbed dye-BN hollow sphere at 3000C for 2h. Expensive solvent such as ethylene glycol was used for washing the catalyst to remove the dye by K. S. Kim⁶⁹ and his co-workers. Most of the reported desorption process need long time as well as hazardous materials and methods was also not eco-friendly. Recently H. Schonherr and his co-workers reported³⁴ an easy method for desorption of dye by changing the pH of the solution. The Au-CN_x catalyst can be reused after removing adsorbed dye from the catalyst simply by changing the pH of the solution with a mild sonication.

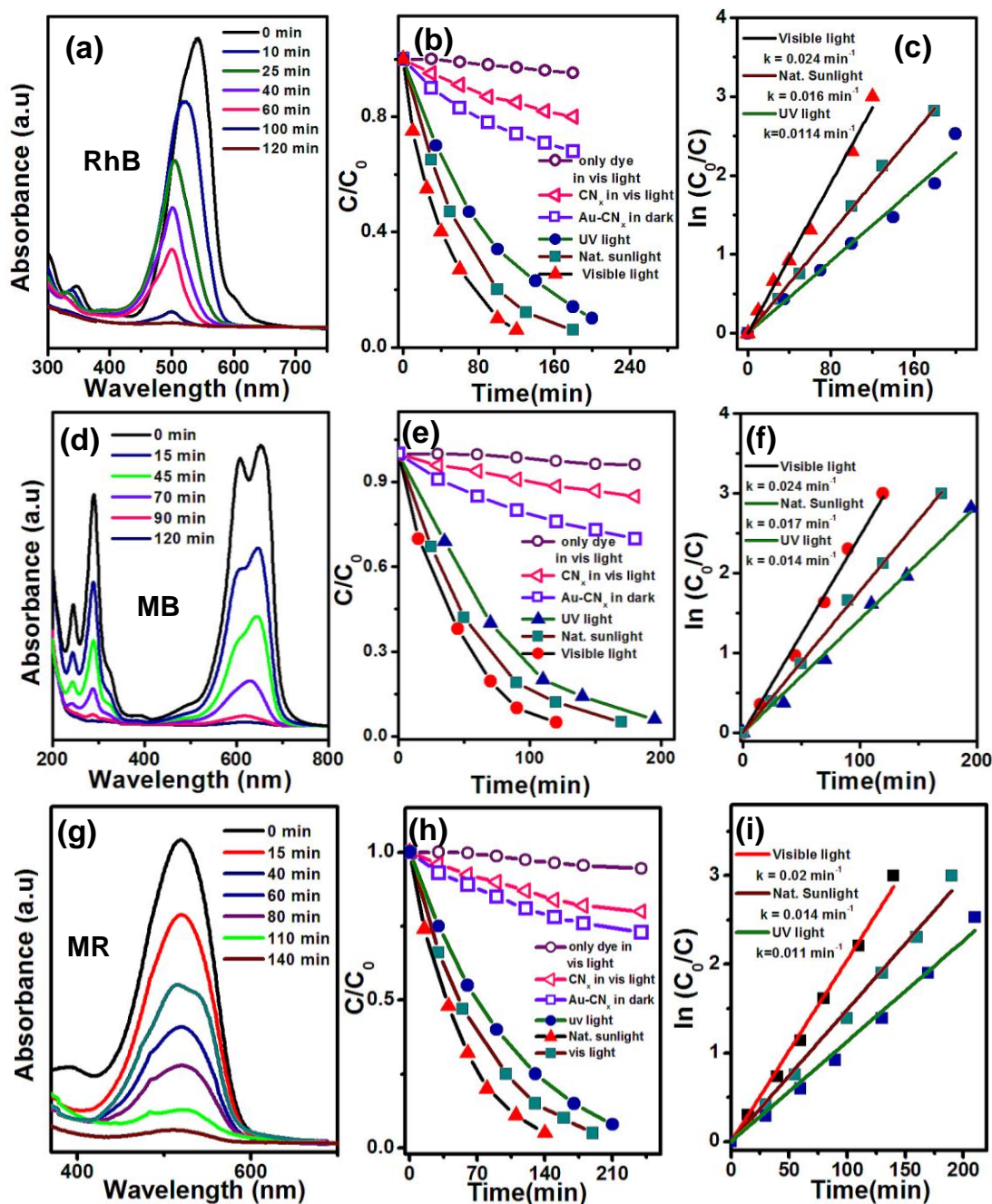


Figure 8.11. Degradation of 30 ppm RhB, 35 ppm MB, and 35 ppm MR dye by Au-CN_x under irradiation of visible light, natural sunlight, and UV light. (a, d, g) The change of UV-Visible absorption spectra of RhB, MB, MR over Au-CN_x catalyst on irradiation of visible light respectively. (b,e,h) Change of the concentration (C) of RhB, MB, and MR relative to their initial values (C₀) with time on irradiation of different lights. (c, f, i) The pseudo first order kinetics plots of RhB, MB, MR degradation under different UV, Visible and natural sunlight respectively.

Figure 8.10 (c and d) show the plot of percentage of adsorption-desorption at different cycle number for RhB and MB respectively. After complete adsorption at pH 6, when pH of the solution is increased to 12 by adding 1(M) NaOH solution, the adsorbed dye gradually desorbed and maximum desorption occurred after a mild sonication. The 89% and 87% of maximum desorption was achieved for RhB and MB at pH 12 in the first cycle. After 4th consecutive adsorption-desorption processes the desorption efficiency of RhB reduced to 81% and the small decrease of desorption efficiency (80%) of MB is also observed after 4th cycle. The de-adsorption process of dyes at high pH can easily be explained by the zeta potential of Au-CN_x and the charge of the dyes. At pH 12, the Au-CN_x surfaces is negatively charged with zeta potential of -55 mV and at the same time these two dyes has also negative charge. The electrostatic repulsion between negatively charged dye molecules and negatively charged Au-CN_x surfaces is responsible for superior desorption of the dyes. Thus it can be concluded that this Au-CN_x catalyst has an efficient recycling ability for the removal of these two cationic dyes.

8.4.4 Photocatalytic degradation of organic dyes

The photo catalytic activity of the Au-CN_x catalyst was evaluated by degradation of Rhodamine B (RhB), Methylene Blue (MB) and Methyl Red (MR) on irradiation of the visible light, UV light and natural sunlight. In typical photo catalytic reaction catalyst was dispersed in the dye solution and then kept in dark with continuous stirring for 1.5 hours before degradation. 130 watt visible light, 84 watt UV light and natural sunlight were used for degradation of organic dyes. A UV-Visible absorption maximum at 544 nm was monitor for RhB degradation whereas 644 nm and 591 nm were used for MB and MR degradation. Since the Au-CN_x composite showed good adsorption of dye, all the photo-catalytic dye degradation experiment was performed after 1.5 hours adsorption of the dyes on Au-CN_x catalyst in dark. Initial concentrations of dyes were 70 ppm. After 1.5 hrs of adsorption, the

remaining dye in solution was considered as initial concentration (C_0) for photocatalysis degradation. Figure 8.11a shows the change of UV-Visible absorption spectrum of ~30 ppm RhB under visible light irradiation. The corresponding changes of ratio, C/C_0 with time on irradiation of UV, Visible and natural sunlight are given in Figure 8.11b and the change of C/C_0 in absence of light (control experiment) is also given for comparison. Similar to the dye degradation the concentration of dye after 1.5h adsorption was taken as C_0 for the control experiment (absence of light). It shows that ~95% of dye was removed in presence of light in 180 minutes whereas only 15% of dye was removed in absence of light due to adsorption. It confirms that enhanced dye removal efficiency of Au-CN_x composite under light is due to photo-catalytic degradation of dye. The 98%, 90% and 82% of RhB dye were degraded in 120 minutes under Visible, natural sunlight and UV light. Figure 8.11b also contains the change of C/C_0 of dye under visible light in presence of CN_x. This indicates the very good photo stability of dye and poor degradation ability of CN_x.

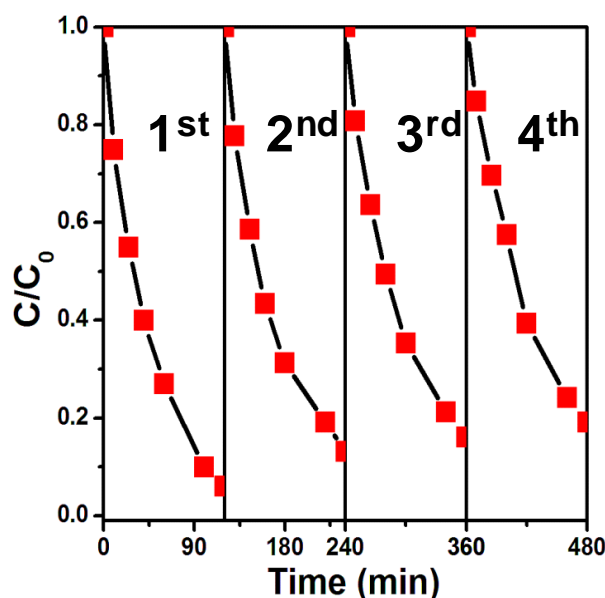


Figure 8.12. (a) Reusability of Au-CN_x catalyst for degradation of 30 ppm RhB dye where conditions of each cycle are kept same.

Figure 8.11 (d and g) shows the change of UV- Visible absorption spectra of 35 ppm MB and 35 ppm MR under visible light respectively. The C/C_0 vs. time plot for under different conditions for MB and MR are shown in Figure 8.11 (e and h). MB and MR also shows excellent photo degradation with Au-CN_x on light irradiation. The 81%, 96% and 90% of MB dye were degraded in 120 minutes under UV, Visible and natural sunlight where as 82%, 96% and 92% of MR dye were removed in 150 minutes. The Au-CN_x composite with different amount of gold loading were prepared by ultrasonic treatment of CN_x sheets and different amount of HAuCl₄. The maximum loading of gold in CN_x sheets we could achieve is 80 wt%. The catalytic activity of Au-CN_x composite is better when gold loading in Au-CN_x composite is 40-50%. All the measurements were done with 40 wt% Au-CN_x composite.

The rate of the photo oxidative degradation of different dye was measured by the Langmuir-Hinshelwood model in equation.

$$r = -\frac{dc}{dt} = \frac{kKC}{1+KC}$$

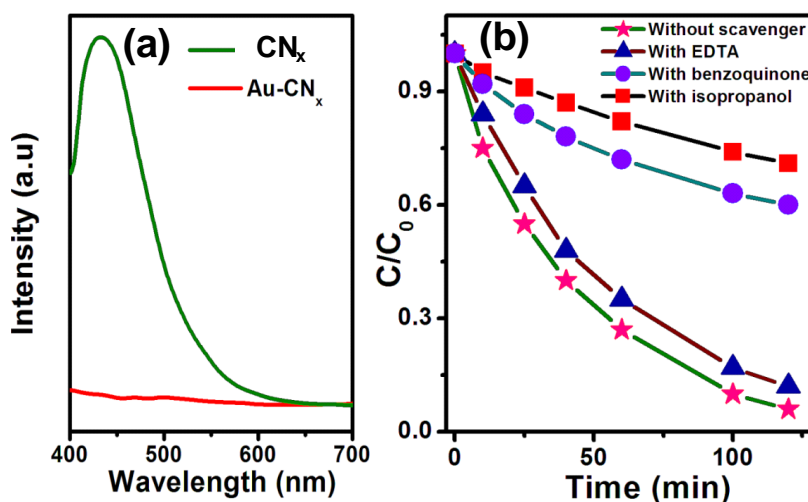


Figure 8.13. (a) Fluorescence emission spectra of g-CN_x and Au-CN_x composite (b) Scavenger effect on rate of 30 ppm RhB dye degradation.

Where r is reaction rate, K is the absorption coefficient, k is reaction rate constant, and C is the reactant concentration. If the reactant concentration is low these equation reduced to

$$\ln \frac{C_0}{C} = kt$$

Where k is the pseudo-first order rate constant, C_0 and C are the initial concentration and concentration after time t respectively.

The plot of $\ln(C_0/C)$ vs. t for RhB as shown in Figure 8.11c gives a straight line going through origin with a positive slope (k). The rate constant for degradation of RhB are 0.024, 0.016 and 0.011 min^{-1} in visible light, natural sunlight and UV light respectively. Figure 8.11 (f and i) shows the plot of $\ln(C_0/C)$ vs. t for MB and MR dye respectively. The rate constant for degradation of MB visible light, natural sunlight and UV light are 0.024, 0.017 and 0.014 min^{-1} respectively whereas rate constant for MR dye is 0.02, 0.014 and 0.011 min^{-1} under natural sunlight, visible light and UV light respectively.

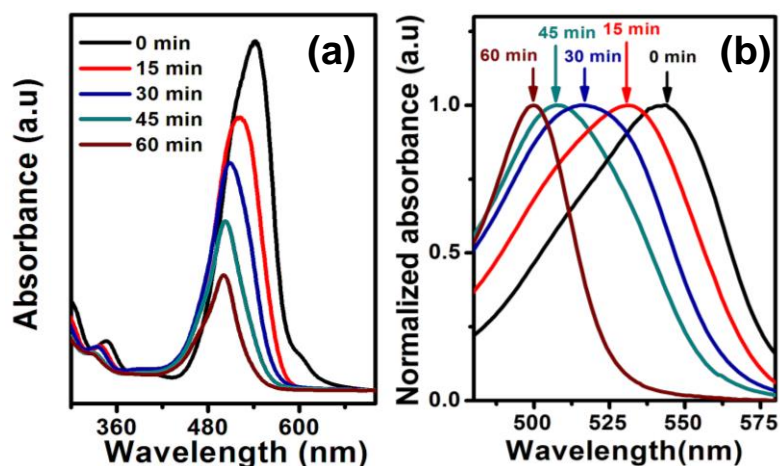


Figure 8.14. (a) UV-vis absorption spectra for degradation of RhB under irradiation of visible light. (b) Normalized absorption spectra of different N-de-ethylated intermediate products taken from Figure 8.14a

The plot of $\ln(C_0/C)$ vs. t for RhB as shown in Figure 8.11c gives a straight line going through origin with a positive slope (k). The rate constant for degradation of RhB are 0.024,

0.016 and 0.011 min⁻¹ in visible light, natural sunlight and UV light respectively. Figure 8.11 (f and i) shows the plot of $\ln(C_0/C)$ vs. t for MB and MR dye respectively. The rate constant for degradation of MB visible light, natural sunlight and UV light are 0.024, 0.017 and 0.014 min⁻¹ respectively whereas rate constant for MR dye is 0.02, 0.014 and 0.011 min⁻¹ under natural sunlight, visible light and UV light respectively. This confirmed that Au-CN_x is efficient catalyst for degradation of dye under irradiation of visible as well as UV light. The comparative study for degradation rate of different dye with Au-CN_x catalyst with different reported catalyst is given in Table 8.2. The photocatalytic rate constant of this Au-CN_x catalyst is comparable to other reported photocatalysts, although high concentration, 30 to 35 ppm of dyes was used in this case. The effect of concentration of dye on degradation rate constant was also studied. Figure 8.15 display the plot of $\ln(C_0/C)$ vs. time for different concentration of RhB. The rate constant for 15, 30 and 45 ppm RhB are 0.036 min⁻¹, 0.024 min⁻¹, and 0.015 min⁻¹. As the concentration of dye increased, rate constant is decreased. The decreases of the rate constant with concentration is due to the less percentage of light properly contact with catalyst as because high concentration of dye hindrance the light.

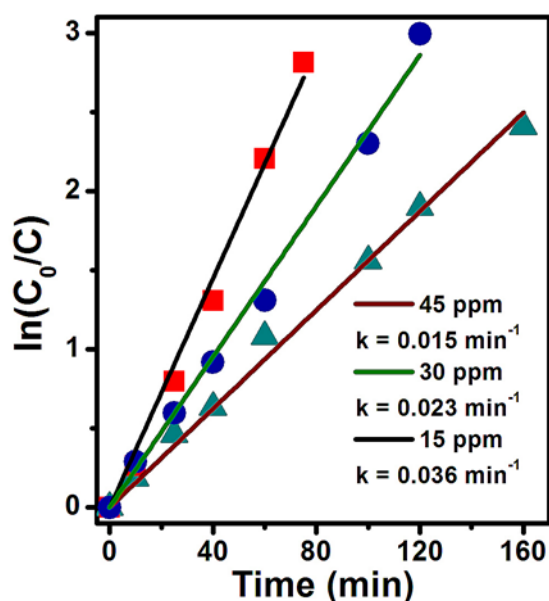


Figure 8.15. $\ln(C_0/C)$ vs. time plot of different concentration of RhB under visible light illumination.

One of the most important properties of the catalyst was the photo stability and reusability of the catalyst. The reusability of the catalyst for degradation of 30 ppm RhB is shown in Figure 8.12. The Au-CN_x catalyst easily degraded 95% RhB dye in 120 min upto 3rd cycle but it take little more time after 4th cycle. The catalyst has high photo-stability upto four cycles with high degradation ability.

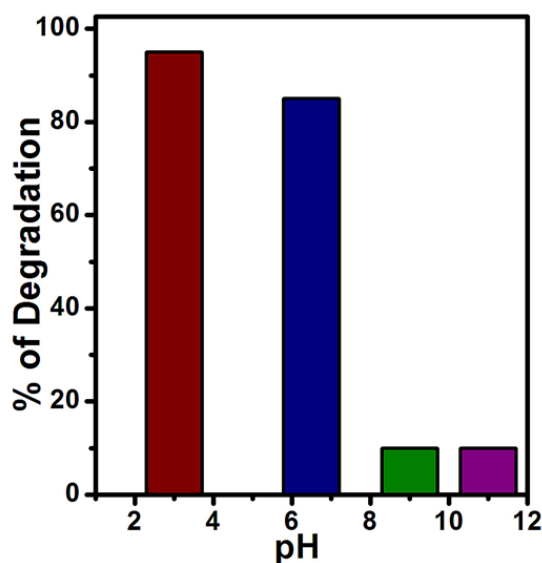


Figure 8.16. pH dependent degradation efficiency of 70 ppm RhB with Au-CN_x catalyst

The recycled catalyst was well characterized by p-XRD. The p-XRD pattern (Figure S8.3) of recycled Au-CN_x catalyst confirms the presence of Au nano-particles on CN_x sheets. Au-CN_x catalyst photo degradation of dyes are highly sensitive to pH. The plot of degradation percentage vs. pH of 30 ppm RhB has shown in Figure 8.16. But the degradation efficiency of RhB at lower pH (pH 3) little higher than neutral pH. Au-CN_x catalyst shows poor degradation efficiency in higher pH compared to neutral pH. So all the degradation experiment was done in acidic pH (pH 3).

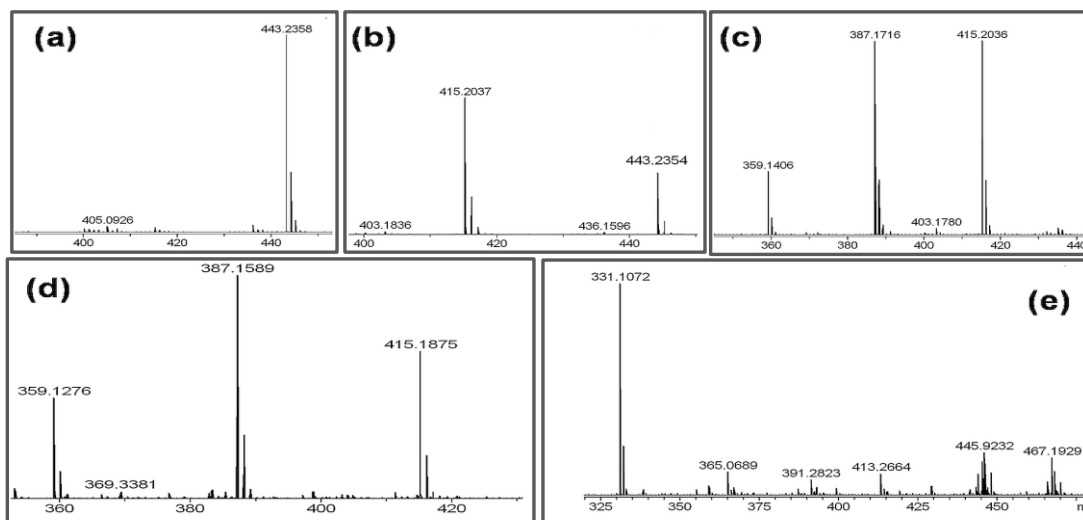
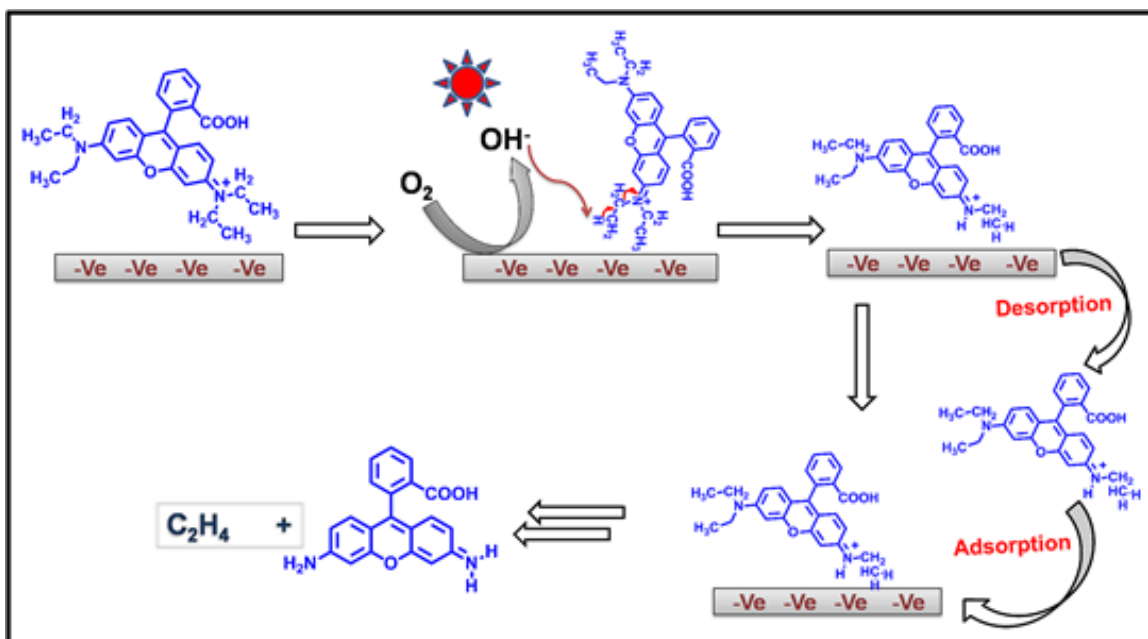


Figure 8.17. (a-e) represent LC-MS mass spectra of different N-alkylated intermediate, formed during degradation of RhB.

Since the catalyst have significant adsorption we have tested the photo degradation of dye of very high concentration of 250 ppm RhB after keeping 12 hours in dark for full adsorption of dye. Figure S8.2 (a and b) (Annexure) shows the change of UV-Visible spectra and corresponding C/C_0 vs. time plot. The Au-CN_x showed excellent degradation in much higher concentration and it can easily degraded 85% within 300 min. Thus, this photocatalyst is effective for removal of low and very high concentration of organic dye by using its dual (adsorbent and photocatalyst) properties. The much higher degradation efficiency of Au-CN_x in compared to CN_x is probably due the hetero junction, made from AuNPs and CN_x sheets. In order to examine the effect of presence of ultra-small AuNPs on CN_x sheets, fluorescence measurements were done to investigate separation efficiency of photo-generated electrons and holes. As fluorescence originated from the recombination of the photo induced electron and hole in valence band, so fluorescence spectra was investigated to understand the separation efficiency of photo excited charge carriers of the photocatalyst. The fluorescence spectra of CN_x and Au-CN_x composite was shown in Figure 8.13a. The highly blue fluorescence of the graphitic carbon nitride was quenched in Au-CN_x due to loading of AuNPs on the graphitic carbon nitride sheets.



Scheme 8.1. Schematic diagram of de-ethylation process of RhB on the surface of Au-CN_x composite under irradiation of light.

The actual relationship is that higher the fluorescence intensity higher is the recombination rate of the electron-hole and lower is the efficiency of photo-excited charge separation. The fluorescence emission spectra of CN_x at ~435 nm represent the band gap of emission light energy equal to the band gap of pure CN_x and this emission was quenched fully after formation of Au-CN_x composite. The less intensity of fluorescence emission spectra of Au-CN_x confirmed the formation of heterostructure where the photo-excited electron traps by the AuNPs and stabilized the photo-induced charge separation. To evaluate active species involved in this photocatalytic dye degradation we studied the RhB degradation under visible light irradiation in presence of different scavenger. EDTA-Na complex is known for hole (h⁺) scavenger, isopropanol is OH radical (·OH) scavenger and benzoquinone (BQ) is a superoxide radical scavenger. Figure 8.13b shows the effect of scavenger on the degradation rate. It can easily be seen that rate of RhB degradations remain unchanged on addition of the EDTA-Na complex. But the rate of the photo-degradation was decreased on addition of isopropanol and benzoquinone. It proved that the hydroxyl and superoxide

radical are the reactive oxygen species (ROS) responsible for the photodegradation of the dye. Photo-degradation mechanism of RhB dye was studied by UV-Visible spectroscopy and LC-MS/MS spectroscopy. The photo-degradation of RhB generally occurs by two ways⁷¹ a) the complete cleavage of chromophores, b) N-de-ethylation of N-substituted groups on chromophores. The change of UV-Visible spectra of RhB under visible light and their normalized spectra are shown in Figure 8.14 (a, b) respectively. It shows that the adsorption maxima of RhB showed hypsochromic shift from 544 nm to 499 nm with increasing the irradiation time. This hypsochromic behavior of absorption maxima is due to the consequence of N-de-ethylation process⁷². As shown in Figure 8.14b, the different adsorption maxima for different de-ethylated intermediates. The 539 nm peak is due to N, N'-tri-ethylated Rhodamine; 522 nm for N, N'-di-ethylated Rhodamine, where as 510 nm and 500 nm are for N-ethylated Rhodamine and Rhodamine respectively. The formation of different intermediate of the de-ethylated products was also confirmed by LC-MS mass spectroscopy. Figure 8.17(a-e) show the mass spectra of different intermediates which was formed during the photo degradation of RhB. Initially RhB shows only one peak at m/z 443 which corresponds to dechlorinated RhB. New peaks were appeared with m/z value at 415, 387, 359, and 331 with increasing the irradiation time. The differences between two consecutive values are 28 m/z that corresponds to mass of ethylene molecule. Based on the UV-Vis and mass spectra it can be concluded that degradation of RhB on Au-CN_x catalyst occurred via de-ethylation process. If the conjugate ring structure is not destroyed then fully de-ethylated RhB should have a maximum at 498 nm with molar extinction co-efficient (ϵ_{\max}) 70% of the initial extinction co-efficient (ϵ_{\max}) of RhB. But intensity of the absorption peak at 498 nm of 30 ppm RhB after visible light irradiation of 120 minutes is reduced to 5% of the initial intensity of RhB. So it confirms that the degradation of RhB on Au-CN_x occurred via the N-de-ethylation process followed by complete mineralization of the

chromophores. The schematic diagram of the proposed mechanism for de-ethylation process is shown in scheme 1. RhB moiety was easily adsorbed on the surfaces of Au-CN_x through the N-alkylated site due to the electrostatic interaction. During the photo irradiation the surface adsorbed oxygen is reduced to form hydroxyl radicals which can easily take the aliphatic proton from N-Ethyl to form ethylene and N,N,N'-tri-ethylated Rhodamine. Some of the N,N,N'-tri-ethylated Rhodamine can desorbed from the catalyst surface and then again adsorbed on AuNPs surfaces.

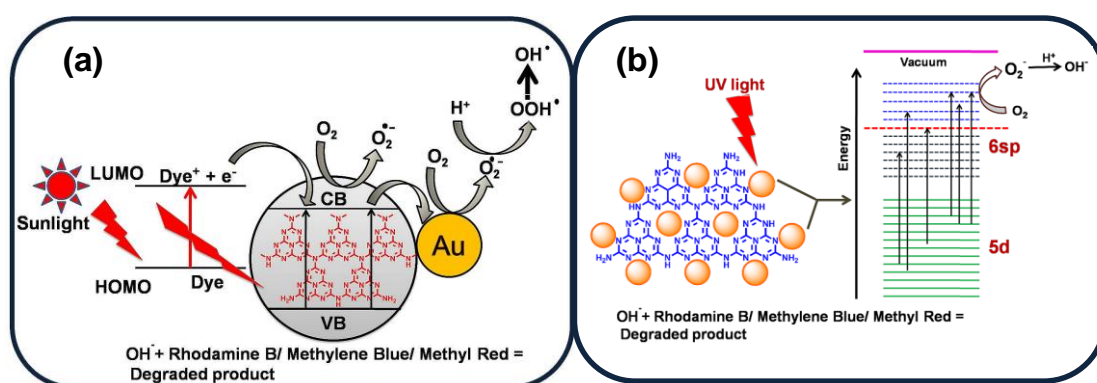


Figure 8.18. A proposed mechanism of photocatalytic degradation of dyes (a) under sunlight or visible light and (b) under irradiation of UV light in presence of Au-CN_x catalyst.

In next step de-ethylation of N,N,N'-tri-ethylated Rhodamine occurs in the same way by the hydroxyl radical to form N,N'-di-ethylated Rhodamine and then released in solution. In the sequential de-ethylation processes Rhodamine B converted to de-ethylated Rhodamine. Finally, Rhodamine was degraded to form UV inactive products.

Based on the above experimental observations we proposed a mechanism for degradation of organic dye over Au-CN_x catalyst on irradiation of visible light as shown in Figure 8.14a. The dye was first excited to dye* and then excited electron transfer to conduction band of CN_x to form cationic dye radical. At the same time on irradiation of visible light, CN_x also form exciton *i.e.* electron excited to conduction band from valence band leading to electron-hole charge separation. Now, the injected electron from dye and excited electron transport

to AuNPs by interfacial electron transports. Then, surfaces adsorbed O_2 molecule reduced on the Au surface to form superoxide radicals which can easily reduce to hydroxyl radical in acidic medium. Finally, hydroxyl radical can easily degrade the dyes easily shown in Figure 8.18a. It is well known that Au and Ag NPs show considerable absorption of UV light due to inter band transition (transition of 5d or 4d electrons to 6sp or 5sp band)⁷³. The degradation of dye over Au-CN_x catalyst under UV light irradiation can be explained by the UV light absorption property of the gold nanoparticles through inter band electron transition. Recently Zhu and his co-worker established the mechanism of phenol degradation by the Ag NPs supported on metal oxide under UV light irradiation through 4d to 5sp inter band transition³¹ and Wang and his co-workers also established the actual mechanism of UV light adsorption by the Au NPs supported on the metal oxide via inter band transition of 5d to 6sp⁷⁴. A proposed mechanism for dye degradation under UV light was depicted in Figure 8.18b. On irradiation of UV light 5d electrons of gold nanoparticles of Au-CN_x composite was excited to 6sp band (inter band transition). Among those excited electrons some of the electrons are in the higher energy state than the energy (red line) of the reduction potential for O_2/O_2^- . These electrons can easily able to reduce the adsorbed oxygen molecule into superoxide radicals which in acidic medium form hydroxyl radicals. The hydroxyl radicals are then available for degradation of dyes. The slight greater the rate constant value under visible light may be due to the synergetic effect of electron transport of supported g-carbon nitride and dye molecule where under UV light only AuNPs responsible for electron transport. The adsorption and photocatalytic degradation of organic dye (RhB) with other noble metal-CN_x composites such as Ag-CN_x were also studied. The Ag-CN_x didn't show any significant absorption and photocatalytic degradation of RhB. The zeta potential of Ag-CN_x was found to be +31 mV whereas Au-CN_x was -25mV at neutral pH. The adsorption and photo-catalytic behaviour of Ag-CN_x composite are similar to pure CN_x compound since

both have positive surface charge. The negative surface charge on the catalyst in solution is important for strong adsorption and photocatalytic degradation of positively charged organic dye such as RhB and MB.

Table 8.4. Comparison of rate constant for photocatalytic degradation of different dyes.

Catalyst	Dye	Concentration of Dye	Light source	Rate constant	Ref.
Graphene- Gold	RhB	2.5 ppm	Visible light	8.3×10^{-3}	32
PD/MW	RhB	2 ppm	Microwave light	1.7×10^{-2}	75
RGO-CuNO ₃	RhB	2.5 ppm	Visible light	1.5×10^{-2}	76
Ag-C ₃ N ₄	RhB	10 ppm	Visible light	2.53×10^{-2}	77
Au-CN_x	RhB	~30 ppm	Visible light	2.4×10^{-2}	This work
Ag/AgCl	MB	20 ppm	Visible light	7.0×10^{-3}	78
Ag/AgCl/g-C ₃ N ₄	MB	10 ppm	Visible light	7.8×10^{-2}	37
Au ⁺³ -TiO ₂ (0.5%)	MB	12 ppm	Visible light	9.2×10^{-3}	79
Au-CN_x	MB	~35 ppm	Visible light	2.4×10^{-2}	This work
TiO ₂	MR	4 ppm	UV light	1.3×10^{-2}	80
Ag ⁺ /TiO ₂	MR	6 ppm	UV light	5.02×10^{-3}	81
Au-CN_x	MR	~35 ppm	Visible light	2.0×10^{-2}	This work

8.5. CONCLUSION

In conclusion, we have demonstrated a facile synthetic route for the formation and very high loading of ultra-small gold nano-particles on two dimensional carbon nitride sheets. This composite was found to be superior catalyst for the reduction of nitro phenol. We have also showed that the Au-CN_x composite has high adsorption capacity for cationic dye (RhB, MB) in neutral medium and anionic dye (MR) in acidic medium with good reusability and easy desorption process. The Au-CN_x composite is not only good adsorbent but also a very

efficient heterogeneous photocatalyst towards the degradation of various dyes. The degradation of RhB, MB and MR over Au-CN_x catalyst was performed on irradiation of UV/Visible light/natural sunlight. The controlled experiment proves that hydroxyl radical is main active species towards photocatalytic degradation of organic dye. The catalyst is also very efficient for removal of high concentration, 250 ppm dye due to its superior photocatalytic activity. This superior catalytic property of Au-CN_x is probably due to naked, ultra small AuNPs on CN_x sheets. Moreover, this Au-CN_x composite can be reused several times for photo-catalytic degradation and as well as for dye adsorption. Thus, this Au-CN_x composite is a suitable catalyst for water cleaning.

8.6. REFERENCES:

- (1) Astruc, D.; Lu, F.; Aranzaes, J. R. *Angew. Chem. Int. Ed.* **2005**, *44*, 7852-7872.
- (2) Jain, P. K.; Huang, X.; El-Sayed, I. H.; El-Sayed, M. A. *Acc. Chem. Res.* **2008**, *41*, 1578-1586.
- (3) Kundu, M. K.; Sadhukhan, M.; Barman, S. *J. Mater. Chem. B* **2015**, *3*, 1289-1300.
- (4) Tian, J.; Liu, Q.; Asiri, A. M.; Qusti, A. H.; Al-Youbi, A. O.; Sun, X. *Nanoscale* **2013**, *5*, 11604-11609.
- (5) Tian, J.; Liu, Q.; Ge, C.; Xing, Z.; Asiri, A. M.; Al-Youbi, A. O.; Sun, X. *Nanoscale* **2013**, *5*, 8921-8924.
- (6) McFarland, A. D.; Van Duyne, R. P. *Nano Lett.* **2003**, *3*, 1057-1062.
- (7) Zhang, Y.; Chang, G.; Liu, S.; Tian, J.; Wang, L.; Lu, W.; Qin, X.; Sun, X. *Catal. Sci. Technol.* **2011**, *1*, 1636-1640.
- (8) Daniel, M.-C.; Astruc, D. *Chem. Rev.* **2003**, *104*, 293-346.
- (9) Lin, J.; He, C.; Zhao, Y.; Zhang, S. *Sensors Actuators B: Chemical* **2009**, *137*, 768-773.

- (10) Qiu, J.-D.; Wang, G.-C.; Liang, R.-P.; Xia, X.-H.; Yu, H.-W. *J. Phys. Chem. C* **2011**, *115*, 15639-15645.
- (11) Yoon, B.; Häkkinen, H.; Landman, U.; Wörz, A. S.; Antonietti, J.-M.; Abbet, S.; Judai, K.; Heiz, U. *Science* **2005**, *307*, 403-407.
- (12) Campelo, J. M.; Luna, D.; Luque, R.; Marinas, J. M.; Romero, A. A. *ChemSusChem* **2009**, *2*, 18-45.
- (13) Geim, A. K. *Science* **2009**, *324*, 1530-1534.
- (14) Ong, W.-J.; Tan, L.-L.; Chai, S.-P.; Yong, S.-T. *Chem. Commun.* **2015**, *51*, 858-861.
- (15) Yeh, T.-F.; Chen, S.-J.; Teng, H. *Nano Energy* **2015**, *12*, 476-485.
- (16) Guo, S.; Dong, S. *Chem. Soc. Rev.* **2011**, *40*, 2644-2672.
- (17) Zheng, Y.; Liu, J.; Liang, J.; Jaroniec, M.; Qiao, S. Z. *Energy Environ. Sci* **2012**, *5*, 6717-6731.
- (18) Gao, H.; Yan, S.; Wang, J.; Zou, Z. *Dalton Trans.* **2014**, *43*, 8178-8183.
- (19) Ong, W.-J.; Tan, L.-L.; Chai, S.-P.; Yong, S.-T.; Mohamed, A. R. *Nano Energy*.
- (20) Wang, Y.; Wang, X.; Antonietti, M. *Angew. Chem. Int. Ed.* **2012**, *51*, 68-89.
- (21) Maeda, K.; Kuriki, R.; Zhang, M.; Wang, X.; Ishitani, O. *J. Mater. Chem. A* **2014**, *2*, 15146-15151.
- (22) Tian, J.; Ning, R.; Liu, Q.; Asiri, A. M.; Al-Youbi, A. O.; Sun, X. *ACS Appl. Mater. Interfaces* **2013**, *6*, 1011-1017.
- (23) Wu, Z.; Gao, H.; Yan, S.; Zou, Z. *Dalton Trans.* **2014**, *43*, 12013-12017.
- (24) Ong, W.-J.; Tan, L.-L.; Chai, S.-P.; Yong, S.-T. *Dalton Trans.* **2015**, *44*, 1249-1257.
- (25) Huang, Z.-F.; Song, J.; Pan, L.; Wang, Z.; Zhang, X.; Zou, J.-J.; Mi, W.; Zhang, X.; Wang, L. *Nano Energy* **2015**, *12*, 646-656.
- (26) McCann, J.; Ames, B. N. *Proc. Natl. Acad. Sci.* **1976**, *73*, 950-954.

- (27) Pradhan, N.; Pal, A.; Pal, T. *Colloids Surf., A: Physicochem. Eng. Aspects* **2002**, *196*, 247-257.
- (28) Chang, G.; Luo, Y.; Lu, W.; Qin, X.; Asiri, A. M.; Al-Youbi, A. O.; Sun, X. *Catal. Sci. Technol.* **2012**, *2*, 800-806.
- (29) Hoffmann, M. R.; Martin, S. T.; Choi, W.; Bahnemann, D. W. *Chem. Rev.* **1995**, *95*, 69-96.
- (30) Tan, B. H.; Teng, T. T.; Omar, A. K. M. *Water Res.* **2000**, *34*, 597-601.
- (31) Chen, X.; Zheng, Z.; Ke, X.; Jaatinen, E.; Xie, T.; Wang, D.; Guo, C.; Zhao, J.; Zhu, H. *Green Chem.* **2010**, *12*, 414-419.
- (32) Xiong, Z.; Zhang, L. L.; Ma, J.; Zhao, X. S. *Chem. Commun.* **2010**, *46*, 6099-6101.
- (33) Lin, S. H.; Peng, C. F. *Water Res.* **1996**, *30*, 587-592.
- (34) Ghorai, S.; Sarkar, A.; Raoufi, M.; Panda, A. B.; Schönherr, H.; Pal, S. *ACS Appl. Mater. Interfaces* **2014**, *6*, 4766-4777.
- (35) Lei, W.; Portehault, D.; Liu, D.; Qin, S.; Chen, Y. *Nat. Commun.* **2013**, *4*, 1777.
- (36) Parker, H. L.; Hunt, A. J.; Budarin, V. L.; Shuttleworth, P. S.; Miller, K. L.; Clark, J. H. *RSC Adv.* **2012**, *2*, 8992-8997.
- (37) Yao, X.; Liu, X.; Hu, X. *ChemCatChem* **2014**, *6*, 3409-3418.
- (38) Sun, H.; Liu, S.; Liu, S.; Wang, S. *Appl. Catal B* **2014**, *146*, 162-168.
- (39) Thapa, R.; Maiti, S.; Rana, T. H.; Maiti, U. N.; Chattopadhyay, K. K. *J. Mol. Cat. A: Chemical* **2012**, *363-364*, 223-229.
- (40) Zhang, J.; Zhang, M.; Sun, R.-Q.; Wang, X. *Angew. Chem. Int. Ed.* **2012**, *51*, 10145-10149.
- (41) Yan, S. C.; Li, Z. S.; Zou, Z. G. *Langmuir* **2009**, *25*, 10397-10401.
- (42) Wang, Y.; Wang, X.; Antonietti, M.; Zhang, Y. *ChemSusChem* **2010**, *3*, 435-439.

- (43) Cheng, N.; Tian, J.; Liu, Q.; Ge, C.; Qusti, A. H.; Asiri, A. M.; Al-Youbi, A. O.; Sun, X. *ACS Appl. Mater. Interfaces* **2013**, *5*, 6815-6819.
- (44) Ge, L.; Han, C.; Liu, J.; Li, Y. *Appl. Catal. A* **2011**, *409–410*, 215-222.
- (45) Xu, H.; Yan, J.; Xu, Y.; Song, Y.; Li, H.; Xia, J.; Huang, C.; Wan, H. *Appl. Catal. B* **2013**, *129*, 182-193.
- (46) Lü, X.; Shen, J.; Wu, Z.; Wang, J.; Xie, J. *J. Mater. Res.* **2014**, *29*, 2170-2178.
- (47) Li, H.; Liu, Y.; Gao, X.; Fu, C.; Wang, X. *ChemSusChem* **2015**, *8*, 1189-96.
- (48) Yang, X.; Tang, H.; Xu, J.; Antonietti, M.; Shalom, M. *ChemSusChem* **2015**.
- (49) Zhang, S.; Li, J.; Zeng, M.; Zhao, G.; Xu, J.; Hu, W.; Wang, X. *ACS Appl. Mater. Interfaces* **2013**, *5*, 12735-12743.
- (50) Zhang, S.; Li, J.; Zeng, M.; Li, J.; Xu, J.; Wang, X. *Chem. Eur. J.* **2014**, *20*, 9805-9812.
- (51) Zhang, S.; Li, J.; Wang, X.; Huang, Y.; Zeng, M.; Xu, J. *ACS Appl. Mater. Interfaces* **2014**, *6*, 22116-22125.
- (52) Barman, S.; Sadhukhan, M. *J. Mater. Chem.* **2012**, *22*, 21832-21837.
- (53) Sadhukhan, M.; Barman, S. *J. Mater. Chem. A* **2013**, *1*, 2752-2756.
- (54) Wagner, C. D.; Muilenberg, G. E. *Handbook of x-ray photoelectron spectroscopy: a reference book of standard data for use in x-ray photoelectron spectroscopy*, Physical Electronics Division, Perkin-Elmer Corp.: 1979.
- (55) Wertheim, G. K.; DiCenzo, S. B. *Phys. Rev. B* **1988**, *37*, 844-847.
- (56) Takahiro, K.; Oizumi, S.; Terai, A.; Kawatsura, K.; Tsuchiya, B.; Nagata, S.; Yamamoto, S.; Naramoto, H.; Narumi, K.; Sasase, M. *J. Appl. Phys.* **2006**, *100*, 084325-01 - 084325-05.
- (57) Turner, M.; Golovko, V. B.; Vaughan, O. P. H.; Abdulkin, P.; Berenguer-Murcia, A.; Tikhov, M. S.; Johnson, B. F. G.; Lambert, R. M. *Nature* **2008**, *454*, 981-983.
- (58) Hövel, H.; Grimm, B.; Pollmann, M.; Reihl, B. *Phys. Rev. Lett.* **1998**, *81*, 4608-4611.

- (59) Wertheim, G. K.; DiCenzo, S. B.; Youngquist, S. E. *Phys. Rev. Lett.* **1983**, *51*, 2310-2313.
- (60) Anderson, D. P.; Alvino, J. F.; Gentleman, A.; Qahtani, H. A.; Thomsen, L.; Polson, M. I. J.; Metha, G. F.; Golovko, V. B.; Andersson, G. G. *Phys. Chem. Chem. Phys.* **2013**, *15*, 3917-3929.
- (61) Arrigo, R.; Havecker, M.; Schlogl, R.; Su, D. S. *Chem. Commun.* **2008**, 4891-4893.
- (62) Li, X.-H.; Wang, X.; Antonietti, M. *Chem. Sci.* **2012**, *3*, 2170-2174.
- (63) Ma, A.; Xu, J.; Zhang, X.; Zhang, B.; Wang, D.; Xu, H. *Sci. Rep.* **2014**, *4*, 4849-4856.
- (64) Zhang, Z.; Xiao, F.; Xi, J.; Sun, T.; Xiao, S.; Wang, H.; Wang, S.; Liu, Y. *Sci. Rep.* **2014**, *4*, 4053-4058.
- (65) Sun, T.; Zhang, Z.; Xiao, J.; Chen, C.; Xiao, F.; Wang, S.; Liu, Y. *Sci. Rep.* **2013**, *3*, 2527-2533.
- (66) Muntean, S. G.; Radulescu-Grad, M. E.; Sfarloaga, P. *RSC Adv.* **2014**, *4*, 27354-27362.
- (67) Dong, Y.; Lin, H.; Jin, Q.; Li, L.; Wang, D.; Zhou, D.; Qu, F. *J. Mater. Chem. A* **2013**, *1*, 7391-7398.
- (68) Zhang, S.; Wang, X.; Li, J.; Wen, T.; Xu, J.; Wang, X. *RSC Adv.* **2014**, *4*, 63110-63117.
- (69) Tiwari, J. N.; Mahesh, K.; Le, N. H.; Kemp, K. C.; Timilsina, R.; Tiwari, R. N.; Kim, K. S. *Carbon* **2013**, *56*, 173-182.
- (70) Lian, G.; Zhang, X.; Zhang, S.; Liu, D.; Cui, D.; Wang, Q. *Energy Environ. Sci.* **2012**, *5*, 7072-7080.
- (71) Wu, T.; Liu, G.; Zhao, J.; Hidaka, H.; Serpone, N. *J. Phys. Chem. B* **1998**, *102*, 5845-5851.
- (72) Yu, K.; Yang, S.; He, H.; Sun, C.; Gu, C.; Ju, Y. *J. Phys. Chem. A* **2009**, *113*, 10024-10032.

- (73) Voisin, C.; Del Fatti, N.; Christofilos, D.; Vallée, F. *J. Phys. Chem. B* **2001**, *105*, 2264-2280.
- (74) Zhu, H.; Chen, X.; Zheng, Z.; Ke, X.; Jaatinen, E.; Zhao, J.; Guo, C.; Xie, T.; Wang, D. *Chem. Commun.* **2009**, 7524-7526.
- (75) Horikoshi, S.; Hidaka, H.; Serpone, N. *Environ. Sci. Technol.* **2002**, *36*, 1357-1366.
- (76) Xiong, Z.; Zhang, L. L.; Zhao, X. S. *Chem. Eur. J.* **2011**, *17*, 2428-2434.
- (77) Hu, S. W.; Yang, L. W.; Tian, Y.; Wei, X. L.; Ding, J. W.; Zhong, J. X.; Chu, P. K. *Appl. Catal. B* **2015**, *163*, 611-622.
- (78) An, C.; Peng, S.; Sun, Y. *Adv. Mater.* **2010**, *22*, 2570-2574.
- (79) Li, X. Z.; Li, F. B. *Environ. Sci. Technol.* **2001**, *35*, 2381-2387.
- (80) Mascolo, G.; Comparelli, R.; Curri, M. L.; Lovecchio, G.; Lopez, A.; Agostiano, A. *J. Hazard. Mater.* **2007**, *142*, 130-137.
- (81) Gupta, A. K.; Pal, A.; Sahoo, C. *Dyes and Pigments* **2006**, *69*, 224-232.

Appendix F

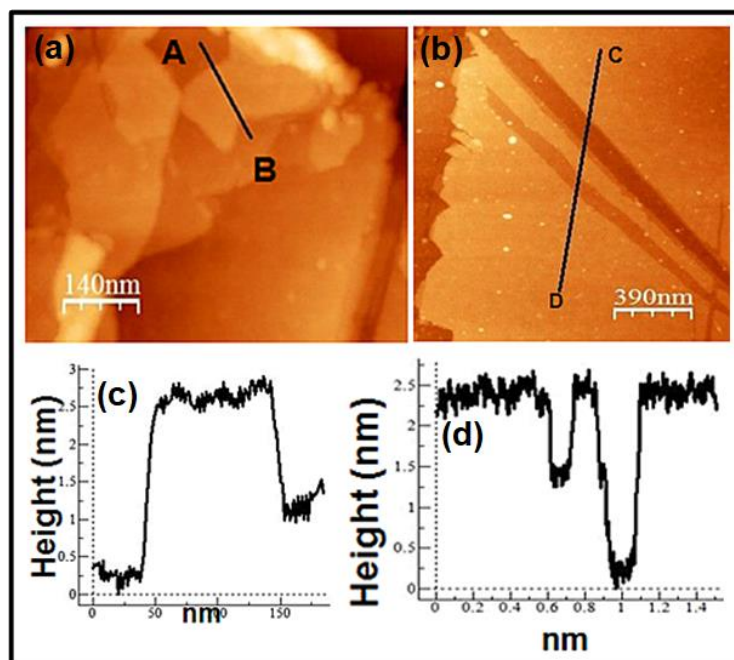


Figure S8.1. AFM images of thin CN_x sheets and its height profile shows thickness 2.0 to 2.5 nm.

Table S8.1. Parameters of different isotherm model of MR dye.

MR dye	Isotherm models		
	Freundlich	Langmuir	sips
Parameter			
K(mg/gm)	30.7	-	-
n	2.7	-	0.54
q _{max} (mg/gm)	-	120	130
b	-	0.05	0.01
R ²	0.89	0.948	0.959

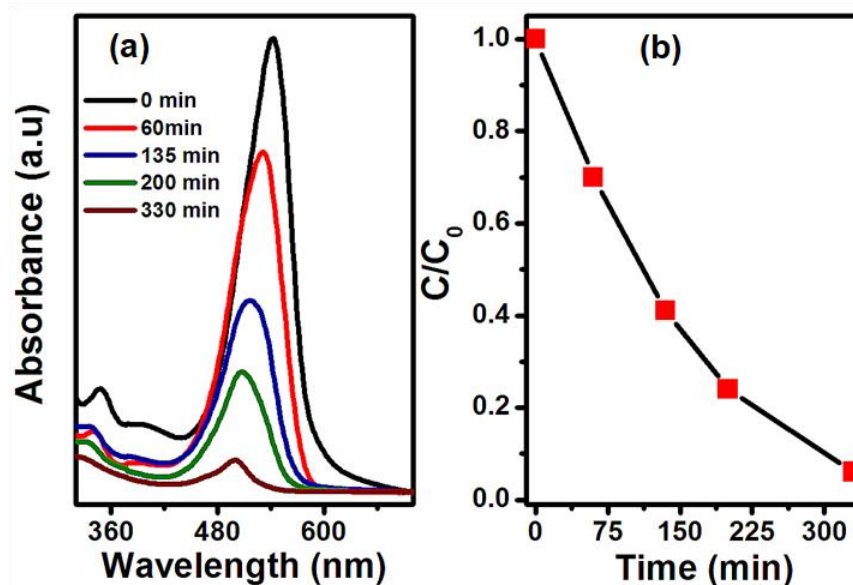


Figure S8.2. Degradation of 250 ppm RhB dye by Au-CN_x under visible light after 10 hour adsorption. (a) The change of UV-Visible Spectra at different time intervals, (b) C/C_0 vs. time plot

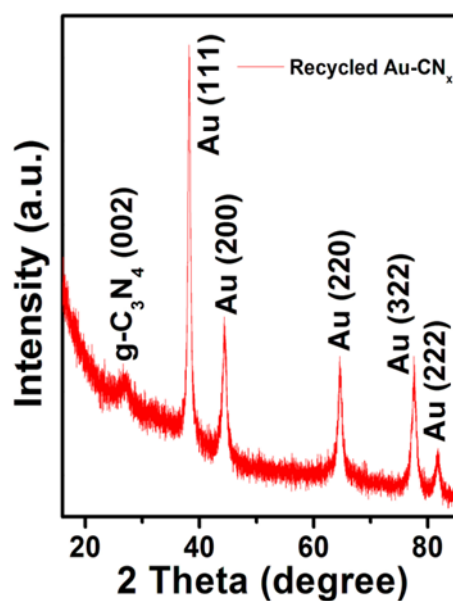


Figure S8.3. pXRD of recycled (after 3rd catalytic cycles) catalyst.

CHAPTER 9

Summary of the Thesis

This dissertation discussed the synthesis of carbon nitride supported 1-D, 2-D, 3-D metal/ metal oxide nanostructures and their applications in fuel cell, water electrolyzers, sensing of hydrogen peroxides, glucose and photocatalysis. The major findings in this thesis work are summarized below

In chapter 1, the current, future energy demand and then need of renewable energy conversion and storage techniques to meet our future energy demands was reviewed. The history and development of fuel cell (FCs) as well as water electrolyzer (Wes) are highlighted. Different fuel cell reactions such as HOR, ORR and water electrolyzer reaction namely HER, OER are mainly concentrated and discussed accordingly. The reaction steps, mechanism and kinetics of those processes and theoretical study to design the best electro catalysts for different FCs and WEs are also revealed here. We have also discussed necessary ideas about glucose sensing, H₂O₂ sensing and environmental pollutant remediation. In the last part a concise discussion about the various nanostructured materials, their properties and several strategies of their synthesis have been exposed.

Chapter 2 describes a brief description of various instrumental techniques which have been exclusively used for this present thesis.

In Chapter 2, we have shown a facile bottom up synthesis of high surface area and porous, Au aerogel supported on CN_x was described. The reduction of HAuCl₄ in presence of CN_x nanosheets using NaBH₄ and ultrasound treatment produces Au-aerogel-CN_x. When the reduction of HAuCl₄ in presence CN_x nano sheets was done only with ultrasound, highly dispersed ultra-small (~2 nm) AuNPs on CN_x sheets were formed. The Au aerogel supported

on CN_x sheets was well characterized by several techniques. The Au-aerogel-CN_x and AuNPs-CN_x composites exhibited superior electro catalytic activity towards oxygen reduction reaction (ORR) in alkaline and acidic media. The Au-aerogel-CN_x composite shows ORR onset potentials at 0.92 V and 0.43 V (vs RHE) in 0.5 M KOH and H₂SO₄ solution. The four electron oxygen reduction process occurs at these supported catalysts in both alkaline and acidic media. In KOH medium the onset potential at Au-aerogel-CN_x is more positive (~ 30 mV) than that of commercial Pt/C catalyst. The composites display excellent methanol tolerance and comparable durability with commercial Pt/C. Furthermore, the Au-aerogel-CN_x composites exhibited high catalytic activity for HER with small onset potential of -30 mV and a Tafel slope of 53 mV dec⁻¹ in acidic medium. At a small Au loading of 0.130 mg cm⁻², this catalyst also exhibit a current density of 10 mA cm⁻² at a low overpotential of -185 mV with an excellent stability. The ORR and HER performances on porous Au-aerogel-CN_x composites is better than that of AuNPs-CN_x catalyst and commercial flat gold electrode. The superior ORR and HER activity at Au-aerogel-CN_x composite are originated from the unique synergistic effects between porous Au network and CN_x support.

The synthesis of Pt nanostructures-N-doped carbon hybrid (Pt-(PtO_x)-NSs/C) and its application towards HER/HOR was demonstrated in chapter 4. The HER activity of this Pt-(PtO_x)-NSs/C catalyst is 4 and 6.5 times better than commercial Pt/C in acid and base. The catalyst exhibits a current density of 10 mA/cm² at overpotentials of 5 and 51 mV with Tafel slopes of 29 and 64 mV/dec in in 0.5 M H₂SO₄ and 0.5 M KOH. The stability test confirmed extraordinary HER stability of the Pt-(PtO₂)-NWs/C catalyst in both medium. This catalyst also showed superior HOR activity at all pH values. The HER/HOR activity of Pt-(PtO₂)-NWs/C and PtO_x-free Pt-Nanostructures/C (PtNSs/C) catalysts are comparable in acid with exchange current (*i*₀) values of 7.2 and 6.1 mA/cm². The presence of PtO_x in Pt-(PtO_x)-

NSs/C makes this Pt-catalyst 5 fold higher HER/HOR active in base media than that of PtO_x free PtNSs/C catalyst although their activity is comparable in acid. Hydrogen binding energy and oxophilicity are the two equivalent descriptors for HER/HOR in basic media. Here we propose a bi-functional mechanism for the enhanced alkaline HER/HOR activity of Pt-(PtO_x)-NSs/C catalyst. In bi-functional Pt-(PtO_x)-NWs/C catalyst, PtO_x provide an active site for OH⁻ adsorption to form OH_{ads} which reacts with hydrogen intermediate (H_{ads}), present at neighbouring Pt sites to form H₂O leading to enhancement of HOR activity in basic medium. For HER in the base, PtO_x favours the adsorptive dissociation of water to form H_{ads} on adjacent Pt sites and then recombination of H_{ads} results to the formation of the hydrogen molecule. This work may provide new opportunity to design and develop bi-functional HER/HOR electro-catalyst for

Chapter 5 describes a facile synthesis method of 3D-hierarchical porous iridium oxide/N-doped carbon hybrid (3D-IrO₂/N@C) was discussed for superior OER and HER activity in acid. In 0.5 M HClO₄, this catalyst exhibited superior activity towards OER with a low overpotential of 280 mV at 10 mA/cm², a low Tafel slope of 45 mV/dec and ~98% faradic efficiency. The mass activity and turnover frequency (TOF) at an overpotential of 350 mV are found to be 833 A/g and 0.432 s⁻¹ which are ~32 times higher that of commercial IrO₂. The HER performance of this 3D-IrO₂/N@C is comparable to that of commercial Pt/C catalyst in acid. This 3D-IrO₂/N@C catalyst requires only 35 mV overpotential to reach 10 mA/cm² current density with Tafel slope of 31 mV/dec in acid. Most importantly, stability test confirmed superior HER and OER stability of this catalyst in acid. This 3D-IrO₂/N@C catalyst was applied as cathode and anode for over-all water splitting and required only 1.55 V to achieve a current density of 10mA/cm² in acid. The outstanding activity of the 3D-IrO₂/N@C catalyst can be attributed to a unique hierarchical porous network, high surface

area, higher electron and mass transportation, synergistic interaction between IrO₂ and carbon support.

Chapter 5 describes a highly active and durable carbon nitride supported interconnected silver nano-wires (AgNWs-CN_x) electrocatalyst for HER and ORR applications was demonstrated. This catalyst exhibited superior HER activity that outperforms commercial Pt/C in both acid and base medium. Like Pt/C, on-set potential of this AgNWs-CN_x electro-catalyst is 0 mV in both medium and the Tafel slopes of this catalyst are 32 mV/dec and 65 mV/dec in acid and base respectively. It requires over-potentials of 25 mV and 85 mV to achieve the current densities of 10 and 50 mA/cm² respectively in acid whereas 110 mV and 290 mV needed to attain the same current densities in base. Most importantly this catalyst showed excellent durability in repeated cycling and long term chronoamperometric studies that confirmed its extraordinary stability in the acid medium. Furthermore, this AgNWs-CN_x catalyst showed superior activity towards ORR in base medium as the one-set potential and half wave potential ($E_{1/2}$) of this Ag catalyst are comparable to that of Pt/C in base. This catalyst also showed excellent methanol tolerance and superior durability in ORR. The superior electro-catalytic activity of the interconnected AgNWs-CN_x are likely due to its hierarchical 3D porous morphology, strong catalyst-support interaction, 1-D wires like structure.

Fabrication of ordered assembly of noble metal nanoparticles on a two dimensional sheets is a very challenging task. We have demonstrated a facile bottom up self-assembly method for the formation of ordered assembly silver nanoparticles on carbon nitride sheets in chapter 7. Ultrasound treatment of aqueous graphitic carbon nitride (g-CN_x) in presence of Ag⁺ ion produces silver-carbon nitride (Ag-CN_x) composite. The ordered assemblies of monodispersed silver nanoparticles on thin carbon nitride sheets are produced by evaporation of aqueous solution of Ag-CN_x composites. On evaporation of this solution,

first two dimensional sheets are formed on a solid substrate and then silver nanoparticles sit on the voids of carbon nitrides on drying. The silver nanoparticles carbon nitride sheets modified glassy carbon electrode can be used as highly sensitive electrochemical non enzymatic sensors for hydrogen peroxide (H_2O_2) and glucose. The lowest detection limits achieved by this Ag-CN_x electrode for H_2O_2 and glucose were 0.6 nM and 0.6 μM respectively.

In chapter 8, a facile method for synthesis of ultra-small gold nanoparticles supported on carbon nitride sheets (Au-CN_x) using ultrasound mediated reduction was discussed. TEM measurements confirm that thin g-CN_x sheets provided two dimensional supports to stabilize 1-3 nm sized gold nanoparticles (AuNPs). The Au-CN_x composite showed excellent catalytic activity towards the reduction of 4-Nitrophenol in aqueous medium in presence of sodium borohydride (NaBH_4) with very fast kinetics and good stability. The Au-CN_x catalyst can be used as an absorbent for the removal of organic dye [Rhodamine B (RhB), methylene blue (MB), and methyl red (MR)] from water. It showed excellent adsorption capacity for RhB and MB due to electrostatic interaction between anionic catalyst and cationic organic dye molecules. The catalyst can easily be reused after removing adsorbed dye from the catalyst simply by changing pH of the solution. In addition, Au-CN_x composite exhibited superior photo catalytic degradation of various dyes (RhB, MB and MR) on irradiation of UV, Visible light and natural sunlight. Excellent photo degradation rate constants for RhB (0.024 min^{-1}), MB (0.024 min^{-1}) and MR (0.02 min^{-1}) were observed although high concentration of dyes were used for degradation. We hope that this Au-CN_x composite will find its application as an effective catalyst for water purification.

Platinum Nanostructure/Nitrogen-Doped Carbon Hybrid: Enhancing its Base Media HER/HOR Activity through Bifunctionality of the Catalyst

Manas Kumar Kundu, Tanmay Bhowmik, Ranjit Mishra, and Sudip Barman^{*[a]}

The design and synthesis of an active catalyst for the hydrogen evolution reaction/hydrogen oxidation reaction (HER/HOR) are important for the development of hydrogen-based renewable technologies. The synthesis of a hybrid of platinum nanostructures and nitrogen-doped carbon [Pt-(PtO_x)-NSs/C] for HER/HOR applications is reported herein. The HER activity of this Pt-(PtO_x)-NSs/C catalyst is 4 and 6.5 times better than that of commercial Pt/C in acids and bases, respectively. The catalyst exhibits a current density of 10 mA cm⁻² at overpotentials of 5 and 51 mV, with Tafel slopes of 29 and 64 mV dec⁻¹ in 0.5 M H₂SO₄ and 0.5 M KOH. This catalyst also showed superior HOR activity at all pH values. The HER/HOR activity of Pt-(PtO_x)-NSs/C and PtO_x-free Pt-nanostructures on carbon (PtNSs/C) catalysts are comparable in acid. The presence of PtO_x in Pt-(PtO_x)-

NSs/C makes this Pt catalyst more HER/HOR-active in basic media. The activity of the Pt-(PtO_x)-NSs/C catalyst is fivefold higher than that of the PtNSs/C catalyst in basic medium, although their activity is comparable in acid. The hydrogen-binding energy and oxophilicity are two equivalent descriptors for HER/HOR in basic media. A bifunctional mechanism for the enhanced alkaline HER/HOR activity of the Pt-(PtO_x)-NSs/C catalyst is proposed. In the bifunctional Pt-(PtO_x)-NSs/C catalyst, PtO_x provides an active site for OH⁻ adsorption to form OH_{ads}, which reacts with hydrogen intermediate (H_{ads}), present at neighbouring Pt sites to form H₂O; this leads to enhancement of the HOR activity in basic medium. This work may provide an opportunity to develop catalysts for various renewable-energy technologies.

Introduction

The rapid rise of global energy demand and environmental problems associated with the use of fossil fuels are the driving force for exploring renewable energy sources and energy storage.^[1,2] Water electrolyzers and fuel cells are two important renewable techniques for energy storage and conversion.^[2,3] Hydrogen is considered to be one of the best clean energy carriers, with high mass density, and the hydrogen evolution reaction (HER) is featured in water electrolyzers that store energy in chemical form by generating molecular hydrogen.^[4] The hydrogen oxidation reaction (HOR) is mainly used in fuel cells, in which chemical energy from hydrogen is converted into electrical energy.^[5] The hydrogen fuel cell consists of two half-cell reactions, such as the HOR at the anode and the oxygen reduction reaction (ORR) at the cathode. Water electrolyzers are based on two reactions: HER at the cathode and the oxygen evolution reaction (OER) at the anode.^[6] Among the various fuel cells, proton exchange membrane fuel cells (PEMFCs) are one of the best renewable energy sources due to better environmental friendliness, high energy conversion efficiency, and high energy and power density.^[2] Platinum is the most active

catalyst for both HER/HOR processes in acid media,^[7] but poor stability of commercial Pt/C under strongly acidic conditions is one of the main obstacles for the commercialization of PEMFCs.^[8] Thus, it is highly desirable to find new highly active and highly durable HER/HOR catalysts. In recent years, alkali membrane fuel cells (AMFCs) and alkaline electrolyzers have been considered as suitable alternatives to PEMFCs and water electrolyzers, respectively, because earth-abundant, transition-metal-based nonprecious-metal catalysts are available for the ORR and OER in alkaline media.^[9] Another advantage of AMFCs over PEMFCs is the high stability of the electrocatalyst in alkaline medium. Although Pt is also the best catalyst for the HER and the HOR in alkaline medium, the HER/HOR activity of commercial Pt/C in basic media is two orders of magnitude lower than that in an acid.^[10] Because of sluggish HER/HOR kinetics at commercial Pt/C catalysts in alkaline media, a very high Pt loading (≈ 0.5 mg cm⁻²) is required at the anode of AMFCs, in comparison to the low Pt loading (≈ 0.05 mg cm⁻²) for PEMFCs.^[11] Therefore, an effective HOR/HER catalyst is highly desirable for the development of AMFCs or alkaline electrolyzers.

Understanding the mechanism of the HOR/HER in alkaline media is important for designing efficient alkaline HOR/HER electrocatalysts. In acidic media, the HOR/HER occurs through either Tafel–Volmer or Heyrovsky–Volmer mechanisms [Eqs. (1)–(3)]:^[10a,11,12]

[a] M. K. Kundu, T. Bhowmik, R. Mishra, Dr. S. Barman
School of Chemical Sciences
National Institute of Science Education and Research (NISER)
Bhubaneswar, HBNI, Orissa-751 005 (India)
E-mail: sbarman@niser.ac.in

Supporting Information and the ORCID identification number(s) for the author(s) of this article can be found under:
<https://doi.org/10.1002/cssc.201800856>.

Cite this: *J. Mater. Chem. A*, 2015, **3**,
23120

Gold aerogel supported on graphitic carbon nitride: an efficient electrocatalyst for oxygen reduction reaction and hydrogen evolution reaction†

Manas Kumar Kundu, Tanmay Bhowmik and Sudip Barman*

Fabrication of a high surface area interconnected porous network of metallic nanomaterials is important for their applications in various fields such as catalysis, sensors, and electrochemistry. Here we report a facile bottom up synthesis of high surface area and porous gold aerogel supported on carbon nitride sheets (CN_x). The reduction of HAuCl₄ in the presence of carbon nitride nanosheets using sodium borohydride and ultrasonic treatment produces gold aerogel supported on carbon nitride (Au-aerogel-CN_x). When the reduction of HAuCl₄ in the presence of CN_x nanosheets was performed using only ultrasonication, highly dispersed ultrasmall (~2 nm) gold nanoparticles on CN_x sheets (AuNPs-CN_x) were formed. The Au aerogel supported on CN_x sheets was well characterized by powder X-ray diffraction, tunneling electron microscopy, selected area electron diffraction, energy dispersive X-ray spectroscopy, scanning electron microscopy, UV-visible and X-rayphotoelectron spectroscopic methods. The Au-aerogel-CN_x and AuNPs-CN_x composites exhibited superior electrocatalytic activity towards oxygen reduction reaction (ORR) in alkaline and acidic media. The Au-aerogel-CN_x composite showed ORR onset potentials at 0.92 V and 0.43 V (vs. RHE) in 0.5 M KOH and H₂SO₄ solution. The four electron oxygen reduction process occurred at these supported catalysts in both alkaline and acidic media. In alkaline (KOH) medium the onset potential at Au-aerogel-CN_x was more positive (~30 mV) than that of commercial Pt/C catalyst. The composites displayed excellent methanol tolerance and comparable durability with commercial Pt/C. Furthermore, the Au-aerogel-CN_x composites exhibited high catalytic activity for the hydrogen reduction reaction (HER) with a small onset potential of -30 mV and a Tafel slope of 53 mV dec⁻¹ in acidic medium. At a small Au loading of 0.130 mg cm⁻², this catalyst also exhibits a current density of 10 mA cm⁻² at a low overpotential of -185 mV with excellent stability. The ORR and HER performances on porous Au-aerogel-CN_x composites were better than those of the AuNPs-CN_x catalyst and commercial flat gold electrode. The superior ORR and HER activities at the Au-aerogel-CN_x composite originated from the unique synergistic effects between the porous Au network and carbon nitride (CN_x) support.

Received 26th August 2015
Accepted 1st October 2015

DOI: 10.1039/c5ta06740e

www.rsc.org/MaterialsA

Introduction

Porous materials have attracted tremendous attention in the last few years due to their exceptionally high catalytic activity,¹⁻³ electrical conductivity⁴ and mechanical properties.⁵ These properties arise due to their ability to interact with the atoms or ions or molecules throughout the bulk of the material, and not only on their surfaces. In the last decade porous metallic network structures have gained tremendous attention for their various kinds of biological sensing applications^{6,7} and catalytic³

and electrocatalytic applications.⁸ Metal aerogels are a new type of porous solid materials that have extremely low density, high porosity, high surface area, high electrical conductivity and catalytic properties. The properties of nanoparticles such as catalytic activities are retained in the metal aerogel and it may thus bridge the gap between nanomaterials and macromaterials. It was reported that the properties of some of the metal aerogels are superior to those of metal nanoparticles because of the combined effects of nanoparticles in the aerogel.⁹ Since the discovery of aerogels in 1963 by Kistler,¹⁰ enormous efforts have been taken to synthesise various aerogels. Several approaches are available in the literature for the synthesis of different non-metal aerogels such as carbon aerogels¹¹ and silica aerogels,¹² organic-inorganic hybrid aerogels,¹³ metal oxide aerogels,¹⁴ and metal chalcogenide aerogels.¹⁵ But only few methods are available for the production of metal aerogels.^{8,16-18} For example, Eychmüller and coworkers^{8,16} have

School of Chemical Sciences, National Institute of Science Education and Research (NISER), Bhubaneswar, Orissa 751 005, India. E-mail: sbarman@niser.ac.in; Fax: +91 674 2304070; Tel: +91 674 2304061

† Electronic supplementary information (ESI) available: TEM images, TGA analysis, IR spectra, deconvoluted XPS spectra of CVs of ORR in acidic medium. See DOI: 10.1039/c5ta06740e

Cite this: *J. Mater. Chem. B*, 2015, **3**,
1289

Ordered assemblies of silver nanoparticles on carbon nitride sheets and their application in the non-enzymatic sensing of hydrogen peroxide and glucose†

Manas Kumar Kundu,‡ Mriganka Sadhukhan‡ and Sudip Barman*

The fabrication of ordered assemblies of noble metal nanoparticles on two-dimensional sheets is very challenging. We report here a facile bottom-up self-assembly method for the formation of ordered assemblies of silver nanoparticles on carbon nitride sheets. The ultrasonication of aqueous graphitic carbon nitride quantum dots (g-CNQDs) in the presence of Ag^+ ions produces a silver–carbon nitride (Ag-CN_x) composite. Ordered assemblies of monodispersed silver nanoparticles on thin carbon nitride sheets are produced by the evaporation of an aqueous solution of these silver–carbon nitride composites. On evaporation of this solution, two-dimensional sheets are formed as a result of the condensation of g-CNQDs on the solid substrate. On drying, the silver nanoparticles are located in the voids of the carbon nitride. A glassy carbon electrode modified with these silver nanoparticle–carbon nitride sheets can be used as a highly sensitive electrochemical non-enzymatic sensor for H_2O_2 and glucose. The lowest detection limits for H_2O_2 and glucose were 0.6 nM and 0.6 μM , respectively. In addition, the ON–OFF–ON fluorescence response of these g-CNQDs was used for the highly sensitive detection of Ag^+ ions and cysteine in aqueous media. The detection limits for Ag^+ ions and cysteine were 50 and 80 nM, respectively.

Received 21st October 2014
Accepted 4th December 2014

DOI: 10.1039/c4tb01740d

www.rsc.org/MaterialsB

Introduction

Nanostructured materials have attracted much interest^{1,2} as a result of their size-, shape- and composition-dependent properties, which lead to their unique performance in electronic,³ optical,⁴ catalytic⁵ and sensor⁶ applications. The preparation and organization of monodispersed nanomaterials is important in many scientific and technological developments. Nanoparticles (NPs) can easily self-assemble into 2D ordered monolayers and 3D nanocrystals.⁷ The ordered 2D assemblies of nanomaterials have different properties from both individual NPs and the bulk material as a result of quantum confinement effects in the individual particles and inter-particle coupling. Several bottom-up methods for the fabrication of 2D superlattice nanomaterials have been published, including evaporation-induced self-assembly,⁸ spin-coating,⁹ the Langmuir–Blodgett method,¹⁰ layer-by-layer assembly,¹¹ adsorption onto self-assembled monolayers¹² and liquid–liquid interface

assembly.¹³ Although these self-assembled monolayers represent a new class of material, there are serious drawbacks resulting from defects in the films and the poor stability of these monolayers. The development of self-assemblies of nanomaterials on 2D sheets is important in achieving the desired properties for applications in surface plasmonics,¹⁴ photovoltaics,¹⁵ photonic devices¹⁶ and in sensors.¹⁷

As a result of its unique properties¹⁸ (e.g. a high specific surface area, excellent electrical conductivity, high charge carrier mobility and high mechanical strength), graphene is a promising candidate as a 2D support for different NPs. Graphene containing metal or semiconductor NPs has been confirmed to be an effective nanocomposite material for use in photovoltaic,¹⁵ catalytic¹⁹ and biosensor²⁰ applications. Graphene-based composite materials doped with noble metal NPs have been reported to have potential applications in catalysis for fuel cells,²¹ sensors²² and gas storage.²³ Semiconductor NP–graphene composites have attracted attention in photocatalytic applications.²⁴ In most instances, graphene oxide or functionalized graphene oxide has been used as a 2D substrate for the synthesis of metal–composite materials. The oxygen-containing functional groups and defects in the graphene oxide are the active sites for the catalytic reactions and the growth of metal NPs. As it is difficult to generate a uniform distribution of functional groups and defects on graphene, the fabrication of

School of Chemical Sciences, National Institute of Science Education and Research (NISER), Bhubaneswar, Orissa 751 005, India. E-mail: sbarman@niser.ac.in; Fax: +91 (674)2304070; Tel: +91 (674)2304061

† Electronic supplementary information (ESI) available: The results of fluorescence life time measurement data, Stern–Volmer equation, FESEM images are provided. See DOI: 10.1039/c4tb01740d

‡ These authors contributed equally.

Cite this: *RSC Adv.*, 2015, 5, 38760

Ultra small gold nanoparticles–graphitic carbon nitride composite: an efficient catalyst for ultrafast reduction of 4-nitrophenol and removal of organic dyes from water†

Tanmay Bhowmik,‡ Manas Kumar Kundu‡ and Sudip Barman*

Synthesis of supported ultra small gold particles is important for their unusual properties and catalytic applications. We report a facile method for synthesis of ultra small gold nanoparticles supported on carbon nitride sheets (Au–CN_x). The ultrasonication was used to form Au–CN_x composite from carbon nitride quantum dots and HAuCl₄ without any aid of external reducing agent. The Au–CN_x composite was well characterized by tunneling electron microscopy, selected area electron diffraction, energy dispersive X-ray spectroscopy, powder X-ray diffraction, X-ray photo electron spectroscopy methods. Electron microscopic measurements confirm that thin graphitic carbon nitride sheets provided two dimensional supports to stabilize ultra small, 1–3 nm sized gold nanoparticles (AuNPs). The Au–CN_x composite showed excellent catalytic activity towards the reduction of 4-nitrophenol in aqueous medium in presence of sodium borohydride (NaBH₄) with very fast kinetics and good stability. The Au–CN_x catalyst can be used as an adsorbent for the removal of organic dye [Rhodamine B (RhB), methylene blue (MB), and methyl red (MR)] from water. It showed excellent adsorption capacity for RhB and MB due to electrostatic interaction between anionic catalyst and cationic organic dye molecules. The catalyst can easily be reused after removing adsorbed dye from the catalyst simply by changing pH of the solution. In addition, Au–CN_x composite exhibited superior photo catalytic degradation of various dyes (RhB, MB and MR) on irradiation of UV, visible light and natural sunlight. Excellent photodegradation rate constants for RhB (0.024 min⁻¹), MB (0.024 min⁻¹) and MR (0.02 min⁻¹) were observed although high concentration of dyes were used for degradation. Au–CN_x is one of the best adsorbent for RhB adsorption with maximum adsorption capacity of 400 mg g⁻¹ and catalyst for nitrophenol reduction. We hope that this Au–CN_x composite will find its application as an effective catalyst for water purification.

Received 19th March 2015
Accepted 20th April 2015

DOI: 10.1039/c5ra04913j

www.rsc.org/advances

Introduction

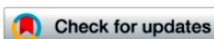
In recent years, noble metal nanoparticles have attracted tremendous attention due to their potential applications in various fields such as catalysis,¹ sensors,^{2–6} optics,⁶ fuel cell.⁷ For example, gold nanoparticles⁸ are being used for a long time in drug delivery, different biological application and catalysis. Silver and platinum nanoparticles show promising capabilities in biosensors⁹ and in fuel cell.¹⁰ Very small metal NPs has an interesting size and shape dependent reactivity¹¹ due to the increase of volume to surface ratio. The reduction in size of metal nanoparticles causes a significant change in reduction

potential of metal nanoparticles as compared to bulk materials because their Fermi potential becomes more negative. This typical important property helps them in electron transfer in various catalysis reactions. But synthesis of ultra small metal nanoparticle is a very challenging task due its high agglomeration property, arises from its high surface energy. In order to avoid aggregation, nanoparticles should be stabilized by using organic molecules or polymer as a capping agent. But their catalytic activity greatly reduced due to the presence of organic or polymer molecules around nanoparticles. Another alternative available method is to stabilize them on the surface of a solid support.¹² Two dimensional (2D) graphene, due to its unique properties¹³ such as high specific surface area, excellent electrical conductivity, high charge carrier mobility, high mechanical strength, became a promising candidate as a support for different nanoparticles. The graphene containing metal or semiconductor nanoparticles have confirmed to be effective nano-composite materials for photovoltaic,^{14,15} catalysis and biosensor applications.¹⁶ In recent year another two

School of Chemical Sciences, National Institute of Science Education and Research (NISER), Bhubaneswar, Orissa-751 005, India. E-mail: sbarman@niser.ac.in; Fax: +91 674 2304070; Tel: +91 674 2304061

† Electronic supplementary information (ESI) available: Materials details, and additional data. See DOI: 10.1039/c5ra04913j

‡ Tanmay Bhowmik and Manas Kumar Kundu equally contributed to this manuscript.

Cite this: *J. Mater. Chem. A*, 2018, **6**,
23531

Rhodium metal–rhodium oxide (Rh–Rh₂O₃) nanostructures with Pt-like or better activity towards hydrogen evolution and oxidation reactions (HER, HOR) in acid and base: correlating its HOR/HER activity with hydrogen binding energy and oxophilicity of the catalyst†

Manas Kumar Kundu,‡ Ranjit Mishra,‡ Tanmay Bhowmik and Sudip Barman^{†*}

Design and synthesis of HER/HOR catalysts are of crucial importance for the development of polymer fuel cells and water electrolyzers. We report the synthesis of Rh–Rh₂O₃ nanoparticles/nitrogen-doped carbon composite (Rh–Rh₂O₃-NPs/C) for HER/HOR applications. The HER activity of this catalyst is ~2.2 times and 1.43 times better than that of commercial Pt/C in base and acid, respectively. Rh–Rh₂O₃-NPs/C exhibited 10 mA cm⁻² current density at an overpotential of 63 mV and 13 mV with Tafel slopes of 70 mV dec⁻¹ and 32 mV dec⁻¹ in base and acid, respectively. The catalyst showed superior HOR activity at all pH values. The exchange current densities were ~0.425 mA cm_{Rh}⁻² and ~0.43 mA cm_{Rh}⁻² in base and acid, respectively. In base, the HOR and HER activities of Rh–Rh₂O₃-NPs/C are 50-fold and 10-fold higher, respectively, in comparison with those of the Rh₂O₃-free RhNPs/C catalyst, although the HER/HOR activity of both the catalysts is comparable in acid. In base, the adsorption of OH⁻ species (OH_{ads}) on Rh₂O₃ sites increases the reactivity of hydrogen intermediate (H_{ads}), which leads to the enhancement of HOR activity of Rh–Rh₂O₃-NPs/C. For HER in base, the adsorptive dissociation of water occurs on the Rh₂O₃ sites to form H_{ads} on the neighboring Rh sites and then, the recombination of H_{ads} results in the formation of hydrogen molecules. This study may provide an opportunity to develop an efficient catalyst for hydrogen-based renewable energy technologies.

Received 10th August 2018
Accepted 24th October 2018

DOI: 10.1039/c8ta07028h

rsc.li/materials-a

1. Introduction

With the increase in energy demand and environmental problems due to the use of fossil fuels, there is an urgent need for alternative energy conversion and storage devices.^{1,2} Electrolysis of water and fuel cells are the two important renewable technologies for energy conversion and energy storage.^{3,4} Hydrogen is considered as one of the greenest fuels and energy carriers,⁴ but production of pure hydrogen is a challenging task. Electrolytic water splitting is one of the renewable ways to produce pure H₂.⁵ Hydrogen evolution reaction (HER) is a cathodic process of electrolysis and hydrogen oxidation reaction (HOR) is generally applied at the anode of fuel cells.^{6,7}

School of Chemical Sciences, National Institute of Science Education and Research (NISER), HBNI, Bhubaneswar, Orissa-751 005, India. E-mail: sbarman@niser.ac.in; Tel: +91 6742494183

† Electronic supplementary information (ESI) available: Details of materials synthesis, extended characterization, ECSA calculation, electrochemical HER/HOR study, stability test, activity comparison table. See DOI: 10.1039/c8ta07028h

‡ Authors with equal contributions.

Pt is the most active catalyst for both processes in acidic media.^{8,9} The high price, scarcity and poor stability of Pt-based catalysts in acidic media are the main drawbacks for its commercialization.¹⁰ In proton exchange membrane fuel cells (PEMFCs), hydrogen and oxygen are used as reactants for HOR at the anode and oxygen reduction reaction (ORR) at the cathode, respectively, in strong acidic conditions. PEMFCs have high power efficiency and are environment-friendly due to their ability to convert hydrogen into water.^{5,11} Pt is also used as ORR catalyst. However, its commercialization is limited because of the very slow kinetics of ORR at the cathode and to overcome this, large amount of Pt is required.¹² Compared with acidic PEMFC-based technologies, alkali membrane fuel cells (AMFCs) or alkaline electrolyzers, which operate in alkaline media, are highly attractive since highly active earth abundant cheap transition metal-based catalysts are available for ORR and OER in alkaline media.^{13–16} However, the main obstacle of AMFCs is that the HER and HOR activity of Pt in basic media is 2–3 orders of magnitude lower than the activity in acidic media.^{9,17,18} Thus, highly efficient HER and HOR catalysts are desirable for the development of AFCs and alkali electrolyzers. The

Palladium Nanoparticle–Graphitic Carbon Nitride Porous Synergistic Catalyst for Hydrogen Evolution/Oxidation Reactions over a Broad Range of pH and Correlation of Its Catalytic Activity with Measured Hydrogen Binding Energy

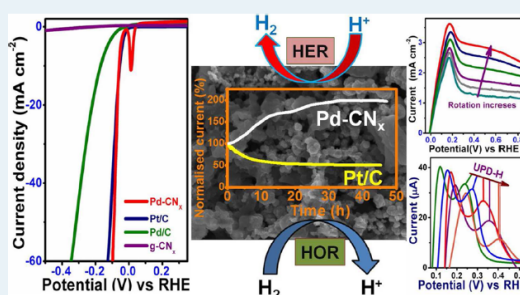
Tanmay Bhowmik, Manas Kumar Kundu, and Sudip Barman*

School of Chemical Science, National Institute of Science Education and Research, Bhubaneswar 751005, India

S Supporting Information

ABSTRACT: The hydrogen evolution reaction (HER) and hydrogen oxidation reaction (HOR) in aqueous medium are two fundamental reactions for the development of non-fossil energy storage and conversion devices. In the polymer electrolyte membrane fuel cell (PEMFC) carbon supported platinum (Pt/C) based catalysts are universally used in cathodes and anodes; however, the poor durability of Pt/C due to degradation of the catalyst in the strongly oxidizing environment prevents its widespread applications. It remains a great challenge to develop new electrocatalysts with superior activity and very high durability for the HER/HOR. Here, we report the synthesis of a porous palladium nanoparticle–carbon nitride composite (Pd-CN_x) for its superior activity and high durability toward the HER/HOR in acidic and alkaline media. The Pd-CN_x composites exhibited high catalytic activity for hydrogen evolution in acidic media with a small onset potential of -12 mV and a Tafel slope of 35 mV dec⁻¹. At a small Pd loading of 0.043 mg cm⁻², this catalyst also exhibits a current density of 10 mA cm⁻² at a low overpotential of -55 mV with an excellent stability. The HER activity on Pd-CN_x composite is comparable to that of commercial Pt/C in acid media. The stability tests of this catalyst were done through a large number of repeated potential cycles and long-term electrolysis. These confirm the exceptional durability of this catalyst, which is much better than that of Pt/C catalysts. Furthermore, this catalyst has also displayed superior HOR activity, measured by a rotating-disk experiment with a broad range of pH (0–14) in different buffer solutions. The HER/HOR activities of porous Pd-CN_x composite in different buffer solutions were correlated with the hydrogen binding energy (HBE) of the catalyst surface. The HER/HOR activity gradually decreases with an increase in the HBE as the solution pH increases. The superior HER/HOR activities and very high durability at porous Pd-CN_x composite are due to strong bonding between Pd and carbon (Pd–C bond), the porous morphology, and synergistic interactions between Pd-NPs and the carbon nitride (CN_x) support.

KEYWORDS: palladium nanoparticle, graphitic carbon nitride, hydrogen evolution and oxidation reaction, underpotential deposition, hydrogen binding energy

**INTRODUCTION**

The rapid depletion of fossil fuels and also various environmental problems arising from the use of fossil fuels are the driving force for developing technologies for energy conversion and storage.¹ Fuel cells and electrolyzers are the most significant renewable energy conversion and storage techniques, respectively. Among the different type of fuel cells, proton exchange membrane fuel cells/polymer electrolyte fuel cells (PEMFCs) are known to be a clean and renewable energy resource due to their high energy conversion efficiency, high energy and power density, and better environmental compatibility.^{2,3} The hydrogen evolution reaction (HER) and hydrogen oxidation reaction (HOR) in aqueous medium are two fundamental reactions for the development of non-fossil energy storage and conversion devices.⁴ The main applicability

of the HOR is predominantly in fuel cells, where chemical energy in hydrogen is converted into electrical energy. The HER is used in electrolyzers, which store the energy in chemical form by liberating the hydrogen. In fuel cells, the anodic hydrogen oxidation reaction (HOR) and cathodic hydrogen evolution reaction (HER) have been catalyzed by the noble metal Pt.^{5,6} In practice, large-scale electrochemical hydrogen production is generally restricted by two main problems: (1) dependence on the precious metal platinum and (2) lack of stability of the electrode materials under the strongly acidic conditions of PEM cells. Research efforts are ongoing to

Received: November 5, 2015

Revised: December 9, 2015

Published: February 5, 2016

Growth of One-Dimensional RuO₂ Nanowires on g-Carbon Nitride: An Active and Stable Bifunctional Electrocatalyst for Hydrogen and Oxygen Evolution Reactions at All pH Values

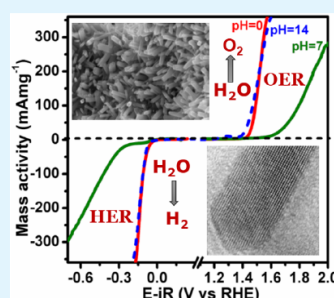
Tanmay Bhowmik, Manas Kumar Kundu, and Sudip Barman*

School of Chemical Science, National Institute of Science Education and Research, HBNI, Bhubaneswar 751005, India

Supporting Information

ABSTRACT: Development of highly efficient and durable bifunctional electrocatalyst for hydrogen and oxygen evolution reactions (HER and OER) is essential for efficient solar fuel generation. The commercial RuO₂ or RuO₂-based catalysts are highly active toward OER, but their poor stability under different operating conditions is the main obstacle for their commercialization. Herein, we report growth of one-dimensional highly crystalline RuO₂ nanowires on carbon nitride (1D-RuO₂-CN_x) for their applications in HER and OER at all pH values. The 1D-RuO₂-CN_x as an OER catalyst, exhibits a low onset overpotential of ~200 mV in both acidic and basic media, whereas Tafel slopes are 52 and 56 mV/dec in acidic and basic media, respectively. This catalyst requires a low overpotential of 250 and 260 mV to drive the current density of 10 mA cm⁻² in acidic and basic media, respectively. The mass activity of 1D-RuO₂-CN_x catalyst is 352 mA mg⁻¹, which is ~14 times higher than that of commercial RuO₂. Most importantly, the 1D-RuO₂-CN_x catalyst has remarkably higher stability compared to commercial RuO₂. This catalyst also exhibits superior HER activity with a current density of 10 mA cm⁻² at ~93 and 95 mV in acidic and basic media. The HER Tafel slopes of this catalyst are 40 mV/dec in acidic condition and 70 mV/dec in basic condition. The HER activity of this catalyst is slightly lower than Pt/C in acidic media, whereas in basic media it is comparable or even better than that of Pt/C at higher overpotentials. The HER stability of this catalyst is also better than that of Pt/C in all pH solutions. This superior catalytic activity of 1D-RuO₂-CN_x composite can be attributed to catalyst–support interaction, enhanced mass and electron transport, one-dimensional morphology, and highly crystalline rutile RuO₂ structure.

KEYWORDS: graphitic carbon nitride, one-dimensional RuO₂ nanowire, hydrogen evolution, oxygen evolution, bifunctional



INTRODUCTION

To solve the energy crisis and environmental problems, worldwide efforts are going on to find renewable energy sources as alternatives to fossil fuels.^{1,2} Hydrogen is considered as one of the cleanest renewable energy sources as an alternative to fossil fuel.^{3,4} Overall, water splitting to produce molecular hydrogen is a promising method to store solar/electric energy into chemical fuels⁵ as H₂. The water splitting consists of two half-cell reactions⁶ such as hydrogen evolution reaction (HER) and oxygen evolution reaction (OER). Without any suitable catalyst both processes are very slow. Apart from H₂ storage application, HER/OER catalysts are also directly coupled with various renewable energy conversion and storage systems^{7,8} such as metal–air batteries, fuel cells, solar cells, etc. OER is a bottleneck process for water splitting because of its sluggish kinetics due to a multistep proton couple electron transfer process.⁹ Although RuO₂ and IrO₂ are highly active electrocatalysts for the OER reaction, IrO₂ is preferred as a state-of-the-art catalyst for OER.¹⁰ The both state-of-the-art catalysts¹¹ still show quite large OER overpotentials as compared to the theoretical value of 1.23 V. The reduction of a large overpotential to reach an appreciable current density for OER

is the major challenge of electrochemical water splitting, which is an obstacle for development of renewable energy conversion devices. Carbon-supported platinum (Pt/C) is a state-of-the-art catalyst for HER. Although Pt/C is highly active in acidic media, its activity in basic media is two orders less as compared to acidic media.¹² The slow kinetics of Pt/C toward HER in basic media restricted fuel efficiency, and a large amount of Pt catalyst is needed in basic media.^{13,14} In addition, the long-term durability of Pt/C catalyst in strong oxidizing condition is another obstacle for its commercialization. The catalysis of HER as well as OER processes in the same medium is attractive, since only one catalyst can be used for their integration. It is known that almost all good OER^{15–19} catalysts are active mainly in basic media, whereas good HER catalysts^{20–24} work well in acidic media. Some HER catalysts^{25–28} are active in acidic, basic, and neutral medium, but OER catalysts,²⁹ which are active in all pH, are relatively very rare. It is thus highly desirable to find superior bifunctional

Received: August 19, 2016

Accepted: October 4, 2016

Published: October 4, 2016

CoFe Layered Double Hydroxide Supported on Graphitic Carbon Nitrides: An Efficient and Durable Bifunctional Electrocatalyst for Oxygen Evolution and Hydrogen Evolution Reactions

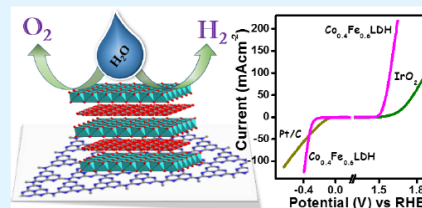
Tanmay Bhowmik, Manas Kumar Kundu, and Sudip Barman*

School of Chemical Science, National Institute of Science Education and Research (NISER), HBNI, Bhubaneswar, Bhubipur-Padanpur, Via Jatni, Khurda, Odisha 752050, India

Supporting Information

ABSTRACT: Finding nonprecious metal based highly active and durable bifunctional electrocatalysts for overall water-splitting is essential for the development of various renewable energy storage and conversion technologies. Herein, we report the synthesis of cobalt iron layered double hydroxide ($\text{Co}_{1-\delta}\text{Fe}_\delta$ LDH) and g-carbon nitride composite ($\text{Co}_{1-\delta}\text{Fe}_\delta$ LDH/g-CN_x) for alkaline water electrolysis. The thin $\text{Co}_{1-\delta}\text{Fe}_\delta$ LDH nanosheets are successfully impregnated on graphitic carbon nitride surface by one pot co-precipitation method at ambient temperature. The optimal composite, $\text{Co}_{0.4}\text{Fe}_{0.6}$ LDH/g-CN_x exhibited superior OER activity in 1 M KOH electrolyte with a small overpotential of 0.28 V for 10 mA cm⁻², low Tafel slope of 29 mV/dec, 100% faradic efficiency, and high TOF of 0.25 s⁻¹ which is superior to commercial (comm) IrO₂. Furthermore, the $\text{Co}_{0.4}\text{Fe}_{0.6}$ LDH/g-CN_x composite also exhibited remarkable HER activity in alkaline media and its HER activity is slightly lower than that of comm Pt/C at low overpotential but it outperforms Pt/C at high overpotential. The catalyst demonstrated its long-term durability and higher stability for HER and OER under alkaline environment. This $\text{Co}_{0.4}\text{Fe}_{0.6}$ LDH/g-CN_x catalyst can serve as both cathode and anode for overall water-splitting and required the small potential of 1.61 V to achieve a current density of 10 mA cm⁻². The superior electrocatalytic activities of the $\text{Co}_{0.4}\text{Fe}_{0.6}$ LDH/g-CN_x composite are due to the high electrochemical surface area (ECSA), easy access of abundant active sites, and easy mass transport owing to 2D sheet morphology of the composite.

KEYWORDS: $\text{Co}_{0.4}\text{Fe}_{0.6}$ LDH, g-carbon nitride, oxygen evolution reaction (OER), hydrogen evolution reaction (HER), overall water splitting.



INTRODUCTION

With increasing concern over rapid depletion of fossil fuels and negative impact on the environment due to excessive use of fossil fuels, there is urgent need of renewable energy resource and storage techniques alternative to the fossil fuels.^{1,2} Hydrogen is considered as a green fuel³ (energy carrier) alternative to fossil fuel due to its high storage density and environment friendliness. The high purity hydrogen (99.6% purity) is mainly produced from chloroalkali industry during the electrocatalytic formation of chlorine and caustic soda.⁴ In recent years, electrolysis of water^{4,5} into molecular hydrogen (H₂) and oxygen (O₂) offers one of most viable alternative approaches for the replacement of fossil fuels. Water electrolysis consists of two half-cell⁶ reactions such as cathodic hydrogen evolution reaction (HER) to produce molecular hydrogen and anodic oxygen evolution reaction (OER) to form molecular oxygen. Both HER and OER kinetics are sluggish without any suitable catalysts. HER is a simple two-step process occurring at low overpotential on noble metal surfaces,⁷ whereas OER is a more complex multielectron process leading to sluggish kinetics of oxygen evolution from water and thus requires large overpotential.⁸ The Pt/C is considered as highly

active, best electrocatalyst^{9,10} for HER, whereas noble metal oxide IrO₂ and RuO₂ are considered as state-of-art electrocatalyst^{11,12} for OER. But the widespread applications of these noble metal based electrocatalysts are limited because of their scarcity and high cost. Thus, it is very important to develop nonprecious metal based highly active and durable electrocatalyst for water-splitting reactions.^{13–15} In recent years, tremendous efforts have been devoted for development of low cost electrocatalyst for HER^{16–19} and OER.^{20–24} Several studies confirmed that first row transition metal dichalcogenide,^{25,26} phosphide,^{18,27} nitride,²⁸ and carbide²⁹ catalysts exhibited superior HER activity whereas transition metal oxide,^{30,31} hydroxides,^{24,32,33} and oxy(hydroxide)²³ based catalysts are active for OER. Generally, most of the good HER catalysts are active in acidic environment^{34,35} whereas most of the nonprecious OER catalysts are active under alkaline environment.^{36,37} The designing of a bifunctional catalyst,^{38–42} where the single catalyst is used as a cathode (HER) and anode

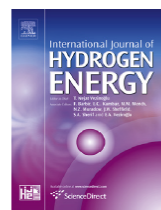
Received: December 19, 2017

Accepted: February 22, 2018

Published: February 22, 2018

Available online at www.sciencedirect.com

ScienceDirect

journal homepage: www.elsevier.com/locate/he

Highly efficient electrocatalytic oxidation of formic acid on palladium nanoparticles-graphitic carbon nitride composite



Tanmay Bhowmik, Manas Kumar Kundu, Sudip Barman*

School of Chemical Science, National Institute of Science Education and Research, HBNI, Bhubaneswar, Odisha 751 005, India

ARTICLE INFO

Article history:

Received 24 June 2016

Received in revised form

5 November 2016

Accepted 13 November 2016

Available online 9 December 2016

Keywords:

Graphitic carbon-nitride

Palladium nanoparticle

Formic acid oxidation

Electrocatalyst

Synergistic interaction

ABSTRACT

The electrochemical formic acid oxidation reaction (FAO) is an anodic process of direct formic acid fuel cells. Carbon supported platinum (Pt/C) and Palladium (Pd/C) catalysts are widely used as anode materials for FAO. The CO poisoning of Pt/C and poor stability of Pd/C are main obstacles for its commercialization. We report here superior electrocatalytic activity of Palladium nanoparticles-carbon nitride composite (PdNPs/CN_x) towards formic acid oxidation (FAO) with high mass activity (1640 mA/mg_{Pd}) in acid media (0.5 M H₂SO₄) which is 7.2 times higher than that of commercial Pd/C catalyst. It also exhibited an outstanding stability for FAO (mass activity of this catalyst was 23 times higher than commercial Pd/C after 1000 cycles).

© 2016 Hydrogen Energy Publications LLC. Published by Elsevier Ltd. All rights reserved.

Introduction

Development of sustainable and renewable energy sources [1] are gaining enormous attentions due to the limited access of natural fossil fuel and the rapid rise of energy demand. The fuel cells are the green energy resources, alternative to fossil fuel [2]. In recent years, Direct Formic Acid Fuel Cells (DFAFCs) have attracted attentions to scientific community due to its unique advantages over hydrogen fuel cell and Direct Methanol Fuel Cells (DMFCs) [3]. For hydrogen fuel cell, hydrogen storage and transportation are the main limitations for its applications, whereas methanol cross over, toxicity of methanol are the disadvantages of DMFCs. The DFAFCs has been

created great attention as a promising alternate to DMFCs due to its higher power density, low fuel crossover, higher energy efficiency and higher electromotive force. The theoretical open circuit potential of DFAFCs is 1.48 V (vs. saturated hydrogen electrode) which is higher than hydrogen and methanol fuel cells [4]. The low fuel crossover in DFAFC is due to dissociation of formic acid to formate ions (HCOO⁻) and their repulsive interaction [5]. The electro-oxidation of formic acid on solid surfaces is known to occur via two different paths – (1) dehydrogenation process, the direct-path involves oxidation of formic acid to carbon dioxide (HCOOH = CO₂ + 2H⁺ + 2e⁻) and (2) the indirect-path (dehydration path) occurs via intermediate formation, oxidation of adsorbed CO species (HCOOH = CO_{ads} + H₂O = CO₂ + 2H⁺ + 2e⁻) [6]. The formic acid

* Corresponding author. Fax: +91 674 2304070.

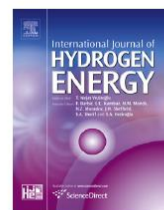
E-mail address: sbarman@niser.ac.in (S. Barman).

<http://dx.doi.org/10.1016/j.ijhydene.2016.11.095>

0360-3199/© 2016 Hydrogen Energy Publications LLC. Published by Elsevier Ltd. All rights reserved.

Available online at www.sciencedirect.com

ScienceDirect

journal homepage: www.elsevier.com/locate/hydro

Highly dispersed platinum nanoparticles on graphitic carbon nitride: A highly active and durable electrocatalyst for oxidation of methanol, formic acid and formaldehyde

Mriganka Sadhukhan, Manas Kumar Kundu, Tanmay Bhowmik, Sudip Barman*

School of Chemical Sciences, National Institute of Science of Education and Research (NISER), Bhubaneswar, HBNI, Orissa, India

ARTICLE INFO

Article history:

Received 25 July 2016
Received in revised form
11 March 2017
Accepted 15 March 2017
Available online 4 April 2017

Keywords:

Electrocatalyst
Onset potential
Tolerance
Durability
Long term stability

ABSTRACT

Finding efficient electrocatalyst for oxidation of small organic molecules such as methanol (CH_3OH), formic acid (HCOOH), formaldehyde (HCHO) etc. is essential for the development of their respective direct fuel cells. We report here highly dispersed platinum nanoparticles (PtNPs) on carbon nitride (CN_x) were successfully synthesized by the ultrasound mediated sodium borohydride reduction of H_2PtCl_6 in presence of CN_x nanosheets. This platinum–carbon nitride (Pt/CN_x) composite exhibited superior electrocatalytic activity towards oxidation of CH_3OH , HCOOH and HCHO in acid media. The mass activity, onset potential, tolerance to carbon monoxide (CO) poisoning and long term durability for the catalytic oxidation of CH_3OH , HCOOH , HCHO on Pt/CN_x catalyst in acid media is much higher than that of commercial Pt/C catalyst. The mass activity of Pt/CN_x catalyst at -0.64 V (forward scan) is $310 \text{ mA/mg}_{\text{Pt}}$ which is 2.7 time higher than that of commercial Pt/C for methanol oxidation. The electrooxidation of HCOOH on Pt/CN_x occurs via dual mechanism with greatly enhanced oxidation through dehydrogenation pathway in comparison with commercial Pt/C . The mass activity on Pt/CN_x at 0.3 V (vs. NHE) is 25 times higher than that of Pt/C for oxidation of HCOOH . The superior catalytic activity and durability of this Pt/CN_x catalyst can be attributed to high dispersion of PtNPs and strong catalyst support interaction.

© 2017 Hydrogen Energy Publications LLC. Published by Elsevier Ltd. All rights reserved.

Introduction

The use of fossil fuel as well as environmental pollution is rising. Therefore, there is a need of green alternate and sustainable energy source. The fuel cells are considered as

alternative green energy sources, transforms the chemical energy of fuel to electrical energy due to electrochemical oxidations of fuel molecule. High efficiency, low cost and low pollutant emission are the main advantages of fuel cells [1]. The electrochemical oxidation of small organic molecules such as methanol (CH_3OH), formic acid (HCOOH) and

* Corresponding author.

E-mail address: sbarman@niser.ac.in (S. Barman).

<http://dx.doi.org/10.1016/j.ijhydene.2017.03.097>

0360-3199/© 2017 Hydrogen Energy Publications LLC. Published by Elsevier Ltd. All rights reserved.

Facile synthesis of carbon quantum dots and thin graphene sheets for non-enzymatic sensing of hydrogen peroxide†

Cite this: *RSC Adv.*, 2014, 4, 4998

Mriganka Sadhukhan, Tanmay Bhowmik, Manas Kumar Kundu and Sudip Barman*

Carbon quantum dots (CQDs) and two dimensional (2D) graphene sheets were prepared from formic acid by microwave mediated thermal method. Microwave irradiation followed by thermal evaporation of formic acid produces fluorescent CQDs. The fluorescence emission of CQDs in water can be tuned between 310 and 820 nm by changing the excitation wavelengths. These quantum dots are found to be sensitive towards hydrogen peroxide in aqueous medium due to quenching of fluorescence. The large area graphene sheets are formed on a solid substrate due to self assembly and 2D growth of CQDs. Graphene sheets modified glassy carbon electrode showed fast electron transfer kinetics for $\text{Fe}(\text{CN})_6^{3-/4-}$ couple. Moreover, these modified electrodes can be used as a highly sensitive and selective metal free, non-enzymatic electrochemical sensor for hydrogen peroxide. The low detection limit was found to be 300 nM.

Received 20th September 2013
Accepted 4th November 2013

DOI: 10.1039/c3ra46050a

www.rsc.org/advances

Introduction

Since the discovery of the single plane layer of honeycomb network of sp^2 hybridized carbon atoms, graphene by Andrew Geim *et al.*¹ it has attracted enormous amount of interest from the scientific community due to its unique properties.^{1,2} The interesting properties of graphene reported in the literature include ballistic electron transport, integer and fractional quantum hall effect, extremely high carrier mobility and ability to sustain very high current densities. Thus, it is considered as a next-generation material for nano-electronics, spintronics, sensors, energy storage. However, the synthesis of large-area graphene on different substrate is hindering its applications. Several methods¹⁻⁵ such as mechanical exfoliation of graphite, chemical exfoliation, synthesis from solid carbon sources, chemical vapor deposition (CVD) of hydrocarbons on metal substrates, sublimation of silicon from silicon carbide (SiC) wafers *etc.* are available to synthesize a single or few layers of graphene. Although mechanical exfoliation of graphite provides excellent quality graphene, it is not suitable for large scale production of graphene. The main difficulty in producing high quality of graphene from graphite is especially due to the high van der Waals energy adhering graphene layers to one another. The most popular solution based approach is the chemical

exfoliation from graphite which involves chemical oxidation of graphite into graphite oxide, followed by exfoliation of graphite oxide in water to form graphene oxide by ultrasonication.³ Chemical oxidation induces defects^{3,6} into the sheets due to presence of oxygenated functional groups such as carboxyl, hydroxyl, epoxy *etc.* Although reduction of graphene oxide by different reducing agent leads to increasing the π -conjugation of graphene,⁶ the restoration of complete π -conjugation is not possible to achieve and hence it has low conductivity. Although chemical vapor deposition (CVD) produces high quality graphene on metal surfaces, there is a need for reliable method(s) for the production of high yield, high quality and large surface area graphene on silicon (Si) substrate. Moreover, compared to 2D graphene less attention has been paid to carbon quantum dots. They are more suitable for various applications as compared to small organic fluorescent molecules and inorganic semiconductor quantum dots, because of their high resistance to photo bleaching, low cytotoxicity and superior biocompatibility. Common methods⁷ for the production of carbon quantum dots include pyrolysis of citric acid, ethylene diamine tetraacetic acid salts, the hydrothermal synthesis from grass and graphene sheets. Highly sensitive and selective determination of hydrogen peroxide is important⁸ since it is the product of several biological enzyme-catalyzed reactions and also plays an active role in food, pharmaceutical, clinical, industrial, and environmental analyses. Several analytical methods⁹ such as titration, chromatographic, fluorometric, colorimetric, chemiluminescent, electrochemical methods are available for determination of H_2O_2 . Among these methods, fluorescence and electrochemical methods for determination of H_2O_2 are the best methods because of their low costs, high sensitivity and portability.

School of Chemical Sciences, National Institute of Science Education and Research (NISER), Bhubaneswar, Orissa - 751 005, India. E-mail: sbarman@niser.ac.in; Fax: +91 (674)2304070; Tel: +91 (674)2304061

† Electronic supplementary information (ESI) available: Details of the experimental techniques, quantum yield measurements, fluorescence lifetimes of CQDs. Additional Table S1 and Figures (Fig. S1-S9). See DOI: 10.1039/c3ra46050a

Available online at www.sciencedirect.com

ScienceDirect

journal homepage: www.elsevier.com/locate/ijhydene

Highly active and durable Pd nanoparticles-porous graphitic carbon nitride composite for electrocatalytic oxygen reduction reaction



Tanmay Bhowmik, Manas Kumar Kundu, Sudip Barman*

School of Chemical Science, National Institute of Science Education and Research, Institute of Physics Campus, Bhubaneswar, Odisha, 751 005, India

ARTICLE INFO

Article history:

Received 20 April 2016

Received in revised form

30 May 2016

Accepted 31 May 2016

Available online 20 June 2016

Keywords:

Graphitic carbon-nitride

Palladium nanoparticle

Oxygen reduction

d-band center band

Durability

Synergistic interaction

ABSTRACT

The electrochemical oxygen reduction reaction (ORR) is a cathodic process of fuel cells. The carbon supported Platinum, Pt/C catalyst is universally used as cathode materials; but poor durability of Pt/C due to degradation of catalyst prevent its wide spread applications. It is thus important to develop new cathode material(s) with high activity and stability. We report here, superior electrocatalytic activity of palladium nanoparticles-carbon nitride (Pd-CN_x) composite towards ORR in both alkaline and acidic media. The ORR activity on Pd-CN_x catalyst is better (half wave potential $E_{1/2}$ of 60 mV more positive) than that of Pt/C in 0.5 M KOH solution and is almost comparable in acid media. Moreover, this porous composite display excellent methanol tolerance and has much better long term durability than that of commercial Pt/C in both acidic and alkaline media. Only 4 and 6 mV positive shift of $E_{1/2}$ after 1500 potential cycles in basic medium and acid media respectively prove the excellent durability of this catalyst. The superior electrocatalytic activity and excellent stability of porous Pd-CN_x composite can be attributed to unique synergistic interaction between CN_x support and Pd nanoparticles (Pd-NPs), lower the d-band center of Pd, easy mass transport, and surface structure of Pd-NPs.

© 2016 Hydrogen Energy Publications LLC. Published by Elsevier Ltd. All rights reserved.

Introduction

The oxygen reduction reaction (ORR) is one of the important redox reaction [1] for development of proton exchange membrane fuel cell (PEMFCs), direct liquid fuel cells (DLFCs) and alkaline fuel cells (AFCs). Without any assistance of suitable catalyst, ORR kinetics becomes very sluggish. Platinum is known to be the universal catalyst for the ORR process. In practice, commercialization is restricted mainly by two major problems: (1) the precious platinum metal dependency and (2) lack of stability of the electrode materials

under strong acidic condition of PEM cells. It is thus important to develop non platinum based highly active and durable ORR catalyst for commercialization of fuel cell. The palladium, another noble metal which has similar crystal structure, surface structure, has created enormous attention as fuel cell catalyst because Pd is more abundance than Pt and has similar activity with Pt [2]. The ORR reaction is highly depended on the size, shape and crystallinity of the electrode materials and also the electrolyte solution [3–5]. Generally, ORR proceeds on the noble metal through two steps process – (a) adsorption or electron transfer to O–O molecule and breaking the O–O bond

* Corresponding author. Tel: +91 (674) 2304061; fax: +91 (674) 2304070.

E-mail address: sbarman@niser.ac.in (S. Barman).

<http://dx.doi.org/10.1016/j.ijhydene.2016.05.295>

0360-3199/© 2016 Hydrogen Energy Publications LLC. Published by Elsevier Ltd. All rights reserved.